NASA Technical Memorandum 86181

Infrared Horizon Sensor Modeling for Attitude Determination and Control: Analysis and Mission Experience

M. C. Phenneger, S. P. Singhal,
T. H. Lee, and T. H. Stengle

MARCH 1985

NASA

NASA Technical Memorandum 86181

Infrared Horizon Sensor Modeling for Attitude Determination and Control: Analysis and Mission Experience

M. C. Phenneger, S. P. Singhal,
and T. H. Lee

Computer Sciences Corporation
Silver Spring, Maryland

T. H. Stengle

Goddard Space Flight Center
Greenbelt, Maryland

National Aeronautics
and Space Administration

**Scientific and Technical
Information Branch**

1985

TABLE OF CONTENTS

TABLE OF CONTENTS (Cont'd)

TABLE OF CONTENTS (Cont'd)

Section 4 (Cont'd)

TABLE OF CONTENTS (Cont'd)

LIST OF ILLUSTRATIONS

LIST OF ILLUSTRATIONS (Cont'd)

Figure

LIST OF ILLUSTRATIONS (Cont'd)

LIST OF ILLUSTRATIONS (Cont'd)

Figure

LIST OF ILLUSTRATIONS (Cont'd)

LIST OF ILLUSTRATIONS (Cont'd)

LIST OF ILLUSTRATIONS (Cont'd)

LIST OF ILLUSTRATIONS (Cont'd)

LIST OF ILLUSTRATIONS (Cont'd)

LIST OF ILLUSTRATIONS (Cont'd)

Figure

LIST OF ILLUSTRATIONS (Cont'd)

Figure

LIST OF TABLES

Table

LIST OF TABLES (Cont'd)

SECTION 1 - INTRODUCTION

This report presents a survey of the work done by the Attitude Determination and Control Section (ADCS) at the National Aeronautics and Space Administration/Goddard Space Flight Center (NASA/GSFC) in analyzing and evaluating the performance of infrared (IR) horizon sensors. A review of some of the IR sensor flight experience and Earth IR radiance modeling analysis prior to 1970 is also included. The missions supported by the ADCS cover the period from 1973 to 1984 and encompass numerous aspects of modeling the response of IR horizon sensors to the Earth's IR horizon as they were applied on various spacecraft attitude systems supported by the ADCS. These missions include

- Atmosphere Explorer (AE)-3
- Small Astronomy Satellite (SAS)-3
- Seasat
- Applications Explorer Mission (AEM)/Stratospheric Aerosol Gas Experiment (SAGE)
- Magsat
- Geostationary Operational Environmental Satellite (GOES)-5
- Dynamics Explorer (DE)-1 and -2
- Earth Radiation Budget Satellite (ERBS)

Analysis of IR sensors on missions not directly under the operational support of the ADCS is reported for

- Television Infrared Observation Satellite (TIROS)-N/ National Oceanic and Atmospheric Administration (NOAA)-7
- Solar Mesosphere Explorer (SME)
- Landsat-4

The role of the ADCS for these missions was to evaluate the attitude determination performance characteristics of a proposed spacecraft attitude sensing system; understand the performance of the attitude sensors as it relates to the attitude determination accuracy requirements placed by the spacecraft attitude control system and by the spacecraft data users; process attitude sensor data to monitor spacecraft health and safety; and support the open-loop control of the spacecraft. Some missions required extensive ground processing of attitude sensor data to provide refined attitude solutions for use in science data reduction. In particular, IR sensor data were analyzed to understand the characteristics of these sensors and to evaluate the effects they may have on spacecraft control system performance and on the ultimate accuracy achievable in the attitude determination process. The results of this analysis were then directed toward establishing attitude data processing methods to enhance the accuracy of the attitude solutions. There has, therefore, been a continuing interest in analyzing IR sensing systems and in refining the performance analysis through flight experience with these systems.

1.1 SURVEY OF PAST SUPPORT

During the first portion of the period from 1973 to 1984, the ADCS developed attitude ground support software (AGSS) to support the AE-3, -4, and -5 and SAS-3 missions. The software was used to process attitude sensor data to determine near-real-time and definitive attitudes. This support involved prelaunch sensor performance analysis of alignments, biases, telemetry digitization, and projected noise levels. Analysis concentrated on developing an autocorrelation technique for fitting data subject to anticipated dynamics problems. It did not include detailed modeling of the bolometer optics or electronics, or variations in the Earth's IR radiation. The postlaunch evaluation was

primarily concerned with the analysis of flight data characteristics and anomalies. In particular, the analysis of AE-3 wheel-mounted horizon sensor and body-mounted horizon sensor data led to the correction of telemetered sensor data for substantial errors ($\pm$0.5 degree) induced by sensor alignment and measurement bias errors. The analysis of the SAS-3 Scanwheel[1] data was performed in conjunction with an attitude reference from star tracker data; it illustrated anomalies characteristic of sensitivity to temperature and calibration nonlinearities.

From these data, it became apparent that the IR sensors were not meeting specifications. Beginning with the Seasat mission support in 1976, an effort was initiated to understand the detailed performance of a specific IR scanner system. The goal was to determine, prior to launch, the performance accuracy of the dual-Scanwheel system to be used on Seasat. The analysis was performed by Computer Sciences Corporation (CSC) with assistance from Lockheed Missiles and Spacecraft Company (LMSC) (the Seasat contractor) and ITHACO, Inc. (the manufacturer of the Scanwheel and the Seasat magnetic attitude control system). The analysis used an IR model of the Earth generated specifically for the Seasat Scanwheel IR passband by LMSC. A program was developed that simulated the optics and electronics of the Scanwheel in the flight geometry and produced analog pitch and roll output. The signal processing electronics was modeled with a linear analysis method using details supplied by ITHACO. Some aspects of this prelaunch analysis were subsequently verified by post-launch analysis using Scanwheel flight data.

Similar analyses were performed for the AEM/Heat Capacity Mapping Mission (HCMM), AEM/SAGE, and Magsat (1977 to 1979) using the Earth radiance model developed for Seasat but with

[1]Scanwheel is a registered trade name of ITHACO, Inc.

the electronics and geometry models specific to each mission. Of these three missions, only Magsat data were analyzed with some rigor by comparing Scanwheel data with data from the fixed-head star tracker (FHST) as a reference. For AEM/SAGE, the prelaunch analysis consisted of studying the performance of a locator logic using signals from the dual-flake bolometer sensor. Postlaunch analysis of a Sun-interference-induced attitude control anomaly provided an unexpected result: the dual-flake locator was coupled to a slightly underdamped response in the Scanwheel signal processing electronics.

Following the Magsat analysis, the ADCS, with CSC support, initiated analyses to produce an IR horizon radiance model tailored more specifically to the properties of the individual IR sensor passbands. To achieve this goal, Earth temperature profile data averaged over longitudes were used as input to the LOWTRAN 5 program to produce Earth IR radiation spectra from 8 to 22 micrometers at 51 different viewing angles from a point in space (the presumed location of the IR sensors). The integrity of this Earth radiance modeling procedure was evaluated by comparing the simulated results with Nimbus-7 LIMS (Limb Infrared Monitor of the Stratosphere) data. Additional work performed since 1980 includes detailed ray tracing through the IR scanner optics to obtain a more precise understanding of field-of-view (FOV) effects for the in-flight system and the system ground calibration configuration. The resulting data were used to evaluate the ERBS IR scanners prior to launch.

In addition to the analyses described above, efforts were made to analyze sensor performance from flight data for DE-1 and GOES-5, each of which were spinning spacecraft using body-mounted IR horizon sensors. An analysis was also performed to predict the response of the Barnes Engineering Company Earth Sensor Assembly (ESA) using the Earth radiance

model tailored to the ESA's IR passband. This report presents a comparison of those results with similar results obtained by Barnes Engineering Company. An analysis to refine attitude measurements on the SME spacecraft was performed by personnel at the University of Colorado under contract to NASA/GSFC, and a summary of their final report is also presented here. Although Landsat-4 attitude support was not the direct responsibility of the ADCS, an analysis of the flight performance of the conical IR scanners flown on Landsat-4 was performed by the ADCS with the support of General Software Corporation (GSC). This analysis used the Landsat-4 onboard solutions derived from FHSTs and inertial reference units (IRUs) as a reference for the analysis of the scanner data.

1.2 IR HORIZON SENSOR HARDWARE

The analysis and experience reported in this document is concerned primarily with scanning horizon sensors and variations on Earth detection methods within that class of sensor. (The only analysis related to the edge-tracking method is for TIROS-N/NOAA-7.) There are three types of sensors in the scanner class: sensors with FOVs that scan by means of spacecraft spin motion (AE-3, GOES-5, DE-1, and SME); sensors that scan through mirrors or germanium prism lenses that rotate in conjunction with reaction and angular momentum control wheels (AE-3, SAS-3, Seasat, AEM/SAGE, Magsat, DE-2, and ERBS); and sensors that scan by constant-speed motors independent of the attitude control loop (Landsat-4).

All IR sensors view the Earth IR spectrum in a passband centered on 15 micrometers. This portion of the Earth's IR spectrum as viewed from outer space is dominated by carbon dioxide (CO_2) absorption bands, and a major portion of the radiation emitted at 15 micrometers originates from altitudes

above the Earth's troposphere. The IR intensity of the Earth in this region is relatively constant, with minimal dependence on the conditions of the atmosphere below the tropopause or on the temperature of the Earth's surface. Figure 1-1 illustrates this point, showing the degree to which the Earth IR intensity changes as a function of latitude for regions above and below the 15-micrometer CO_2 absorption band. The degree to which the center of the Earth IR image can be used as an attitude reference depends on the stability of the sensed IR horizon. This in turn is a function of the width of the IR passband, the design of the bolometer Earth-pulse-processing electronics, and the method used to detect the Earth edges using this pulse (referred to as the horizon locator logic).

Table 1-1 lists the IR sensor configurations and Earth horizon detection methods that have been the subject of analyses performed by the ADCS. Figure 1-2 illustrates the passbands for most of the missions considered in this report, including some examples from sensors on earlier Nimbus and Landsat spacecraft. It can be seen that those sensors with transmittance extending below 14 micrometers and above 16 micrometers will have significant input signal variation when scanning from warm to cold regions on the Earth, such as represented by the spectra in Figure 1-1. Conversely, the signal from the narrower passbands will have less variation. The instantaneous signal-to-noise ratio of the narrower passband sensors will, however, be lower.

The effects of input signal noise on the attitude measurement are determined by the signal processing electronics, the details of which depend on the scan rate and locator logic design. For a high scan rate, the circuits must be fast with equivalent increases in electronic bandwidth. For

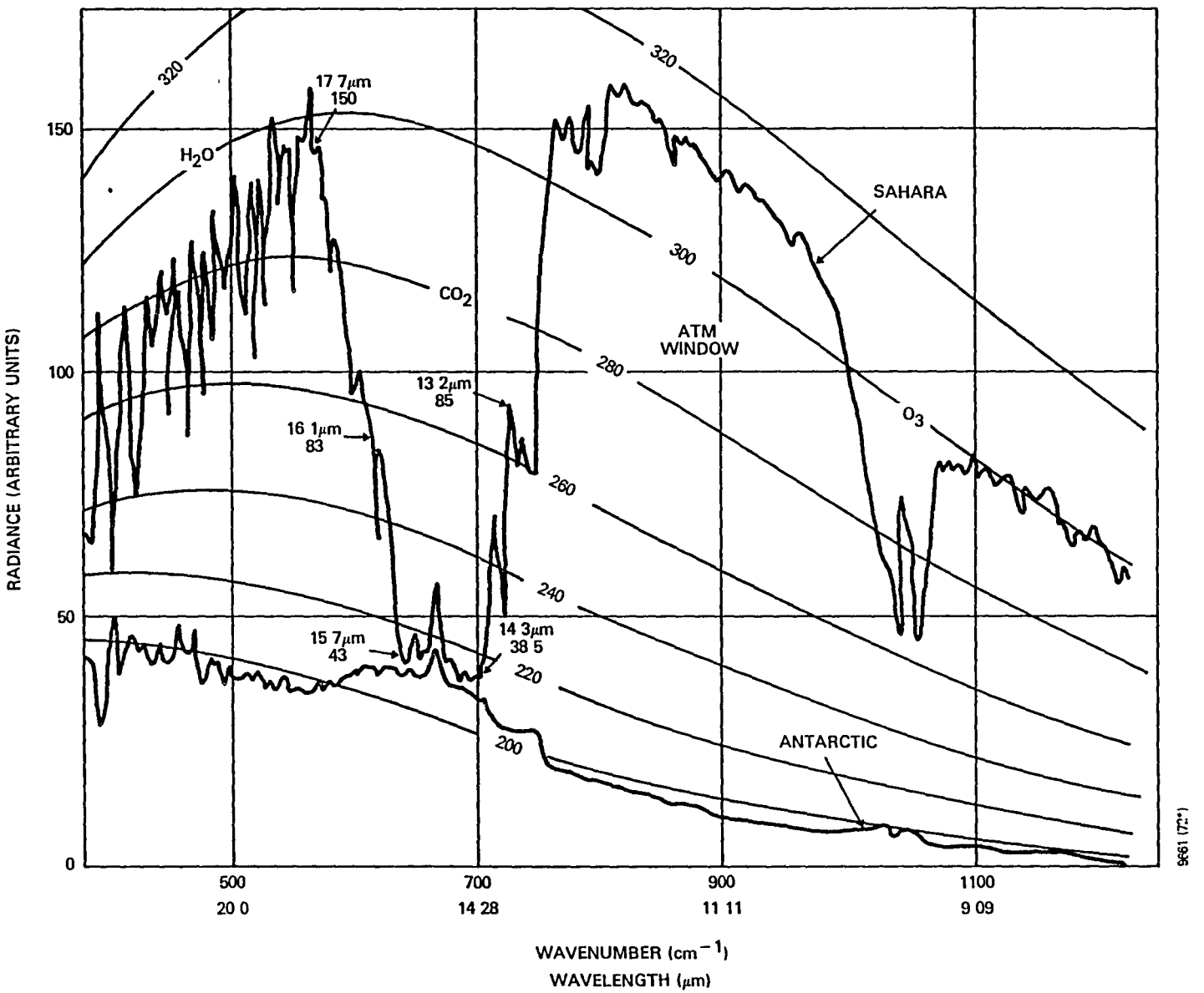

Figure 1-1. Earth IR Spectrum as Viewed From Space for Two Extremes, the Sahara and the Antarctic

Table 1-1. Earth Sensor Specifications for the Twelve Missions

MISSION/DATE	DETECTOR TYPE(S)	LOCATOR TYPE	PASS BAND 10% RISING TO 10% FALLING (microns)	FIELD OF VIEW* (degrees)	SCAN RATE (rpm)	SCAN HALF-CONE ANGLE (degrees)	SPIN AXIS-TO-NADIR ANGLE, NOMINAL (degrees)
AE-3/1973	DUAL WHEEL-MOUNTED HORIZON SENSORS DUAL-FLAKE THERMISTOR ROTATING WHEEL-MOUNTED MIRROR	FIXED THRESHOLD 25% OF EXPECTED PEAK	13.67 TO 16 77	2.5 × 2.5 SQUARE	180 TO 3001	107, 118	90
	TWO REDUNDANT BODY-MOUNTED HORIZON SENSORS	FIXED THRESHOLD 25% OF EXPECTED PEAK	12.3 TO 16 77	2.5 × 2 5 SQUARE	4	110	90
SAS-3/1975	SINGLE SCANWHEEL DUAL-FLAKE THERMISTOR ROTATING GERMANIUM PRISM LENS	FIXED THRESHOLD	12.3 TO 17 7	2 × 2 SQUARE	1400 TO 1600	45	UP TO 10
SEASAT/1978	DUAL SCANWHEELS SINGLE-FLAKE THERMISTOR ROTATING GERMANIUM PRISM LENS	NORMALIZED THRESHOLD @ 40 % OF AVERAGE BETWEEN 5° AND 11° FROM AOS AND LOS	13.3 TO 17 4	2 × 2 SQUARE	700 TO 1100	45, 135	64, 116
TIROS-N/ NOAA-7/1978	EDGE-TRACKING METHOD FOUR ARRAYS OF FOUR SIX JUNCTION THERMOPILES	DIRECT-CURRENT DIFFERENCES BETWEEN OPPOSING THERMOPILE ARRAYS	13 9 TO 16 0	FOUR EQUILATERAL TRIANGLES, 6 ON A SIDE	STATIC		CENTER OF THERMOPILE ARRAY 62.6
AEM/SAGE/1979	DUAL SCANWHEELS DUAL-FLAKE THERMISTOR ROTATING GERMANIUM PRISM LENS	FIXED THRESHOLD "ANDed" FLAKE SIGNALS, 33% OF EXPECTED PEAK	12.3 TO 17 7	2 × 2 SQUARE	825, 1900 ± 40	45, 45	90, 90
MAGSAT/1979	SINGLE SCANWHEEL DUAL-FLAKE THERMISTOR ROTATING GERMANIUM PRISM LENS	FIXED THRESHOLD "ANDed" FLAKE SIGNALS, 25% OF EXPECTED PEAK	12.3 TO 17 4	2 × 2 SQUARE	1500	45	90
GOES-6/1981	DUAL BODY-MOUNTED HORIZON SENSORS SINGLE-FLAKE THERMISTOR	NORMALIZED THRESHOLD 50% OF PEAK EARTH PULSE	14 TO 16	1.5 × 1 5 SQUARE	69.2	85, 95	90
DE-1/1981	DUAL BODY-MOUNTED HORIZON SENSORS SINGLE-FLAKE THERMISTOR	NORMALIZED THRESHOLD ON THE DERIVATIVE OF THE EARTH PULSE, 50% OF PEAK	13 67 TO 16 77	2 5 × 2 5 SQUARE	10	81, 99	90
DE-2/1981	TWO REDUNDANT WHEEL-MOUNTED HORIZON SENSORS SINGLE-FLAKE THERMISTOR ROTATING WHEEL-MOUNTED MIRROR				750 AND 1500	130	90
SME/1981	DUAL BODY-MOUNTED HORIZON SENSORS SINGLE-FLAKE THERMISTOR	NORMALIZED DERIVATIVE OF THE EARTH PULSE, 50% OF DERIVATIVE PULSE, AVERAGE OF THE ASCENDING AND DESCENDING 50% POINTS	13 4 TO 16 7	0 7 × 0 7 SQUARE	5	55, 125	85
LANDSAT-4/1982	DUAL CONICAL SCANNERS SINGLE-FLAKE THERMISTOR ROTATING GERMANIUM PRISM LENS	NORMALIZED DERIVATIVE OF THE EARTH PULSE, 50% OF DERIVATIVE PULSE, AVERAGE OF THE ASCENDING AND DESCENDING 50% POINTS	14 0 TO 16 1	1 1 × 1 1 SQUARE	120	45	RIGHT SIDE, 66, AFT, 66
ERBS/1984	DUAL SCANWHEELS SINGLE-FLAKE THERMISTOR ROTATING GERMANIUM PRISM LENS	NORMALIZED THRESHOLD @ 40% OF AVERAGE BETWEEN 20° AND 25° AOS, 15° AND 20° LOS	14 0 TO 16 1	1 13 × 1 13 SQUARE	2000 ± 500	45	80, 280

*UNDISTORTED FOV WITHOUT THE EFFECT OF THE PRISM, WHERE APPLICABLE

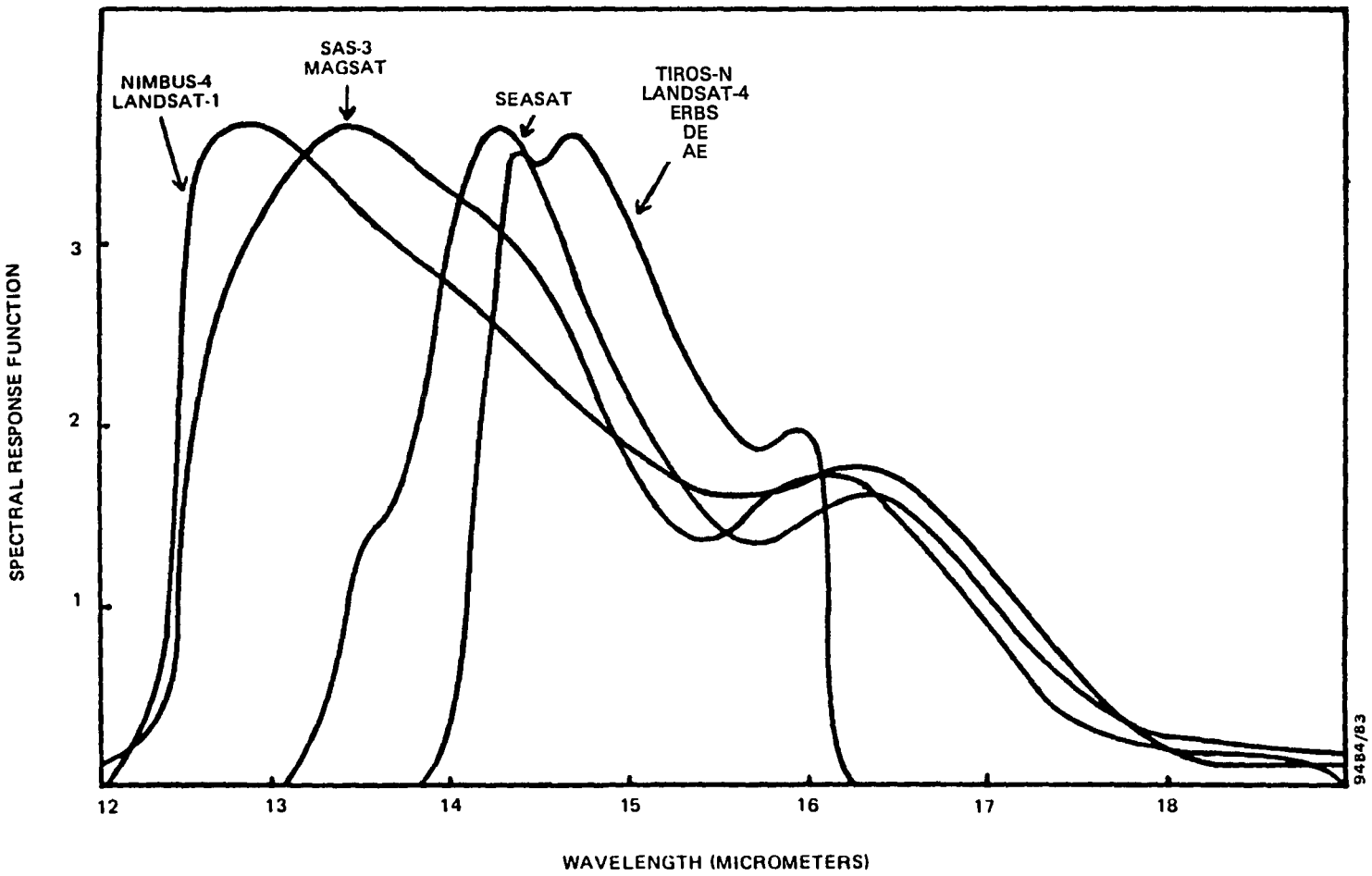

Figure 1-2. Normalized IR Horizon Sensor Spectral Response Function for Ten Missions

a slow scan rate, such as those for the body-mounted IR horizon sensors and constant 100-rpm conical scanners of Landsat, designs with narrower, more highly tuned electronic passbands can be used.

Two types of horizon locator logic dominate the missions discussed in this report: fixed and normalized threshold. Fixed threshold locator logic from a single flake uses a processed Earth pulse or its derivative as the sensed signal. When the signal level or its derivative exceeds a fixed reference voltage on the rising portion of the pulse, the Earth acquisition-of-signal (AOS) detection pulse is generated and a logic pulse is started. When the signal level falls below a fixed reference voltage, an Earth loss-of-signal (LOS) pulse is generated and the logic pulse is stopped. On the other hand, fixed threshold locator logic from a pair of bolometer flakes scanning through the same optics in near-coincident scan cones uses the logic pulse from each flake in an "ANDed" logic gate. The output logic pulse width is the minimum output from the latest AOS threshold to the earliest LOS threshold from the two-flake combination. Fixed threshold sensors are primarily sensitive to variations in the brightness of the Earth horizon as it is defined by the flight geometry and the angular size of the FOV.

Normalized threshold locator logic can be applied to either the slightly integrated Earth pulse or its derivative. This method uses a sample-and-hold circuit or its equivalent to automatically adjust the threshold voltage. Numerous normalized threshold determination procedures are possible. The threshold voltage is determined as a percentage of the average value of the peak Earth pulse, of the Earth pulse sampled between two preset scan angles relative to AOS or LOS, or of the peak derivative of the AOS or LOS Earth pulse edge.

1.3 DOCUMENT OVERVIEW

The remainder of this document provides a discussion of the three main aspects of IR horizon sensor modeling: Earth IR radiation modeling, sensor optical and electronics modeling to simulate attitude errors, and mission experience.

Section 2 discusses various models of the Earth's IR radiation, including (1) a review of the IR horizon sensor experience during the 1960s; (2) the results of Earth IR radiance simulation studies by Honeywell, Inc., and the experimental results obtained from Project Scanner; (3) the LMSC simulation of an Earth radiance model for the Seasat mission; (4) a CSC model independent of the passband of a specific IR sensor; and (5) the experimental results of the Nimbus-6 and -7 limb observations in the IR region of interest.

Section 3 provides an overview of the Horizon Radiance Modeling Utility, which is the software used by CSC to model the IR sensor optics and electronics processing for most of the missions discussed in this report. Section 3 also discusses the detailed optics modeling, as well as the sensitivity of this software to changes in the electronics and locator logic parameters.

Section 4 discusses 12 different missions, grouped according to sensor type. Each subsection includes a description of the basic mission configuration as it relates to attitude sensors; predicted and mission data analysis, if available; and an overall summary of results for that particular mission.

Section 5 summarizes the experience as it relates to IR sensors and recommends future directions for this work.

SECTION 2 - EARTH RADIATION MODELS

The performance of IR sensors in spacecraft attitude determination and the accuracy of the achievable results depend heavily on the level of understanding of the Earth's IR radiation profiles and the Earth edge-detection technology. The performance of the IR sensor is degraded considerably, for example, if the sensor system is picking up radiation over a larger portion of the electromagnetic spectrum than that included in the modeling of the sensor. Similarly, the results are affected if the sensor modeling assumed a pattern of Earth IR radiation profiles contrary to realistic situations. This section reviews the work performed in developing models of the Earth IR radiation profiles for use with the IR sensors over the last two decades by various groups.

By 1973, the timeframe of the earlier missions discussed in this report, significant progress had been made in understanding the nature of the problem of spacecraft attitude determination using IR sensors. A survey of the experience obtained with IR sensors on the Mercury, Vela, Orbiting Geophysical Observatory (OGO), and Gemini spacecraft (Reference 1) established guidelines for the design, implementation, preflight testing, and limitations of IR sensors. Theoretical research performed under contract to NASA/ Langley Research Center (LRC) by personnel at Honeywell Inc., GCA Corporation, and Florida State University established an analytical method for synthesizing Earth IR radiance profiles for the 15-micrometer CO_2 band from meteorological input data (Reference 2). This method was then used to establish the existence of systematic radiance profile variations over latitude and season. The work performed under contract to LRC by Honeywell and GCA (Reference 3) suggested that the profile intensities had a direct

dependence on the atmospheric temperature at the 10-millibar (mbar) altitude (32 kilometers) and the lapse rates (the rate of drop in temperature with altitude) at the 500-millibar (16 kilometers) and 50-millibar (22 kilometers) altitudes.

To test the theoretical approach for synthesizing radiance profiles established in Reference 2, an experiment was conducted in 1966 to make direct measurements of the horizon radiance profiles of North America. The experiment, named Project Scanner, consisted of two suborbital rocket flights in August and December 1966 that measured profiles from the atmosphere under summer and winter conditions, respectively (References 4 and 5). The conclusion of the experiment was that the theoretical approach established for 15-micrometer profile synthesis was adequate and in agreement with the experimental measurements of the atmosphere for summer conditions. The theoretical approach was determined inadequate, however, for a reliable synthesis of profiles under winter conditions. The high degree of horizontal nonuniformity in the atmosphere, in the mid to high latitudes during winter, was counter to the assumptions of homogeneity in the theory.

An estimate of the upper limit of horizon sensing accuracy achievable by IR horizon sensors, based on the experimental and theoretical works performed by and for LRC, is presented in Reference 6. This paper concludes that, for a hypothetically perfect (no sensor errors) dual IR sensing system operating with an IR passband between 14.0 and 16.3 micrometers at an altitude of 540 kilometers, a potential attitude accuracy of 0.033 degree (1σ) is achievable. The estimate is based on the assumption that an oblateness-like correction to the horizon sensor measurement has been applied to compensate for the variability of the sensed horizon. The performance is quoted for a hypothetical edge-tracking

sensor with a threshold determined by a limit on the integral of a normalized radiance profile. This corresponds to located horizon altitude uncertainty of 1.5 kilometers for a dual-scan sensor and is reported as being the limit of sensing accuracy using horizon radiance models to derive the oblateness-like horizon altitude variation compensation function.

When GSFC initiated attitude support for the Seasat mission, CSC began to estimate the flight performance accuracy of the Seasat IR sensing system (Reference 7). In support of the effort to establish the oblateness-like compensation function, LMSC developed a global set of radiance profiles for the Seasat IR scanner passband. The LMSC method (Reference 8) was similar to that of Reference 2, with the exception that two atmospheric constituents, ozone and water vapor, were added. This was done to accommodate the wider IR passband of the Seasat scanner, whose IR sensitivity extended beyond the edges of the well-defined 15-micrometer CO_2 absorption band. The CSC study included a simulation of the IR scanner Earth-sensing flight geometry, the scanner FOV integration over the LMSC Earth IR radiance model, and the IR scanner signal processing and locator logic. This analysis (Reference 9) concluded that sensitivity to variations in the ozone and water vapor densities were insignificant, but that scanner flight performance would be degraded significantly due to its sensitivity to cold clouds.

The Earth IR profiles provided by LMSC were later used to evaluate IR sensor performance and postlaunch IR sensor data correction on the AEM/HCMM, AEM/SAGE, Magsat, and DE-2 missions, even though the IR passbands for these missions were different from those used in the LMSC profiles. In 1980, CSC, under contract to GSFC, initiated an effort to establish the capability of computing the systematic seasonal and latitudinal horizon radiance corrections for IR scanners with

passbands different from those of Seasat. To accomplish this, the LOWTRAN 5 Atmospheric Transmittance/Radiance Computation Code (Reference 10) was adopted, along with a world average of radiosonde observation (RAOBS) data (Reference 11), as the climatological input to the LOWTRAN 5 program.

The new procedure was first applied to ERBS attitude data processing. Prior to this, however, an analysis was performed to check the procedure by direct comparison of RAOBS-1972/LOWTRAN 5 generated profiles with profiles from the Nimbus-7/LIMS experiment. This work was performed under contract to GSFC by CSC and its subcontractor GSC (Reference 12). In addition, analyses of horizon-radiance-induced attitude errors for the SME and Landsat-4 spacecraft were performed under contract to GSFC by personnel at the University of Colorado Laboratory for Atmospheric and Space Physics (LASP) and GSC, respectively (References 13 and 13a).

The following sections provide a more detailed description of the work just surveyed. The intent is to provide a high level of understanding of the evolution of horizon sensor attitude determination technology. The analysis related to various models of the Earth IR profiles, the characteristics of the profiles with regard to their seasonal and geographical systematic variations, and the characteristics of the random (nonsystematic) variations in these profiles are discussed.

2.1 EARLY EXPERIENCE WITH IR SENSORS

Reference 1 presents the experience with spacecraft attitude IR sensors up to 1969. IR sensors used during that period can be divided into three basic classes: scanners, edge trackers, and radiance balancers. The early sensors used germanium optical elements that transmit IR radiation in the interval from 1.8 to 20 micrometers. The sensors on the Mercury vehicles were conical with wide IR passbands of the

germanium optics and used a fixed percentage of the peak signal for threshold determination. Consequently, these sensors were sensitive to IR radiation from the Earth's surface and the atmosphere. The Earth pulse amplitude was primarily dependent on Earth surface temperatures and on the temperature of opaque clouds that came into the sensor FOV. This susceptibility to clouds initially caused attitude errors as high as 35 degrees. These errors were subsequently reduced by lowering the detector threshold to a minimum value consistent with the detector noise. The Mercury sensors were also affected by solar IR radiation entering along a direct path into the FOV at the full intensity, this saturating the sensor electronics. Interference also occurred at sunset, when the Sun pulse amplitude was low enough to be confused with the Earth pulse, and along an indirect reflected path from the Earth IR albedo. This effect occurred because Earth-reflected IR radiation was greater than expected at the shorter wavelengths below 7 micrometers. The Mercury sensors were also susceptible to electromagnetic interference (EMI) caused by inadvertently mounting the sensor heads in the ground plane of the spacecraft antennas.

Because of the early Mercury experience, conical scanner development proceeded with the following improvements:

- The spectral passband was shifted to above 14 micrometers to reduce Earth temperature effects and reduce solar IR radiation by a factor of 100.
- The aperture was increased and the number of optical elements was reduced to reduce absorption.
- The angular width of the detector FOV was reduced in the scan direction to increase the accuracy in this direction.
- Hyperimmersed thermistor bolometers were incorporated to improve optical gain.

- Preamplifier designs were improved to reduce noise.
- Low-speed motors were used instead of high-speed motor gear reduction drives with wick lubrication and labyrinth shields, to restrict lubricant evaporation and reduce optical element contamination.
- EMI filtering was incorporated.
- High-reliability components were incorporated.
- Sun sensing and compensation to reduce Sun interference errors were incorporated into some sensors.

The Vela satellite incorporated a scanning horizon sensor viewing the Earth through an oscillating mirror. The spectral passband for this sensor was between 13.2 and 22 micrometers, and thus sensitivity to clouds for that spacecraft was not a problem. Sun interference was a problem, however, occurring when the Sun was near the scan path where the Sun pulse was comparable to the Earth pulse. The problem was alleviated by predicting the location of solar interference and inhibiting the sensor output to the spacecraft control system during that period. Other problems with internal reflection of IR radiation in the lens barrel necessitated a redesign of the barrel to increase attenuation of reflected radiation.

After some testing of the edge-tracking sensors for the OGO satellite, and a blocked sensor FOV due to the failed deployment of an experiment boom on the first OGO mission, flight data were obtained from the edge tracker in the second OGO mission. During the OGO-2 mission, the edge-tracking sensor tracked the edges of clouds drifting into the FOV, stimulating excessive attitude control activity and depleting the intended 1-year supply of reaction control fuel in 10 days. This problem was not anticipated before the flight because of insufficient dynamic simulation of

clouds drifting through the FOV. The problem was corrected by blocking the input IR radiation below 13 micrometers and biasing the edge-tracking dither toward space. Dynamic simulation of clouds verified the approach, and subsequent OGO flights did not experience this problem. It was also discovered during redesign and testing after OGO-2 that Sun interference could occur when the Sun was 1.6 degrees from the scan plane, causing similar problems with thruster fuel depletion. The problem was prevented by increasing the scan plane offset to 5.8 degrees from the Sun. On the flight of OGO-4, the IR sensors tracked moonrise, but the reaction control jets had been disabled at that time and the vehicle did not track the Moon.

It was therefore recommended (Reference 1) that sensing be limited to the 15-micrometer CO_2 absorption band; the number of moving parts be limited; and procedures for avoiding Sun and Moon interference, thermal runaway of thermistor bolometers, optical ghosts, and EMI be developed. The report also pointed out that the relationship between the detected Earth horizon and the hard Earth horizon depends on the detection technique. This is a key point in understanding the procedures to derive the oblateness-like corrections for systematic horizon radiance variations for a specific sensing system. For example, the Earth horizon radiance profiles vary in shape and intensity with latitude and season. The accuracy of estimating the effect of these variations on the sensor output depends on the theory of radiation transfer, the Earth atmospheric physical parameters input to that computation, and, very significantly, on the model of the IR sensor. In short, the profiles are unique to the sensor and the optical passband. After the characteristics of the Earth IR model have been accurately estimated, showing both the shape and amplitude variations of the profiles that have been obtained, the response of the

IR scanner optics and electronics must be modeled. The systematic variations of the sensed horizon altitude will vary, depending on the sensor FOV size, the orbital geometry, the time constants in the Earth pulse processing, and the horizon locator electronics. Some electronics will be sensitive to IR brightness gradients along the Earth scan track, and others will be sensitive to the slope of the rising and falling portions of the processed Earth pulse. The objective of the sensor modeling effort is to accurately determine this response, which is highly dependent on the sensor system design.

2.2 HONEYWELL/LRC RADIANCE MODELING ANALYSIS

The early mission experience with IR sensors indicated that accurate and reliable performance could be obtained if the optical passband was limited to the 15-micrometer CO_2 absorption band. To improve the understanding of the characteristics of the Earth radiance profile at 15 micrometers, LRC initiated a series of theoretical and experimental studies. Section 2.2.1 reviews the theoretical approach to generate Earth radiation profiles performed by Honeywell. Section 2.2.2 reports on the study of radiance variations, also performed by Honeywell, and Section 2.2.3 presents the results of the Project Scanner experiment at LRC. Section 2.2.4 interprets these analytical and experimental results as they pertain to the attitude determination accuracy achievable with IR sensors.

2.2.1 SYNTHESIS OF 15-MICROMETER HORIZON RADIANCE PROFILES

The purpose of the work by LRC and Honeywell was to define, with a degree of statistical confidence, the variations in the Earth's horizon radiance profiles in the 15-micrometer CO_2 band. The study extended the theoretical treatment of the 15-micrometer radiance profiles by including the effects of Doppler broadening of the absorbing line width and the

effect of the absence of local thermodynamic equilibrium (LTE). The analysis investigated a range of spectral intervals to determine the spectral interval of highest radiance stability with respect to the meteorological input. Computational procedures were used to include the effects of the atmospheric constituents water vapor and ozone, which affect radiance intensities at the edges of the 15-micrometer CO_2 band at the higher and lower wavelengths. This augmented version of the radiance profile synthesizer is called the Comprehensive Radiance Profile Synthesizer (CORPS).

To address the objective of defining the Earth's 15-micrometer horizon with a reasonable degree of statistical confidence, the CORPS program was used with 448 sets of input temperature-pressure profiles. Radiance profiles were generated to study profile characteristics for four types of variations: seasonal variations represented by meteorological data from an 8-month span ending on February 10, 1965; geographical variations from meteorological data taken every 100 kilometers from Antigua Island to White Sands, New Mexico; temporal variations from meteorological data taken hourly, daily, and weekly; and climatological variations from meteorological data taken in January, April, July, and October from 5 latitudes between $20^{o}N$ and $75^{o}N$ and 10 longitudes between $60^{o}W$ and $150^{o}W$. A summary of the CORPS computational model is provided below.

The 15-micrometer radiation intensity, N(h), received by a sensor with a point FOV and unit acceptance area, viewing the Earth from outer space along a path, S, is given by the following equation (Reference 2):

$$N(h) = -\int_{\nu_1}^{\nu_2}\int_{1}^{\tau_{\nu_o}} J_\nu(T)\, d\tau_\nu\, d\nu + \int_{\nu_1}^{\nu_2} J_\nu(T_o)\, \tau_{\nu_o}\, d\nu \quad (2\text{-}1)$$

where h = tangent height of the optical path

ν_1, ν_2 = wave numbers of the spectral band

τ_{ν_o} = spectral transmittance at the Earth's surface

τ_ν = spectral transmittance of the Earth's atmosphere along the line of sight

$J_\nu(T)$, $J_\nu(T_o)$ = source terms for the atmosphere and the Earth, respectively

T, T_o = temperatures of an atmospheric layer and the Earth, respectively, at the point where it intersects the line of sight

The source term for the Earth is nonzero only when the tangent height is less than zero, at which point the line of sight intersects the Earth. The geometry of the computation is illustrated in Figure 2-1. The source terms are assumed to be Planck black-body radiation functions of the form

$$J_\nu(T) = \frac{C_1 \nu^3}{(e^{C_2 \nu / T} - 1)} \qquad (2\text{-}2)$$

where $C_1 = 1.1909 \times 10^{-5}$ erg·cm^2/sec/sr

$C_2 = 1.4389$ cm·deg

The assumption of LTE in the region of the atmosphere contributing to a specific source term justifies the use of Planck functions at low tangent heights. At higher tangent heights (near 50 kilometers), the assumption of LTE is not valid, and a modified Planck source function must be used.

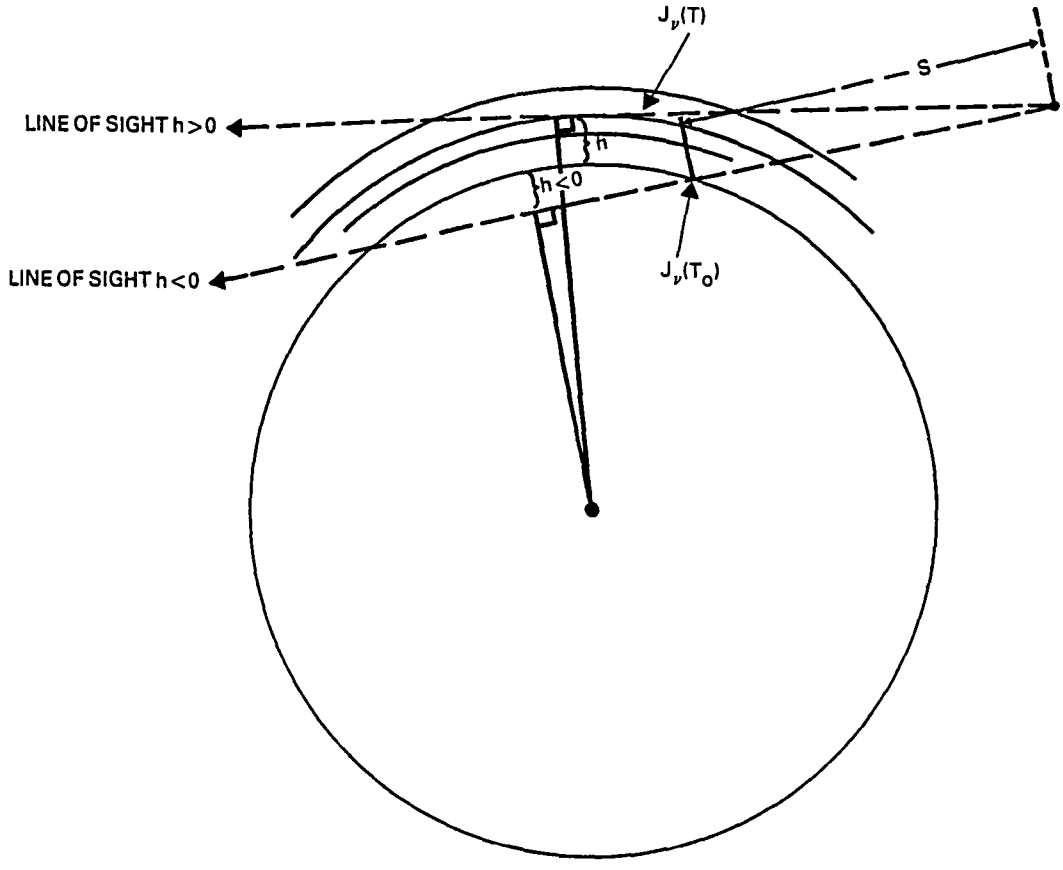

Figure 2-1. Geometry of the Line of Sight for Tangent Height h > 0 and h < 0 Showing the Assignment of the Source Terms for the Atmosphere and the Earth

To simplify the description of the physics of the radiative transfer equation, the following discussion refers to a line of sight that does not intercept the Earth. In that case, the second term on the right-hand side of Equation (2-1) is zero, and the first term can be rewritten as

$$N(h) = \int_{\nu_1}^{\nu_2} \int_{h}^{\infty} J_\nu(x) \frac{d\tau_\nu(h,x)}{dx} dx\, d\nu \qquad (2\text{-}3)$$

where h is the tangent point altitude; $J_\nu(x)$ is the Planck function for the volume of gas at point x; x is the variable along the line of sight; and $\tau_\nu(h, x)$ is the spectral transmissivity from point x to the spacecraft for the path whose tangent point is h kilometers from the hard Earth. In Reference 6, Equation (2-3) is further transformed into a vertical integral along the altitude coordinate z to define the weighting function W(z, h):

$$N(h) = \int_{\nu_1}^{\nu_2} \int_{h}^{\infty} J_\nu(z)\ W_\nu(z,h)\ dz\ d\nu \qquad (2\text{-}4)$$

The weighting function accounts for the effects of the complex phenomena relating to atmospheric conditions and composition between the source function and the observer who, for these computations, is assumed to be at some point $z = \infty$ on the vertical scale. One special characteristic of this function is that it has two values for each value of z above h. This can be seen from the illustration of the geometry of Equation (2-4) in Figure 2-2. The line of sight from point O to the tangent point P receives radiation from a source at an altitude z greater than h at two points along X. The value of $W_\nu(z,h)$ for the location z(X > OP) is less than the value of $W_\nu(z,h)$ for the point z(X < OP) because of the increased atmospheric absorption along a longer optical path. It can also be seen from the figure that a large fraction of the source and absorber is within a few kilome- ters of the altitude of the tangent point. The weighting function reflects this by increasing the contributions made to the integral by the atmosphere near the tangent altitude. Thus, the physical characteristics of the atmosphere near the tangent point altitude, in particular

the temperature, greatly influence the radiance profile intensity at that point on the profile.

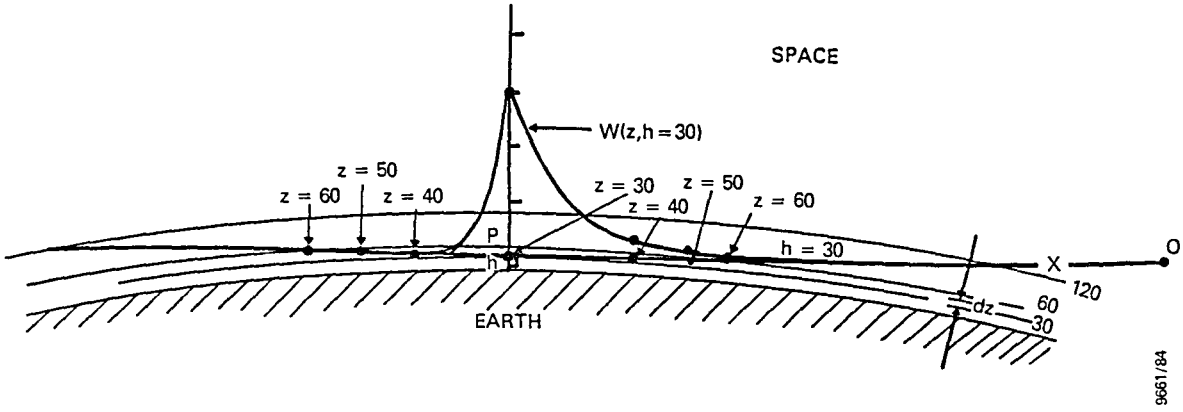

Figure 2-2. Approximately Scaled Geometry of a Single Horizon Profile Ray

Examples of the weighting functions for three 5-centimeter^{-1} (cm^{-1}) intervals at the edges and center of the 15-micrometer CO_2 absorption band are illustrated in Figures 2-3, 2-4, and 2-5. It is clear from these figures that the center of the band at 15 micrometers is insensitive to atmospheric conditions below the tropopause and that a major portion of the radiation for the whole band from 14 to 16 micrometers originates from above 10 kilometers. The work by Honeywell established an analytical representation of the 15-micrometer CO_2 band transmittance, the effect of Doppler broadening, the effect of the absence of LTE, the effect of atmospheric refraction to alter the path of the ray along which a given profile intensity is computed, and the definition and significance of the weighting functions in the computational model. The work extended the analysis to include the effects of water vapor and ozone in the more comprehensive version of the CORPS program. This analysis further established the optimum atmospheric model shell density necessary to preserve the resolution of the temperature-pressure measurements, and it evaluated the characteristics of 10 wavelength

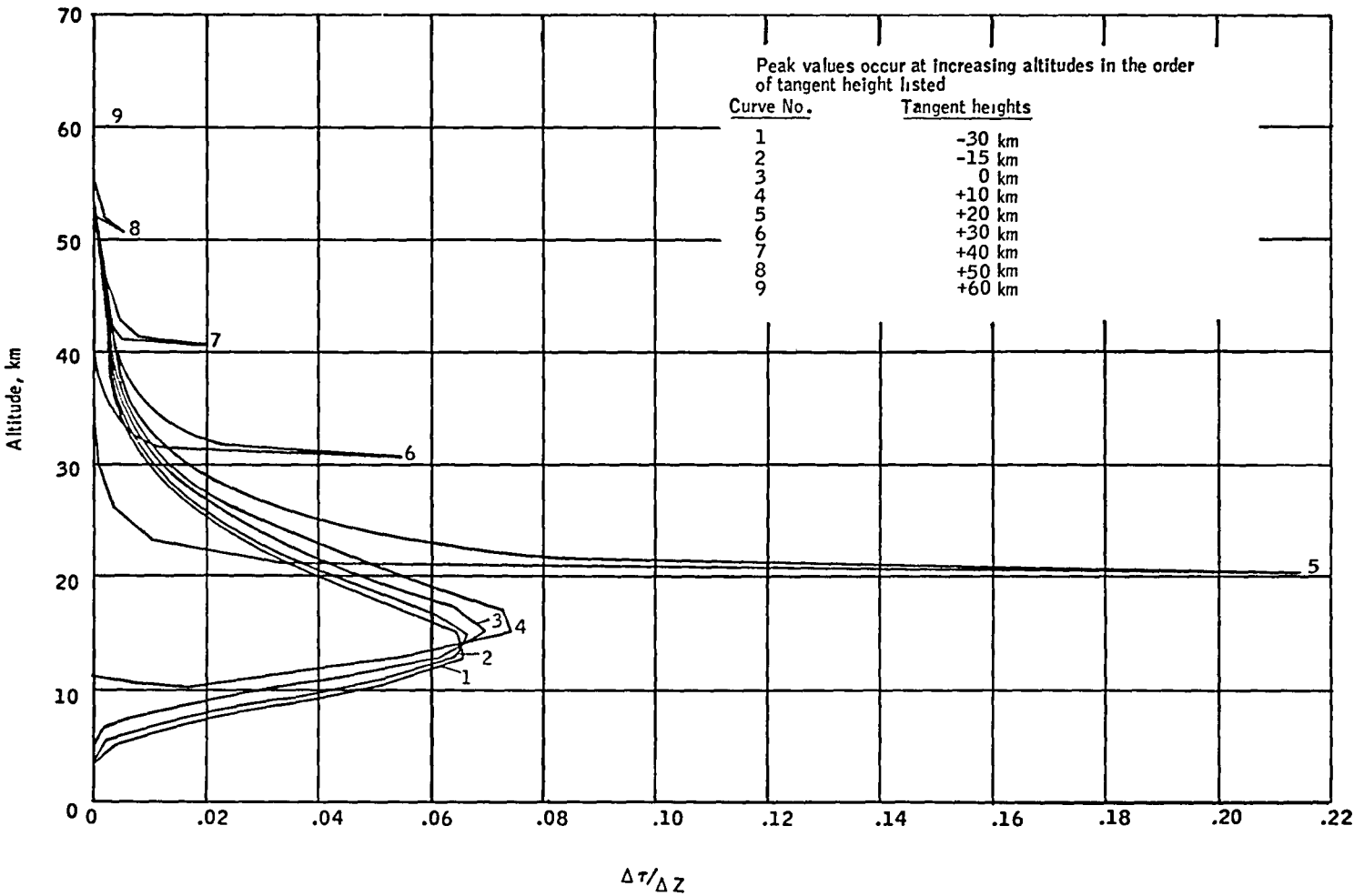

Figure 2-3. Weighting Functions for Spectral Interval 705-715 cm^{-1}, 1962 Standard Atmosphere (13.98 to 14.18 Micrometers)

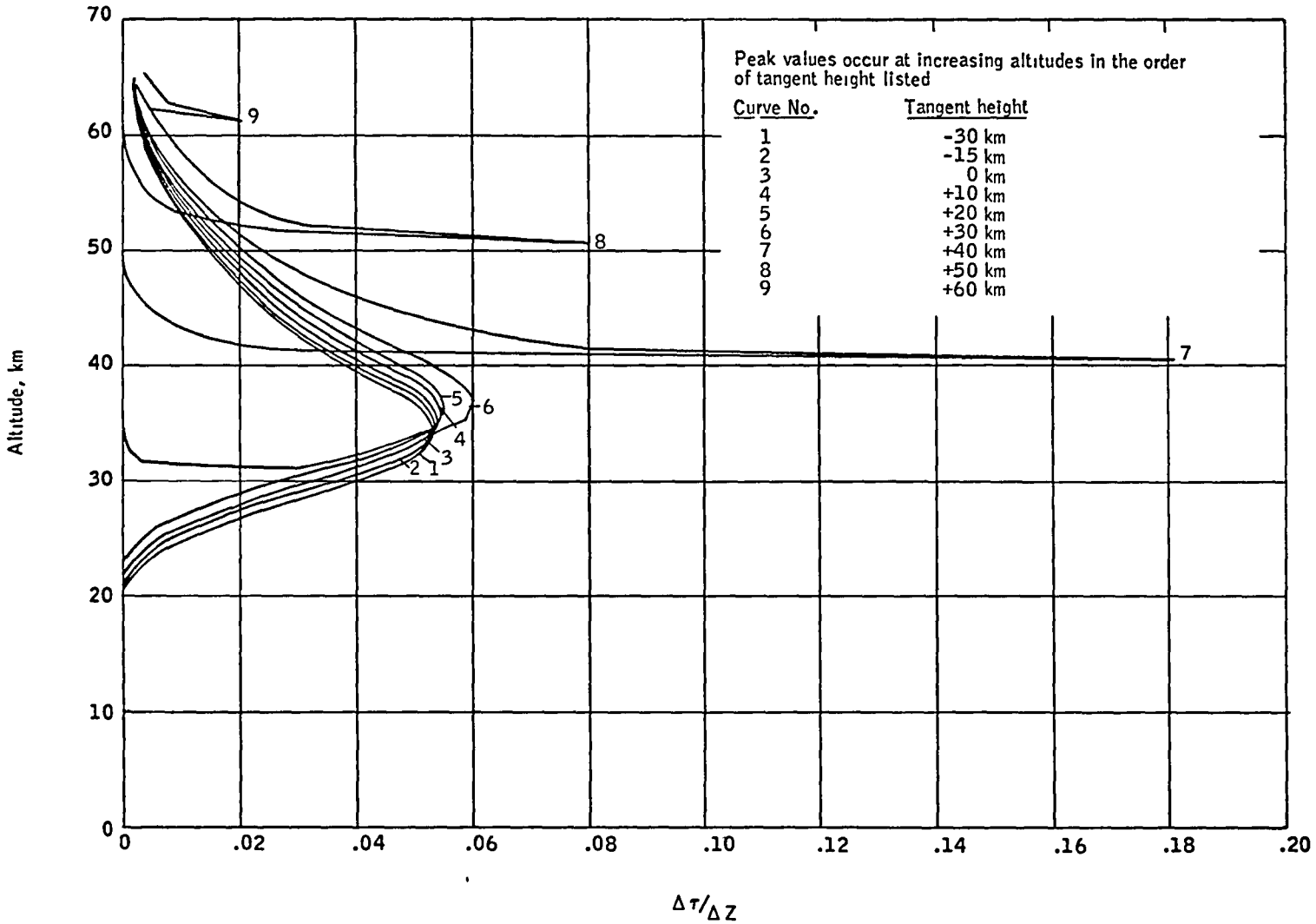

Figure 2-4. Weighting Functions for Spectral Interval 665-670 cm^{-1}, 1962 Standard Atmosphere (14.9 to 15.0 Micrometers)

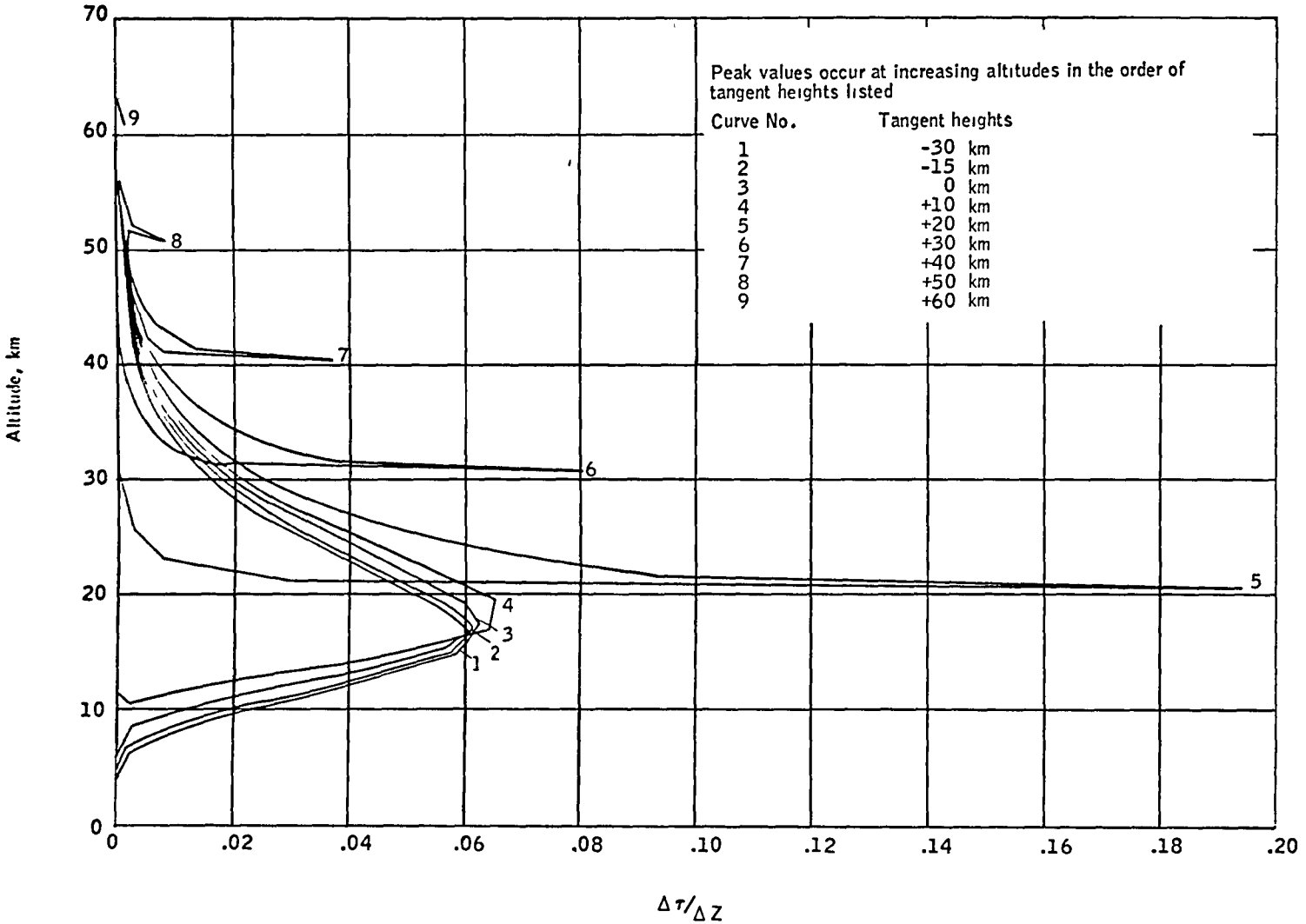

Figure 2-5. Weighting Functions for Spectral Interval 625-635 cm^{-1}, 1962 Standard Atmosphere (15.75 to 16.0 Micrometers)

intervals between 13.8 and 16.67 micrometers to aid in selecting a sensor passband that is relatively immune to the phenomena that complicate the problem of horizon definition in this band.

2.2.2 RADIANCE VARIATIONS

The work by Honeywell that is directly associated with the attitude analysis is their study of the effects of clouds, the effect of scanning from different azimuth views through an atmospheric volume with neighboring volumes of different temperature-pressure profiles, and the establishment of the existence of systematic radiance variations. This study, using the CORPS program, demonstrated the existence of the systematic variations of profiles from seasonal and latitude-dependent phenomena using 1085 atmospheric temperature-pressure profiles from balloon and rocket sounding.

Although Reference 2 does not provide details of the systematic variation over season and latitude of the profiles generated using this meteorological data, it does provide figures illustrating the systematic variations in the characteristics of the whole band from 13.98 to 16.67 micrometers and five other subbands within that band. In particular, it clearly illustrates the existence and characteristics of systematic variations in intensity and tangent height of the profiles for a band between 13.98 and 16.00 micrometers. The analysis of cloud effects indicates significant effects due to clouds for vertical scan paths on a passband between 13.98 and 16.26 micrometers. Here a 27-percent reduction in radiance is estimated. The maximum effect is at the near-equatorial latitude of 20^{o}N, where the cloud and Earth are in highest contrast. Because these effects were derived from clouds at simulated altitudes of 16 to 20 kilometers, the report concludes that, 99 percent of the time, cloud effects will be smaller than 27 percent of the nadir point

profile intensity for this passband. Figures 2-6 and 2-7 illustrate the estimated amount of radiance attenuation expected from clouds at various altitudes for scanner views from the nadir to the horizon for July at 20^{o}N and 75^{o}N, respectively, in the 13.78- to 16.26-micrometer passband. The radiance attenuation due to clouds increases with cloud height up to an altitude that corresponds with the tropopause and then decreases again. This happens because the clouds are simulated at the ambient temperature, which decreases up to tropopause altitudes and then starts to rise again.

The effects of horizontal nonuniformity of the temperature and pressure profiles in the volume of atmosphere being scanned from space were also estimated. The computation used two isothermal atmospheric temperature-pressure profiles, one at 210K and one at 220K. The computation illustrated that the brightness from the limb to the nadir view can be modified significantly (20 percent) when the boundary of the warm to cold atmospheres is within 5 geodetic degrees of arc from the point of tangency. Figure 2-8 (Reference 6) illustrates this result. In the figure, the boundary between the hot and cold atmospheres is at the tangent point for curve 1 and at 5 degrees forward of the nadir for curve 2.

The analysis of the systematic effect of horizon profile variations is not treated as a separate topic in Reference 2; however, it is apparent from a review of the synthesized profiles presented that a systematic variation exists in the radiance amplitude with season and latitude. This can be seen in a review of Figures 2-9 through 2-14 (Appendix D of Reference 2), which show the radiance curves for a number of spectral intervals. In these figures, the profile labeled C is close to that for the ERBS scanner, and the discussion below refers to this case only.

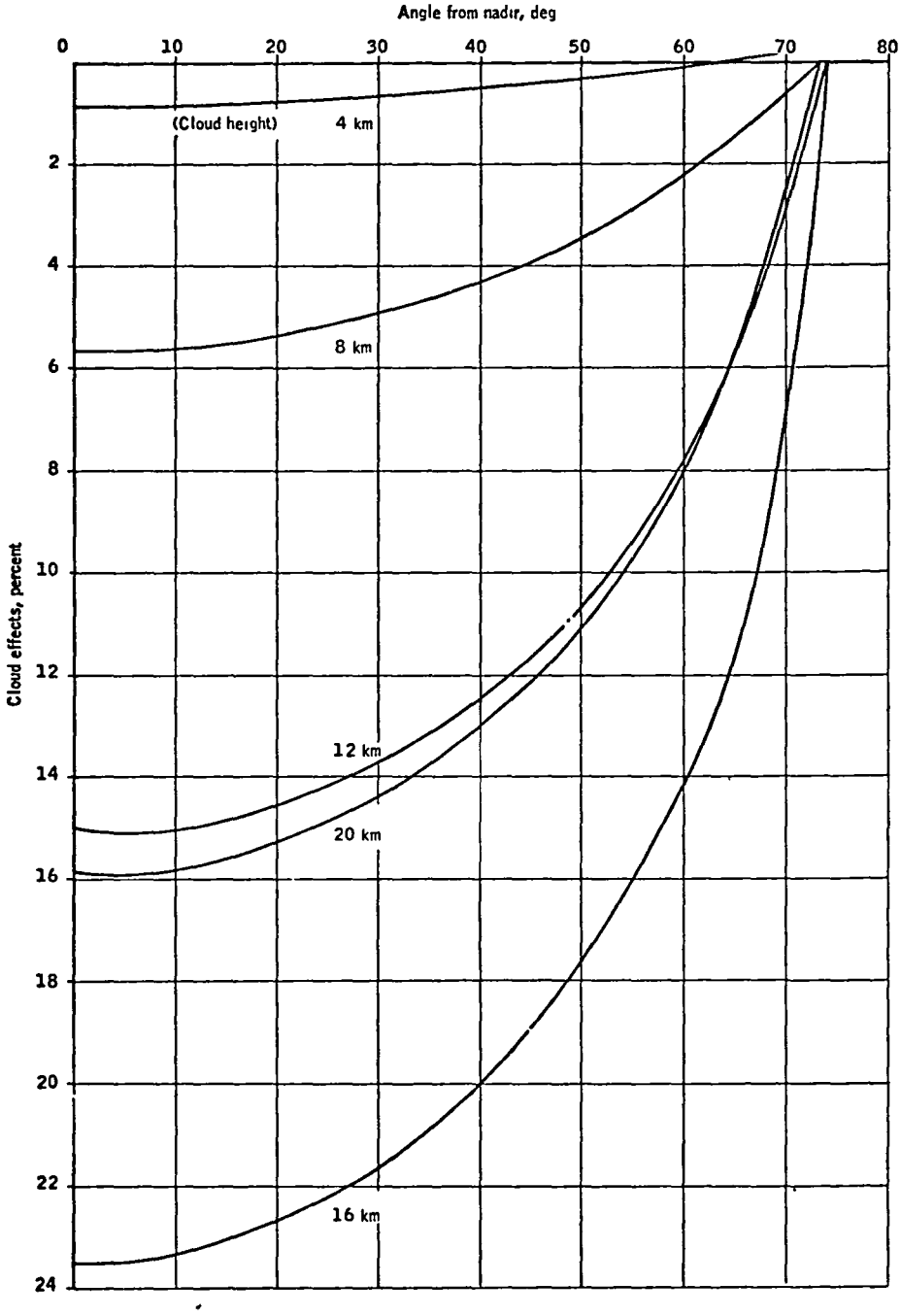

Figure 2-6. Percentage Cloud Effects, July, 20°N

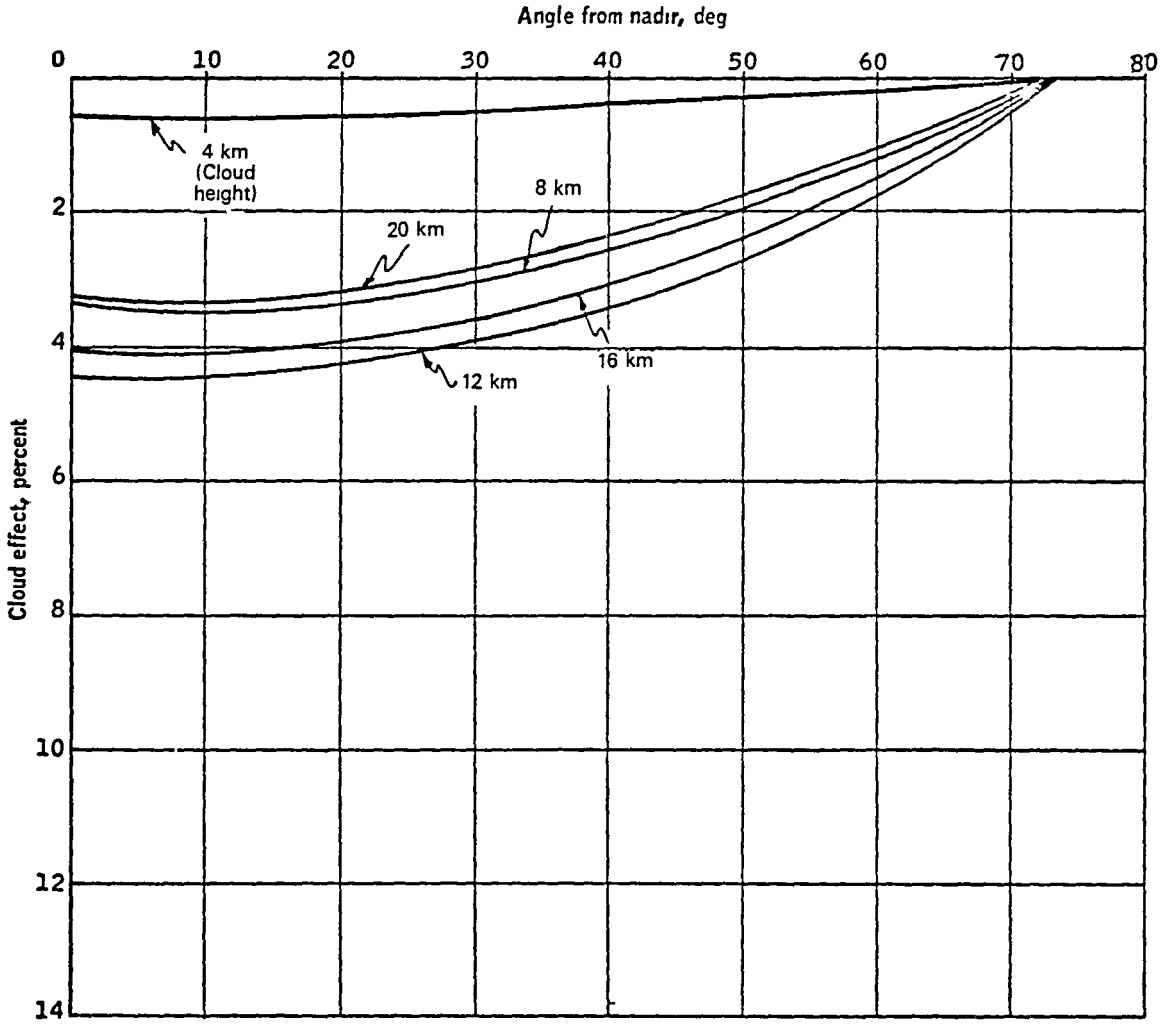

Figure 2-7. Percentage Cloud Effects, July, 75°N

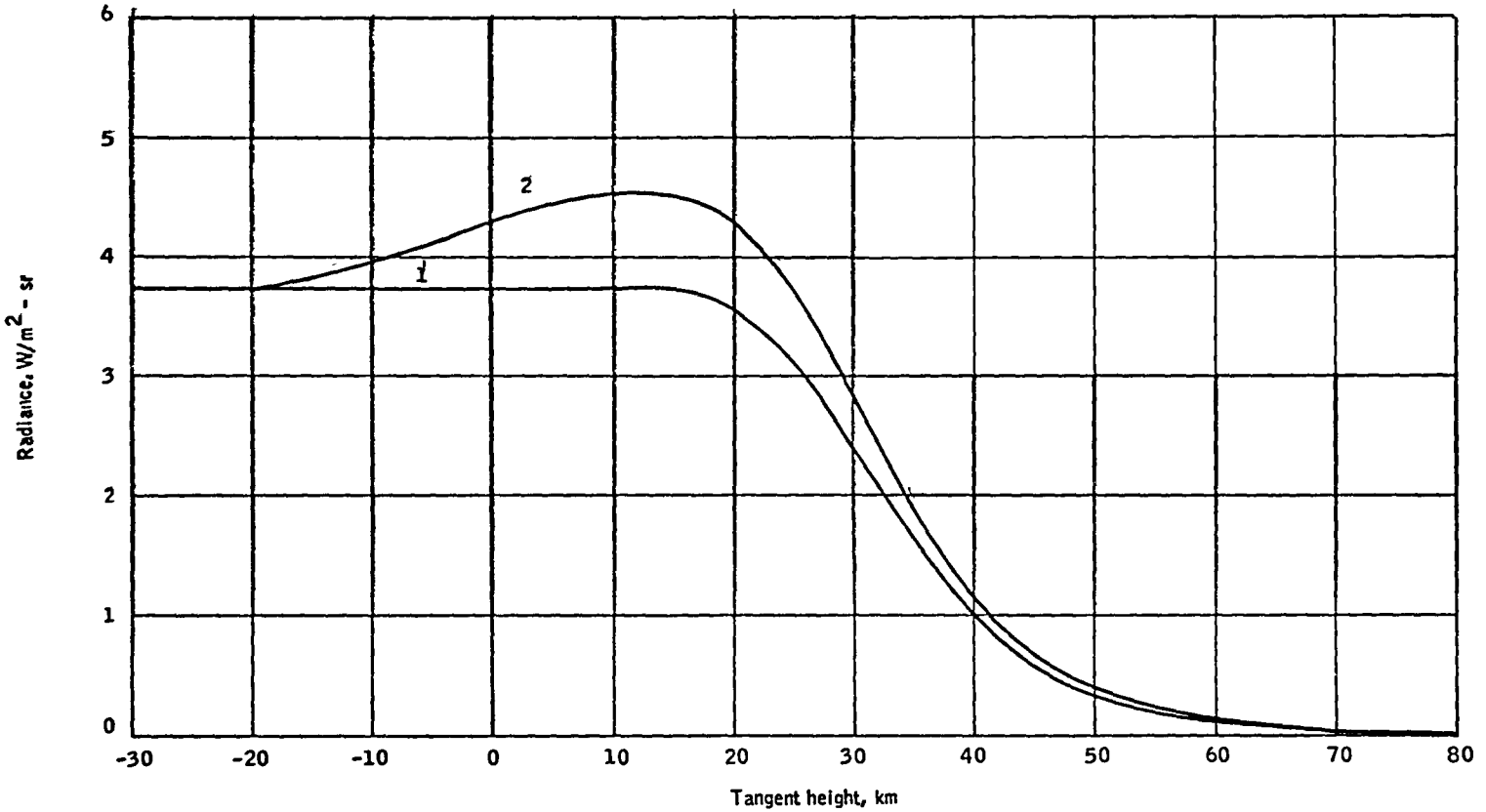

Figure 2-8. Evaluation of Azimuth Model With Two Isothermal Atmospheres (Curves 1 and 2 represent an atmosphere at 220K and 210K, respectively.)

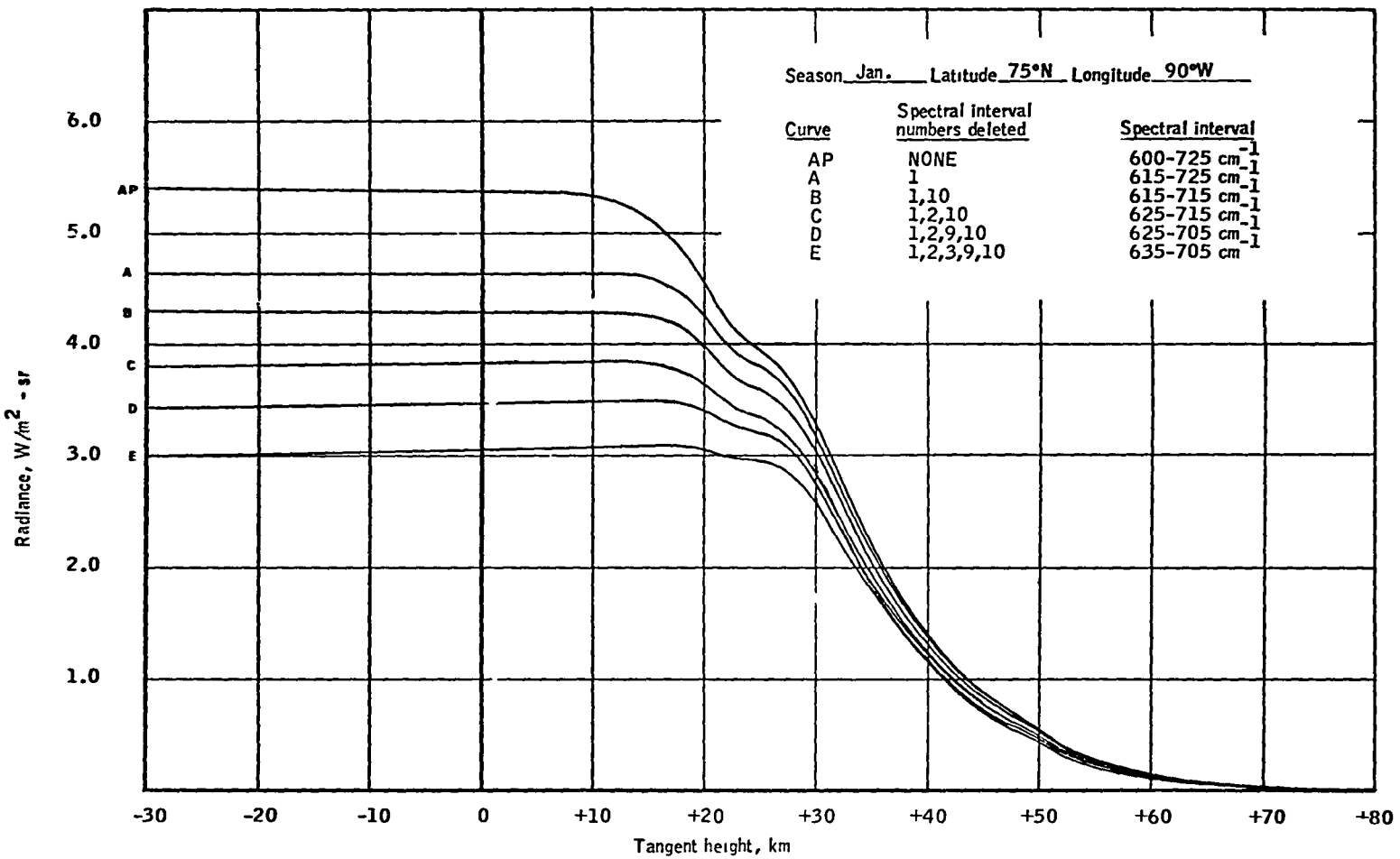

Figure 2-9. Effects of Spectral Interval Variations on the 15-Micrometer CO_2 Horizon Profile, January, 75°N

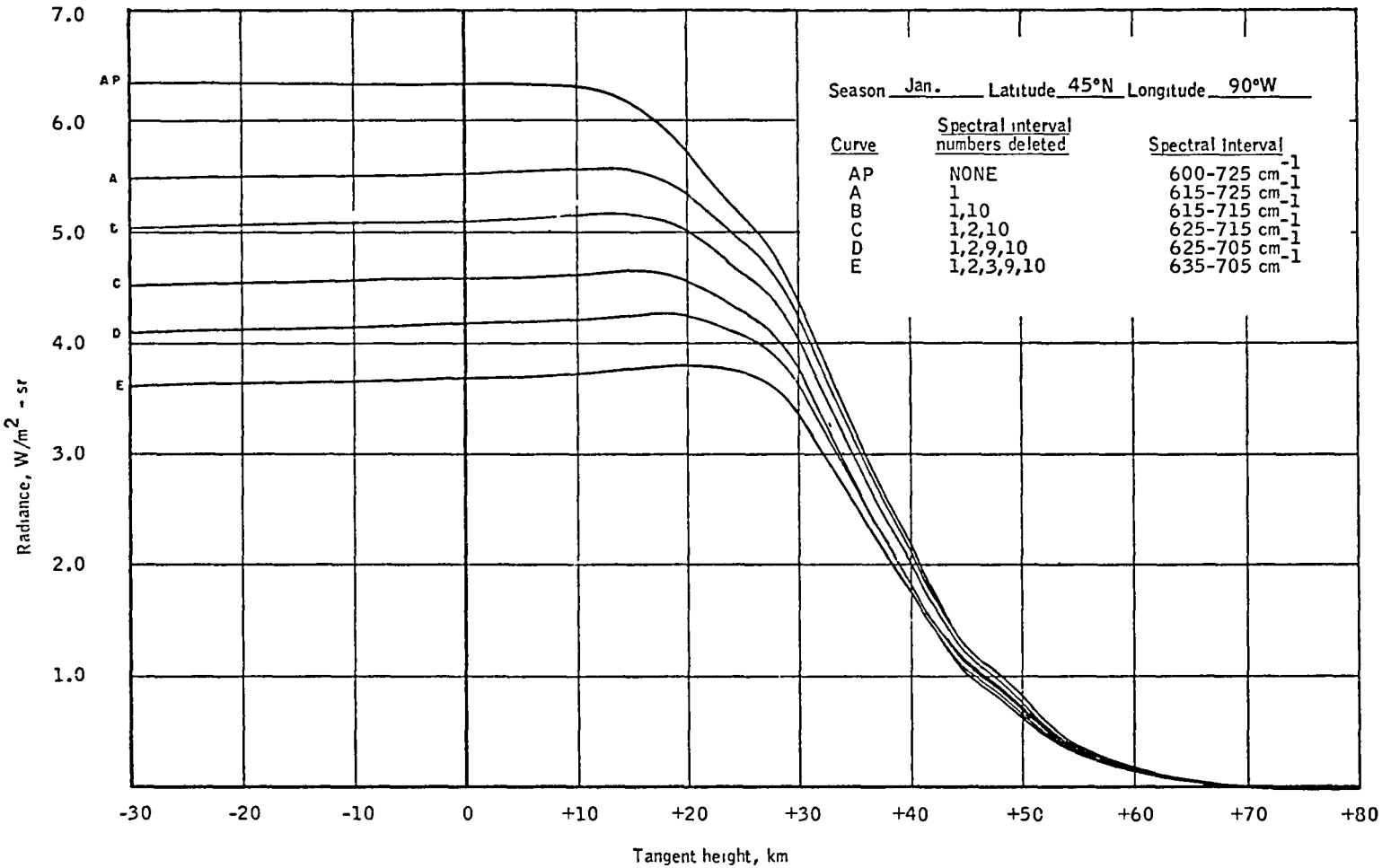

Figure 2-10. Effects of Spectral Interval Variations on the 15-Micrometer CO_2 Horizon Profile, January, 45°N

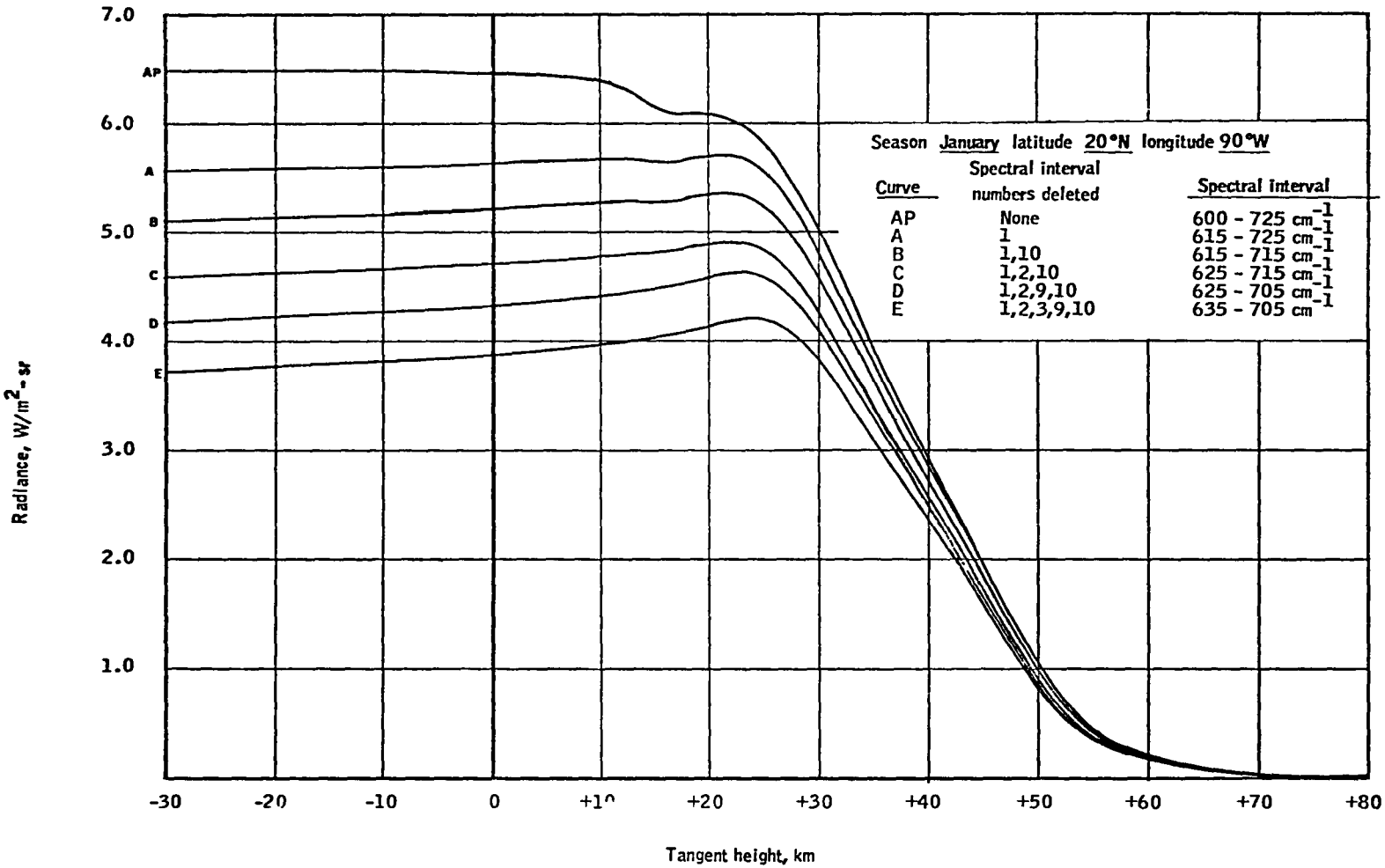

Figure 2-11. Effects of Spectral Interval Variations on the 15-Micrometer CO_2 Horizon Profile, January, 20°N

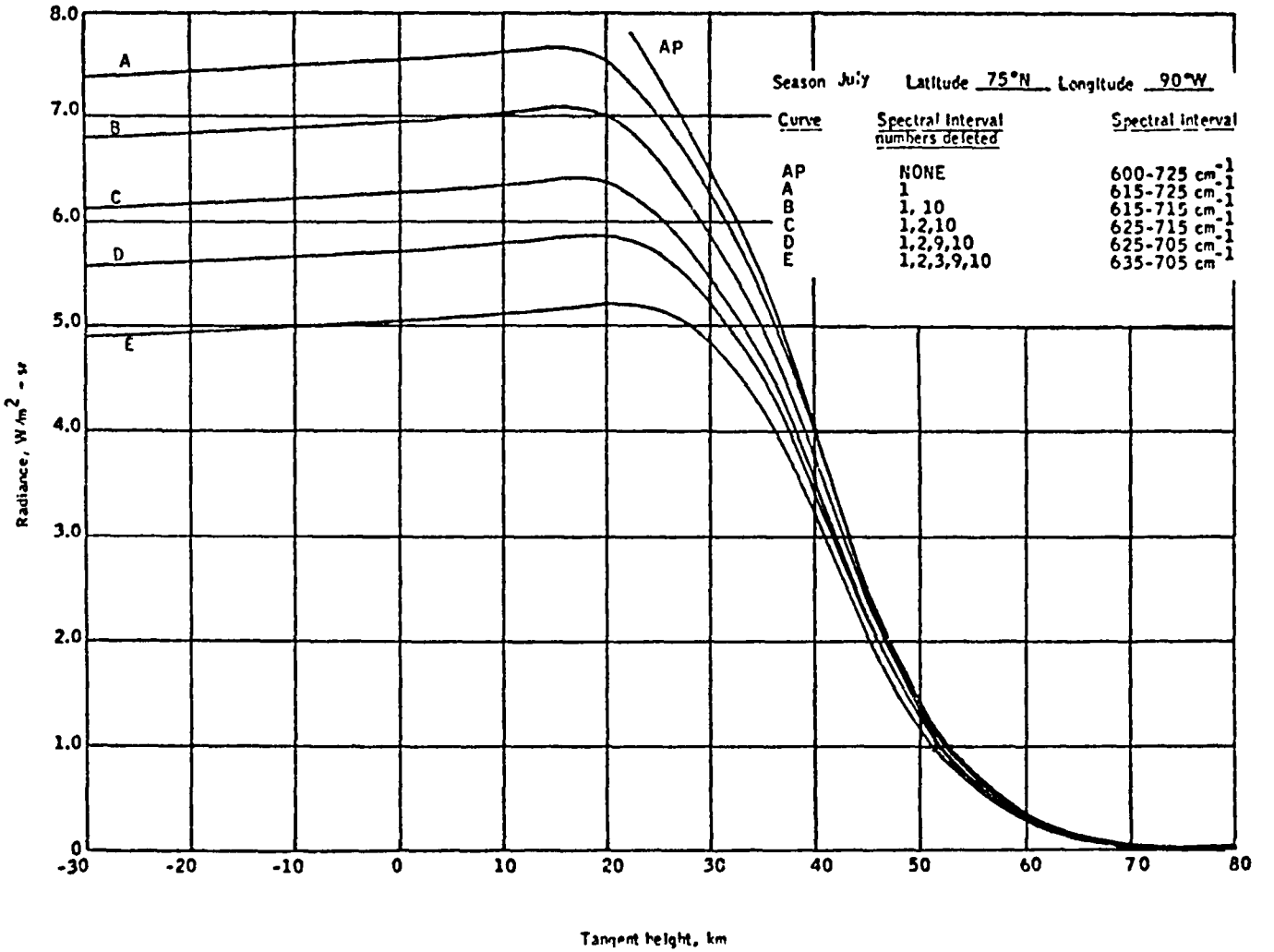

Figure 2-12. Effects of Spectral Interval Variations on the 15-Micrometer CO_2 Horizon Profile, July, 75°N

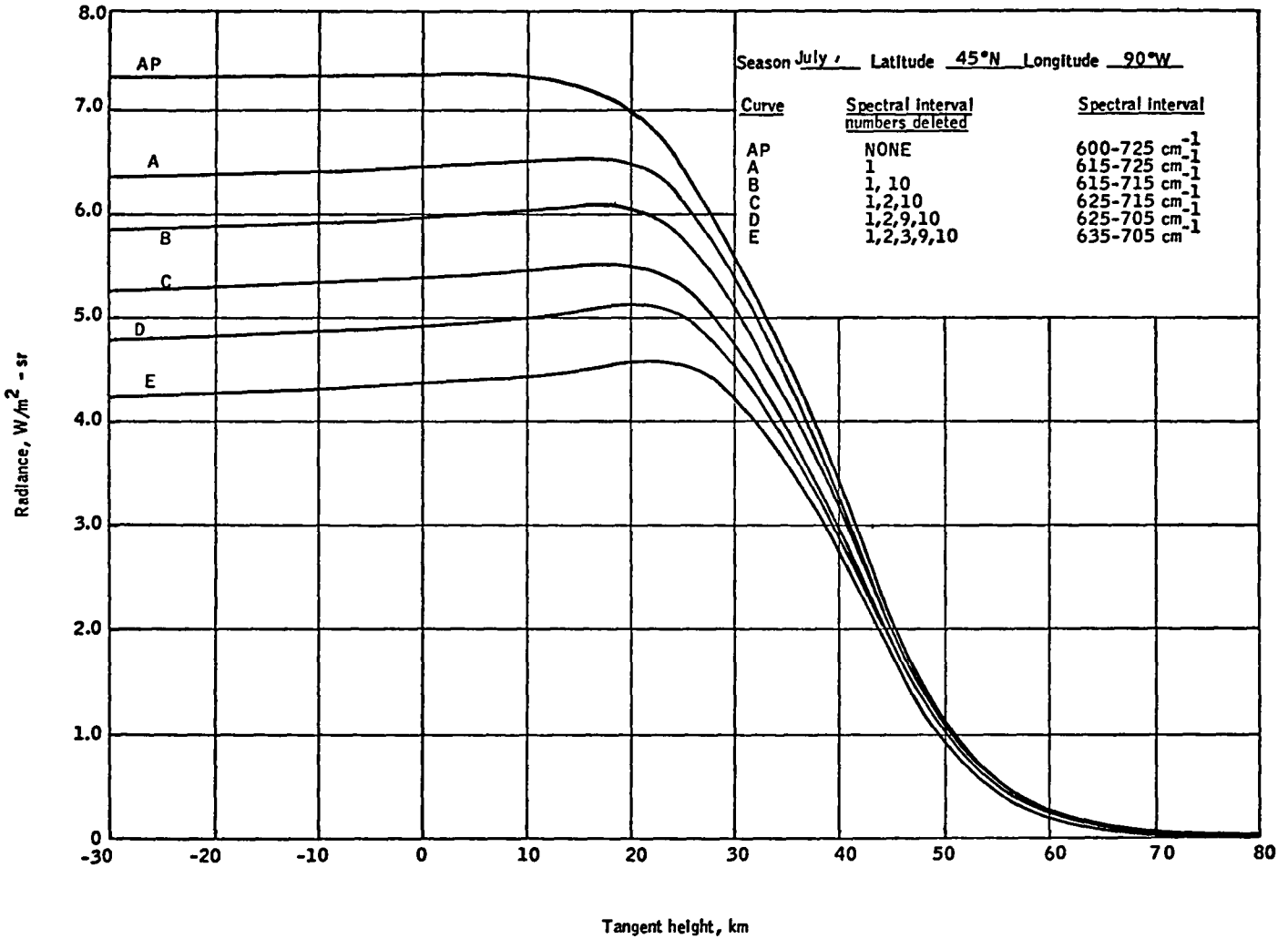

Figure 2-13. Effects of Spectral Interval Variations on the 15-Micrometer CO_2 Horizon Profile, July, 45°N

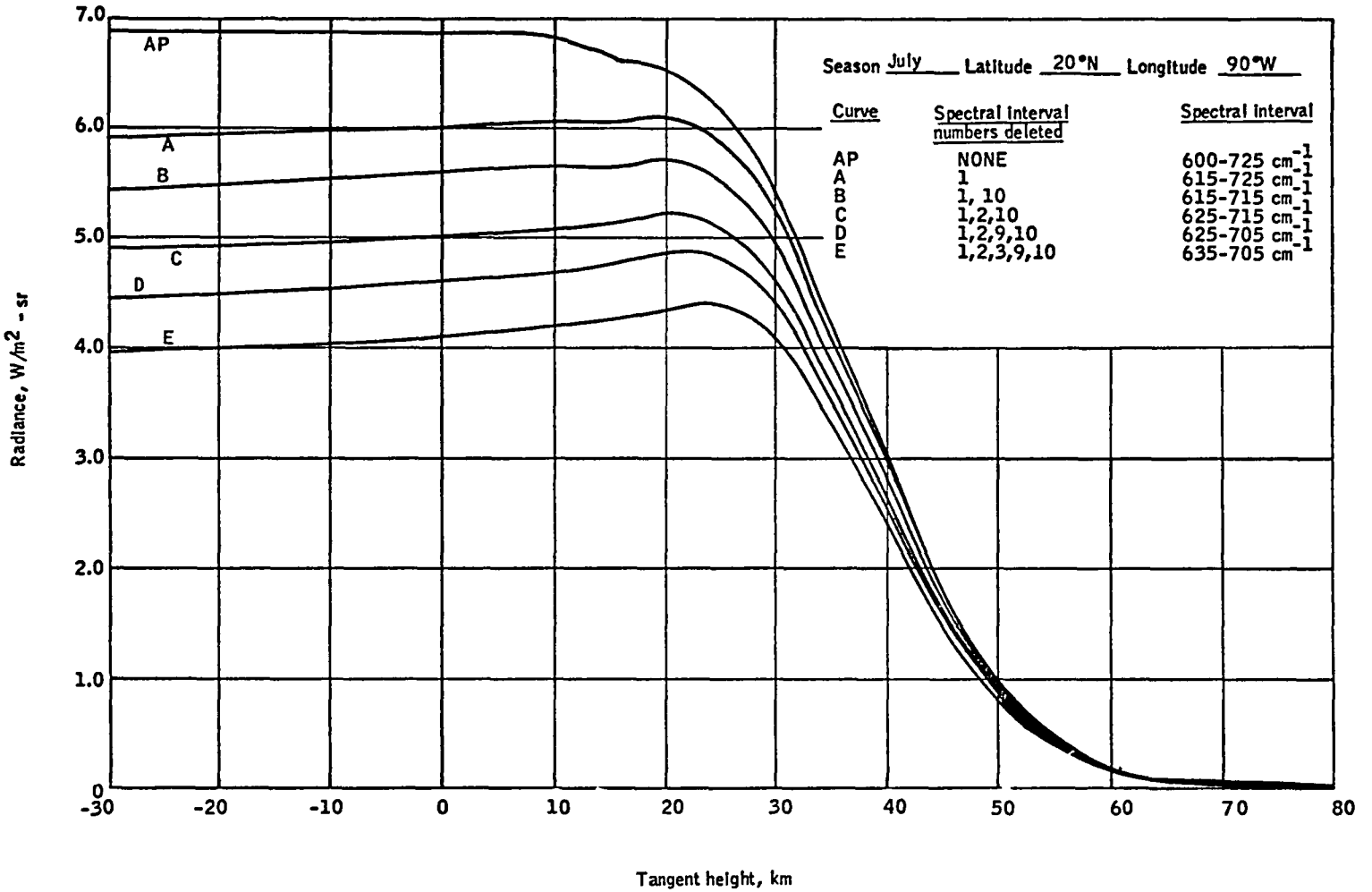

Figure 2-14. Effects of Spectral Interval Variations on the 15-Micrometer CO_2 Horizon Profile, July, 20°N

A systematic variation in the tangent height of the profile 50-percent point, which appears to range between 37 and 42 kilometers for January and between 41 and 42 kilometers for July is evident from the data presented. Figure 2-15 summarizes the 0-kilometer radiance versus latitude and tangent height of the 50-percent point versus latitude for the month of January. For this illustration, the July data have been used to represent the southern latitudes in January. The left-hand scale is for radiance at the 0-kilometer point, plotted as O; the right-hand scale is for the tangent height of the 50-percent (of the radiance at a 0-kilometer tangent height) point, plotted as X. A systematic trend in both of these quantities is evident. The apparent irregularity in the tangent height of the 50-percent point for the January 20^{o}N data (Figure 2-11) may reflect the accuracy of the temperature-pressure profile input to the CORPS program. If this apparent outlier is ignored, the figure provides evidence for a systematic variation of 6 kilometers pole to pole in some seasons for the measured horizon altitude.

A discussion of the Honeywell/LRC statistical study of the systematic behavior of the 15-micrometer CO_2 band profiles is presented in Reference 3. The statistics were compiled on 839 synthesized profiles for the passband between 615 cm^{-1} (16.26 micrometers) and 715 cm^{-1} (13.98 micrometers). The profiles were evaluated as 99 subsets of profiles, where each subset was characterized by a common feature. Features of interest for this report were as follows: the latitude of the atmospheric temperature-pressure profile, the time of year, and the diurnal variations and the standard deviation of the data about the average profile for each representative latitude and month. The systematic variation of profile amplitude with latitude in the winter is illustrated by the synthesized profiles in Figure 2-16. The variation in tangent height of the 50-percent point is illustrated in Figure 2-17, which is a

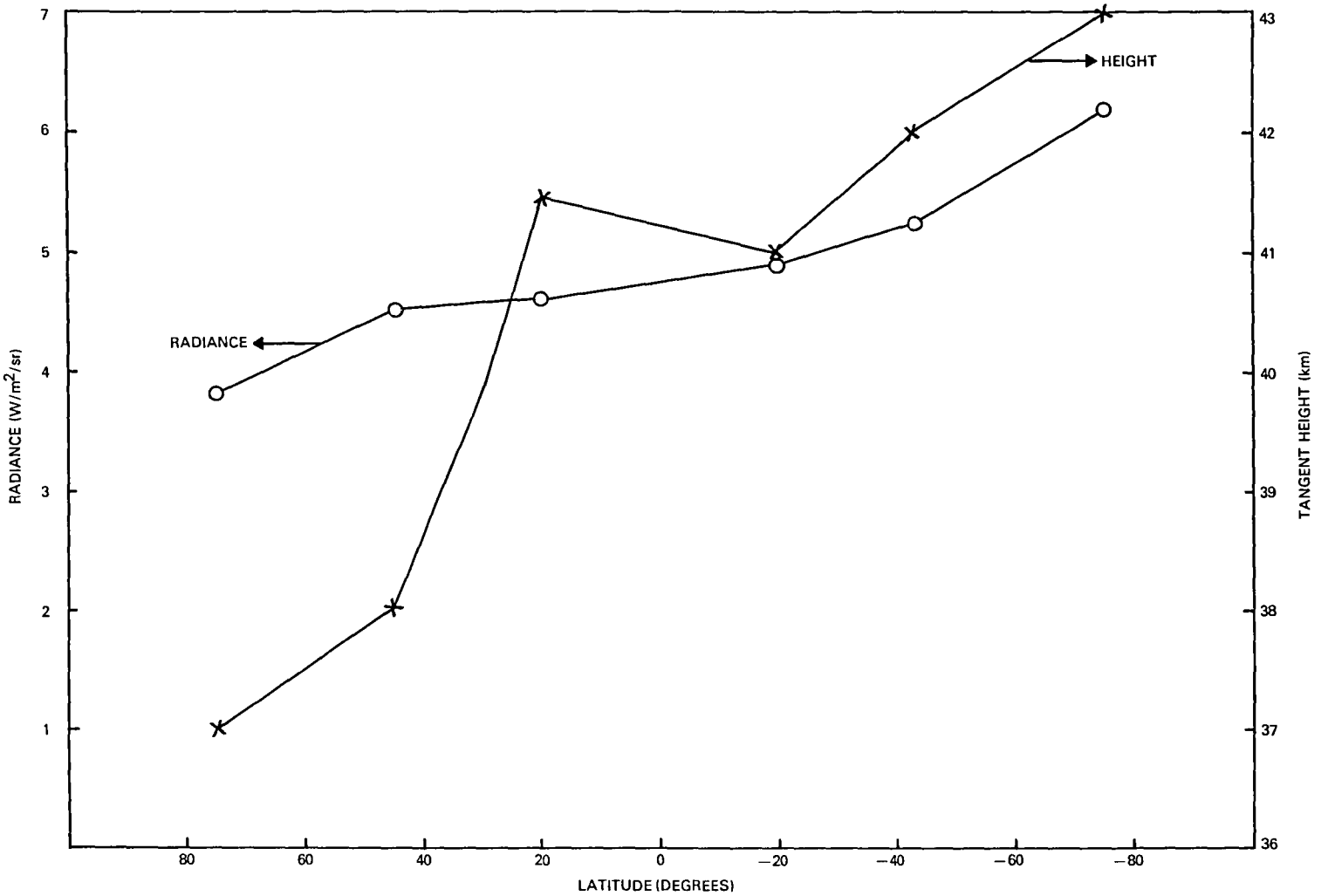

Figure 2-15. Radiance Intensity at a 0-Kilometer Tangent Height and Tangent Height of the 50-Percent Point Versus Latitude (January)

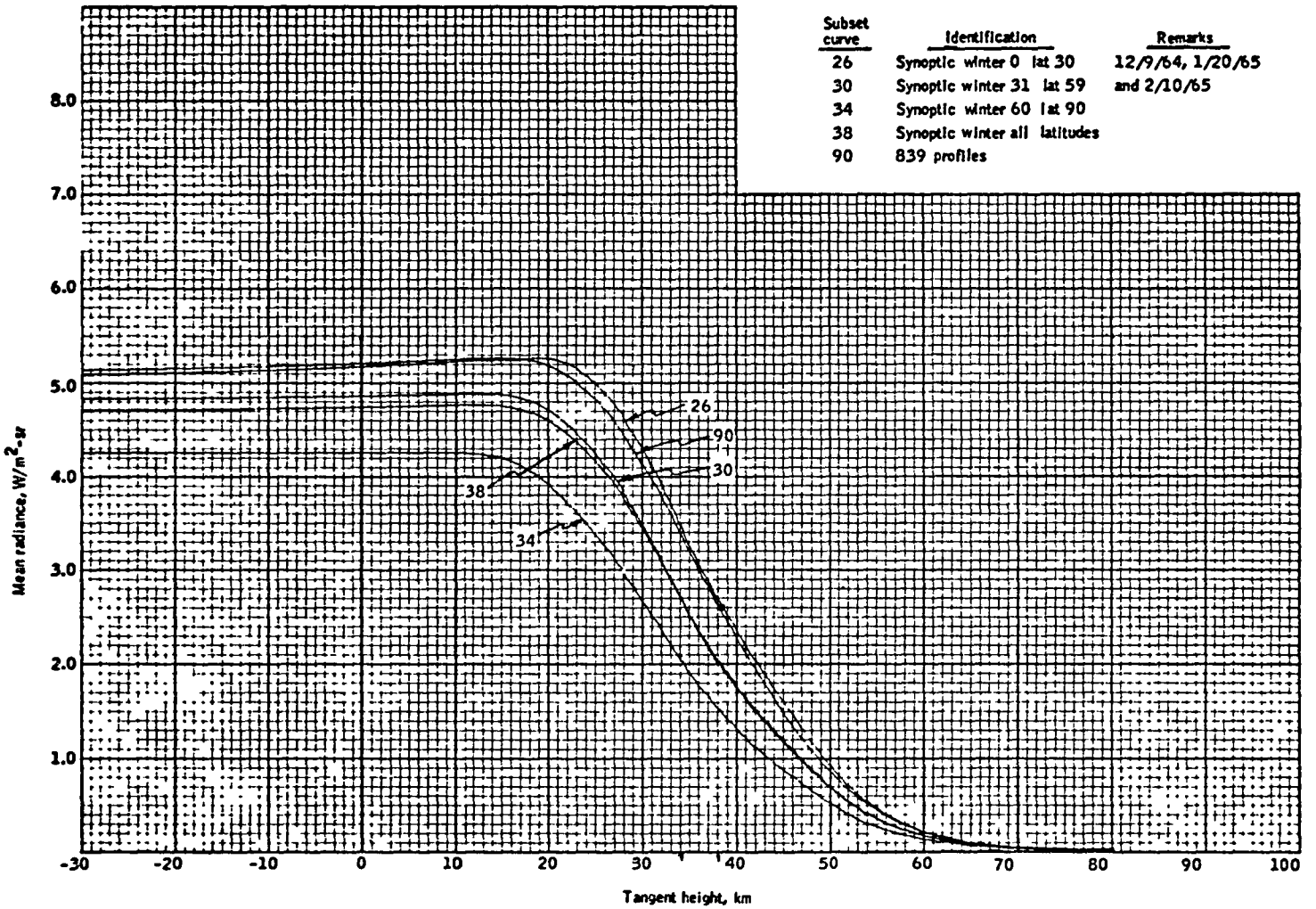

Figure 2-16. Mean Radiance Versus Tangent Height for the Winter Hemisphere

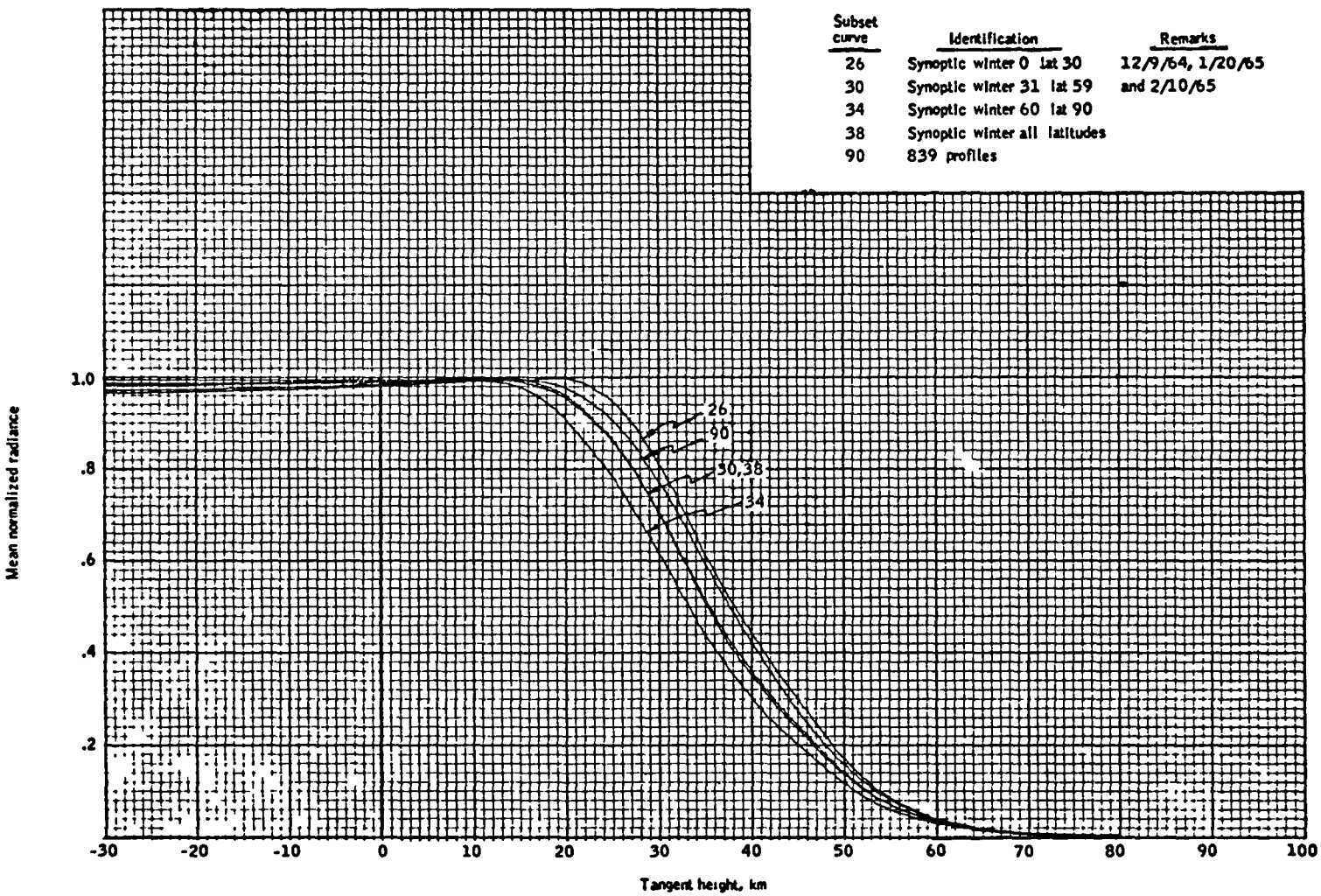

Figure 2-17. Mean Normalized Radiance Versus Tangent Height for the Winter Hemisphere

display of the normalized profiles from Figure 2-16. Similar characteristics for the summer profiles are illustrated in Figures 2-18 and 2-19. The diurnal variations were estimated to be smaller than the resolution of the analysis accuracy, and the standard deviation for the winter profiles was reported to be higher than the standard deviation of the summer profiles.

The analysis of systematic effects reported in Reference 3 also noted an apparent linear dependence of the radiance on the temperature of the 10-millibar pressure level. Citing the correlation of radiance with the 10-millibar temperature, procedures to compute radiance profiles from empirical and phenomenological representations of the synthesized profiles were investigated. This profile computational approach was also analyzed by CSC (Reference 7) during the early stages of the analysis to establish IR sensor correction for Seasat-1. It was not implemented, however, because it was specific to a passband that was narrower than that of the Seasat-1 IR scanner.

2.2.3 PROJECT SCANNER PROFILE MEASUREMENTS

The Project Scanner measurements were made during single rocket flights in August and December of 1966. References 4 and 5 describe these experiments and compare the results with the synthesized profiles using the methods of Reference 2. The profiles were measured by a dual-radiometer assembly with a Cassegrian optical system and scanning mirrors. The FOV was 0.625 degree in the scan direction (vertical), consisting of an array of five bolometer flakes. Each of the five flakes subtended 0.025 degree in the vertical direction and 0.10 degree in the horizontal direction.

The radiometer had two IR passbands: one centered on the 15-micrometer CO_2 absorption band and one on a part of the

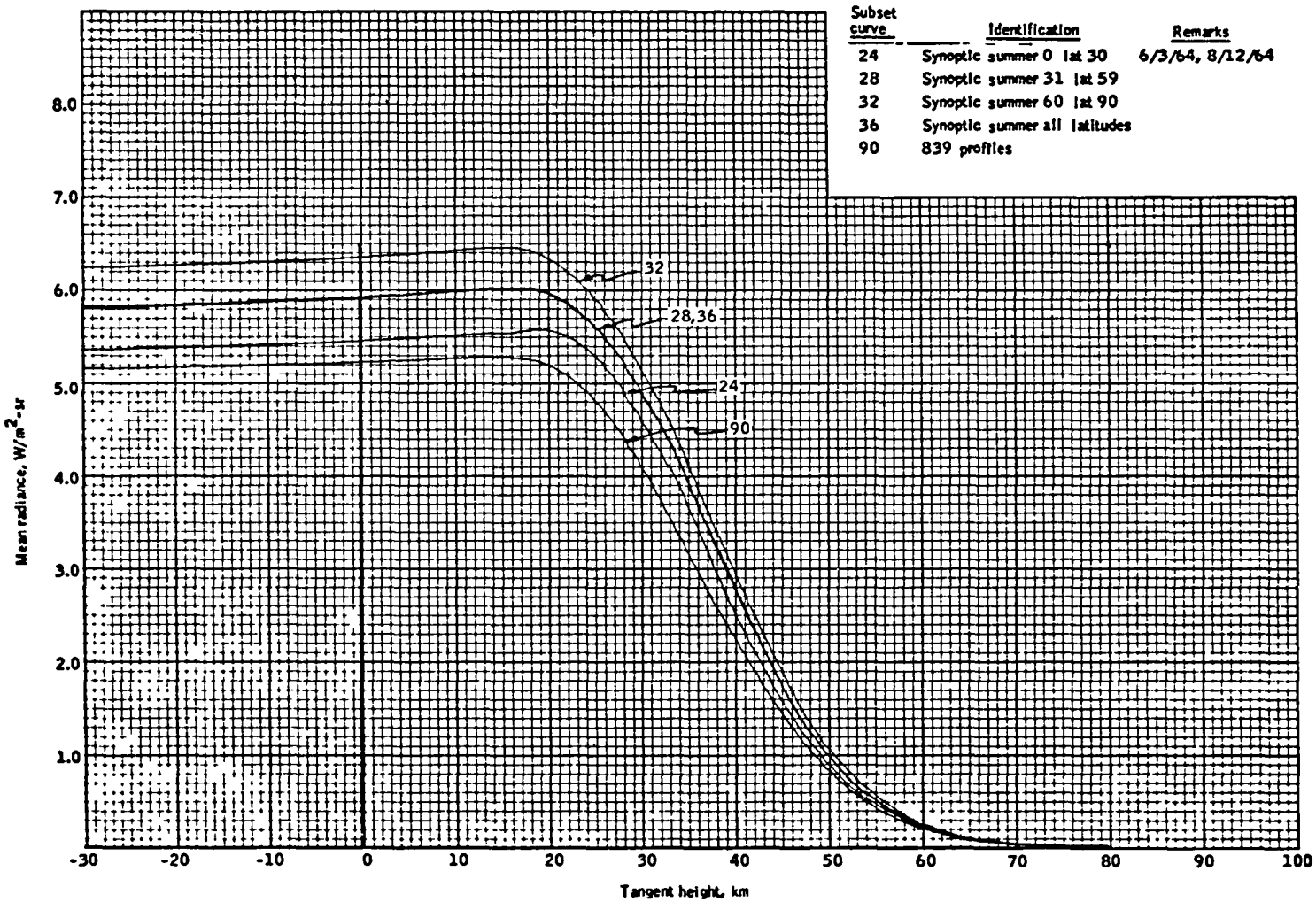

Figure 2-18. Mean Radiance Versus Tangent Height for the Summer Hemisphere

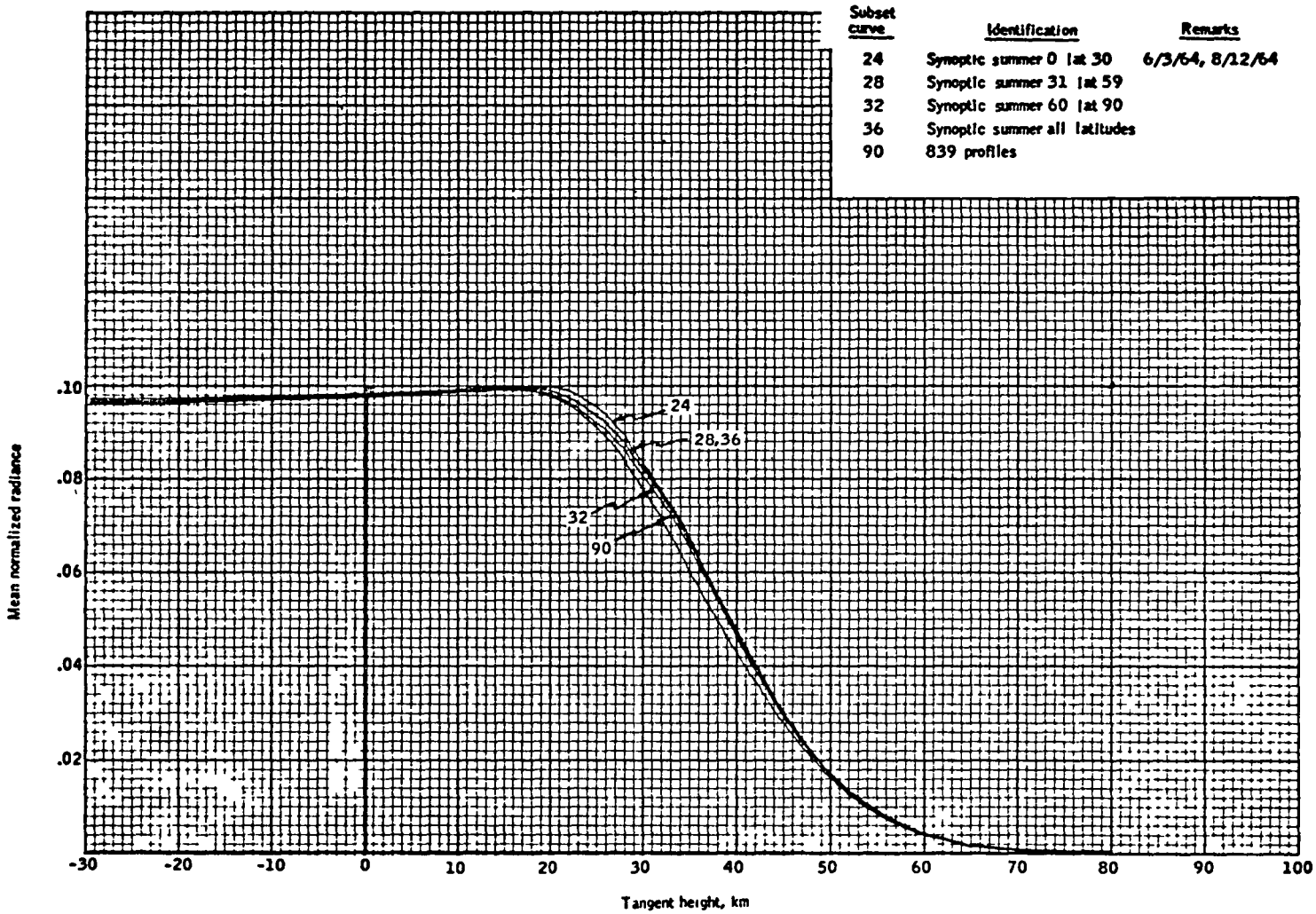

Figure 2-19. Mean Normalized Radiance Versus Tangent Height for the Summer Hemisphere

water vapor rotational band 10 micrometers wide centered near 26 micrometers. These passbands are illustrated in Figure 2-20. Geographical regions for the profile measurements are illustrated in Figures 2-21 and 2-22 for the summer and winter conditions, respectively. These measurements were performed in coordination with near-simultaneous radiosonde data taken at ground sites near the location of the profile measurements. Figure 2-23 compares the measured profiles with the synthesized counterparts in the 15-micrometer CO_2 band for the summer experiment. The quoted accuracy of the Project Scanner data was 4 to 6 percent (1σ) for the radiance between 3 and 6 watts per meter^2 per steradian ($W/m^2/sr$) and 1.3 kilometers (1σ) for the tangent height. Table 2-1 summarizes the error sources for tangent height calibration.

Table 2-1. Errors in Tangent Height Determination for Project Scanner

Error Source	Error	Tangent Height Accuracy (km)
Radiometer mirror position ($\pm 1\sigma$)	$\pm$0.02 deg	$\pm$1.0
Radiometer time delay	$\pm$0.001 sec	$\pm$0.5
Star mapper ($\pm 1\sigma$)	$\pm$0.008 deg	$\pm$0.4
Alignment of instruments	$\pm$0.005 deg	$\pm$0.25
Altitude ($\pm 1\sigma$)	$\pm$0.5 km	$\pm$0.45
Total system error		$\pm$1.3

The comparison of Project Scanner profiles with the synthesized profiles (using the CORPS program) confirmed the validity of the profile synthesis analysis for summer atmospheric conditions. This positive result is a consequence of the high degree of horizontal uniformity at all altitudes in the summer atmosphere.

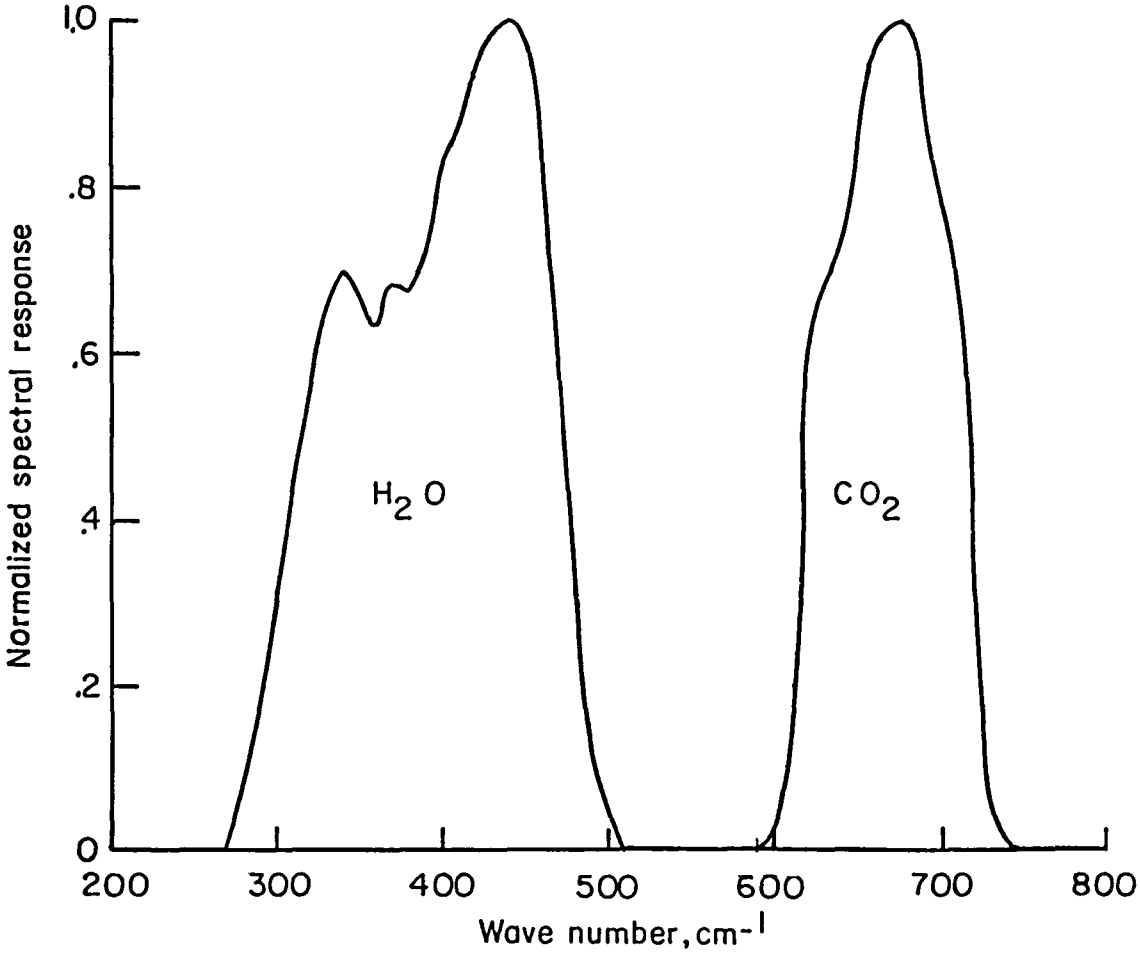

Figure 2-20. Normalized Spectral Response of the Dual Radiometers of Project Scanner

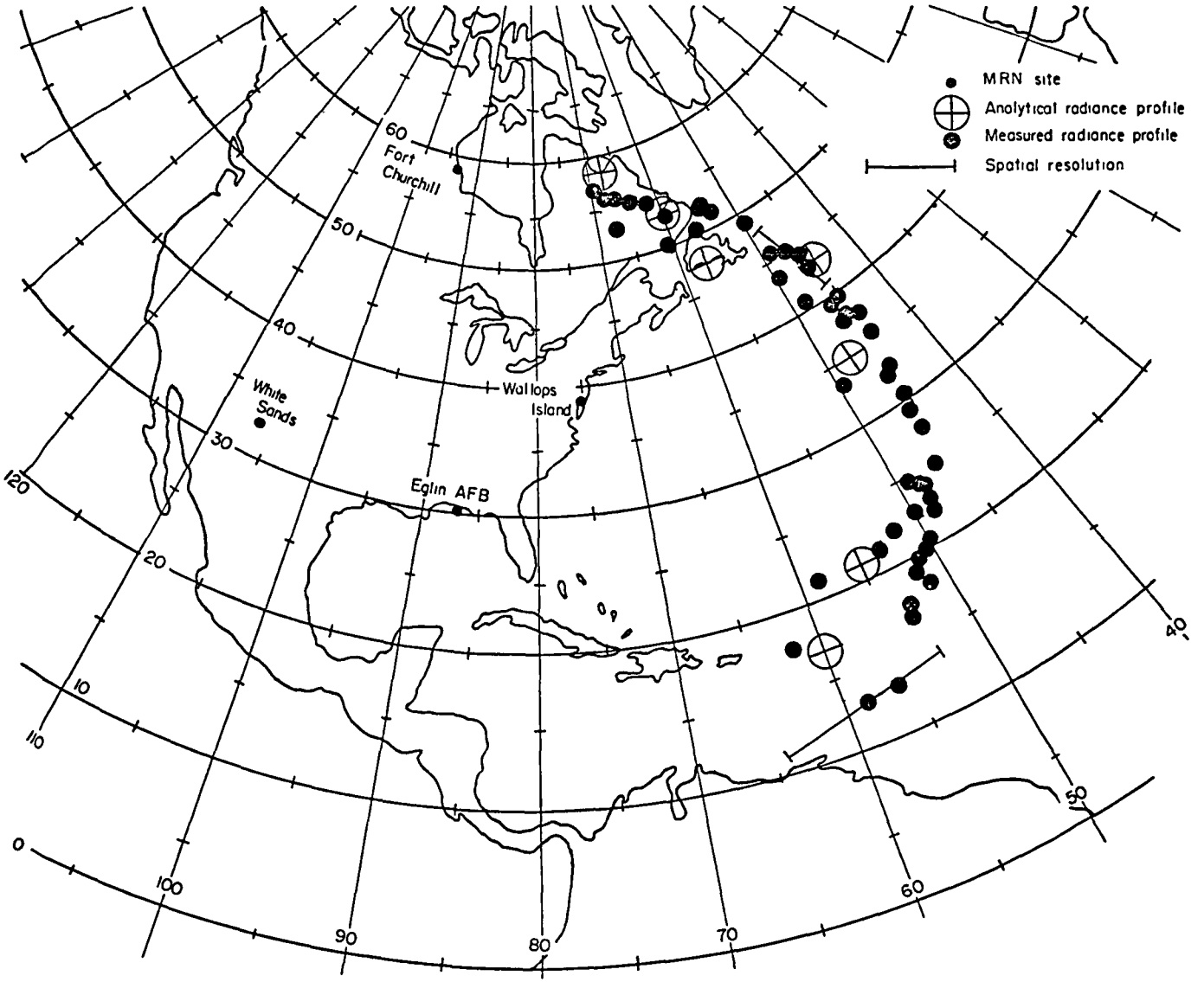

Figure 2-21. Geographic Location of Horizon Radiance Profiles for Summer Conditions

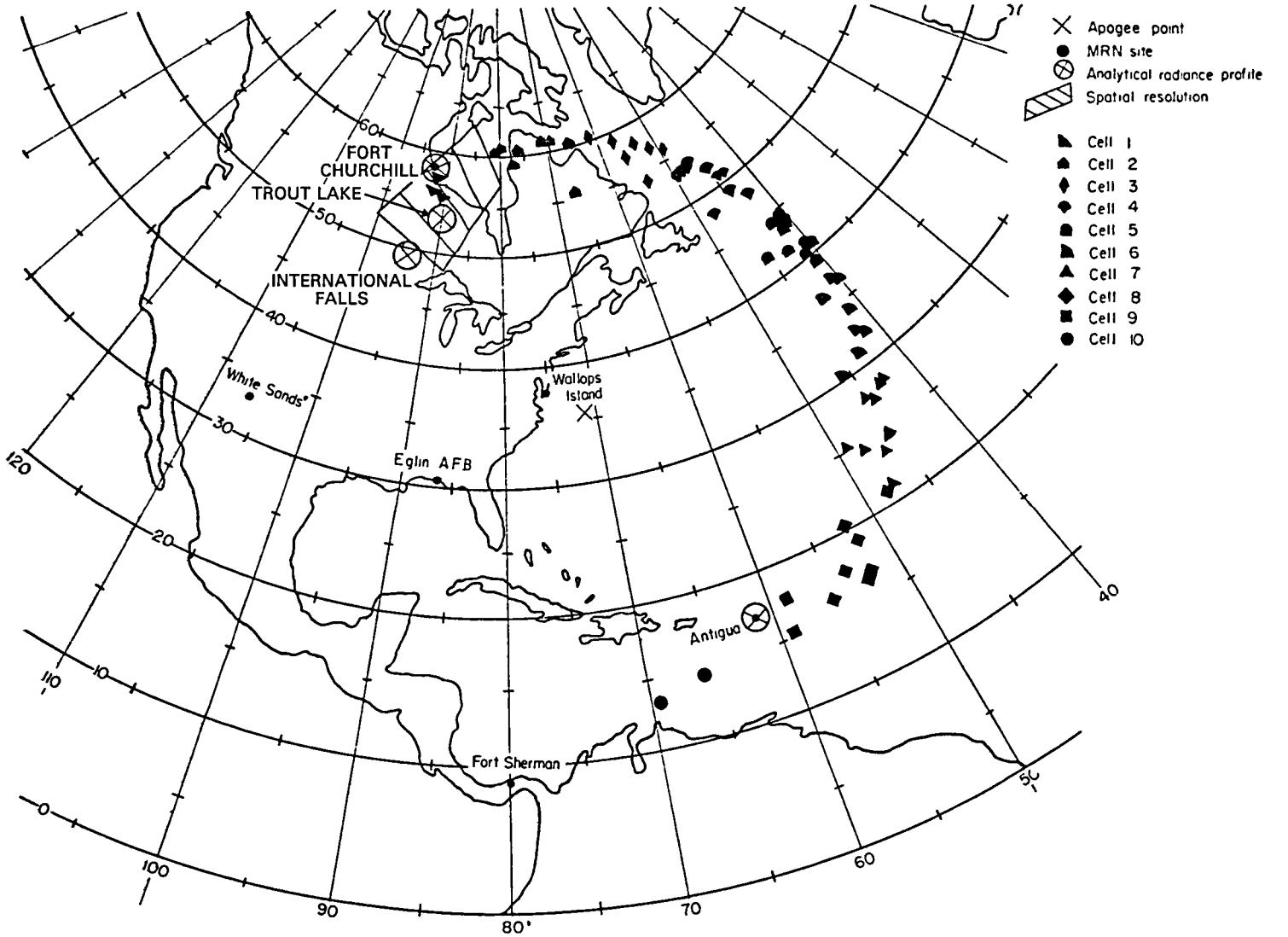

(a) 615 cm^{-1} to 715 cm^{-1} (CO_2).

Figure 2-22. Geographic Location of Horizon Radiance Profiles for Winter Conditions

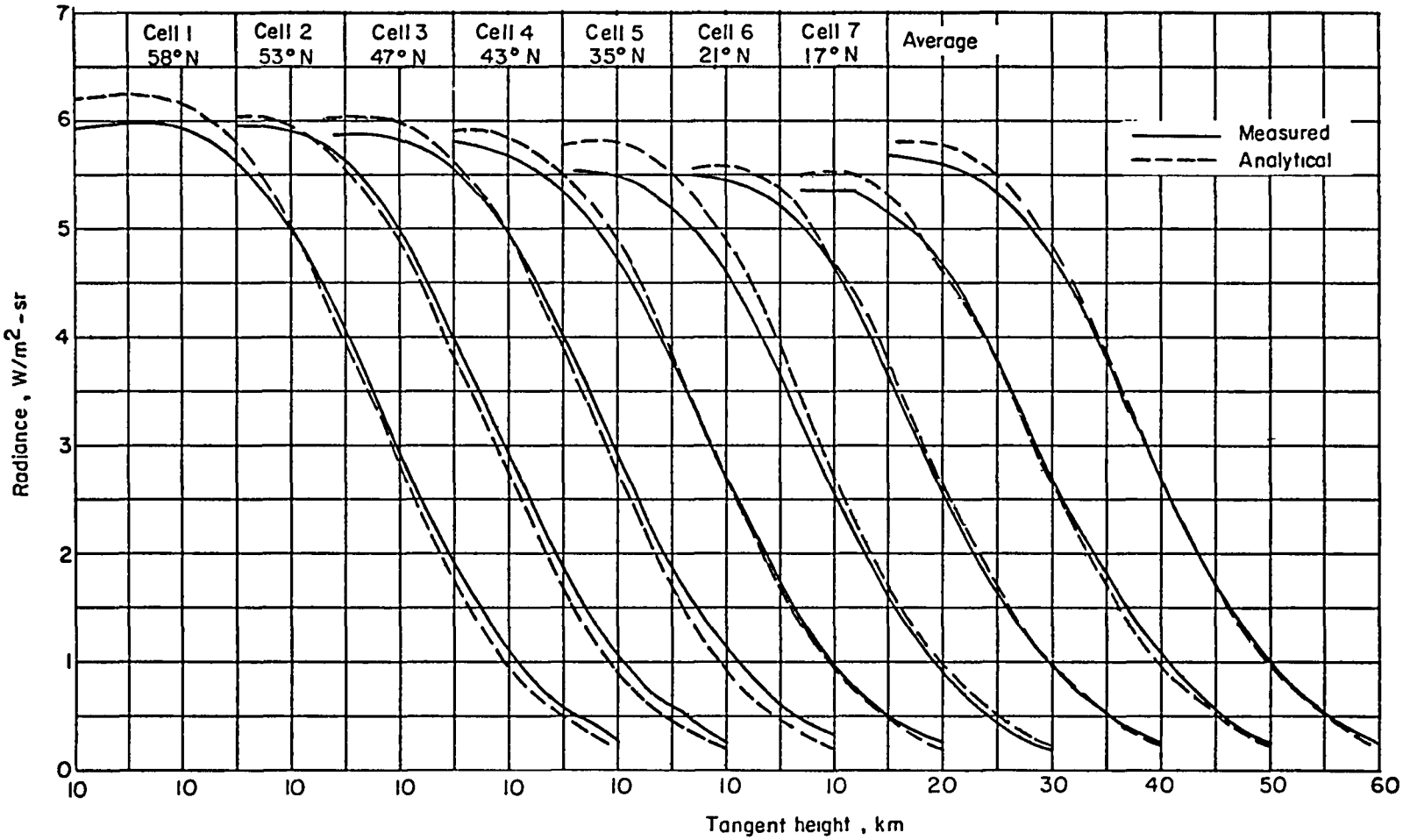

Figure 2-23. Comparison of Measured and Analytical Horizon Radiance Profiles for Summer Conditions in the CO_2 Band

In contrast, the comparison of winter profiles was not as straightforward. This is a result of the high horizontal temperature gradients that exist in the winter atmosphere at altitudes above 20 kilometers, where most of the radiance in the CO_2 band originates. Figure 2-24 illustrates the range of profiles that resulted from radiosonde data from three locations within the cell (illustrated by the box in Figure 2-22) associated with the measurement. This is evidence that the application of a correction to IR scanner attitude data based on average atmospheric conditions during the winter months may result in less improvement in attitude accuracy than similar corrections for summer, spring, and fall conditions, when conditions are more typical of the equatorial latitudes. One further result of the Project Scanner measurements was direct evidence for the seasonal and latitude-dependent variations of the radiance profiles for the CO_2 absorption band. These results are presented in Figure 2-25.

2.2.4 IR SCANNER ACCURACY LIMITS

The results of the Honeywell analysis and the LRC Project Scanner measurements were translated into an estimate of the IR scanner attitude determination performance accuracy by Dodgen and Curfman (Reference 6). The estimate is based on the assumption that the raw IR sensor data are corrected by the application of a deterministic oblateness-like correction, derived from mean atmospheric data, to compensate for the effects of seasonal and geographic IR radiance variations. The estimate also assumes that the IR sensor is ideal and that all of the attitude error originates from uncertainties associated with the response of the sensor to nonsystematic (and, therefore, not modeled) variations in the Earth IR profile. The highest accuracy is estimated to occur for a hypothetical IR scanner with a passband between 14 and 16 micrometers and a locator detecting a threshold

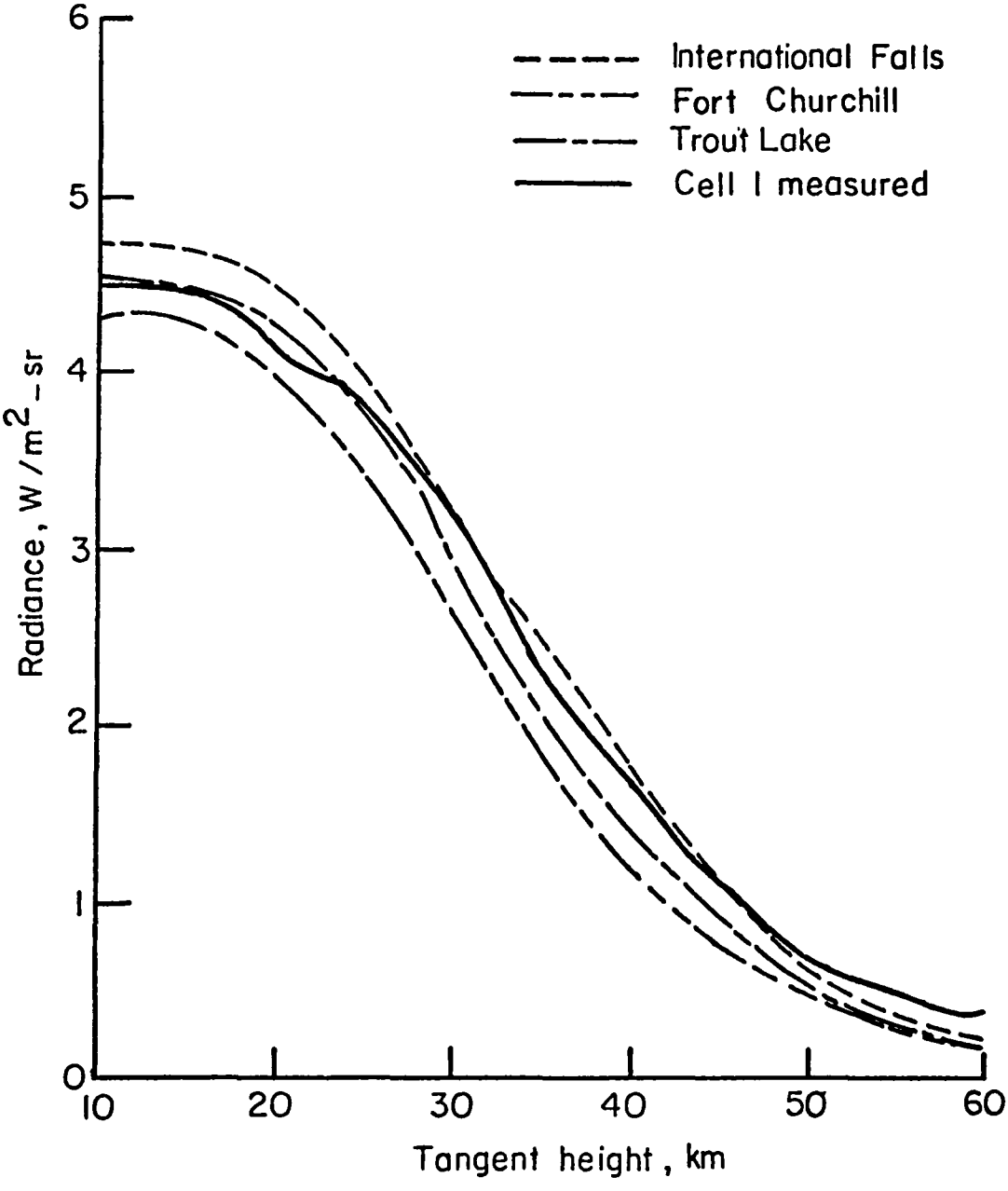

Figure 2-24. Comparison of Measured and Analytical Horizon Radiance Profiles for Winter Conditions in the CO_2 Band

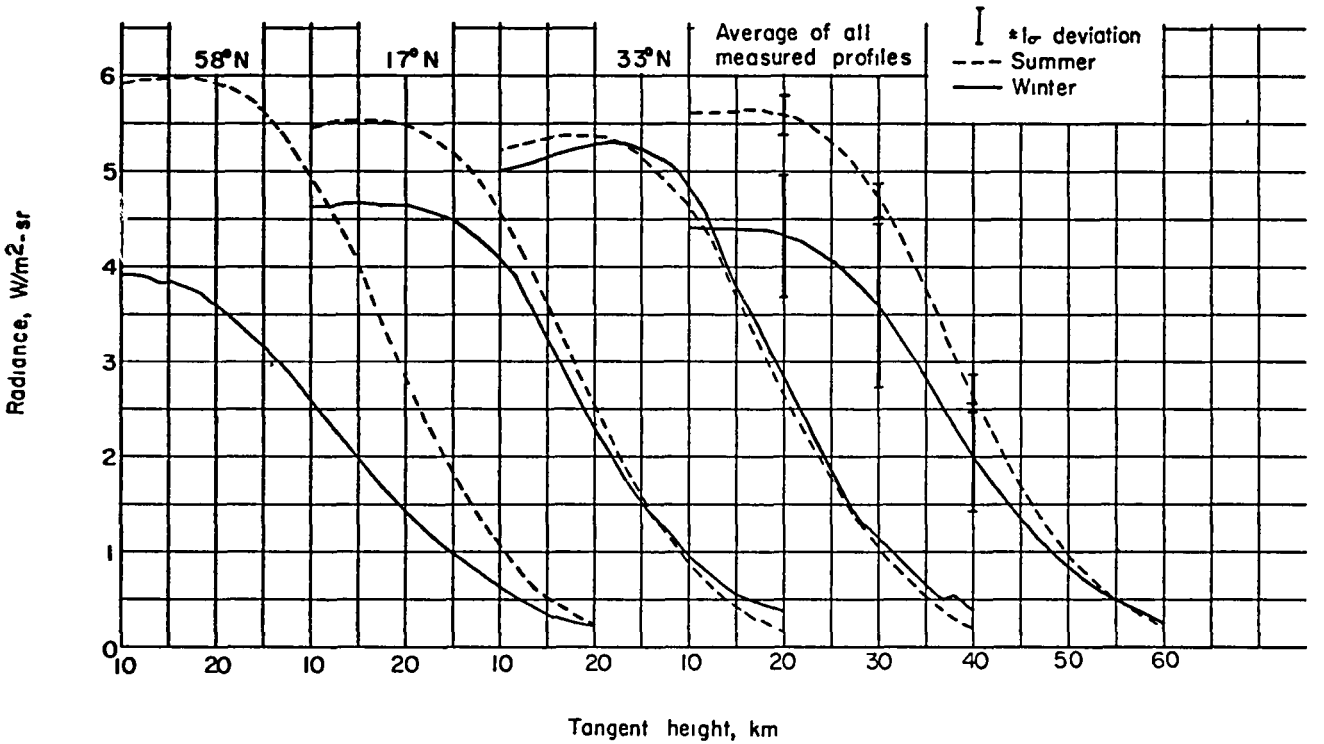

Figure 2-25. Seasonal Variation of Measured Radiance Profiles From Project Scanner in the CO_2 Band

based on the integral of a normalized radiance profile. The results for horizon altitude detection accuracy in November are reproduced here in Figures 2-26, 2-27, and 2-28 for examples of hypothetical sensors with fixed-threshold detection logic and integral locator logic with the following characteristics:

- Edge tracker--5 degrees by 2 hertz vertical dither
- Detector--thermistor bolometer
- Optics--2 inches in diameter
- FOV--1 degree by 4 degrees
- Radiometric efficiency--18 percent
- Detection logic
  - Threshold of integrated radiance
  - Threshold of normalized integrated radiance
- Noise equivalent radiance-- 0.025 $W/m^2/sr$
- Horizon sensitivity-- 2 kilometers, signal-to-noise ratio equal to 10

The 1σ limits of attitude determination uncertainty for a single-beam integral of the normalized radiance detector are presented as a function of spacecraft altitude in Figure 2-29 (Reference 6). The results shown correspond to tangent height-sensing accuracies of 3 kilometers (the "best" estimate), 6 kilometers, and a shaded region corresponding to the then-current range of accuracy. The results for a dual-beam sensor with an estimated horizon altitude sensing accuracy of 1.5 kilometers (1σ) are also shown.

The Dodgen and Curfman analysis shows the lower limits of error for a hypothetical IR sensor based on the observed stability of the atmospheric profiles relative to an average atmosphere for all latitudes in November. The translation of this estimate into an operational performance accuracy

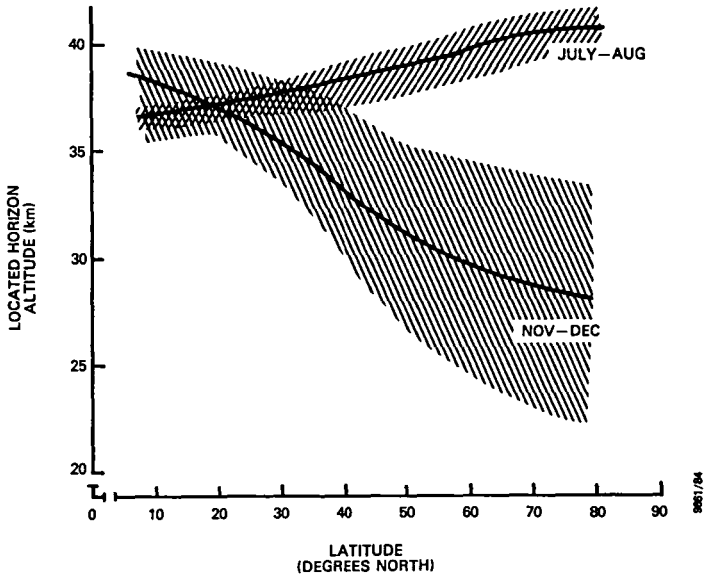

Figure 2-26. Variation of the Located Horizon Altitude for a 3-W/m^2/sr Fixed Threshold With Latitude for Two Seasons (Data Based on 3 Years)

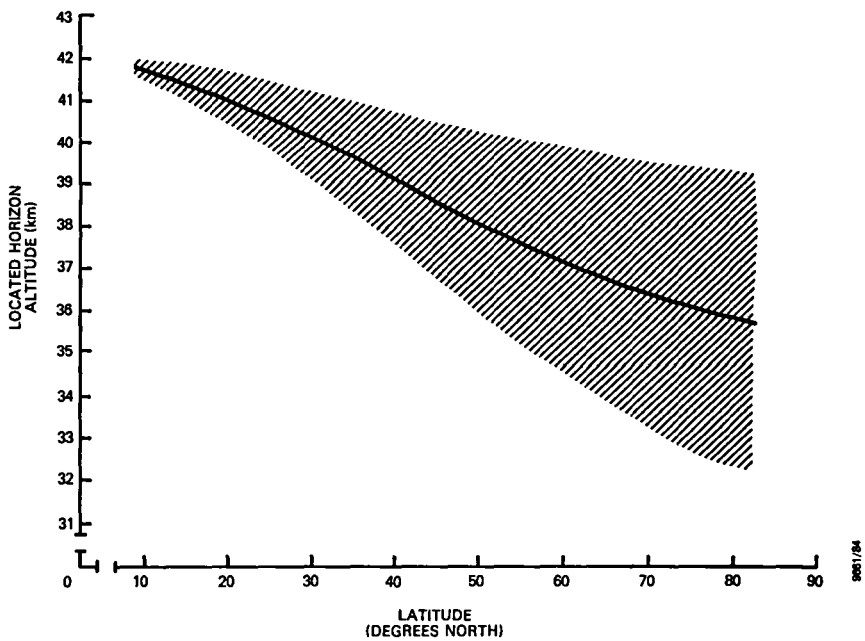

Figure 2-27. Variation of the Located Horizon Altitude for a 20-W/m^2/sr Threshold on Integrated Radiance With Latitude for November

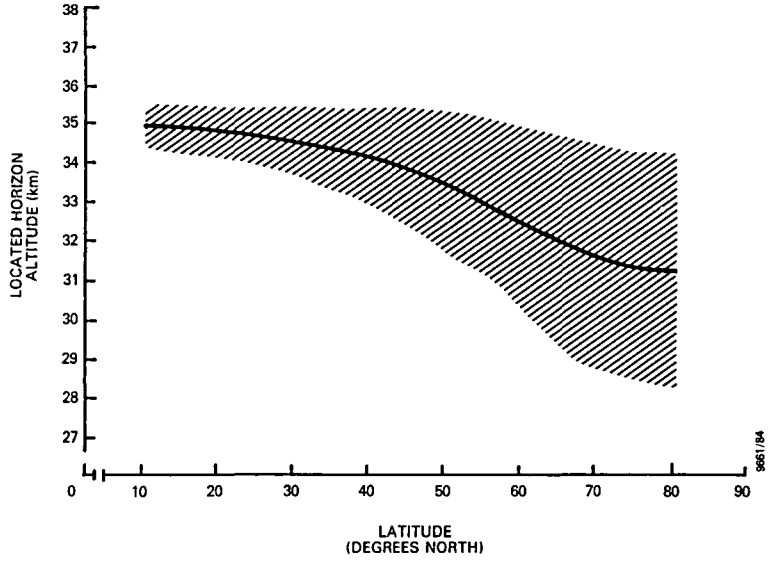

Figure 2-28. Variation of the Located Horizon Altitude for a Threshold Using Normalized Integrated Radiance With Latitude for November (Data Based on 3 Years)

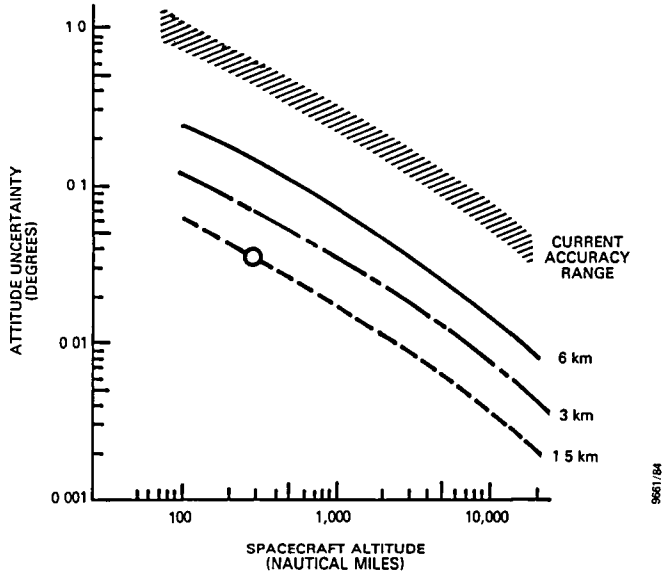

Figure 2-29. Single-Beam Horizon Sensor Angular Uncertainty Caused by Horizon Radiance Variations

for a real IR sensing hardware system requires detailed analysis of the optical and electronics properties of the hardware. IR sensors have been flown since the time of the Dodgen and Curfman report with fixed threshold, normalized threshold, and normalized derivative threshold locator logic. The Dodgen and Curfman results can be applied directly only for estimates of the performance of the fixed threshold sensor and, in this application, accuracy falls short of the estimate because of the wider passbands used on the fixed threshold sensors for SAS-3, AEM, and Magsat. The sensors with normalized threshold locator logic have horizon altitude detection responses that are determined by the variation in radiance in the portion of the scan used for threshold level computation. This portion of the scan typically corresponds to negative tangent heights near -1000 kilometers. The analysis of radiance variations at this viewing location is highly dependent on the width of the IR passband and the degree to which the passband encroaches on the portion of the Earth IR spectrum that originates from the Earth with limited clear air attenuation. Even if the passband is confined to the narrow region analyzed in the LRC reports, the effect of variations in the threshold level on the altitude of the detected horizon is greatly influenced by the scanner rotation rate and the rise time and delay of the Earth pulse signal processing electronics.

Aside from the details of the IR sensor hardware, there are other factors to be resolved regarding the sensor calibration and alignment, the effects of telemetry digitization, and the availability of an absolute attitude reference or a procedure to perform good in-flight calibration and verification of the IR sensing system to get a good estimate of the performance accuracy of the system. These comments have been offered here to ensure that a clear understanding of

the meaning of the Dodgen and Curfman result is obtained, i.e., that reaching their high accuracy estimate is clearly a challenge to the technology.

2.3 LMSC IR RADIANCE MODEL

The LMSC radiance modeling analysis was performed in preparation for Seasat, to provide more accurate estimates of the radiance profile for the wider spectral passband filter of the ITHACO IR scanner. The passband for the Seasat IR scanner is illustrated in Figure 2-30 (Reference 8). The extended regions of transmittance below 14 micrometers and above 16 micrometers indicated the need to include the effects of water vapor and ozone in the CORPS program. Also because of the wider passband, it was necessary to perform an analysis to determine the degree of sensitivity of this system to clouds occurring at altitudes up to the top of the tropopause.

To compute horizon radiance profiles necessary for modeling the systematic seasonal and geographic IR radiance variation, LMSC used two sources of atmospheric temperature data (Reference 8). These were balloon data, averaged over several years, for altitudes up to 25 kilometers, and rocket data for altitudes above 25 kilometers. Temperature averages were performed for every 10 degrees of latitude between 0^{o}N and 70^{o}N for January, April, July, and October. These averages were then used 6 months out of phase to represent the southern latitudes (i.e., January 60^{o}N was used for July 60^{o}S). The data for latitudes 80^{o} and 90^{o} were constructed by interpolating the 60^{o} and 70^{o} data maintaining zero slope at 90^{o}. Parametric studies were performed to evaluate changes in the Seasat radiance profiles resulting from water vapor ratios of 30 percent, 65 percent, and 135 percent of nominal and from ozone levels 300 percent of nominal.

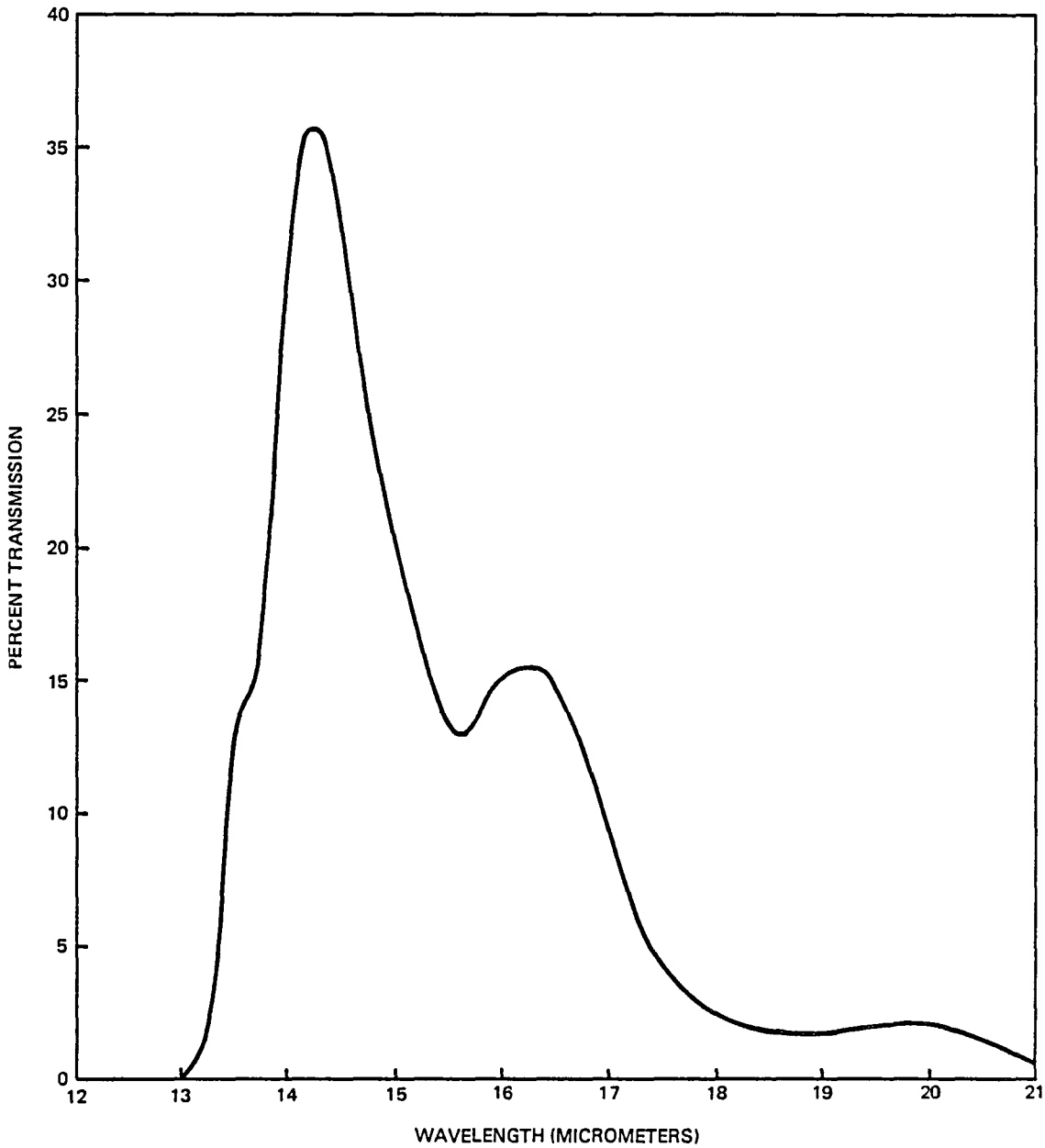

Figure 2-30. Spectral Response Function of the ITHACO Filter Used on the Seasat IR Scanner

2.3.1 SEASAT IR RADIANCE MODEL

During the prelaunch phase of the Seasat attitude support provided by GSFC, an analysis was performed to evaluate the flight performance accuracy of the Seasat IR scanners (References 9 and 14). It was concluded that, to achieve the attitude determination accuracy required for support of the Seasat science data, a correction to IR scanner pitch and roll for systematic horizon radiance variations was required. These systematic pitch and roll radiance-induced corrections were computed by CSC using horizon radiance profiles generated by LMSC, tailored specifically to the broader Seasat IR scanner passband.

The profiles were used as the Earth IR model input to a program that simulated the flight geometry and signal processing electronics of the Seasat IR scanners (see Section 3). The program produced a horizon altitude correction for the four horizon contact points corresponding to every 10 degrees of subsatellite latitude around the orbit. The corrections for April and July, with north and south latitudes interchanged, were assumed to be equivalent to corrections for October and January, respectively. These data were then interpolated over latitude and date to obtain daily corrections for all orbital positions throughout the year. To evaluate the accuracy of the model for radiance-induced pitch and roll corrections, LMSC prepared radiance profile data for various mixing ratios of water vapor and ozone and simulating the effects of clouds at equatorial latitudes. The analysis concluded that the effects of extreme variations in water vapor and ozone mixing ratios were minimal for the Seasat scanner, but that sensitivity to cold clouds was severe when comparing the effects with the attitude determination accuracy requirement. The following discussion summarizes the LMSC radiance modeling procedure (References 8 and 15) and the analysis performed by CSC, using

that data, to establish the pitch and roll errors for Seasat attitude determination.

The CO_2 and water vapor contributions were computed using the absorption coefficients of Anding, Kauth, and Turner (Reference 16) augmented to 18 additional wavelengths to accommodate the wide passband of the Seasat scanner. The LMSC analysis begins with the expression for radiance $N(\lambda)$ at wavelength λ sensed along an optical path viewing from space to Earth:

$$N(\lambda) = \beta(\lambda) \cdot \varepsilon(\lambda) \cdot \tau(\lambda)\Big|_{s=s_0} + \int_{s_0}^{s} \beta(\lambda)\ \varepsilon(\lambda)\ \frac{d\tau(\lambda)}{ds}\, ds \quad (2\text{-}5)$$

where $\beta(\lambda)$ is the Planck radiation function for the path increment ds, $\varepsilon(\lambda)$ is the emissivity of the increment ds, $\tau(\lambda)$ is the transmissivity of the path increment ds, and s is the optical path. The subscript 0 refers to the boundary, nominally the Earth. The radiance along path s for wavelength λ is then integrated over the IR scanner passband response function $F(\lambda)$ to obtain one point on the radiance profile:

$$R_s = \int_{\lambda_1}^{\lambda_2} F(\lambda)\ N(\lambda)\ d\lambda \quad (2\text{-}6)$$

where the subscript s assigns the radiance to the specific optical path used in Equation (2-5).

The LMSC model divides the Earth's atmosphere into 31 shells and computes radiance through this representative volume of gas as a function of viewing geometry. When the optical path passes from space through the volume and intersects the

Earth, the computed radiance is labeled according to zenith angle. (The angle between the line of sight and the local vertical at the point of intersection with the Earth.) When the optical path passes through the volume without intersecting the Earth, the radiance point is labeled according to tangent height (h), where tangent height is the minimum altitude from the hard Earth surface to the optical path. This geometry is illustrated in Figure 2-1. A single horizon radiance profile is a list of 43 radiance values for 8 zenith angles and 35 tangent heights up to 80 kilometers. There are 19 profiles (one for each 10-degree latitude bin), in a set, and one set each for January, April, July, and October.

Profiles for April and July are presented in Tables 2-2 through 2-5. The January and October profiles can be obtained by inverting the latitude assignments on the July and April data, respectively. Graphs of the January and April profiles are presented in Figures 2-31 and 2-32. Because little latitude-dependent variation occurs in the April data, only the extreme profiles are plotted. The solid circles illustrate the point at which the profile reaches 50 percent of its amplitude between 70 and 80 degrees zenith angle, thus illustrating profile tangent height variations.

2.3.2 PARAMETRIC STUDIES

Because of the wider passband of the Seasat IR scanners, radiance profiles were synthesized by LMSC, including the effects from the atmospheric constituents water vapor and ozone. The analysis showed that various percentages of water vapor and ozone had little effect on the shape of the radiance profiles for Seasat. To illustrate this, the integrand of Equation (2-6) is plotted in Figure 2-33 (Reference 8) for various values of water vapor and ozone

Table 2-2. Horizon Radiance Data (April-North) Average Atmosphere (Radiance is in $W/m^2/sr$)

ZETA/TNGT	0N	10N	20N	30N	40N	50N	60N	70N	80N	90N
0.0	0.2225E-03	0.2247E-03	0.2235E-03	0.2189E-03	0.2164E-03	0.2098E-03	0.2063E-03	0.1971E-03	0.1944E-03	0.1970E-03
45.0	0.2134E-03	0.2153E-03	0.2145E-03	0.2106E-03	0.2096E-03	0.2048E-03	0.2027E-03	0.1944E-03	0.1924E-03	0.1947E-03
60.0	0.2057E-03	0.2075E-03	0.2070E-03	0.2039E-03	0.2041E-03	0.2010E-03	0.1999E-03	0.1922E-03	0.1907E-03	0.1928E-03
70.0	0.1994E-03	0.2010E-03	0.2009E-03	0.1983E-03	0.1995E-03	0.1980E-03	0.1978E-03	0.1902E-03	0.1893E-03	0.1912E-03
75.0	0.1961E-03	0.1975E-03	0.1976E-03	0.1953E-03	0.1971E-03	0.1965E-03	0.1968E-03	0.1891E-03	0.1886E-03	0.1904E-03
80.0	0.1927E-03	0.1940E-03	0.1944E-03	0.1924E-03	0.1948E-03	0.1953E-03	0.1959E-03	0.1881E-03	0.1879E-03	0.1896E-03
85.0	0.1894E-03	0.1905E-03	0.1914E-03	0.1896E-03	0.1927E-03	0.1944E-03	0.1952E-03	0.1869E-03	0.1871E-03	0.1887E-03
87.5	0.1878E-03	0.1887E-03	0.1899E-03	0.1882E-03	0.1915E-03	0.1939E-03	0.1948E-03	0.1862E-03	0.1867E-03	0.1881E-03
0.0	0.1867E-03	0.1876E-03	0.1889E-03	0.1873E-03	0.1907E-03	0.1934E-03	0.1944E-03	0.1858E-03	0.1863E-03	0.1877E-03
5.0	0.1846E-03	0.1856E-03	0.1870E-03	0.1858E-03	0.1866E-03	0.1900E-03	0.1892E-03	0.1806E-03	0.1815E-03	0.1831E-03
10.0	0.1736E-03	0.1778E-03	0.1750E-03	0.1718E-03	0.1736E-03	0.1779E-03	0.1791E-03	0.1728E-03	0.1738E-03	0.1750E-03
15.0	0.1509E-03	0.1513E-03	0.1543F-03	0.1558E-03	0.1615E-03	0.1658E-03	0.1668E-03	0.1597E-03	0.1608E-03	0.1626E-03
20.0	0.1441E-03	0.1446E-03	0.1463F-03	0.1437F-03	0.1447E-03	0.1468E-03	0.1451E-03	0.1347E-03	0.1378E-03	0.1404E-03
22.0	0.1397E-03	0.1404E-03	0.1414F-03	0.1380E-03	0.1368E-03	0.1384F-03	0.1350E-03	0.1217E-03	0.1256E-03	0.1283E-03
24.0	0.1352E-03	0.1358E-03	0.1361E-03	0.1305E-03	0.1274E-03	0.1286E-03	0.1234E-03	0.1093E-03	0.1125E-03	0.1150E-03
26.0	0.1294F-03	0.1299E-03	0.1297E-03	0.1231E-03	0.1189E-03	0.1199E-03	0.1133E-03	0.9896E-04	0.9924E-04	0.1001E-03
28.0	0.1231E-03	0.1234E-03	0.1226E-03	0.1155E-03	0.1109E-03	0.1120E-03	0.1043E-03	0.8959E-04	0.8577E-04	0.8271E-04
30.0	0.1151E-03	0.1155F-03	0.1134E-03	0.1064F-03	0.1021E-03	0.1036E-03	0.9464E-04	0.8012E-04	0.7366E-04	0.6609E-04
32.0	0.1045E-03	0.1048E-03	0.1017E-03	0.9513E-04	0.9161E-04	0.9346E-04	0.8391E-04	0.7022E-04	0.6320E-04	0.5561E-04
34.0	0.9205F-04	0.9213F-04	0.8870E-04	0.8263E-04	0.7985E-04	0.8186E-04	0.7249E-04	0.5970E-04	0.5323E-04	0.4646E-04
36.0	0.7833E-04	0.7804E-04	0.7496E-04	0.6957E-04	0.6771E-04	0.6952E-04	0.6138E-04	0.4920E-04	0.4520E-04	0.3978E-04
38.0	0.6555E-04	0.6504E-04	0.6250F-04	0.5798E-04	0.5661E-04	0.5774E-04	0.5147E-04	0.4199E-04	0.3945E-04	0.3463E-04
40.0	0.5372F-04	0.5307E-04	0.5107E-04	0.4780E-04	0.4680E-04	0.4735E-04	0.4277E-04	0.3518E-04	0.3369E-04	0.2929E-04
42.0	0.4368F-04	0.4295E-04	0.4145E-04	0.3874E-04	0.3750E-04	0.3791E-04	0.3443E-04	0.2817E-04	0.2822E-04	0.2537E-04
44.0	0.3420E-04	0.3348E-04	0.3241E-04	0.3036E-04	0.2975E-04	0.3024E-04	0.2750E-04	0.2284E-04	0.2403E-04	0.2192E-04
46.0	0.2654E-04	0.2594F-04	0.2512F-04	0.2358F-04	0.2330E-04	0.2356E-04	0.2165E-04	0.1830E-04	0.1984E-04	0.1821E-04
48.0	0.2028F-04	0.1978E-04	0.1917E-04	0.1797E-04	0.1789E-04	0.1806E-04	0.1662E-04	0.1416E-04	0.1592E-04	0.1470E-04
50.0	0.1497F-04	0.1454E-04	0.1408E-04	0.1331E-04	0.1323E-04	0.1341E-04	0.1236E-04	0.1061E-04	0.1224E-04	0.1137E-04
52.0	0.1081E-04	0.1045F-04	0.1015E-04	0.9639E-05	0.9560E-05	0.9776E-05	0.8934E-05	0.7736E-05	0.8850E-05	0.8366E-05
54.0	0.7577E-05	0.7275E-05	0.7107E-05	0.6815E-05	0.6769E-05	0.6947E-05	0.6365E-05	0.5523E-05	0.6287E-05	0.6050E-05
56.0	0.5143F-05	0.4926F-05	0.4854E-05	0.4720E-05	0.4700E-05	0.4803E-05	0.4445E-05	0.3853E-05	0.4408E-05	0.4172E-05
58.0	0.3380E-05	0.3256E-05	0.3254E-05	0.3238E-05	0.3263E-05	0.3318E-05	0.3090E-05	0.2644E-05	0.3046E-05	0.2884E-05
60.0	0.2191E-05	0.2119E-05	0.2174F-05	0.2207E-05	0.2227E-05	0.2271E-05	0.2219E-05	0.1796E-05	0.2086E-05	0.1925E-05
62.0	0.1384E-05	0.1354L-05	0.1442E-05	0.1492E-05	0.1508E-05	0.1547E-05	0.1449E-05	0.1216E-05	0.1407E-05	0.1294E-05
64.0	0.8652E-06	0.8555E-06	0.9481E-06	0.9958E-06	0.1011E-05	0.1042E-05	0.9807E-06	0.8200E-06	0.9396E-06	0.8543E-06
66.0	0.5397E-06	0.5383E-06	0.6101E-06	0.6596E-06	0.6731E-06	0.6943E-06	0.6576E-06	0.5493E-06	0.6174E-06	0.5588E-06
68.0	0.3394E-06	0.3401E-06	0.4023E-06	0.4324E-06	0.4414E-06	0.4555E-06	0.4328E-06	0.3610E-06	0.4000E-06	0.3620E-06
70.0	0.2179E-06	0.2176E-06	0.2590F-06	0.2854E-06	0.2896E-06	0.2984E-06	0.2848E-06	0.2360E-06	0.2547E-06	0.2306E-06
72.0	0.1418E-06	0.1404E-06	0.1659E-06	0.1847E-06	0.1856E-06	0.1898E-06	0.1829E-06	0.1503E-06	0.1622E-06	0.1434E-06
74.0	0.9333E-07	0.9178E-07	0.1067E-06	0.1180E-06	0.1167E-06	0.1173E-06	0.1149E-06	0.9360E-07	0.1017E-06	0.8777E-07
76.0	0.6236E-07	0.6093E-07	0.6901E-07	0.7464E-07	0.7197E-07	0.7054E-07	0.7032E-07	0.5680E-07	0.6326E-07	0.5326E-07
78.0	0.4170E-07	0.4033E-07	0.4432E-07	0.4677E-07	0.4383E-07	0.4182E-07	0.4207E-07	0.3386E-07	0.3948E-07	0.3250E-07
80.0	0.2760E-07	0.2625E-07	0.2810E-07	0.2894E-07	0.2642E-07	0.2457E-07	0.2475E-07	0.2001E-07	0.2487E-07	0.2019E-07

Table 2-3. Horizon Radiance Data (April-South) Average Atmosphere

ZETA/TNGT	90S	80S	70S	60S	50S	40S	30S	20S	10S
0.0	0.1840E-03	0.1923E-03	0.1955E-03	0.2063E-03	0.2115E-03	0.2147E-03	0.2220E-03	0.2269E-03	0.2255E-03
45.0	0.1796E-03	0.1875E-03	0.1911E-03	0.2007E-03	0.2049E-03	0.2072E-03	0.2134E-03	0.2174E-03	0.2161E-03
60.0	0.1760E-03	0.1835E-03	0.1875E-03	0.1961E-03	0.1995E-03	0.2010E-03	0.2061E-03	0.2094E-03	0.2082E-03
70.0	0.1729E-03	0.1799E-03	0.1843E-03	0.1921E-03	0.1948E-03	0.1958E-03	0.2000E-03	0.2027E-03	0.2017E-03
75.0	0.1711E-03	0.1779E-03	0.1826E-03	0.1899E-03	0.1922E-03	0.1928E-03	0.1965E-03	0.1989E-03	0.1981E-03
80.0	0.1693E-03	0.1757E-03	0.1808E-03	0.1876E-03	0.1894E-03	0.1897E-03	0.1929E-03	0.1951E-03	0.1944E-03
85.0	0.1674E-03	0.1733E-03	0.1790E-03	0.1852E-03	0.1863E-03	0.1866E-03	0.1892E-03	0.1912E-03	0.1909E-03
87.5	0.1663E-03	0.1720E-03	0.1780E-03	0.1840E-03	0.1846E-03	0.1850E-03	0.1872E-03	0.1891E-03	0.1891E-03
0.0	0.1656E-03	0.1700E-03	0.1773E-03	0.1831E-03	0.1835E-03	0.1840E-03	0.1861E-03	0.1879E-03	0.1879E-03
5.0	0.1600E-03	0.1643E-03	0.1723E-03	0.1783E-03	0.1776E-03	0.1821E-03	0.1844E-03	0.1860E-03	0.1860E-03
10.0	0.1496E-03	0.1536E-03	0.1611E-03	0.1664E-03	0.1609E-03	0.1679E-03	0.1706E-03	0.1722E-03	0.1733E-03
15.0	0.1348E-03	0.1387E-03	0.1473E-03	0.1532E-03	0.1493E-03	0.1529E-03	0.1535E-03	0.1540E-03	0.1545E-03
20.0	0.1115E-03	0.1165E-03	0.1255E-03	0.1321E-03	0.1310E-03	0.1379E-03	0.1417E-03	0.1456E-03	0.1460E-03
22.0	0.1017E-03	0.1071E-03	0.1154E-03	0.1231E-03	0.1233E-03	0.1307E-03	0.1352E-03	0.1396E-03	0.1404E-03
24.0	0.9403E-04	0.9904E-04	0.1067E-03	0.1143E-03	0.1146E-03	0.1224E-03	0.1282E-03	0.1331E-03	0.1349E-03
26.0	0.8835E-04	0.9260E-04	0.1001E-03	0.1060E-03	0.1064E-03	0.1144E-03	0.1201E-03	0.1255E-03	0.1285E-03
28.0	0.8367E-04	0.8721E-04	0.9330E-04	0.9747E-04	0.9827E-04	0.1063E-03	0.1118E-03	0.1175E-03	0.1215E-03
30.0	0.7914E-04	0.8077E-04	0.8455E-04	0.8824E-04	0.8988E-04	0.9728E-04	0.1026E-03	0.1083E-03	0.1129E-03
32.0	0.7011E-04	0.7175E-04	0.7415E-04	0.7787E-04	0.8039E-04	0.8674E-04	0.9154E-04	0.9711E-04	0.1018E-03
34.0	0.6066E-04	0.6204E-04	0.6278E-04	0.6654E-04	0.6960E-04	0.7515E-04	0.7936E-04	0.8494E-04	0.8934E-04
36.0	0.5174E-04	0.5270E-04	0.5247E-04	0.5547E-04	0.5881E-04	0.6336E-04	0.6666E-04	0.7208E-04	0.7589E-04
38.0	0.4381E-04	0.4441E-04	0.4329E-04	0.4573E-04	0.4877E-04	0.5254E-04	0.5544E-04	0.6038E-04	0.6353E-04
40.0	0.3746E-04	0.3790E-04	0.3582E-04	0.3796E-04	0.4009E-04	0.4333E-04	0.4579E-04	0.4961E-04	0.5205E-04
42.0	0.3072E-04	0.3097E-04	0.2833E-04	0.3014E-04	0.3158E-04	0.3460E-04	0.3728E-04	0.4056E-04	0.4235E-04
44.0	0.2513E-04	0.2524E-04	0.2280E-04	0.2408E-04	0.2481E-04	0.2716E-04	0.2927E-04	0.3201E-04	0.3322E-04
46.0	0.2039E-04	0.2036E-04	0.1821E-04	0.1906E-04	0.1946E-04	0.2150E-04	0.2313E-04	0.2532E-04	0.2590E-04
48.0	0.1576E-04	0.1580E-04	0.1407E-04	0.1459E-04	0.1479E-04	0.1645E-04	0.1784E-04	0.1936E-04	0.1993E-04
50.0	0.1165E-04	0.1159E-04	0.1051E-04	0.1075E-04	0.1079E-04	0.1202E-04	0.1322E-04	0.1444E-04	0.1480E-04
52.0	0.8276E-05	0.8236E-05	0.7627E-05	0.7771E-05	0.7634E-05	0.8524E-05	0.9552E-05	0.1063E-04	0.1082E-04
54.0	0.5788E-05	0.5791E-05	0.5414E-05	0.5558E-05	0.5323E-05	0.5898E-05	0.6753E-05	0.7681E-05	0.7705E-05
56.0	0.3991E-05	0.4096E-05	0.3867E-05	0.3897E-05	0.3604E-05	0.3952E-05	0.4685E-05	0.5441E-05	0.5312E-05
58.0	0.2713E-05	0.2733E-05	0.2612E-05	0.2684E-05	0.2396E-05	0.2624E-05	0.3193E-05	0.3794E-05	0.3616E-05
60.0	0.1836E-05	0.1849E-05	0.1774E-05	0.1813E-05	0.1560E-05	0.1715E-05	0.2195E-05	0.2602E-05	0.2396E-05
62.0	0.1231E-05	0.1239E-05	0.1189E-05	0.1202E-05	0.9938E-06	0.1100E-05	0.1482E-05	0.1748E-05	0.1563E-05
64.0	0.8208E-06	0.8302E-06	0.7864E-06	0.7908E-06	0.6425E-06	0.7129E-06	0.9766E-06	0.1155E-05	0.1008E-05
66.0	0.5446E-06	0.5541E-06	0.5098E-06	0.5157E-06	0.4143E-06	0.4568E-06	0.6256E-06	0.7489E-06	0.6448E-06
68.0	0.3576E-06	0.3759E-06	0.3324E-06	0.3326E-06	0.2575E-06	0.2933E-06	0.4036E-06	0.4779E-06	0.4122E-06
70.0	0.2377E-06	0.2513E-06	0.2154E-06	0.2133E-06	0.1732E-06	0.1908E-06	0.2587E-06	0.3084E-06	0.2667E-06
72.0	0.1561E-06	0.1770E-06	0.1395E-06	0.1360E-06	0.1120E-06	0.1246E-06	0.1647E-06	0.1972E-06	0.1737E-06
74.0	0.1042E-06	0.1286E-06	0.8991E-07	0.8595E-07	0.7193E-07	0.8057E-07	0.1047E-06	0.1260E-06	0.1136E-06
76.0	0.6812E-07	0.9816E-07	0.5761E-07	0.5384E-07	0.4584E-07	0.5167E-07	0.6687E-07	0.8074E-07	0.7480E-07
78.0	0.4449E-07	0.7478E-07	0.3647E-07	0.3368E-07	0.2912E-07	0.3304E-07	0.4282E-07	0.5184E-07	0.4919E-07
80.0	0.2852E-07	0.5209E-07	0.2284E-07	0.2132E-07	0.1864E-07	0.2118E-07	0.2736E-07	0.3350E-07	0.3221E-07

Table 2-4. Horizon Radiance Data (July-North) Average Atmosphere

ZETA/TNGT	0N	10N	20N	30N	40N	50N	60N	70N	80N	90N
0.0	0.2237E-03	0.2256E-03	0.2258E-03	0.2299E-03	0.2304E-03	0.2339E-03	0.2359E-03	0.2362E-03	0.2430E-03	0.2441E-0
45.0	0.2143E-03	0.2162E-03	0.2165E-03	0.2208E-03	0.2223E-03	0.2275E-03	0.2311E-03	0.2319E-03	0.2396E-03	0.2411E-0
60.0	0.2064E-03	0.2082E-03	0.2087E-03	0.2134E-03	0.2159E-03	0.2226E-03	0.2276E-03	0.2290E-03	0.2373E-03	0.2390E-0
70.0	0.1997E-03	0.2015E-03	0.2022E-03	0.2071E-03	0.2107E-03	0.2191E-03	0.2254E-03	0.2273E-03	0.2369E-03	0.2391E-0
75.0	0.1958F-03	0.1977E-03	0.1986E-03	0.2037E-03	0.2079E-03	0.2174F-03	0.2247E-03	0.2269E-03	0.2374E-03	0.2398E-0
80.0	0.1919F-03	0.1939E-03	0.1951E-03	0.2002E-03	0.2052E-03	0.2163E-03	0.2246E-03	0.2272E-03	0.2392E-03	0.2420E-0
85.0	0.1880E-03	0.1900E-03	0.1916E-03	0.1968E-03	0.2029E-03	0.2157E-03	0.2254E-03	0.2284E-03	0.2425E-03	0.2458E-0
87.5	0.1860E-03	0.1881E-03	0.1899E-03	0.1951E-03	0.2017E-03	0.2155E-03	0.2258E-03	0.2290E-03	0.2441E-03	0.2477E-0
0.0	0.1848F-03	0.1869E-03	0.1888E-03	0.1941E-03	0.2009E-03	0.2152E-03	0.2258E-03	0.2292E-03	0.2448E-03	0.2484E-0
5.0	0.1826E-03	0.1845E-03	0.1869E-03	0.1922E-03	0.1986E-03	0.2132E-03	0.2227E-03	0.2266E-03	0.2426E-03	0.2464E-0
10.0	0.1691F-03	0.1705E-03	0.1724E-03	0.1779E-03	0.1836E-03	0.1986E-03	0.2117E-03	0.2167E-03	0.2330E-03	0.2369E-0
15.0	0.1498F-03	0.1516E-03	0.1554E-03	0.1612E-03	0.1685E-03	0.1864E-03	0.2017E-03	0.2066E-03	0.2240E-03	0.2289E-0
20.0	0.1412E-03	0.1431E-03	0.1465E-03	0.1503E-03	0.1566E-03	0.1704E-03	0.1834E-03	0.1869E-03	0.2043E-03	0.2107E-0
22.0	0.1351F-03	0.1372E-03	0.1404E-03	0.1433E-03	0.1492E-03	0.1628F-03	0.1743E-03	0.1767E-03	0.1957E-03	0.2021E-0
24.0	0.1295E-03	0.1317E-03	0.1344E-03	0.1361F-03	0.1421E-03	0.1538E-03	0.1637E-03	0.1651E-03	0.1861E-03	0.1920E-0
26.0	0.1246E-03	0.1255E-03	0.1272E-03	0.1277E-03	0.1343E-03	0.1451F-03	0.1540E-03	0.1546E-03	0.1762E-03	0.1812E-0
28.0	0.1175F-03	0.1186E-03	0.1196E-03	0.1196E-03	0.1264E-03	0.1366E-03	0.1445E-03	0.1446E-03	0.1662E-03	0.1704E-0
30.0	0.1099F-03	0.1098E-03	0.1104E-03	0.1105E-03	0.1168E-03	0.1268E-03	0.1345E-03	0.1346E-03	0.1563E-03	0.1600E-0
32.0	0.9947E-04	0.9836E-04	0.9857E-04	0.9950F-04	0.1053E-03	0.1148E-03	0.1224E-03	0.1228E-03	0.1444E-03	0.1469E-0
34.0	0.8685E-04	0.8549E-04	0.8631E-04	0.8710C-04	0.9220E-04	0.1010E-03	0.1085E-03	0.1092E-03	0.1285E-03	0.1315E-0
36.0	0.7288E-04	0.7172E-04	0.7285E-04	0.7380E-04	0.7837E-04	0.8654E-04	0.9369E-04	0.9441E-04	0.1121E-03	0.1150E-0
38.0	0.6015F-04	0.5935E-04	0.6074E-04	0.6167E-04	0.6561E-04	0.7264E-04	0.7931E-04	0.8076E-04	0.9707E-04	0.9990E-0
40.0	0.4863E-04	0.4822F-04	0.4983E-04	0.5048E-04	0.5389E-04	0.6005E-04	0.6607E-04	0.6801E-04	0.8221E-04	0.8481E-0
42.0	0.3922F-04	0.3914E-04	0.4078E-04	0.4103E-04	0.4406E-04	0.4833E-04	0.5358E-04	0.5570E-04	0.6813E-04	0.7032E-0
44.0	0.3075F-04	0.3079E-04	0.3225E-04	0.3222E-04	0.3470E-04	0.3833E-04	0.4290E-04	0.4544E-04	0.5620E-04	0.5806E-0
46.0	0.2413E-04	0.2420E-04	0.2538E-04	0.2517E-04	0.2706E-04	0.2988E-04	0.3381E-04	0.3601E-04	0.4530E-04	0.4695E-0
48.0	0.1906E-04	0.1912E-04	0.1971E-04	0.1942E-04	0.2080E-04	0.2306E-04	0.2647E-04	0.2860C-04	0.3685E-04	0.3779E-0
50.0	0.1451E-04	0.1454E-04	0.1474E-04	0.1446E-04	0.1544E-04	0.1710E-04	0.2007E-04	0.2192E-04	0.2881E-04	0.3007E-0
52.0	0.1089E-04	0.1087E-04	0.1080E-04	0.1055E-04	0.1125E-04	0.1257E-04	0.1480E-04	0.1633E-04	0.2209E-04	0.2329E-0
54.0	0.7914F-05	0.7895E-05	0.7702E-05	0.7465E-05	0.7955E-05	0.9020E-05	0.1068E-04	0.1192E-04	0.1653E-04	0.1765E-0
56.0	0.5565E-05	0.5555E-05	0.5323E-05	0.5126E-05	0.5409E-05	0.6294E-05	0.7525E-05	0.8452E-05	0.1176E-04	0.1266E-0
58.0	0.3800E-05	0.3809E-05	0.3607E-05	0.3384E-05	0.3646E-05	0.4264E-05	0.5143E-05	0.5846E-05	0.8226E-05	0.8979E-0
60.0	0.2472E-05	0.2480E-05	0.2331E-05	0.2172E-05	0.2344E-05	0.2773F-05	0.3438E-05	0.3884E-05	0.5370E-05	0.5977E-0
62.0	0.1566E-05	0.1574E-05	0.1463E-05	0.1346E-05	0.1465E-05	0.1750E-05	0.2202E-05	0.2529E-05	0.3377E-05	0.3732E-0
64.0	0.9681E-06	0.9744E-06	0.9044E-06	0.8282E-06	0.8962E-06	0.1076E-05	0.1371E-05	0.1600E-05	0.1992E-05	0.2216E-0
66.0	0.5886F-06	0.5927E-06	0.5522E-06	0.5071E-06	0.5355E-06	0.6413E-06	0.8255E-06	0.9738E-06	0.1107E-05	0.1207E-0
68.0	0.3575E-06	0.3598E-06	0.3383E-06	0.3118E-06	0.3151E-06	0.3711E-06	0.4786E-06	0.5700E-06	0.5786E-06	0.6131E-0
70.0	0.2233E-06	0.2252E-06	0.2135E-06	0.1946E-06	0.1852E-06	0.2088E-06	0.2659E-06	0.3171E-06	0.2841E-06	0.2960E-0
72.0	0.1423E-06	0.1450E-06	0.1374E-06	0.1219E-06	0.1082E-06	0.1139E-06	0.1412E-06	0.1666E-06	0.1293E-06	0.1339E-0
74.0	0.9139E-07	0.9488E-07	0.8820E-07	0.7557E-07	0.6221E-07	0.5927E-07	0.7143E-07	0.8270E-07	0.5737E-07	0.5784E-0
76.0	0.5914E-07	0.6311E-07	0.5644E-07	0.4638E-07	0.3482E-07	0.3017E-07	0.3402E-07	0.3808E-07	0.2533E-07	0.2401E-0
78.0	0.3776E-07	0.4179E-07	0.3575E-07	0.2818E-07	0.1964E-07	0.1513E-07	0.1595E-07	0.1710E-07	0.1190E-07	0.1041E-0
80.0	0.2338E-07	0.2704E-07	0.2221E-07	0.1670E-07	0.1120E-07	0.7870E-08	0.7810E-08	0.8064E-08	0.6761E-08	0.5706E-0

Table 2-5. Horizon Radiance Data (July-South) Average Atmosphere

ZETA/TNGT	90S	80S	70S	60S	50S	40S	30S	20S	10S
0.0	0.1619E-03	0.1648E-03	0.1695E-03	0.1804E-03	0.1923E-03	0.2027E-03	0.2111E-03	0.2212E-03	0.2247E-03
45.0	0.1579E-03	0.1607E-03	0.1649E-03	0.1759E-03	0.1876E-03	0.1973E-03	0.2034E-03	0.2115E-03	0.2150E-03
60.0	0.1542E-03	0.1569E-03	0.1608E-03	0.1719E-03	0.1835E-03	0.1929E-03	0.1970E-03	0.2033E-03	0.2068E-03
70.0	0.1504E-03	0.1532E-03	0.1568E-03	0.1682E-03	0.1798E-03	0.1897E-03	0.1915E-03	0.1963E-03	0.1997E-03
75.0	0.1480E-03	0.1507E-03	0.1542E-03	0.1658E-03	0.1777E-03	0.1880E-03	0.1885E-03	0.1924E-03	0.1958E-03
80.0	0.1450E-03	0.1478E-03	0.1511E-03	0.1632E-03	0.1755E-03	0.1866E-03	0.1854E-03	0.1882E-03	0.1916E-03
85.0	0.1412E-03	0.1442E-03	0.1474E-03	0.1600E-03	0.1730E-03	0.1856E-03	0.1823E-03	0.1839E-03	0.1873E-03
87.5	0.1391E-03	0.1421E-03	0.1454E-03	0.1583E-03	0.1717E-03	0.1850E-03	0.1807E-03	0.1816E-03	0.1851E-03
0.0	0.1379E-03	0.1409E-03	0.1442E-03	0.1572E-03	0.1709E-03	0.1845E-03	0.1796E-03	0.1802E-03	0.1837E-03
5.0	0.1336E-03	0.1369E-03	0.1399E-03	0.1524E-03	0.1685E-03	0.1830E-03	0.1776E-03	0.1780E-03	0.1812E-03
10.0	0.1283E-03	0.1236E-03	0.1270E-03	0.1402E-03	0.1544E-03	0.1687E-03	0.1634E-03	0.1621E-03	0.1660E-03
15.0	0.1055E-03	0.1087E-03	0.1111E-03	0.1255E-03	0.1398E-03	0.1541E-03	0.1459E-03	0.1427E-03	0.1451E-03
20.0	0.8741E-04	0.9092E-04	0.9154E-04	0.1054E-03	0.1197E-03	0.1377E-03	0.1338E-03	0.1338E-03	0.1379E-03
22.0	0.7942E-04	0.8341E-04	0.8426E-04	0.9788E-04	0.1122E-03	0.1310E-03	0.1283E-03	0.1292E-03	0.1336E-03
24.0	0.7135E-04	0.7487E-04	0.7806E-04	0.8995E-04	0.1035E-03	0.1232E-03	0.1211E-03	0.1244E-03	0.1292E-03
26.0	0.6225E-04	0.6459E-04	0.7023E-04	0.8150E-04	0.9463E-04	0.1159E-03	0.1142E-03	0.1189E-03	0.1235E-03
28.0	0.5179E-04	0.5362E-04	0.6062E-04	0.7226E-04	0.8538E-04	0.1095E-03	0.1067E-03	0.1126E-03	0.1170E-03
30.0	0.4189E-04	0.4379E-04	0.5185E-04	0.6257E-04	0.7555E-04	0.1035E-03	0.9765E-04	0.1044E-03	0.1087E-03
32.0	0.3359E-04	0.3555E-04	0.4383E-04	0.5248E-04	0.6522E-04	0.9593E-04	0.8702E-04	0.9402E-04	0.9773E-04
34.0	0.2662E-04	0.2839E-04	0.3576E-04	0.4261E-04	0.5468E-04	0.8590E-04	0.7595E-04	0.8242E-04	0.8503E-04
36.0	0.2173E-04	0.2315E-04	0.2903E-04	0.3497E-04	0.4521E-04	0.7350E-04	0.6502E-04	0.7006E-04	0.7134E-04
38.0	0.1782E-04	0.1903E-04	0.2374E-04	0.2945E-04	0.3751E-04	0.6077E-04	0.5452E-04	0.5863E-04	0.5903E-04
40.0	0.1453E-04	0.1554E-04	0.1938E-04	0.2439E-04	0.3075E-04	0.4936E-04	0.4514E-04	0.4826E-04	0.4796E-04
42.0	0.1196E-04	0.1279E-04	0.1595E-04	0.1981E-04	0.2458E-04	0.3906E-04	0.3616E-04	0.3911E-04	0.3887E-04
44.0	0.9821E-05	0.1047E-04	0.1300E-04	0.1610E-04	0.1965E-04	0.3049E-04	0.2877E-04	0.3088E-04	0.3054E-04
46.0	0.8093E-05	0.8535E-05	0.1066E-04	0.1310E-04	0.1577E-04	0.2376E-04	0.2261E-04	0.2450E-04	0.2422E-04
48.0	0.6255E-05	0.6531E-05	0.8415E-05	0.1029E-04	0.1233E-04	0.1780E-04	0.1735E-04	0.1882E-04	0.1892E-04
50.0	0.4443E-05	0.4630E-05	0.6448E-05	0.7923E-05	0.9409E-05	0.1310E-04	0.1286E-04	0.1411E-04	0.1432E-04
52.0	0.2991E-05	0.3138E-05	0.4788E-05	0.5921E-05	0.6990E-05	0.9359E-05	0.9367E-05	0.1031E-04	0.1060F-04
54.0	0.2052E-05	0.2174E-05	0.3469E-05	0.4414E-05	0.5090E-05	0.6550E-05	0.6691E-05	0.7347E-05	0.7603E-05
56.0	0.1477E-05	0.1534E-05	0.2487E-05	0.3187E-05	0.3673E-05	0.4488E-05	0.4651E-05	0.5051E-05	0.5280E-05
58.0	0.1018E-05	0.1118E-05	0.1750E-05	0.2268E-05	0.2600E-05	0.3026E-05	0.3188E-05	0.3416E-05	0.3568E-05
60.0	0.8000E-06	0.8615E-06	0.1215E-05	0.1589E-05	0.1809E-05	0.2024E-05	0.2123E-05	0.2238E-05	0.2320E-05
62.0	0.6406E-06	0.6892E-06	0.8240E-06	0.1113E-05	0.1253E-05	0.1354E-05	0.1394E-05	0.1438E-05	0.1471E-05
64.0	0.5227E-06	0.5652E-06	0.5554E-06	0.7714E-06	0.8633E-06	0.8914E-06	0.9003E-06	0.9030E-06	0.9170E-06
66.0	0.4399E-06	0.4662E-06	0.3721E-06	0.5256E-06	0.5889E-06	0.5815E-06	0.5695E-06	0.5539E-06	0.5642E-06
68.0	0.3694E-06	0.3871E-06	0.2456E-06	0.3525E-06	0.3967E-06	0.3763E-06	0.3557E-06	0.3395E-06	0.3480E-06
70.0	0.3052E-06	0.3200E-06	0.1632E-06	0.2352E-06	0.2643E-06	0.2458E-06	0.2240E-06	0.2136E-06	0.2200E-06
72.0	0.2492E-06	0.2620E-06	0.1084E-06	0.1565E-06	0.1735E-06	0.1603E-06	0.1425E-06	0.1363E-06	0.1412E-06
74.0	0.1965E-06	0.2074E-06	0.7218E-07	0.1028E-06	0.1139E-06	0.1032E-06	0.9069E-07	0.8692E-07	0.9111E-07
76.0	0.1624E-06	0.1744E-06	0.4764E-07	0.6732E-07	0.7425E-07	0.6596E-07	0.5765E-07	0.5543E-07	0.5903E-07
78.0	0.1137E-06	0.1223E-06	0.3112E-07	0.4397E-07	0.4787E-07	0.4204E-07	0.3616E-07	0.3501E-07	0.3765E-07
80.0	0.7567E-07	0.8039E-07	0.2030E-07	0.2882E-07	0.3099E-07	0.2679E-07	0.2237E-07	0.2165E-07	0.2323E-07

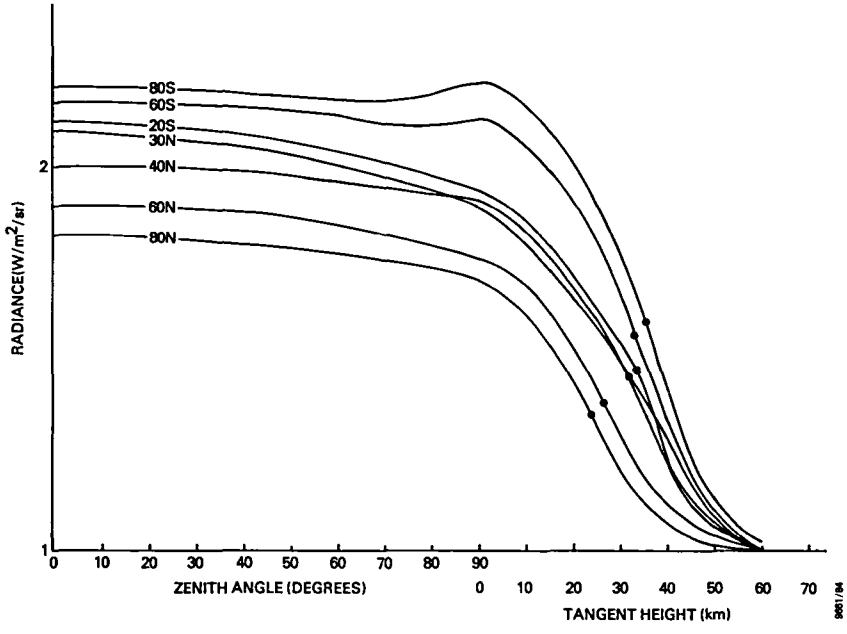

Figure 2-31. LMSC January Profiles for Seasat-1

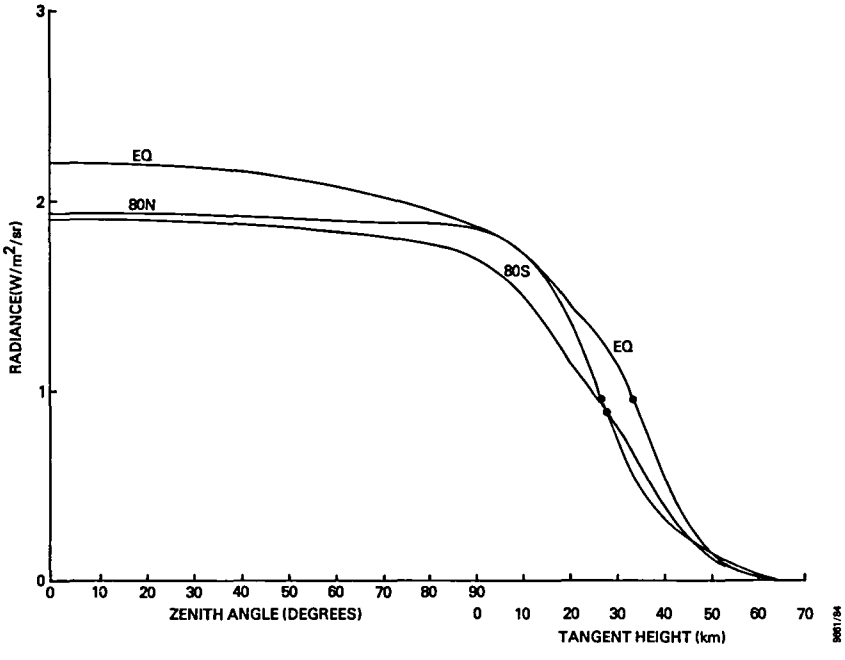

Figure 2-32. LMSC April Profiles for Seasat-1

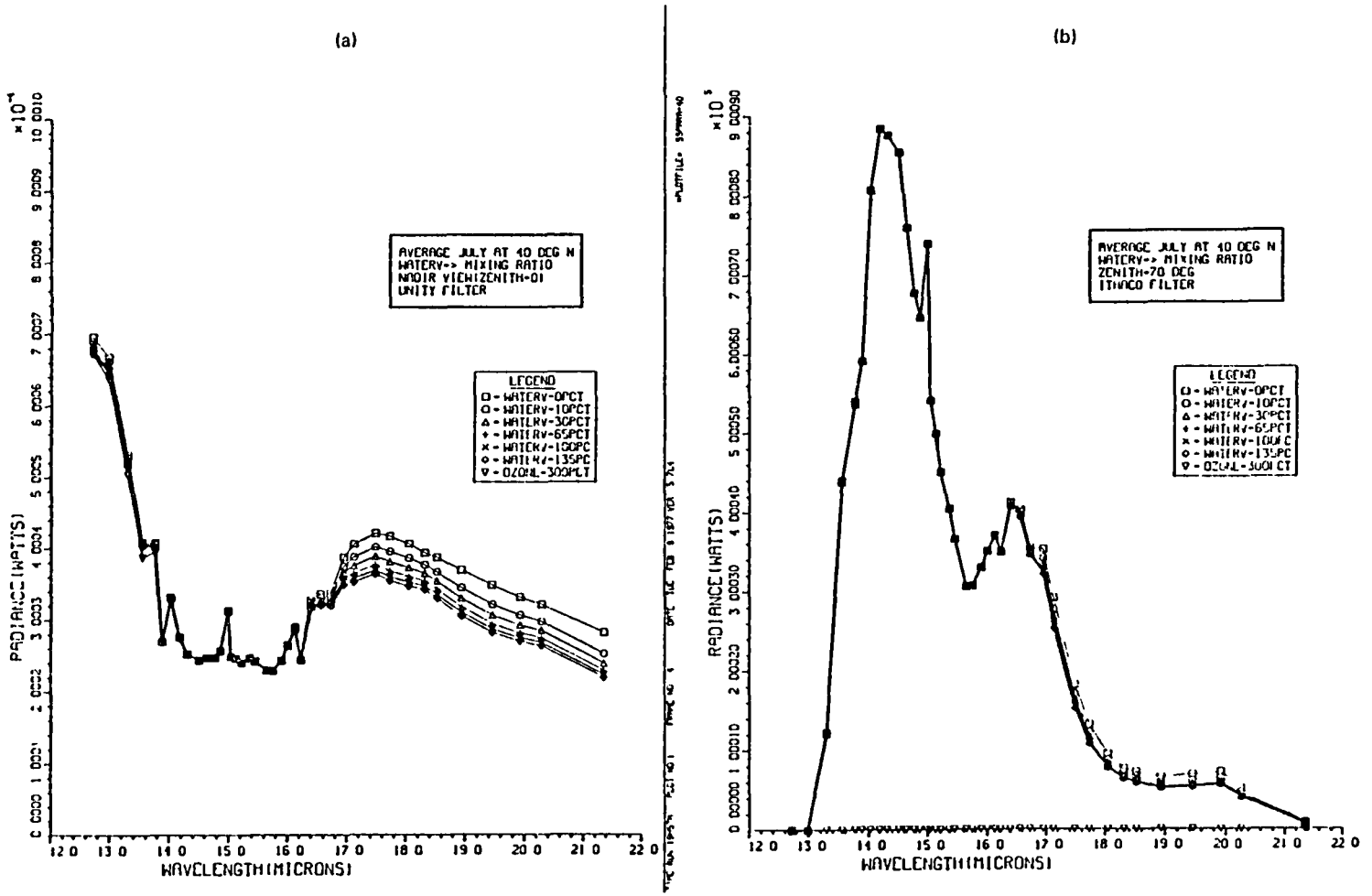

Figure 2-33. July Spectral Radiance Comparisons for 40°N Latitude
(a) Zenith angle = 0, unity filter
(b) Zenith angle = 70 degrees, ITHACO filter

percentages for July radiance profiles. Figure 2-33a shows the effects on the Earth IR radiance between 12 and 22 micrometers for the nadir view (zenith angle = 0) with a unity filter (i.e., $F(\lambda) = 1$), and Figure 2-33b shows the effects for a 70-degree zenith angle path using the ITHACO filter. Note that the inverted triangles on the abscissa of Figure 2-33b appear to be spurious; the 300-percent ozone effect is quoted in Reference 8 as being indistinguishable from nominal for the Seasat passband.

2.3.3 CLOUD ANALYSIS

In addition to the generation of the nominal radiance profiles, another significant result of the LMSC analyses was the evaluation of the sensitivity of the IR scanners to cold clouds. Some of this analysis is reported in Reference 8; a more detailed discussion of the cloud modeling analysis procedure and results is presented in Reference 15, along with a discussion of the frequency and distribution of clouds at various altitudes for the Northern Hemisphere in January, April, July, and October.

The cloud profiles were synthesized assuming opaque clouds at altitudes 1/3, 2/3, and 3/3 the height of the tropopause. The procedure was to compute the integral portion of the radiation equation (Equation (2-5)) from an initial optical path position s_0 corresponding to the cloud height. In addition to this, the source term $N_0(\lambda)\tau_0$ was evaluated for a source at the temperature of the cloud (which is considered at the same temperature as the atmosphere at that altitude) with a transmittance, τ_0, equivalent to the transmittance from the cloud top to the observer in outer space. Figure 2-34 (Reference 15) illustrates the sensor geometry and cloud altitude distribution for the nadir view, as well as the altitude of the tropopause versus latitude. The effect of clouds at various altitudes on the nadir view

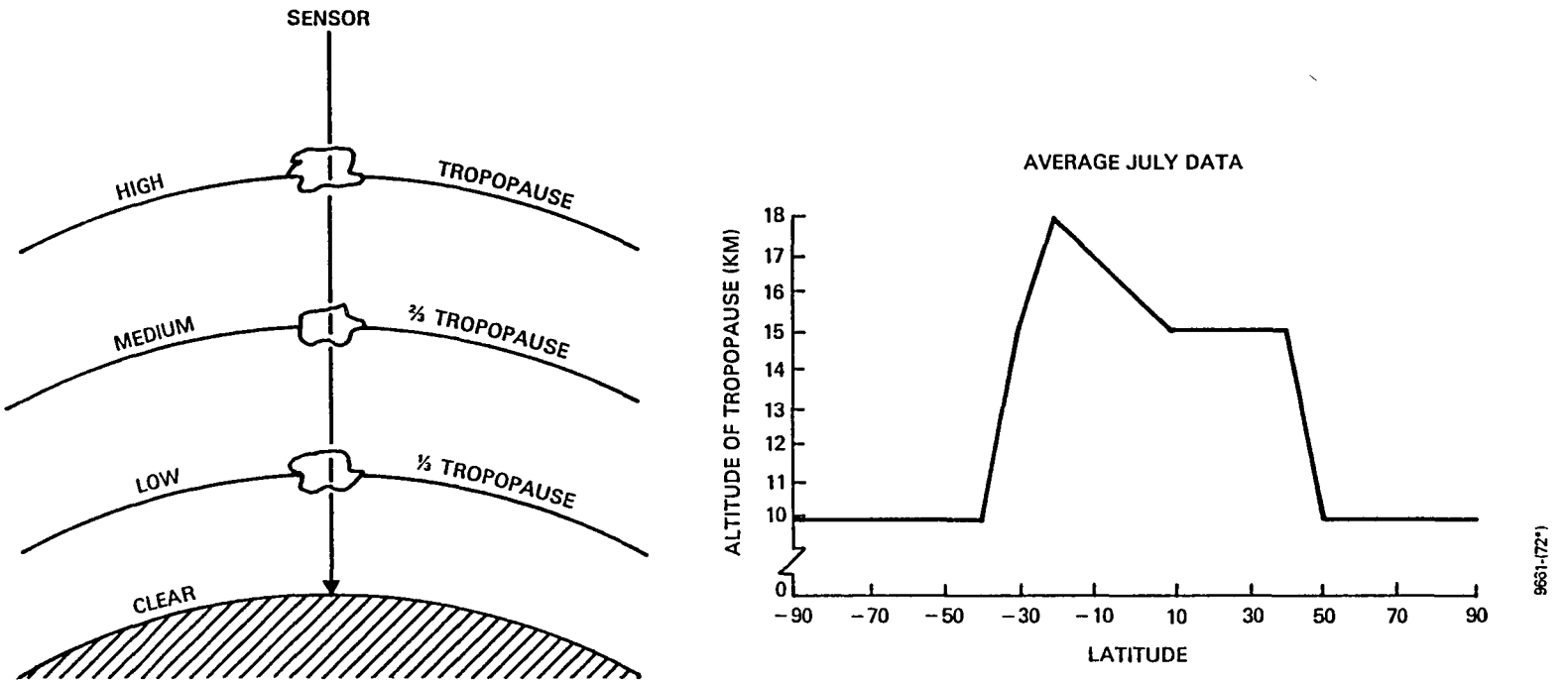

Figure 2-34. Computational Model for Cloud Simulation

radiance for a July equatorial Earth IR spectrum is illustrated in Figure 2-35. A comparison of a profile perturbed by a high-altitude cold cloud with a normal profile for July at the Equator is illustrated in Figure 2-36. Seasat scanners detected the Earth using the normalized threshold locator logic, with the normalized threshold level determined by the average value of the radiance between 5 and 11 scan degrees from the horizon. This averaging region is also shown in Figure 2-36 at the corresponding zenith angle values.

Using the profile in Figure 2-36 and ignoring effects due to scanner geometry FOV integration and signal processing electronics, it can be seen that the drop in radiance near zenith angles of 70 degrees moves the detected horizon out 4 kilometers, as indicated by arrows on the abscissa near 35 kilometers. Translating this into a pitch or roll error for Seasat yields 0.03 degree. Using a similar technique, LMSC concluded that the worst-case cold cloud effect could result in occasional disturbances of 0.1 degree.

More detailed analysis of the cold cloud effects using the LMSC profiles in a horizon sensor optics and electronics simulation program by CSC confirmed these results (Reference 14). This analysis and IR scanner flight data from the Seasat mission are summarized in Section 4.

2.4 HRDB (CSC/LOWTRAN 5/RAOBS-1972) MODEL

The horizon radiance modeling efforts of LRC and LMSC described in the previous sections suffered from two major drawbacks: (1) the data simulation dealt mostly with the Northern Hemisphere, using a seasonal mirroring for the Southern Hemisphere, and (2) the generated profiles covered either a very narrow region of the IR spectrum or were specific to a certain passband. Consequently, the profiles were limited in their usefulness in support of attitude determination efforts at GSFC. CSC, under contract to GSFC,

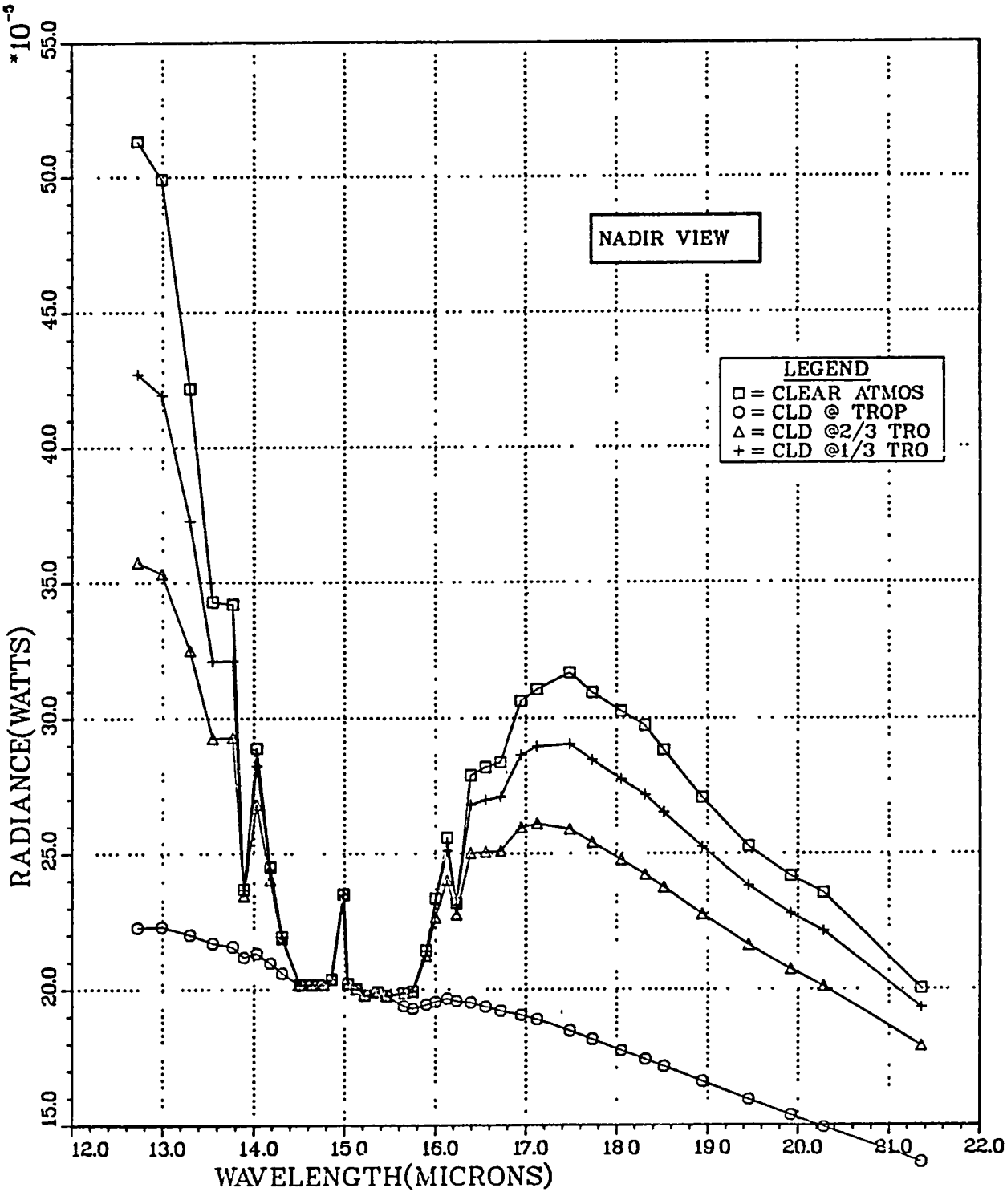

Figure 2-35. Spectral Radiance for Cloud Conditions at the Equator in July

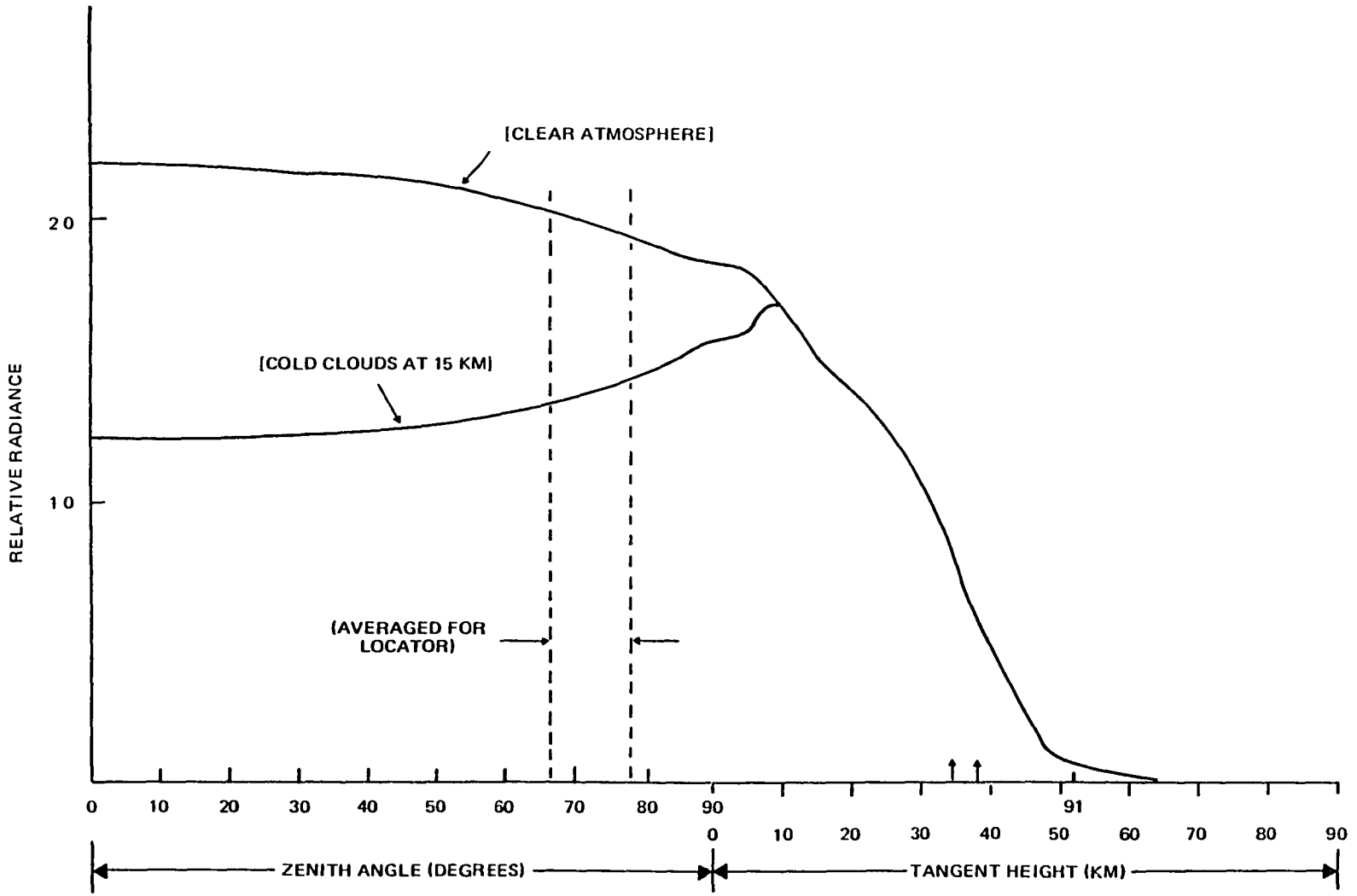

Figure 2-36. Nominal and Cold Cloud Radiance Profiles at the Equator in July

undertook the project of generating a comprehensive data base, starting with a feasibility study in 1980 (Reference 17). The study examined several options, including the techniques of numerical synthesis and the compilation of observed satellite data. The comprehensive data base, called the Horizon Radiance Data Base (HRDB), was generated in 1982 (Reference 18) using the computer program LOWTRAN 5 obtained from the U.S. Air Force Geophysical Laboratory (Reference 10). The climatological data base from 1972 radiosonde observations (RAOBS-1972) (References 11 and 19) provided the atmospheric temperature and humidity profiles required as input to the LOWTRAN 5 program.

The HRDB provides a global data base of IR intensities due to the Earth and its immediate environment. Its major features are as follows:

- The radiance profiles are provided for the IR region of 8 to 22 micrometers at steps of 0.2 micrometer.

- The HRDB provides seasonal variations in monthly steps.

- Geographic variations are included by providing data for nine latitude bins of 20 degrees width centered at $80^{o}N$, $60^{o}N$, $40^{o}N$, $20^{o}N$, Equator, $20^{o}S$, $40^{o}S$, $60^{o}S$, and $80^{o}S$ latitudes.

- The two hemispheres and the seasonal effects are based on independent observations of the climatological data without incorporating seasonal mirroring.

- The viewing geometry is represented by 51 different optical paths from the observer (the sensor on board the satellite) to the Earth's atmosphere. These are subdivided into two groups: paths intersecting with the Earth's surface are represented by zenith angles (ζ) ranging from 90 degrees (tangential to the Earth's surface) to 0 degrees

(nadir view) in steps of 10 degrees; paths passing through the atmosphere are characterized by a tangent height (h) (along the local vertical at the point of closest approach to the Earth) ranging from 0 to 80 kilometers in steps of 2 kilometers. Figure 2-37 defines ζ and h.

- The HRDB can be used for any mission by generating profiles specific to the passband of the horizon sensor in use. This can be achieved by integrating the product of the IR spectral data from the HRDB and the spectral response function of the sensor optics over the wavelength parameter.

The radiance profiles represented by the HRDB were used to simulate data corresponding to the specific CO_2 channels used in the LIMS experiment on board Nimbus-7, and the results were compared with the observed data. That study is described in Reference 12 and will be discussed further in Section 2.5.

2.4.1 LOWTRAN 5 PROGRAM

The LOWTRAN 5 program (Reference 10) calculates atmospheric transmittance and radiance emitted by the atmosphere and the Earth in the IR region of the electromagnetic spectrum. The program, which is written in FORTRAN, has the following general features:

- Computes either transmittance or transmittance and radiance data in steps of 5 cm^{-1} from 350 to 40,000 cm^{-1} (28.5 to 0.25 micrometer).
- Uses a single parameter band model for molecular absorption and includes the effects of continuum absorption, molecular scattering, and aerosol extinction.
- Includes the effects of refraction and Earth curvature in the calculation for slanted atmospheric paths.

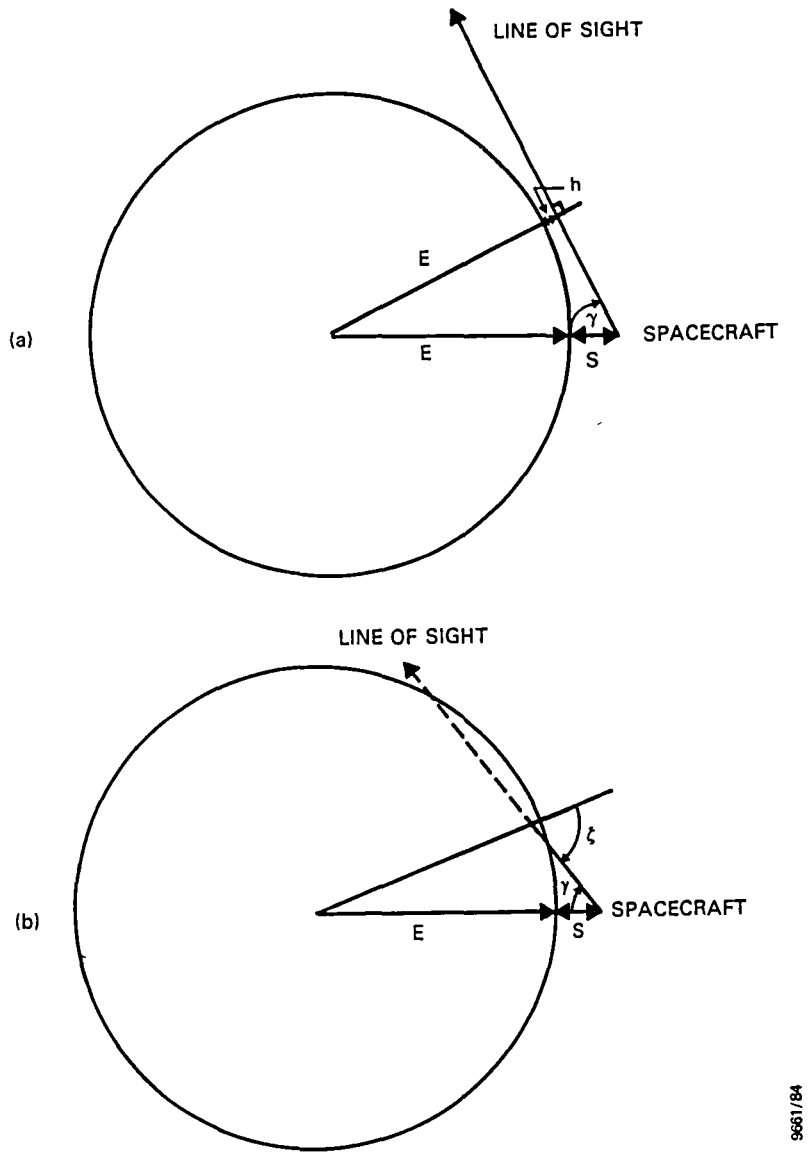

Figure 2-37. Definitions of (a) Tangent Height, h, and (b) Zenith Angle, ζ

- Contains six representative atmospheric models and many representative aerosol models.
- Has an option for a user-supplied atmospheric model providing temperature and water vapor profiles as a function of pressure and altitude. The model may optionally provide data relating to ozone and aerosol densities.
- Uses a spherical model of the atmosphere with up to 34 shells at various altitudes defined by the internal models or the user-supplied atmospheric model.
- Assumes LTE in each layer. This condition is satisfied at lower altitudes in the atmosphere but not at higher altitudes (as discussed in Section 2.2); however, no provision is made to correct for this.
- Includes absorption curves and mixing ratios for water vapor, ozone, nitric acid, and the uniformly mixed gases (carbon dioxide, nitrous oxide, methane, carbon monoxide, oxygen, and nitrogen).
- Allows for inclusion of cloud effects via a source term at the boundary; however, this source term can only be included by artificially changing the size of the Earth to coincide with the location of the cloud.

Details of the two major functions of the LOWTRAN 5 program, the computation of radiance and transmittance, are discussed in the following sections.

2.4.1.1 Computation of Atmospheric Radiance

The LOWTRAN 5 program has the option of calculating atmospheric radiance and Earth radiance. A numerical analog of the integral form of the radiative transfer equation is used in the program. The emission from aerosols and the treatment

of aerosol and molecular scattering is considered only in the zero-th order. Additional contributions to atmospheric emission from radiation scattered one or more times are neglected. LTE is assumed in the atmosphere.

The average atmospheric radiance (over a 20-cm^{-1} interval) at the wave number, ν, along a given line of sight in terms of the LOWTRAN transmittance parameters is given by

$$I(\nu) = \int_{\bar{\tau}_a^b}^{1} d\bar{\tau}_a \, B(\nu, T)\bar{\tau}_s + B(\nu, T_b)\bar{\tau}_t^b \qquad (2\text{-}7)$$

where the integral represents the atmospheric contribution and the second term is the contribution of the boundary (for example, the surface of the Earth or a cloud top) and

where $\bar{\tau}_a^b$, $\bar{\tau}_t^b$ = average transmittances from the boundary to the observer

$\bar{\tau}_a$ = average transmittance due to absorption

$B(\nu, T)$ = average Planck (black body) function corresponding to the wave number, ν, and the temperature, T, of an atmospheric layer

$\bar{\tau}_s$ = average transmittance due to scattering

T_b = temperature of the boundary

$\bar{\tau}_t = \bar{\tau}_a\bar{\tau}_s$ = average total transmittance

The emissivity of the boundary is assumed to be unity.

The LOWTRAN 5 band model approach used here assumes that, because the black-body function is a slowly varying function of frequency, the average value of the radiance can be represented in terms of the average values of the transmittance and the black-body function. The parameters $\bar{\tau}_a$, $\bar{\tau}_s$, and $\bar{\tau}_t$ vary from 1 to $\bar{\tau}_a^b$, $\bar{\tau}_s^b$, and $\bar{\tau}_t^b$, respectively, along the observer's line of sight. For lines of sight that do not

intersect the Earth or a cloud layer, the second term in Equation (2-7) is omitted.

The numerical analog of Equation (2-7) has been incorporated in the LOWTRAN 5 program. The numerical integration of the radiance along a line of sight for a given model atmosphere defined at N levels is given by

$$I(\nu) = \sum_{i=1}^{N-1} \left\{ [(\bar{\tau}_a(i) - \bar{\tau}_a(i+1)]\ B\left[\nu, \frac{T(i) + T(i+1)}{2}\right] \right. \left. \left[\frac{\bar{\tau}_s(i) + \bar{\tau}_s(i+1)}{2}\right] \right\} + B(\nu, T_b)\bar{\tau}_t^b \tag{2-8}$$

Thus, the spectral radiance along a given line of sight in the atmosphere is calculated by dividing the atmosphere into a series of isothermal layers at constant pressure and density, and then summing the radiance contribution from each of these layers along the line of sight. Figure 2-38 shows a simple example of this numerical procedure. Ignoring the contribution due to scattering, the total upward spectral radiance as seen by an observer in space for a three-layered atmosphere at T_1, T_2, and T_3 is given by

$$I(\nu) = (1 - \tau_1')\ B(\nu, T_3) + (\tau_1' - \tau_2')\ B(\nu, T_2) + (\tau_2' - \tau_3')\ B(\nu, T_1) + \tau_3'\ B(\nu, T_b) \tag{2-9}$$

It should be emphasized that, in the calculation of radiance as given by Equation (2-7), scattering is treated only as a loss mechanism and is not included as a source.

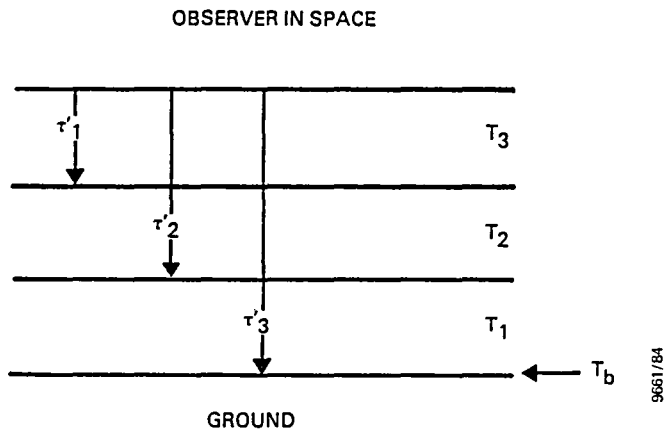

Figure 2-38. Downward Atmospheric Paths Through a Three-Layered Atmosphere for Radiance Calculations

2.4.1.2 Computation of Atmospheric Transmittance

In the LOWTRAN 5 program, the total atmospheric transmittance at a given wave number averaged over a 20-cm^{-1} interval is given by the product of the average transmittances due to molecular band absorption, molecular scattering, aerosol extinction, and molecular continuum absorption. The molecular band absorption consists of four components; namely, the separate transmittances of water vapor, ozone, nitric acid, and the uniformly mixed gases.

The average transmittance ($\bar{\tau}$) due to molecular band absorption is represented by a single-parameter empirical transmittance function. The argument of the transmittance function is the product of a wave-number-dependent absorption coefficient and "an equivalent absorber amount" for the atmospheric path:

$$\bar{\tau} = f(C_\nu \rho' DS) \qquad (2\text{-}10)$$

where C_ν is the LOWTRAN 5 wave-number-dependent absorption coefficient, and ρ' is an "equivalent absorber density"

for the atmospheric path, DS. The density ρ' is defined in terms of the pressure, P(z); temperature, T(z); concentration of absorber, ρ, at an altitude z of the atmospheric layer; and an empirical constant, n, as follows:

$$\rho' = \rho \left\{ \frac{P(z)}{P_o} \sqrt{\frac{T_o}{T(z)}} \right\}^n \qquad (2\text{-}11)$$

where T_o and P_o correspond to standard temperature and pressure (STP) (1 atmosphere, 273K) conditions.

The form of the function f (Equation (2-10)) and the value of the parameter n have been determined empirically using both laboratory transmittance data and available molecular line constants. Mean values of n are 0.9 for water vapor, 0.75 for the uniformly mixed gases, and 0.4 for ozone.

For sufficiently small values of the argument of f (i.e., $C_\nu \rho'$ DS << 1), the transmittance function $\bar{\tau}$ is modified to perform calculations for atmospheric layers of small optical thickness. For cases where $0.999 \leq \bar{\tau} \leq 1$, the transmittance function has been computed from the following analytic expression:

$$\bar{\tau} = 1 - a \, (C_\nu \rho' \, DS)^b \qquad (2\text{-}12)$$

where a = 0.088 and b = 0.81 for water vapor and the uniformly mixed gases, and a = 0.055 and b = 1.03 for ozone, obtained from empirical transmittance data fitting.

Empirically determined absorption coefficients for water vapor, ozone, nitric acid, and the combined effect of the uniformly mixed gases are included as data in the computer code. The transmittance spectra from which the coefficients were derived were first degraded in resolution to 20 cm^{-1},

and the data points were digitized at steps of 5 cm^{-1}. For the ultraviolet and visible ozone bands, the absorption coefficients were digitized at 500-cm^{-1} and 200-cm^{-1} intervals, respectively.

The absorption coefficients for water vapor are shown in Figures 2-39(a) and (b). Those for ozone are shown in Figures 2-40(a), (b), and (c), and those for the uniformly mixed gases, in Figures 2-41(a) and (b).

The transmittance due to nitric acid has been assumed to lie in the weak-line or linear region. Absorption coefficients digitized at 5-cm^{-1} intervals for the 5.9-, 7.5-, and 11.3-micrometer bands of nitric acid are also included in the LOWTRAN 5 program. These coefficients are shown in Figure 2-42.

2.4.2 RAOBS-1972 CLIMATOLOGICAL DATA

A data base of well-screened, worldwide observations of temperature and water vapor distributions is required to simulate the transport of IR radiation along a line of sight through the atmosphere into space. One such data base was constructed at GSFC using radiosonde observations of temperature and relative humidity in the troposphere and stratosphere for the 12 months of 1972 (References 11 and 19). The profiles in the RAOBS-1972 data base are constructed by selecting the best 2 days of data available from the first 5 days of each month in 1972. Data were taken twice daily, at noon and at midnight. The data were obtained from the National Climatic Center (NCC) at Asheville, North Carolina.

The RAOBS profiles supplied by NCC are lists of pressures, temperatures, and relative humidities at the 40 standard pressure levels listed in Table 2-6. The radiosonde temperature profiles were constrained to join smoothly onto a

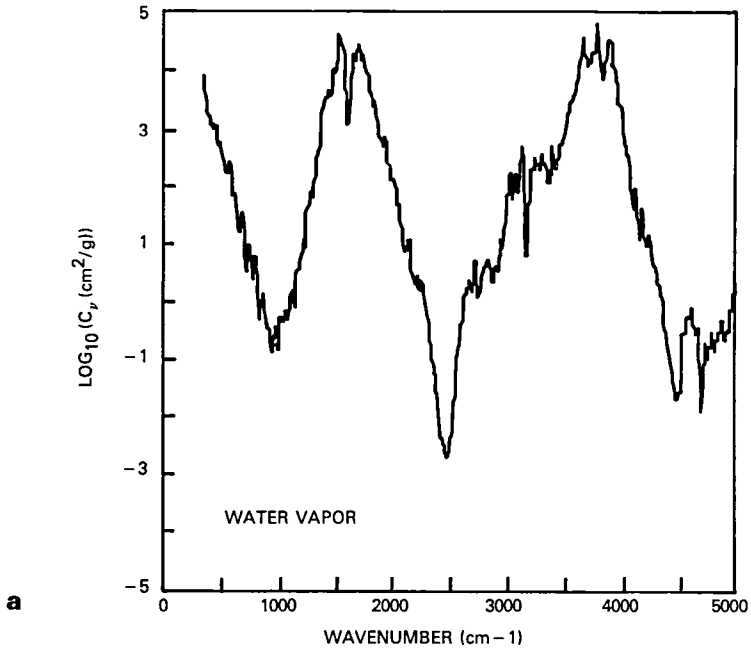

a

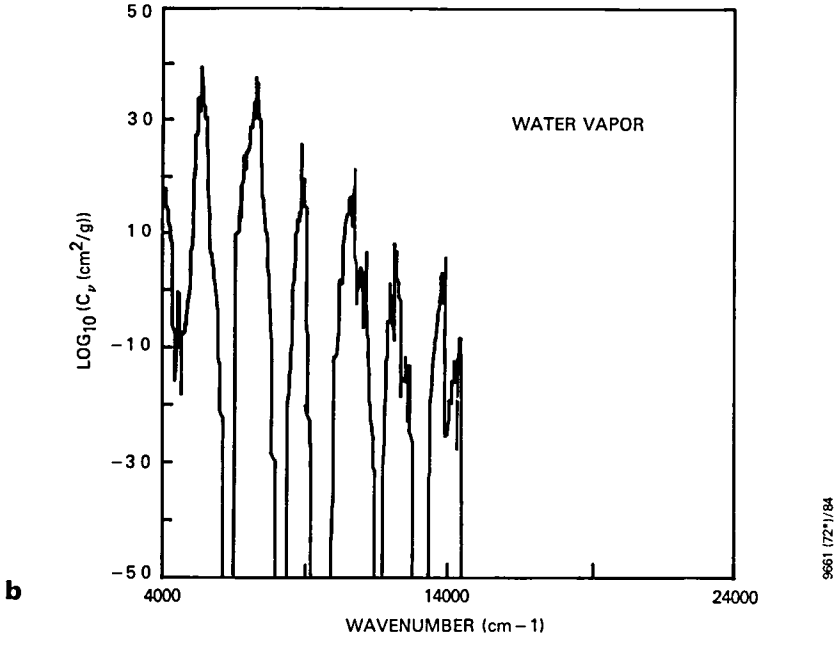

b

Figure 2-39. Absorption Coefficient C_ν for Water Vapor
a. From 350 to 5000 cm^{-1}
b. From 4000 to 24,000 cm^{-1}

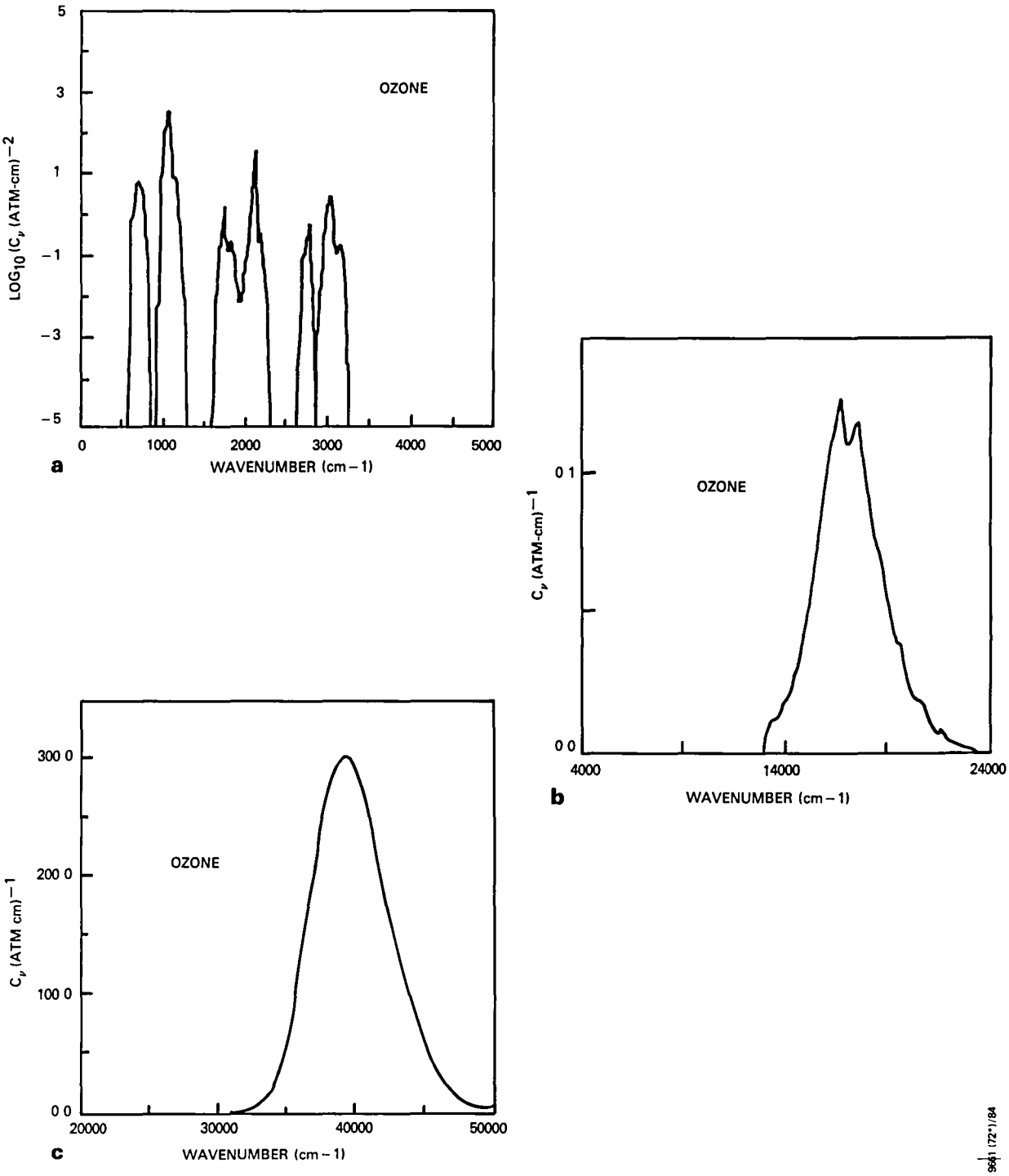

Figure 2-40. Absorption Coefficient C_ν for Ozone

a. From 350 to 5000 cm^{-1}
b. From 4000 to 24,000 cm^{-1}
c. From 20,000 to 50,000 cm^{-1}

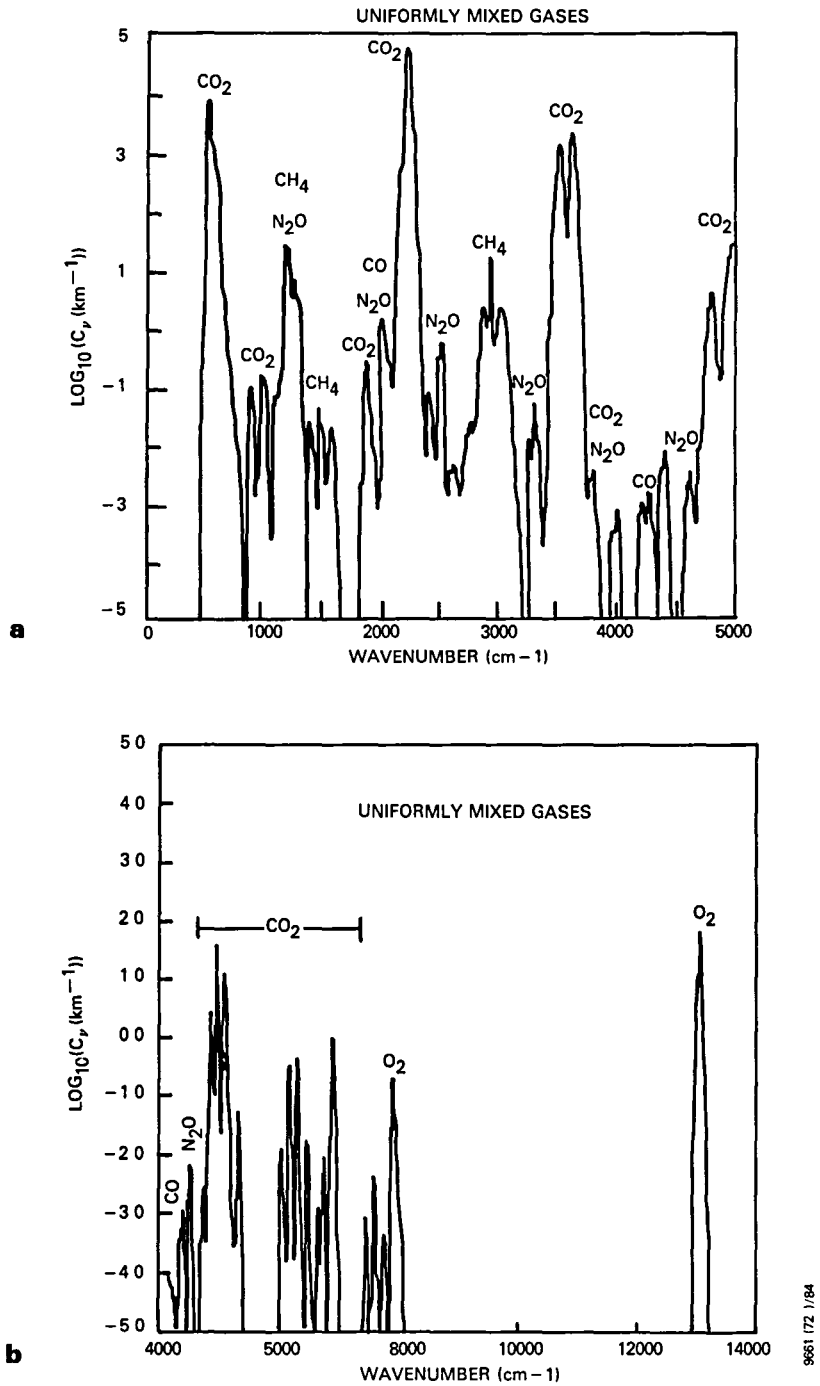

Figure 2-41. Absorption Coefficient C_ν for the Uniformly Mixed Gases
a. From 350 to 5000 cm^{-1}
b. From 4000 to 14,000 cm^{-1}

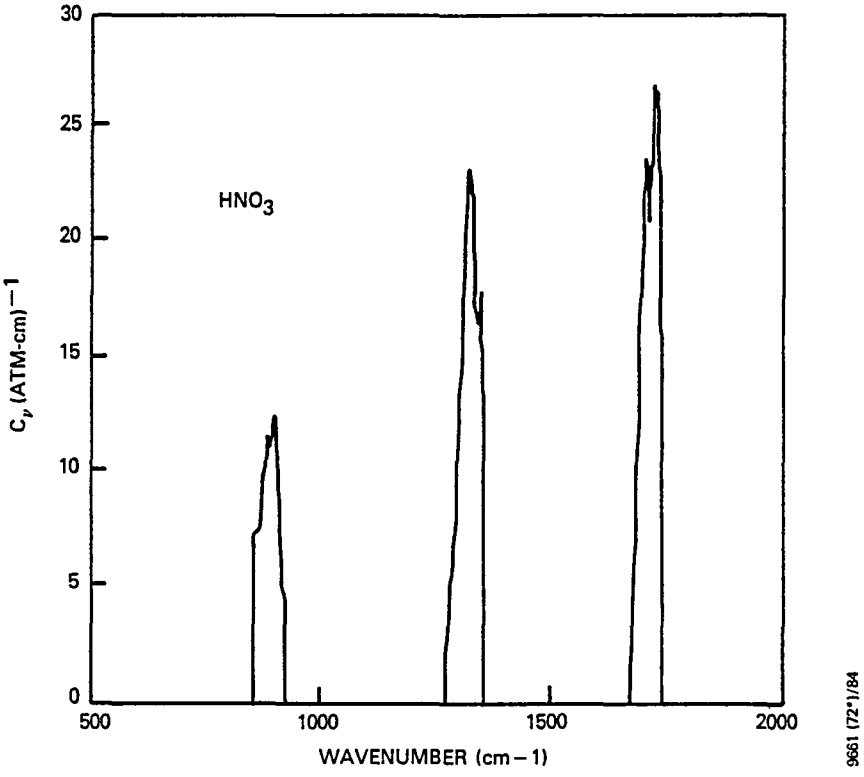

Figure 2-42. Absorption Coefficient C_ν for Nitric Acid (From 500 to 2000 cm^{-1})

standard stratospheric temperature profile (based on the U.S. standard atmosphere). To simulate the troposphere more realistically, missing temperatures were filled by linear interpolation where possible, or by linear extrapolation over a limited pressure range with the assumption of an isothermal troposphere over a wider pressure range. An alphabetic code is associated with each temperature in the profile, indicating how the temperature was determined at that pressure level.

Because only temperatures and relative humidities appear in the RAOBS-1972 data base, each water vapor mixing ratio must be calculated from the corresponding temperature and humidity

Table 2-6. RAOBS-1972 Standard Pressure Levels

LEVEL NO.	PRESSURE (mb)	LEVEL NO	PRESSURE (mb)
1	0 2	21	40
2	0 3	22	50[1]
3	0 5	23	60
4	0 7	24	70[1]
5	1 0	25	85
6	2 0	26	100[1]
7	3 0	27	125
8	4 0	28	150[1]
9	5 0	29	175
10	6 0	30	200[1]
11	7.0	31	250[1]
12	8 5	32	300[1]
13	10 0[1]	33	350
14	12 5	34	400[1]
15	15 0	35	500[1]
16	17 5	36	600
17	20.0[1]	37	700[1]
18	25.0	38	850[1]
19	30 0[1]	39	920
20	35	40	1000[1]

9661 (70*)/84

[1]MANDATORY RAOBS PRESSURE LEVEL UP TO 10 MILLIBARS.

at that pressure level. Because the measured stratospheric relative humidity is less than 1 percent and appears as a zero in the humidity list, the default stratospheric mass mixing ratio for water vapor is 0.0 grams per kilogram (g/kg) in this data base. The actual default stratospheric value is usually not important. Simulations of radiation transport through the atmosphere are not sensitive to the actual stratospheric mixing ratio if it is small (much less than 1.0 g/kg). The tropospheric mixing ratios are determined by linearly extrapolating/interpolating the measured relative humidities. Water vapor mixing ratios are more variable than atmospheric temperatures. The average water vapor mixing ratio at 1000 millibars varies from nearly 15 g/kg during tropic summer to less than 1 g/kg during arctic winter. A factor of five change in this ratio during the year in polar regions is not uncommon.

More than 12,000 individual profiles from over 600 different stations reside in this data base. These profiles were segregated into nine latitude bins, each 20 degrees wide. As a result, the observations from stations located in the Southern Hemisphere are separated from the more numerous Northern Hemisphere reports. Table 2-7 shows the location and seasonal distribution of the profiles in the RAOBS-1972 data base. By retaining the identity of each station in the RAOBS-1972 data base, it is possible to select stations within a small geographical area for further study. Later, if needed, the data base could be reorganized on the basis of geography (e.g., highlands, coastal areas, continental interiors) or on the basis of weather at the reporting stations (e.g., by particular mesoscale event or by air mass sampled). Provisions were made for extracting the actual radiosonde profile from the data base by coding each temperature according to how it was determined.

Table 2-7. Distribution of RAOBS-1972 Profiles

LATITUDE BIN	NUMBER OF STATIONS	WINTER	SPRING	SUMMER	FALL	TOTAL
70°N–90°N	22	94	94	115	122	425
50°N–70°N	175	938	995	1000	1001	3934
30°N–50°N	260	1273	1334	1343	1328	5278
10°N–30°N	87	386	390	377	394	1547
10°S–10°N	28	104	101	101	99	405
10°S–30°S	20	82	92	70	87	331
30°S–50°S	15	61	62	53	60	236
50°S–70°S	12	38	45	35	44	162
70°S–90°S	6	20	9	7	11	47
TOTAL	625	2996	3122	3101	3146	12365

Although the specially selected high-altitude reports are prescreened by NCC, further testing was required. Minor errors were detected in some data, which would have reduced the quality of the data base. The most common mistake was a sign error in the measured Celsius temperature. Occasionally, the block-station number identifying the station was incomplete or missing; as a result, the location of the profile was unknown. On rare occasions, only stratospheric data were present, or too few temperatures were measured for meaningful interpolation or extrapolation onto the 40 standard pressure levels. Whenever any of these errors were found, the entire observation was discarded. Despite these precautions, some erroneous data still reside in the RAOBS-1972 data base. Approximately one profile per thousand contains bad data.

The profiles from the RAOBS-1972 data base were used as input to the LOWTRAN 5 program. The large number of profiles make it a very good statistical sample. The difference in Southern and Northern Hemisphere profiles 6 months apart is evidence that season mirroring to obtain Southern Hemisphere data from the Northern Hemisphere data is not entirely adequate. However, some features of this data base are questionable. The data base represents only a single year,

1972. In addition, the upper stratospheric data are artificially uniform because the profiles were constrained to join smoothly to a standard atmospheric temperature profile for altitudes where measured data were not available. These and other statistical variations of the data base are discussed in some detail in Reference 11.

2.4.3 HRDB PARAMETRIC VARIATIONS

Samples of the radiance profile data (in units of watts per centimeter^2 per steradian per micrometer) from the HRDB are shown in Figures 2-43 and 2-44. The data are for optical path tangent heights of 2 and 38 kilometers in January for the 40^{o}N latitude bin. The local peak in the vicinity of 15 micrometers wavelength shows the CO_2 radiance used for the horizon sensors. The data shown represent midlatitudes in the winter hemisphere.

The HRDB data were studied for sensitivity to changes in the atmospheric temperature, relative humidity, ozone concentration, different aerosol models built into the LOWTRAN 5 program, and presence of clouds. Figures 2-43 and 2-44 show the results for two of these changes. The numerals indicate the total number of overlapping data points. Figure 2-45 shows the fractional change in the radiance due to two perturbations, temperature and humidity, as a function of optical path at 15 micrometers, center of the CO_2 band. The abscissa represents tangent height (positive values) or zenith angle minus 90 (negative values) to provide a continuous scale. The results of the sensitivity analysis are summarized as follows:

- No appreciable change is observed, especially in the 15-micrometer CO_2 band, for changes in the relative humidity ranging from half the RAOBS values to almost 99-percent relative humidity.

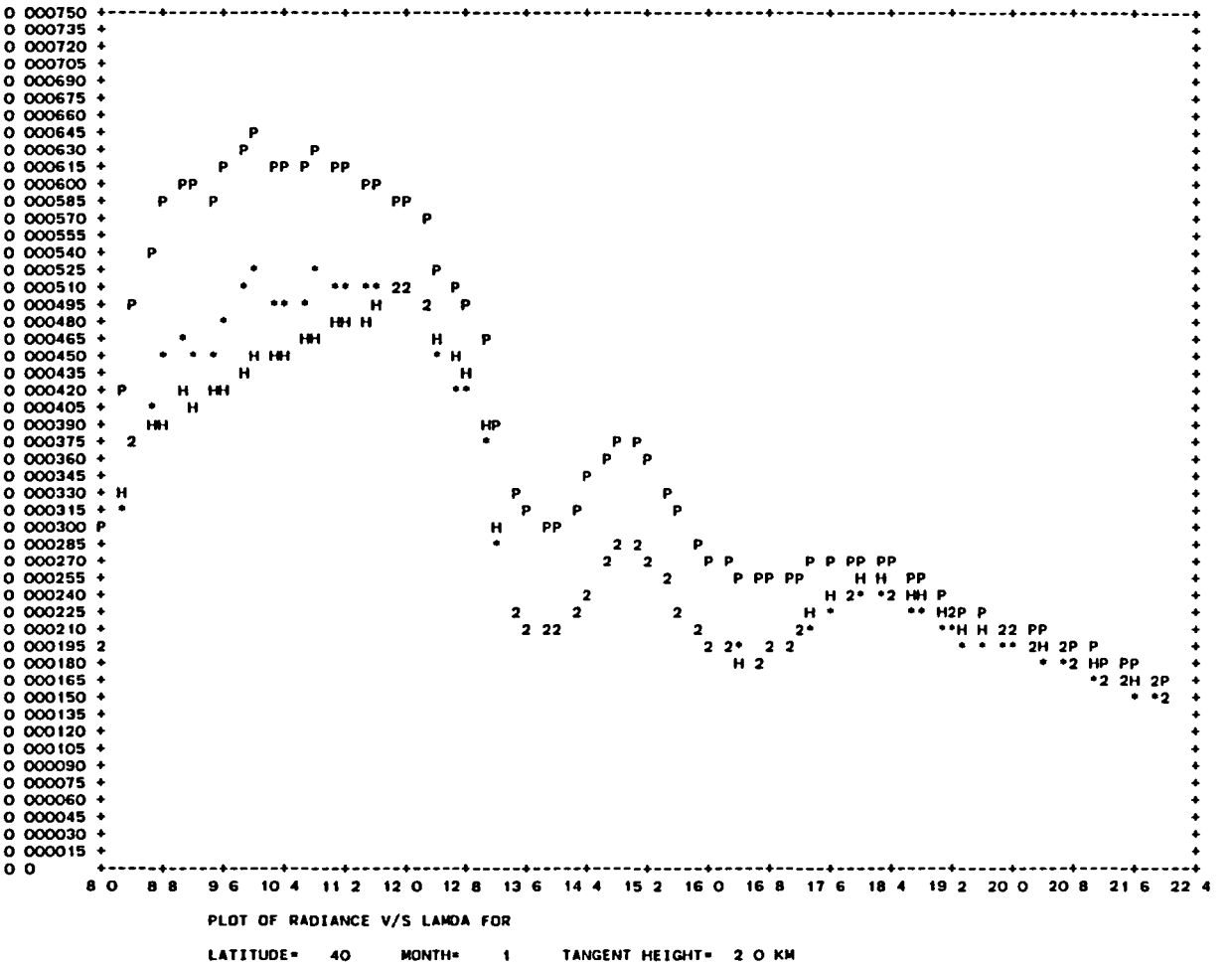

Figure 2-43. Radiance Profiles for January 40°N Latitude, h = 2 Kilometers (Nominal HRDB data (*) compared with uniformly heated (by 20 degrees) atmosphere (P) and relative humidity at half the nominal value (H).)

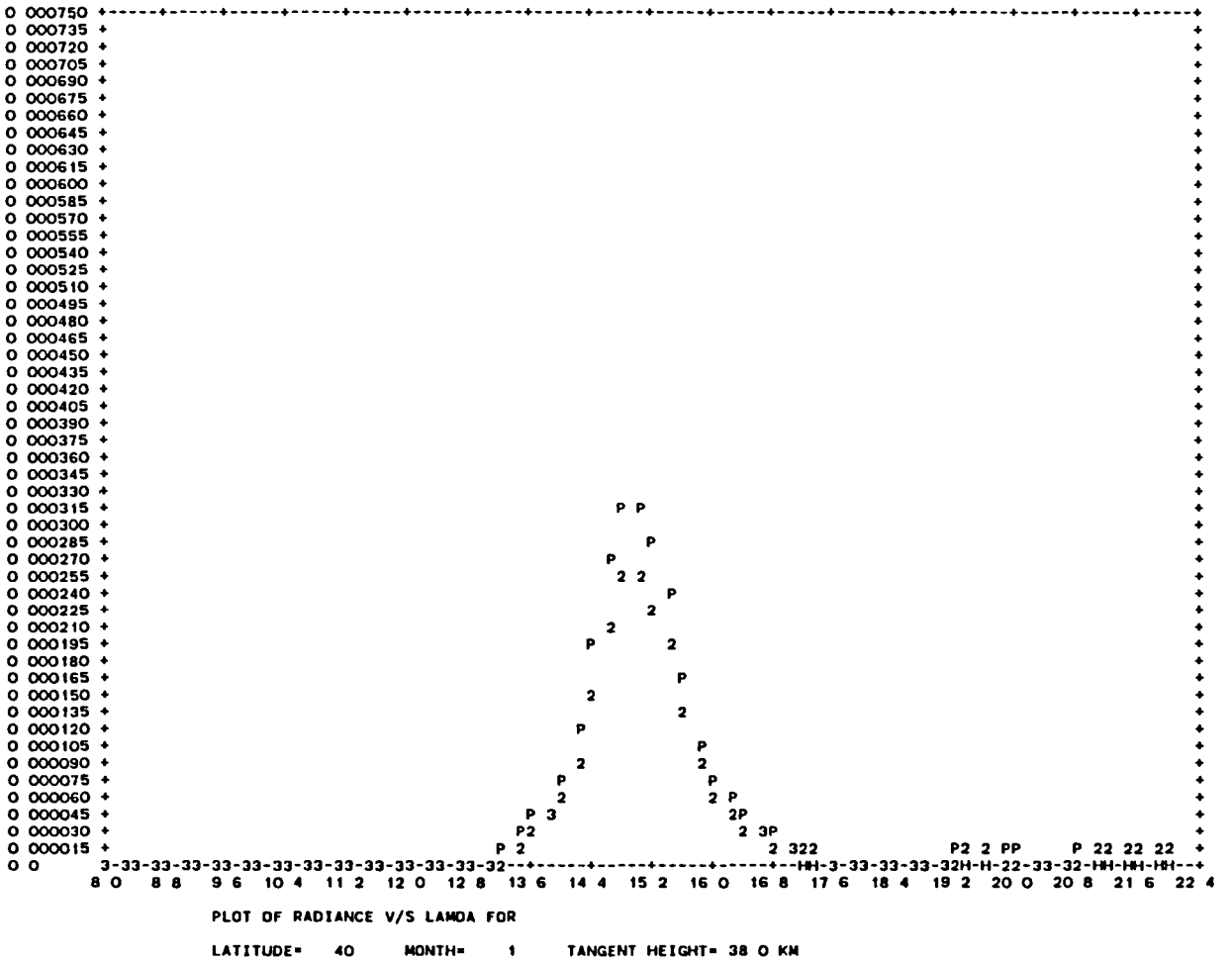

Figure 2-44. Radiance Profiles for January 40°N Latitude, h = 38 Kilometers (Nominal HRDB data (*) compared with uniformly heated (by 20 degrees) atmosphere (P) and relative humidity at half the nominal value (H).)

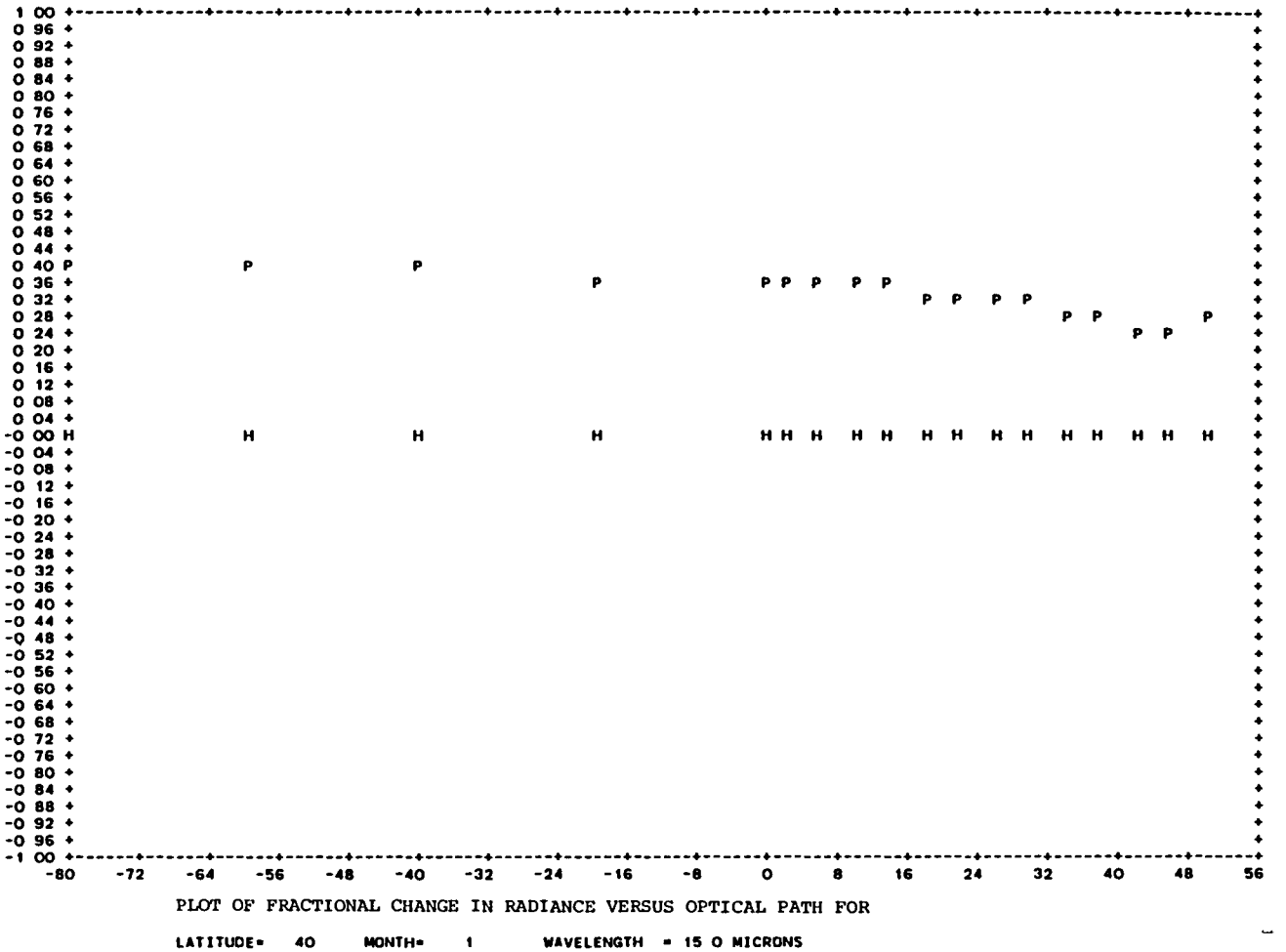

Figure 2-45. Fractional Changes in the Radiance Profiles at 15 Micrometers (Uniform heating of the atmosphere by 20 degrees (P) compared to halving the relative humidity data (H).)

- No change is observed in the CO_2 band for changes in the ozone concentration or from the use of different aerosol models.

- Fractional changes in radiance are larger for the same amount of uniform heating than for cooling of the atmosphere.

- The derivative of $\ell n(R)$ with respect to temperature [i.e., $1/R\ (\Delta R/\Delta T)$], where R is the radiance and T is the temperature, stays approximately constant, for a given optical path and wavelength, as a function of season and geography. The maxima in this derivative occur for optical paths that are nearly tangential to or intersecting with the Earth. Table 2-8 lists results for three wavelengths in the 15-micrometer CO_2 band that show an approximate 2-percent change in radiance per 1-degree change in atmospheric temperature.

The effects of cloud simulation at the top of the troposphere on the Earth IR spectrum are shown in Figures 2-46 and 2-47 for the month of January for the $80^{o}N$ latitude nadir view and in the equatorial region for a view at h equal to 10.0 kilometers. The results, using the LOWTRAN 5 program, again demonstrate the insensitivity of the 15-micrometer band to weather phenomena, in agreement with previous Project Scanner and LMSC studies (see Sections 2.2 and 2.3).

2.5 NIMBUS-6 AND -7 OBSERVATION MODEL

The Limb Radiance Inversion Radiometer (LRIR) experiment, flown on the Nimbus-6 spacecraft in 1975, was conducted to determine the vertical distribution of temperature, ozone, and water vapor from the lower stratosphere ($\sim$15 kilometers) into the lower mesosphere ($\sim$60 kilometers) on a global scale (Reference 20). These vertical distributions were to be determined by inverting measured limb radiance profiles obtained by the LRIR, an infrared, multispectral scanning

Table 2-8. Maximum Fractional Change in the Radiance Profiles per Degree Change in the Atmospheric Temperature for the CO_2 Band

MONTH	LATITUDE BIN	$(\Delta R/R)/\Delta T$[a]		
		14 μ	15 μ	16 μ
1 (JAN)	0	0 024	0 020	0 020
	40 S	0 022	0 019	0 019
	80 S	0 020	0 020	0 020
4 (APRIL)	0	0 026	0 021	0 021
	40 S	0 025	0 021	0 021
	80 S	0 021	0 021	0 017
7 (JULY)	0	0 024	0 020	0 020
	40 S	0 023	0 020	0 020
	80 S	0 028	0 023	0 024
10 (OCTOBER)	0	0 024	0 021	0 021
	40 S	0 023	0 020	0 020
	80 S	0 027	0 022	0 022

9661 (70*1/84

[a]R VALUE CORRESPONDS TO NOMINAL RAOBS-1972 TEMPERATURE, T, ΔR IS THE DIFFERENCE BETWEEN THE NOMINAL RADIANCE VALUE AND THAT OBTAINED USING A TEMPERATURE OF T+ΔT, WHERE ΔT REPRESENTS THE CONSTANT CHANGE APPLIED TO THE ATMOSPHERIC TEMPERATURE

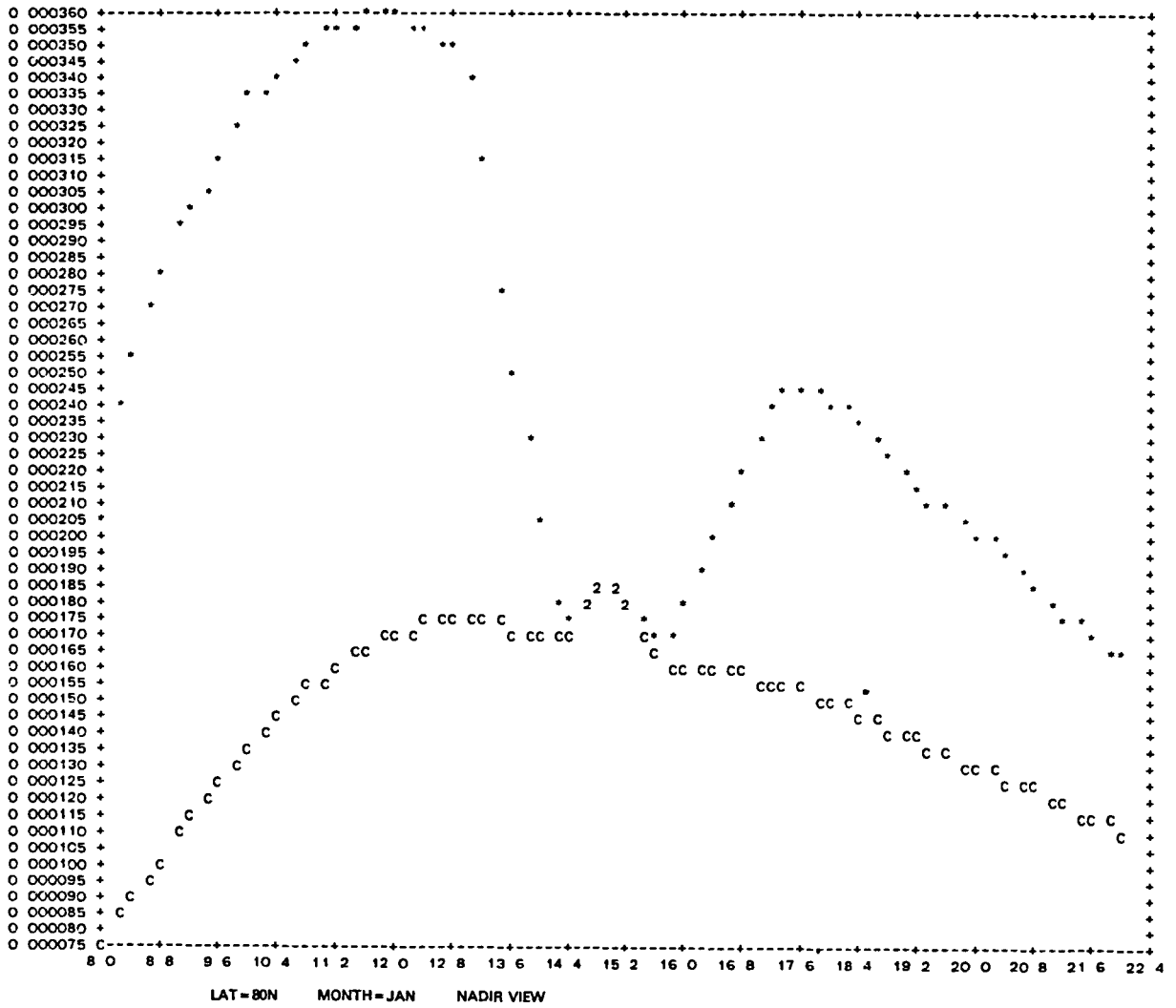

Figure 2-46. Nominal HRDB Radiance Profiles for January, 80°N Latitude, Nadir View (Nominal HRDB radiance profiles (*) are compared to those with a uniform cold cloud at the top of the troposphere (C).)

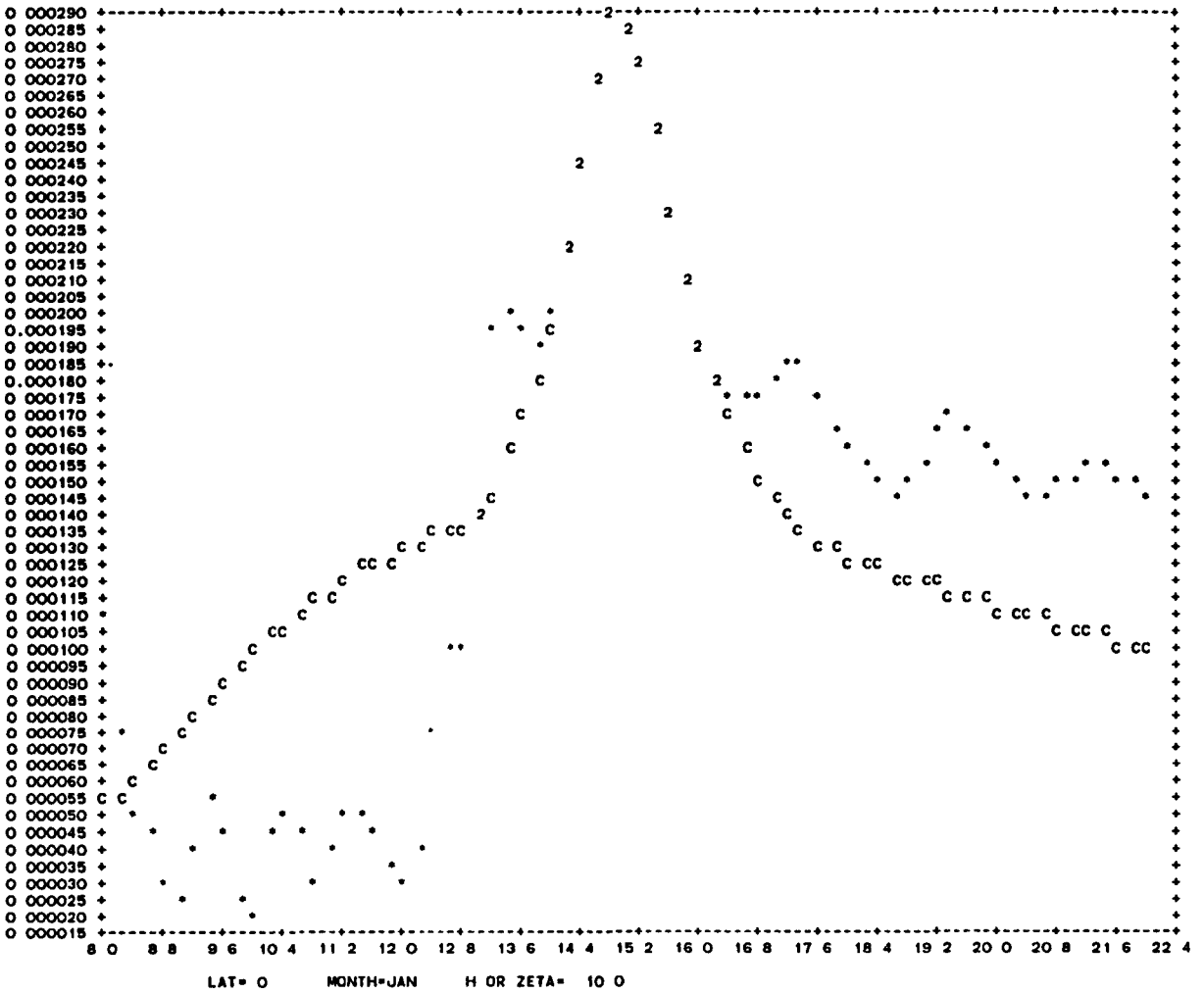

Figure 2-47. Nominal HRDB Radiance Profiles for January, Equatorial Region, h = 10 Kilometers (Nominal HRDB radiance profiles (*) are compared to those with a uniform cold cloud at the top of the troposphere (C).)

radiometer. Measurements were made in four spectral regions: two in the 15-micrometer CO_2 band; one in the 9.6-micrometer ozone band; and one in the 23- to 27-micrometer water vapor band.

The LRIR experiment was followed by the Limb Infrared Monitor of the Stratosphere (LIMS) experiment, flown on the Nimbus-7 spacecraft in 1978 (Reference 21). LIMS was designed to determine global-scale vertical distributions of temperature and several gases involved in the chemistry of the ozone in the stratosphere. It employed a multispectral scanning radiometer similar to that for the LRIR experiment. Measurements were made in six spectral regions: one in the 9.6-micrometer ozone band, one in the 6.3-micrometer nitrogen dioxide band, one in the 6.2-micrometer water vapor band, one in the 11.3-micrometer nitric acid (HNO_3) band, and two in the 15-micrometer CO_2 band. The nominal viewing geometry for LIMS is shown in Figure 2-48.

One of the CO_2 channels used in the two experiments is quite similar in width to the spectral bands typically used for IR horizon scanners; LRIR channel BCO_2 (broad) has a passband range (based on 50-percent peak response) from 14.4 to 16.9 micrometers and LIMS channel CO_2W (wide) has a passband range from 13.2 to 17.3 micrometers. The data coverage extends from 83°N to 64°S latitude for LRIR and from 84°N to 64°S latitude for LIMS. This provides an opportunity to compile either an IR data base directly from observed profiles or a global temperature data base to be used with an analytical model like LOWTRAN 5. Unfortunately, neither of these goals can be realized at this time due to the limited amount of processed science data currently available. At the time of this report, the LRIR/LIMS science groups, via the National Space Science Data Center (NSSDC) at GSFC, had released only 1 month (June 20 to July 30, 1975) of inverted temperature profiles from LRIR and

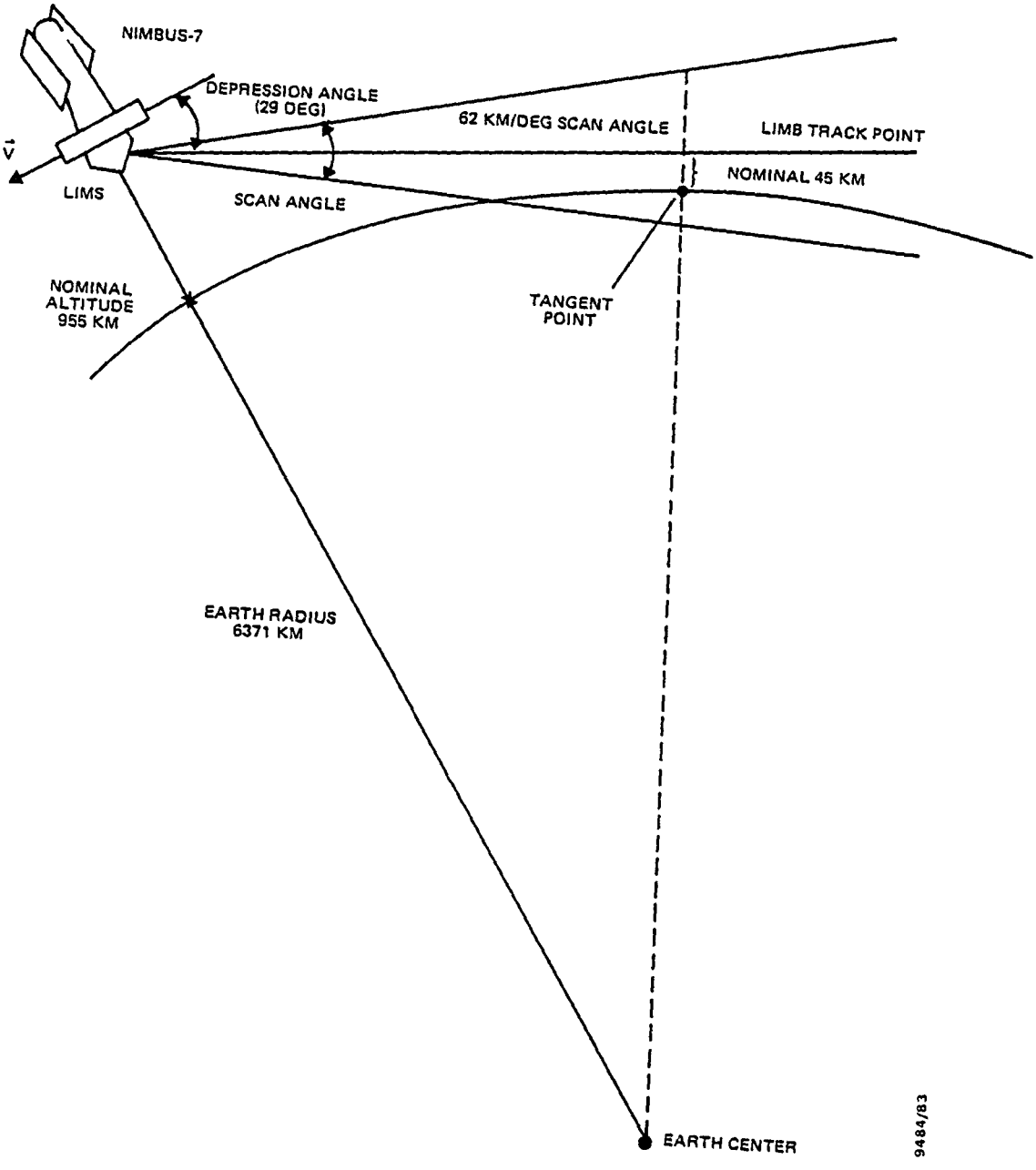

Figure 2-48. Nominal LIMS Viewing Geometry

approximately 7 months (October 25, 1978, to May 30, 1979) of Profile-R (radiance versus scan angle) data from LIMS. Nevertheless, these experiments provide a rich source of data for comparison with the HRDB (Section 2.4) and for help in identifying the strengths and weaknesses of the current efforts.

2.5.1 LRIR AND LIMS OBSERVATIONS

The LRIR data, consisting of an Inverted Profile Archival Tape (IPAT) (Reference 22) for each month, were obtained from NSSDC for the month of July 1975. The IPAT provides ancillary data (e.g., orbit number, time of day, and latitude and longitude of the subsatellite point and of the tangent point) as well as the profile data, including the inverted profile of temperature, pressure, and ozone mixing ratio. The data were grouped together in 20-degree latitude bins (using the latitude of the tangent point) at the standard RAOBS pressure levels (Section 2.4.2) and averaged over all scans for the desired timeframe. Temperatures at the pressure levels not represented in the observed data were generated by logarithmic interpolation (but no extrapolation). The resulting temperature averages for July 1-5, 1975, are shown in Figure 2-49 as a function of altitude, represented by the logarithm of pressure. A value of -1.0 on the vertical scale represents a pressure of 10 millibars, corresponding to an altitude of approximately 32 kilometers. The figure shows curves for the eight latitude bins and is a clear demonstration of the latitude dependence of the temperatures in the stratosphere. This is in sharp contrast to the RAOBS-1972 data used for the HRDB, in which the observed data were joined smoothly to a standard atmosphere for high altitudes. Figures 2-50 through 2-52 compare LRIR temperature data with the corresponding RAOBS-1972 data for the 80^{o}N, equatorial, and 60^{o}S latitude bins. The results show that RAOBS-1972 underestimates the temperature (and

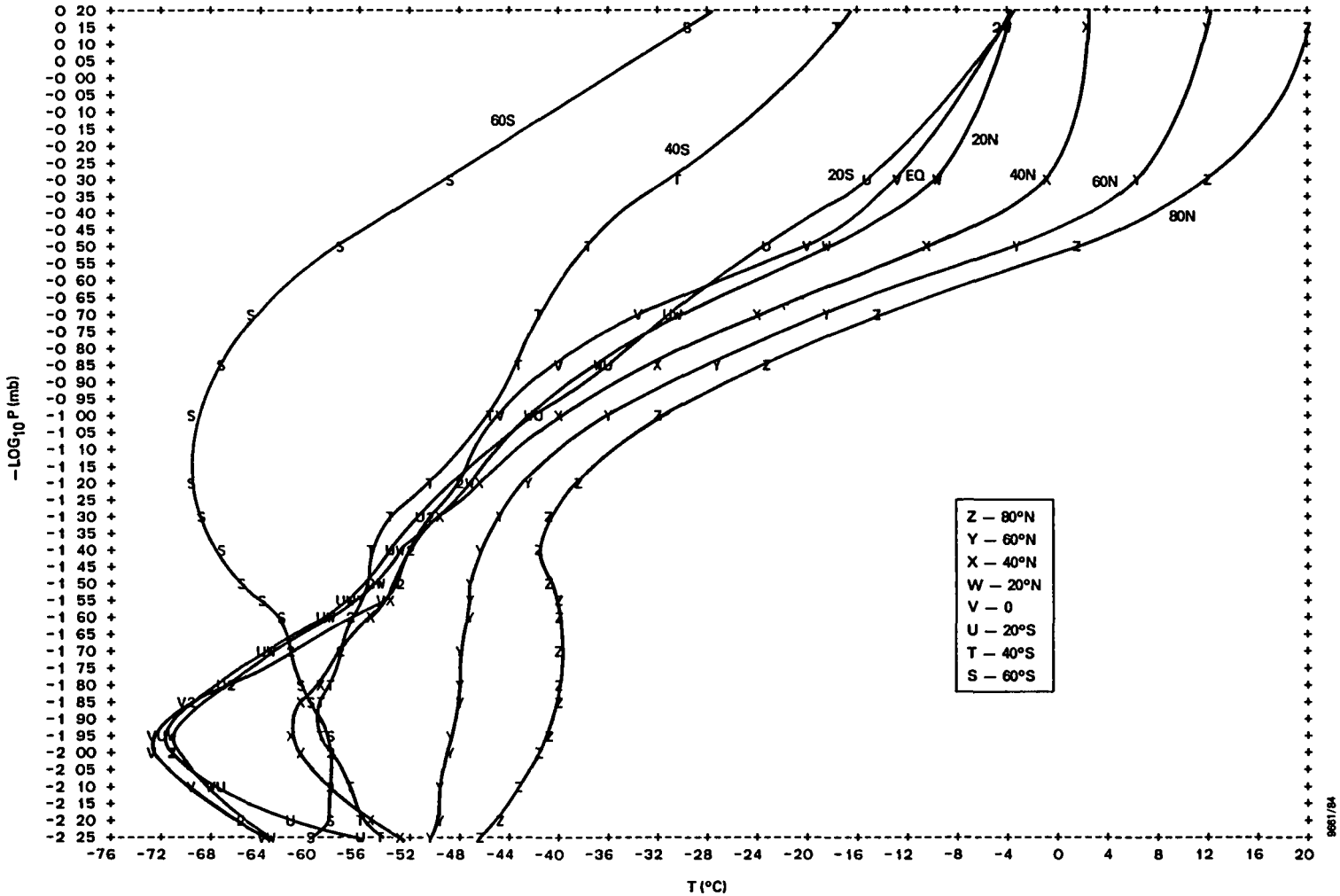

Figure 2-49. Temperature Versus Altitude (Plotted as -Log P) From LRIR Data, July 1975

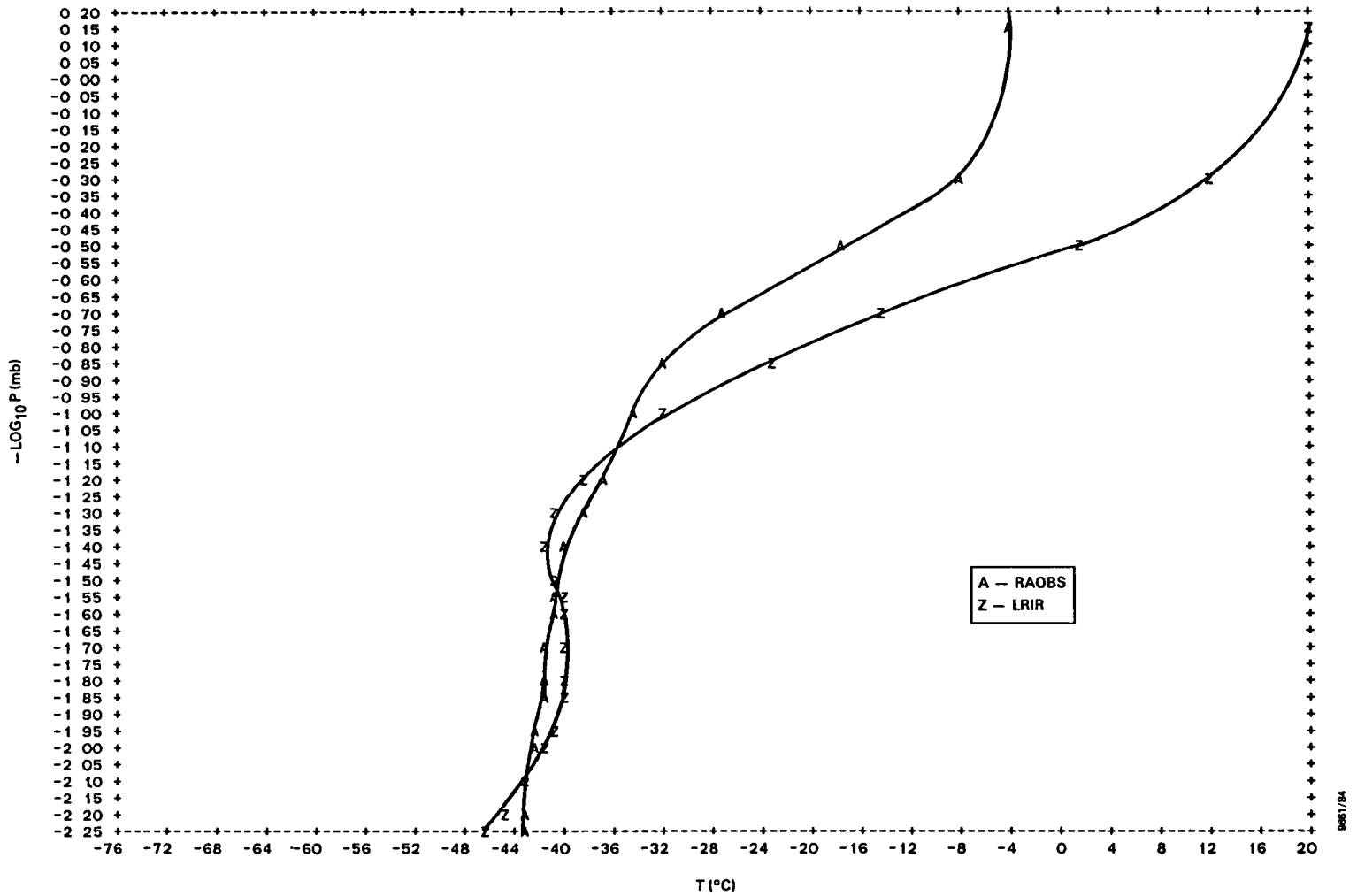

Figure 2-50. LRIR Temperature Data for July Compared With RAOBS-1972 Data for 80°N Latitude

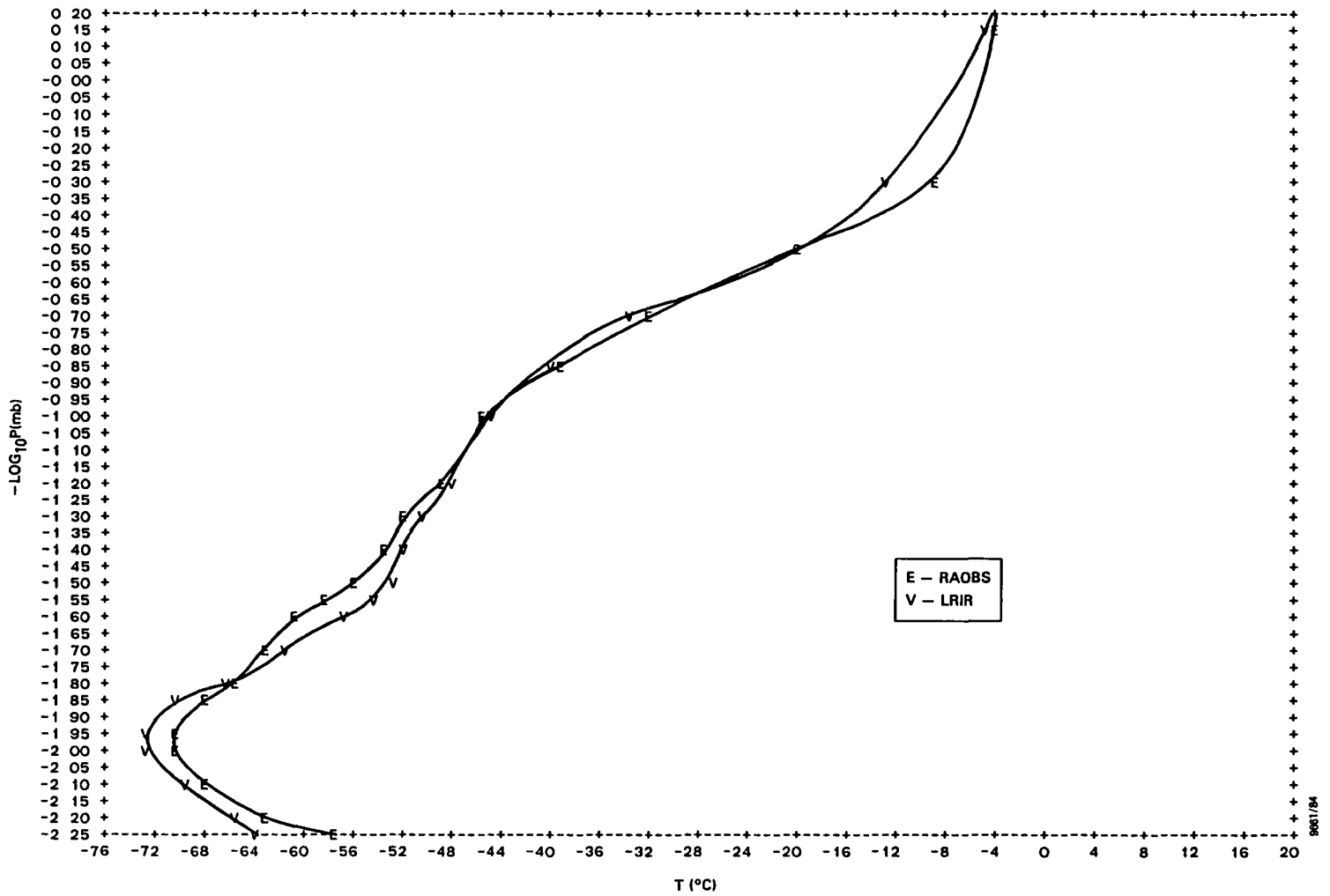

Figure 2-51. LRIR Temperature Data for July Compared With RAOBS-1972 Data for the Equatorial Region

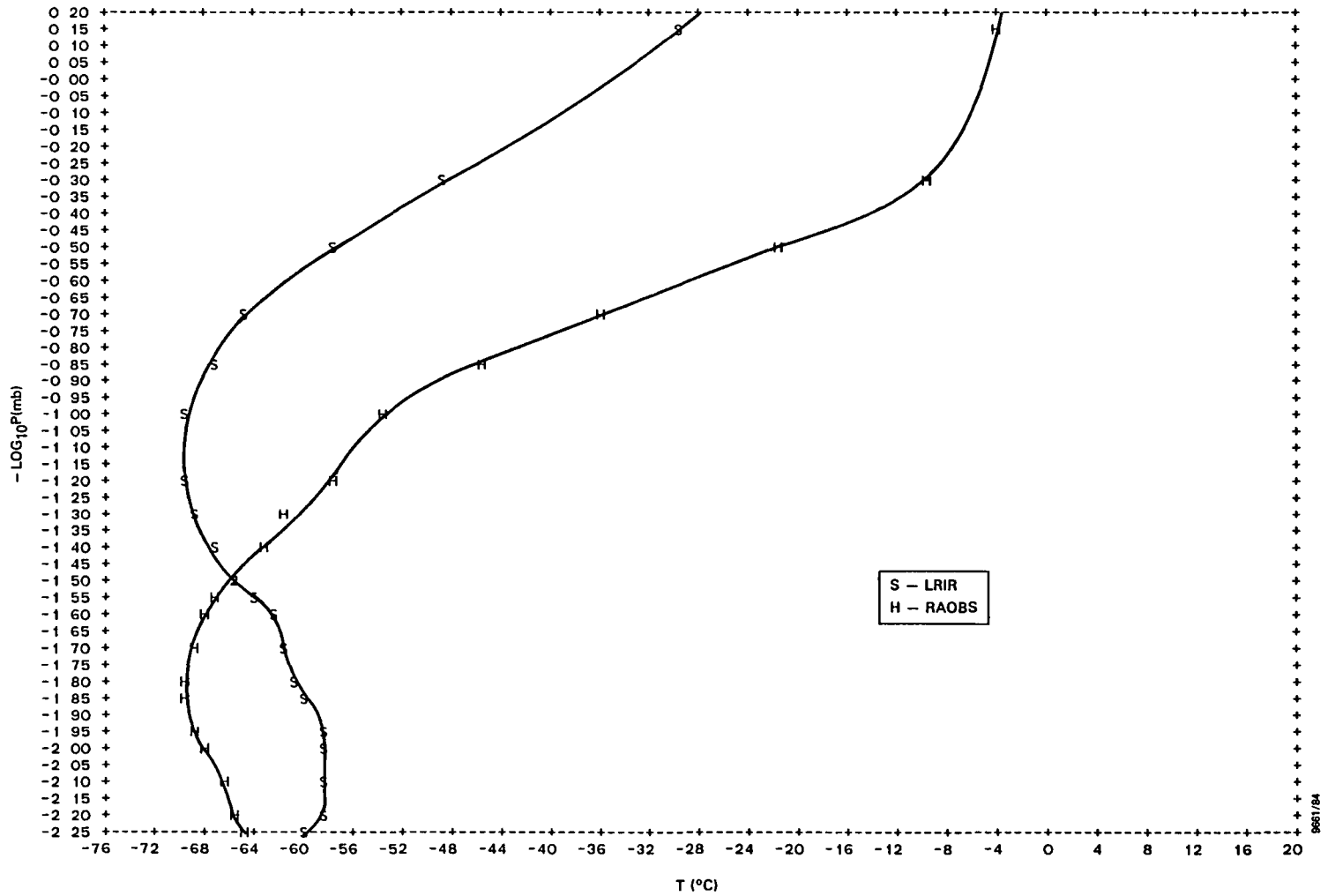

Figure 2-52. LRIR Temperature Data for July Compared With RAOBS-1972 Data for 60°S Latitude

thus the resulting radiance profile) of the stratosphere for the summer hemisphere and overestimates it for the winter hemisphere.

NSSDC provides Profile-R data tapes as Nimbus-7 LIMS Profile-R microfilm product tapes. (A detailed description of the generation and content of these data tapes is presented in References 12, 21, and 23. Reference 12 also describes the software used to analyze the LIMS data.) LIMS data include a reference scan angle corresponding to a tangent height of 30 kilometers for each profile. This scan angle provides a rough calibration of IR horizon scanner viewing heights and is expected to provide a conversion accurate to 3 kilometers for most conditions. A greater uncertainty is expected for the polar winter conditions, where the radiance variability is larger.

The 30-kilometer reference scan angle was determined by ground data processing at the National Center for Atmospheric Research (NCAR) using a procedure similar to that used on board for limb track point adjustment. The onboard limb track point is the angular position of 40 percent of peak CO_2N (narrow) channel radiance. Similarly, during ground data processing, the scan angle at 85 percent of peak radiance for the CO_2N channel is defined as a scanner viewing height of 30 kilometers. This correlation is based on a statistical average from a detailed simulation of Earth radiance.

As an independent check of the accuracy of the LIMS 30-kilometer reference scan angle, profiles of the LIMS nitric acid (HNO_3) band were plotted. Figure 2-53 shows concurrently measured LIMS profiles of the CO_2N channel, CO_2W (wide) channel, and nitric acid band as a function of tangent height based on the 30-kilometer reference scan angle conversion for sample scans on January 17, 1979. The

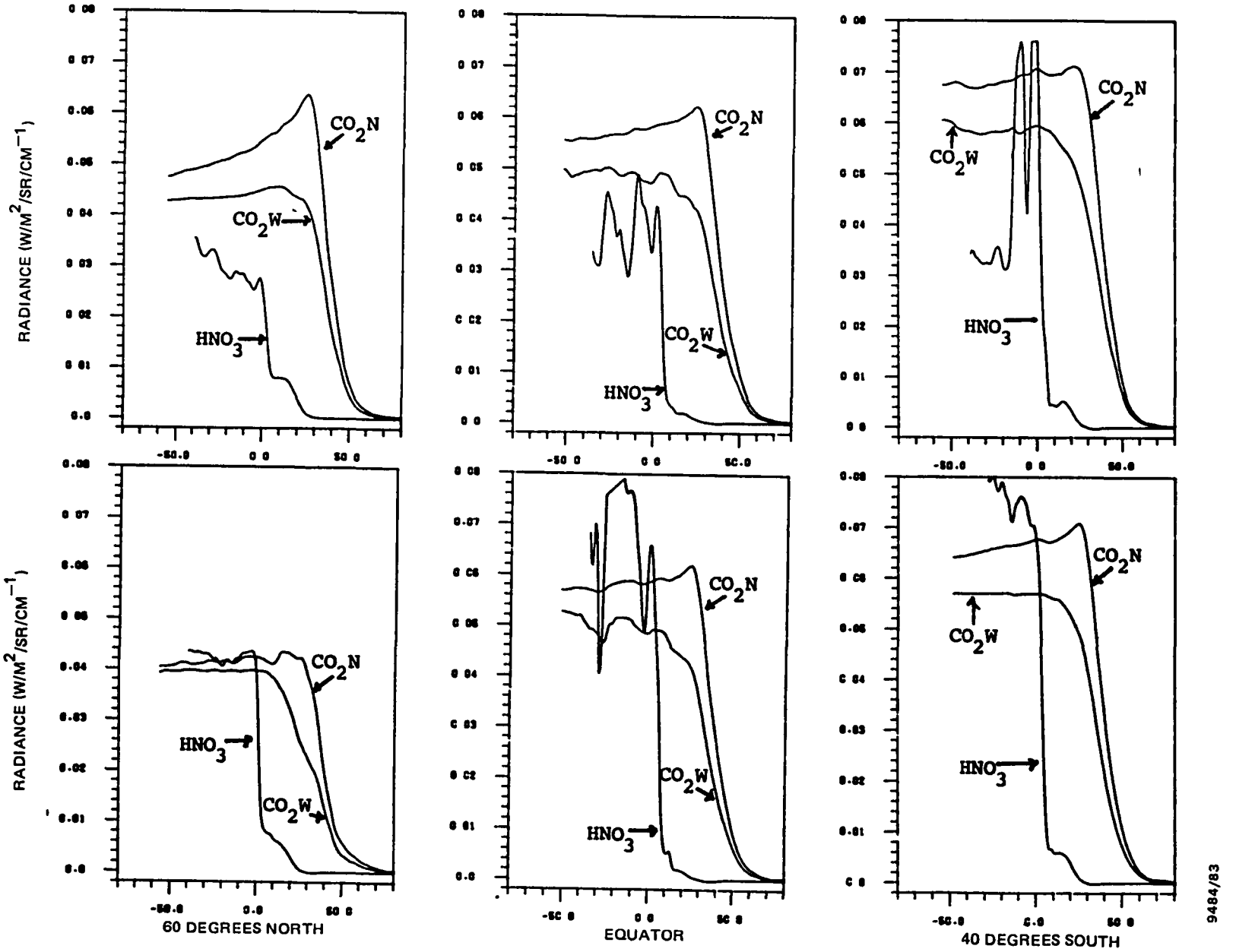

Figure 2-53. Sample LIMS Profiles of CO_2N, CO_2W, and HNO_3 Radiance Versus Tangent Height

sharp change in nitric acid radiance occurs between a tangent height of 0 and 10 kilometers with an approximate 6-kilometer variation in the 50-percent point. Calculations of the nitric acid profile using the LOWTRAN 5 program indicated that, for cloud-free conditions, a rapid rise of nitric acid radiance is expected to occur at a tangent height between 2 and 6 kilometers. Checks of occasional, clear-sky nitric acid radiance profiles measured by LIMS appear to support the use of the 30-kilometer reference scan angle for tangent height scale calibration to ± 6 kilometers accuracy. The 60^{o}N latitude profile set in the lower left corner of Figure 2-53 is the only set on the figure containing a nitric acid profile that is likely to be free of atmospheric cloud effects. The other five examples show obvious cloud disturbances in the 11.5-micrometer data. These data were used to estimate the effects of clouds on the corresponding CO_2N and CO_2W channel profiles, and the results confirm the accuracy of simulations that have been made using the LOWTRAN 5 program for the effects of clouds on the ERBS IR horizon scanners.

The conversion from scan angle to tangent height was computed using the 30-kilometer reference scan angle and a linear relationship between scan angle and tangent height resulting from the flight geometry. Negative tangent heights indicate positions below the physical horizon.

2.5.2 COMPARISON WITH HRDB

The observed Earth IR profiles just discussed were compared with the synthesized profiles (HRDB) discussed in Section 2.4, in an attempt to assess the accuracy of the HRDB data (Reference 12). The following is a review of that study and its results.

The HRDB profiles were integrated over the spectral passband for the CO_2N channel or the CO_2W channel in the LIMS

experiment. However, because the LIMS data are provided per wave number unit, an equivalent bandwidth, W_E, was derived for the two channels by

$$W_E = \sum_{i=1}^{N} \left[\frac{1}{(\lambda_i - 0.1)} - \frac{1}{(\lambda_i + 0.1)} \right] t_i \qquad (2\text{-}13)$$

where λ_i is the center wavelength in micrometers and t_i is the corresponding fractional transmittance for each of the N segments for the channel of interest in 0.2-micrometer steps. The use of W_E allowed a direct comparison of LIMS data with corresponding HRDB data.

The set of LIMS profiles from one day, the day nearest mid-month, were selected for comparison with the HRDB profiles for each month. From these, all profiles measured within 1 degree of the center latitude of each of the HRDB latitude bins were selected for comparison with the corresponding profile predicted by the HRDB. Figure 2-54 illustrates the LIMS/HRDB comparison for the CO_2N channel on November 16, 1978, at 80^oN latitude. Radiance is in units of watts per meter^2 per steradian per centimeter^{-1}. Figures 2-55 and 2-56 provide similar comparisons for the CO_2W channel, for 80^oN and 60^oS latitude, respectively.

The measured and predicted radiances for the optical path corresponding to a 0-kilometer tangent height are shown as a function of latitude for each of seven months in Figures 2-57 and 2-58 for the CO_2W and CO_2N channels, respectively. The HRDB data show good agreement with LIMS data in the tropics, but poor agreement near the North and South Poles in the winter and summer months. At higher latitudes, the HRDB tends to slightly underestimate LIMS in the summer hemisphere and to significantly overestimate LIMS in the winter hemisphere. The underestimation in the summer

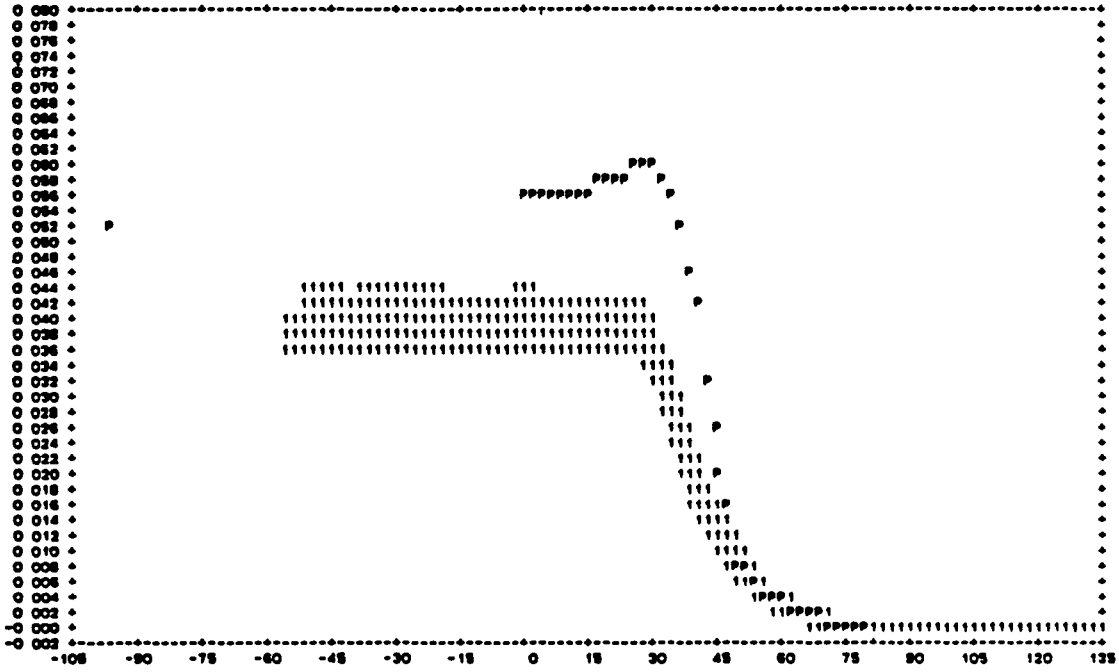

CO2N RADIANCE -VRS- TANGENT HEIGHT IN KM

OBSERVED DATA WITH PREDICTED OVERLAID

MONTH: NOV LATITUDE 80N

OBSERVED DATA	
-------- ----	
	NUMBER OF PROFILES(SCANS REPRESENTED) 58
	SUB-TANGENT POINT LATITUDE RANGE 79 0 81 0
	SUB-TANGENT POINT LONGITUDE RANGE 0 0 360 0
	TIME SPAN REPRESENTED 781118 021659000 781116 005507000
	TIME OF DAY DAY AND NIGHT
	SCAN: UP AND DOWN
	NUMBER OF DATA VALUES 12690
	OBSERVED DATA SCALING FACTOR 1 000
	PREDICTED DATA SCALING FACTOR 903 080
	30KM REFERENCE SCAN ANGLE USED FOR SCAN ANGLE/TANGENT HEIGHT CONVERSION

Figure 2-54. LIMS/HRDB Profile Comparison for the CO_2N Channel, November, 80°N Latitude (1-LIMS, P-HRDB)

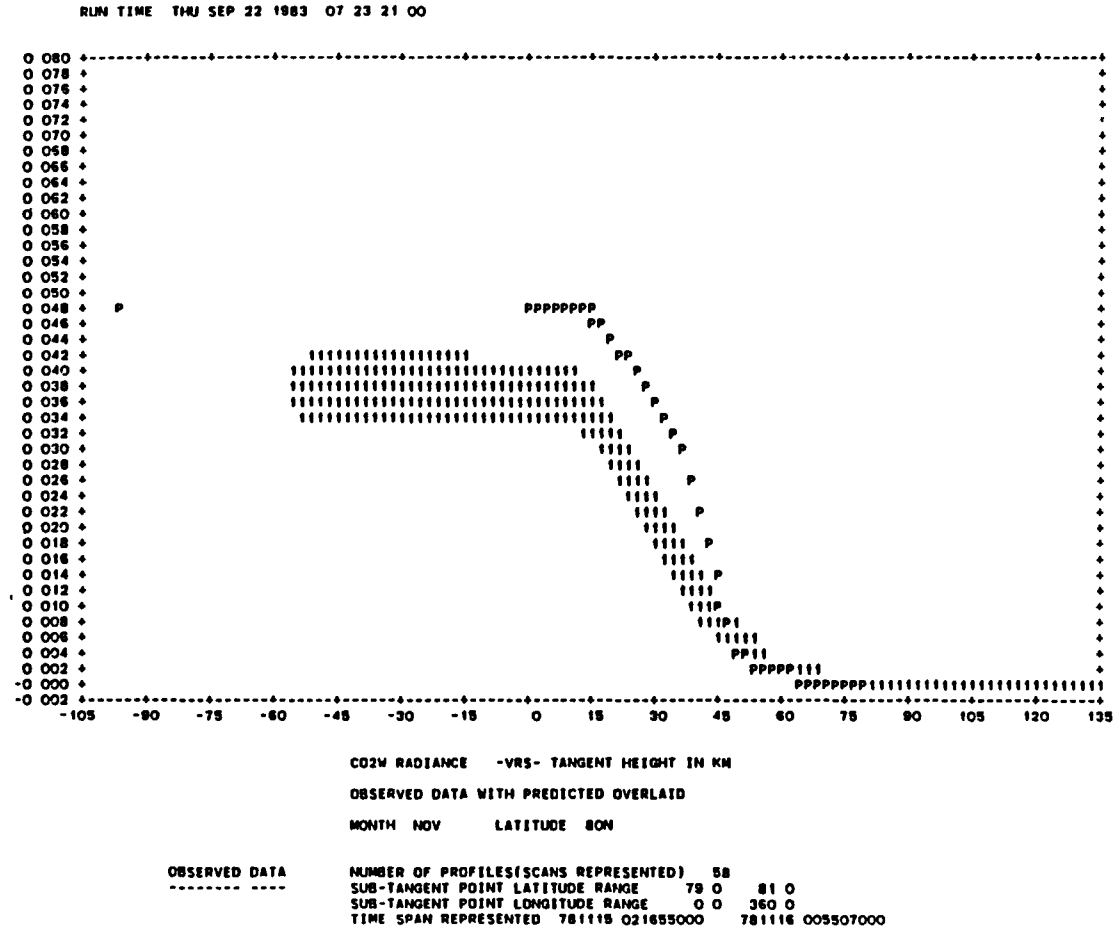

Figure 2-55. LIMS/HRDB Profile Comparison for the CO_2W Channel, November, 80°N Latitude (l-LIMS, P-HRDB)

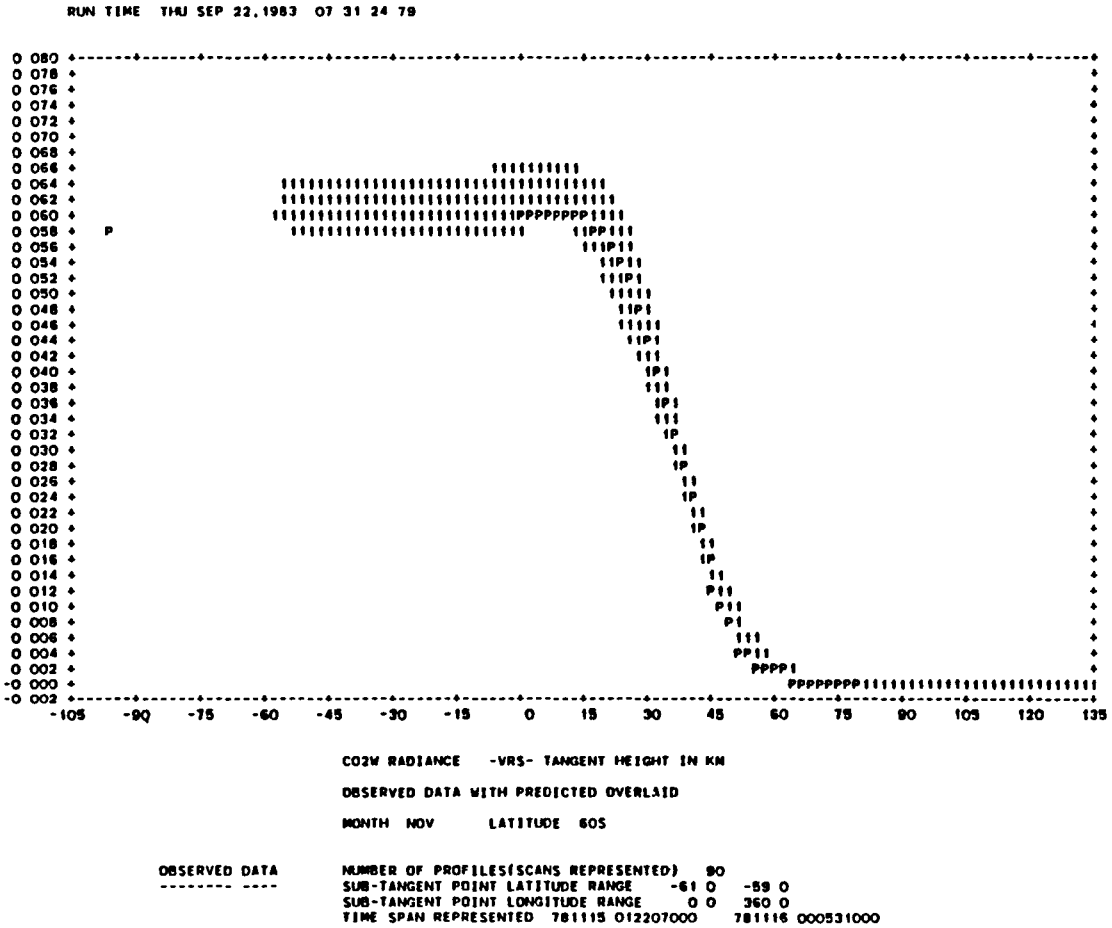

Figure 2-56. LIMS/HRDB Profile Comparison for the CO_2W Channel, November, 60°S Latitude (1-LIMS, P-HRDB)

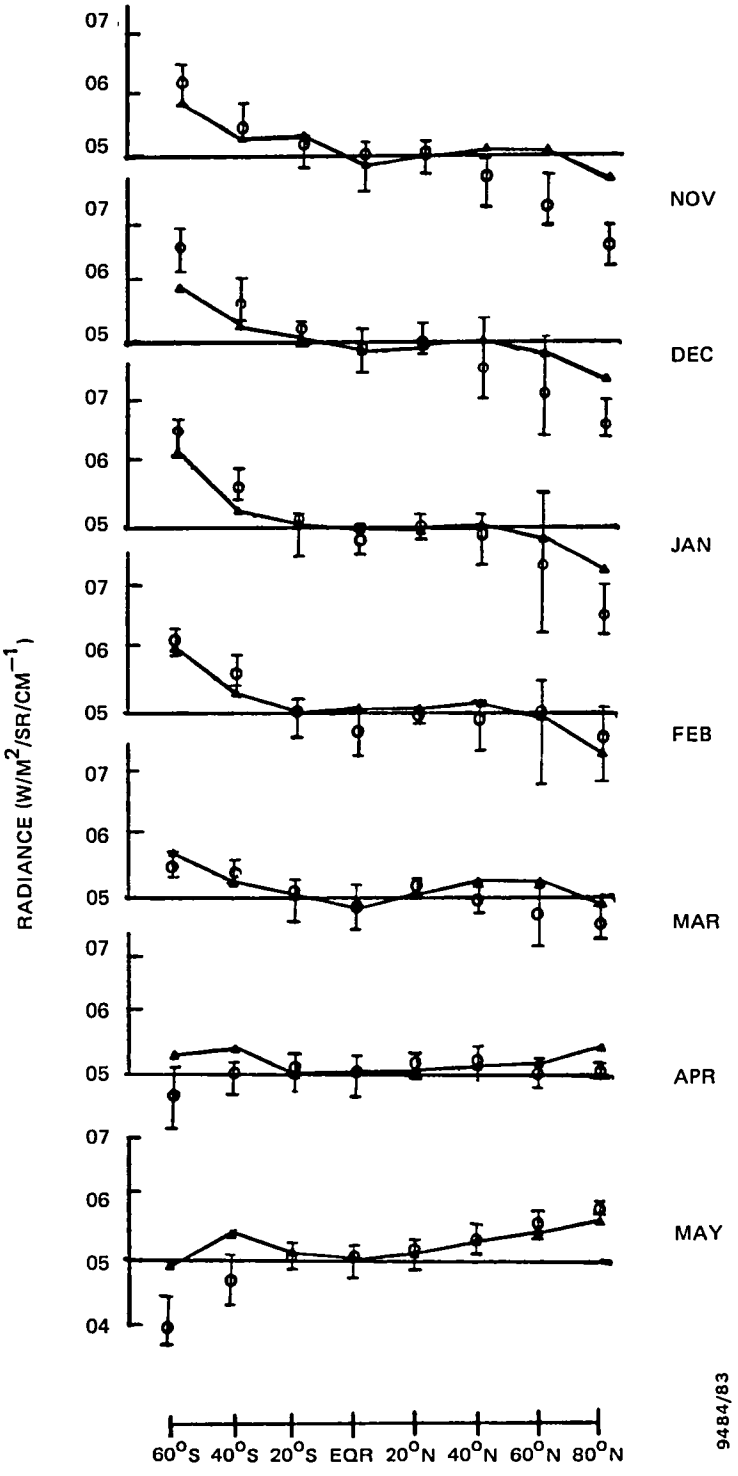

Figure 2-57. CO_2W Radiance Intensities at a 0-Kilometer Tangent Height (O-LIMS, Δ-HRDB; bars indicate maximum and mimimum LIMS values.)

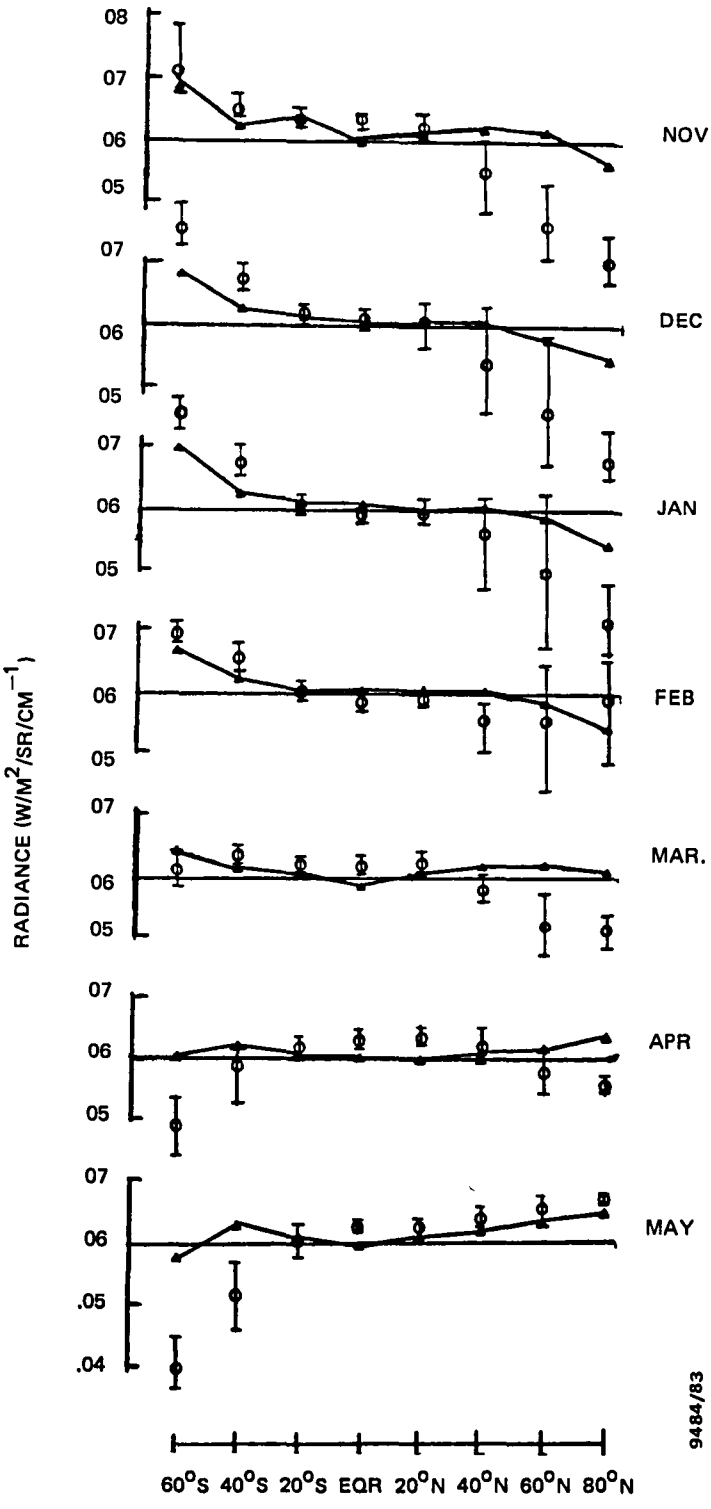

Figure 2-58. CO_2N Radiance Intensities at a 0-Kilometer Tangent Height (O-LIMS, Δ-HRDB; bars indicate maximum and minimum LIMS values.)

hemisphere varies from 3 to 10 percent, and the overestimation in the winter hemisphere varies from 15 to 30 percent. The HRDB generally shows better agreement with the CO_2W channel than with the CO_2N channel. Although agreement is generally poor in the polar regions, particularly at $80^{o}N$ in the winter, agreement appears to be good during the months of February and March. This is a result of a polar stratospheric warming event occurring in late January 1979.

The tangent height at which 50 percent of peak radiance occurs on the rising portion of radiance profiles is important because it provides an absolute indication of the changes in the effective IR Earth radius viewed by sensors over latitude and season. However, a comparison of the 50-percent tangent heights predicted by the HRDB with those indicated by LIMS yields little information about the HRDB model tangent height accuracy, because the uncertainty of tangent height at 50 percent of peak for LIMS profiles is on the order of ± 6 kilometers.

Figure 2-59 shows residual tangent height at 50 percent of peak radiance for the CO_2W channel as a function of latitude for each month. Generally, the HRDB predicts 50 percent of peak radiance to occur about 4 kilometers higher than LIMS. Due to the estimated 6-kilometer uncertainty in the LIMS tangent heights, however, this comparison between the HRDB and LIMS is inconclusive.

Because of the lack of an accurate absolute tangent height calibration in the LIMS Profile-R data, little information can be derived from this analysis about the HRDB model or about the actual systematic variation of the altitude of the profile 50-percent point. Moreover, the interpretation of the data presented in Figure 2-59 is not straightforward. It therefore remains as an analysis problem to present evidence and measurements of the systematic seasonal and

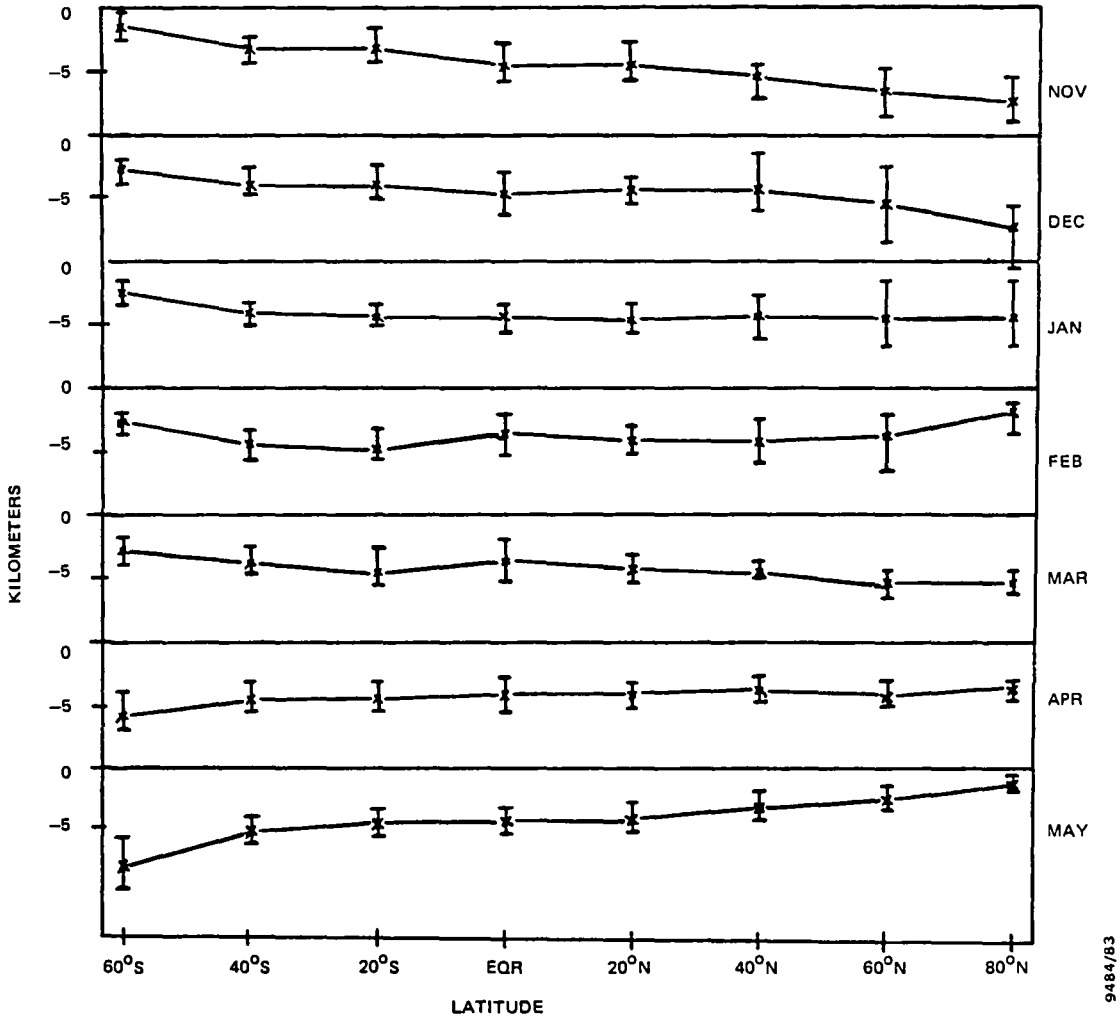

Figure 2-59. CO_2W Residual Tangent Height at 50 Percent of Peak Radiance (Observed-Predicted) (X's indicate mean residuals; bars indicate maximum and minimum residuals.)

latitude-dependent variation of the altitude of the profile 50-percent point. IR horizon scanner attitude systems with derivative locator logic, such as those on Landsat-4, have a chance of demonstrating this effect, and more accurately calibrated Nimbus-7 and TIROS-N data could contribute to the resolution of this problem.

2.5.3 DISCUSSION AND CONCLUSIONS

Comparison of the LIMS CO_2W channel data and the CO_2N channel data with the HRDB model of the LIMS data produced the following results: The HRDB model underestimates the radiance gradient between the Equator and the poles in the winter and summer seasons. The LOWTRAN 5 estimate of the LIMS data is better for the CO_2W channel data than for the CO_2N channel data and is primarily controlled by the accuracy of the input temperature profiles. The LOWTRAN 5 analysis appears to provide a sound analytical translation of temperature profiles into radiance profiles with good agreement in the midlatitudes for the amplitude of the radiance. The January North Pole LIMS profiles are modeled too brightly (i.e., more like equatorial data) by the LOWTRAN 5 program, and the January South Pole LIMS profiles are modeled slightly dimmer than the LIMS data; both are attributable to the input data from RAOBS-1972. The LOWTRAN 5 estimate of the tangent height of the 50-percent point of the LIMS CO_2W channel data is within ± 4 kilometers of the data, which is consistent with the tangent height calibration accuracy of the LIMS data. Not only has LIMS data provided a useful reference for comparison with the radiance model, it has also provided information about atmospheric radiance variability and structure caused by clouds and stratospheric warming phenomena. The LIMS/HRDB comparison analysis has not, however, provided a clear measurement of the dependence of the altitude of the 50-percent point of maximum radiance on season and latitude.

The significance of this last item on the horizon radiance model is as follows: If there is a large (5- to 10-kilometer) systematic variation in the altitude at which the profile intensities drop to 50 percent, the HRDB will have omitted a significant portion of the horizon radiance model. This omission has more significance for derivative locator logic and fixed threshold logic than it does for the normalized threshold locator logic.

If there is not a large (less than 5 kilometers) systematic variation in the altitude of the 50-percent point, the HRDB accounts for the major reason for triggering height changes with latitude and season for the normalized threshold locator logic. For the derivative threshold locator logic, however, the effects of systematic variation in the altitude of the 50-percent point of less than 5 kilometers pole to pole may be comparable to the changes in triggering height induced by profile brightness variation. For this latter case, the HRDB accounts for only part of the modeled source of triggering height variations.

It is important, therefore, for normalized threshold system modeling, either to acquire data showing the variations in the altitude of the 50-percent point to be less than 5 kilometers or to determine what these variations are to an accuracy of about 2 kilometers. For the modeling of derivative locator logic systems, the systematic variations of the altitude of the 50-percent point are the most important aspect of the model, especially if the variations are greater than 5 kilometers pole to pole. Data that could provide this information are Landsat-4 IR horizon scanner data compared with star tracker data, and Nimbus-6 and -7 and TIROS-N data converted to temperature profiles with accurate ($\leq$ 2 kilometers) geodetic altitude scales.

SECTION 3 - HORIZON RADIANCE MODELING UTILITY

The Horizon Radiance Modeling Utility (HRMU) is a standalone program that determines the effective height of the IR horizon as sensed by one or two IR horizon scanners. It is executed in the batch mode to compute heights of the predicted horizon at AOS and LOS (for a given set of radiance profiles) as a function of the time of year and the subsatellite latitude. The height data can also be converted to pitch and roll errors assuming a null spacecraft attitude. The HRMU is capable of generating intermediate computation results and printer plots in addition to horizon altitude data sets for modeling analysis, simulation studies, or mission support.

The HRMU was originally designed for Seasat and AEM/HCMM (Reference 24) but has been modified repeatedly for greater flexibility and better quality output. Several versions of the program exist. Some have extensive options to facilitate detailed analyses and sensitivity studies, and some were used operationally for mission support. The latest versions were created for simulation analysis and operational support of the ERBS mission (Reference 25).

3.1 OVERVIEW

The HRMU is used for both operational support and prelaunch analysis of the IR horizon scanners. The important characteristics and capabilities of this utility program can be summarized as follows:

- Accepts a data base of IR radiances specific to the scanner system being studied. The data base provides radiance profiles as a function of optical viewing paths, month or season, and latitude.

- Interpolates input radiance data to generate profiles for a finer latitude grid, using an adjustable number of input data points.
- Uses an internal orbit generator that requires the Keplerian orbital elements.
- Models the IR scanner mounting geometry using NAMELIST parameters and the assumption of a nominal attitude for the spacecraft.
- Performs the FOV integration to obtain the IR radiation accumulated at the bolometer flake for a specific position in the orbit and scan angle.
- Accepts electronics parameters (e.g., time constants and amplifier frequencies) as input data. Computes the electronics transfer function and convolves it with the bolometer input signal to produce the output pulse.
- Computes the scan angle of the detected Earth horizon at AOS and LOS according to the locator logic specific to the scanner electronics model.
- Converts AOS and LOS scan angles into horizon triggering altitudes and writes output to a data base for use in mission support attitude operations.
- Converts AOS and LOS data to simulated pitch and roll errors for one or two IR scanners.
- Plots the AOS and LOS altitudes and pitch and roll errors as a function of some orbital parameter (e.g., subsatellite latitude or phase angle from node).

A more detailed description of the program is provided in References 24 and 25. Some of the functions described above vary in the different versions of the program. The primary

functions that differ are the FOV integration, the electronics transfer function, and the locator logic.

The FOV integration was performed for an equivalent square FOV in all versions of the HRMU except the two most recent: the one used to simulate bolometer input pulses for use by ITHACO in the ERBS prelaunch IR scanner analysis (see Section 4.6) and that developed for ERBS operational support (Reference 25). The simulation version (not documented separately) uses detailed ray-tracing results through the optical system; the operational version uses an analytical model to simulate the FOV distortion. These models are discussed in more detail in Section 3.2.

The electronics transfer function is a linear model in all versions of the HRMU except that for the DE-2 mission, which uses a state variable approach. The individual models also differ in the number of electronics components included. The original Seasat version used three time constants and two amplifier frequencies, the Magsat version used only one amplifier frequency, and the recent ERBS version uses five time constants. Furthermore, the ERBS version has two separate branches: one for the locator logic and one for the threshold determination subsystem.

The locator logic implemented in the different versions of the HRMU is based on two broad categories: fixed threshold and normalized threshold. The Seasat and ERBS versions use the normalized threshold, in which detector pulse is generated when the output pulse matches a specified percentage of the threshold pulse accumulated from a previous scan. The AEM and Magsat versions used a fixed-threshold as a fixed percentage of expected peak signal, and the DE-2 version used a variation on the normalized threshold logic that used the derivative of the Earth pulse instead of the pulse itself. The details of the locator logic used on the

missions discussed in this report are summarized in Table 1-1.

The HRMU program has been used for IR scanner analysis for six missions: Seasat, AEM/HCMM (not discussed in this report), AEM/SAGE, Magsat, DE-2, and ERBS. The Landsat-4 IR scanner analysis was performed by a somewhat different version of the HRMU developed by GSC under contract to the ADCS. Application of the HRMU analysis to the Seasat and Magsat missions was very useful and led to improved understanding of these systems. For example, the effects of clouds on the horizon-triggering altitudes for the wide passband scanner used on Seasat are now better understood. For Magsat, the IR scanner data residuals, using FHST data for reference attitudes, were compared to the simulated results and provided some insights into the behavior of the scanner performance as a function of triggering threshold. CSC and ITHACO, Inc., performed simulations for the ERBS mission using a detailed optics model; CSC used the transfer function model of the electronics, and ITHACO, the state variable model. These predictions will be compared with the mission data analysis in the near future. The three other applications of the HRMU program (AEM/HCMM, AEM/SAGE, and DE-2) led to indefinite results. The analysis of the mission data in these cases was incomplete; no effort was made to properly compute sensor biases or to check the IR scanner simulated results against mission data. For the DE-2 mission, the horizon triggering altitude data base was generated but was not used for mission support due to unresolved questions about its accuracy and usefulness and the loss of an accurate attitude reference caused by partial failure of the electronics in the fine Sun sensor. Further details of these applications are provided in Section 4 under the appropriate mission.

3.2 FOV INTEGRATION

The HRMU program accepts the Earth IR radiance profiles specific to the IR scanner. The IR radiation is focused by the optical system onto a bolometer flake to generate the input pulse to the electronics. The energy received at the bolometer depends on a number of factors. Some of these depend on the specific scanner (e.g., the size of the active region of the bolometer, the focusing characteristics of the optical system, or the spectral response function of the filter window); others depend on the geometry of the orbit and the scanner mounting alignment. The energy impinging on the bolometer flake is computed by integrating the radiance profiles over the FOV, the size and shape of which depend not only on the scanner system but also on the actual scan angle at that instant.

The optical system for the IR scanner used on ERBS is shown schematically in Figure 3-1. The major optical components are a filter window that provides the spectral selection, a rotating germanium lens/wedge (consisting of a prism and a plano-convex lens) that provides a change in direction from the actual line of sight to the optical axis and partial focusing of the rays, and a hyperhemispherical lens that completes the focusing process. The bolometer flake is embedded in the stationary hyperhemispherical lens. The scanner collects radiation centered on the FOV vector at 45 degrees from the optical axis (the specific value of this angle is determined by the apex angle of the prism part of the lens/wedge and the refractive index of the material). The line-of-sight cone rotates about the optical axis of the scanner as the lens/wedge portion rotates. The bolometer flake, however, remains fixed, which results in distortion in the angular size and shape of the FOV.

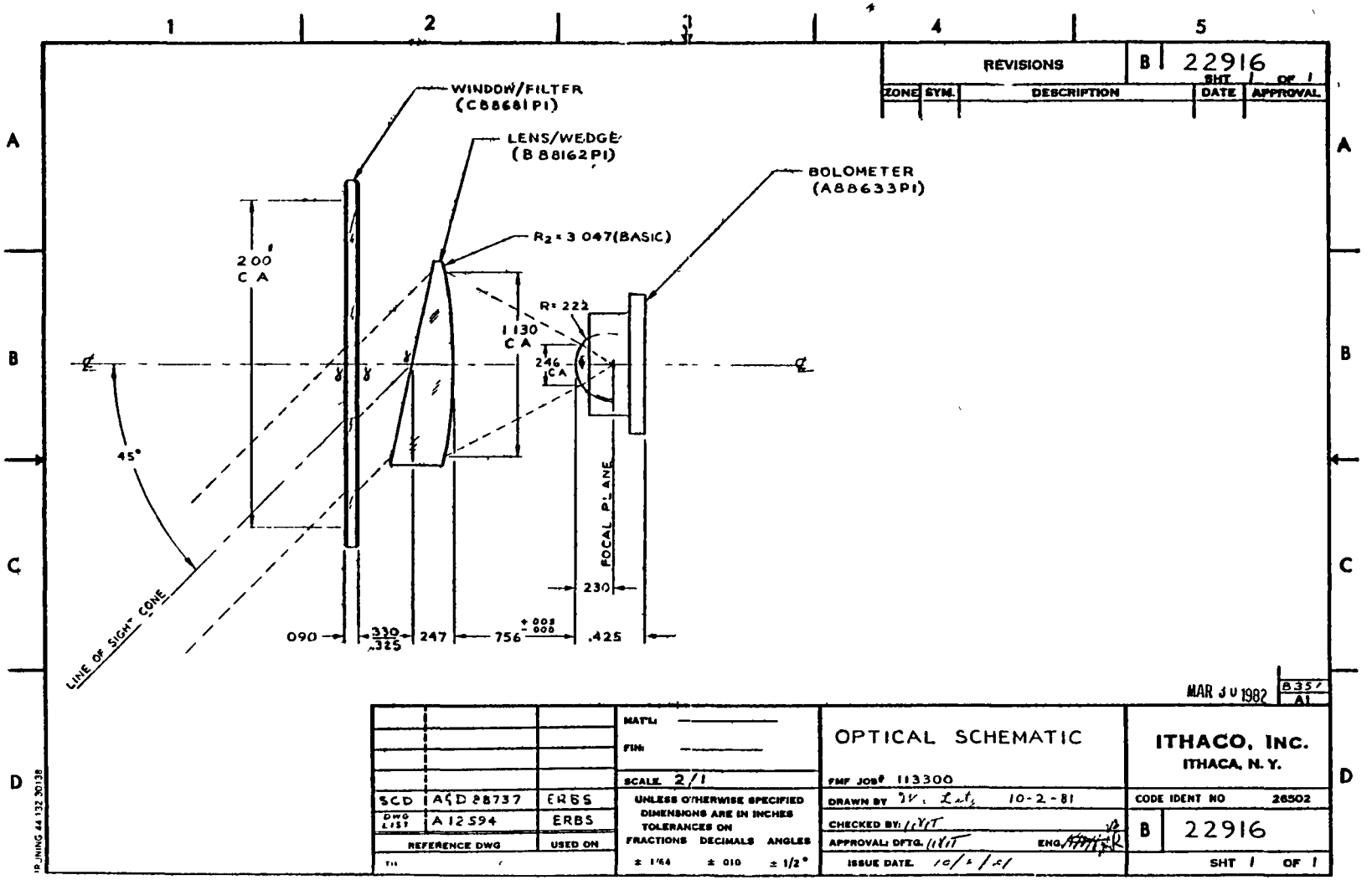

Figure 3-1. ERBS IR Scanner Optical Schematic (Compliments of ITHACO, Inc.)

The FOV integral has generally been modeled by an analytical method assuming that the radiance profiles vary only slowly in one direction within the FOV and that the FOV edges are abrupt. The early FOV model simply rotates a geometrically square FOV with the scan angle; the ERBS software models rotation and distortion of the FOV. The numerical method developed for ERBS prelaunch analysis uses an FOV model based on ray tracing performed by the Geometric Optical Analysis of Lens Systems (GOALS) Program (References 26 and 27). The distribution of rays focused onto the bolometer flake is normalized relative to the FOV center for far field to generate the optical intensity distribution (OID) function. The FOV integral is then performed numerically by summing the product of the OID function and the radiance intensity corresponding to that specific point in the FOV. Details of this method and some of the computed OID functions are discussed in Section 3.2.2.

3.2.1 THE ANALYTIC METHOD

All operational versions of the HRMU program have used the analytic method because the detailed optical model was not thought to be essential for modeling accuracy, and because of the computational speed. For mission support, the HRMU is typically executed for a number of circular orbits at varying heights and different months. For each orbit, it generates a set of AOS and LOS triggering altitudes for a number of subsatellite latitudes around the orbit. This data base of horizon altitudes is then used during mission support to correct for IR-related attitude errors. It provides a triggering altitude for the specified time and position of the satellite using a multistep interpolation scheme.

The FOV is limited by the square mask (0.1 by 0.1 millimeter in the ERBS scanner) over the bolometer flake. Without the prism part of the lens/wedge, the FOV would be a square on

the unit sphere centered on the outgoing Scanwheel axis (optical axis) direction. The presence of the prism, however, shifts the FOV line of sight by 45 degrees and changes the shape of the FOV. The resulting FOV is a rectangle for scan angles of 0, $\pm$90, and 180 degrees; a diamond for $\pm$45 and $\pm$135 degrees; and a parallelogram for other scan angles. Figure 3-2 shows the ERBS FOV model for several scan angles. One of the cases included is for a scan angle of approximately 67 degrees, corresponding to LOS. The square FOV, in the absence of the prism, is also shown for reference.

Figure 3-3 shows the geometry of the left IR scanner relative to the nominal spacecraft axes for the ERBS mission. The scanner spin axis is in the body Y-Z plane at a tilt angle α from the orbit normal. The scanner line of sight sweeps out a cone around the spin axis of half angle λ (cone angle). Figure 3-4 depicts the relationship between α; λ; the scan angle, η; and the line of sight angle, γ. The scan angle is the positive angle about the scanner spin axis from the nadir to the instantaneous line of sight, and γ is the arc length from the line of sight to the nadir. Angle γ is related to the other three angles by

$$\cos \gamma = \cos \lambda \sin \alpha + \sin \lambda \cos \alpha \cos \eta \qquad (3\text{-}1)$$

The horizon crossing angle ψ, between the scan direction ($\hat{n}$) and the unit normal to the Earth isoradiance contours ($\hat{x}$) (illustrated in Figures 3-2 and 3-5) is related to the angles α, λ, and γ by

$$\sin \psi = (\sin \alpha - \cos \lambda \cos \gamma)/(\sin \lambda \sin \gamma) \qquad (3\text{-}2)$$

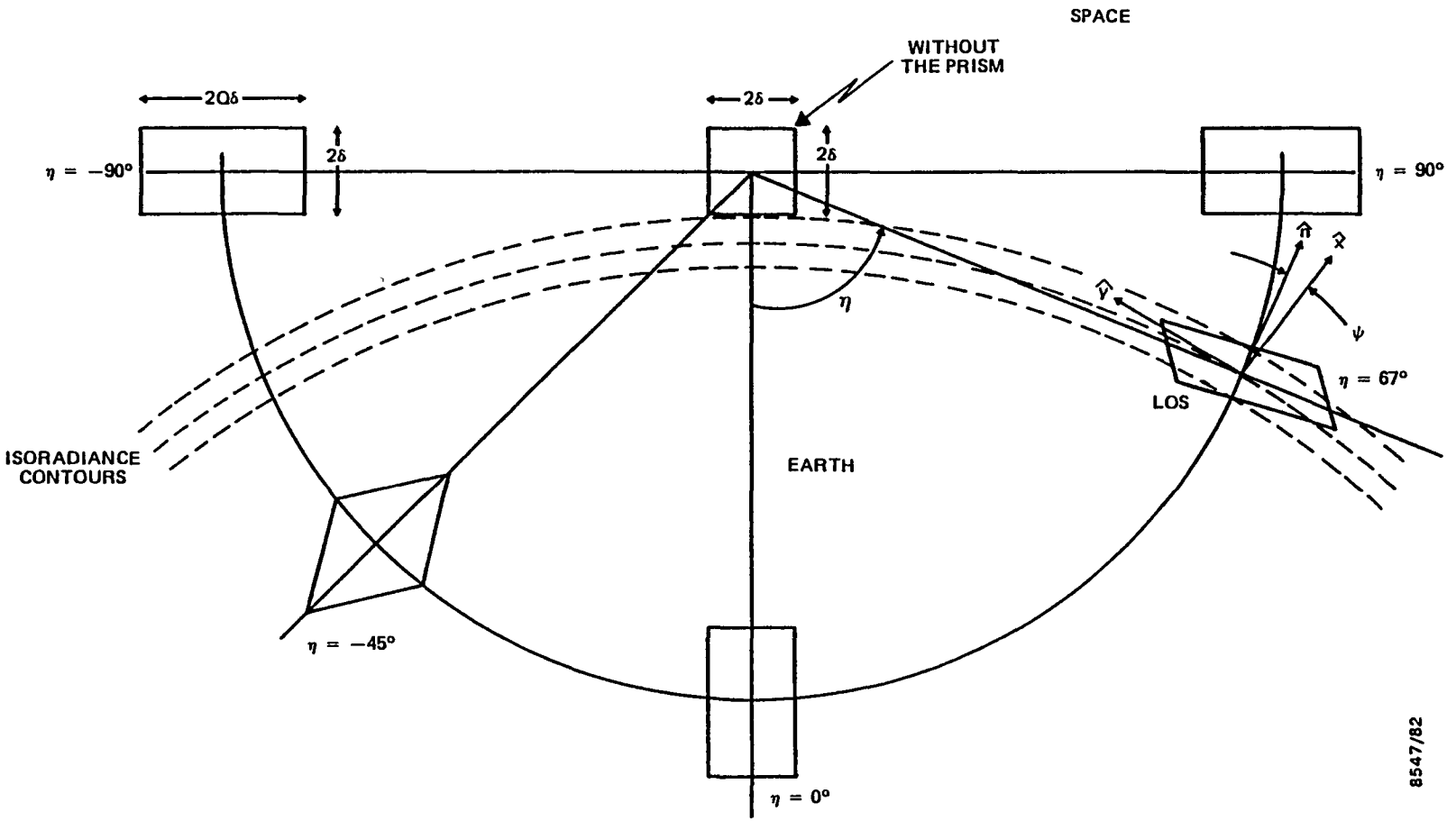

Figure 3-2. Shapes of Scanner FOVs for Various Scan Angles (η)

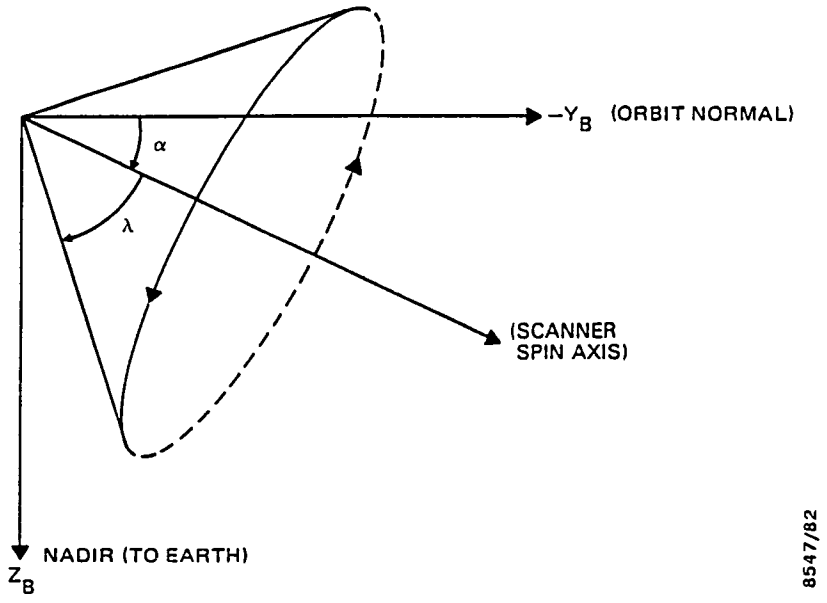

Figure 3-3. Left IR Horizon Scanner Geometry for ERBS

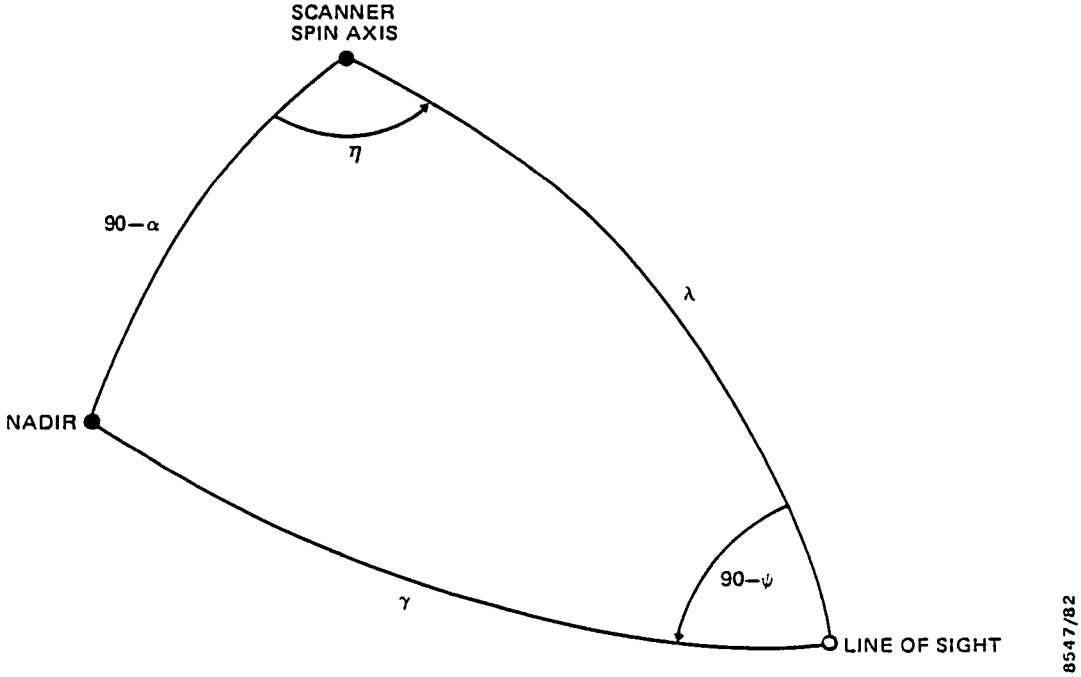

Figure 3-4. Scanner Geometry on the Celestial Sphere

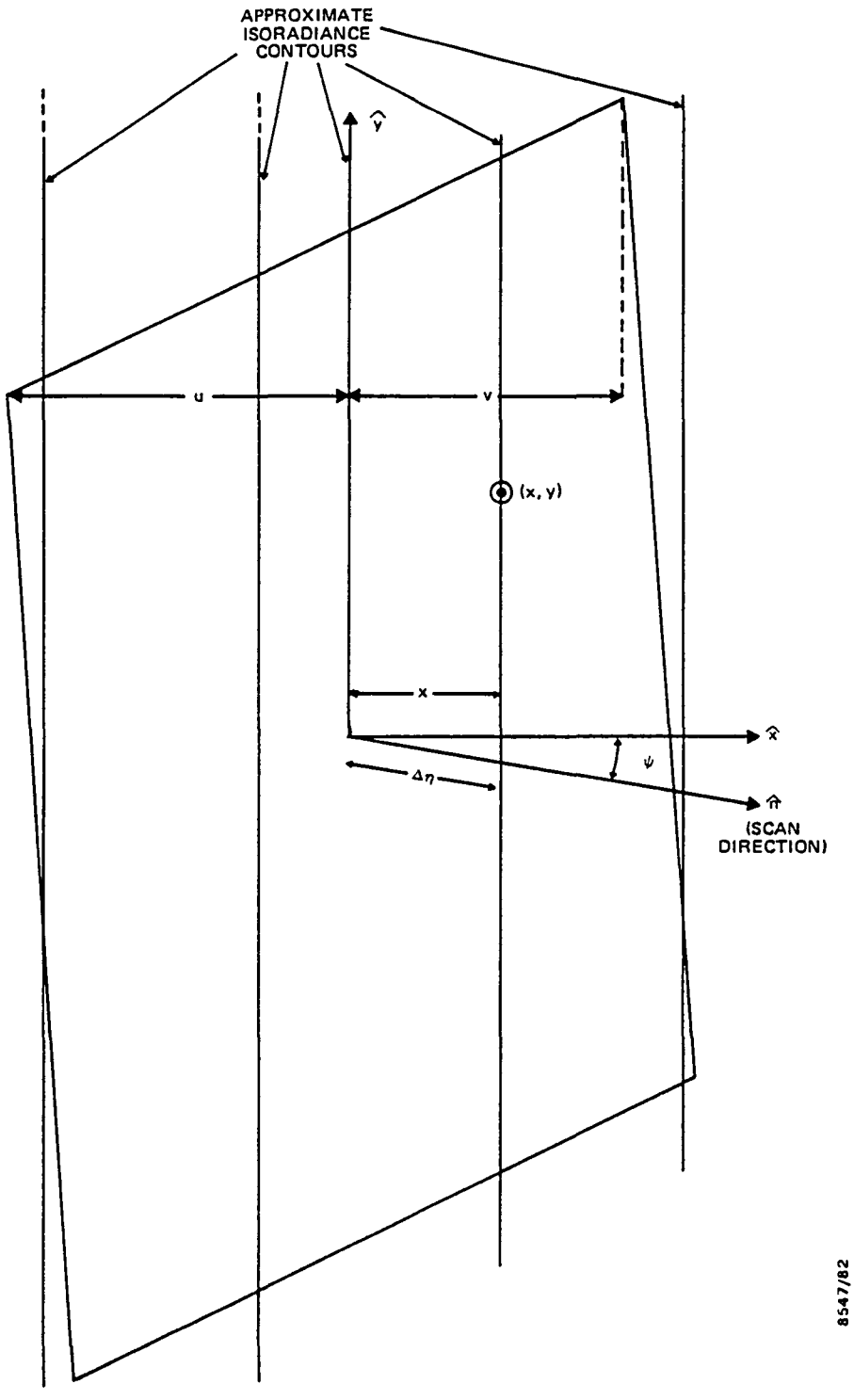

Figure 3-5. Geometry of FOV Integral

The FOV integral computed at a given scan angle, η, results in the average radiance, $R_{AV}(\eta)$:

$$R_{AV}(\eta) = \frac{1}{A} \iint_{FOV} R(\eta + \Delta\eta)\, dx\, dy \qquad (3\text{-}3)$$

where A is the angular area of the FOV, $R(\eta + \Delta\eta)$ is the radiance within the FOV for a subscan angle displaced from the nominal value, and x and y are directions perpendicular and parallel to the isoradiance lines. Figure 3-5 illustrates the geometry for the ERBS FOV model. The two-dimensional integral of Equation (3-3) is reduced to a simple integral:

$$R_{AV}(\eta) = \int_{-u}^{u} f(x)\, R(\eta + \Delta\eta)\, dx \qquad (3\text{-}4)$$

where f(x) is a weighting function whose functional form changes at $\pm u$ and $\pm v$. Parameters u and v are defined by Figure 3-5.

The ERBS FOV model differs from the previous versions in accounting for the distortion and thus the definitions of the u and v parameters. Further details on these models are presented in References 28 and 9.

3.2.2 THE DETAILED OPTICS NUMERICAL METHOD

The numerical method was used in the prelaunch analysis for the ERBS IR scanners. This detailed optical system analysis was performed by CSC using the GOALS program (References 26 and 27) to compute an OID data base. This data base was used in a numerical sum to provide a refined analytical estimate of the input IR pulse to the bolometer flake. These pulses were computed for the ERBS orbital geometry using

nominal radiance profiles, cloud profiles, and direct Sun IR interference conditions for the mission orbit and for the ITHACO calibration test facility conditions. These bolometer input pulses were used by ITHACO to simulate the attitude errors using a state variable model of the electronics, which is discussed in Section 4.6.

The GOALS program is a general-purpose ray-tracing program used to study the response of an optical system. The version used in the ERBS IR scanner study was obtained from GSFC Code 717 (Optics Branch) and is executed on the VAX-11/780 computer. The details of the GOALS program are described in References 26 and 27.

A detailed study was performed on the ERBS scanner optics (Figure 3-1) for two distinct conditions: one dealing with the mission mode for object points at a very large distance (approximately 500 kilometers) along the optical axis, and the other for the ITHACO test/calibration fixture for object distances varying from 14 to 27 inches. The region of the object area to be investigated was divided into pixels of equal solid angles subtended at the scanner location. The evaluated region was sufficiently large to ensure that none of the rays originating at the edges entered the bolometer flake. A total of 100 rays were traced from each object point for a single wavelength (400 in the case of the near field study). The number of rays from each pixel in the object plane focused on the flake was normalized to provide the OID function. The function thus had a value of 1.0 for pixels at infinity at the FOV center.

Figures 3-6, 3-7, and 3-8 present the resulting mission mode OID function for scan angles of 0, 20, and 45 degrees, respectively. The region shown is a 3- by 3-degree field (with a granularity of 0.05 degree) corresponding to a grid size of 3 degrees in the scan direction and 4.2 degrees in

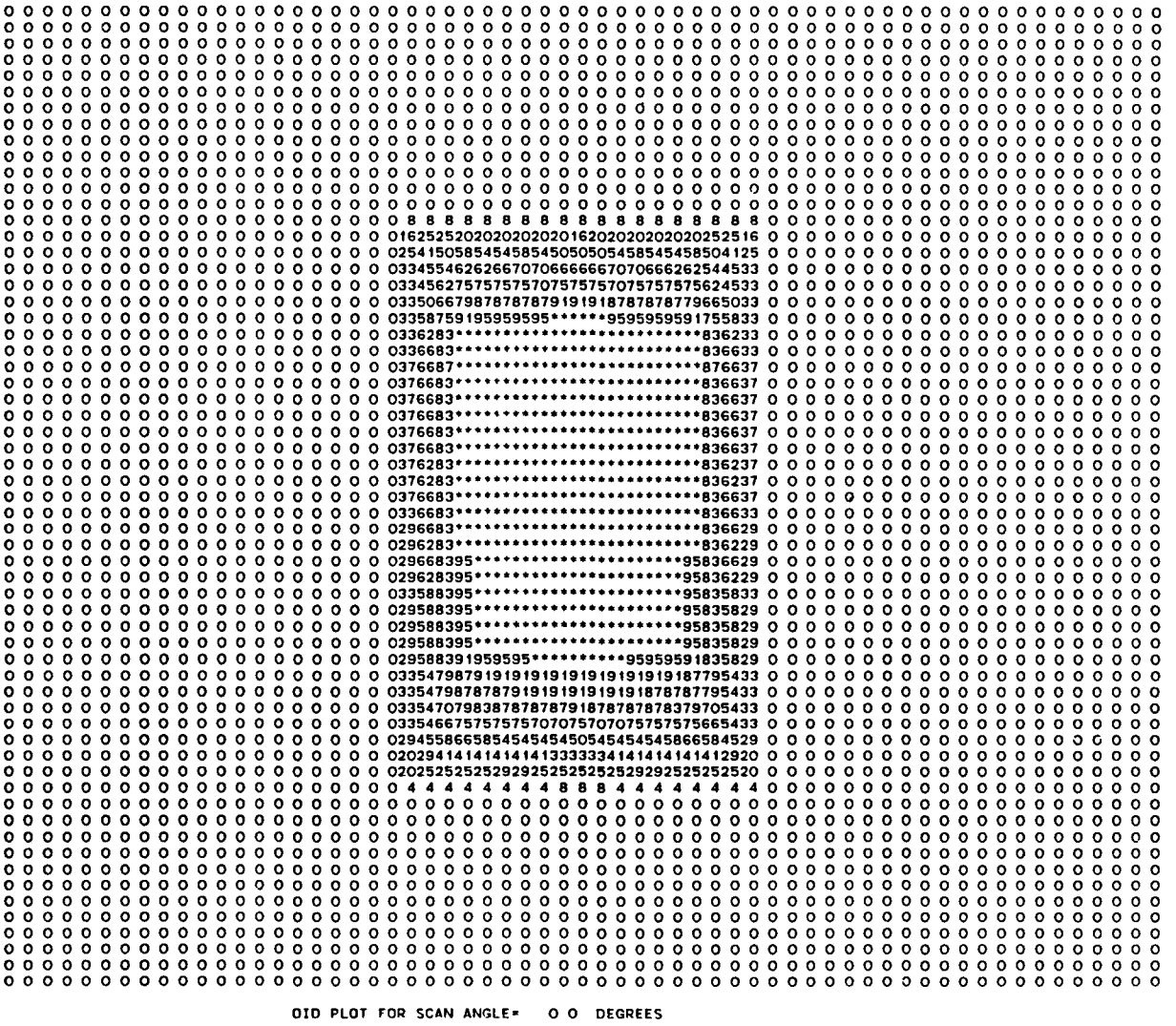

Figure 3-6. Optical Intensity Distribution Function for Mission Mode (Far Field) at 0-Degree Scan Angle

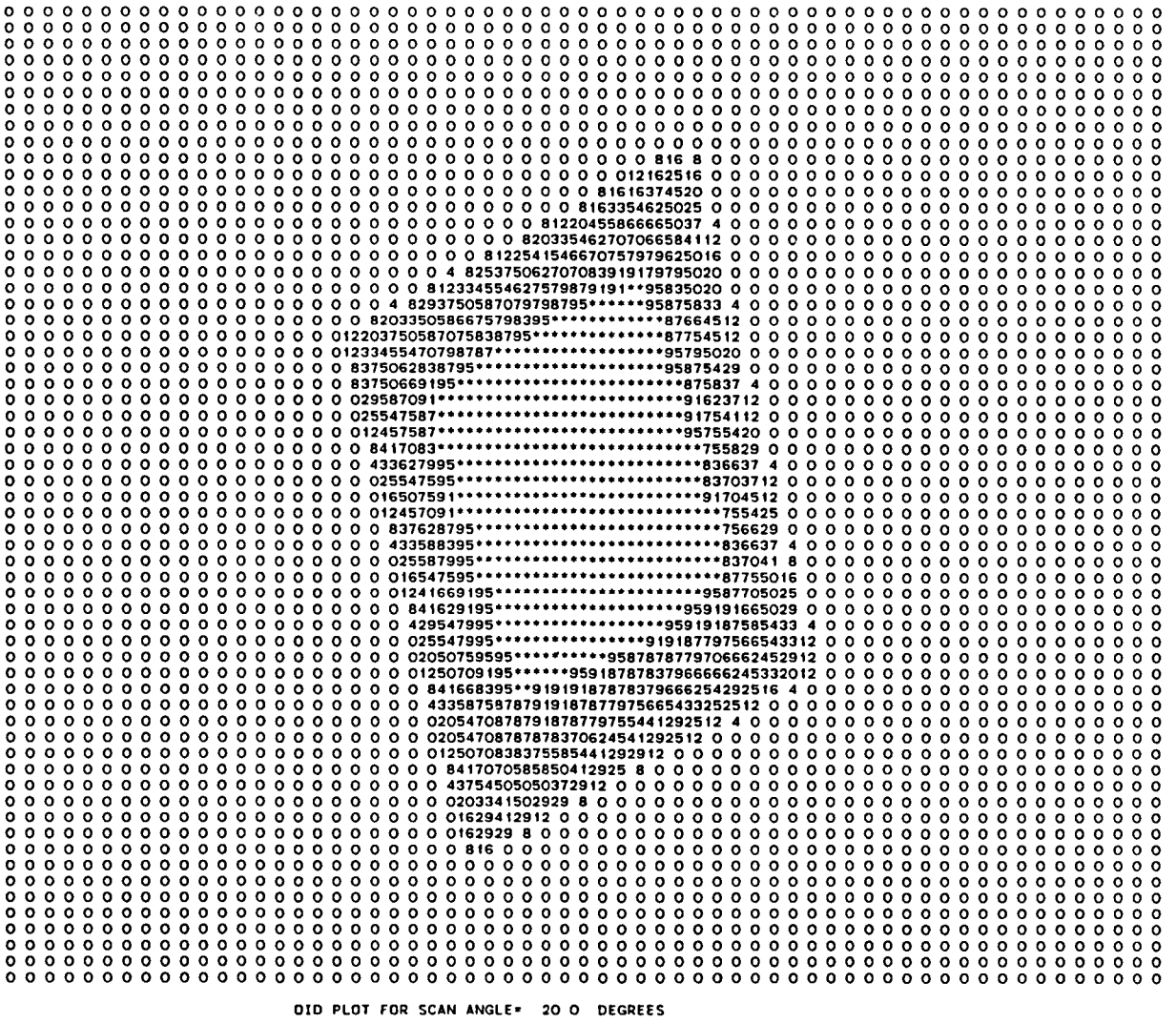

Figure 3-7. Optical Intensity Distribution Function for Mission Mode (Far Field) at 20-Degree Scan Angle

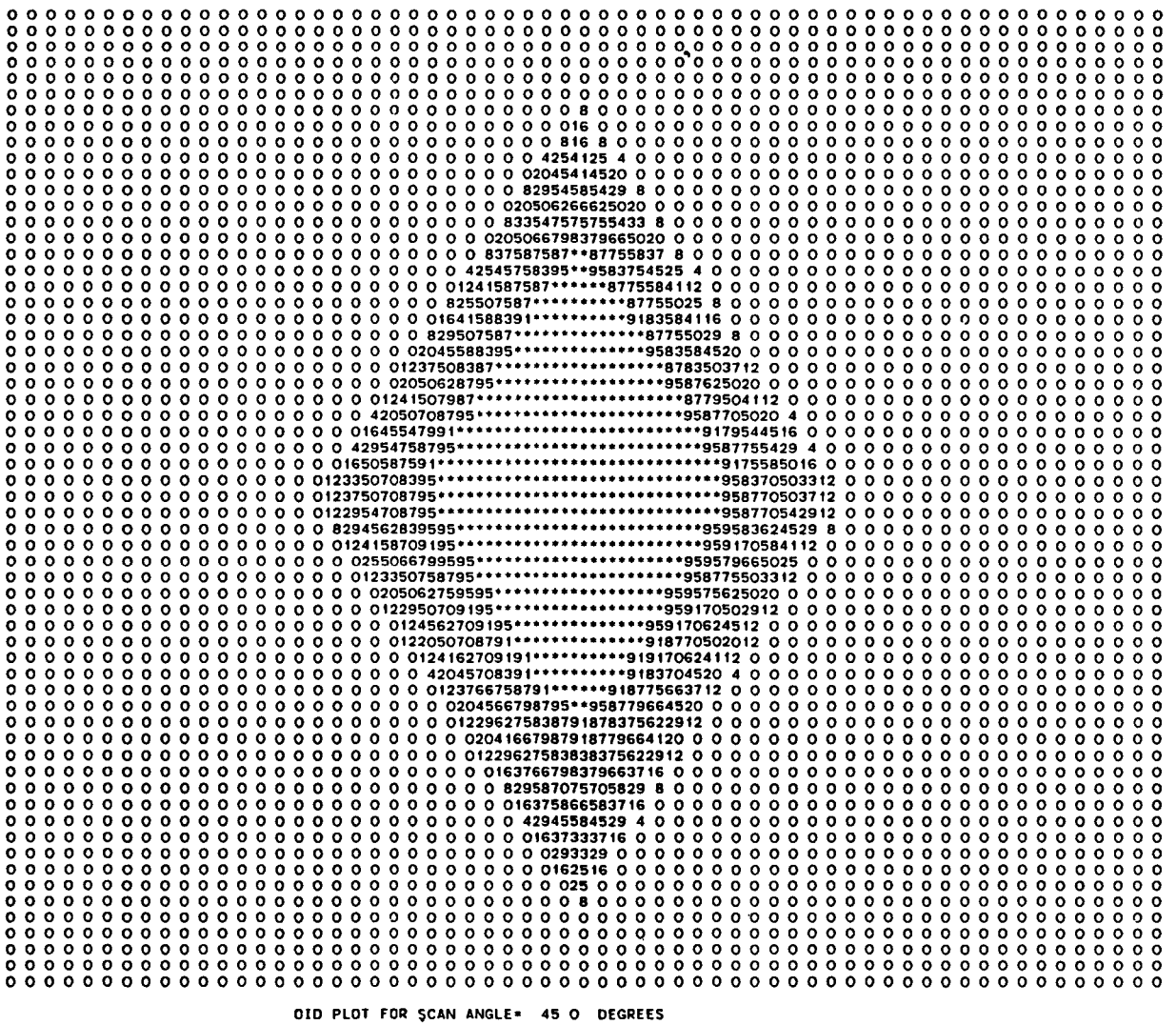

Figure 3-8. Optical Intensity Distribution Function for Mission Mode (Far Field) at 45-Degree Scan Angle

the cone angle direction due to the distortion effects of the prism. The OID data are shown as two-digit percentages. The center of the FOV is filled with asterisks, indicating the normalized value of 100 percent. The figures clearly demonstrate the distortion of the FOV from a rectangle at η equal to 0 (Figure 3-6), to a parallelogram at η equal to 20 degrees (Figure 3-7), and finally to a diamond at η equal to 45 degrees (Figure 3-8). The figures also illustrate the gradual fall-off near the edges of the FOV.

For the near field case, the dimensions of the surfaces of the test/calibration setup shown in Figure 3-9 were measured to obtain realistic object distances for the structure surfaces at different scan angles. Figures 3-10 and 3-11 show the OID function for a scan angle of 20 degrees with a Z-distance (object distance along the optical axis) of 27 inches and 14 inches, respectively. The data are plotted for a 4- by 4-degree region with a granularity of 0.1 degree, to accommodate the defocusing of the image. The smearing of the image over a larger area, loss of clarity of the image, and an absence of object points with a 100-percent focusing are clearly demonstrated by these figures.

3.3 HRMU ELECTRONICS MODELING

The electronics signal processing system was considered as a linear system between the input signal received by the bolometer (S_I) and the output signal at the locator logic (S_O). The relationship is expressed by

$$S_O(t) = \int_{-\infty}^{t} S_I(t')\, F(t - t')dt' \qquad (3\text{-}5)$$

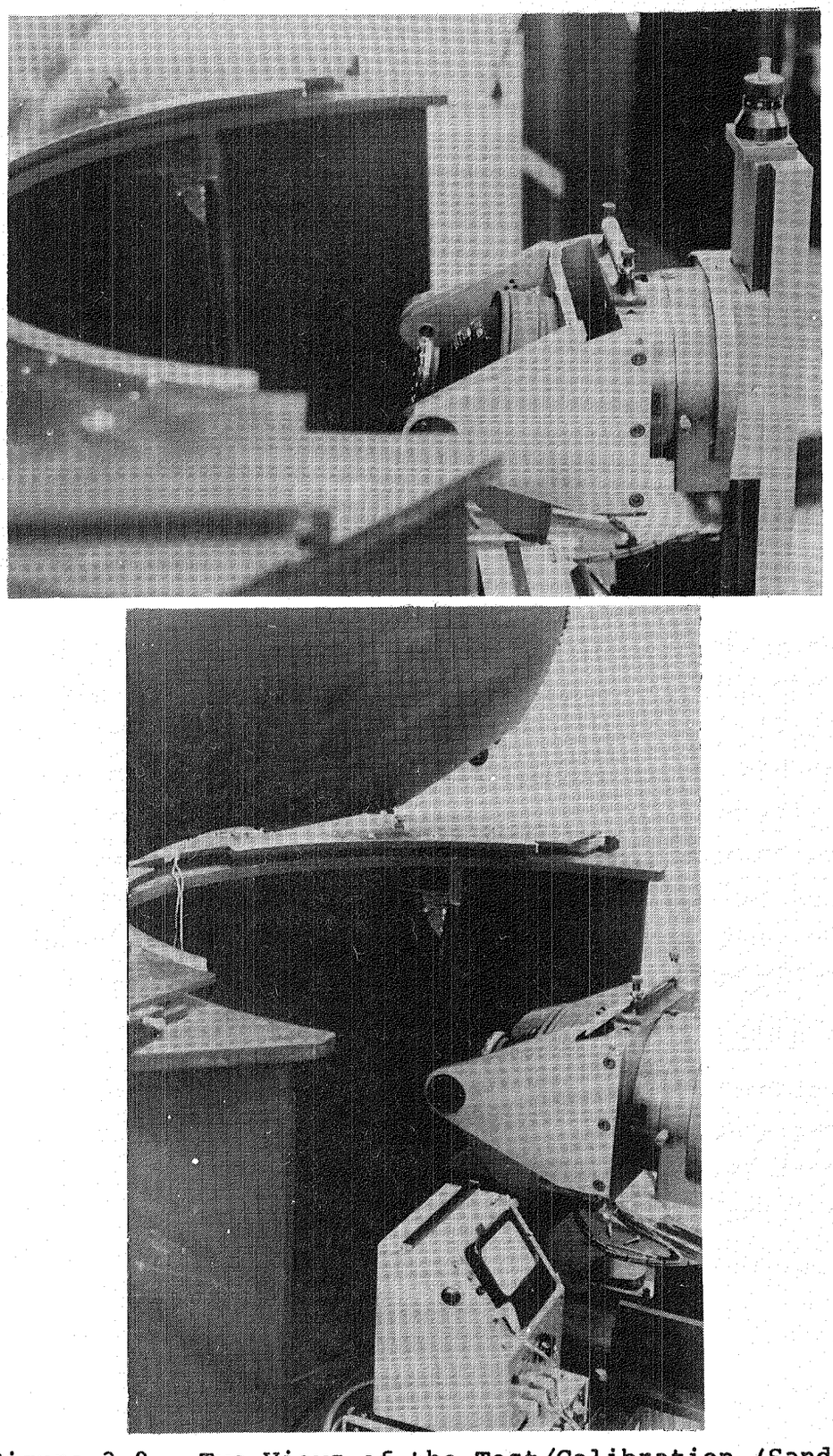

Figure 3-9. Two Views of the Test/Calibration (Sandbox) Setup Used by ITHACO, Inc.

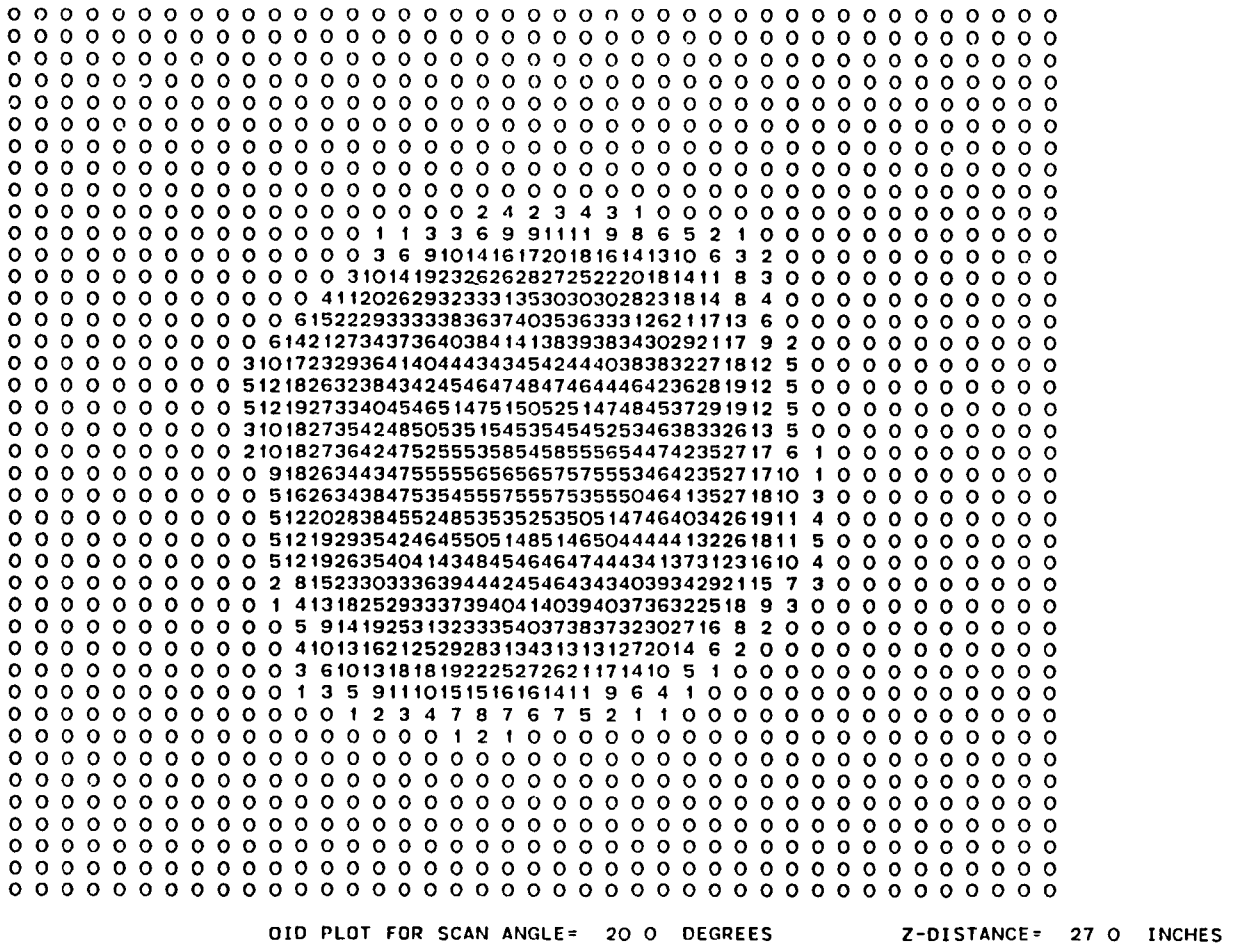

Figure 3-10. Optical Intensity Distribution Function for Test Setup (Near Field) at 20-Degree Scan Angle, Object Plane at 27 Inches

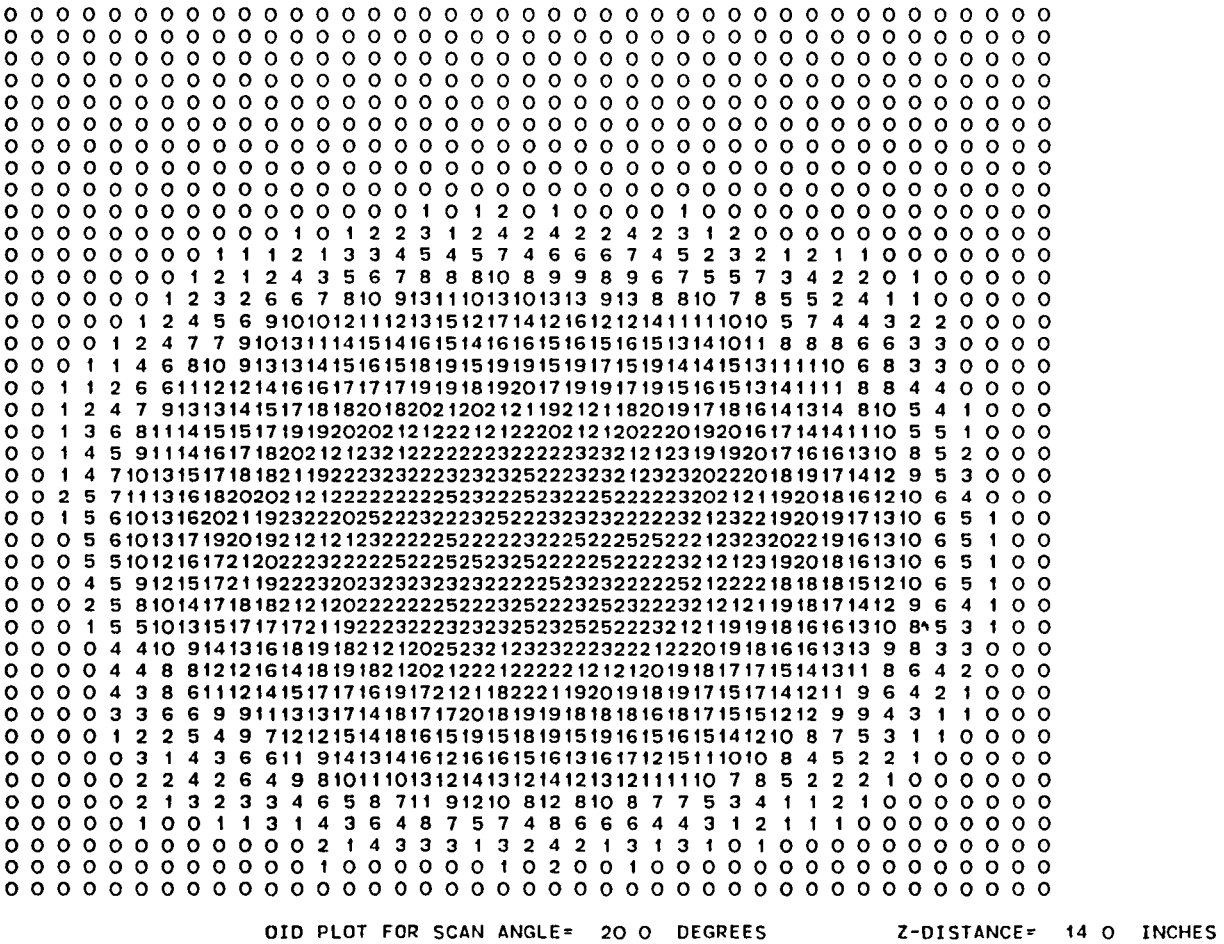

Figure 3-11. Optical Intensity Distribution Function for Test Setup (Near Field) at 20-Degree Scan Angle, Object Plane at 14 Inches

where F is called the impulse response function. The input signal $S_I(t)$ is related to $R_{AV}(\eta)$ by the radiance-to-volts conversion of radiance received at scan angle η corresponding to time t. However, the electronic circuits are conventionally expressed as a transfer function, $H(i\omega)$, in the frequency domain by the Fourier transform of the impulse response function, i.e.,

$$F(t) = \frac{1}{2\pi}\int_{-\infty}^{\infty} H(i\omega)\ e^{+i\omega t}\ d\omega \qquad (3\text{-}6)$$

3.3.1 TRANSFER FUNCTION

The electronics for IR horizon sensor signal processing generally contain various stages for bolometer, amplifier, peaking, direct current (DC) restore, frequency filters, and voltage limiters. The transfer function is thus a product of many terms involving different time constants. The terms with very long and very short time constants compared with scanner cycling time can be ignored. Hence, a general form of the transfer function will be (Reference 28):

$$H(i\omega) = A\left[\prod_{k=1}^{n} (1 + i\omega\ T_k)^{-1}\right] \cdot \left[(i\omega + \omega_a)^2 + \omega_b^2\right]^{-1} \qquad (3\text{-}7)$$

where A is a proportionality constant for radiance-to-volts conversion, T_k are the time constants and ω_a and ω_b are the noise filter frequencies. The number of terms included in the model (n) can be specified, depending on the degree of accuracy desired. In the original version of the HRMU, only three components (n = 3) were used for Seasat (Magsat). The option to add two more terms was implemented in the ERBS simulation studies and mission support version.

Using the method of residues, the impulse response function can be obtained analytically:

$$F(x > 0) = A\left(\omega_a^2 + \omega_b^2\right)\left\{\sum_{i=1}^{n} \frac{T_i^n \exp(-x/T_i)\left[1 - 2T_i\omega_a + T_i^2\left(\omega_a^2 + \omega_b^2\right)\right]^{-1}}{\prod_{\substack{j=1 \\ j\neq i}}^{n}(T_i - T_j)} + \exp(-x\omega_a)\sin(x\omega_b - \alpha)/(\rho\omega_b)\right\} \tag{3-8}$$

and

$$F(x \leq 0) = 0$$

where ρ and α are real numbers determined by the complex equation

$$\rho e^{i\alpha} = \prod_{j=1}^{n} [1 - T_j(\omega_a - i\omega_b)] \tag{3-9}$$

Figure 3-12 shows an example of the impulse response function simulated for ERBS.

The convolution of average radiance $R_{AV}(\omega_o t)$ and F(t) to obtain the output signal is performed in the HRMU by numerical integration. Figures 3-13 and 3-14 are sample plots of input signal and corresponding output signal, for the IR scanner on ERBS. Tradeoffs between numerical accuracy and computation time were studied by changing the time step,

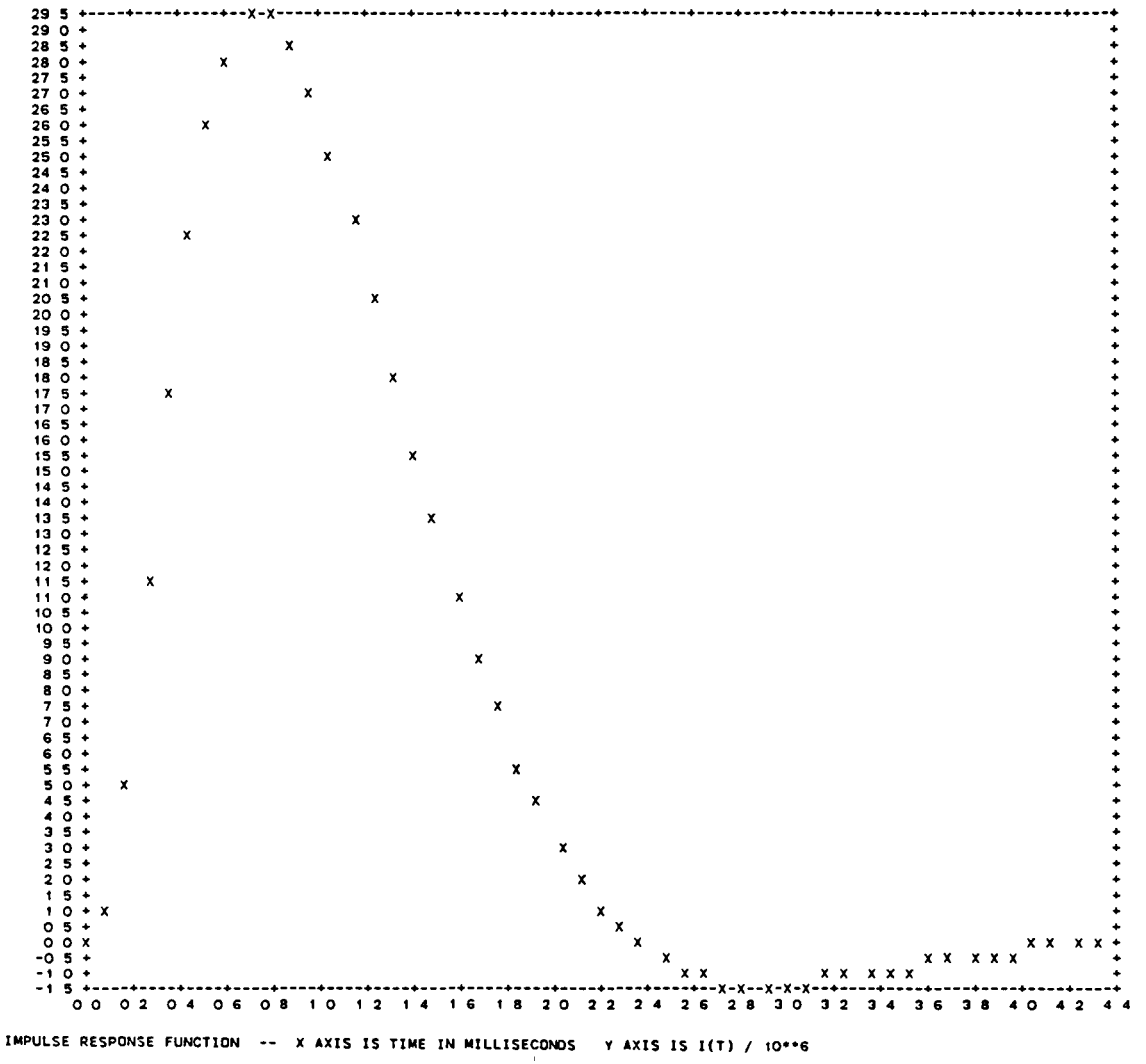

Figure 3-12. Impulse Response Function for IR Horizon Scanner on ERBS

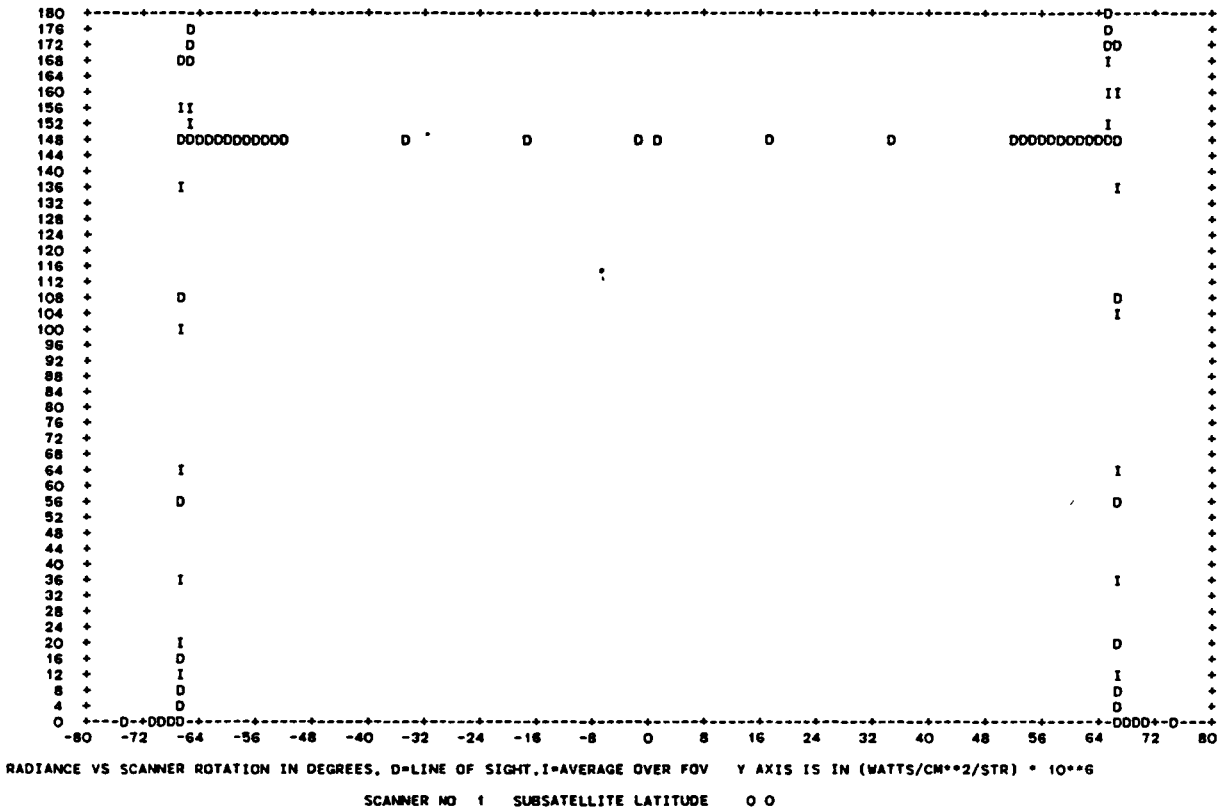

Figure 3-13. Input Radiances as a Function of Scanner Rotation Angle for January Data at Zero Subsatellite Latitude

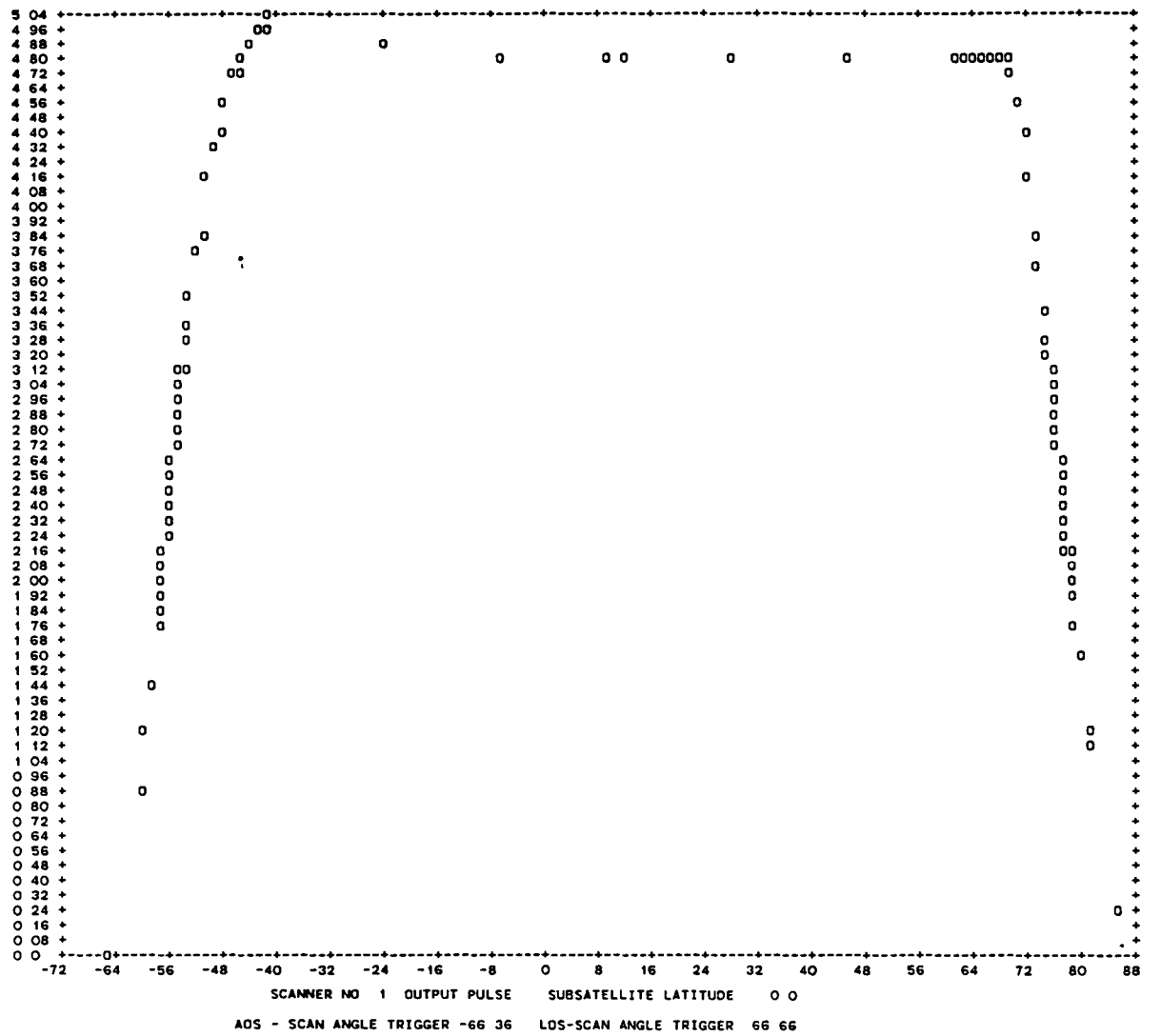

Figure 3-14. Output Pulse Signal From ERBS January Simulation, Corresponding to the Input Radiance in Figure 3-13

time interval, and numerical integration method. The effects of changes in some of the model parameters is discussed in Section 3.5.2.

3.3.2 LOCATOR LOGIC

The algorithm for the fixed threshold locator logic computes the horizon triggering when the voltage of the output Earth pulse rises or falls to a fixed value. The normalized locator logic changes the threshold in proportion to a fraction, β, of an average value of the Earth pulse between two preset scan angles. The horizon is thus detected for AOS (and similarly for LOS) when:

$$S_O^{AOS}(\bar{\eta}) - \beta \bar{R}_{AOS}(\bar{\eta}) = 0 \qquad (3\text{-}10)$$

where

$$\bar{R}_{AOS} = \frac{1}{2b} \int_{\bar{\eta}+a-b}^{\bar{\eta}+a+b} S_O(\eta)\, d\eta$$

and constants a and b define the region of the normalization process. In the HRMU, η is solved by an iterative (Newton-Raephson) technique. The normalized threshold locator logic method is illustrated in Figure 3-15.

3.4 PROGRAM OPTIONS

The HRMU offers options enabling the user to control the computation process and select output forms via NAMELIST variables. Some of the user options are as follows:

- Processing time--The start, stop, and step times can be specified to control the number of orbit points and the time interval for horizon triggering computation.

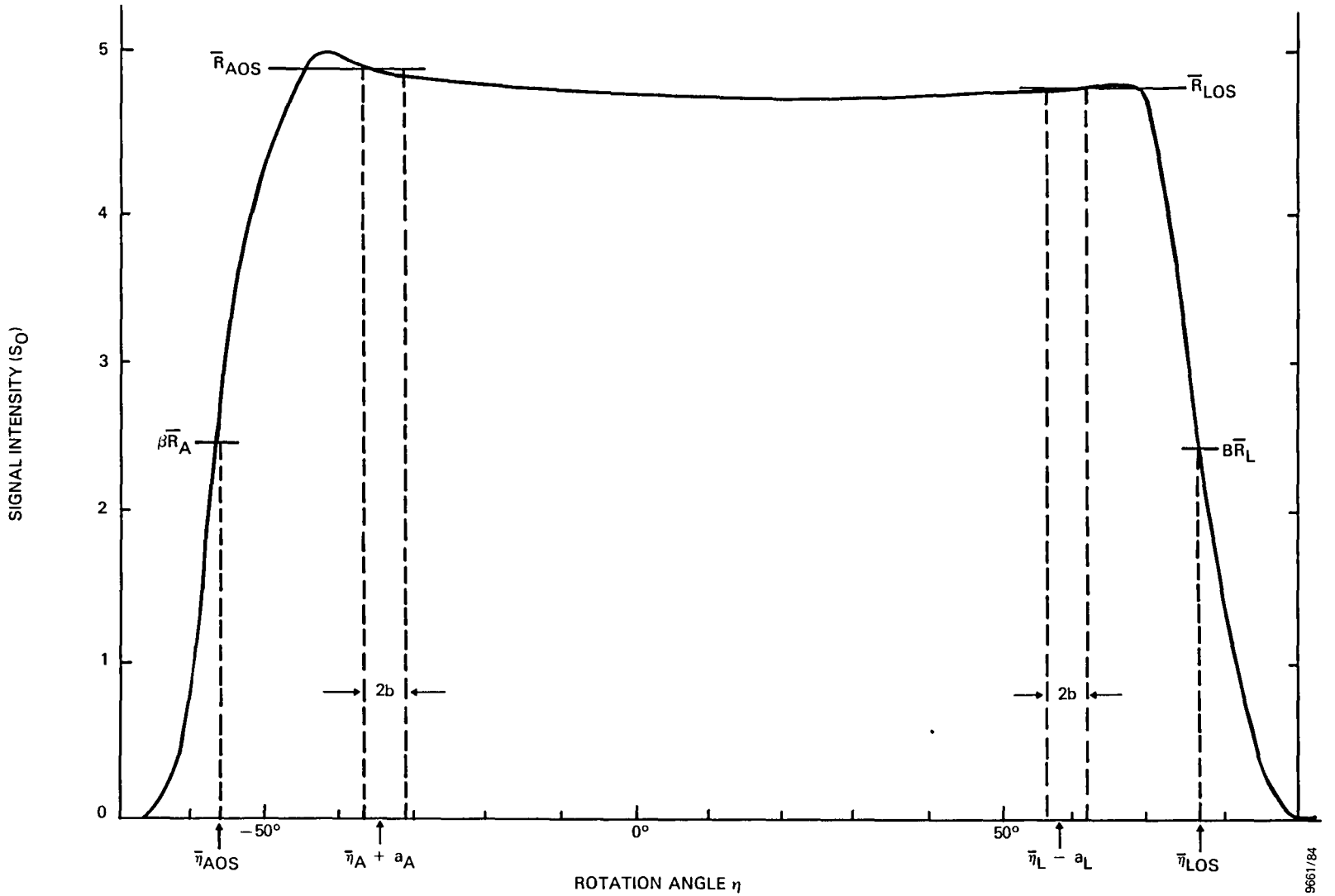

Figure 3-15. Schematic Diagram of Triggering Point Determination for a Normalized Threshold Locator Logic

- Size and shape of the FOV--FOV half-width, cone angle, spin axis angle, prism refractive index, and FOV distortion can be specified.

- Numerical integration and interpolation--The number of points to be used in the interpolation process, in the integration for average FOV radiance, and in the integrations for convolving the transfer function and output pulse are selectable. Options are also offered to select either Gaussian quadrature or Simpson rule as the numerical integration scheme and to select a five- to nine-point iterative least squares fit to the rising or falling portions of the output pulse.

- Electronics modeling--In addition to time constants and other components of the electronics circuit, the spin rate and angular time lag adjustment can be specified.

- Triggering angle, height, pitch, and roll error calculation--The number of scanners and configuration (left, right, or dual), nominal triggering height, pitch angle bias, locator logic averaging regions, and threshold fraction or a constant voltage are selectable.

- Output controls--The type and number of plots and graphs can be specified. Printer plots include impulse response function; input radiance versus scanner rotation angle; output pulse versus rotation angle; pitch and roll errors versus subsatellite latitude; elapse time or phase from node; and AOS and LOS triggering heights versus latitude, time, or phase. Three selected examples of plots are shown in Figures 3-16 through 3-18. Better quality graphics are also available using the CalComp plotter.

3.5 SENSITIVITY ANALYSIS OF THE ELECTRONICS MODEL

Many different approximations and integration methods built into the HRMU are likely to affect the accuracy of the final

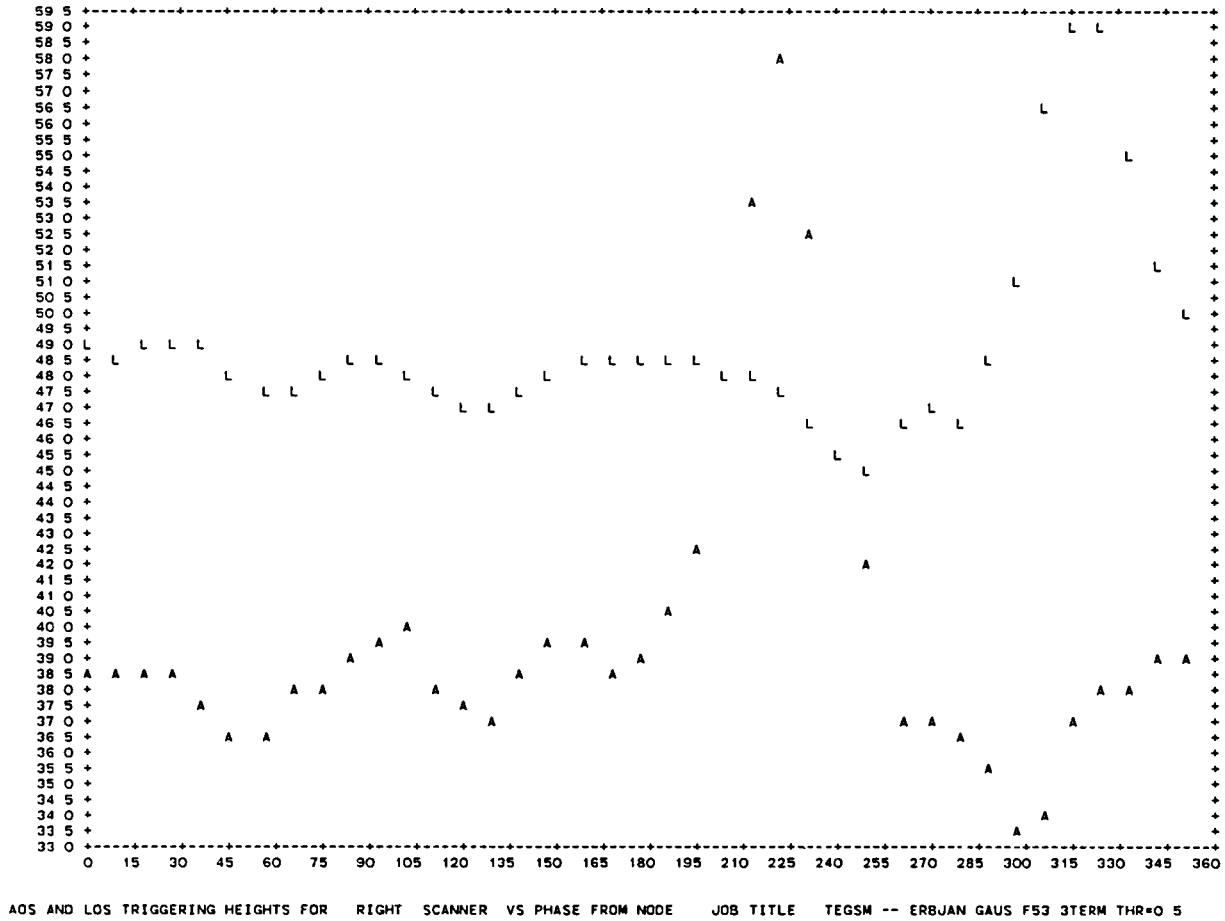

Figure 3-16. AOS and LOS Triggering Heights as a Function of Orbit Phase Angle From Ascending Node

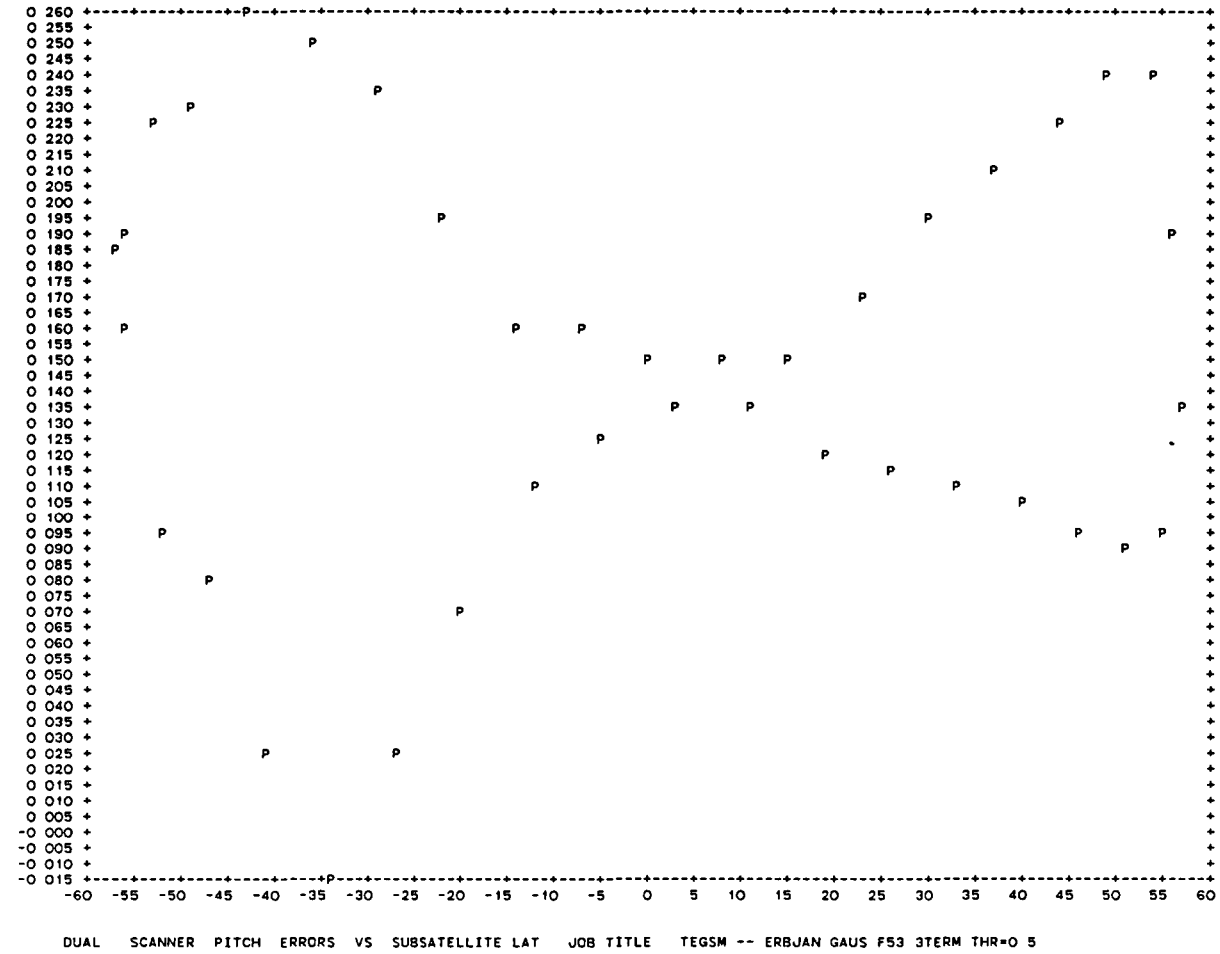

Figure 3-17. Pitch and Roll Errors as a Function of Subsatellite Latitude for a Sample ERBS Orbit (1 of 2)

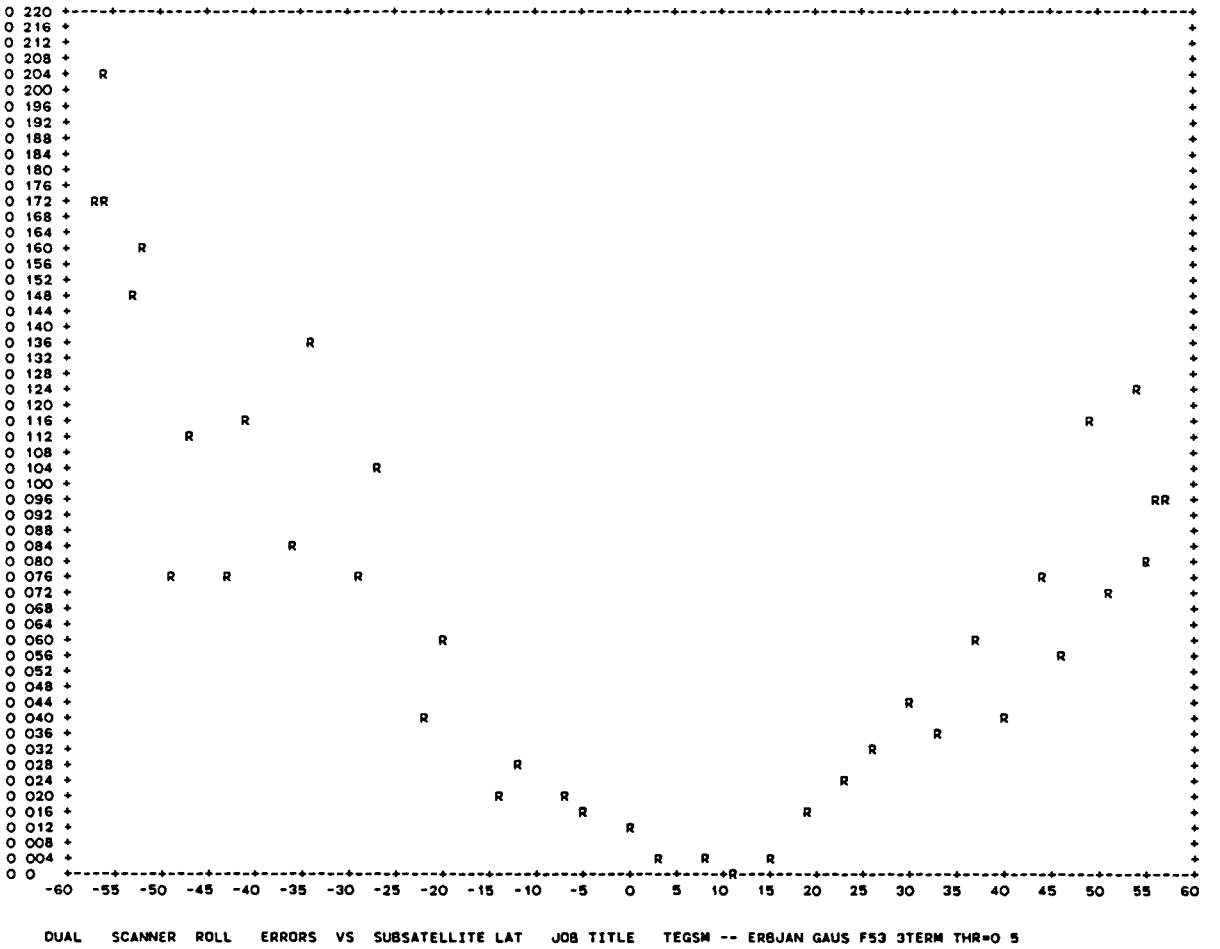

Figure 3-17. Pitch and Roll Errors as a Function of Subsatellite Latitude for a Sample ERBS Orbit (2 of 2)

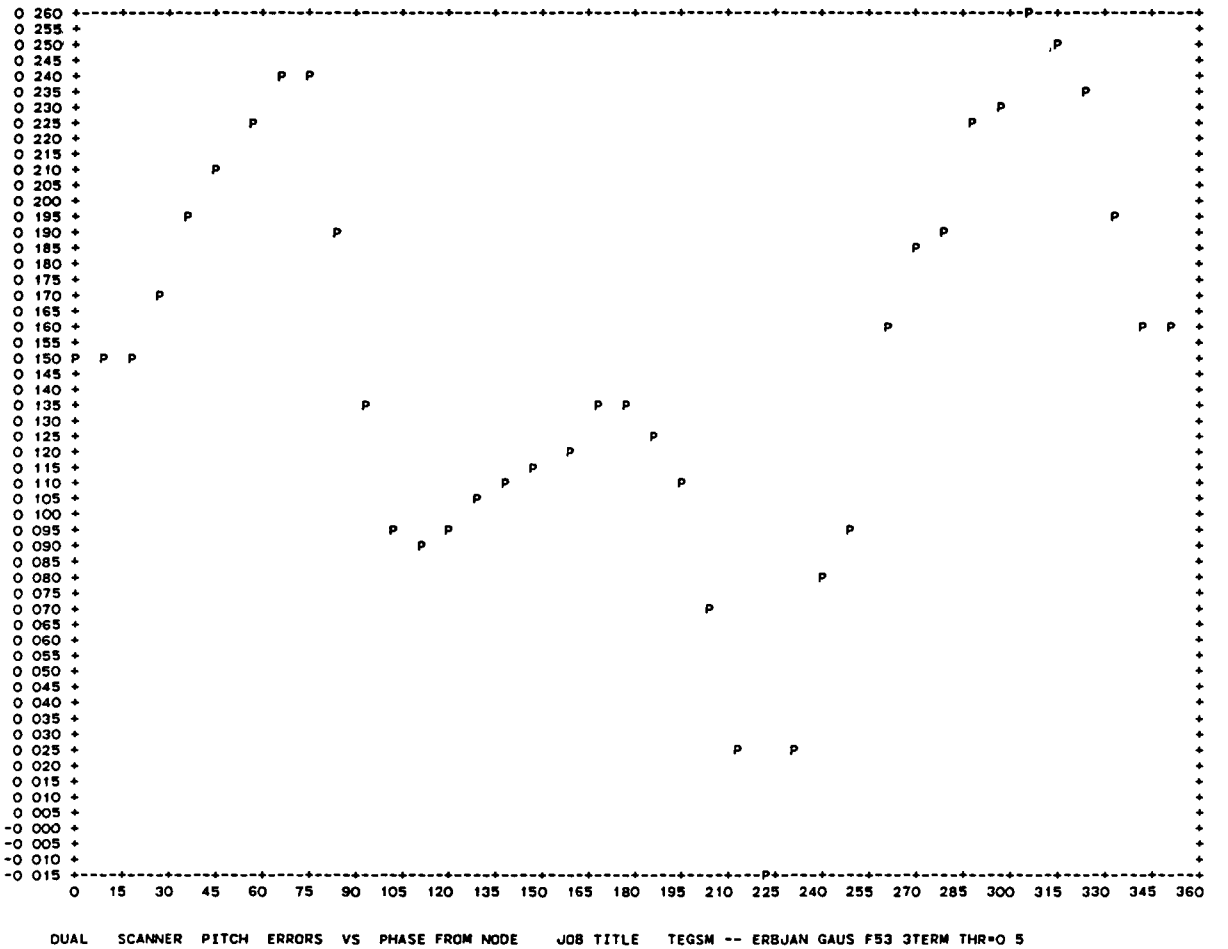

Figure 3-18. Pitch and Roll Errors as a Function of Orbit Phase Angle From Ascending Node (1 of 2)

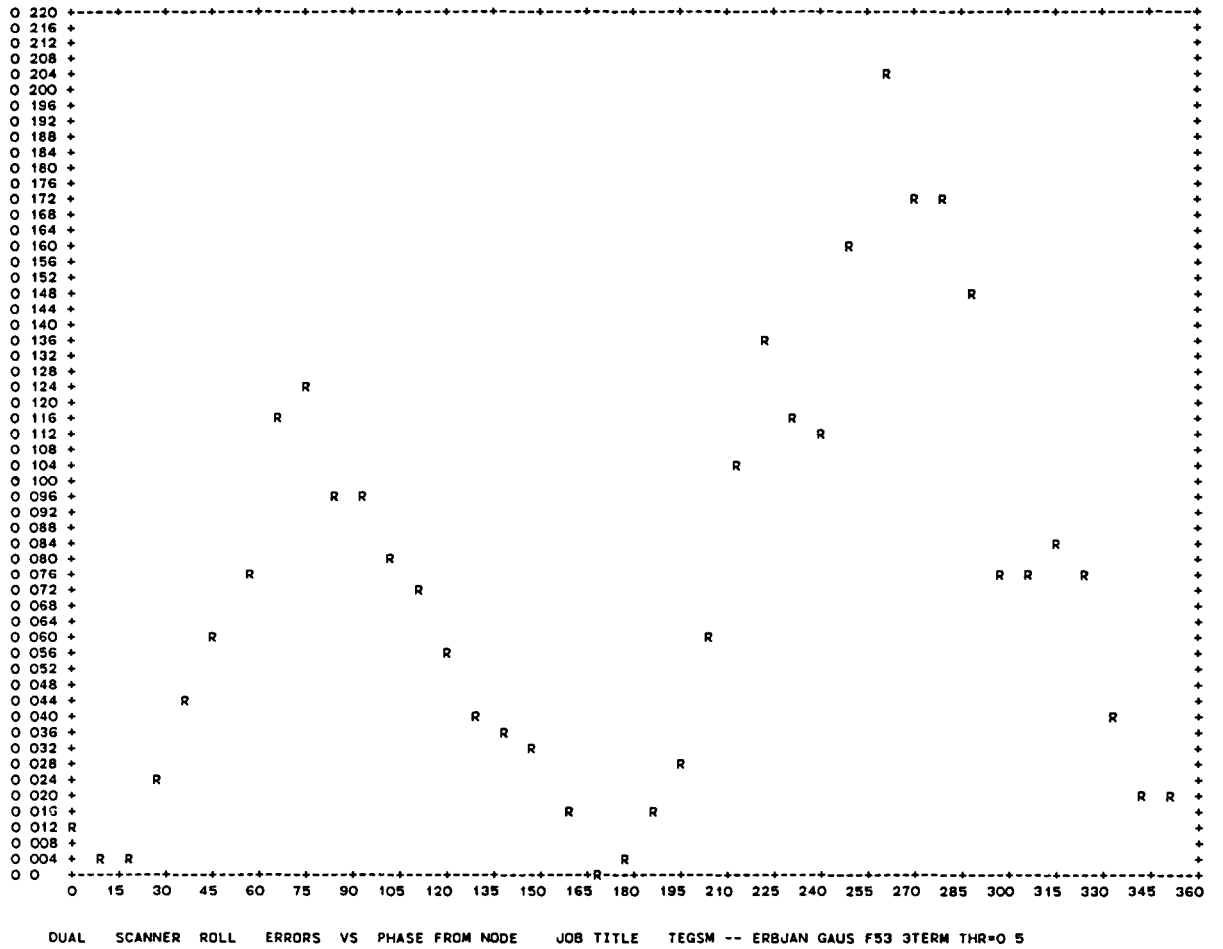

Figure 3-18. Pitch and Roll Errors as a Function of Orbit Phase Angle From Ascending Node (2 of 2)

results. The HRMU provides enough flexibility to change parameters or algorithms in the computational process to be suitable for a sensitivity analysis of the electronics modeling. CSC performed a detailed sensitivity study of the HRMU for ERBS horizon sensors with January, July, and October radiance data from the horizon radiance data base (HRDB) (Reference 29).

In general, two major sources of inaccuracies exist in the electronics modeling in the software. The first is the simplification of the electronics circuits by using only a few linear terms to compute the impulse response function. Usually, the very long and the very short time constants are neglected. The effect of switching from a three- to a five-component electronics model on the resultant pitch and roll errors is discussed in Section 3.5.1. The second major source of error is the numerical integration scheme used for calculating input and output signals. The computational resolution and accuracy in the convolution process play a particularly important role in the stability of the modeling results and are discussed in Section 3.5.2.

3.5.1 VARIATIONS WITH TRANSFER FUNCTION COMPONENTS

In the electronics model of the ERBS horizon scanners, two time constants associated with preamplifiers are close to the smaller constant for the peaking amplifier (Table 3-1). This suggested that a three-component approximation may be adequate for modeling the electronics.

Comparison of the calculated impulse response functions showed that the change from a three- to a five-component model causes an increase of mean time lag of about 0.05 millisecond. The resultant output pulses are also changed by a shift of about 0.2 to 0.3 degree, which appears as a bias in the absolute pitch and roll output. The pulse shape shows

Table 3-1. HRMU Input Parameters for ERBS and Seasat

PARAMETER	DESCRIPTION	NOMINAL VALUE	
		ERBS	SEASAT
α	SCANNER TILT ANGLE	+10° DEGREES (LEFT) −10 DEGREES (RIGHT)	26 DEGREES OR −26 DEGREES
λ	SCANNER CONE ANGLE	+45 DEGREES (LEFT) 135 DEGREES (RIGHT)	45 DEGREES OR 135 DEGREES
E	EARTH RADIUS	6371 KILOMETERS	6367 4 KILOMETERS
E + S	ORBITAL RADIUS	6971 KILOMETERS	7153 KILOMETERS
h_o	NOMINAL HORIZON HEIGHT	41 67 KILOMETERS	NOT APPLICABLE
a	LOCATOR CONSTANT	22 5 DEGREES	8 DEGREES
b	LOCATOR CONSTANT	2 5 DEGREES	3 DEGREES
c	LOCATOR CONSTANT	17 5 DEGREES	8 DEGREES
d	LOCATOR CONSTANT	2 5 DEGREES	3 DEGREES
η	ROTATION ANGLE AT NOMINAL HORIZON	66 9 DEGREES	77 5 DEGREES
β	THRESHOLD CONSTANT	50 PERCENT	40 PERCENT
Q	FOV DISTORTION	1 80	1 80 (ASSUMED 1 0)
δ	FOV SIZE CONSTANT	0 5 DEGREE	1 0 DEGREE
ω_0	WHEEL SPIN RATE	209 4 RADIANS/ SECOND (2000 RPM)	94 25 RADIANS/ SECOND (900 RPM)
T_1	PEAKING AMPLIFIER TIME CONSTANT	18 MICROSECONDS	22 5 MICROSECONDS
T_2	PEAKING AMPLIFIER TIME CONSTANT	118 1 MICROSECONDS	67 2 MICROSECONDS
T_3	DC RESTORER AMPLIFIER TIME CONSTANT	48 4 MICROSECONDS	46 4 MICROSECONDS
T_4	PREAMPLIFIER TIME CONSTANT	18 MICROSECONDS	0 (3 3 MICROSECONDS)
T_5	PREAMPLIFIER TIME CONSTANT	15 8 MICROSECONDS	0 (3 2 MICROSECONDS)
T_6	THRESHOLD NORMALIZER TIME CONSTANT	225 MICROSECONDS	NOT APPLICABLE
T_C	THRESHOLD NORMALIZER CHARGING TIME CONSTANT	3200 MICROSECONDS	NOT APPLICABLE
ω_a	NOISE FILTER AMPLIFIER FREQUENCY	1437 RADIANS/SECOND	4915 RADIANS/SECOND
ω_b	NOISE FILTER AMPLIFIER FREQUENCY	1468 RADIANS/SECOND	5200 RADIANS/SECOND

8547/82

no obvious changes, especially at the AOS and LOS slopes, where the horizon threshold is detected.

The results of this study (Reference 29) show that there are no outstanding differences in error patterns between the three- and the five-component models. Figure 3-19 shows the results for the five-component model for comparison with the three-component model of Figure 3-18. The changes in the peak-to-peak amplitudes of the pitch and roll errors are less than 0.05 degree and 0.02 degree, respectively. These variations are about the same magnitude as the modeling accuracy estimates established for the ERBS IR system.

3.5.2 COMPUTATIONAL STABILITY

Computational noise appears as irregularities in the pitch and roll functions. Examples of this scatter of values near the maxima in the roll errors from the three- and the five-component models are illustrated in Figures 3-18 and 3-19.

Another type of noise evaluated in the sensitivity study, appears as abrupt changes in pitch or roll amplitudes that occur as the threshold value or certain parameters in the model are varied slightly. An example of this type of noise is illustrated in Table 3-2. As the threshold level increases from 0.50 to 0.55, the maximum pitch amplitude decreases from 0.28 to 0.26 degree and then suddenly jumps to 0.41 degree for the Gaussian integration without smoothing. The roll amplitude responds in a similar fashion.

The source of the behavior described above is believed to be the numerical integration process. The accuracy of the convolution process depends on the size of the step, range, and integration schemes. More accurate integration should stabilize the irregular fluctuation of amplitudes in the pitch and roll results. Data from detailed analysis showed, however, that even with very high integration resolution, a

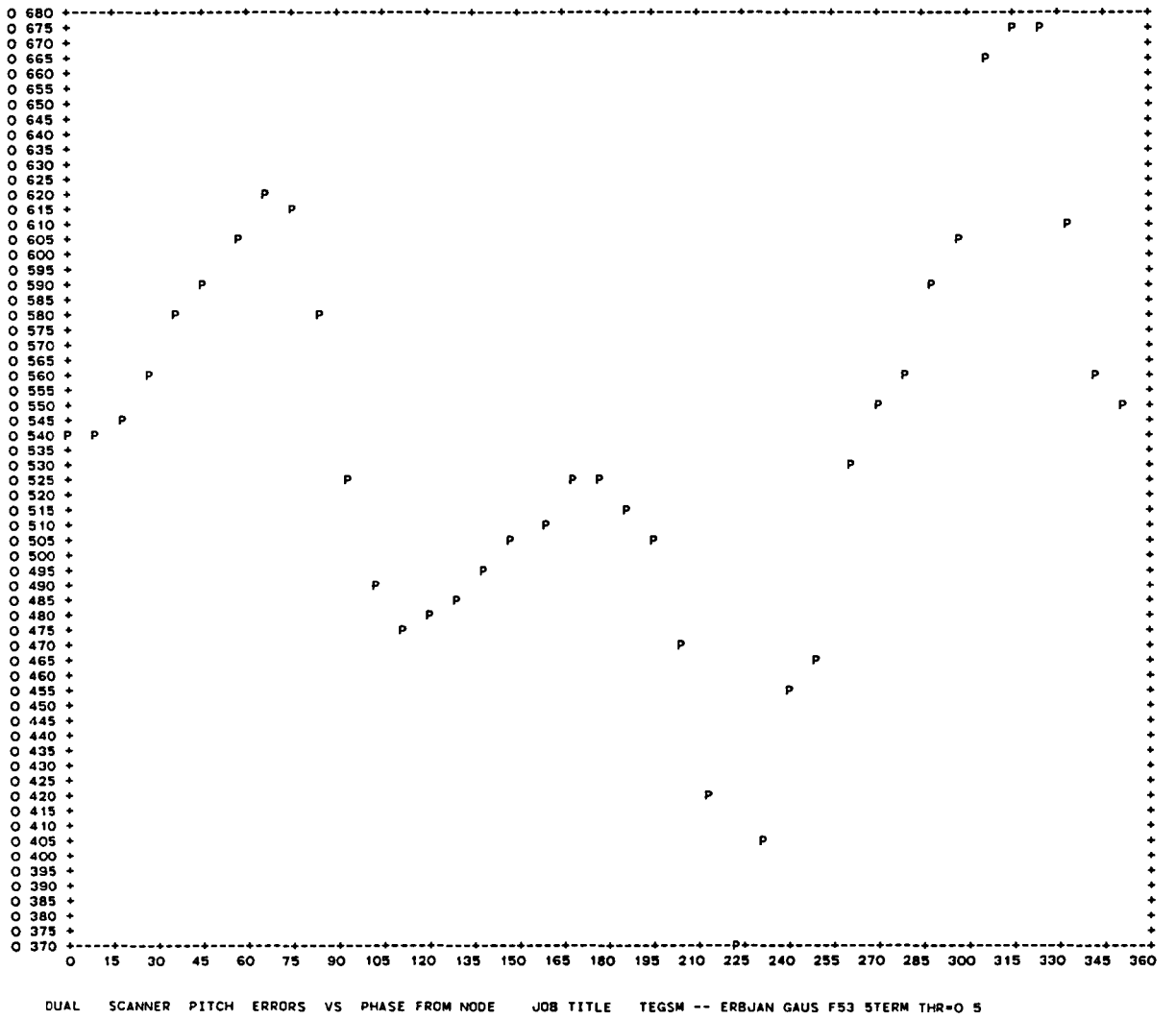

Figure 3-19. Pitch and Roll Errors for the Five-Component Model (1 of 2)

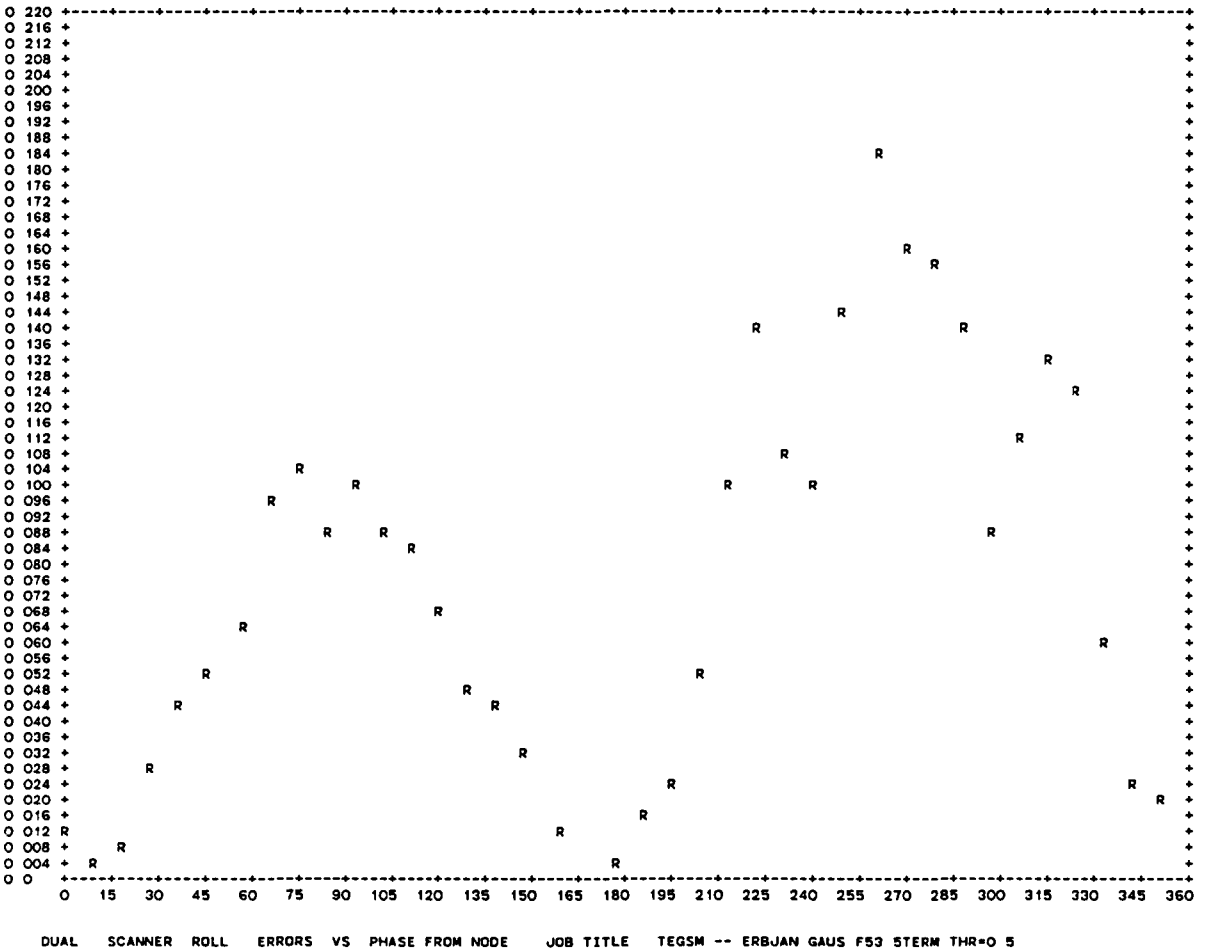

Figure 3-19. Pitch and Roll Errors for the Five-Component Model (2 of 2)

Table 3-2. Differences in Peak-to-Peak Pitch and Roll Errors Due to Changes in Threshold Levels for Three Computational Models

THRESHOLD LEVEL	SIMPSON WITHOUT SMOOTHING (WITH SMOOTHING)				GAUSSIAN WITHOUT SMOOTHING (WITH SMOOTHING)				GAUSSIAN WITH NEW ANGLE DISTRIBUTION			
	PITCH		ROLL		PITCH		ROLL		PITCH		ROLL	
	MAXIMUM	SECONDARY[a]	MAXIMUM	SECONDARY[a]	MAXIMUM	SECONDARY[a]	MAXIMUM	SECONDARY[a]	MAXIMUM	SECONDARY[a]	MAXIMUM	SECONDARY[a]
0.45	0 26 (0.31)	0.15 (0.14)	0.20 (0.20)	0.09 (0.10)	0.36 (0.34)	0.19 (0.15)	0.28 (0.22)	0.16 (0.11)	0.33	0.15	0.23	0.13
0.475	0.29 (0.29)	0.14 (0.14)	0.20 (0.20)	0.11 (0.10)	0.34 (0.31)	0.14 (0.15)	0.20 (0.20)	0.12 (0.11)	0.34	0.13	0.18	0.10
0.50	0.30 (0.29)	0.14 (0.15)	0.21 (0.22)	0.10 (0.10)	0.28 (0.29)	0.14 (0.15)	0.21 (0.21)	0.13 (0.12)	0.29	0.13	0.18	0.11
0.525	0.31 (0.31)	0.17 (0.16)	0.24 (0.23)	0.11 (0.11)	0.26 (0.30)	0.14 (0.15)	0.21 (0.23)	0.11 (0.11)	0.28	0.13	0.19	0.11
0.55	0.33 (0.32)	0.16 (0.17)	0.24 (0.25)	0.13 (0.12)	0.41 (0.34)	0.27 (0.18)	0.31 (0.26)	0.21 (0.12)	0.35	0.17	0.24	0.13

9568 (29*) 83

[a]SECONDARY REFERS TO PEAK-TO-PEAK ERROR FOR NORTHERN HEMISPHERE ONLY.

small variation in the output pulse at the slopes is enough to cause variations in the attitude results. This suggested an additional error source in the earlier stages of signal processing. For example, an irregular interpolation of the input IR radiance profiles results in an irregular input pulse to the electronics. Furthermore, the resolution of the input pulse can also influence the variability of integration results. Further studies should be performed to identify the error sources and to assess their sensitivities to attitude results.

The tradeoff between accuracy and computer time is frequently a subject of consideration. For practical purposes, simple approaches are used to correct these computational errors and improve the HRMU model performance. The smoothing of output pulse data in the AOS and LOS slopes was found to be very effective, as demonstrated by the results in Table 3-2. The smoothing filter used in this analysis was a nine-point, third-degree, least squares fit with five iterations and was applied to the output pulse computed from a 40-point Gaussian quadrature. Another useful approach is the redistribution of scan angles selected for the output pulse calculation. The experience with the ERBS simulation shows that the oversampling on the output pulse slope actually introduces more unevenness and hence larger instability in the final results. Table 3-2 also shows the effects of changing the scan angle distribution on pitch and roll amplitudes.

The results of the parametric studies (Reference 29) showed the sensitivity of pitch and roll errors to changes in modeling constants and computational schemes and algorithms. Table 3-3 summarizes these results for the ERBS IR scanner system. The results were derived from HRMU runs using the Gaussian quadrature with a pulse edge smoothing option for mean January radiance data. The major parameters

Table 3-3. Sensitivity of Pitch and Roll Errors to Changes in Various Parameters, Based on Results of Gaussian Model With Smoothing (1 of 2)

PARAMETERS		PITCH ERROR AMPLITUDE		ROLL ERROR AMPLITUDE	
		MAXIMUM	SECONDARY[a]	MAXIMUM	SECONDARY[a]
INTEGRATION TIME (SECONDS)					
0 004 (NOMINAL)		0.29	0 15	0 21	0.12
0 0035		0 31	0.15	0 22	0.12
0 0045		0.34	0.15	0 22	0.12
0 005		0 40	0 24	0 30	0 17
0.006		0 50	0.29	0 29	0 26
THRESHOLD LEVEL RATIO					
0 50 (NOMINAL)		0 29	0 15	0 21	0 12
0.45		0 34	0 15	0.22	0 11
0 475		0 31	0.15	0 20	0.11
0 525		0 30	0.15	0.23	0.11
0 55		0 34	0.18	0.26	0.12
THRESHOLD ADJUST REGION (DEGREES)					
ACQUISITION OF SIGNAL	LOSS OF SIGNAL				
20–25	15–20 (NOMINAL)	0 29	0 15	0.21	0.12
20–25	20–25	0.32	0 16	0 23	0 12
25–30	15–20	0.31	0.16	0 22	0 13
30–35	15–20	0 33	0 16	0 23	0 13
35–40	15–20	0.35	0 17	0 24	0.13
NUMBER OF ELECTRONIC COMPONENTS					
3 (NOMINAL)		0.29	0.15	0 21	0.12
5		0.35	0.15	0.20	0.10
5 (SIMPSON)		0 31	0.15	0 21	0.10

9568-(29*1-84

Table 3-3. Sensitivity of Pitch and Roll Errors to Changes in Various Parameters, Based on Results of Gaussian Model With Smoothing (2 of 2)

PARAMETERS		PITCH ERROR AMPLITUDE		ROLL ERROR AMPLITUDE	
		MAXIMUM	SECONDARY[a]	MAXIMUM	SECONDARY[a]
ELECTRONIC TIME CONSTANTS (MICROSECONDS)					
T_1 = 18, T_2 = 118 1;					
T_3 = 48 4, (NOMINAL)		0 35	0 15	0 21	0 12
T_4 = 18, T_5 = 15 8					
ALL CONSTANTS NOMINAL EXCEPT.					
T_2 x 0 75		0 30	0 15	0 21	0 12
T_2 x 1 25		0 38	0.18	0 24	0.13
T_3 x 0.5		0 30	0 15	0 21	0 12
T_3 x 1 5		0 38	0.17	0 24	0 12
T_3 x 2 0		0 33	0 21	0 27	0 14
FILTER AMPLIFIER FREQUENCY (RADIANS/ SECOND)					
ω_a	ω_b				
1437	1468 (NOMINAL)	0 35	0 15	0 21	0 12
1437 x 0 75	1468	0 38	0 21	0 28	0.16
1437 x 1.25	1468	0 25	0 15	0 21	0 11
1437 x 1 5	1468	0 32	0 16	0 22	0 11
1437	1468 x 0.75	0 32	0 12	0 19	0 10
1437	1468 x 1.25	0 32	0 21	0 22	0 11
1437	1468 x 1 5	0.20	0.07	0 10	0 05

9568 39*-84

[a]SECONDARY REFERS TO PEAK-TO-PEAK ERROR FOR NORTHERN HEMISPHERE ONLY

9568-39*-84

under study were number of electronic components, threshold percentage, integration time range, threshold level adjust region, electronic time constants, and filter amplifier frequency. The variations in the pitch and roll error amplitudes are generally smaller than 0.05 degree, as compared to variations due to the latitude dependence of the radiance input of about 0.3 degree in pitch and 0.2 degree in roll. These results were obtained from only one study specifically conducted for ERBS simulation. Previous experience and current understanding lead to the conclusion that the HRMU is a reliable and indispensable tool for IR horizon sensor simulation for spacecraft mission support.

SECTION 4 - MISSION EXPERIENCE

This section documents 10 years of experience in IR horizon sensor data modeling and sensor calibration resulting from satellite attitude determination mission support at GSFC. This experience began with IR sensor calibration analysis for the AE-3 and SAS-3 missions, which focused primarily on in-flight sensor calibration and sensor misalignment modeling to provide data corrections. The work continued with detailed analysis to assess the attitude determination accuracy of IR scanners for Seasat-1 and subsequent missions.

Efforts to enhance the Seasat IR scanner attitude determination accuracy included the application of a deterministic oblateness-like pitch and roll correction, based on an Earth IR horizon radiance model. Attempts were made to assess the accuracy of this Earth radiance model correction procedure for the Seasat, Magsat, and DE-2 missions. The analysis was further extended to acquire the capability of generating an Earth IR radiance profile model that was true to the IR passband of the sensors in each individual mission. This work included the incorporation of the LOWTRAN 5 radiance modeling program to build a data set of Earth IR spectra, and evolved into the generation of the Earth radiance profile model for the ERBS mission IR scanner passband.

In addition to these efforts, postlaunch data analyses were performed on a variety of other missions. These include the less detailed analysis performed by CSC for the AE, GOES-5, and TIROS-N/NOAA-7 IR sensors; the analysis performed by GSC for the Landsat-4 conical IR scanner; and the analysis performed at the University of Colorado at Boulder for the SME. All of these analyses contributed to understanding the performance of various IR sensor systems and the response of various sensor designs to the Earth IR radiance. The analyses served to determine the latitude and time dependence of

the Earth IR radiance profile, the predictability of the radiance, the magnitude of the random variations in the radiance, and the response of the various IR scanner configurations to the radiance variations. Each of the missions described experienced some of the IR sensor anomalies encountered in the Mercury and Vela missions (Section 1), thus indicating that knowledge gained from mission experience is sometimes lost and that the IR sensor space applications technology is still evolving.

The mission experience described in the following subsections covers 12 different missions, arranged by sensor type and not chronologically. The first group includes mission experience from SAS-3, Seasat, AEM/SAGE, Magsat, DE-2, and ERBS (Sections 4.1 through 4.6), all of which employed ITHACO Scanwheels or wheel-mounted horizon sensors (WHSs), which make use of reaction and angular momentum control wheels for scanning and detecting the Earth edge. The second group includes the AE-3, GOES-5, DE-1, and SME missions (Sections 4.7 through 4.10), employing the body-mounted IR horizon sensors (BHSs), which make use of the spacecraft spin motion. The AE-3 mission was unique in that it used both types of sensors, WHS and BHS. Finally, Section 4.11 discusses Landsat-4, which employed conical scanners that scan by a constant-speed motor independent of the angular momentum control loop, and Section 4.12 discusses NOAA-7, which employed the edge-tracking method of the Earth Sensor Assembly.

4.1 SMALL ASTRONOMY SATELLITE-3

SAS-3 provided one of the earliest examples of analysis to evaluate the accuracy of attitude determination using IR scanner data. It also offered an excellent opportunity to extract detailed information about the IR scanner flight performance and the characteristics of the Earth IR image. The full potential was not realized, however, because the mission analysis was focused primarily on sensor calibration.

4.1.1 MISSION REQUIREMENTS AND HARDWARE

SAS-3 was launched by a Scout rocket from the San Marco platform in the sea off the east coast of Kenya, South Africa, in May 1975. The SAS-3 spacecraft is illustrated in Figure 4.1-1. The mission can be summarized as follows:

- Orbit--Circular, 485-kilometer altitude at 2.9-degree inclination
- Attitude configuration--Spin stabilized with the spin axis (+Z) inertially fixed to point toward a preselected target
- Attitude determination hardware
  - Spin-mode Sun sensor, with a $\pm$90- by 2-degree FOV
  - Two solid-angle Sun sensors, with a $\pm$64- by $\pm$64-degree FOV mounted about the spin plane at -135 and 45 degrees
  - N-slit Applied Physics Laboratory (APL) star sensor mounted in the spin plane at -45 degrees from the +X-axis, with a 5- by 10-degree FOV
  - Two Massachusetts Institute of Technology (MIT) star cameras (Figure 4.1-2 from Reference 30),

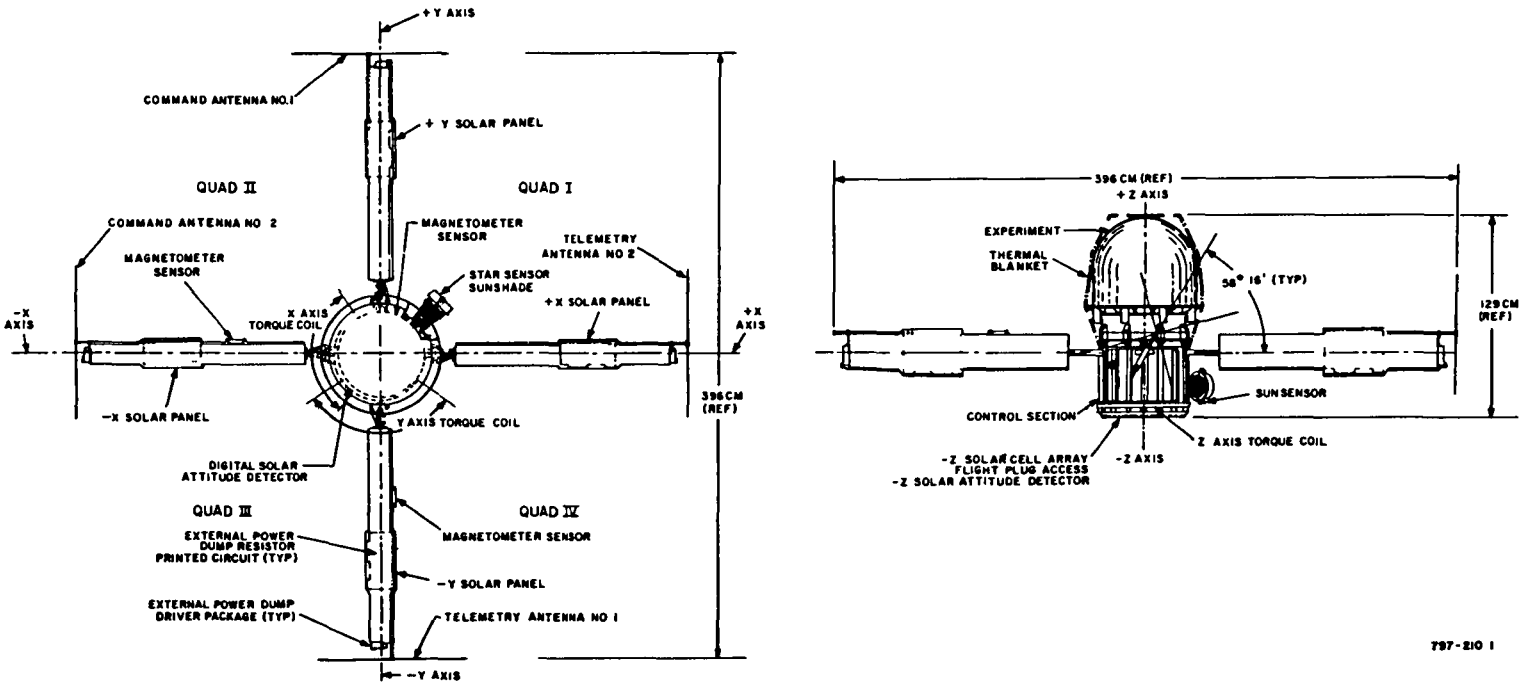

Figure 4.1-1. SAS-3 Spacecraft Geometry

one mounted along the +Z-axis and the other in the spin plane at -45 degrees from the +X-axis, 8- by 8-degree FOV

- Orthogonal set of magnetometers
- ITHACO Scanwheel IR horizon scanner (Figure 4.1-3) mounted along the -Z-axis with the magnetic pickup for the index at 135 degrees from the +X-axis
- Two gyroscopes (also used for attitude control)

- Attitude control hardware
  - Momentum wheel
  - Two gyroscopes (also used for attitude determination)
  - Z-axis magnetic torquing coil
  - Three-axis magnetic trim system
  - Nutation damper
  - X, Y torquing coils for momentum wheel unloading
  - Closed-loop pitch control unit
  - Three-axis closed loop attitude control system
- Accuracy requirement
  - Attitude determination--Spin axis to within 0.5 degree
  - Attitude control--Position spin axis to within 3 degrees of desired source, maintain spin axis within a 2-degree range of attitude acquired, maintain spin rate of momentum wheel between 1400 and 1600 revolutions per minute (rpm)

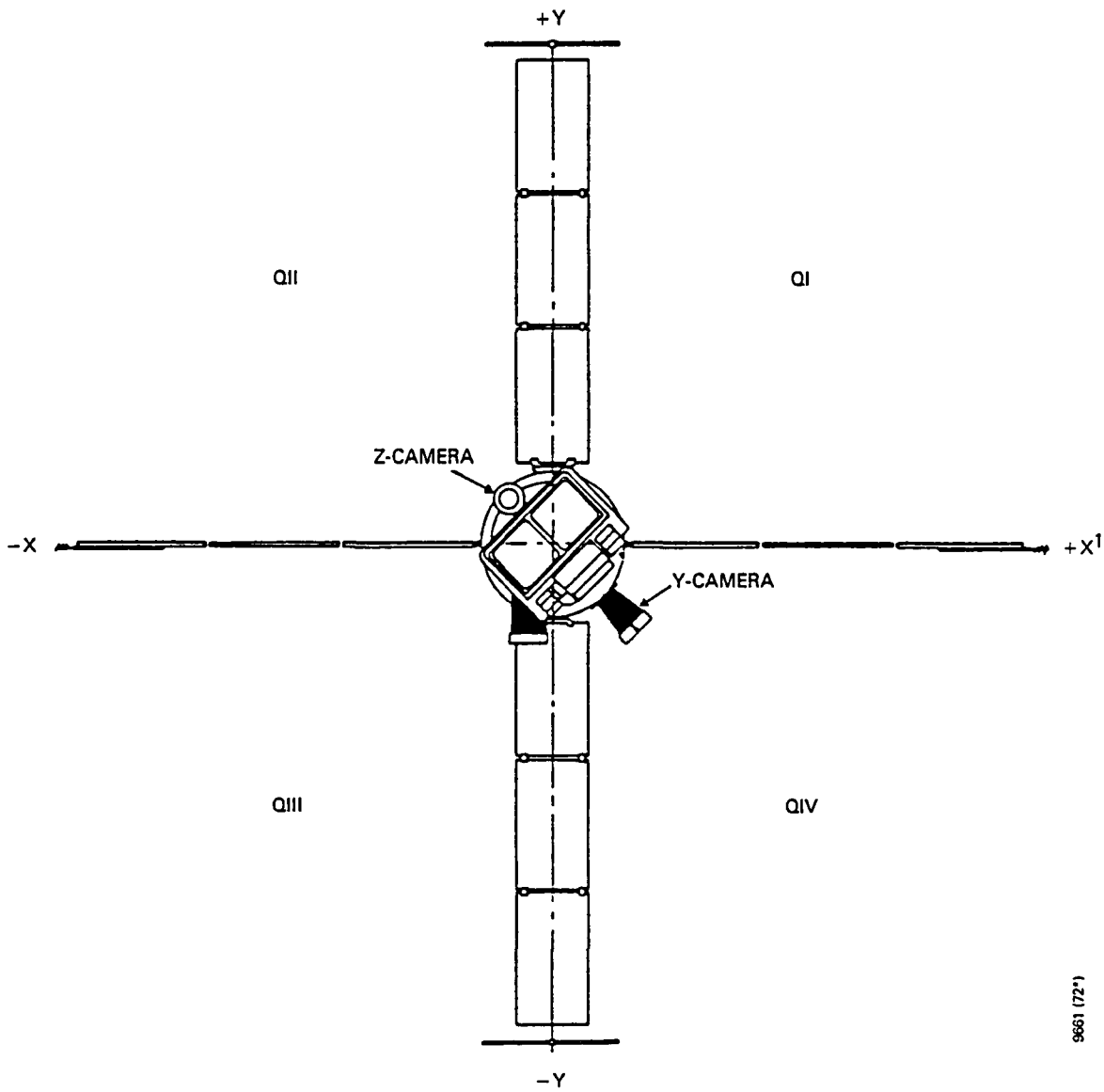

[1]COORDINATE AXES AS DESIGNATED BY APL

Figure 4.1-2. Star Camera Locations on SAS-3 Satellite

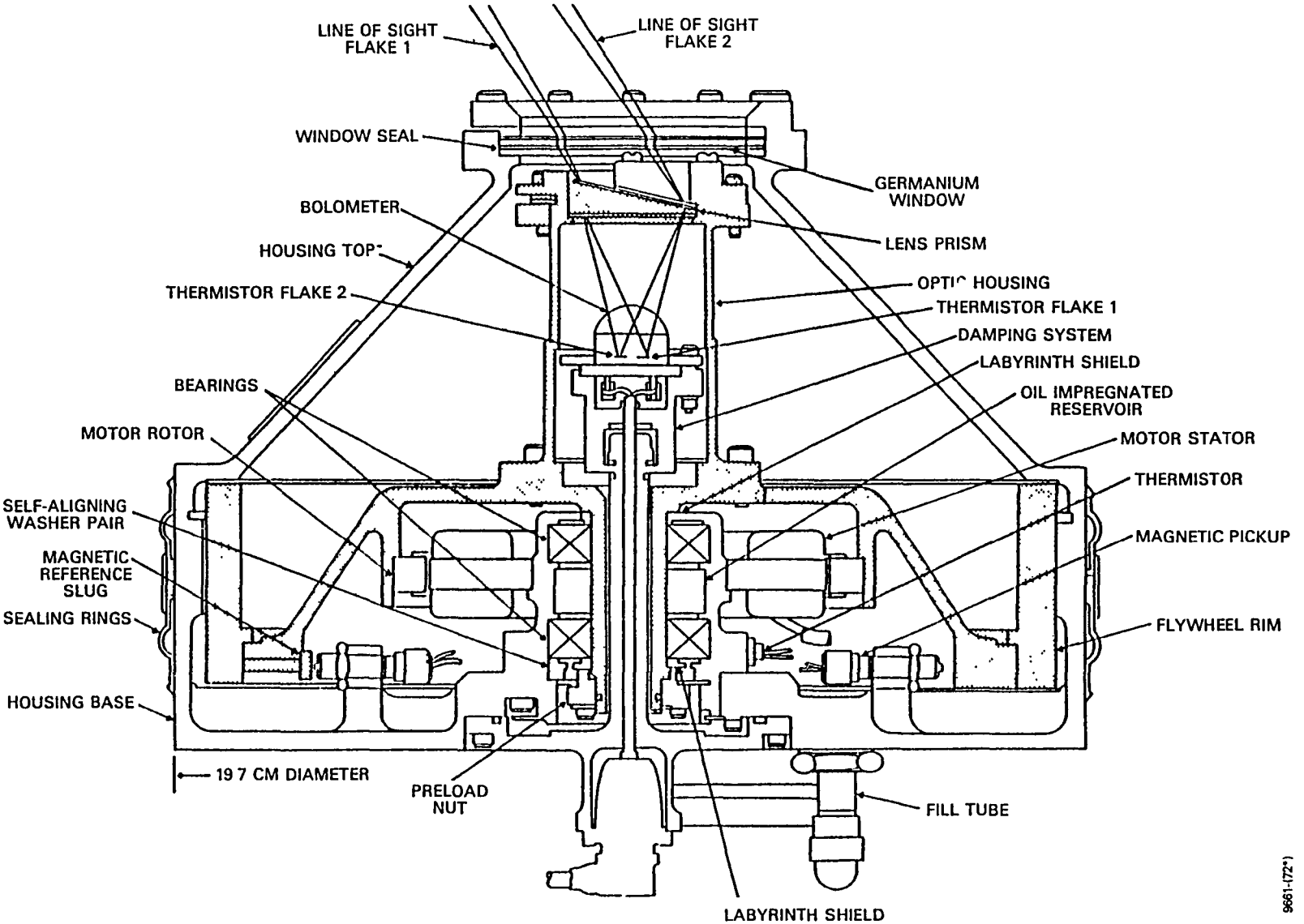

Figure 4.1-3. SAS-3 Type-B Scanwheel (Shading indicates rotating components consisting of flywheel and prism assembly. Courtesy of ITHACO, Inc.)

- Ground support system--Interactive processing
- Data processing requirements--Determine spin axis attitude within a half-hour of receipt of playback data for up to five daily passes

4.1.2 MISSION DATA ANALYSIS

The results of the analysis performed for SAS-3 IR scanner data calibration and assessment are reported in Reference 31. The ITHACO Scanwheel on SAS-3 was a dual-flake system with fixed-threshold locator logic for each flake, as illustrated in Figure 4.1-4. The Earth chord length and spacecraft pitch were computed with "ANDed" logic signals from the two flakes. For the IR scanner analysis, an attitude reference derived from star camera data was used to calibrate the IR scanner data. The pitch and roll angles were then computed from the calibrated IR scanner data and compared with the pitch and roll angles derived from the more accurate star camera data. The residuals between these two sets of pitch and roll data were used to evaluate the IR scanner data for other sources of error. These error sources included the percent Earth/roll angle model (a function of IR scanner optical characteristics), bolometer thermal effects, and Earth oblateness.

The analysis of Reference 31 was successful in the in-flight recalibration of telemetered roll voltage to percent Earth conversion. However, the application of a correction that included a model of the dual-flake locator logic was inconclusive (i.e., the data residuals were not reduced by the application of corrections originating from the dual-flake geometry and logic). The dual-flake model applied to SAS-3 data was based on reflective mirror optics to obtain the 45-degree deflection of the IR scanner FOV. This was probably inherited as a result of experience with the AE-3 IR

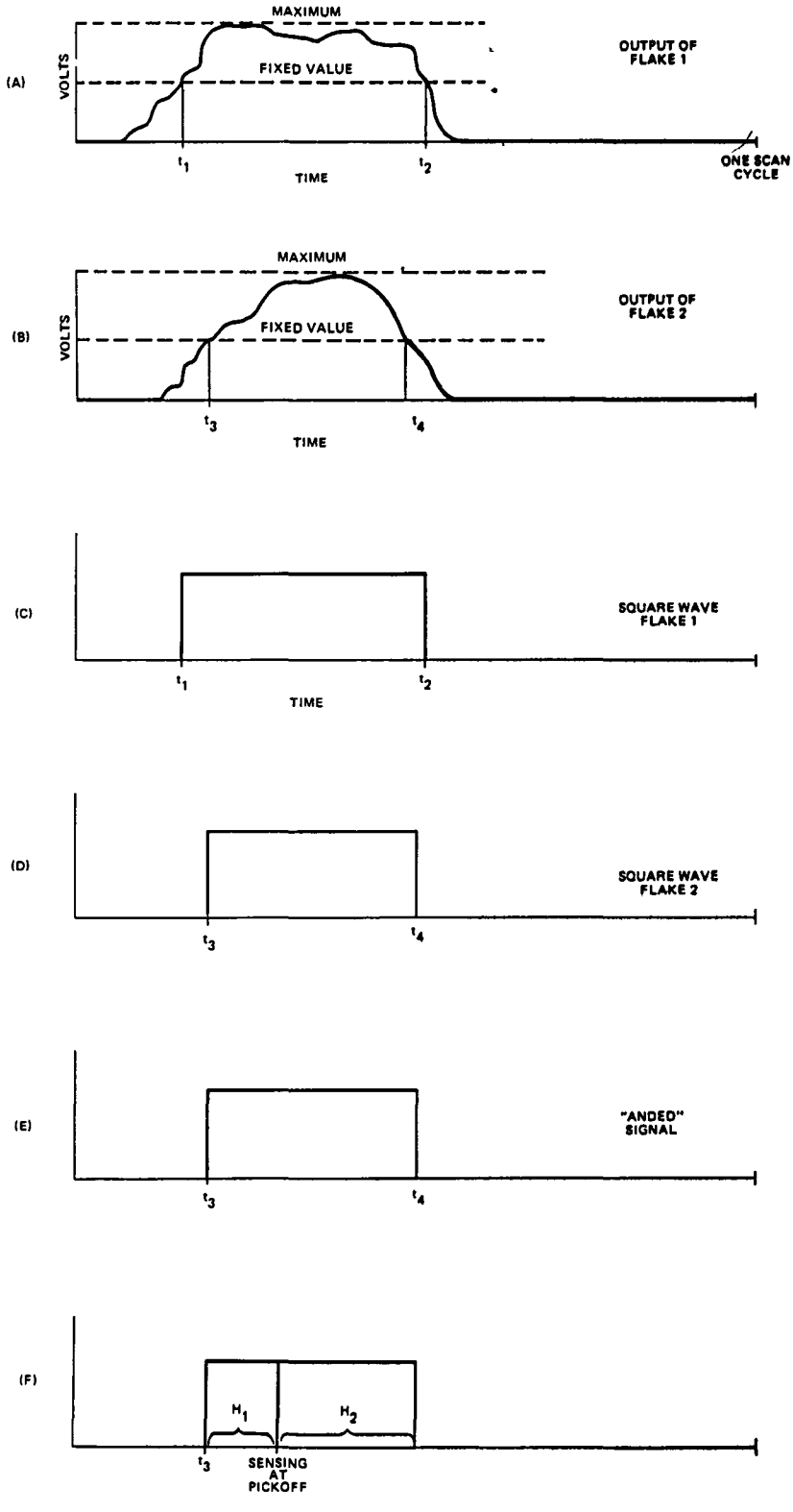

Figure 4.1-4. IR Scanner Dual-Flake Signal Processing for SAS-3 and AEM/SAGE

scanners, which did use a rotating mirror assembly. The SAS-3 system was a germanium prism lens system, and it was discovered during analysis for the AEM/SAGE mission that the optical geometry for a dual-flake mirror configuration does not adequately represent the prism lens geometry.

4.1.3 RESULTS AND DISCUSSION

The SAS-3 analysis represented one of the early attempts to apply an optics model and a primitive version of the electronics response function model (the "ANDed" logic). The effort to model the "ANDed" logic was not completely successful, however, due to the erroneous assumption that the dual-flake mirror geometry was an adequate representation of the optics. The effects of the unmodeled Earth oblateness were discounted because of the geometry of the near-equatorial orbit and the south polar attitude, which restricted the range of IR scanner Earth paths to a small region of latitudes as illustrated by Figure 4.1-5 (Reference 31). Likewise, any effect of systematic changes in the Earth IR radiance with season and latitude would not have affected the SAS-3 data.

The SAS-3 IR data analysis did discover a trend in the residuals that was highly correlated with the ambient temperature of the IR scanner bolometer. Figure 4.1-6 (Reference 31) illustrates the roll angle residuals between the calibrated IR data and the star camera data. The peak in the residual at 2400 seconds is just before orbit day, 4 a.m. local time at the Earth subsatellite point. The minimum in the residual at 5200 seconds corresponds to 4 p.m. local time. Bolometer temperature was determined to be the cause of these residuals, and this was reinforced by subsequent information from ITHACO indicating that the SAS-3 IR scanner bolometers were not temperature compensated.

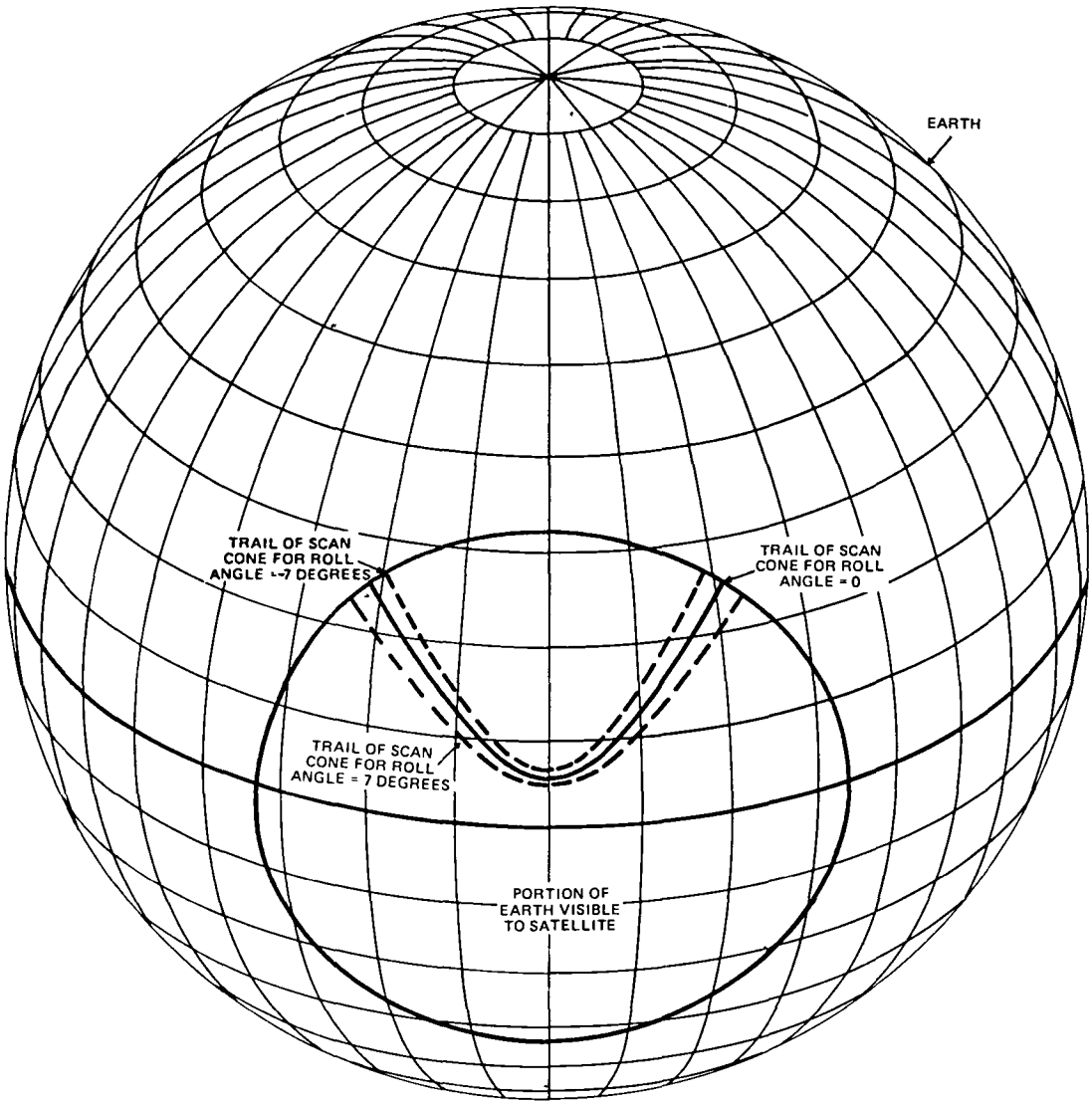

Figure 4.1-5. Earth as Seen by the SAS-3 IR Scanner Assuming a Zero Inclination Orbit

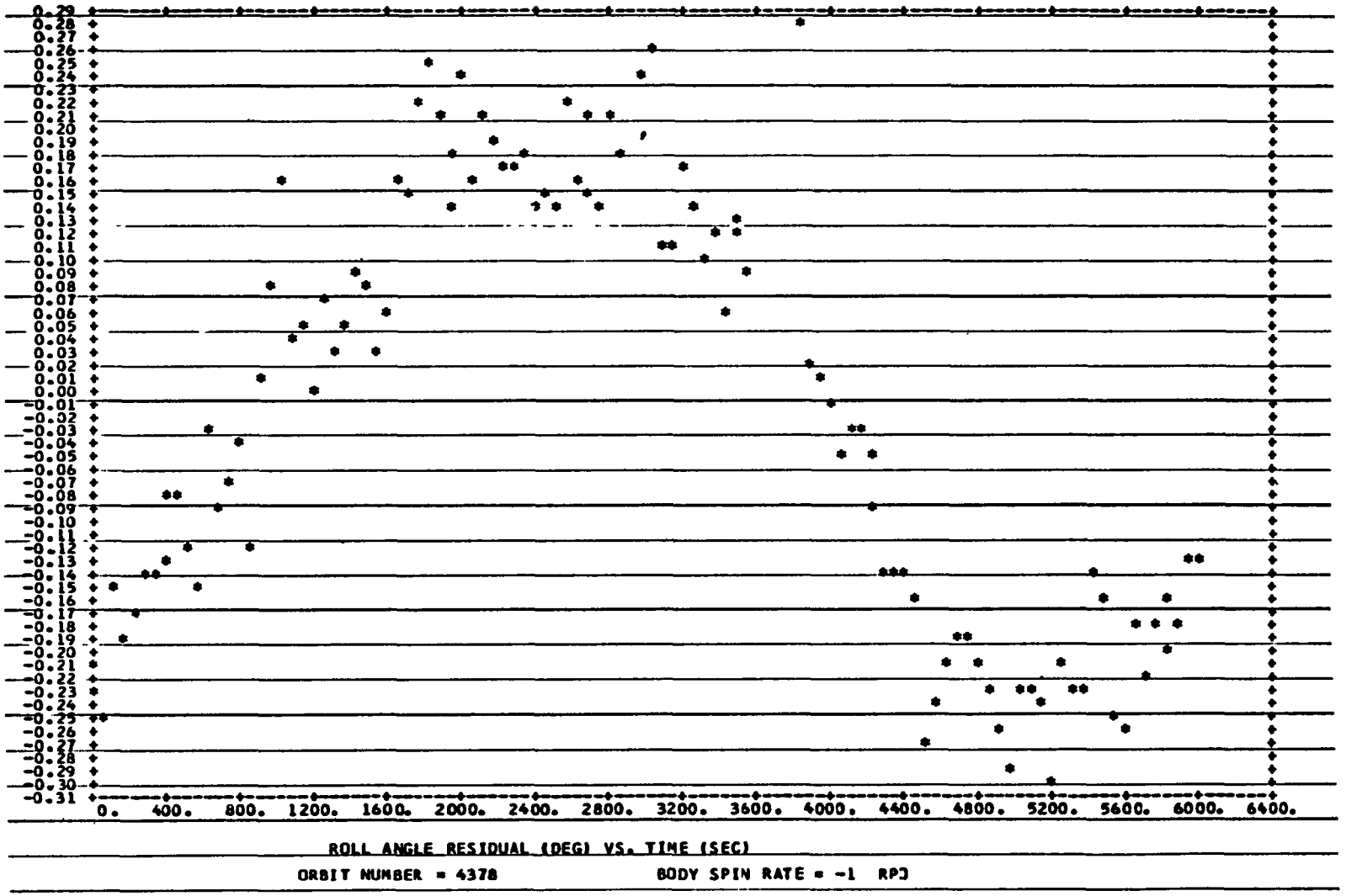

Figure 4.1-6. Roll Angle Residual (Degrees) Versus Time (Seconds) for SAS-3 Orbit Number 4378

4.2 SEASAT

Attitude analysis for the Seasat mission began at GSFC in 1976. Part of this analysis was directed at estimating the attitude determination accuracy that could be achieved by a ground attitude data processing system using the Seasat IR scanner and fine Sun sensor (FSS) data. Another goal of the analysis was to establish a deterministic pitch and roll data correction function that would compensate for pitch and roll sensing errors caused by systematic seasonal and latitudinal variations in the Earth IR radiance. These Earth horizon radiance profiles, provided by LMSC (Reference 8), were generated by integrating a computed Earth IR radiation spectrum over the passband response function of the ITHACO IR horizon scanner.

The pitch and roll errors from the horizon radiance model were determined by simulating the optical and electronic response of the ITHACO IR horizon sensing system in the flight configuration. Questions about the accuracy of this model were addressed to establish the overall accuracy of a ground attitude computation that included corrections for horizon radiance variations. For this purpose, LMSC produced special IR profiles simulating the effects of cold clouds and variations in the percentage of the atmospheric constituents ozone and water vapor (Reference 15). The Seasat error analysis for the prelaunch phase of mission support is documented in Reference 14. An update to that analysis, which includes flight data from the sensor performance evaluation analysis, is documented in Reference 32.

4.2.1 MISSION REQUIREMENTS AND HARDWARE

Seasat-1 was part of the Earth and Ocean Dynamics Application Program of the NASA Office of Applications. The primary experimental objective of the mission was to study the world's oceans and to determine if microwave instrumentation

scanning the oceans from space could provide useful scientific data for oceanographers, meteorologists, and commercial users of the seas. Experimental considerations dictated an 800-kilometer, near-circular orbit, circling the Earth 14.4 times a day, with the spacecraft's instruments sweeping across 95 percent of the oceans' surface every 36 hours. The Seasat-1 spacecraft is illustrated in Figure 4.2-1. The mission can be summarized as follows:

- Orbit--Near-circular at 800-kilometer altitude and 108-degree inclination
- Attitude configuration--One revolution per orbit (rpo) with the spacecraft Z-axis toward Earth, the Y-axis along negative orbit normal, and the X-axis along the approximate direction of flight
- Attitude determination hardware
  - Two ITHACO Scanwheel IR horizon scanners (also used for attitude control)
  - Four Adcole 18960 two-axis fine Sun sensors with a $\pm$32- by $\pm$32-degree FOV and 0.04-degree (3σ) quoted accuracy
  - Three-axis Schoenstedt flux-gate magnetometer
- Attitude control hardware
  - Two ITHACO Scanwheel IR horizon scanners (also used for attitude determination)
  - Electromagnet assembly
  - Pitch and roll reaction wheels
- Accuracy requirement--Absolute accuracy of 0.17 degree (3σ) on each axis (proven to be beyond the limits of the Seasat hardware)

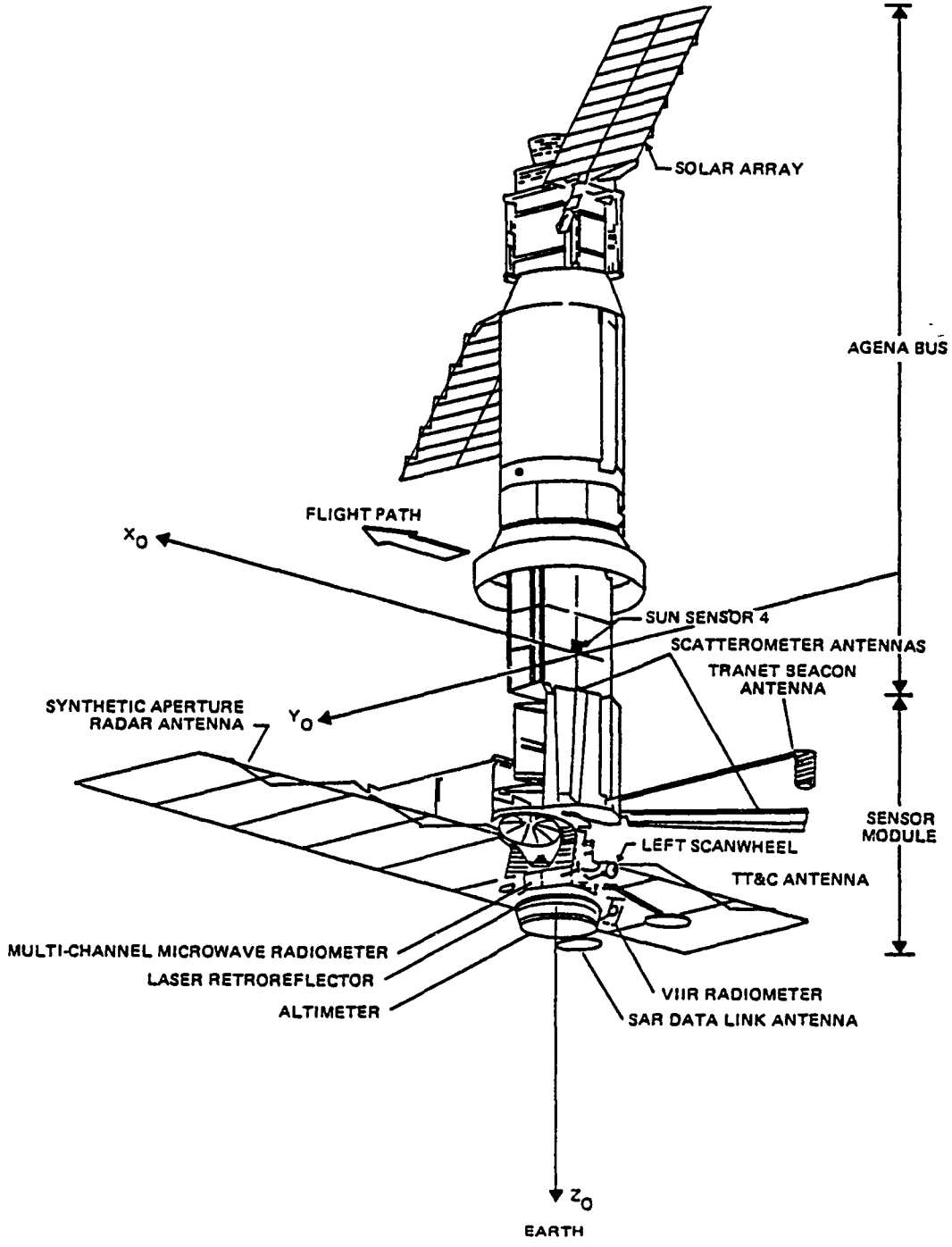

Figure 4.2-1. Seasat-1 Spacecraft Configuration

- Ground support system--Interactive processing
- Data processing requirements
  - Definitive solutions generated in 1-day segments for 24 hours per day
  - Output interval of 5 to 60 seconds such that linear interpolation caused less than 0.02-degree error
  - Turnaround within 24 hours from receipt of telemetry data and definitive orbit
- Problems encountered
  - Regular once-per-orbit Sun interference in the right IR scanner due to failure of blanking electronics to perform as specified
  - Intermittent Sun interference in the left IR scanner due to reflected sunlight from the synthetic aperture radar downlink antenna
  - Sun sensor measurement discontinuities as the Sun entered or exited the FOV
  - Sun sensor alignment errors that necessitated postlaunch recalibration

A Barnes Engineering horizon scanner and three gyroscopes were used for ascent attitude control, but were unavailable for definitive attitude determination. The three-axis magnetometer could only provide coarse data with a resolution of 1 to 2 degrees. Attitude determination was therefore based on data from the Scanwheels and the fine Sun sensors.

The four Adcole 18960 two-axis fine Sun sensors were configured in two electronics systems, each with two sensors. Normally the Sun data were obtained from only one sensor in the system. The output was a 32-bit word that encoded the position of the Sun in increments of 1/256 degree.

Seasat-1 had two single-flake, normalized threshold IR scanners that could be configured in either the dual- or single-scanner mode for pitch and roll sensing. Attitude control in the single-scanner mode was less accurate than in the dual-scanner mode due to altitude dependency, an increase in measurement noise, and increased oblateness and horizon radiance effects. The scanner axes were mounted in the Y-Z plane of the spacecraft, tilted 26 degrees down from the horizontal. Right and left scanners were defined with respect to an observer facing in the direction of flight. Nominal wheel speed was 900 $\pm$ 300 rpm. The pitch and roll data were generated from the corresponding voltage and telemetered to the ground as 8-bit words every 1.024 seconds. Pitch and roll were considered valid only when within the range of $\pm$10 degrees. Both fine ($\pm$1 degree) and coarse ($\pm$10 degrees) pitch and roll angle data were provided simultaneously. The flight geometry of the dual IR scanner system for Seasat is illustrated in Figure 4.2-2, showing the portion of the scan cone where Sun interference is considered unavoidable.

The normalized threshold locator logic is illustrated in Figure 4.2-3. The threshold level computation is performed by averaging the processed Earth pulse for scan angles that are several degrees inside the scan angles of the previously detected Earth horizons. For Seasat, the AOS and LOS threshold level averaging was performed between 5 and 11 degrees from each Earth edge. The procedure tends to make the Earth edge detection errors sensitive to variations in the amplitude of the Earth pulse at scan locations that correspond to points thousands of kilometers inside the horizon of the Earth.

Because the IR scanners are frequently integral components in the spacecraft attitude control loop, the spin rates are determined by the angular momentum requirements for attitude

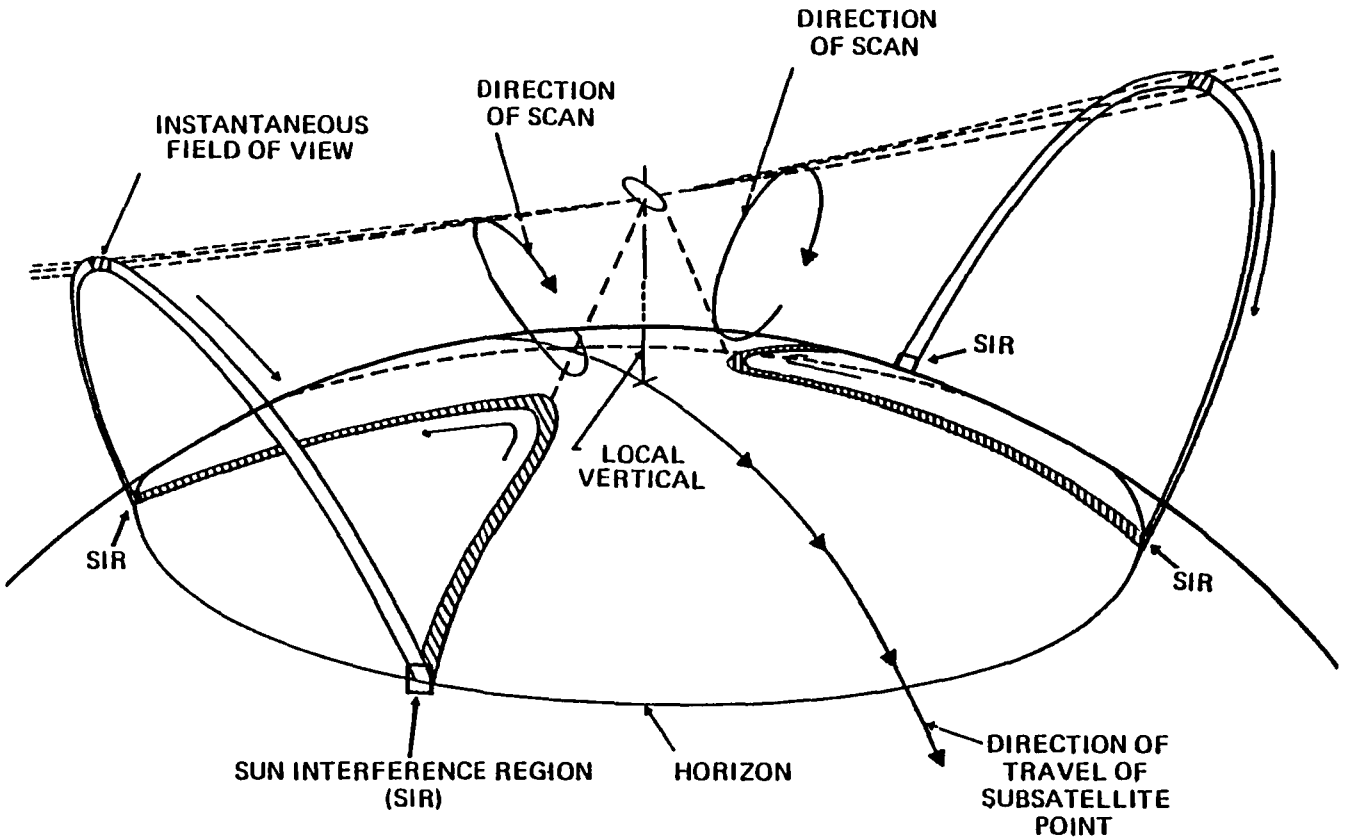

Figure 4.2-2. Seasat-1 Dual-Scanwheel Configuration

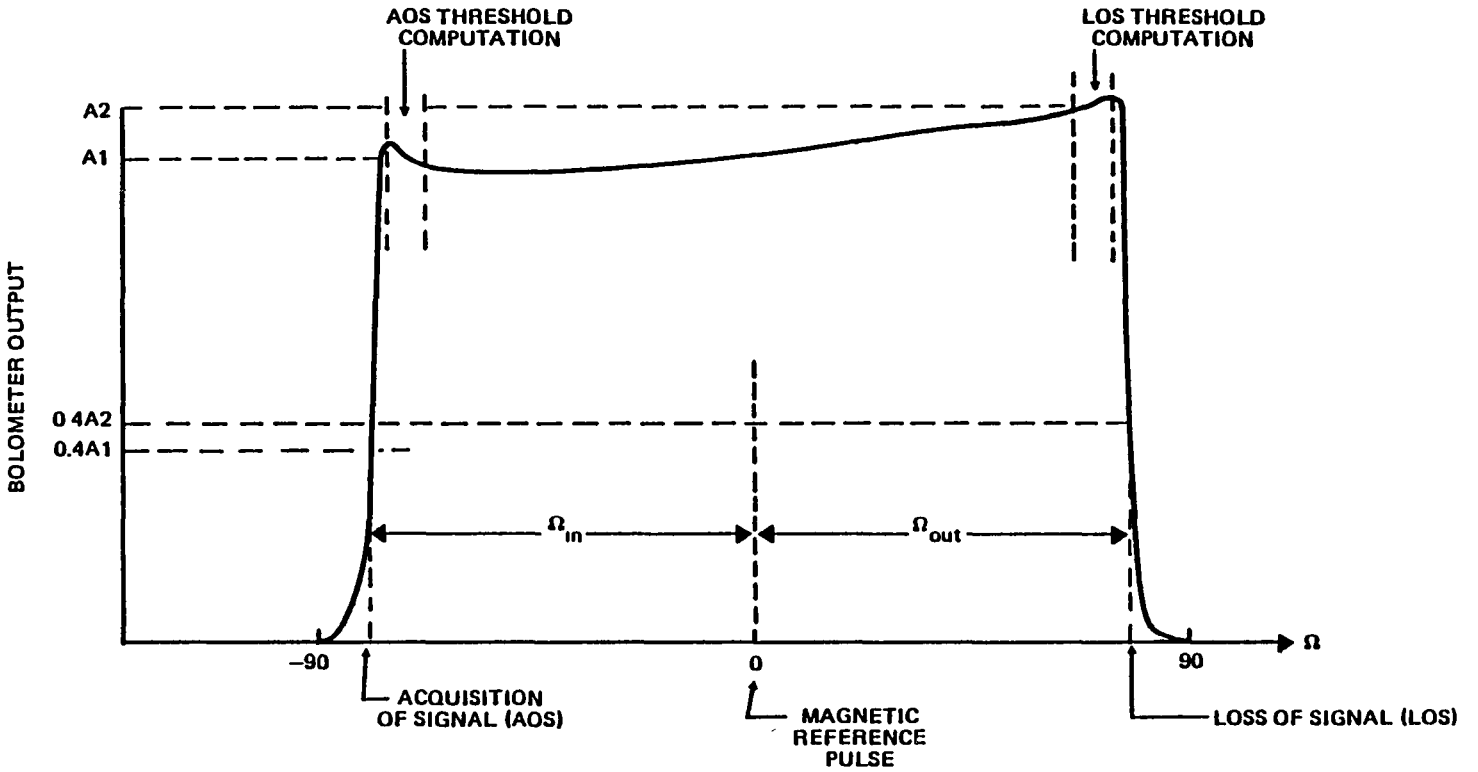

Figure 4.2-3. IR Scanner Output Signal Processing With Normalized Threshold Locator Logic

control (e.g., 900 $\pm$ 300 rpm for Seasat-1 and 2000 $\pm$ 500 rpm for ERBS). The output error signal from such systems (a measure of the attitude error sensed by the IR scanner horizon detection logic) is typically the result of an electronic average of 15 to 30 Earth scans. The details of the signal processing electronics have changed from mission to mission to accommodate conditions specific to the mission and to improve the Earth detection performance.

4.2.2 PREDICTED ATTITUDE ERRORS

LMSC provided an Earth horizon radiance profile for 10-degree intervals from 90°N to 90°S latitude for the months of January, April, July, and October. The profiles were used as input to the HRMU program (Section 3) to determine the roll and pitch errors induced on the scanners mounted on a spacecraft flying at a null geocentric pitch and roll attitude. A spherical Earth model was used to delineate only the horizon-radiance-induced errors. Estimates of the variations in the flight data relative to the average radiance model were made by inserting a cold-cloud-perturbed profile at one latitude into the data set of profiles representing the 19 latitude bins. Figures 4.2-4 through 4.2-7 show the dual-scanner pitch and roll errors simulated for April and July using LMSC profiles.

These values were subtracted from the telemetered IR scanner pitch and roll angles to remove the effects of Earth radiance variations on the sensed pitch and roll. Similar adjustments were made to the IR data for Earth oblateness and scanner electronics and for alignment and calibration biases, to get the best estimate of the geocentric pitch and roll. The effects of localized cold clouds on the Seasat IR scanners simulated during the prelaunch analysis are illustrated in Figures 4.2-8 and 4.2-9 for the pitch and roll errors, respectively.

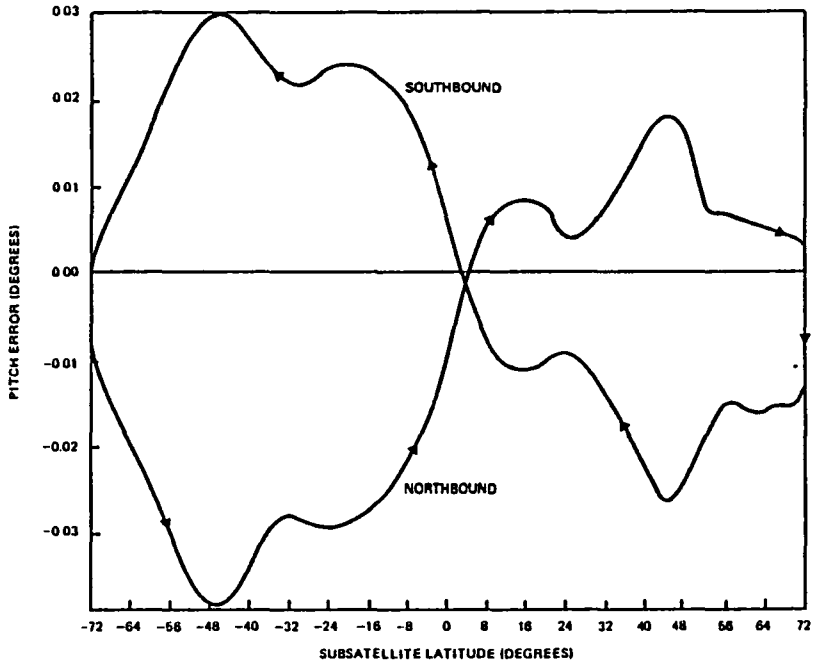

Figure 4.2-4. Seasat-1 Pitch Errors for April 1978 Radiances

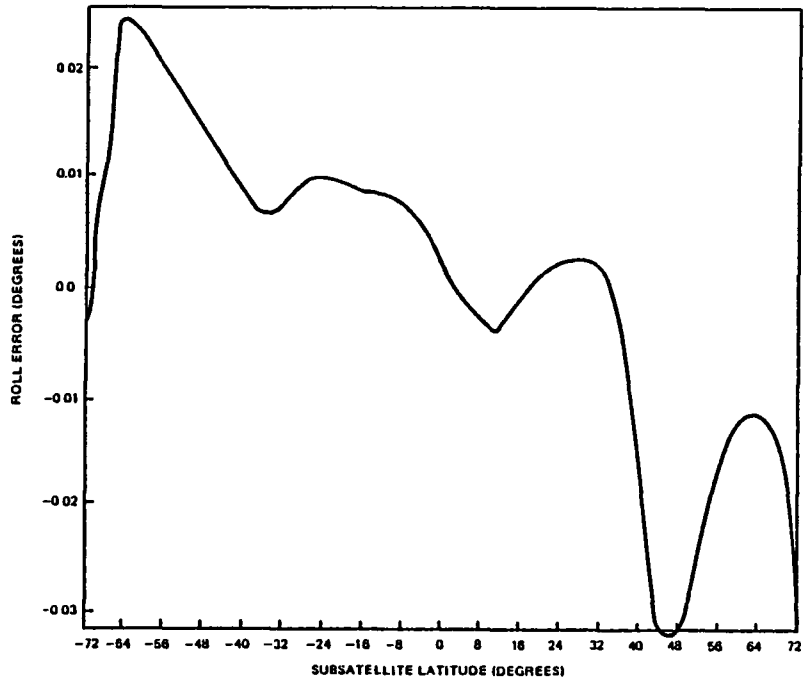

Figure 4.2-5. Seasat-1 Roll Errors for April 1978 Radiances

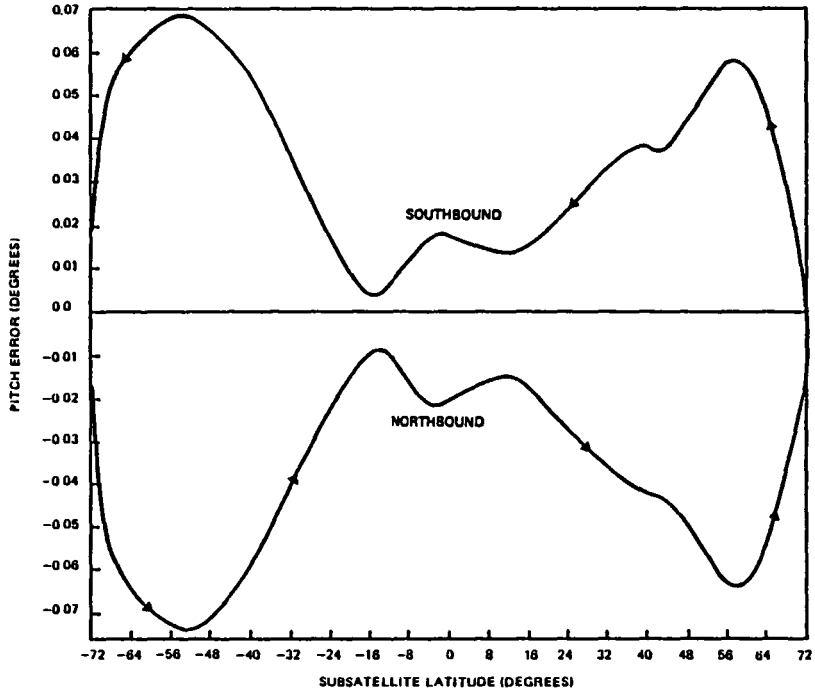

Figure 4.2-6. Seasat-1 Pitch Errors for July 1978 Radiances

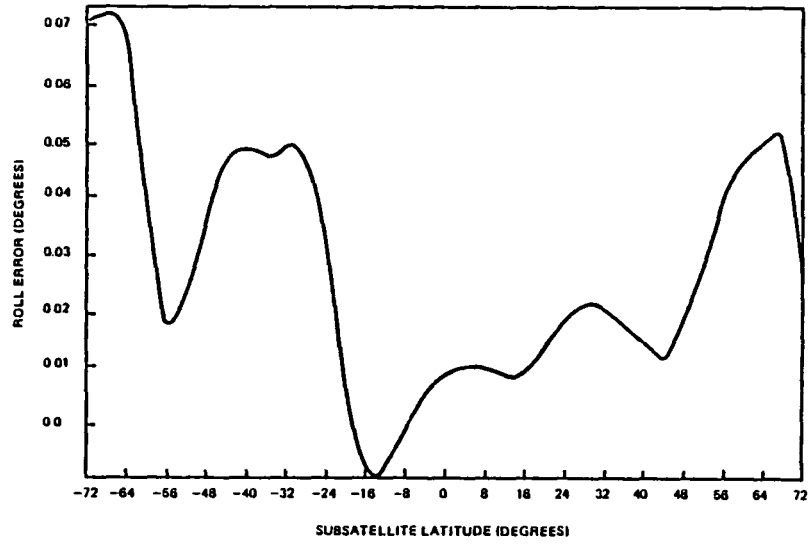

Figure 4.2-7. Seasat-1 Roll Errors for July 1978 Radiances

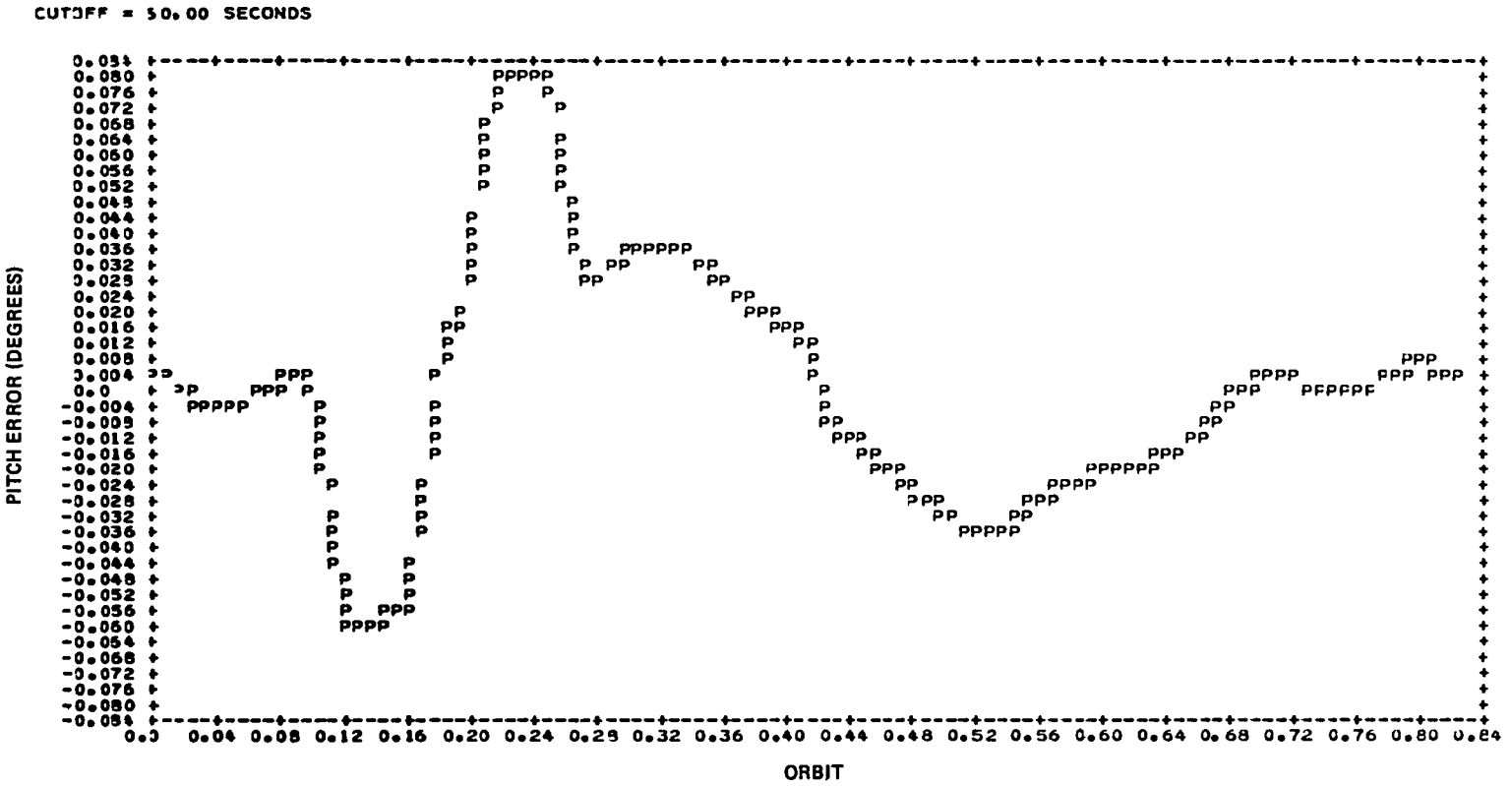

Figure 4.2-8. Effect of Simulated Clouds on Seasat-1 Pitch Errors

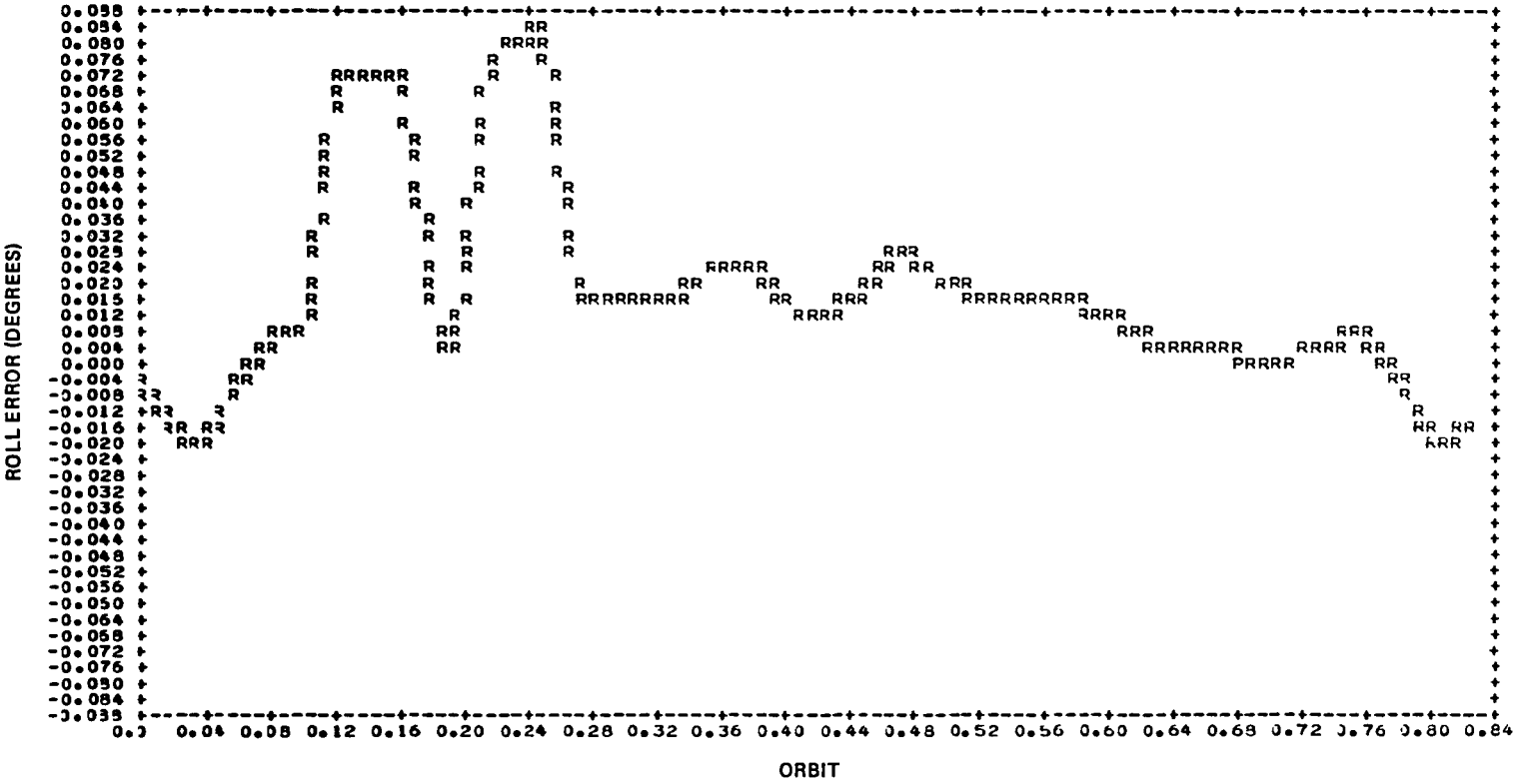

Figure 4.2-9. Effect of Simulated Cold Clouds on Seasat-1 Roll Errors

Based on the analysis discussed above and discussions with the spacecraft manufacturer (LMSC) and IR scanner system subcontractor (ITHACO), a detailed list of attitude sensing error sources, error magnitudes, and error distributions was compiled to estimate overall end-to-end attitude determination accuracy. This list and the resultant accuracy estimates compiled from prelaunch analysis for Seasat-1 are presented in Table 4.2-1 (Reference 32). The interpretation of this table of errors is as follows.

The prelaunch estimates of the end-to-end attitude determination (3σ) of geocentric pitch, roll, and yaw accuracy during Sun data coverage are 0.2 degree, 0.2 degree, and 0.18 degree, respectively. Significant contributions to the roll and pitch errors are from the 0.08-degree errors associated with the predicted magnitude of the cold cloud effects, which were expected to occur with maximum intensity and frequency in the tropical latitudes. Table 4.2-1 also indicates that the correction of the 0.075-degree errors from systematic effects is assumed to be performed accurately and that all calibration and alignment biases are removed without error. The Sun sensor is used to determine IR scanner alignments, biases, and calibration errors in the augmented data. The difference between the nominal and the augmented data is that the Sun sensor errors are substituted for the corresponding IR scanner errors. The 0.06-degree accuracy improvement in the augmented pitch and roll results primarily from the application of a systematic horizon radiance correction.

4.2.3 MISSION DATA ANALYSIS

The responsibility of the ADCS was to provide definitive attitude determination on a daily basis for spacecraft data spans 1 day in length at data periods of 1 second. No real-time support was planned; however, because of problems that

Table 4.2-1. Seasat-1 Pitch and Roll Attitude Error Summary[a]

ERROR SOURCE	FREQUENCY	NOMINAL		AUGMENTED		
		PITCH	ROLL	PITCH	ROLL	YAW
SYSTEMATIC HORIZON RADIANCE VARIATION[b]	ORBITAL	0 074	0 075	0	0	NA[c]
RANDOM HORIZON RADIANCE VARIATIONS[b]	ORBITAL	0 08	0 08	0 08	0 08	0 07[d]
COMPONENT AGING[e]	LOW	0 025	0 025	0	0	NA
NOISE (WITH SOFTWARE FILTER)[e, f]	HIGH	0 01	0 01	0 01	0 01	0 01[d]
SCANWHEEL SPEED (±300 RPM)[e, f]	ORBITAL + LOW	0 004	0 059	0 002	0 03	0 03[d]
TEMPERATURE VARIATIONS (17 TO 25° C)[e]	LOW	0 04	0 04	0 04	0 04	NA
THRESHOLD STABILITY[e]	LOW/ORBITAL	0 04	0 04	0 04	0 04	0 04[d]
ATTITUDE COMPUTER DRIFT[e]	LOW/ORBITAL	0 032	0 032	0 032	0 032	0 03[d]
INTERNAL ALIGNMENT KNOWLEDGE[e]	LOW	0 05	0 05	0	0	NA
EXTERNAL ALIGNMENT KNOWLEDGE[e, f]	LOW	0 002	0 0025	0	0	NA
MISCELLANEOUS INCLUDING TRIMMING OR CALIBRATION[e]	LOW	0 05	0 03	0	0	NA
LAUNCH SHOCK (SCANNER)[e]	LOW	0 025	0 025	0	0	NA
SUN SENSOR ACCURACY[d, e, f, g, h]	HIGH	NA	NA	0 05	0 05	0 072
LAUNCH SHOCK (SUN SENSOR)[g]	LOW	NA	NA	0 006	0 006	0 006
SUN SENSOR ALIGNMENT[e, f]	LOW	NA	NA	0 0033	0 0032	0 0025
MAXIMUM THERMAL DISTORTION AT ν = 90 DEGREES[e] (SUN SENSOR FIXTURE TO SARA)	ORBITAL	NA	NA	0 042	0 042	0 031
BIAS DETERMINATION OBSERVABILITY[i]	LOW	NA	NA	0 01	0 01	0 01
TOTAL (3σ, GAUSSIAN)		0 26	0 26	0 20	0 20	0 18

9661 (72*1)/84

[a] ALL ERROR SOURCES ARE ASSUMED UNIFORM WITH THE TABULATED UPPER BOUND EXCEPT THOSE DENOTED OTHERWISE

[b] FROM CSC REPORT CSC/TR-78/6007, *SEASAT-A ATTITUDE ANALYSIS AND SUPPORT PLAN,* APRIL 1978

[c] NOT APPLICABLE

[d] THESE ERRORS ARE A RESULT OF YAW CORRELATIONS WITH PITCH AND ROLL

[e] JPL INTEROFFICE MEMORANDUM 343-78-098, A J TREDOR TO E H POUNDER, JANUARY 26, 1978

[f] GAUSSIAN ERROR DISTRIBUTION, 3σ VALUE TABULATED

[g] FROM LMSC REPORT GCS/3900/6211, *SEASAT-A ATTITUDE DETERMINATION SYSTEM (ADS) PERFORMANCE ANALYSES,* 1976

[h] THESE ARE WORST-CASE 3σ ERRORS NOMINAL ERRORS MAY BE AS LOW AS 0 025 DEGREE

[i] FROM CSC REPORT CSC/TR-76/6012, *EVALUATION OF AN INFRARED HORIZON SCANNER BIAS DETERMINATION ALGORITHM FOR SEASAT-A,* 1977

occurred with the IR scanners and their influence on the degradation of spacecraft control, a significant amount of near-real-time support was provided in the first month. Activities that had not been anticipated, such as IR data problem diagnosis and data filtering analysis, end-to-end attitude sensor alignment, and analysis for alternative methods of yaw determination, dominated the first 2 months of mission support. After this, the effort shifted to a period of intense definitive data processing support to clear a 40-day backlog of data days and to catch up to the planned schedule of mission data flow. The high degree of near-real-time support, along with diverse problems in the definitive data that resulted from the evolution of orbit/Sun geometry, taxed the attitude determination system (ADS) software. The software design had anticipated a less hectic schedule of processing definitive data with minimal scanner problems. Because of the high level of activity that was required to achieve the nominal support, insufficient time was available to evaluate comprehensively the accuracy of the application of the systematic horizon radiance correction to the pitch and roll data. Approximately 100 days of data became available from launch on June 28, 1978, to the failure of the spacecraft in the first week of October. From these, 3 days of data were analyzed to assess the IR scanner data for information about the accuracy of the systematic correction and the magnitude of the errors due to unmodeled horizon radiance variations.

4.2.3.1 IR Scanner Anomalies

Sun interference in the Seasat IR scanner data was predicted, before launch, to occur 78 days from nominal launch (i.e., near day 256) for approximately 3 to 4 days. It was during these times that the Sun appeared on the horizon in the unblanked portion of the IR scanner cone near the Earth edge triggering point. In fact, Sun interference in the IR

scanner data was a principal cause of IR data anomalies from launch (day 178) to day 184 and from day 225 through day 256.

Soon after launch, real-time IR scanner telemetry data displayed an anomaly characterized by a large instantaneous positive roll error signal of 7.0 degrees and a pitch error signal of -3.5 degrees. Examples of these data are shown in Figures 4.2-10 and 4.2-11. This anomaly occurred regularly every 100 minutes (orbital period), 36 minutes from the time of the ascending node. Calculations indicated that the angle between the IR scanner axis and the Sun direction was consistently near 45 degrees at this time. It was concluded that the anomaly was due to the failure of the blanking electronics to suppress the effects of Sun IR radiation entering the right IR scanner. This conclusion was verified by turning off the right IR scanner signal processor just before the expected anomaly and observing no occurrence. After a series of observations, it was further concluded that the blanking electronics was not effective for certain geometrical configurations. The failure of the blanking electronics to perform as designed was related to a power supply problem. It was found that blanking performance could be improved by selecting the appropriate power supply and that IR scanner bias determination results were dependent on power supply selection.

While using only the left IR scanner, another data anomaly was observed. This anomaly was characterized by an intermittent large negative roll error signal to -10.0 degrees and a negative pitch error signal to -5.0 degrees; it is illustrated in Figures 4.2-12 and 4.2-13. This left IR scanner anomaly occurred when the Sun was well away from the scan cone and did not occur with the regularity of the right scanner anomaly. It was concluded from the high-frequency structure of the anomaly that the cause was reflected sunlight from some surface near the left IR scanner cone.

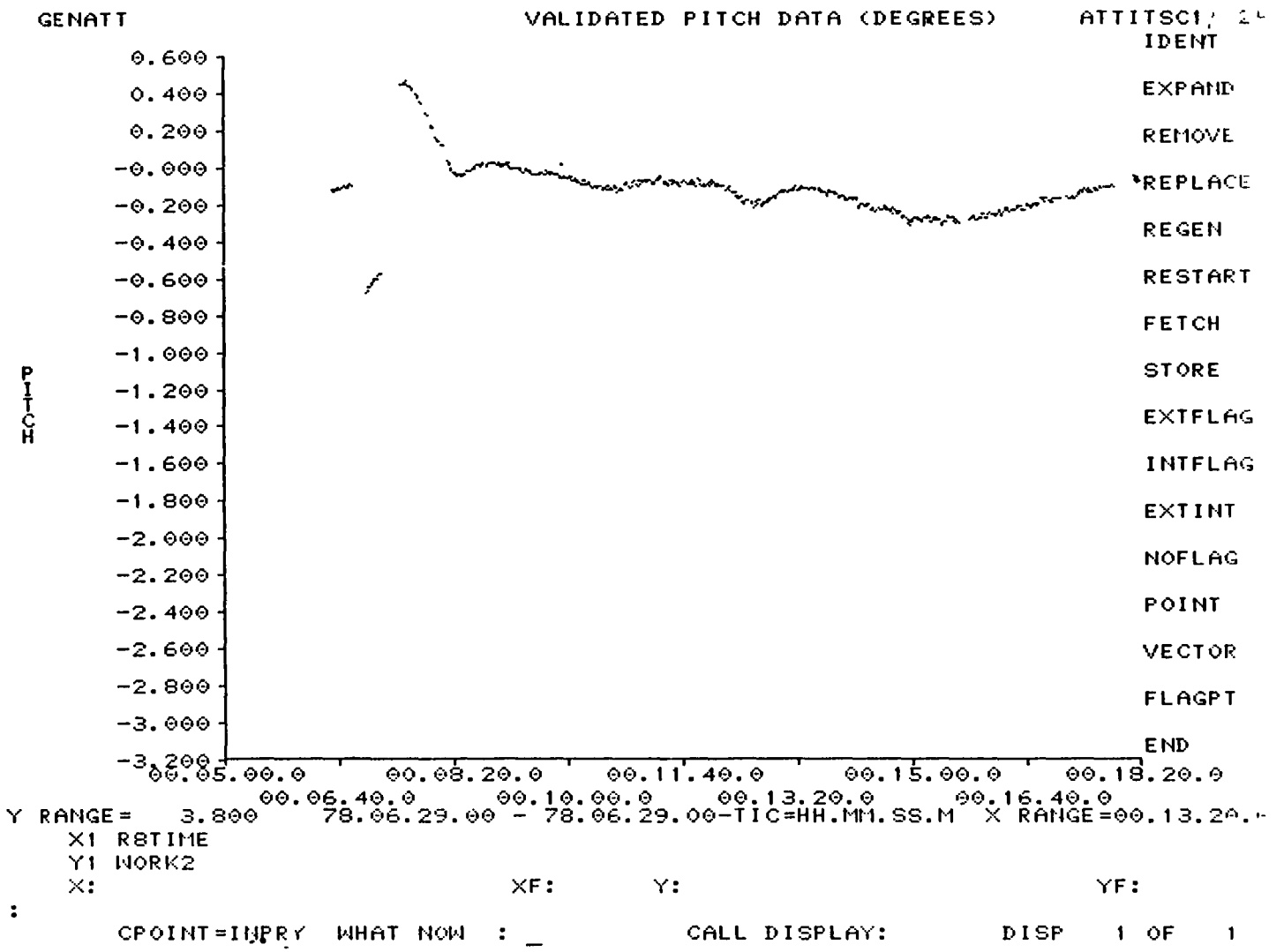

Figure 4.2-10. Dual-Scanner Pitch Anomaly for Revolution 28

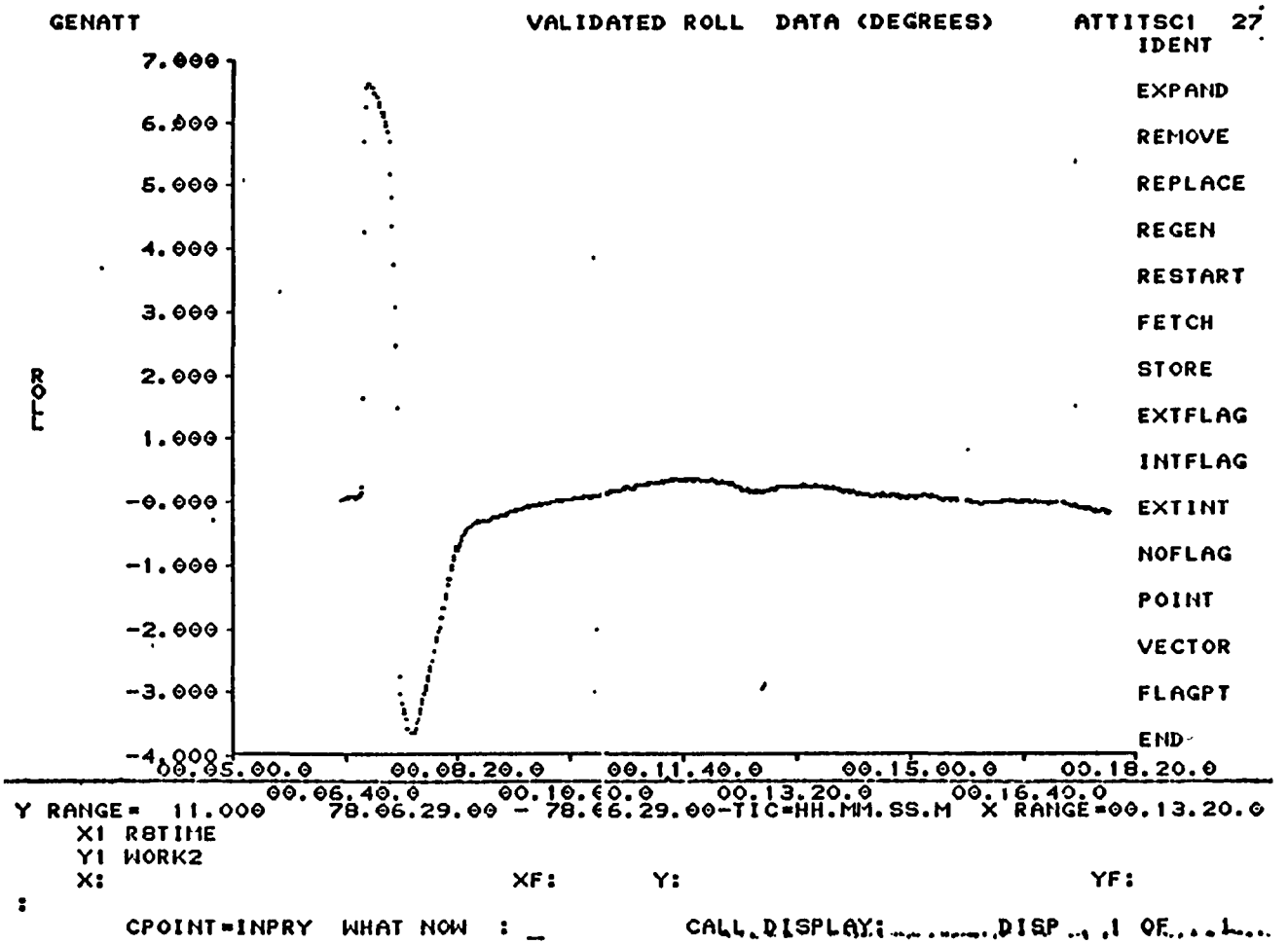

Figure 4.2-11. Dual-Scanner Roll Anomaly for Revolution 28

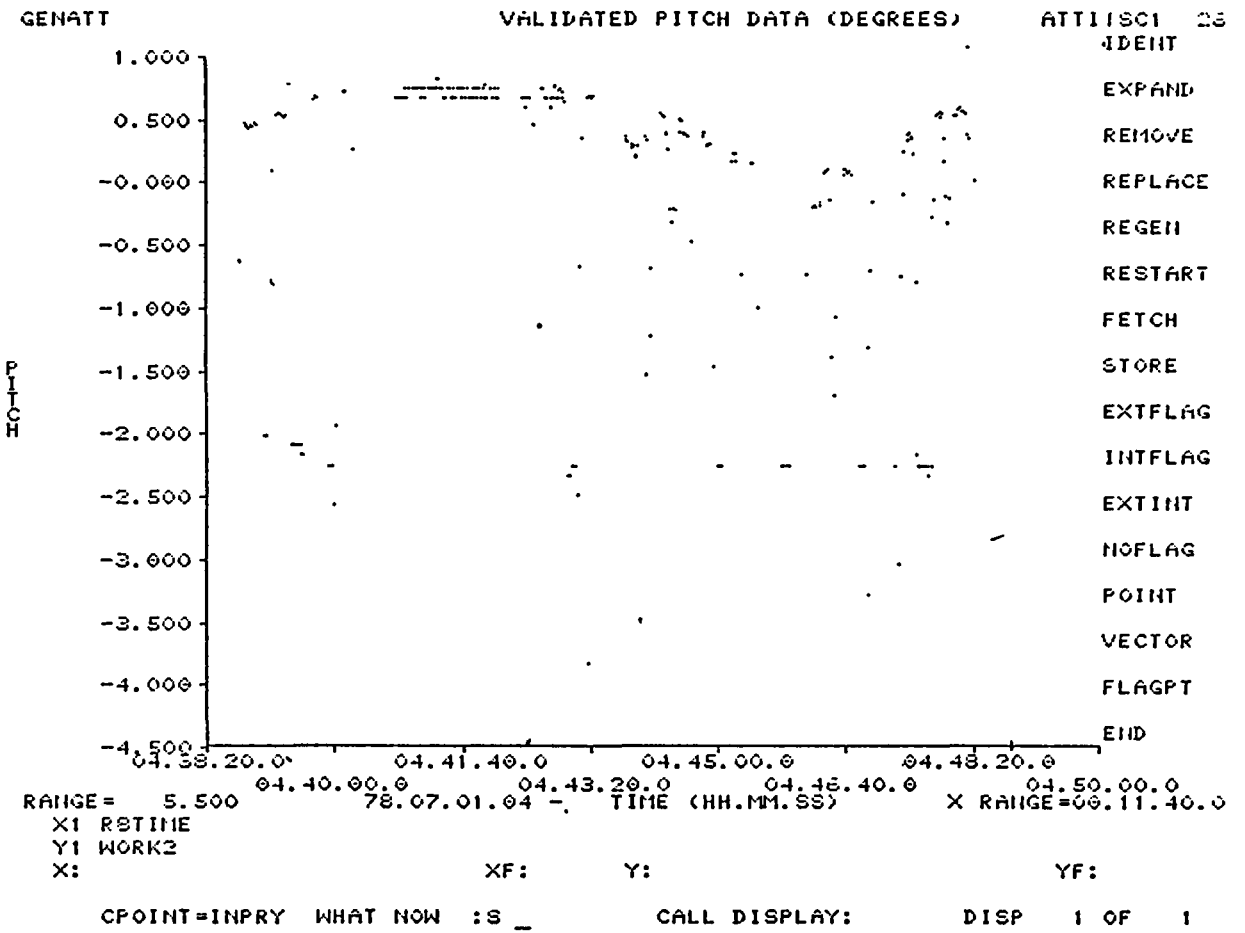

Figure 4.2-12. Left Scanner Pitch Anomaly Signature on Revolution 60

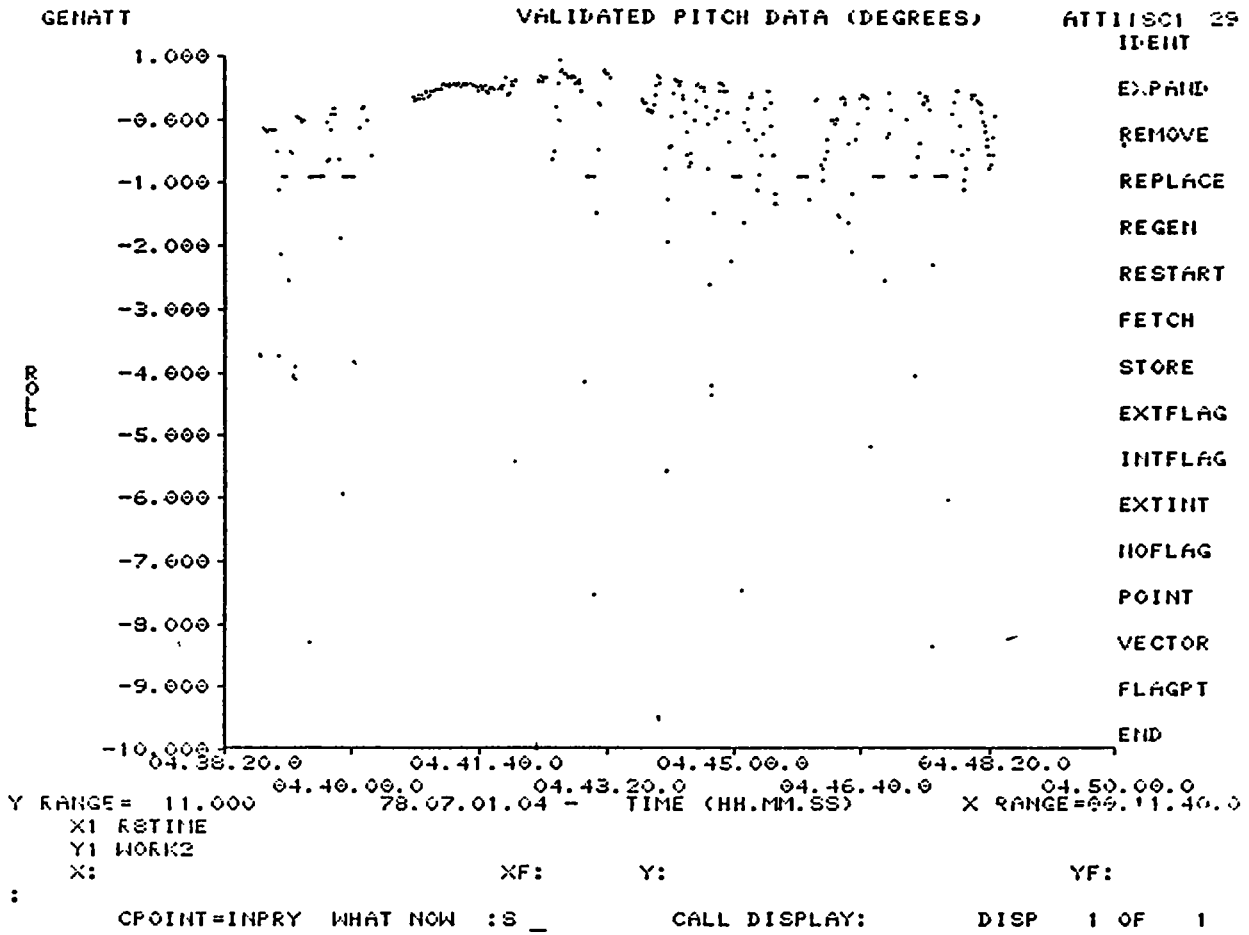

Figure 4.2-13. Left Scanner Roll Anomaly Signature on Revolution 60

Investigation by LMSC showed that the Synthetic Aperture Radar downlink antenna was within 1 or 2 degrees of the left IR scanner cone, near the Earth horizon at the AOS portion of the scan.

Because Sun interference in the left IR scanner was totally unpredictable, it was decided to disable the left IR scanner signal processor and develop operational spacecraft control procedures to work around the more predictable anomalies occurring in the right IR scanner. During the analysis of IR scanner data anomalies, Sun sensor data were used as a reference for interpreting true spacecraft behavior.

4.2.3.2 Sun Sensor Anomalies

Another level of confusion was introduced into the attitude determination system analysis when Sun sensor data anomalies occurred. Sun sensor data anomalies occurred as discontinuities in the Sun sensor measurement angles α and β. The nominal FOV of the Sun sensors was from -32 degrees to +32 degrees for both α and β. For the Sun within this FOV, coarse 6-bit Gray-coded α and β values with 1.6-degree resolution and fine 9-bit binary-coded α and β values with 1/256-degree resolution were generated by the sensor. When the Sun left the FOV, a Sun presence bit in the telemetry word was to be set from 1 to 0.

It was found that Sun sensor data anomalies occurred as the Sun approached and exited the sensor FOV. These errors resulted from the attitude determination system's reliance on the Sun presence bit to signal the occurrence of valid Sun data for data processing logic and the imprecise adjustment of the Sun presence indicator threshold. The sensor indicated Sun presence at times when the Sun was beyond the nominal FOV and when the actual Sun angle was beyond the range of the telemetry word length. As the Sun approached the edge of the FOV, one of two effects occurred: a discontinuity

from positive maximum to negative maximum (coarse word discontinuity) or a discontinuity of 1.6 degrees (fine word discontinuity). Figures 4.2-14 and 4.2-15 illustrate the two effects. These effects were eliminated in the data processing system by limiting the Sun sensor α and β values to a range of $\pm$30 degrees.

From the analysis of the valid Sun sensor data (not containing discontinuities), other inconsistencies were observed. These were in two forms. First, when data from different Sun sensors were used for IR scanner bias determination, different biases resulted. Second, when the FOVs of two Sun sensors provided overlapping Sun coverage, data from the two sensors produced different yaw solutions. These results suggested sensor alignment errors and required an unanticipated postlaunch recalibration.

Fine Sun sensor 1 (FSS-1) was chosen as the reference sensor for calibration because it produced the most comprehensive Sun data coverage. An extensive study was then performed to obtain IR scanner biases and to estimate the alignment errors in FSS-2 and -3 relative to FSS-1. FSS-4 was not evaluated because no data were obtained for that sensor.

4.2.3.3 Attitude Sensor Alignment

Unanticipated problems with the application of an IR scanner bias determination algorithm that used Sun sensor data as a reference made it necessary to perform an in-flight alignment analysis of the attitude sensor complement. Different pitch and roll biases resulted from batches of data from different Sun sensors. The sensor alignment procedure was essentially a manually iterative process that involved changing the sensor alignment angle data base to obtain self-consistent attitudes between the IR scanner pitch and pitch derived from an optional algorithm using the Sun sensor data.

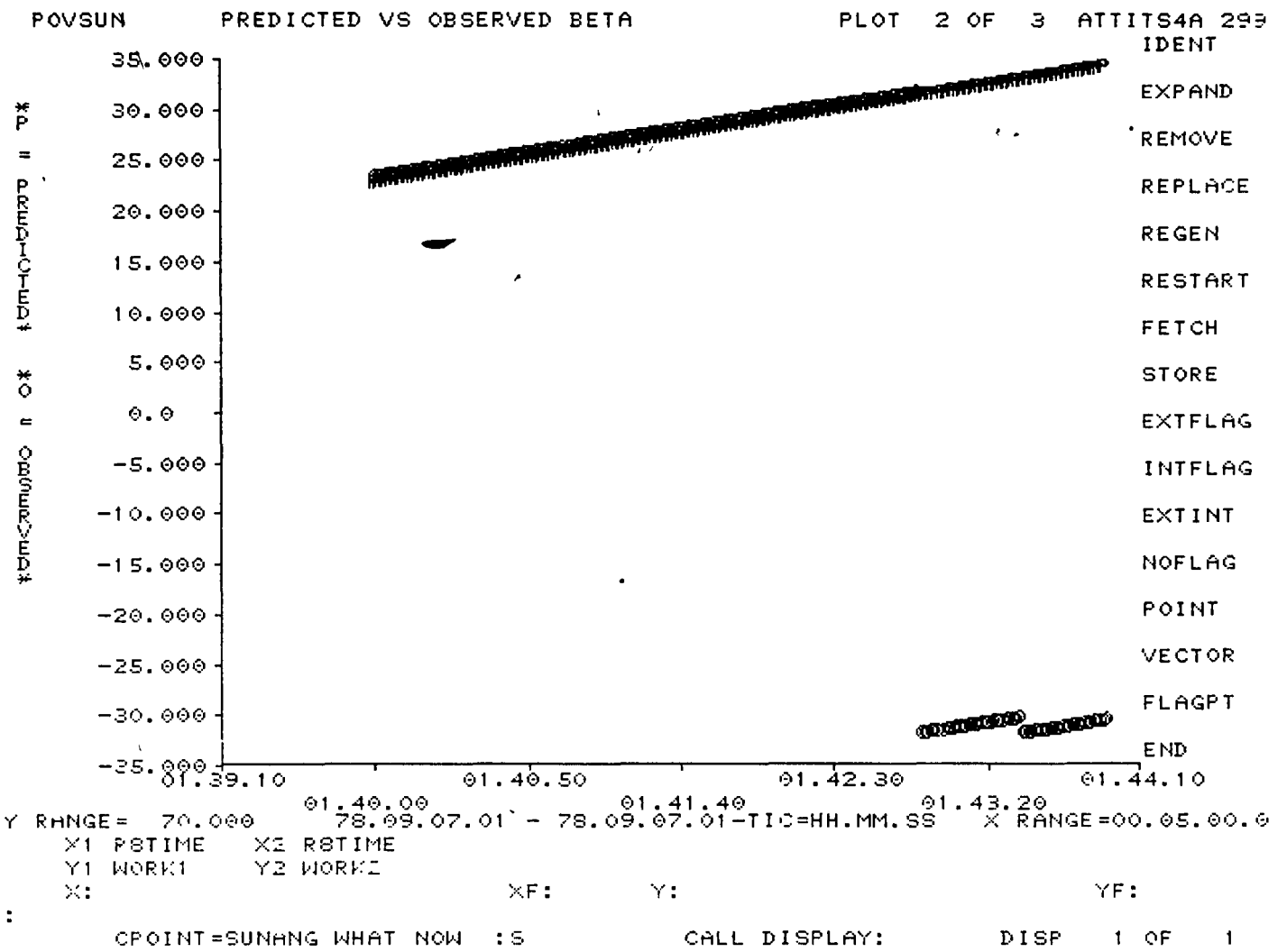

Figure 4.2-14. An Abrupt Change in β-Angle Value From +32 to -32 Degrees as the Sun Leaves the Upper Edge of FSS-2 FOV Followed by a 1.6-Degree Jump

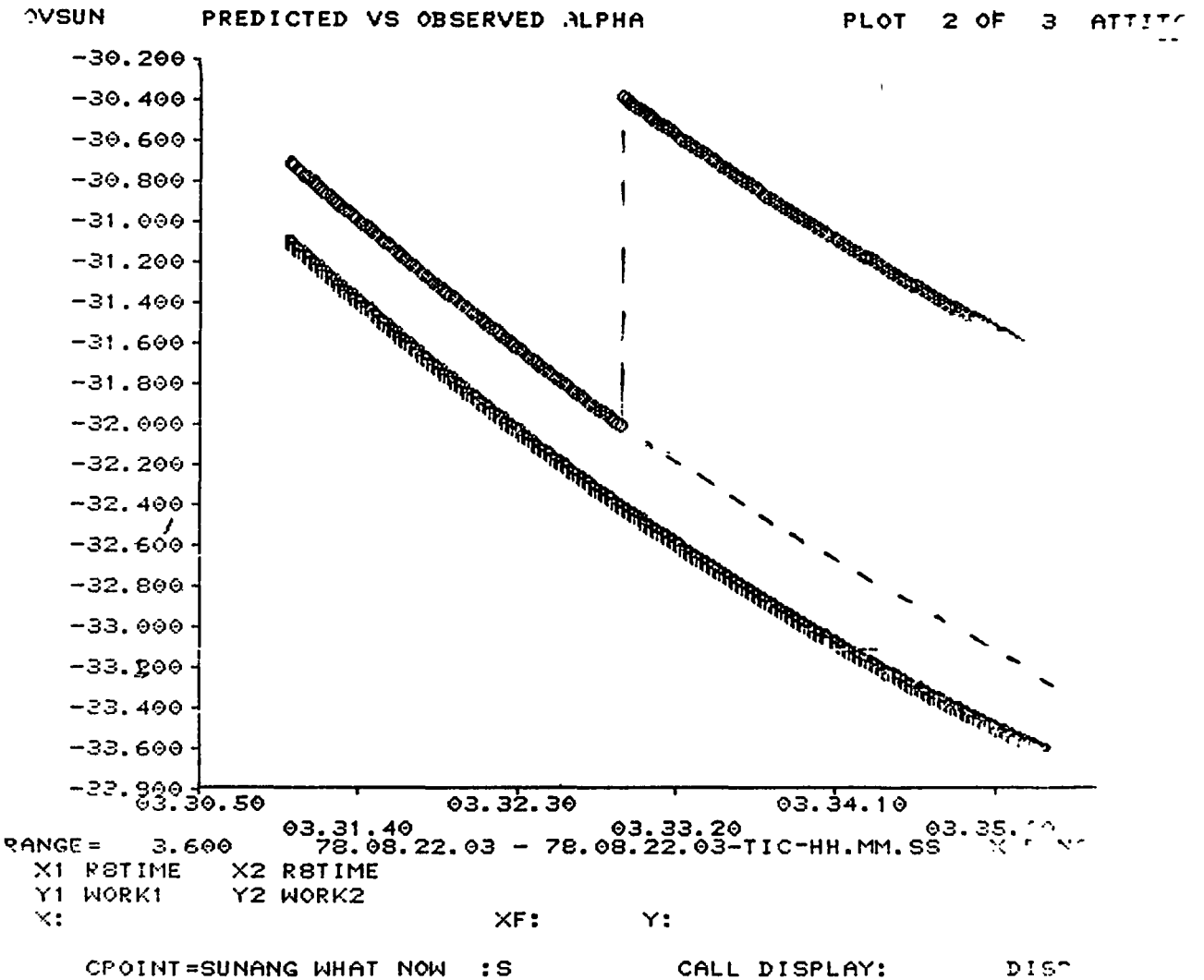

Figure 4.2-15. First 1.6-Degree Jump in α-Angle as the Sun Leaves FSS-1 FOV

A fundamental assumption in this procedure was that FSS-1, which was oriented to view along the spacecraft pitch axis, was the reference sensor for the attitude sensing system. Figure 4.2-16 illustrates the FOV geometry at FSS-1 and FSS-2 showing the overlap region. This overlap was planned to permit in-flight assessment of the accuracy of the FSS ground alignment knowledge. Data retrieved when the Sun passed through this region clearly indicated that the in-flight relative azimuthal alignment of FSS-1 and FSS-2 differed from the relative azimuthal alignment derived from the prelaunch measurements by 0.264 degree. (Tables of these data are presented in Reference 32.) Estimates of the elevation alignment error and boresight rotation alignment error for FSS-2 and FSS-3 were obtained by the manual method described above, using IR scanner and Sun sensor pitch comparisons for data days when the Sun traversed widely separated regions of the FSS-2 FOV. Figure 4.2-17 shows the geometry of the FSS-2 FOV and the Sun paths for the data used in this manual alignment procedure.

Figure 4.2-18 illustrates the graphical analysis of consecutive iterations used to align the pitch derived from the IR scanner (P_{IR}) and Sun sensor data (P_{SUN}) for day 282. The figure also shows P^1_{SUN} and P^2_{SUN}, which are reconstructed pitch angles obtained by application of cone angle and cone and twist angle corrections (Set 1, Table 4.2-2), respectively, to the Sun data. Table 4.2-2 summarizes the results of the alignment effort on FSS-2. FSS-3 data were also available for day 282; however, conclusive alignment of that sensor was not established as the Seasat-1 mission ended prematurely with a power subsystem failure on day 283 (October 10, 1978).

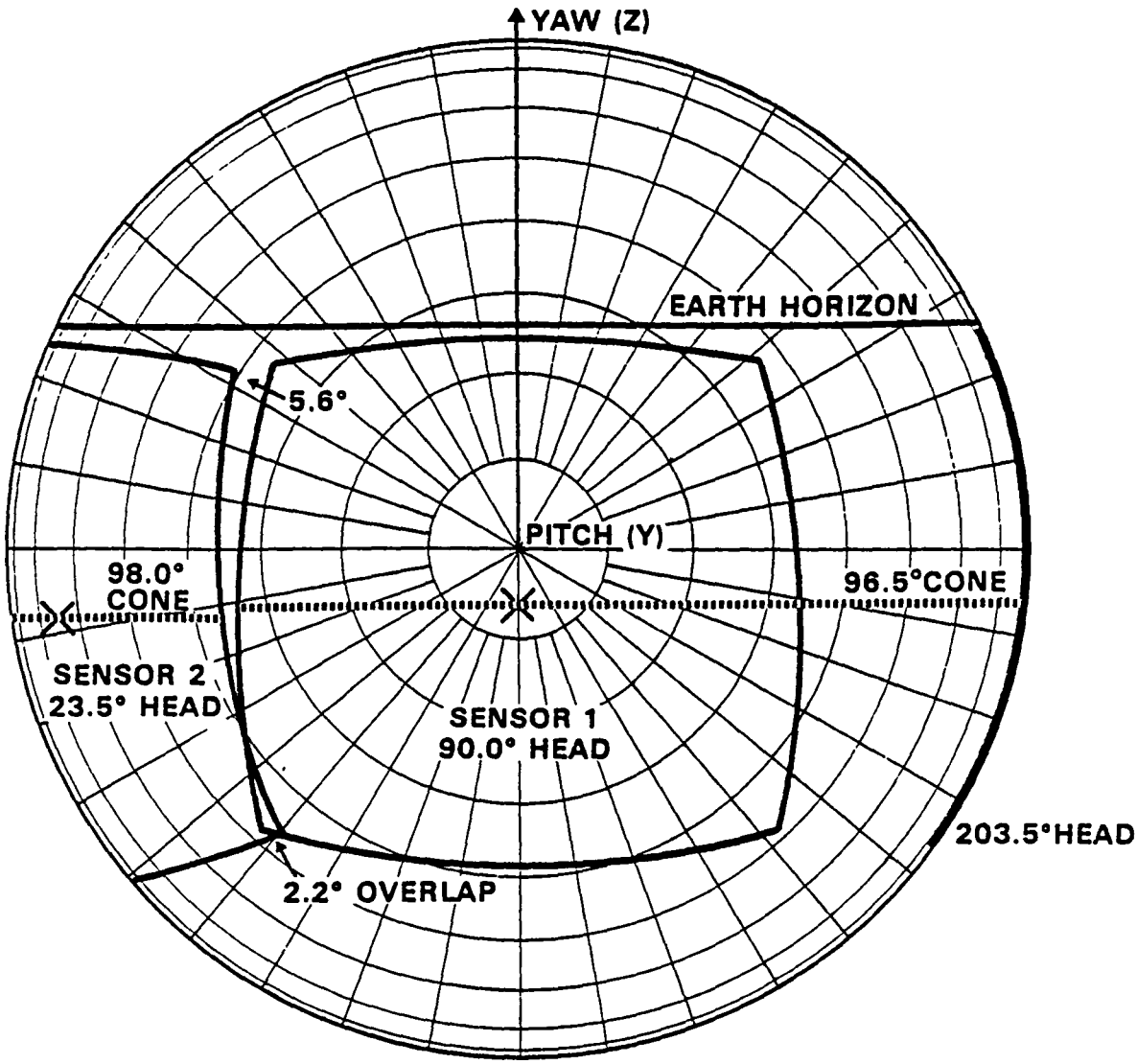

Figure 4.2-16. Seasat-1 Sun Sensor Configuration Looking Down on the Y (Pitch) Axis

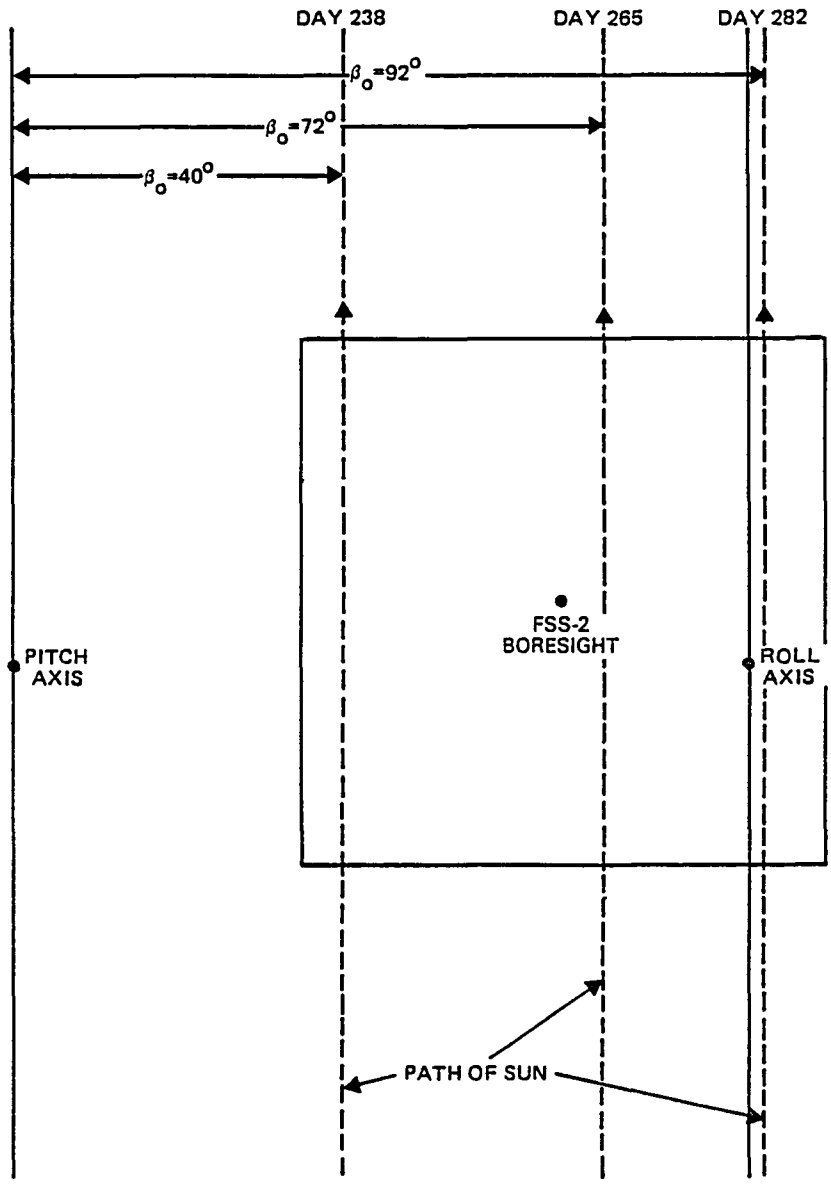

Figure 4.2-17. Sun/Spacecraft Geometries on Days 238, 265, and 282 With FSS-2 FOV

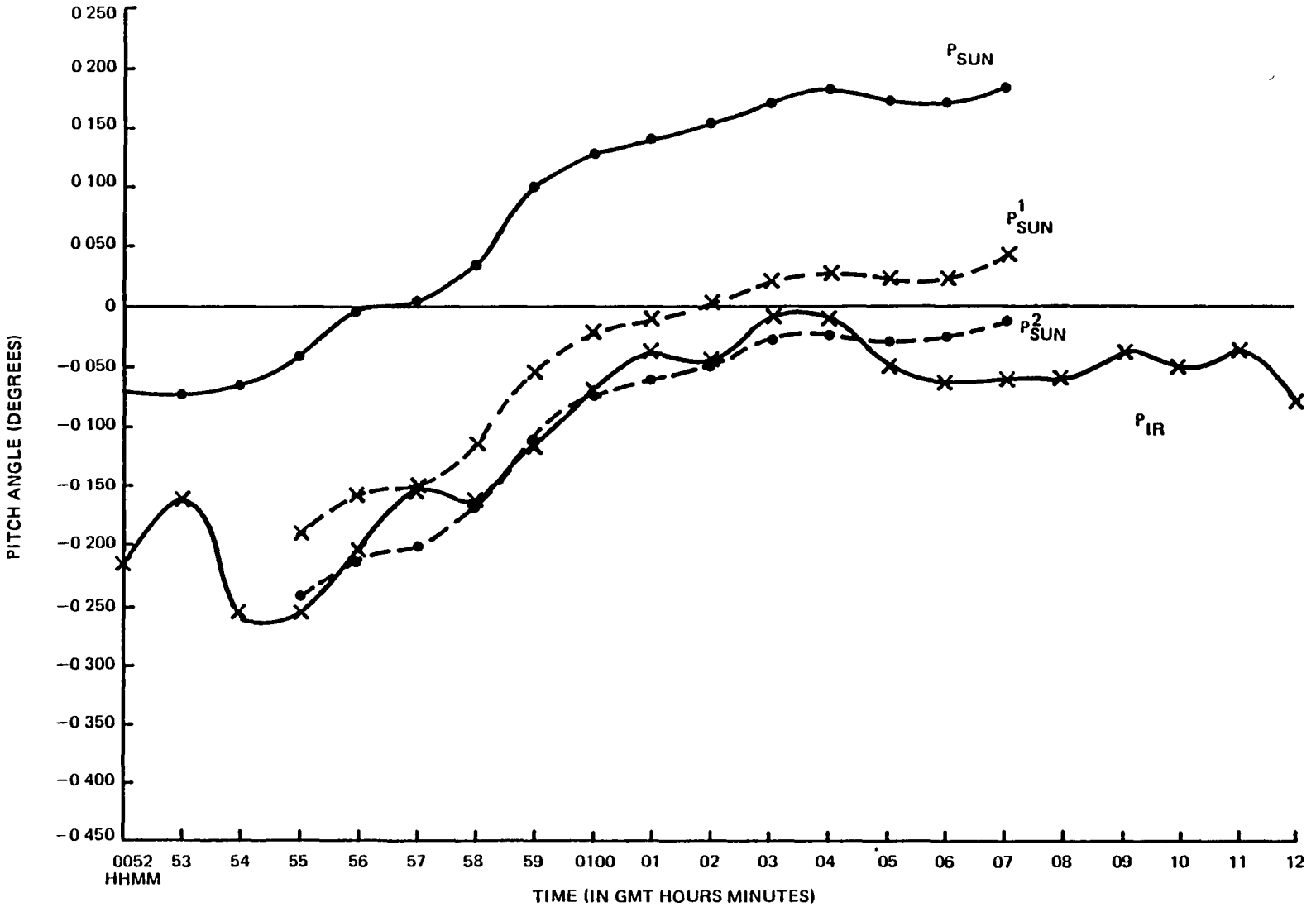

Figure 4.2-18. Comparison of IR Scanner and Sun Sensor Pitch Angles for Day 282

Table 4.2-2. FSS-2 Alignment Angle Results*

	CONE		TWIST		CLOCK	
	θ	$\Delta\theta$	ψ	$\Delta\psi$	ϕ	$\Delta\phi$
PRELAUNCH ANGLES	98 017	–	–90 012	–	23.509	–
POSTLAUNCH (SET 1)	98 187	0 17	–89.892	0 12	23.250	–0 259
POSTLAUNCH (SET 2)	98 177	0 16	–89.862	0.15	23.260	–0.249
POSTLAUNCH** ANGLES	98 170	0.153	–89.890	0.122	23.245	–0.264

*THESE RESULTS WERE OBTAINED ASSUMING
FINE PITCH BIAS = 0.11°, FINE ROLL BIAS = 0.10° IN THE IR DATA

**THESE ANGLES WERE INCORPORATED INTO THE DATA BASE NAMELIST FOR DATA DAYS FOLLOWING DAY 225 (AUGUST 13)

4.2.3.4 Verification of the Accuracy of the Seasat-1 Earth IR Horizon Model

To establish a measure of the accuracy of the IR scanner pitch and roll data, the corrected IR scanner roll data were compared with roll data derived from the FSS-1 data. This comparison was most valid when the Sun was near the spacecraft pitch axis and thus near the center of the FSS-1 FOV. Figure 4.2-19 illustrates the geometry for the Sun in the FSS-1 FOV on day 219 with a Sun angle of 19 degrees.

Figures 4.2-20 and 4.2-21 compare IR scanner and Sun sensor roll data from day 219 and day 205, respectively. The second case represents conditions when the Sun was closer to the center of the sensor (i.e., Sun angle of 3.7 degrees). Although these examples represent a very limited amount of data, evidence exists for the achievement of higher accuracy in the summer hemisphere (+72 degrees) than in the winter hemisphere (-72 degrees). Long-duration IR data excursions

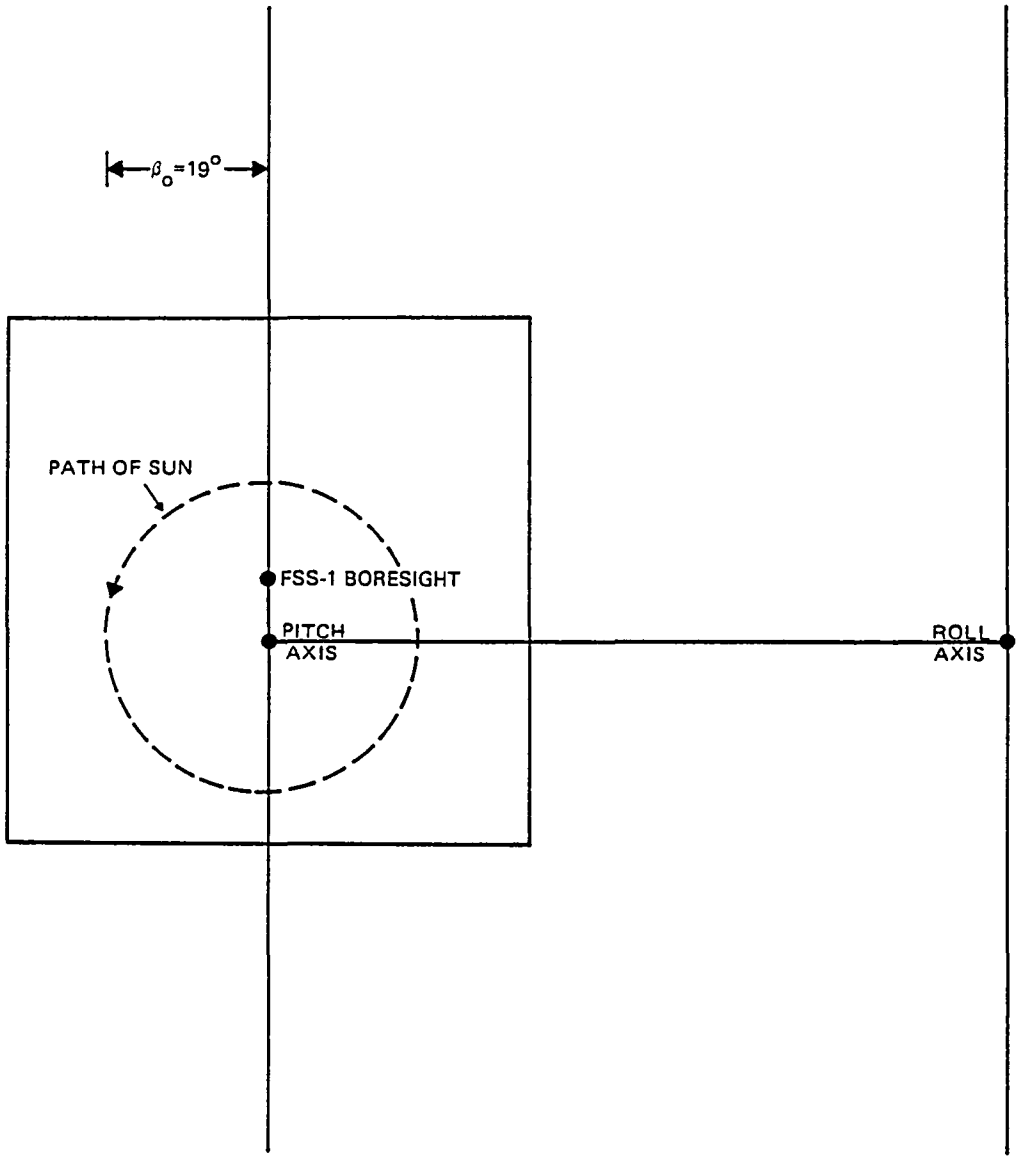

Figure 4.2-19. Sun/Spacecraft Geometry on Day 219 With FSS-1 FOV

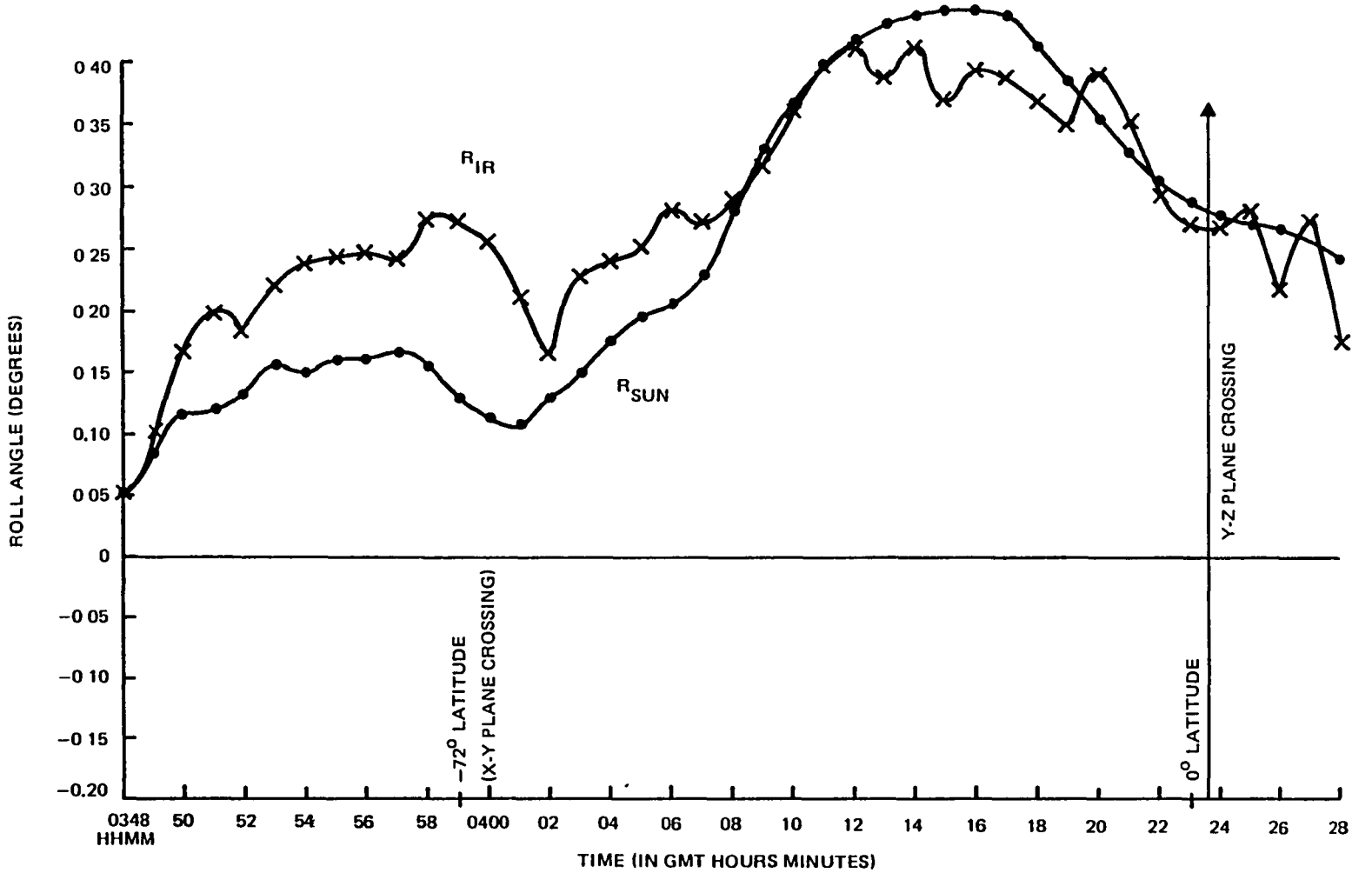

Figure 4.2-20. Comparison of IR Scanner and Sun Sensor Roll Angles for Day 219 (Reconstruction of roll with FSS-1 prelaunch angles) (1 of 2)

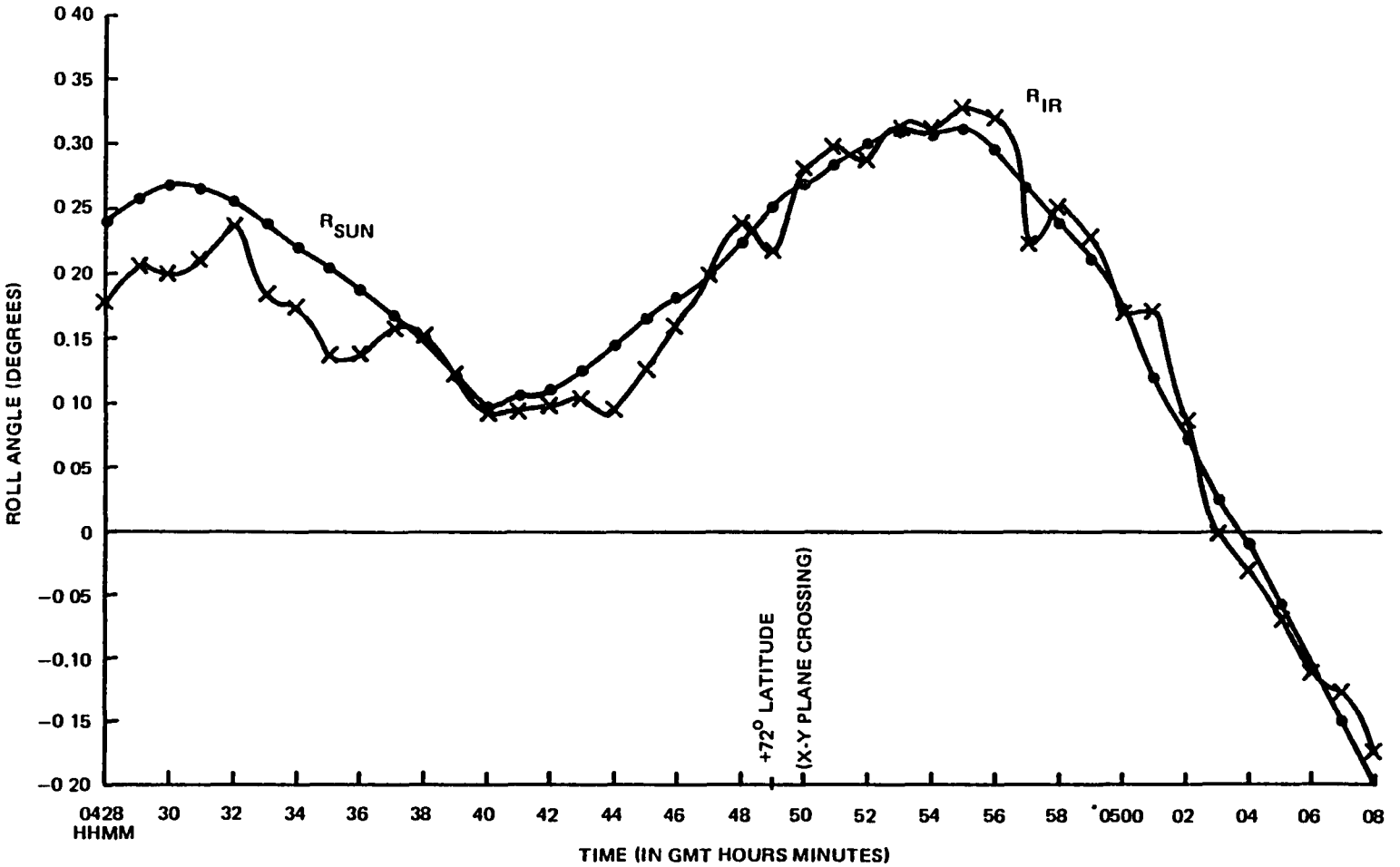

Figure 4.2-20. Comparison of IR Scanner and Sun Sensor Roll Angles for Day 219 (Reconstruction of roll with FSS-1 prelaunch angles) (2 of 2)

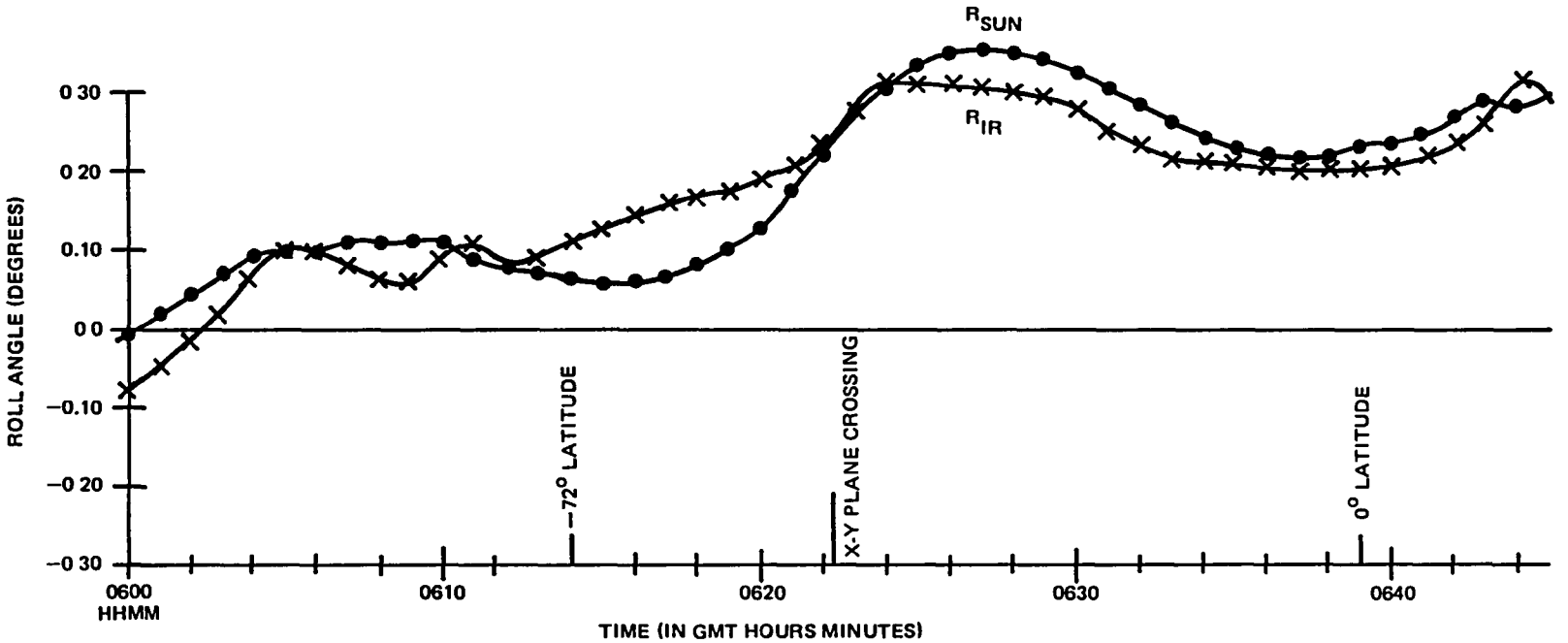

Figure 4.2-21. Comparison of IR Scanner and Sun Sensor Roll Angles for Day 205 (1 of 2)

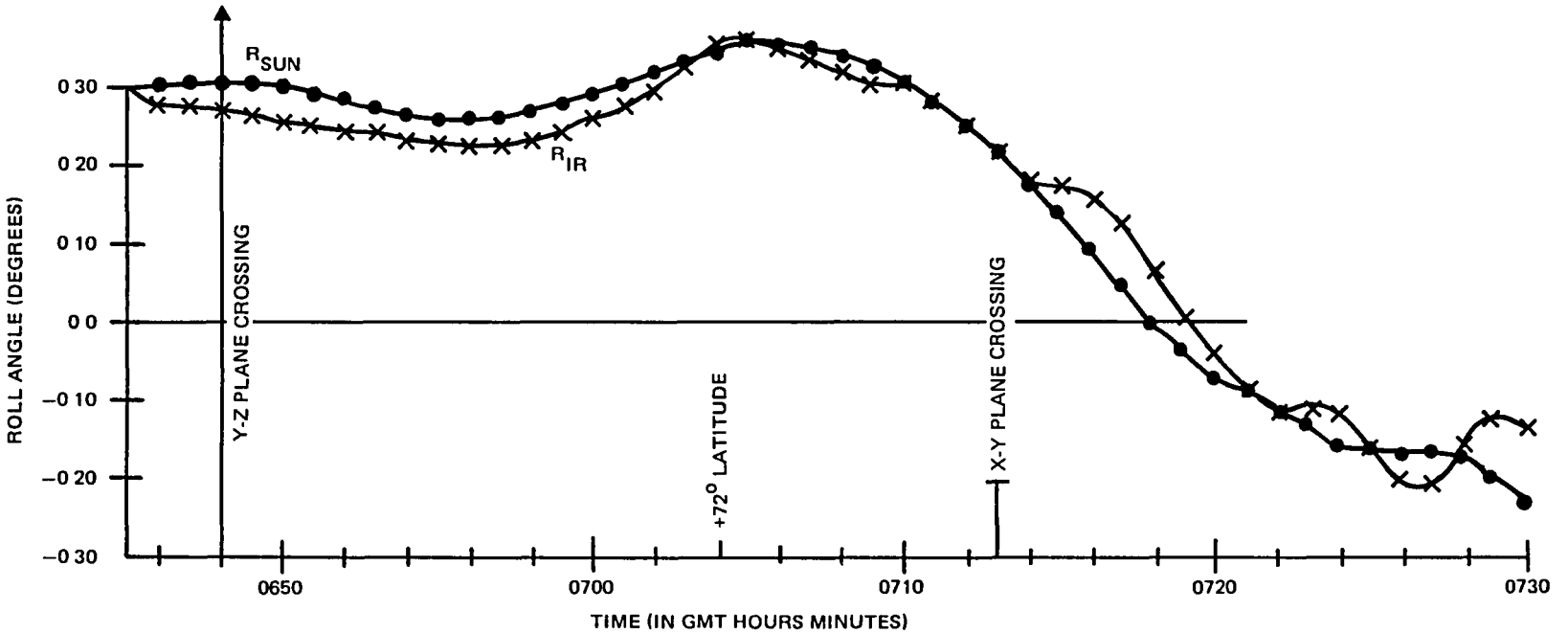

Figure 4.2-21. Comparison of IR Scanner and Sun Sensor Roll Angles for Day 205 (2 of 2)

on day 219 near 03:56 universal time (UT) are approximately 0.1 degree over the winter hemisphere. Near the Equator and midlatitudes, excursions of 0.05 degree lasting up to 10 minutes occur. Short-duration variations in the IR roll signal within 0.05 degree occur throughout the orbit. The explanation for the variations at the different locations and frequencies is as follows.

The Southern (winter) Hemisphere is dominated by a geographically large atmospheric anomaly in the stratosphere. The equatorial and midlatitude regions are dominated by more localized cold cloud anomalies occurring as single events of 2- to 5-minute duration and as simultaneous and consecutive-to-multiple events lasting up to 20 minutes (1/4 orbit). The Northern (summer) Hemisphere is a region of higher overall IR data stability, with errors from cold clouds occurring frequently with amplitudes less than 0.05 degree.

The amplitude and frequency of cold cloud effects on the Seasat-1 IR scanner data predicted by prelaunch analysis and illustrated in Figures 4.2-8 and 4.2-9 were verified in the Seasat IR scanner flight data. Figure 4.2-22 illustrates an error pattern in the pitch and roll caused by an isolated cold cloud on data from October 6, 1978.

To clearly demonstrate that the source of these data anomalies was correlated with the clouds, a Synchronous Meteorological Satellite-2 (SMS-2) (12-micrometer band) IR photo of the Earth was overlaid with the IR scanner threshold normalization zone groundtrack and is shown in Figure 4.2-23. The spacecraft roll data from orbits including those traced on the Earth image in Figure 4.2-23 are illustrated in Figure 4.2-24. Correlations between the roll errors in orbits 4 and 6 (starting from the pole at 05:15 UT and 08:35 UT) can be seen 25 minutes from the start, as the scanner threshold region groundtrack passes over a tropical

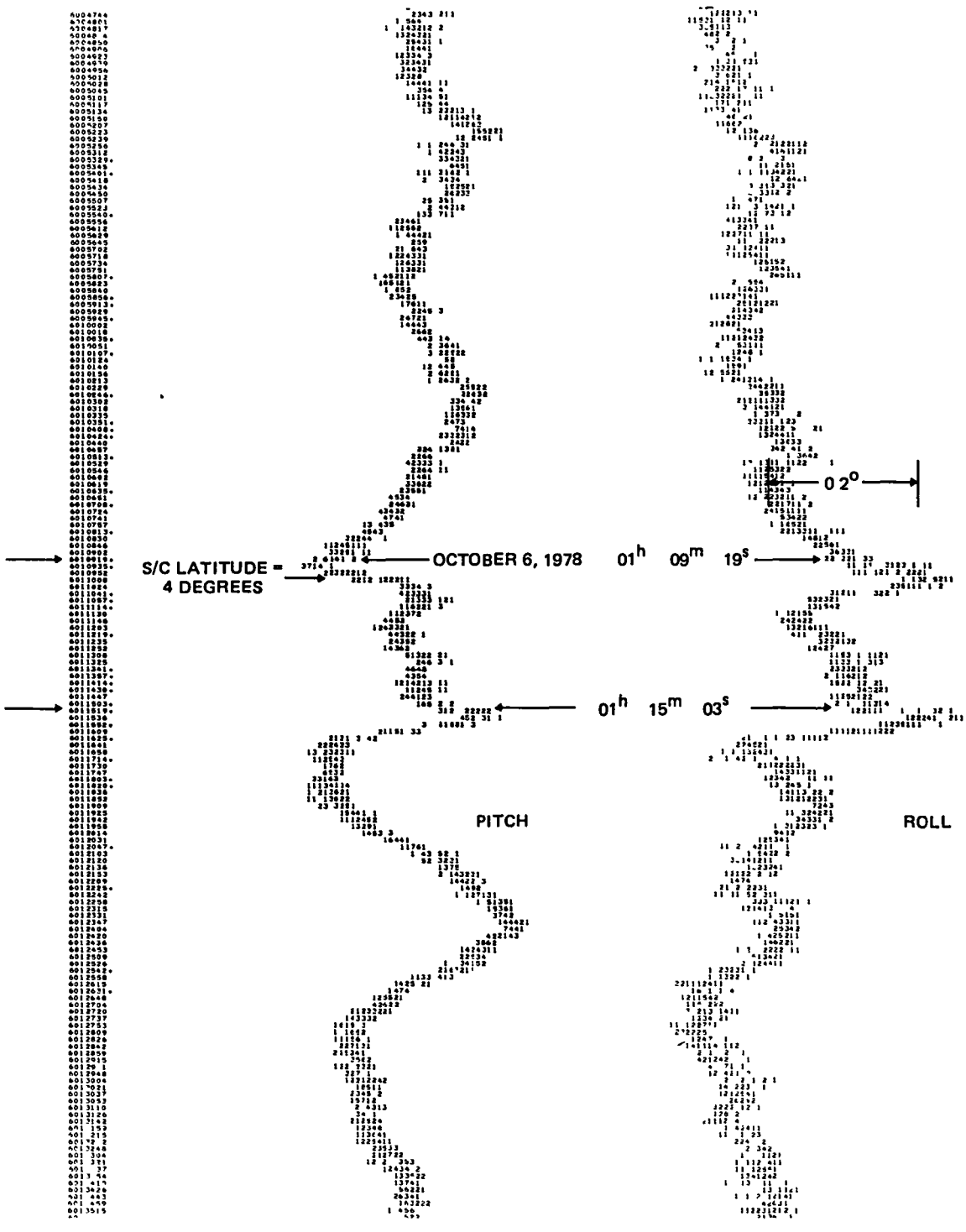

Figure 4.2-22. Seasat-1 Fine Pitch and Roll Telemetry Data on October 6, 1978

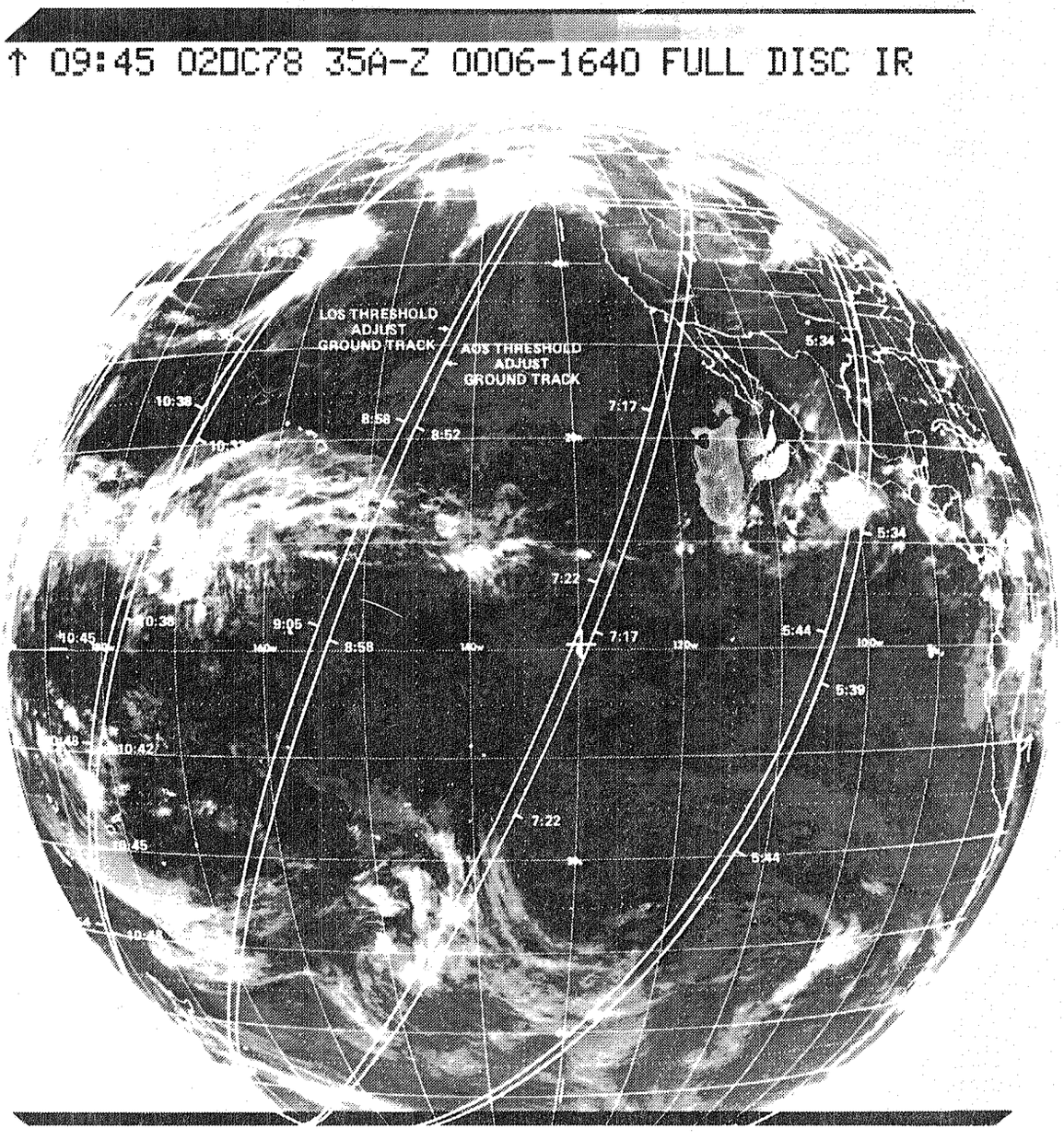

Figure 4.2-23. SMS-2 Earth Photo on October 2, 1978, With Scan Threshold Adjustment Region Groundtrack Overlaid (Photo From the Environmental Data Service of NOAA)

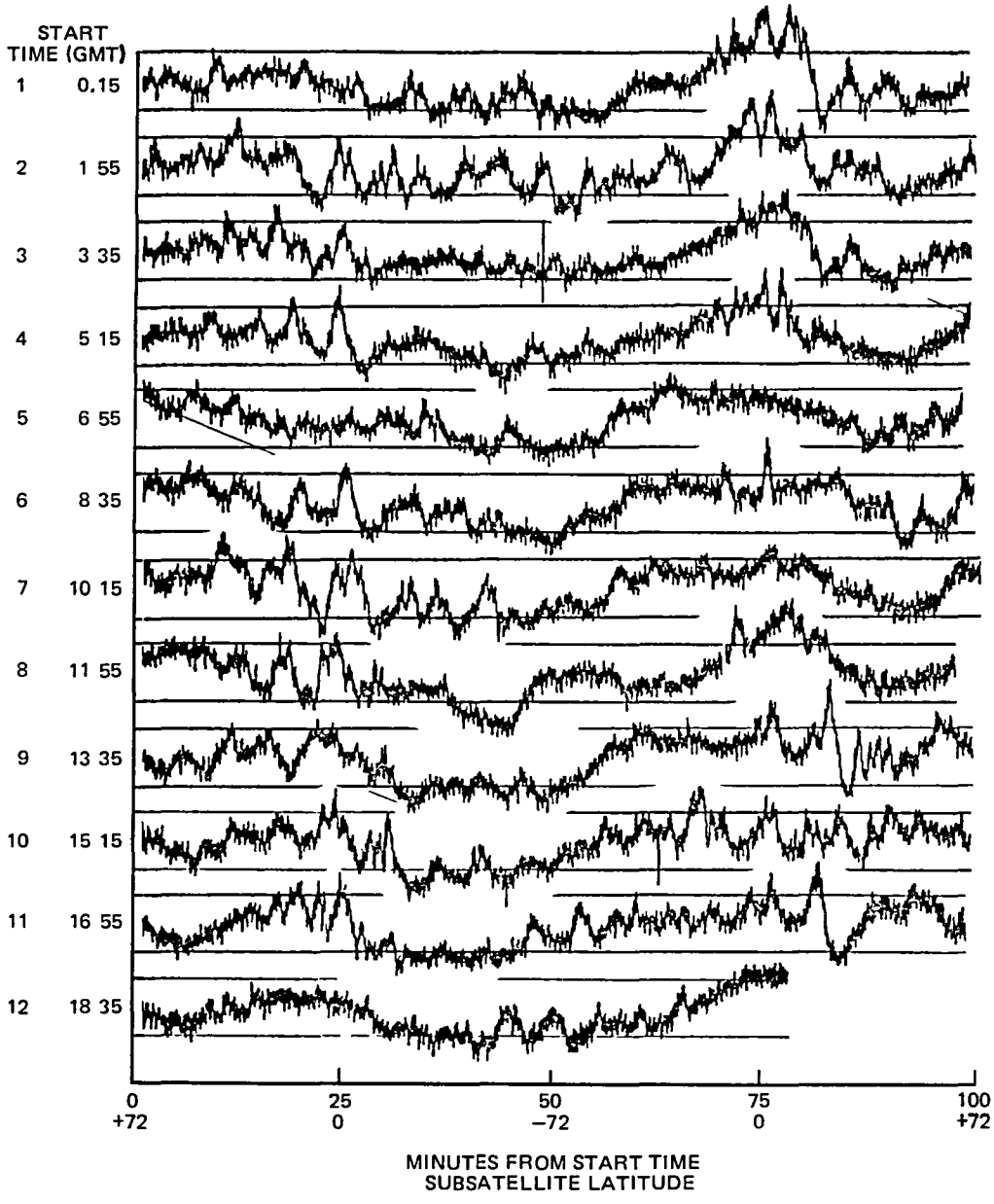

Figure 4.2-24. Seasat-1 Roll Telemetry for 12 Orbits on October 2, 1978 (Day 275) Illustrating Cold Cloud Anomalies at the North and South Equator Crossings

storm off the west coast of Central America and over a distributed cloud near the Equator south of Hawaii. In Figure 4.2-23, the double ground trace is formed by the AOS threshold moving southward over a geographical location followed by the LOS threshold moving southward 5 minutes later at the same latitude. The LOS track is slightly westward due to the Earth's eastward rotation.

4.2.4 RESULTS AND DISCUSSION

From the analysis of Seasat-1 flight data, the following conclusions were drawn about the success of the application of the correction for systematic horizon radiance variations to the IR scanner pitch and roll data:

- After data correction, the IR scanner data appear to agree with equivalent measurements from the Sun sensor to within 0.05 degree in the summer hemisphere and to within 0.1 degree in the winter hemisphere for the data analyzed (days 205 and 219).

- The largest excursions in the single-scanner IR pitch and roll data associated with cold cloud effects were approximately 0.25 degree (Figure 4.2-22). This translates to a roll error of 0.12 degree for the associated peak in the dual-scanner mode. However, there is no reduction in the pitch data for the near-polar orbit of Seasat-1 and the longitudinally extended cloud distributions evident near the Equator in Figure 4.2-23. Thus, the 3σ accuracy estimates for the pitch and roll data in the dual-scanner mode include contributions by these amounts.

- Cold cloud effects are additive, and thus wide distributions of clouds can cause complex and sustained error patterns (note orbit 7 in Figure 4.2-24).

- For the Seasat-1 application, the use of the correction appears to have improved the accuracy of the data by

removing the predicted 0.074-degree systematic error, illustrated by Figures 4.2-6 and 4.2-7. However, because the flight data showed that the cold cloud errors were three and two times greater than predicted for pitch and roll, respectively, the overall errors (from horizon radiance variations) estimated from the flight were larger than the prelaunch predictions. The magnitude of the systematic correction was a small fraction of the random component.

- No clear and independent estimate of the size of the systematic horizon radiance correction was made using the Seasat-1 data. The assumption, however, was that the variation of the IR scanner roll data relative to the corresponding Sun sensor roll data was totally due to unmodeled cold clouds and stratospheric effects.

The analysis of the Seasat-1 attitude sensor flight data contributed significantly to the understanding of the performance of an IR scanner/fine Sun sensor attitude determination system. The mission offered the opportunity to compare attitude sensing accuracy estimates, based on prelaunch specifications and analysis of the system performance, with an accuracy estimate established by analysis of the flight data.

Major surprises were that the Sun sensor relative alignment offsets were near 0.25 degree, compared to a prelaunch statement of alignment knowledg at an accuracy that did not exceed 0.01 degree, and that the electronic calibration changed by 0.1 degree when the system was powered by one or the other of the two electronics power supplies.

Table 4.2-3 is a revised table (compared to its counterpart in Table 4.2-1) of attitude sensing errors based on flight data analysis. The new values assume that the observed 0.1-degree change in the calibration due to switching electronics power supplies and the 0.25-degree offset observed

Table 4.2-3. Seasat-1 3σ Errors From In-Flight Analysis of the Attitude Determination Data

		Pitch	Roll	Yaw	[d](SS2 & 3)
Horizon Radiance Modeling Errors		0.25	0.13	0.20	
Noise with Software Filter[a]		0.01	0.01	-	
Scanwheel Speed Variations		0.02	0.02	0.02	
Component Aging, Trimming, and Calibration[b] Attitude Computer Drift		0.30	0.30	0.29	
Temperature Variations[a]		0.04	0.04	0.04	
Threshold Stability[a]		0.04	0.04	0.04	
Sun Sensor 1 Accuracy[a]		0.05	0.05	0.07	
Sun Sensor 1 Alignment[b]	Estimate 1	0.043	0.04	0.03	(0.077)
	Estimate 2	0.18	0.23	0.40	(0.406)
	Estimate 3	0.37	0.46	0.79	(0.795)
RSS Total	Estimate 1	0.40	0.34	0.37[c]	(0.37)
RSS Total	Estimate 2	0.44	0.41	0.54	(0.55)
RSS Total	Estimate 3	0.54	0.57	0.87	(0.87)

[a] These values remain unchanged from the prelaunch analysis.

[b] These components were assumed to be measured by inflight observations.

[c] This value is obtained either by the RSS of the yaw column or by combining the total pitch and roll errors with the estimates of SS1 accuracy and alignment errors.

[d] Yaw accuracy estimates from sensors 2 and 3 must include an additional 0.7-degree error in the inflight determination of the alignment angles.

between the Sun sensors occurred with a 30-percent probability. The individual estimates assigned all of the 0.25-degree offset to FSS-2 (estimate 1), assumed one-half of the 0.25-degree offset was a 1σ number (estimate 2), and attributed all alignment errors (flight and preflight) to FSS-2 with no error in FSS-1.

The performance of the IR scanners with respect to their sensitivity to clouds was also explained by the analysis as follows. An amplitude-normalized threshold locator logic was used primarily to lower the sensitivity of the pitch and roll error output to latitude variations in the IR profile brightness. This is justified if the profiles vary in amplitude by a simple scale factor, with no change in shape. Because of the wide IR passband (Figure 2-30) of the Seasat IR scanners, the profile shape was significantly influenced (40 percent) by the presence of clouds in the portion of the Earth scan used for threshold level adjustment. Unpredictable changes of up to 40 percent in threshold level caused errors in single-scanner pitch and roll of 0.3 degree, nullifying improvements acquired by reduced response to the systematic brightness variation. A reduction in the width of the IR passband, confining it strictly between 14 and 16 micrometers, would have significantly improved the performance of the Seasat IR scanners by reducing the response to clouds to 0.05 degree. Unavoidable intensity variations at this 15-micrometer band due to stratospheric warming events would still, however, limit the accuracy of such an IR scanner in the winter hemisphere.

4.3 APPLICATIONS EXPLORER MISSION/STRATOSPHERIC AEROSOL GAS EXPERIMENT

The attitude mission analysis for AEM/SAGE contributed to the understanding of the performance of the dual-flake germanium prism lens IR scanner. Prelaunch analysis of the prism lens optics using point FOVs and a spherical Earth model demonstrated the effects of the "ANDed" logic on the dual-flake Earth signals and established a framework for understanding the effects of Sun interference on the IR scanner signals. Postflight analysis of IR scanner data during Sun-interference-induced control anomalies demonstrated how subtle effects in the signal processing electronics coupled to control system responses caused drastic differences between the prelaunch estimates of Sun interference and the flight experience. Additional information was also obtained from this flight data about the Sun-sensitive angular width of the IR scanner FOV. Most of the material for the following discussion has been derived from References 33 through 37.

4.3.1 MISSION REQUIREMENTS AND HARDWARE

The SAGE spacecraft was launched from Wallops Island, Virginia, on a Scout rocket on February 18, 1979. SAGE (Figures 4.3-1 and 4.3-2) was the second in a series of satellites using the basic, modularly designed launch vehicle and satellite support system called the Applications Explorer Mission. The first satellite in this series was the Heat Capacity Mapping Mission (AEM/HCMM). The AEM/SAGE spacecraft and supporting systems were identical with AEM/HCMM in most respects; however, there were differences that affected the attitude system.

The purpose of SAGE was to determine the spatial distribution of stratospheric aerosols and ozone on a global scale by measuring the attenuation of solar radiation at four

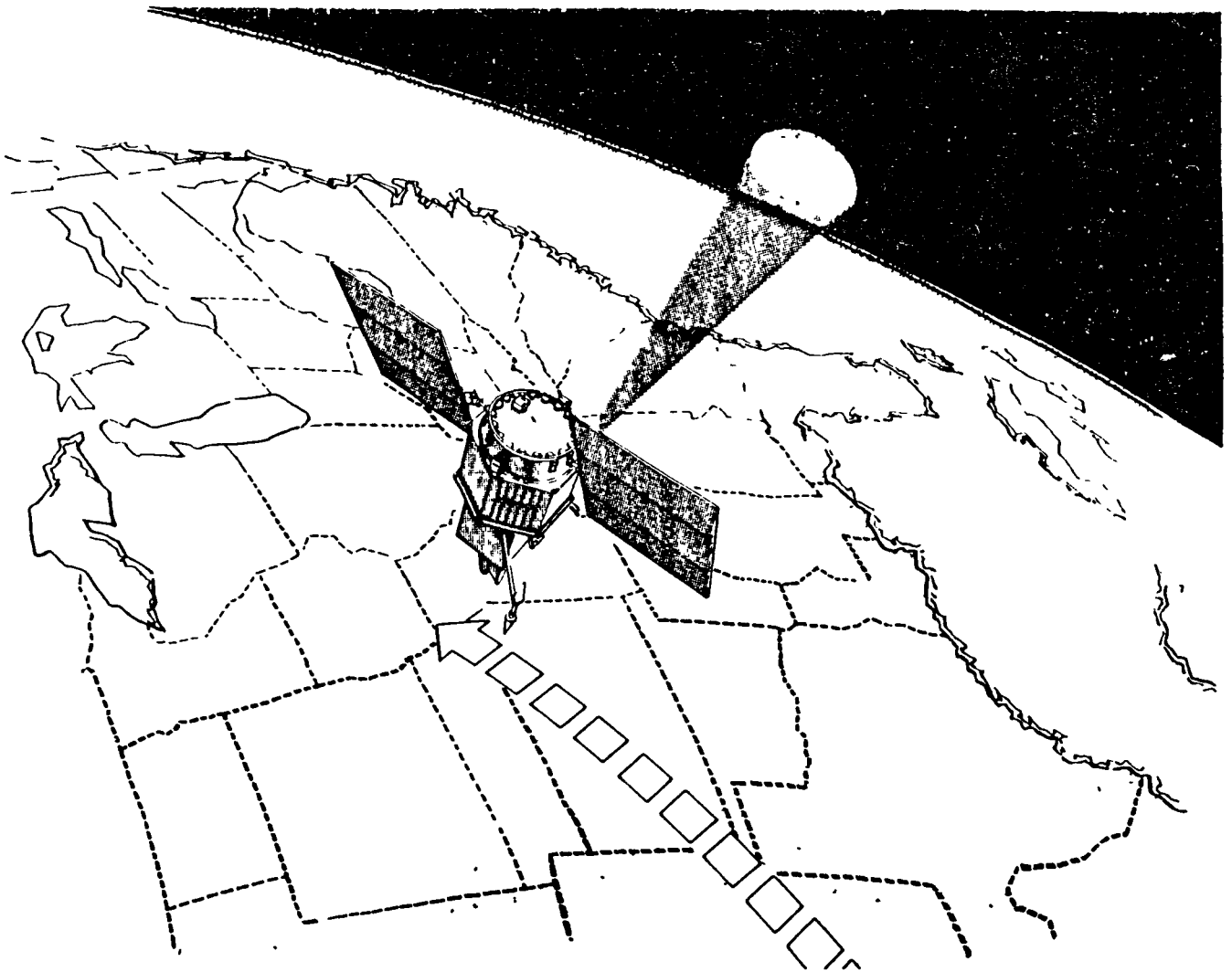

Figure 4.3-1. Applications Explorer Mission/Stratospheric Aerosol and Gas Experiment

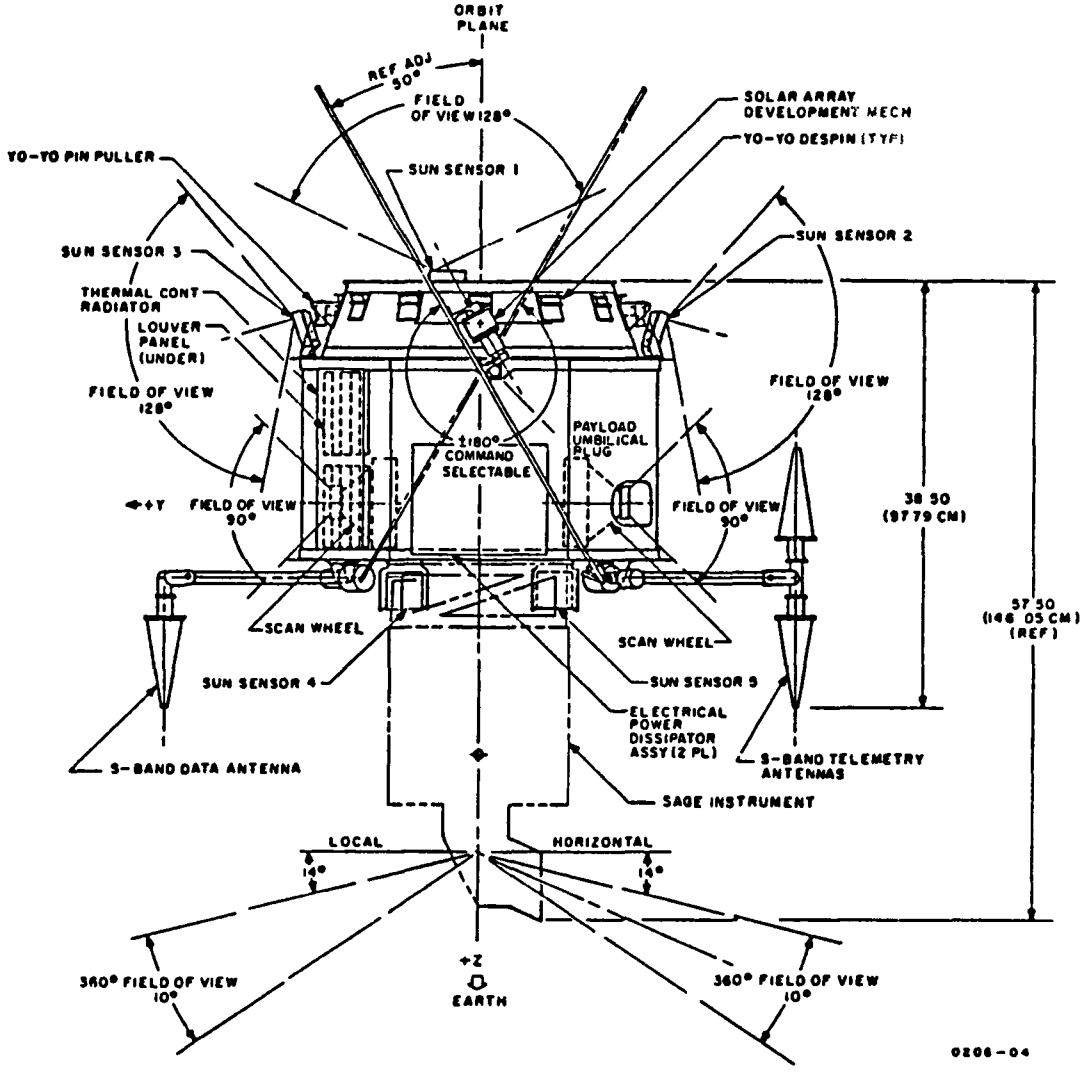

Figure 4.3-2. Geometric Front View of AEM/SAGE

distinct wavelengths during solar occultation. This technique of using the extinction of solar radiation at several wavelengths was employed to derive the stratospheric aerosol extinction coefficient and ozone concentration profile during every satellite sunrise and sunset (i.e., about 30 measurements per day). The mission can be summarized as follows:

- Orbit--Near-circular at 600-kilometer altitude and 55-degree inclination
- Attitude configuration--One rpo, with spacecraft Z-axis pointing toward Earth, Y-axis along negative orbit normal, and X-axis in the approximate direction of flight (Figure 4.3-3)
- Attitude determination hardware
  - Two ITHACO Scanwheel dual-flake IR horizon scanners (also used for attitude control)
  - Five Adcole Model 16764 Sun sensors (0.5-degree resolution)
  - Three-axis Schoenstedt flux-gate magnetometer
- Attitude control hardware
  - Two ITHACO Scanwheel dual-flake IR horizon scanners (also used for attitude determination)
  - Electromagnet assembly
  - Pitch reaction wheel
- Accuracy requirement--$\pm$0.5 degree in pitch, $\pm$0.5 degree in roll, $\pm$2 degrees in yaw (3σ)
- Ground support system--Interactive processing

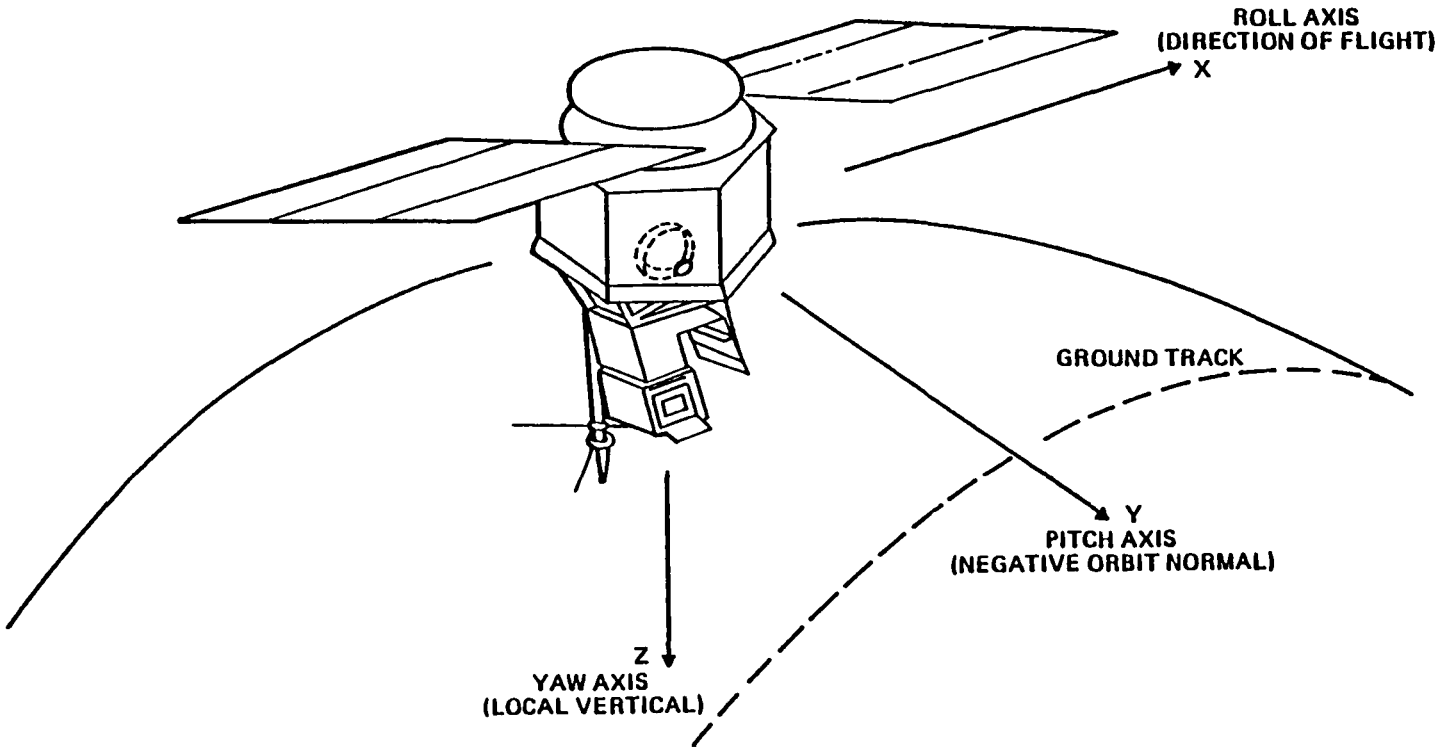

Figure 4.3-3. SAGE Orbital Coordinate System

- Data processing requirements
  - Definitive solutions generated only during time segments centered on spacecraft sunrise and sunset for each of ∿15 orbits per day
  - Output data interval of 10 seconds
  - One-week turnaround from receipt of definitive orbit and raw attitude data
- Problems encountered
  - Sun interference in the IR scanners more serious than predicted
  - Unpredicted Sun interference effects in the IR scanners
  - Oscillatory behavior in control system response due to anomalous IR scanner data

SAGE had two similar, but not identical, IR scanners. The larger Scanwheel assembly (SWA-B) had its boresight along the +Y-axis; the smaller (SWA-A) had its boresight along the -Y-axis. These scanners provided the following:

- Angular momentum along the pitch axis for spacecraft gyroscopic stability
- Attitude control about the pitch axis by variations in the SWA-B wheel speed
- Pitch and roll angle data for ground-based attitude determination and for onboard use by the attitude control electronics

The scanner FOV rotated at a nominal speed of 825 rpm for SWA-A and 1900 rpm, in the mission mode, for SWA-B. The two angular momentum vectors pointed in the -Y direction, providing spacecraft gyroscopic stabilization. The onboard

analog controller used a sensed pitch error to vary the wheel speed of SWA-B to provide pitch control.

The Sun sensors flown on SAGE were Adcole Model 16764. A complement of five sensors like those used on AEM/HCMM provided continuous Sun coverage during daylight passes. The magnetometers, electromagnets, and attitude control system (ACS) electronics were the same as those for AEM/HCMM, except for the changes in the ACS that were necessary to accommodate a control configuration with dual IR scanners and a single-pitch reaction wheel.

Attitude determination requirements for SAGE included the following:

- Processing IR scanner data, Sun sensor data, and magnetometer data received over the data link from the Information Processing Division (IPD)--SAGE had two onboard tape recorders storing data for time intervals centered on sunrise and sunset. Attitude data were obtained from the spacecraft twice per orbit via playback of these onboard recorders. Attitude solutions were required only during the two nonoverlapping segments centered on sunrise and sunset.

- Correction of IR scanner data for Earth oblateness and horizon radiance variations

- Calculation of a three-axis attitude solution expressed as pitch, roll, and yaw angles for a 2-1-3 (pitch-roll-yaw) Euler angle sequence at a 10-second spacing between points

- Calculation of attitude solutions either deterministically or by using a differential corrector algorithm employing a time-dependent polynomial model for attitude propagation

- Determination of pitch, roll, and yaw rate information
- Quality control of attitude solution data before transmission to IPD
- Generation of definitive solutions within 1 week from receipt of definitive orbit and raw attitude data
- Support of real-time monitoring functions in addition to definitive attitude determination functions with interactive graphics capability

4.3.2 PREDICTED ATTITUDE ERRORS

Prelaunch analysis predicted Sun interference anomalies in the IR scanner data. The actual data displayed effects similar to those predicted, as well as effects drastically different from the predictions.

Before launch, it was predicted that the precession of the orbit at -4.16 degrees per day and the 23.44-degree obliquity of the ecliptic would periodically bring the Sun close to the scan cones of the IR scanners. Because the scanner axes lie along the positive and negative orbit normals for a nominal mission attitude, the value of the Sun angle with respect to orbit normal (β) directly indicates when the Sun is close to the scanner cone. Figure 4.3-4 shows the evolution of Sun angle. Points on the curve near β angles of 45 or 135 degrees are the times when Sun interference was expected, i.e., at irregular intervals of 2 to 4 weeks. Detailed modeling of the Earth-Sun-horizon scanner geometry predicted interference for 2 to 3 days at each occurrence. The length of the orbital segment affected was predicted as a function of β angle. The predicted duration of interference ranged up to 38 minutes per orbit.

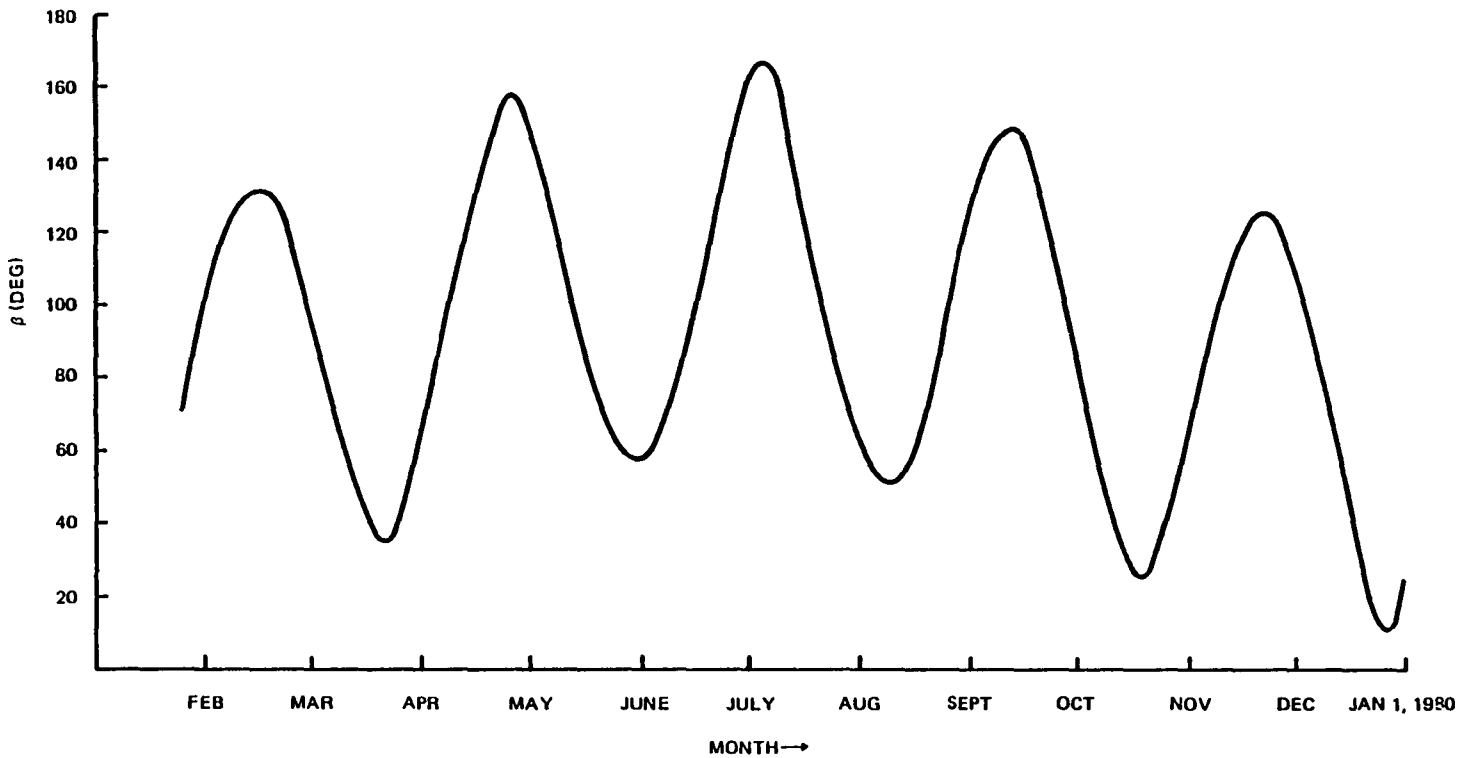

Figure 4.3-4. Angle Between the Pitch Axis (Negative Orbit Normal) and the Sun Versus Time

Maximum pitch and roll errors from Sun interference events were predicted to be 0.22 degree and 0.17 degree, respectively. Errors of this magnitude did not present any problem, because the required accuracy for pitch or roll was considerably less stringent (e.g., $\pm$0.5 degree). In addition, analysis indicated that, even if no effort were made to compensate for Sun interference, the accuracy requirement could be met. Maximum pitch and roll rates from Sun interference events were predicted to be 0.015 and 0.004 degree per second, respectively. The specified limits for pitch and roll rate were $\pm$0.01 degree per second. Sun interference did not, therefore, appear to present any significant problem to pitch and roll rate requirements.

A more detailed prelaunch analysis of the dual-flake bolometer geometry and electronics indicated that the candidate β angles for Sun interference were slightly below and slightly above the nominal values of 45 degrees and 135 degrees. Thus, for SWA-B, interference was predicted for β angles of 43 and 47 degrees. For SWA-A, interference was predicted for a β angle of 138 degrees. Interference was not expected for a β angle of 132 degrees, because the slower speed of SWA-A would allow the Sun transient to decay before it could affect signal voltage at Earth horizon crossing time.

The largest in-flight interference effects were observed for β angles of approximately 47, 133, and 137 degrees. The full range of angles for which any interference occurred was 40 to 50 degrees for SWA-B and 131 to 140 degrees and 160 to 165 degrees for SWA-A. Although, as stated above, Sun interference for a β angle of 133 degrees was not expected, data showing a typical Sun interference event at sunrise for β equal to 132.3 degrees is presented in Figure 4.3-5. An initial roll error of about 0.8 degree is shown with a

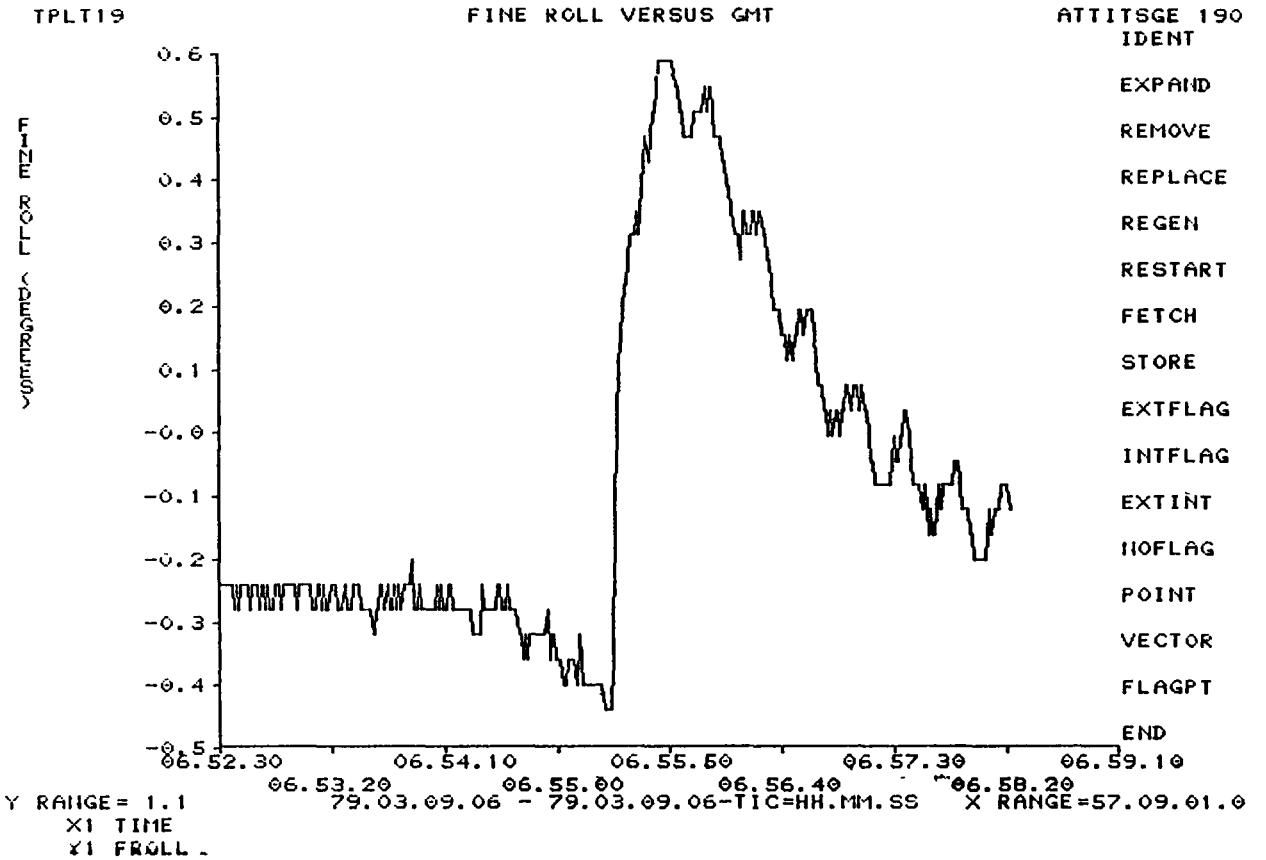

Figure 4.3-5. Scanwheel A Sun Interference on Roll at Sunrise for β Angle of 132.3 Degrees

sinusoidal decay to zero. This oscillatory decay of roll error was also unexpected. Data from a typical Sun interference event at sunrise for a β angle of 137 degrees are presented in Figure 4.3-6. The roll error induced by this event was about 1 degree. The oscillatory behavior of roll after the start of interference was also observed in Scanwheel speed (Figure 4.3-6). Sun interference roll errors in these and other events were considerably larger than the predicted maximum of 0.17 degree. Although not shown, the pitch error in such events ranged up to 1.25 degrees, which was considerably larger than the predicted maximum value of 0.22 degree. Sun interference events such as those shown produced maximum pitch and roll rates of 0.2 and 0.02 degree per second, respectively. These exceeded both the requirement of 0.01 degree per second and the predicted values of 0.015 and 0.004 degree per second.

The Sun interference events shown in Figures 4.3-5 and 4.3-6 were accounted for by the effect of capacitive coupling in the Scanwheel electronics. Capacitive coupling and the intense Sun pulse produced a positive pulse followed by a negative undershoot, which held the trailing Earth pulse below the threshold value. The effect is diagrammed in Figure 4.3-7. The sinusoidal decay of the error was explained by the variation of the negative undershoot pulse due to the decay of Sun pulse amplitude as the Sun moved along the scan cone away from the Earth edge. This IR scanner step pulse into the control system caused the momentum wheel to drive the Sun out of the FOV, eliminating the sensor error and revealing a true attitude error, thus resulting in an unstable attitude oscillation. The condition was damped out with time as the Sun moved further from the horizon.

Unpredicted Sun interference effects were also observed for β angles of 155 and 165 degrees. An example of scanner

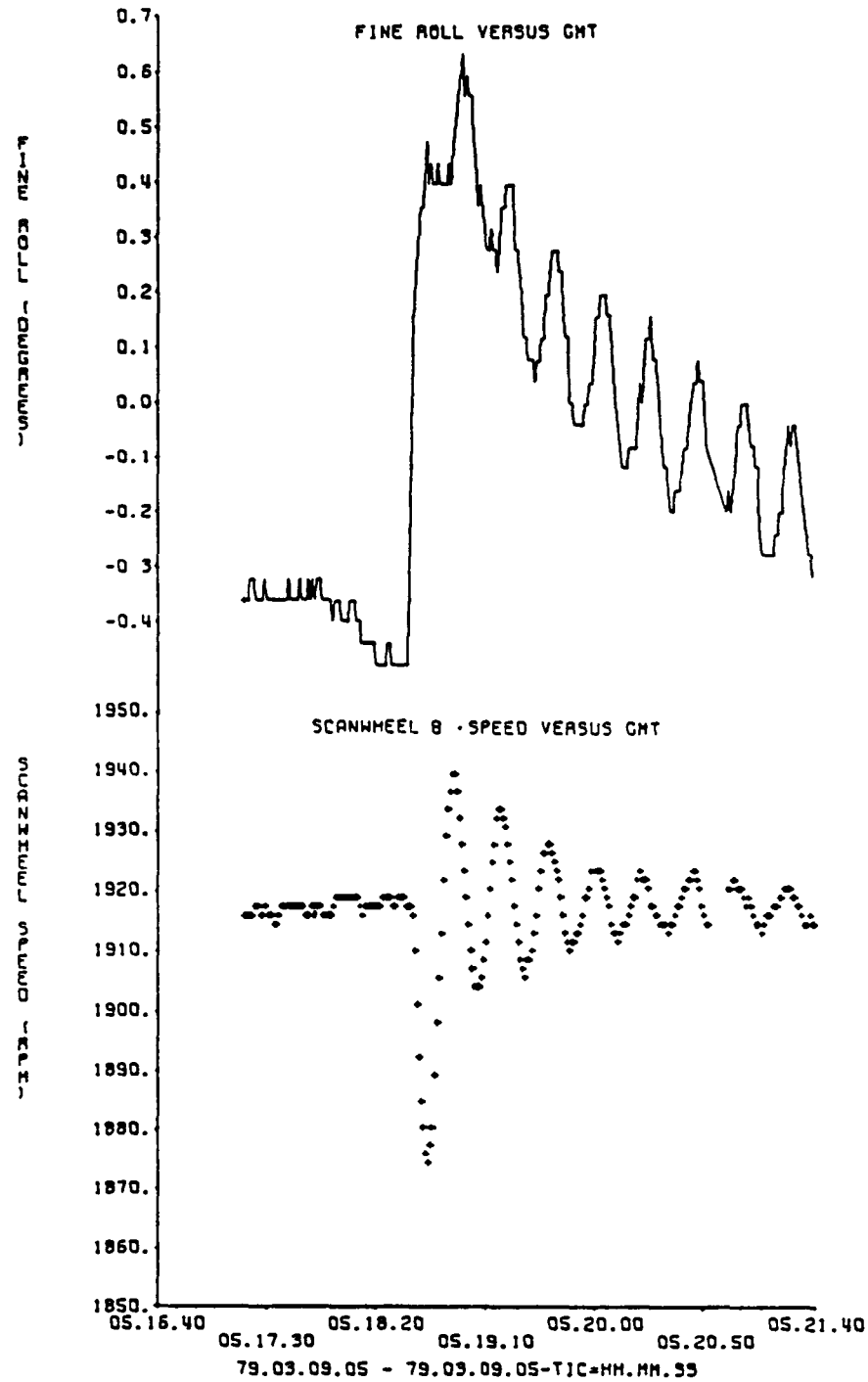

Figure 4.3-6. Sunrise Data for β Angle of 137 Degrees

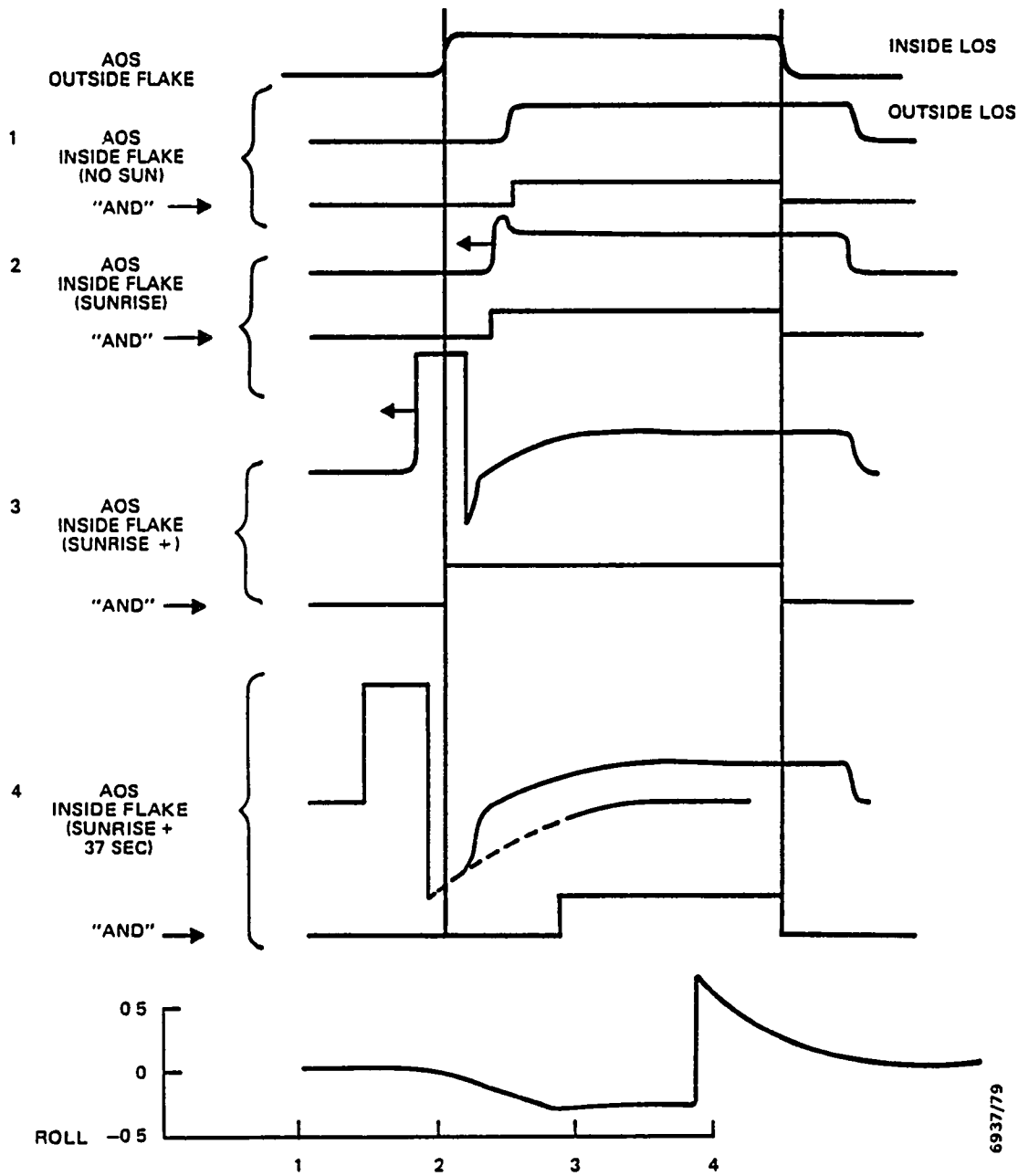

Figure 4.3-7. Earth Pulses and Resultant Roll Signal

data for these events is shown in Figure 4.3-8. These events were attributed to increased ambient temperature effects as the Sun illuminated the IR scanner optical assembly from a position near the scan cone axis.

4.3.3 MISSION DATA ANALYSIS

Extensive postlaunch ground support was required for SAGE due to the effects of Sun interference on IR scanner data. Interference occurred at times when it was not predicted and was more intense than expected at the predicted occurrences. Through the generation of Sun and magnetometer data attitude solutions during periods of Sun interference, it was determined that IR scanner data from the affected scanner was invalid and did not represent true attitude motion. The actual change in attitude induced by anomalous signals from the scanner that was experiencing interference departed substantially from the expected performance. The fitting algorithm designed for attitude data smoothing could not meet specifications in attempting to fit the rapidly varying attitude during a Sun interference event. Tailoring the algorithm to spacecraft behavior during Sun interference reduced its validity for the nominal, slowly varying attitude.

Spacecraft body rates were also a problem during Sun interference events. Experiment requirements placed limits of $\pm$0.01 degree per second on attitude rates. The attitude determination algorithm was designed to compute attitude rates from the polynomial fit of the attitude angle solutions. Attitude rates during Sun interference events substantially exceeded the limits of the polynomial fit. Some uncertainty about the severity of the control problem was induced by poor polynomial fitting of the anomalous data. A thorough investigation of alternatives for calculating attitude rates was performed. Numerous samples of raw and

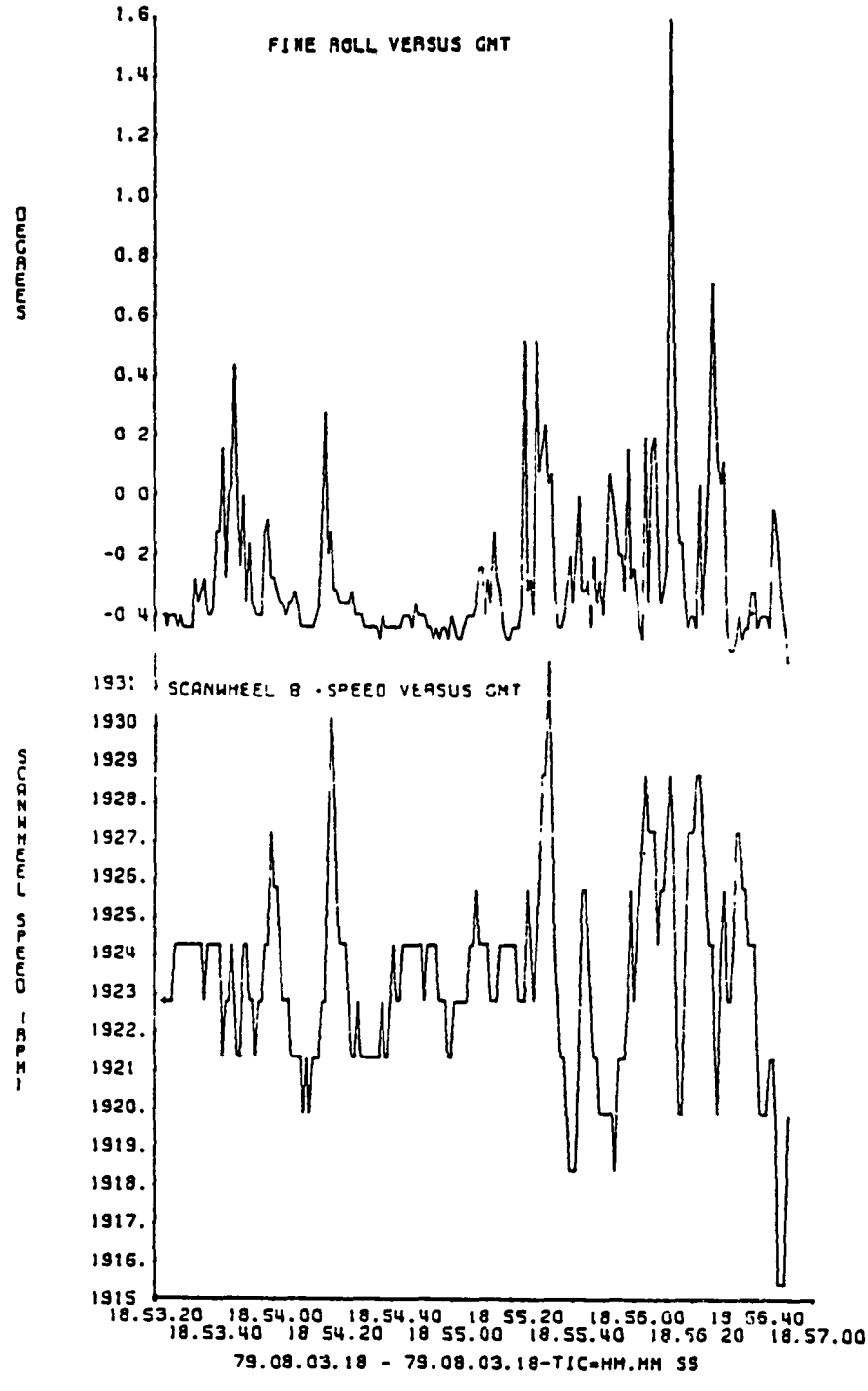

Figure 4.3-8. Sunset Data for β Angle of 155 Degrees

processed attitude data were used to discriminate between valid and anomalous effects and to check the accuracy of proposed improved modeling techniques.

The application of a correction for systematic horizon radiance variations to the pitch and roll data was a requirement of the definitive attitude data processing function. To implement this correction for SAGE, the HRMU was run using the Earth radiance profiles generated for Seasat and the IR sensor electronics model for AEM/HCMM. This AEM model incorporated a single-flake geometry and fixed-threshold locator logic. The effects of the dual-flake scan geometry within the "ANDed" Earth chord output were therefore not included in the Earth horizon attitude model.

The opportunity to check the accuracy of the horizon radiance correction analysis for SAGE using the flight data did not occur, primarily because of the limited Earth coverage offered by the definitive data, which was recorded only at spacecraft sunrise and sunset. Another factor was the relatively low resolution of the Sun sensor data (0.5 degree), which is the standard attitude reference for IR data evaluations. Finally, the extremely strong control loop and the low resolution of the control system angular momentum wheel rates rendered both the IR data accuracy and the wheel tachometer data accuracy insufficient for any meaningful analysis of the flight response to the Earth horizon radiance.

Analyses of other spacecraft control anomalies were also performed. The effect of stray inductive fields from the slew motor of the SAGE experiment on the magnetic nutation control loop was analyzed, as were the erratic IR scanner signals that occurred when Scanwheel assembly temperatures were high and spacecraft voltage was low.

4.3.4 RESULTS AND DISCUSSION

Although the SAGE ACS was considered to have performed well, close analysis of the SAGE pitch angle sensor and control loop performance highlighted a significant problem in its design. Graphics-generated plots of wheel speed, scanner output, and Sun and magnetometer data revealed the nature of the problem. The SAGE pitch control loop was designed to null the pitch error signal from the IR scanner with a "strong-control" control law. Because of this, the control loop's response to error signals in the IR scanner was rapid pitch displacement of the spacecraft body. The control loop was so effective at keeping the pitch error sensor signal at null that the information about spacecraft pitch attitude errors was lost, and it was impossible to evaluate the pitch control performance based on signals from the IR scanners.

The lesson learned from this experience is that close attention should be paid to the role of the attitude sensors in the attitude control loop. A control loop should not be capable of inducing spacecraft rates much higher than are required to offset the rates expected from environmental or disturbance torques (except for special, high-rate control modes where attitude slews are required). For attitude determination, the changes in the sensor signal induced by attitude motion must be separated from those induced by other effects, such as electronic noise, thermal variations, or aberration of the sensor reference source (such as the Earth's horizon). To perform this function with a sensor that is also an integral part of the control loop requires a good understanding of the control laws and also requires attitude algorithms that incorporate some telemetered control system data, such as reaction wheel tachometer data.

Definitive data processing for SAGE, which was to be very similar in procedure to that of AEM/HCMM, was stopped after

analysis of the SAGE attitude control performance and evaluation of the postlaunch attitude determination. Only real-time support was provided for this mission. Definitive support was discontinued because the SAGE experimenter actually needed highly accurate spacecraft pitch and roll rates for the science data reduction problem. Analysis of optional techniques to derive pitch and roll rates using attitude dynamics modeling software such as the SAGE/ADGEN or SAGEN programs yielded no improvement in the solution for attitude determination with the sensors and data available for SAGE. After meetings with attitude analysts who explained the attitude determination system output and SAGE spacecraft control anomalies, the experimenter subsequently developed techniques for data reduction that did not require an attitude solution.

The ground support system for SAGE was not useful for routine definitive support because, although attitude accuracy met the specification, the rates derived from these attitude solutions did not. The attitude rate determination accuracy, which was not specifically defined as a requirement for the SAGE attitude determination system, was in fact the most important attitude parameter for science data reduction. The results indicate that the attitude sensors and control system flown on SAGE and the ground support system specified to process the sensor data were developed without a clear understanding of SAGE attitude performance requirements.

SAGE attitude support experience reveals something about anticipated anomalies with the IR scanner response to the Sun. Before launch, it was expected that Sun interference would occur, but the in-flight experience was drastically different than had been anticipated, even though prelaunch analysis was based on prior mission experience. It is

therefore clear that as much caution should be exercised when venturing into new applications of old systems as with first applications of new systems.

4.4 MAGSAT

The Magsat mission offered a unique opportunity to evaluate the IR scanner response to the Earth horizon radiance variations using the highly accurate attitude references from fine Sun sensor and fixed-head star tracker data. The material in this section is derived primarily from three sources: an evaluation of the Magsat IR scanner data (Reference 38) and two reviews of the Magsat definitive attitude support software and operations experience (References 33 and 39). A more detailed description of the Magsat fine attitude determination system and mission experience with that system is provided in Reference 39.

4.4.1 MISSION REQUIREMENTS AND HARDWARE

The Magsat spacecraft was launched on October 30, 1979; it reentered the Earth's atmosphere on June 11, 1980. The mission was a cooperative effort between NASA and the United States Geological Survey (USGS) as part of the Earth and Ocean Dynamics Applications Program in the NASA Office of Applications. The objectives were to update the USGS worldwide magnetic field model and to compile a global scalar and vector crustal magnetic anomaly map.

The Magsat spacecraft is illustrated in Figure 4.4-1. A detailed description of the mission requirements is presented in Reference 38. The mission can be summarized as follows:

- Orbit--Sun synchronous, with 97-degree inclination, 560-kilometer-apogee and 350-kilometer-perigee altitude, and argument of perigee precession at 3.7 degrees per day
- Attitude configuration--Three-axis stabilized at 1 rpo; Earth-oriented

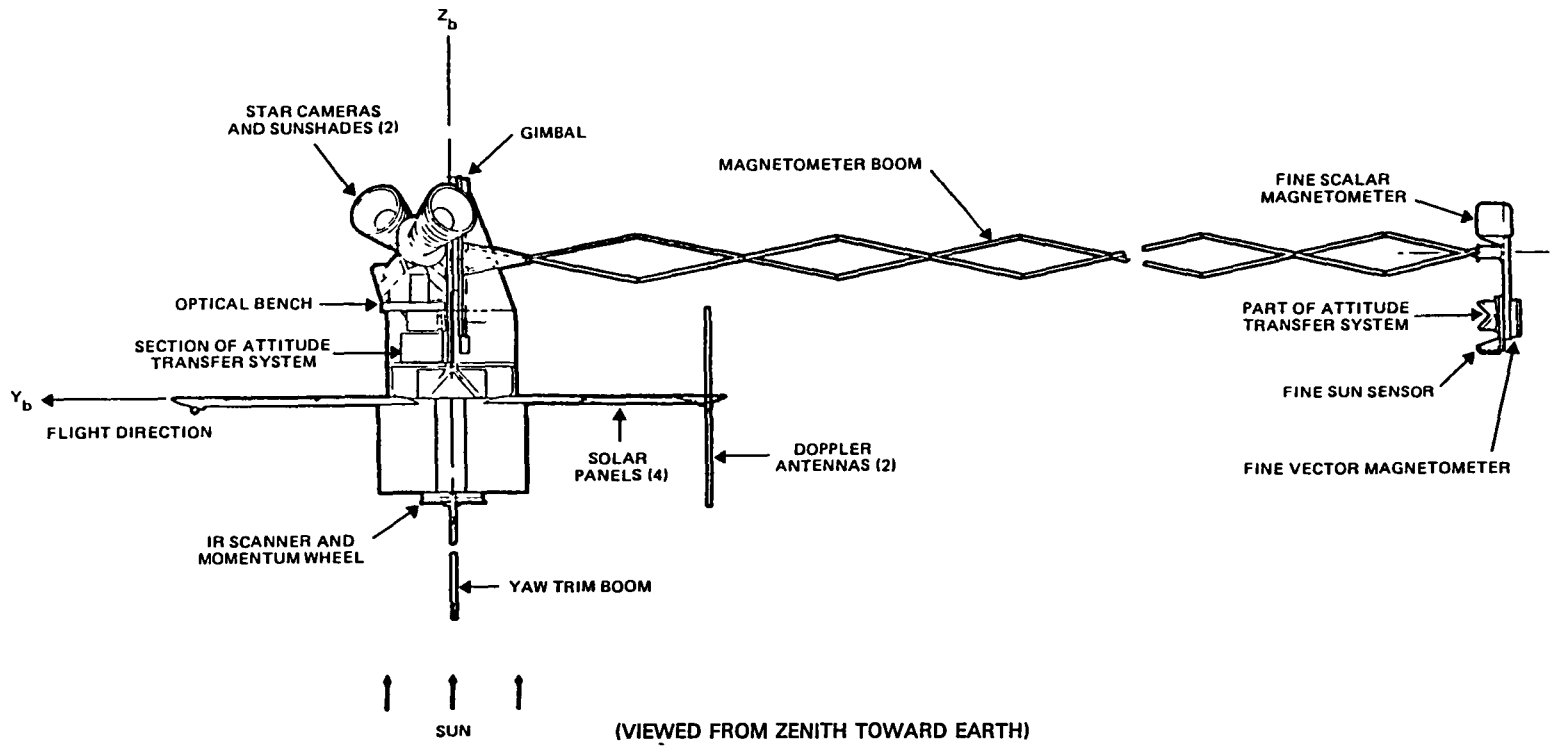

Figure 4.4-1. Magsat Spacecraft Components and Spacecraft Body Reference Frame

- Attitude determination hardware
  - ITHACO Scanwheel IR horizon scanner (also used for attitude control)
  - Spinning single-axis Sun sensor (digital solar aspect indicator (DSAI))
  - Coarse Sun sensor
  - Coarse vector magnetometer
  - Adcole two-axis fine Sun sensor with a $\pm$32- by $\pm$32-degree FOV and a quoted accuracy of 12 arc-seconds
  - Two Ball Brothers star trackers, model CT401
  - Attitude transfer system
  - Pitch inertial reference unit (IRU) (also used for attitude control)
  - Scientific payload
- Attitude control hardware
  - ITHACO Scanwheel IR horizon scanner (also used for attitude determination)
  - Nutation damper
  - Spin axis torque coil
  - Wheel spin rate control coil
  - Pitch IRU (also used for attitude determination)
  - Yaw-axis trim boom
- Accuracy requirement
  - Intermediate system (IR scanner and fine Sun sensor data)--20 arc-minutes

  - Fine system (star tracker, pitch IRU, and fine Sun sensor data)--20 arc-seconds or better

- Ground support system--Interactive processing
- Data processing requirements
  - Continuous definitive attitude solutions
  - Output data interval of 2 to 30 seconds for intermediate system, 0.25 second for fine system
  - Turnaround within 5 weeks for intermediate system or 5 months for fine system after receipt of all necessary data with a throughput processing of 1 day's data each day
- Problems encountered
  - Anomalous IR scanner data caused by the shadow of the yaw trim boom
  - Anomalous IR scanner data caused by cold clouds
  - Inaccurate IR scanner voltage conversion calibration necessitating in-flight recalibration
  - Sun interference on star camera data
  - Failure of the coarse Sun sensor to produce good data (possibly due to reflections from spacecraft appendages such as the yaw boom)
  - Early postlaunch discontinuities in the attitude transfer system roll output
  - Changes in the attitude transfer system/fine Sun sensor system alignment throughout the mission

The attitude determination and control strategy for Magsat was loose pointing control with high-accuracy attitude determination. To minimize the potential disturbance to the Earth magnetic field measurement experiments, a minimum amount of activity to control spin axis precession was requested. The attitude control procedure was to trim the spacecraft attitude and angular momentum drift aerodynamically with pitch offset biases and an extendable yaw trim boom. The attitude was permitted to drift freely in a 4-degree deadband within a zone of 10 degrees around orbit normal. Spin axis precession control activity was used infrequently so as to center this zone on a control point near orbit normal.

Three attitude determination systems supported the Magsat mission. The coarse ADS was used for only a short time in the early postlaunch phase when the spacecraft was spinning. It was used to process the magnetometer and DSAI data to compute the spin mode attitudes.

The intermediate ADS was used when the spacecraft became operational in the despun 1-rpo mode. It was used for near-real-time attitude determination in support of spacecraft control, sensor performance evaluation, and definitive support (e.g., processing playback data from the IPD) of the intermediate accuracy attitude requirements. The intermediate ADS software was an adapted version of the AEM/HCMM and AEM/SAGE software, which used IR scanner and fine Sun sensor data as the principal source of attitude solutions.

The fine ADS was developed primarily in support of high-accuracy definitive data processing using the star tracker, fine Sun sensor, and attitude transfer system data. This system was also used throughout the flight of Magsat in a near-real-time mode with approximate alignment bias and

calibration parameters to monitor the performance of the fine ADS hardware.

The IR scanner used on Magsat was a dual-flake bolometer with fixed-threshold locator logic. The spectral passband for the system is illustrated is Figure 4.4-2. The Earth scan geometry is illustrated in Figure 4.4-3 for the Magsat spacecraft going north at the Equator. The scan path is for a single-flake angular FOV, 2 by 2 degrees in size.

For the flight system scan path, two bolometer flake FOVs at cone angles of 43 degrees and 47 degrees were simulated in the scan geometry model of the HRMU. The signals from both flakes are processed in identical channels of the electronics to determine a square-wave Earth pulse or an Earth-crossing envelope for each flake. The envelope is constructed to represent the portion of the scan during which the flake FOV is on the Earth.

Figure 4.4-4 schematically shows the nature of the changes to an Earth radiance signal in the various stages of signal processing; the figure also includes a transfer function block diagram. (The transfer functions describing the circuit elements of the Magsat Scanwheel are adapted from Reference 40.) The bolometer converts the radiation signal into a voltage signal. According to ITHACO, Inc., the bolometer outputs approximately 500 microvolts for radiation from a 230K Earth and 0 volts for the outer space background radiation. The circuit gain following this conversion is a factor of approximately 4700. The bolometer has a fairly long time constant (approximately 3 milliseconds), which is a significant fraction of the Earth pulse duration. At 1500 rpm, the spin period is 40 milliseconds and the scanner sees the Earth for approximately one-third of the spin period, i.e., about 13 milliseconds.

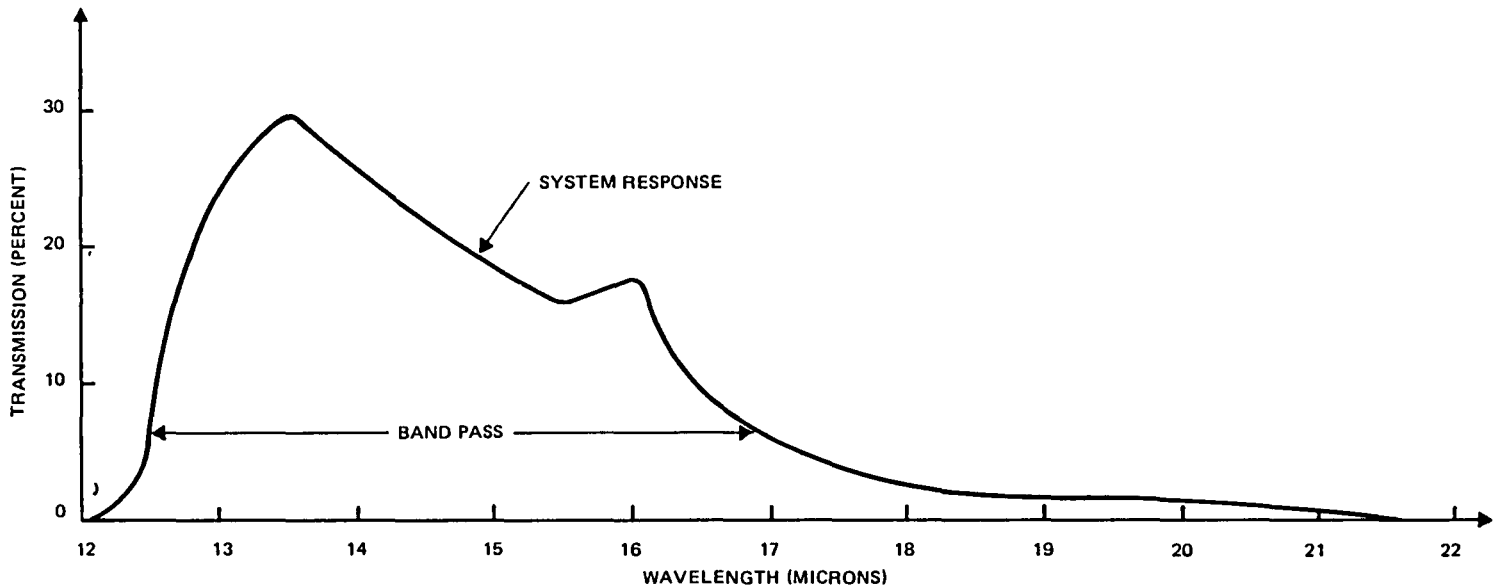

Figure 4.4-2. Magsat IR Scanner Spectral Response

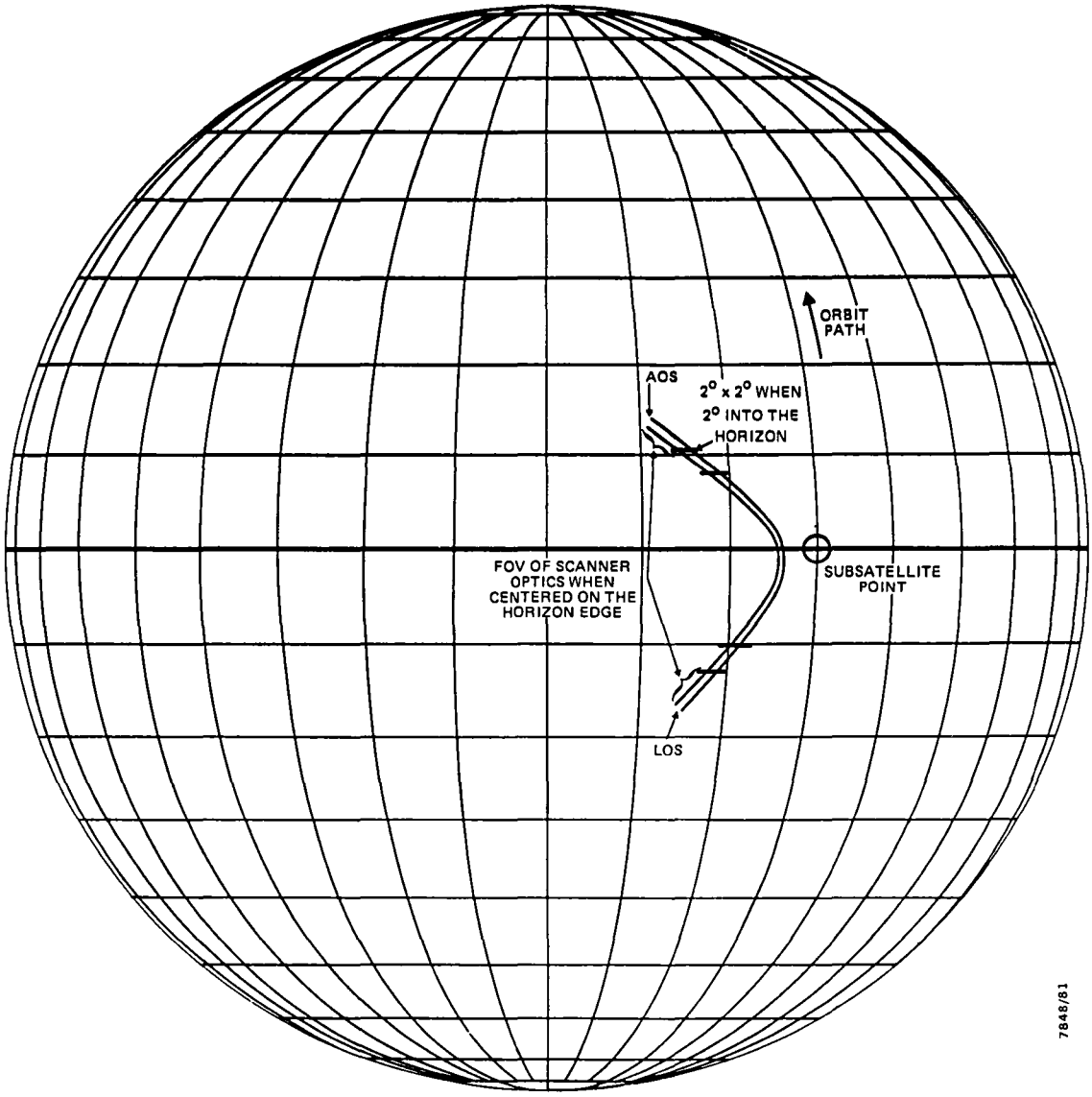

Figure 4.4-3. Magsat IR Scanner FOV Path Over an Earth Grid for a 45-Degree Scan Cone Half-Angle

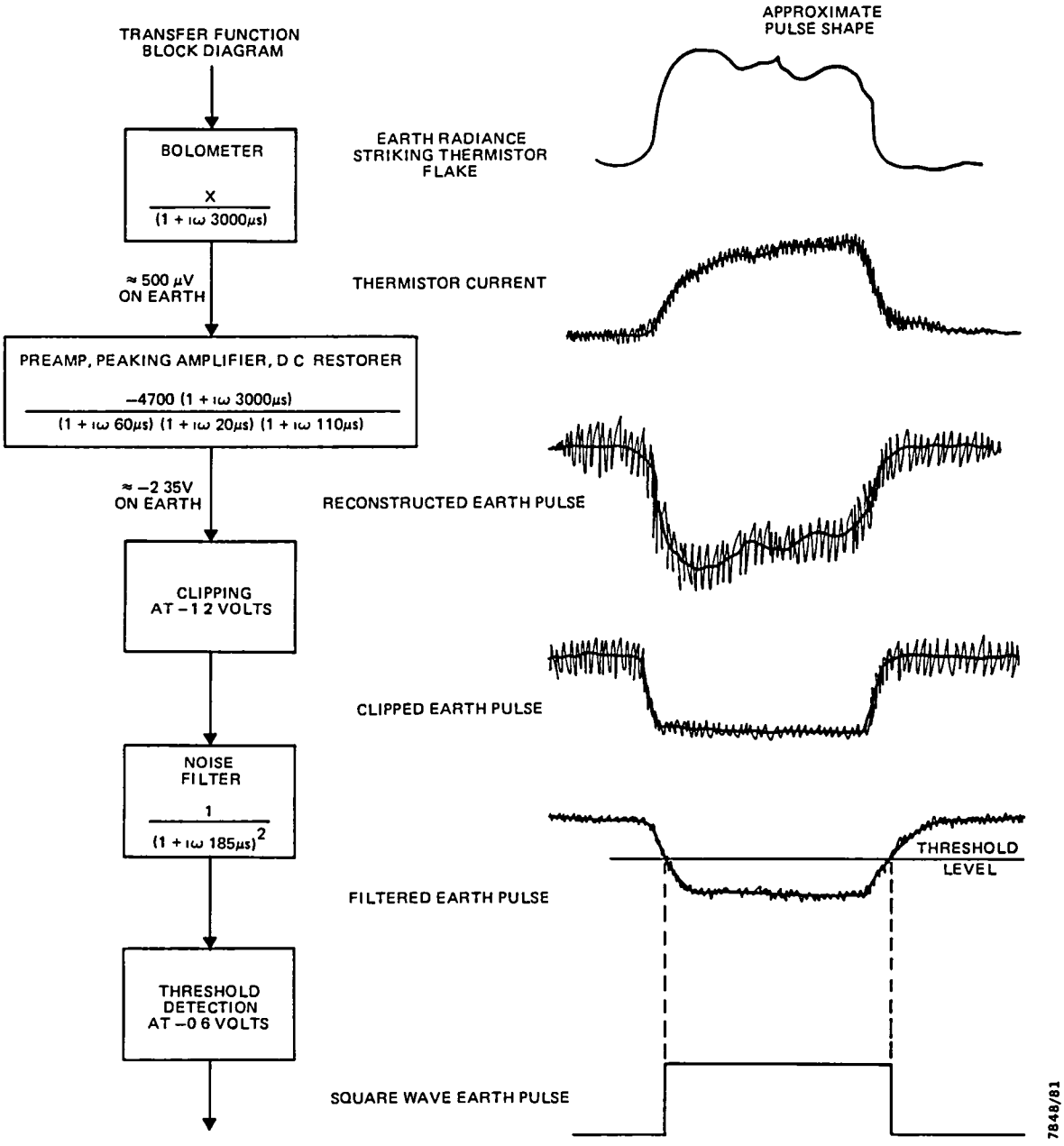

Figure 4.4-4. Magsat IR Scanner Earth Signal Processing Model

The Earth-crossing envelope from each thermistor flake and a blanking signal are logically "ANDed" for the purposes of Sun and Moon interference rejection. Because the Sun can enter only one flake FOV at a time, the effect of this is to extend one end of either flake's Earth-crossing envelope. This type of interference was not experienced during the Magsat mission because of the geometry of the orbit and attitude relative to the Sun.

4.4.2 PREDICTED ATTITUDE ERRORS AND MISSION DATA ANALYSIS

4.4.2.1 Systematic Horizon Radiance Errors

The response of the Magsat IR scanner was computed using the LMSC Earth IR model previously generated for Seasat. The resulting pitch and roll errors are illustrated in Figure 4.4-5 for one full orbit. To evaluate this radiance correction model for the IR scanner pitch and roll data, the attitude computed from the Magsat fine Sun sensor and star tracker was used as a reference to compute the IR scanner pitch and roll signal from an oblate Earth. This computed signal was subtracted from the telemetered and bias-corrected IR scanner pitch and roll data to form the pitch and roll residuals.

Figure 4.4-6 illustrates this method with examples of the data at various stages in the analysis for November 21, 1979. In Figure 4.4-6(a), the IR scanner pitch data are plotted with the high-accuracy attitude solutions computed from star tracker data; the computed data are shown with hash marks. Figure 4.4-6(b) shows the raw data as IR pitch voltage. The difference between the two versions of the IR pitch data of Figure 4.4-6(a) are plotted in Figure 4.4-6(c). Corresponding roll data are shown in Figure 4.4-6(d).

The functional form of the data in Figures 4.4-6(c) and (d) identifies the IR scanner sensing error after the attitude-dependent component of the sensor signal has been removed.

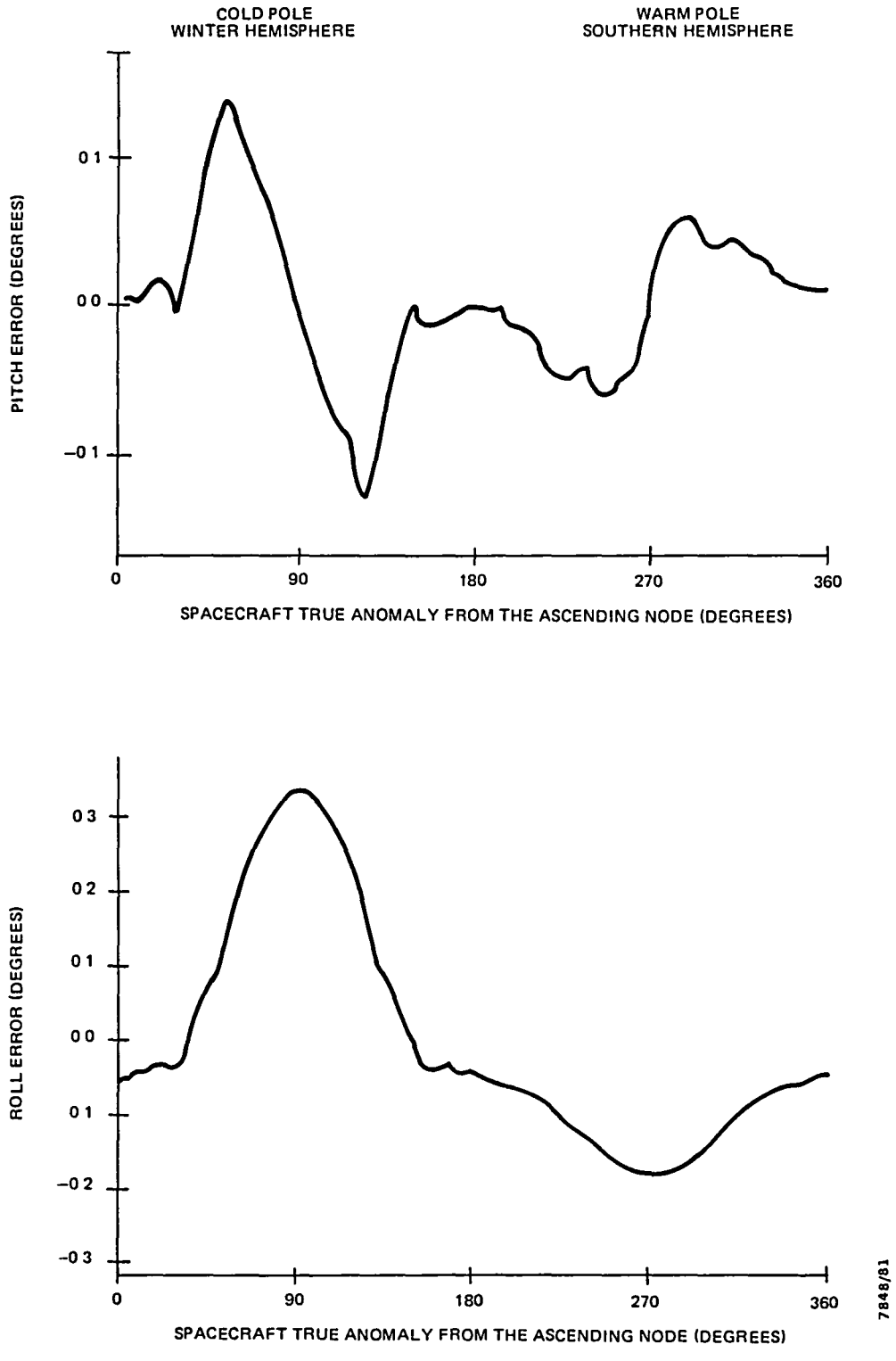

Figure 4.4-5. Systematic Horizon Radiance Correction for January at 350-Kilometer Altitude

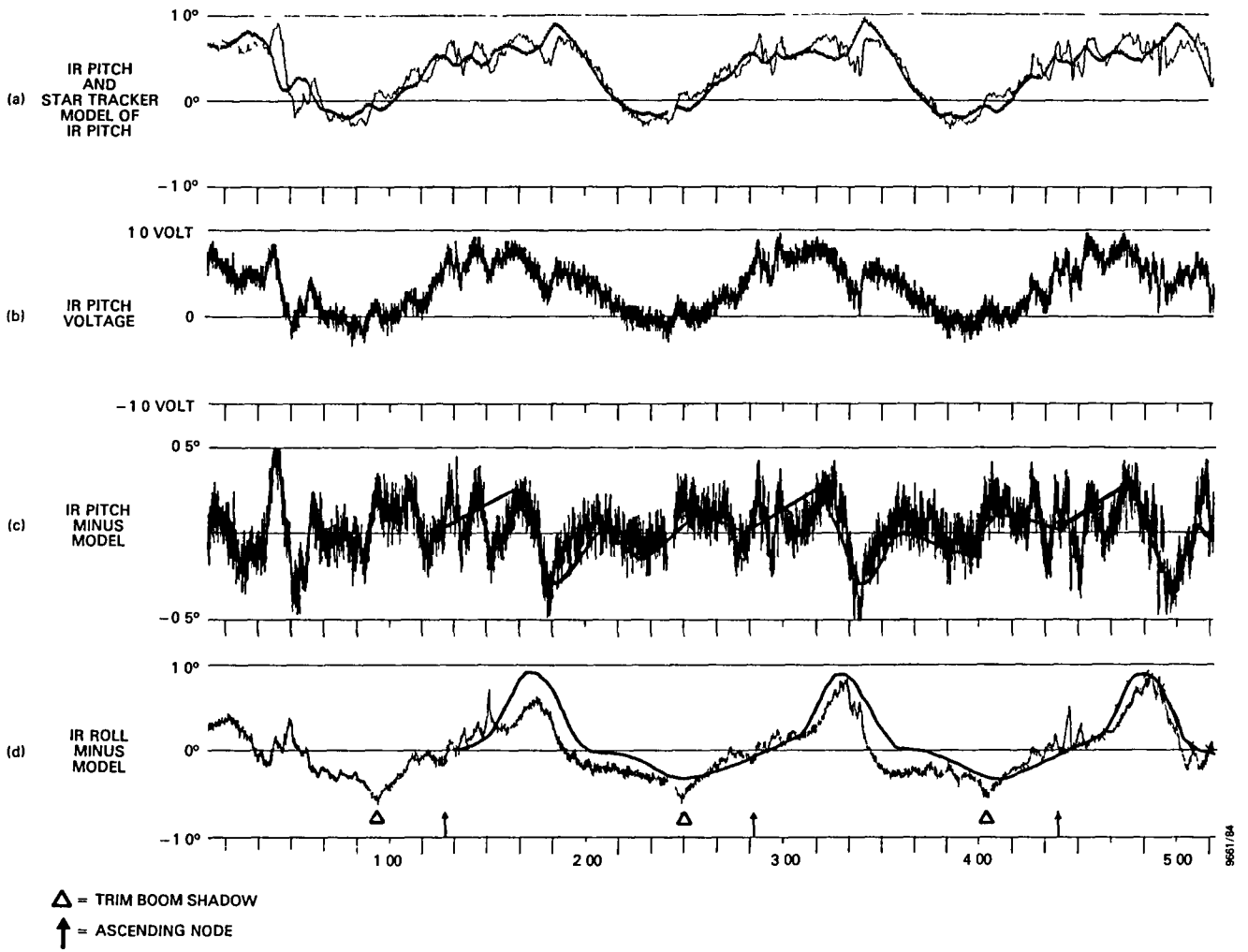

Figure 4.4-6. Magsat IR Data Analysis Comparing the IR Pitch and Roll and a Model of the Data Using the Star Tracker Attitudes (1 of 2)

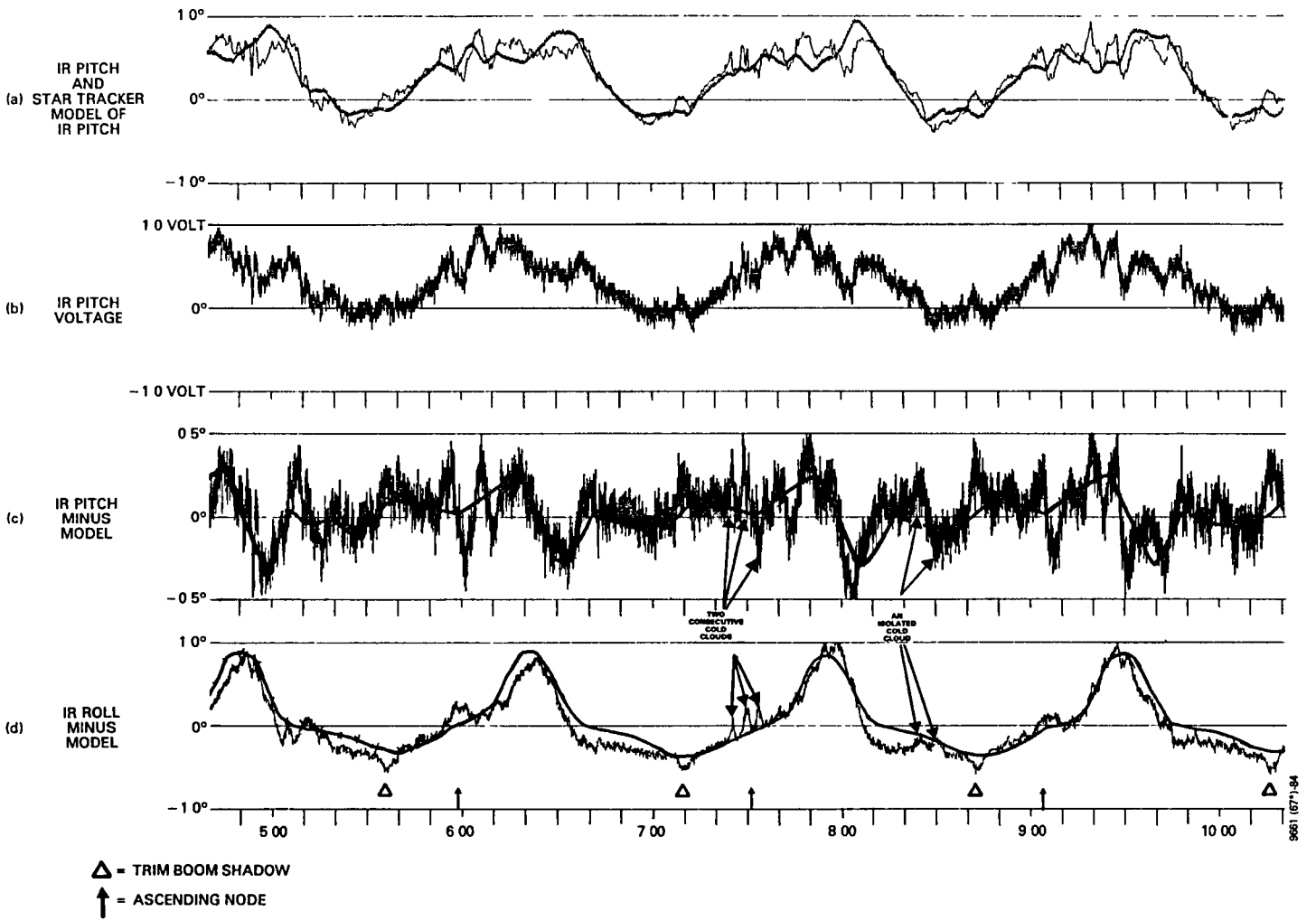

Figure 4.4-6. Magsat IR Data Analysis Comparing the IR Pitch and Roll and a Model of the Data Using the Star Tracker Attitudes (2 of 2)

The sources of this error function are systematic horizon radiance variations; random Earth radiance anomalies such as cold clouds; and other IR signal modulation sources such as spacecraft structural components, the Sun, and the Moon. To compare the residuals with the functional form of the effects of systematic variations in the Earth's IR radiation with latitude, the computed HRMU pitch and roll errors for January (smooth solid curves) are overlaid with the corresponding November data residuals. The HRMU results were obtained using the January Seasat-1 radiance profiles in the Magsat HRMU. The threshold voltage was set at 0.6 volt, but the bolometer radiance-to-volts gain was lowered to one-half the value used to generate the results for the original analysis (those results are displayed in Figure 4.4-5).

The above example shows that a systematic horizon radiance effect was apparent in Magsat. A change in the gain of the electronics model by a factor of 1/2 raised the roll error estimates by a factor of 3 and the pitch error estimates by a factor of 2. This brought both the pitch and roll predictions in approximate agreement with the residuals data and demonstrated the sensitivity of the prediction model to uncertainties in factors associated with the gain parameter. These factors include the IR passband sensitivity and width, the entrance aperture area, the bolometer flake size and subtended angular width of the FOV at the object, and the electronics constants.

Because the Seasat IR passband used in the above analysis was narrower than the Magsat passband, using the Magsat passband in the model would have increased the overall system gain. Another significant increase would also occur in sensitivity to latitude temperature gradients in the atmosphere nearer the Earth's surface. The model seems, however, to accommodate the data with a simple lowering of the radiance-to-volts gain factor. It is likely that the flight

data could be predicted more accurately using horizon radiance profiles generated with the wider Magsat passband and a more detailed analysis of the IR scanner, filter window, and optical acceptance efficiency. This assumes that the model of the electronics processor does not contribute significantly to the simulation problem, even though a parameter in that model was adjusted to force agreement with the data for this report.

Although the November data for Magsat readily conform to the interpretation that the residuals for roll and pitch are primarily due to a systematic horizon radiance effect, the data from March and April do not. More detailed analysis of the Magsat IR scanner data and the flight data might explain the March and April data. The analysis results presented here do not include a refined voltage-to-Earth chord calibration. Because some of the examples of roll residuals appear to have extremes correlated with the extremes in the null voltage, this calibration would have to be studied for a better understanding. Other factors that may have contributed to the discrepancy in the March and April data are as follows: the Magsat passband was not used to generate the Earth IR profile model, the detailed modeling of the bolometer dual-flake FOVs and their associated efficiencies was not applied, and effects due to solar illumination of the IR scanner assembly were experienced. On the other hand, an overestimate in the scanner optical gain would cause the flight signal processing circuit to operate in a region of marginal performance. This would lead to subtle effects induced by changes in any one of the factors influencing the scanner performance (e.g., the solar illumination).

4.4.2.2 Cold Cloud Effects

Figure 4.4-6 shows many examples of IR data anomalies induced by cold clouds. These anomalies are identifiable in

the data as positive and negative spikes in the pitch data lasting a few minutes each and separated by 5 minutes and as pairs of positive spikes separated by 5 minutes in the roll data. The pairs of positive spikes in the roll data are directly correlated with the negative-then-positive pairs of spikes in pitch. The peak amplitudes of the cold cloud effects in the Magsat data appear to be 0.3 degree for the pitch and roll data. This is comparable in size to the zero-to-peak systematic correction visible in the pitch data and adds to the confusion in recognizing the signature of the systematic effect in that data. Direct evidence that the anomalies described above are caused by cold clouds is presented in Figures 4.4-7 and 4.4-8. Figure 4.4-7 is an IR image of the Earth from the synchronous orbit of a weather satellite on November 21, 1979, at 15:45 UT. Overlaid on that image are Magsat subsatellite points, indicated by ⊕, and boundaries of the IR scanner Earth traces for the attitude control limits at the corresponding subsatellite point. The IR data from these orbits are presented in Figure 4.4-8. Data anomalies in these figures that can be directly correlated with clouds in Figure 4.4-7 are those centered on times near 14:28, 16:00, and 17:34 UT. These times are correlated with the equatorial clouds right of center, at the center, and west of center of the image. More well-defined cloud anomalies at 14:05 and 18:30 occur over Eastern North America at the edge of the image and on the opposite side of the Earth at the ascending node, respectively. The interaction of cold cloud effects with the pitch control loop results in a complex IR data noise structure.

The response time of the pitch control loop is about 150 seconds. A close look at the overlaid IR scanner and star tracker derived data shows how the initial position error induced by the cloud in the IR scanner data causes an attitude control response of the opposite sign. The spacecraft

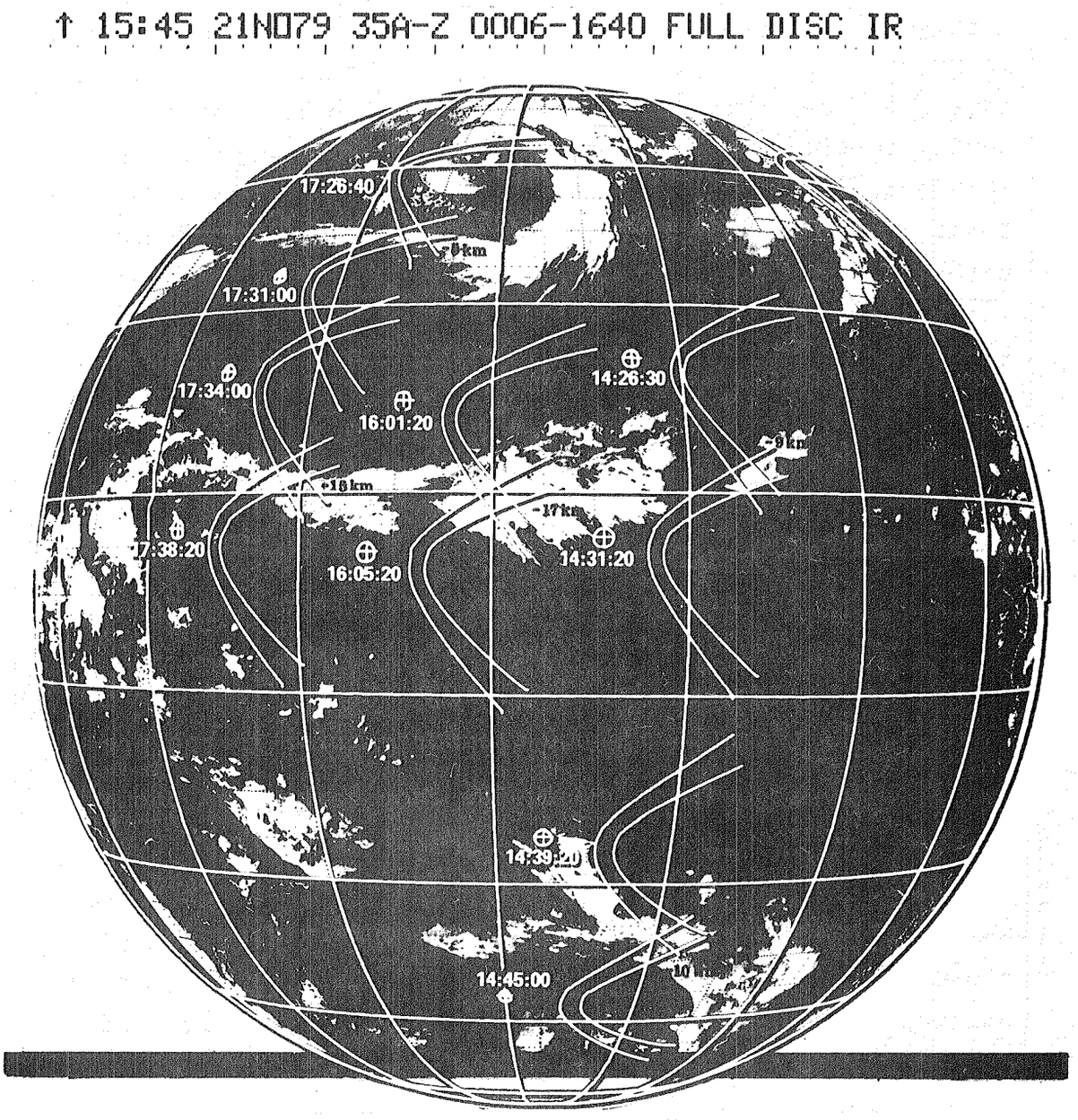

Figure 4.4-7. Magsat Scan Path on Earth Horizons on November 21, 1979

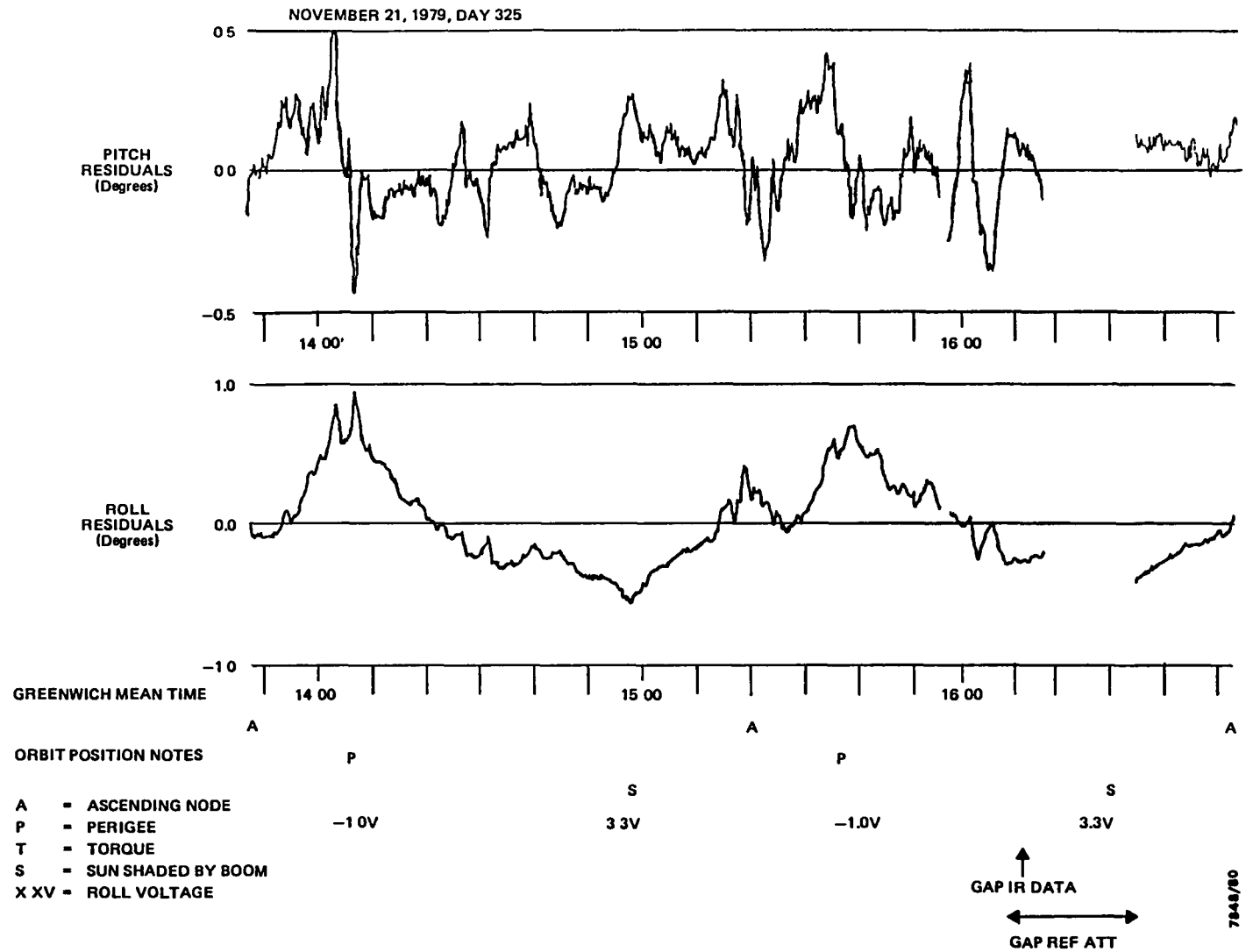

Figure 4.4-8. Pitch and Roll Residuals for November 21, 1979 (1 of 2)

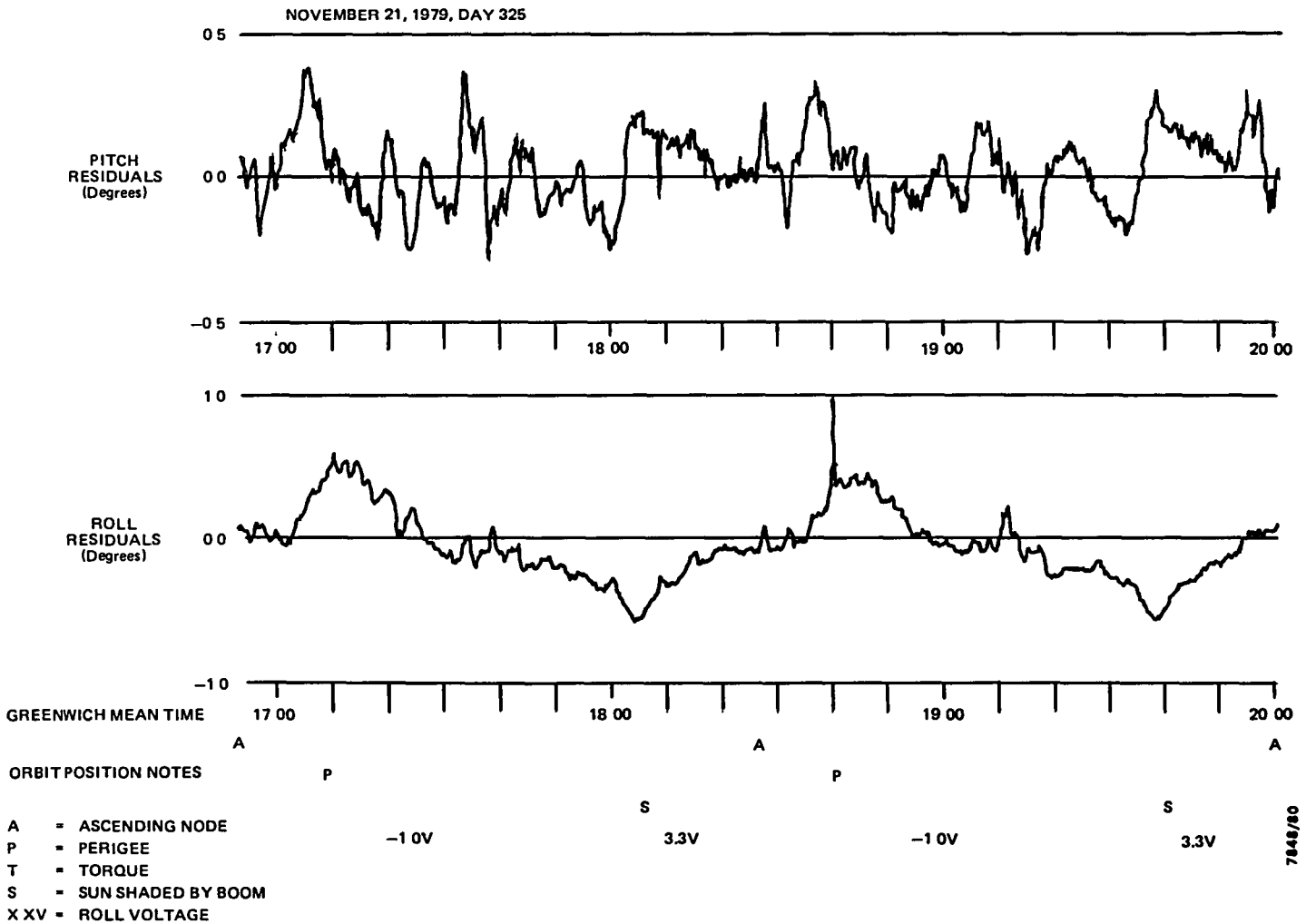

Figure 4.4-8. Pitch and Roll Residuals for November 21, 1979 (2 of 2)

pitch angle, as indicated by the star tracker pitch function, shows a minimum a few minutes later than the initial positive impulse.

4.4.2.3 Solar IR Radiation Effects

The IR scanner assembly was mounted on the sunlit side of the Magsat spacecraft, with the scan cone axis aligned along the spacecraft -Z-axis. For the duration of the mission, the scanner axis was within a few degrees of positive orbit normal. The angle between the scanner cone axis and the Sun varied slowly with time as the declination of the Sun changed with the seasons. Ignoring the Magsat attitude control offset, which could deviate as far as 10 degrees from orbit normal, the angles from the scan cone to the Sun vector changed from 16 degrees in midwinter to 30 degrees at the end of the mission in June.

The study of the effect of solar IR radiation on the pitch and roll output from the Magsat IR scanners was centered on an event that regularly eliminated sunlight from the IR scanner assembly. This event, the periodic shading of the IR scanner by the yaw trim boom assembly, occurred once per orbit. For the midwinter months, the shadow of the yaw trim boom passed over the IR scanner optics when the spacecraft was at its southernmost latitude. The effect of the absence of solar IR radiation can be seen in the November 21 data in Figure 4.4-6 delineated by the open triangles. There are -0.2-degree changes in the roll residuals data with corresponding positive 0.25-degree changes in the pitch residuals data. It can thus be concluded that, for the November 21 geometry, sunlight caused the roll and pitch IR data to be in error by these amounts at this time in the orbit.

Because no systematic analysis of the change in the amplitude of this effect versus the change in Sun/orbit geometry was performed, no conclusion can be drawn concerning the

time dependence of the errors due to solar IR radiation either at the orbital rate or as a function of season. The significance of the observation is not, however, diminished by the lack of detailed analysis. A large number of missions have flown IR scanner optical assemblies that have been subjected to varying conditions of solar illumination. The orbital period effects can be caused by spacecraft day/night effects, spacecraft appendage shadowing (e.g., Magsat, Reference 38), and solar elevation angle variation relative to the Earth (again as for Magsat). The longer period effects would be caused by the change in the amplitude of the above-mentioned effects due to ascending node precession and seasonal changes in solar declination. Overall attitude determination accuracy using IR scanner data can be improved by controlling or eliminating such effects through improved design, or by a better understanding of the effects so that data processing procedures can be established to compensate for the errors.

4.4.3 RESULTS AND DISCUSSION

The analysis of Magsat flight data comparing the attitudes obtained from the IR scanner to those from the fine Sun sensor and star trackers showed that the IR scanner attitudes were altered by a number of effects (Reference 38). These included cold clouds, electronic calibration changes for the pitch loop, systematic horizon radiance variations, sunlight on the IR scanner optical tube entrance, and errors in the preflight roll calibration. Significant accomplishments were made in the Magsat analysis in understanding the effects of systematic variations in the Earth IR profiles on the pitch and roll data. The analysis showed that, with the aid of the star tracker reference attitudes, peak-to-peak roll error amplitudes up to 1.5 degrees due to radiance variations with latitude can be explained. The hypothesis is that an improved analysis (of the Earth IR model and the IR

scanner detection efficiency) could have predicted this 1.5-degree effect. In missions without star trackers, where sufficient attitude sensing accuracy is available only periodically with Sun sensors, it is frequently possible to spot check and adjust the IR scanner/Earth radiance model to agree with the more accurate, but less frequent, attitude reference data.

The results of the Seasat-1 flight data analysis (Section 4.2) indicated that a more accurate estimate of the pitch and roll attitudes for that mission could have been obtained if the Seasat IR scanners had been fixed-threshold sensors. That observation was based on the severe effect caused by the cold clouds on the threshold level adjustment function of the normalized threshold locator logic. It was argued that a fixed-threshold locator logic would be less sensitive to cold clouds because the fixed-threshold horizon triggering point would occur before the FOV began to be influenced by IR anomalies below a 20-kilometer tangent height. It was also thought that the integrity of systematic corrections computed with the Earth IR and sensor component models would be higher because of the insensitivity of the flight system to cold clouds. Magsat data appear to refute this argument. It appears, however, that the success of a fixed-threshold Earth horizon detection system depends critically on accurate estimates of the IR radiation collection and detection efficiency of the optical system. This analysis, showing a reduction by one-half of the gain parameter in the sensor model, indicates that the scanner system may have been operating in a marginal performance region near the top of the sensed Earth pulse, thereby increasing the scanner system's sensitivity to all effects that significantly alter the Earth pulse. These effects for Magsat are cold clouds and the geographical temperature variation on the Earth, which are associated with the seasons. A detailed analysis

of the Magsat sensor optics and bolometer assembly (like that performed for ERBS) would, however, be necessary to confirm the hypothesis that Magsat was operating in a marginal performance region. The above hypothesis is based on the observation that the modeled performance with the nominal Magsat system (with the gain factor unchanged) did not predict systematic errors greater than 0.5 degree.

4.5 DYNAMICS EXPLORER-2

The DE-2 spacecraft was launched with the DE-1 spacecraft on a Delta 3913 launch vehicle. The DE spacecraft were designed to continue the work of the AE spacecraft series. The DE-2 orbit was similar to that of AE-4. Although the DE-2 hardware was also similar to that of the AE spacecraft, some of the AE subsystems were not included on or were modified for DE-2. DE-2 did not have a hydrazine propulsion system for orbit adjustment and yaw inversion control and did not have the dual wheel- and body-mounted IR horizon sensors (WHSs and BHSs). The two DE-2 WHS bolometers scanned the Earth at the same cone angles, through the wheel-mounted scanning mirror, and therefore the attitude information from WHS1 and WHS2 for DE-2 was redundant. The DE wheel speed, which determined the Earth scanning rate, was 750 rpm when DE-2 was despun and near 1300 rpm when DE-2 was spinning.

DE-2 had two Adcole two-axis fine Sun sensors that provided for potentially higher accuracy attitude solutions than the AE solutions, which relied on 0.5-degree-resolution DSAI data for most near-real-time processing. As it turned out, however, the DE-2 fine Sun sensors had a fine reticle electronics failure within the first month of the mission, reducing the Sun data accuracy to approximately $\pm$0.8 degree. Because of this loss of an accurate attitude reference, in-flight analysis of the effects of systematic variations in the Earth IR radiance on the DE-2 IR data could not be performed, and the opportunity to evaluate the DE-2 IR sensor modeling analysis performed in the prelaunch phase of mission support was lost. A review of the DE-2 WHS flight data is still important, however, for understanding the effect of spacecraft design on the WHS performance. The following discussion is derived from References 33, 41, 42, and 43.

4.5.1 MISSION REQUIREMENTS AND HARDWARE

DE-2 was launched from the Western Test Range on August 3, 1981. The launch apogee was low, which shortened the mission lifetime. With no active orbit restoration capability, the length of the mission was governed by the rate of decay of the orbit. The mission ended with reentry on February 19, 1983. The DE-2 spacecraft is illustrated in Figure 4.5-1. The mission can be summarized as follows:

- Orbit--Polar with a 90-degree inclination, 305-kilometer perigee altitude, and 1300-kilometer apogee altitude
- Attitude configuration--Three-axis stabilized at 1 rpo, Earth-oriented
- Attitude determination hardware
  - Two redundant wheel-mounted horizon sensors (WHSs) similar to AE
  - Two Adcole 18960 fine Sun sensors with $\pm$32- by $\pm$32-degree FOV; quoted accuracy of 0.016 degree
- Attitude control hardware
  - Momentum wheel assembly
  - Two air-core attitude coils
  - Two air-core momentum coils
  - Passive nutation damper
- Accuracy requirement--0.7 degree (3σ) for Z-axis half-cone angle and 0.5 degree (3σ) for X-axis azimuth
- Ground support system--Interactive processing
- Data processing requirements
  - Definitive solutions packaged as nonoverlapping passes; solutions generated for an average 30-percent duty cycle

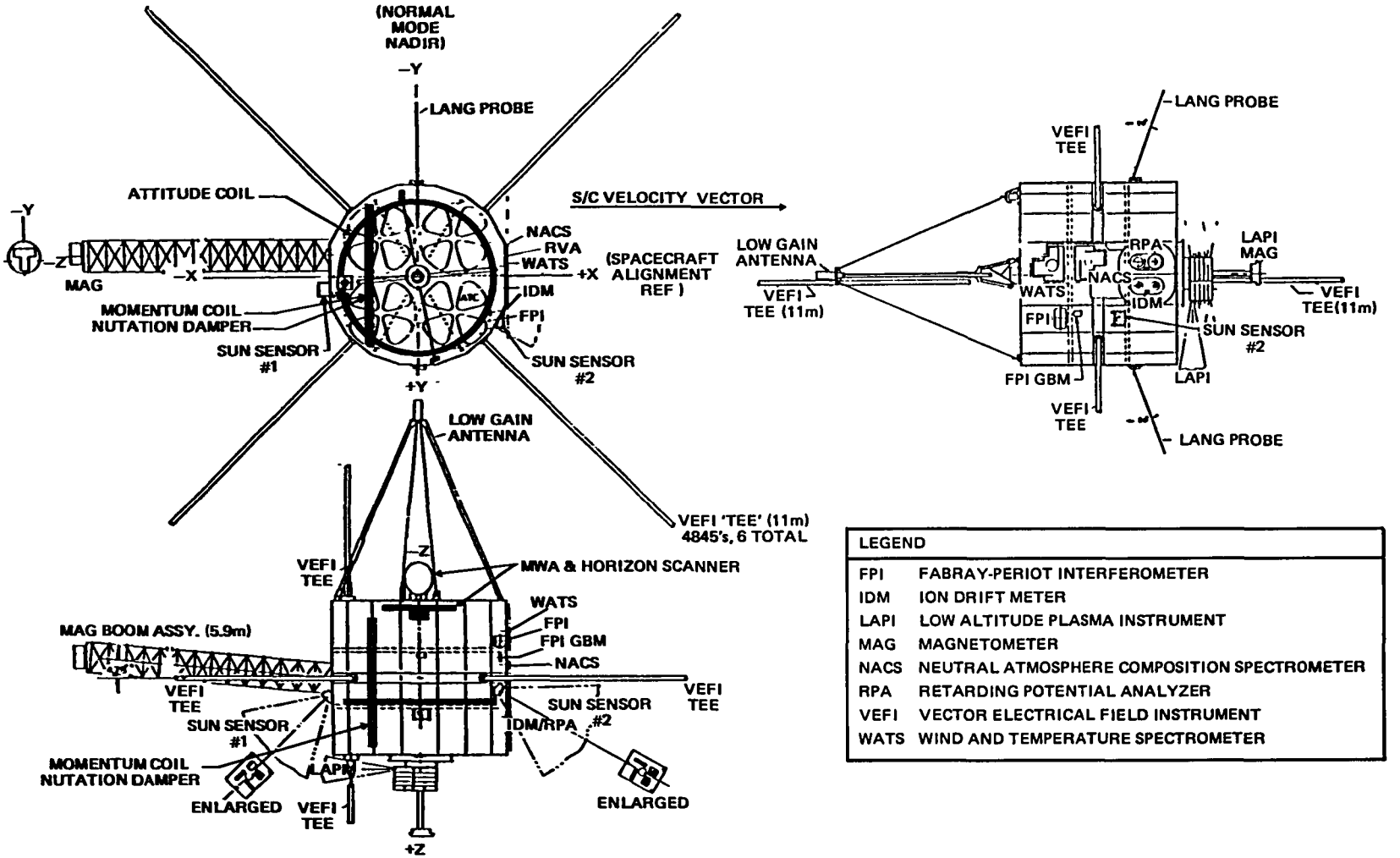

LEGEND	
FPI	FABRAY-PERIOT INTERFEROMETER
IDM	ION DRIFT METER
LAPI	LOW ALTITUDE PLASMA INSTRUMENT
MAG	MAGNETOMETER
NACS	NEUTRAL ATMOSPHERE COMPOSITION SPECTROMETER
RPA	RETARDING POTENTIAL ANALYZER
VEFI	VECTOR ELECTRICAL FIELD INSTRUMENT
WATS	WIND AND TEMPERATURE SPECTROMETER

Figure 4.5-1. DE-2 Spacecraft External Configuration

- Output data interval of 15 seconds
- Special processing at a 0.5-second output interval performed as requested for passes with Sun and Earth IR data available simultaneously
- Turnaround in 2 to 5 days from receipt of telemetry and definitive orbit data

• Problems encountered

- Interaction of control system with IR anomalies caused errors in azimuth angle solutions.
- Early failure of the fine reticle electronics in the Adcole fine Sun sensor assembly degraded sensor accuracy to $\pm$0.8 degree.
- Transponder activity induced pitch sensing errors and stimulated control system offsets.
- Some evidence exists for Sun-angle-dependent and orbit-angle-dependent thermal radiation interference in the WHS nadir angle data.
- Pitch sensor output was not a good indicator of the spacecraft pitch angle because this output was nulled continuously by the control loop (as for SAGE). With the degraded Sun data and frequent periods of partial Sun coverage, pitch angle determination and, therefore, definitive azimuth solutions were degraded.

The Earth scan geometry of DE-2 was similar to that of the AE spacecraft (Figure 4.7-2). The scan cone angle was 30 degrees, measured from the wheel spin axis. The WHS bolometers were also similar to those used on the AE spacecraft. The IR passband of the bolometer telescope extended from 13.5 to 16.6 micrometers for the 10-percent-of-peak

transmittance points. The width of the band at half maximum was 2.5 micrometers. Figure 4.5-2 is a block diagram of the DE-2 Earth sensor electronics model used by CSC (Reference 44). The AOS and LOS horizon locator technique for the DE-2 WHS was a fixed percentage of the peak derivative of the Earth pulse at the rising (space to Earth) and falling (Earth to space) portions of the pulse, respectively. The automatic threshold adjust feature in the DE-2 WHS electronics was a change from the earlier AE WHS electronics.

4.5.2 PREDICTED ATTITUDE ERRORS

The DE-2 WHS electronics model was incorporated into the HRMU using the state variable approach (Reference 42). This model and approach followed similar analysis by RCA (Reference 44). The RCA analysis calculated the response of the WHS to Earth radiance profiles obtained from an analysis by NASA and Honeywell (Reference 3). The CSC analysis was based on the same Earth IR profile model used for Seasat. The major difference in the implementation of the radiance correction function between DE-2 and Seasat was that, for DE-2, the horizon altitudes data set was generated for every 200 kilometers of possible spacecraft altitude and for the positive and negative orbit normal spin axis alignments. The DE-2 ADS then used the data set to compute the WHS pitch and roll correction as a function of spacecraft altitude. The primary effect of attitude alignment with negative or positive orbit normal was to reverse the sign of the spacecraft pitch correction. The simulated input and output pulses from the CSC analysis are illustrated in Figures 4.5-3 and 4.5-4 for a spacecraft altitude of 400 kilometers and a subsatellite latitude of 60°N. Figures 4.5-5 through 4.5-8 show the results of the CSC analysis converted to WHS pitch and roll errors for January and April in the DE-2 normal attitude (spacecraft Z-axis and WHS spin axis toward negative orbit normal) and an altitude of 400 kilometers.

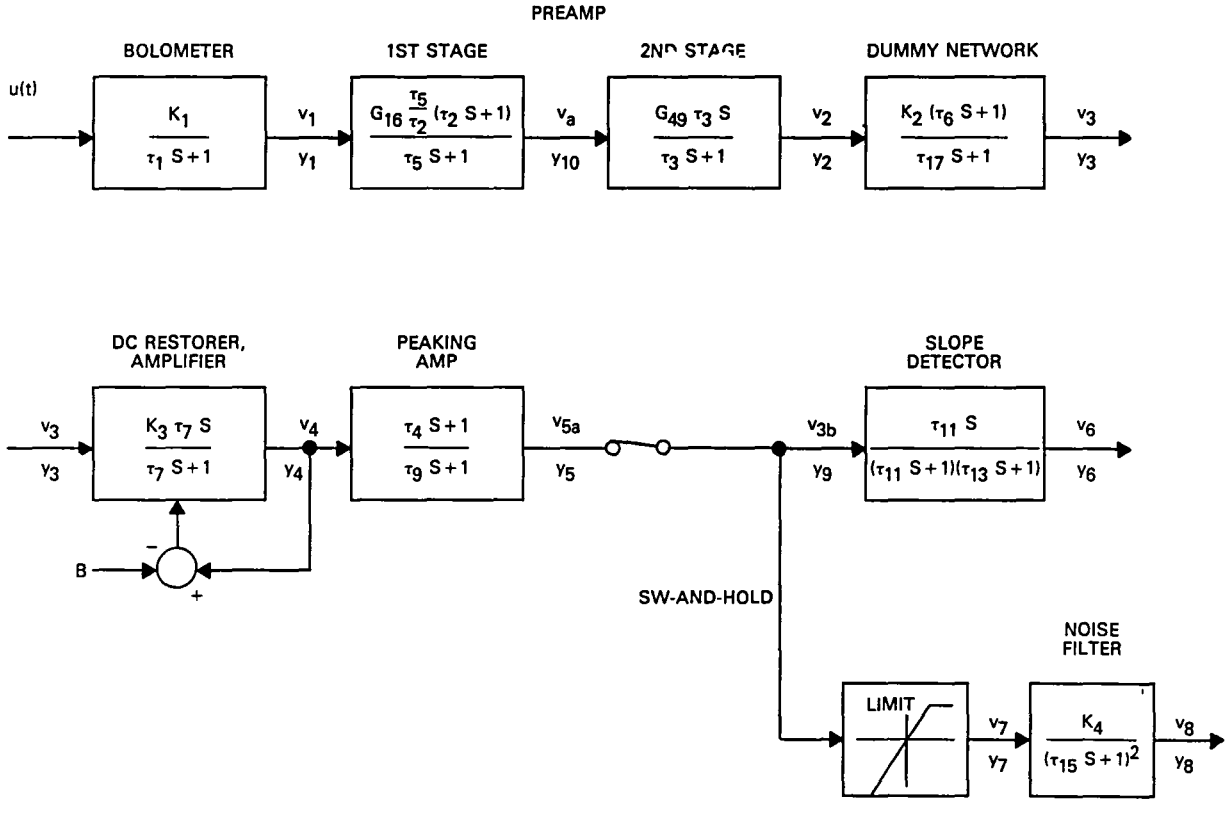

NOMINAL PARAMETER VALUES

B = 0 2 V	τ_1 = 1/270	τ_9 = 1/2010
K_1 = 3 525E−5 V/W	τ_2 = 1/0 021	τ_{11} = 1/300
K_2 = 1	τ_3 = 1/0 077	τ_{13} = 1/2000
K_3 = 5 2	τ_4 = 1/250	τ_{15} = 1/6000
K_4 = 0 85	τ_5 = 1/0 595	τ_{17} = 1
LIMIT = 1 5	τ_6 = 1	
G_{16} = 28	τ_7 = { 0 0067 FOR $v_4 < B$	
G_{49} = 55	0 0010 FOR $v_4 \geq B$	

9661 (70a*1)/84

Figure 4.5-2. Block Diagram of the DE-2 Earth Sensor Electronics Model

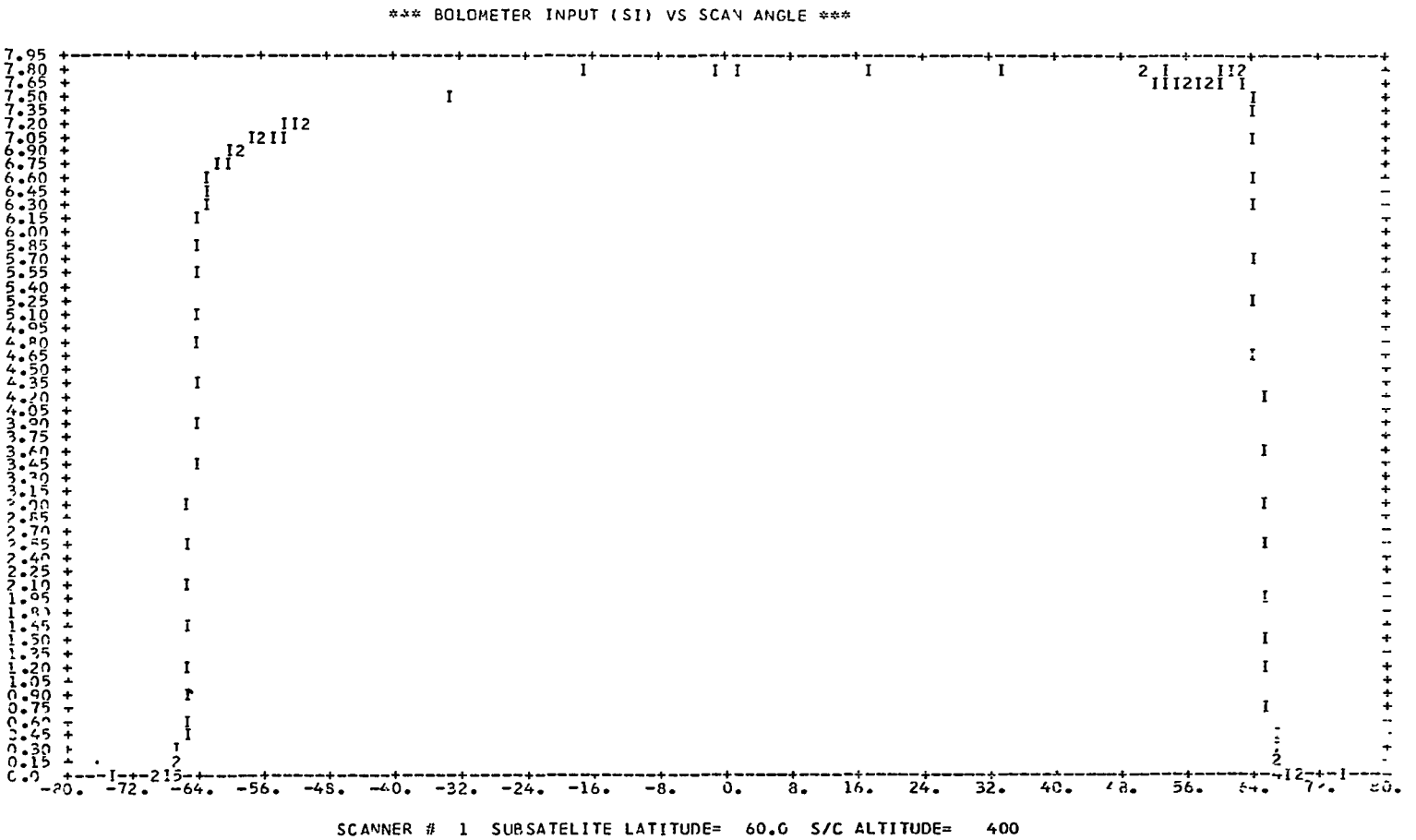

Figure 4.5-3. Input Radiance to the DE-2 Bolometer Versus Scan Angle

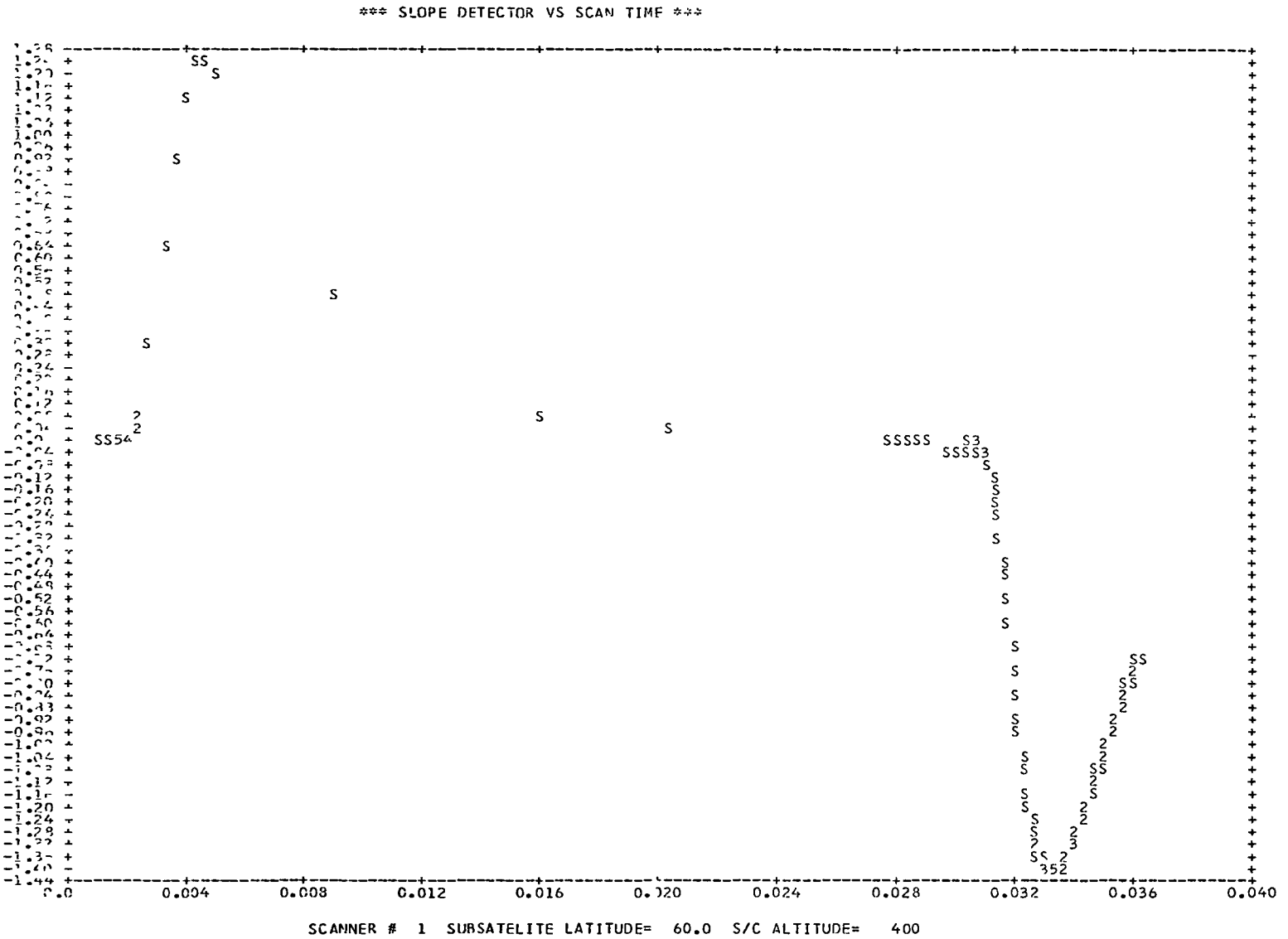

Figure 4.5-4. DE-2 Slope Detector Output Voltage Versus Scan Time

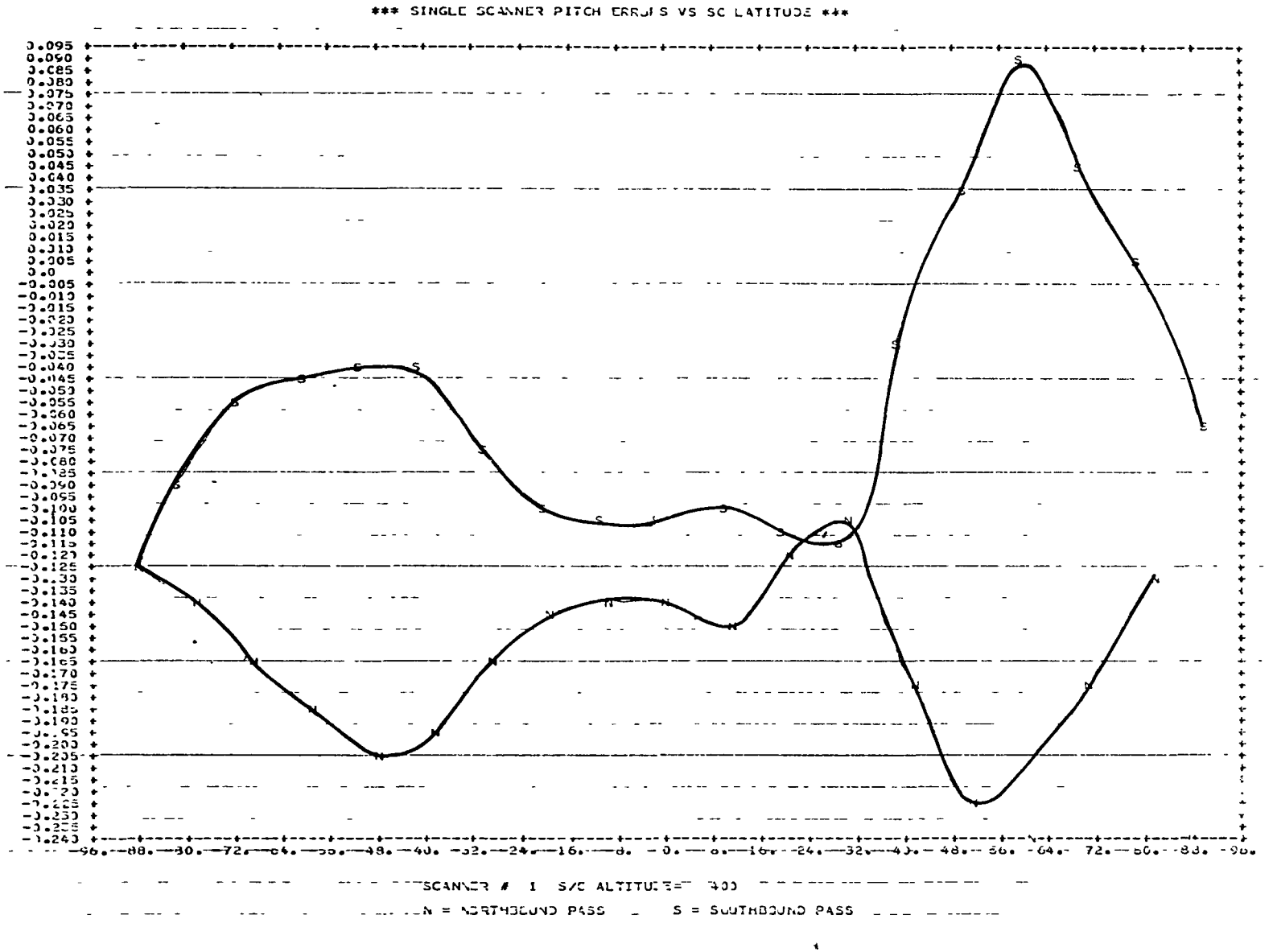

Figure 4.5-5. Simulated Pitch Errors for DE-2 in January

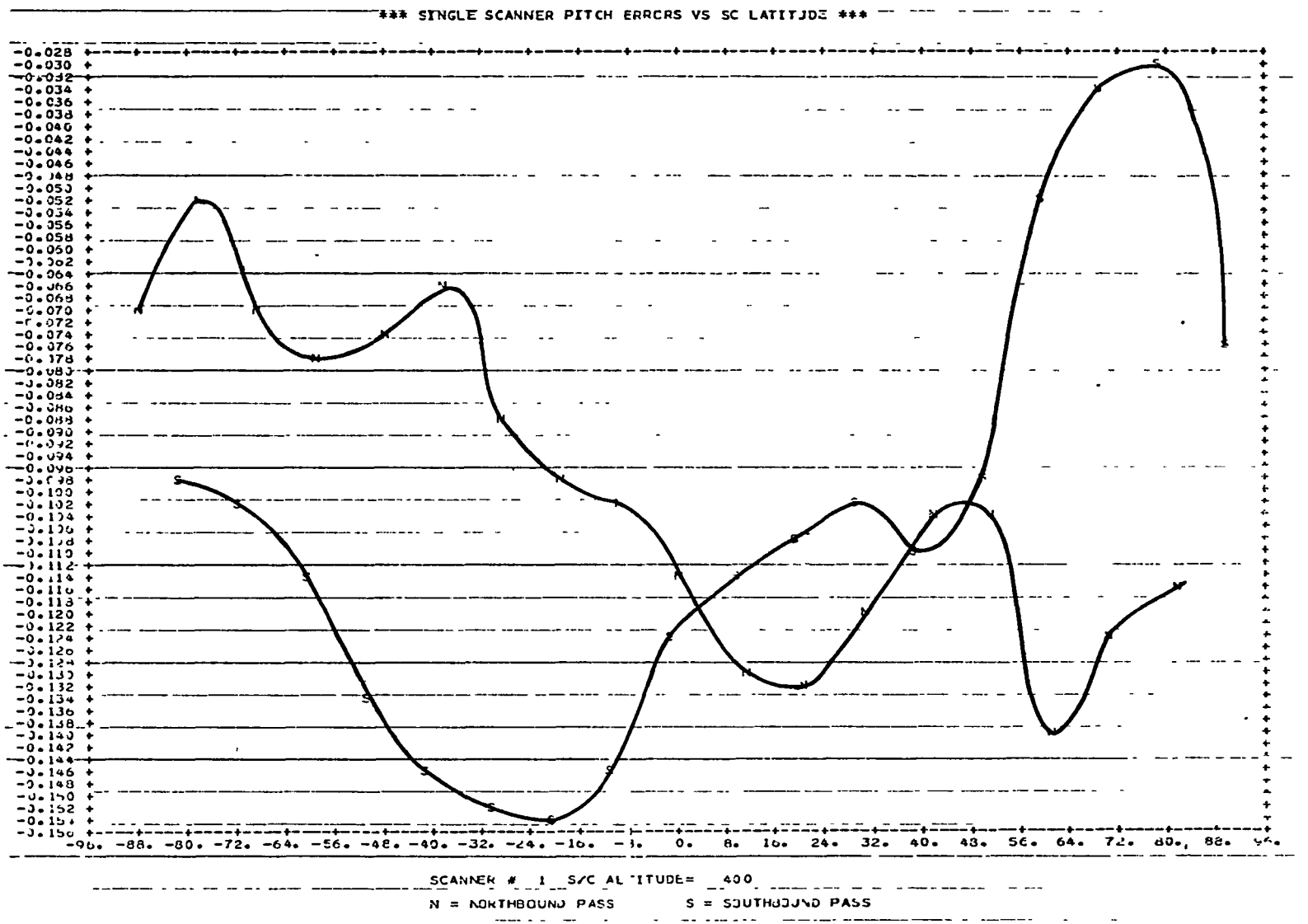

Figure 4.5-6. Simulated Pitch Errors for DE-2 in April

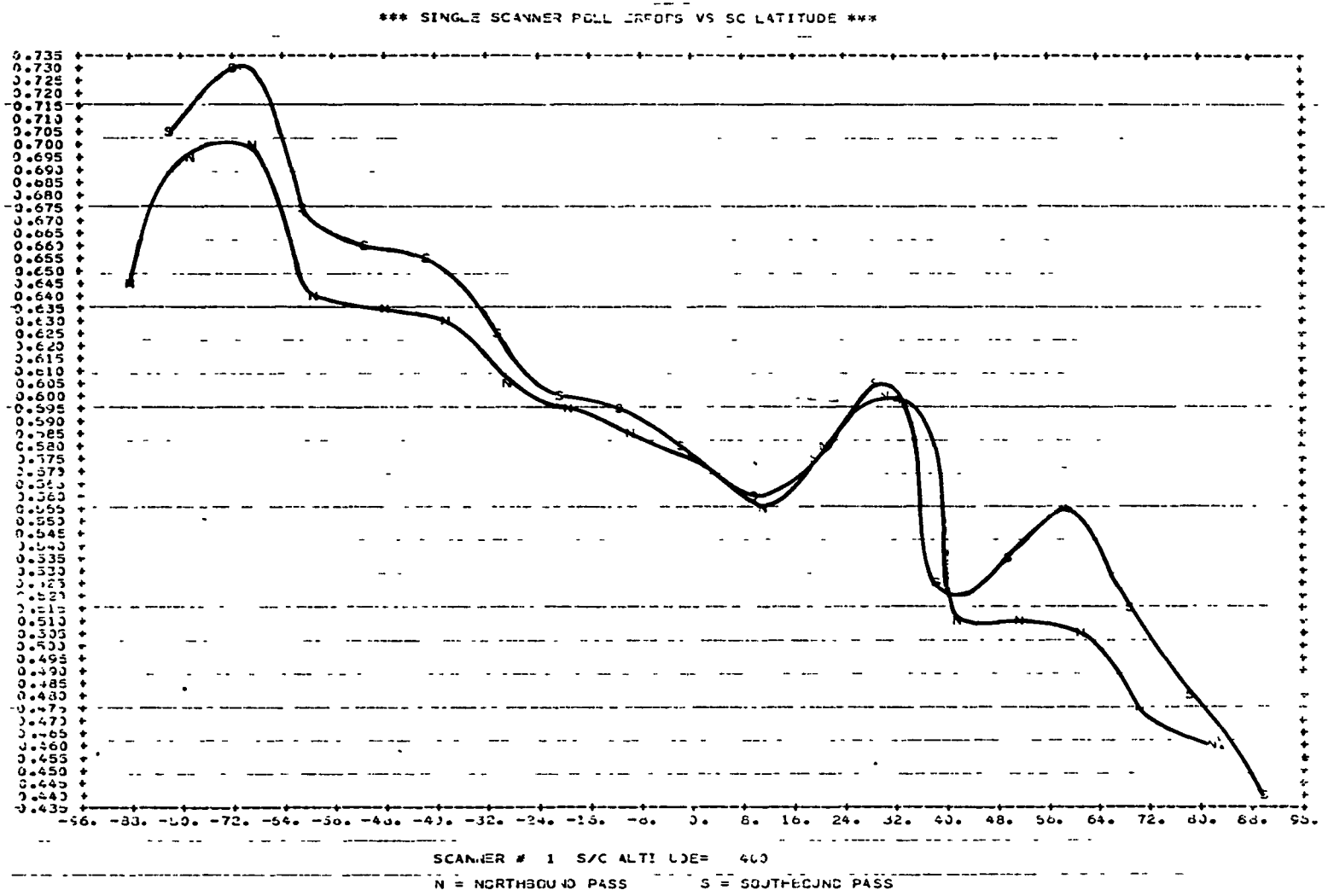

Figure 4.5-7. Simulated Roll Errors for DE-2 in January

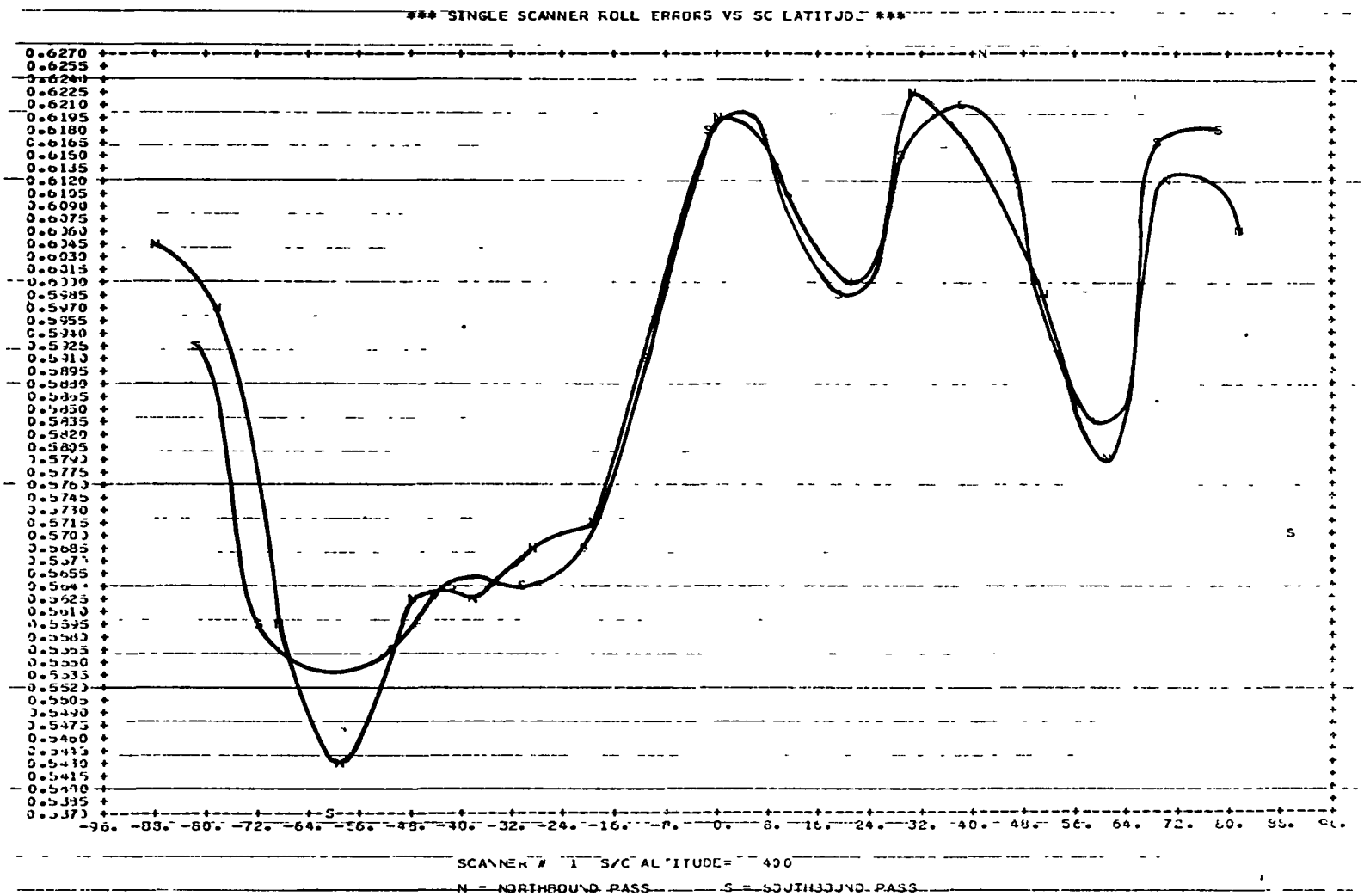

Figure 4.5-8. Simulated Roll Errors for DE-2 in April

These results compare favorably with data points at an altitude of 290 kilometers from the RCA analysis for pitch but show differences of up to 0.15 degree for roll.

The explanation for these differences could be differences in the Earth radiance profile models. A review of the DE-2 version of the HRMU used by CSC, however, showed that the FOV integration to construct the input radiance pulse was performed at scan angles 0.5 degree apart. Because the Earth radiance profile typically rises from 10 percent to 90 percent in less than 1 degree of scan, the possibility exists for analytical errors in the computation of the derivative of the processed Earth pulse. Neither a sensitivity analysis of the HRMU simulation of the DE-2 WHS errors nor a direct check of the accuracy of the predicted DE-2 horizon radiance corrections was ever made to study these possibilities in detail.

Spacecraft orbital motion can cause variations in WHS sensed Earth width that are not related to the attitude motion. The nadir angle variation for a constant inertial spin axis attitude can be understood as follows. Figure 4.5-9 shows the geometry of the inertial spin axis and the nadir vector. The nadir vector rotates around the orbit normal at the orbital rate. The nadir angle has a functional form dependent on orbit phase angle and spin axis orientation in the orbital reference frame, as follows:

$$\cos \eta = \sin \delta \cos \Omega$$

where η is the nadir angle, δ is the angle between orbit normal and the spin axis, and Ω is the orbital phase angle measured from the projection of the spin axis on the orbit plane to the nadir vector. For the DE-2 and AE-3 spacecraft,

the attitude control requirement was to maintain δ less than 2 degrees.

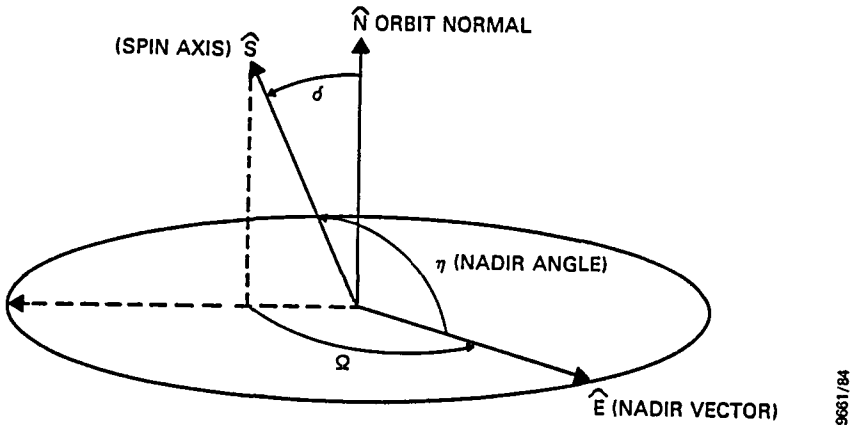

Figure 4.5-9. Geometry of the DE-2 Spin Axis and Earth Vector Defining the Nadir Angle (η)

4.5.3 MISSION DATA ANALYSIS

Data from the performance-degraded fine Sun sensor (Figure 4.5-10) prevented any evaluation of the IR horizon radiance corrections using flight data. A review of the WHS data does, however, provide some estimate of its accuracy.

The WHS performance analysis relied on interactive data processing sessions involving the review of output in the form of nadir angle residuals. The corrected Earth width data from the DE-2 WHS was compared with a model of the nadir angle based on the assumption of an inertially constant spacecraft spin axis attitude. The analysis showed the differences between the time history of the nadir angles derived from bias- and oblateness-corrected data and a model of the nadir angle that is the complement of the roll

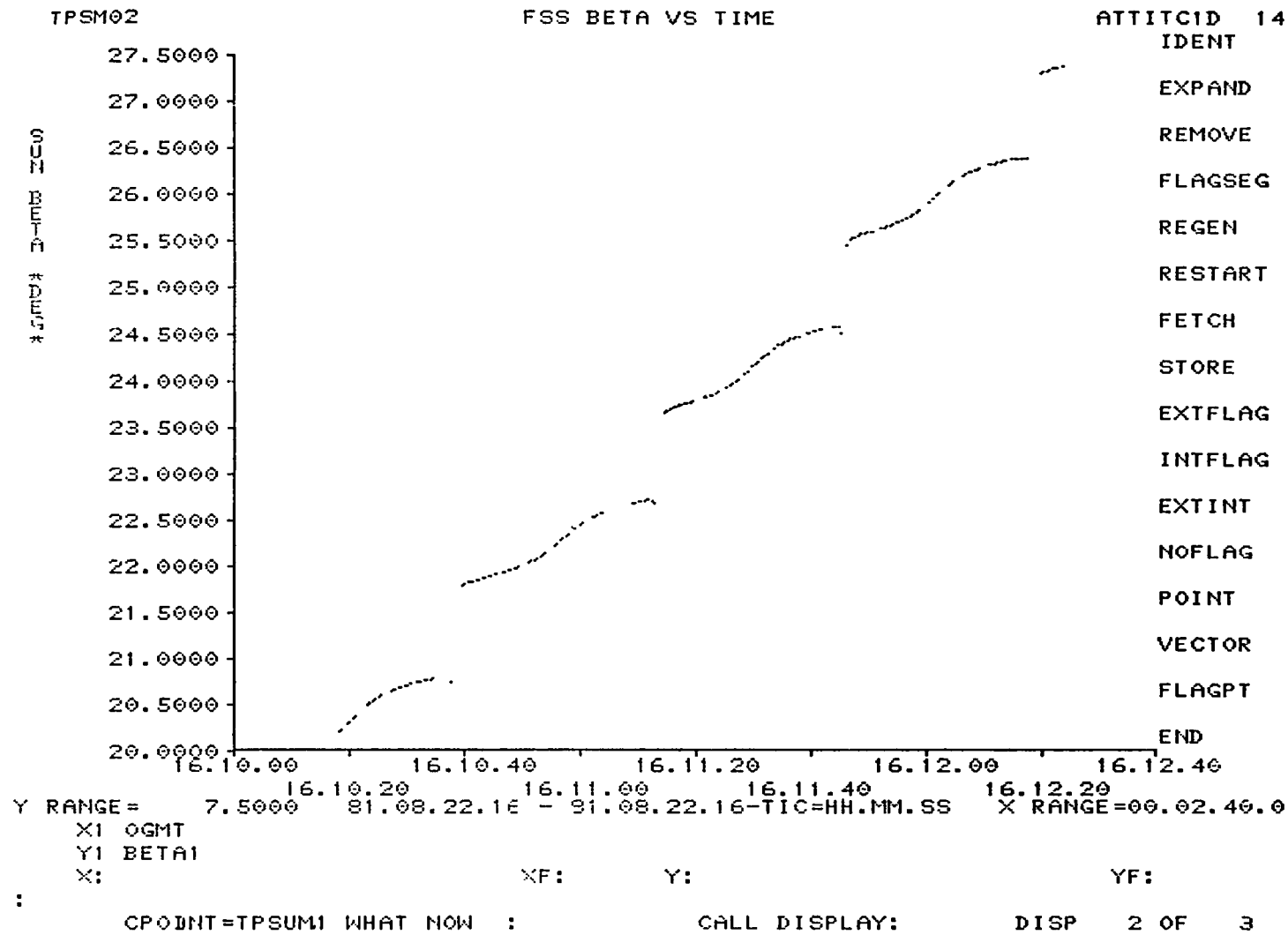

Figure 4.5-10. Degraded Fine Sun Sensor β Angle Data From DE-2

angle. Writing the nadir angle equation with roll angle yields

$$\sin r = \cos \eta = \sin \delta \cos \Omega$$

and, for small r and δ,

$$r \cong \delta \cos \Omega$$

Thus, if a near-null attitude ($r \cong 0$) is assumed for the constant attitude model ($\eta = \pi/2$), this functional form for the roll angle describes the anticipated shape of the residuals. In other words, when the model provides the correct function for $\Omega(t)$ and the correct offset δ, the residuals between the model for roll and the roll derived from the data should be random around zero for a data interval during which the attitude is constant. Figure 4.5-11 shows an example of the nadir angle residuals from perigee to perigee that were computed from simulated data. Here the spin axis attitude is constant from a few minutes after the first perigee until a few minutes before the next perigee.

A second example of the residuals from the least squares estimator on a simulated data interval centered on perigee is provided in Figure 4.5-12. Here the nadir angle data have the functional form caused by one attitude before perigee and another attitude after perigee. The solution model converges on an average of these two attitudes, and the residuals are therefore somewhat discontinuous during perigee when the attitude changed. A sinusoidal residual is obtained from the difference between the model cosine function and the individual cosinusoidal data functions before and after perigee.

Figure 4.5-13 shows the nadir angle residuals for a high Sun angle (near 75 degrees) on September 18, 1981, when the

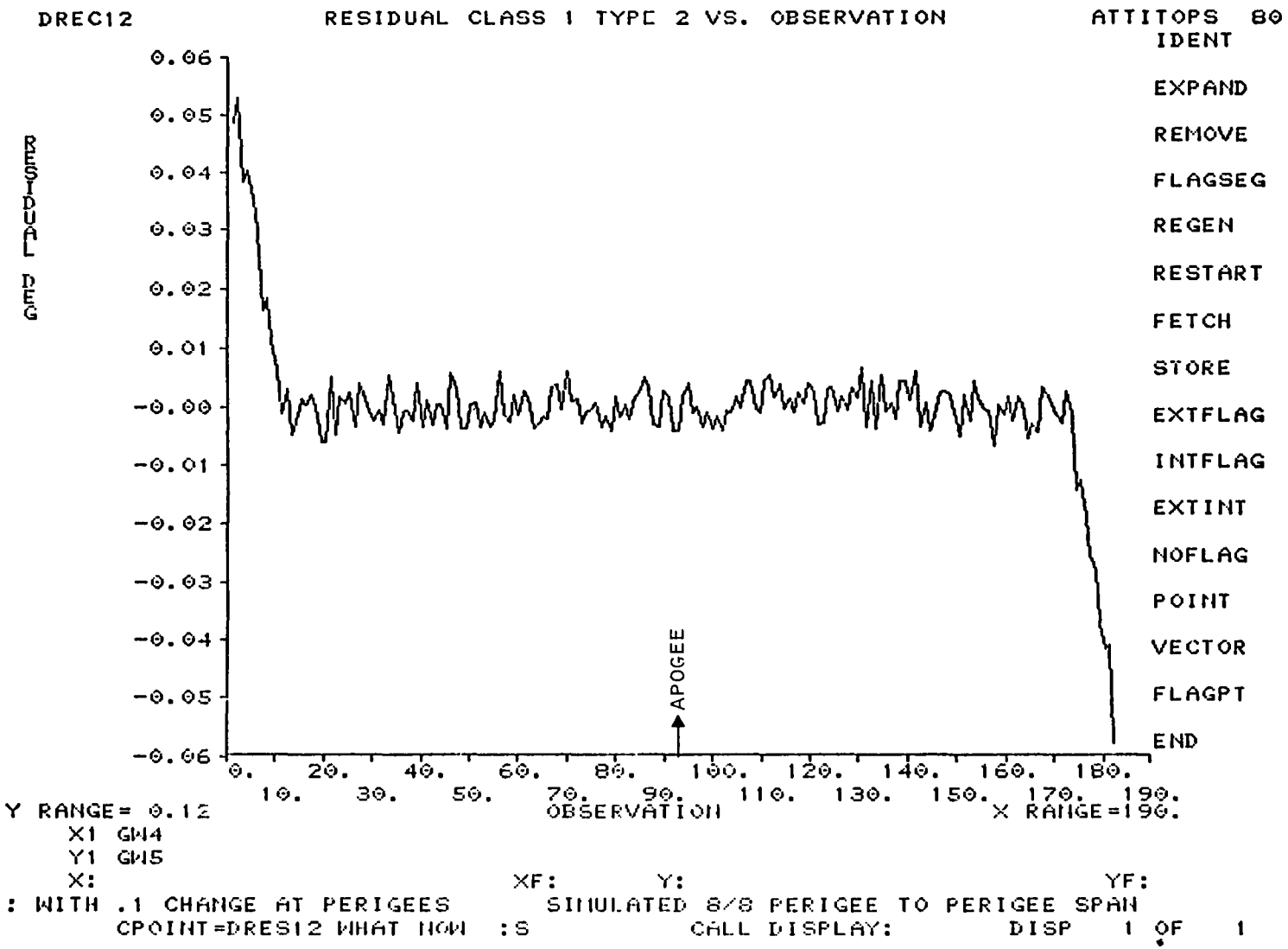

Figure 4.5-11. Nadir Angle Residuals From Simulated Data (Perigee to Perigee) With a 0.1-Degree Attitude Change at Perigee

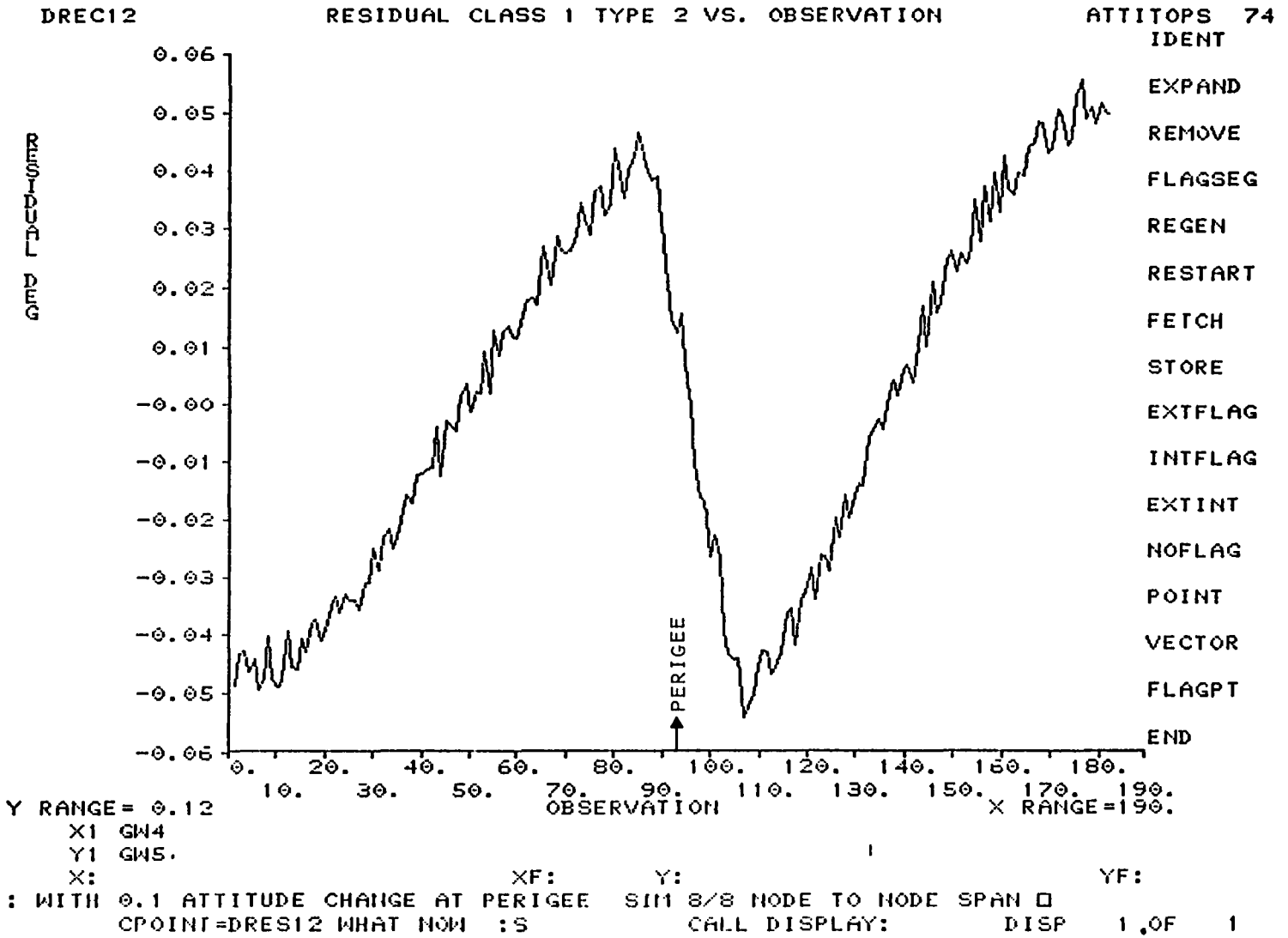

Figure 4.5-12. Nadir Angle Residuals From Simulated Data (Centered at Perigee) With a 0.1-Degree Attitude Change at Perigee

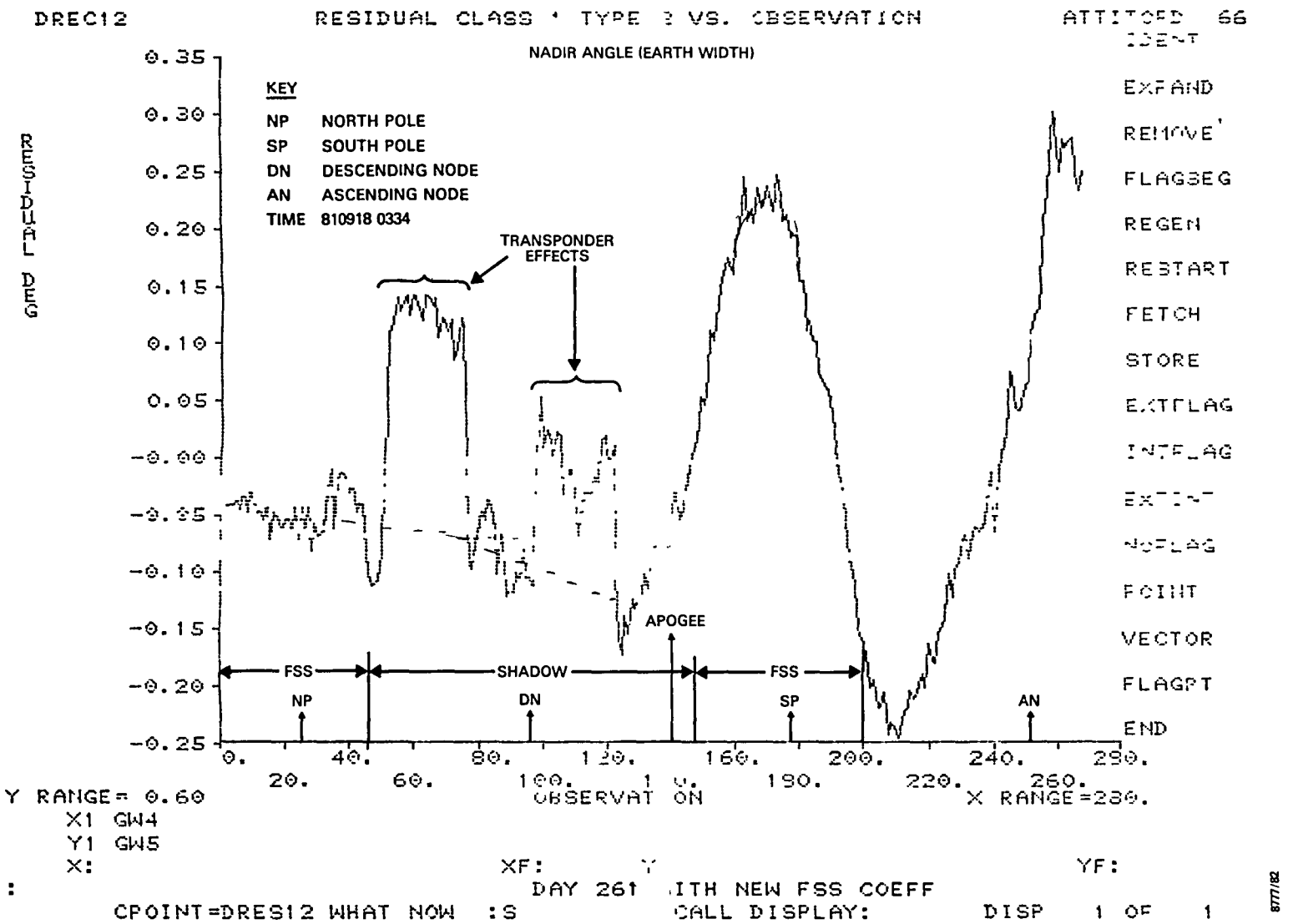

Figure 4.5-13. DE-2 Nadir Angle Residuals for a Negative Orbit Normal Attitude Mode Showing Transponder Interference Effects

spacecraft was at negative orbit normal. The effects of the operation of the spacecraft transponder can be seen in these data to cause a roll error of up to 0.15 degree. A positive roll error in this attitude mode is consistent with an increase in the sensed Earth chord. Other data showed that the IR split-to-index changes due to transponder interference were consistent with an extension of the LOS Earth horizon by 0.5 degree. The spacecraft pitch control loop responded to these errors within a fraction of a minute by offsetting the spacecraft pitch attitude +0.25 degree. Figure 4.5-14 shows residuals from the same span of data as shown in Figure 4.5-13, with a correction applied to cancel the transponder-induced errors. Still remaining in the residuals for this data span (which is centered on apogee and should look more like the residual in Figure 4.5-11) are two large 0.4- to 0.5-degree peaks. The same pattern in the residuals can be seen in data from 6 days later (at a Sun angle of 70 degrees) in Figure 4.5-15. Some of the variation at the end of this data span is characteristic of the effect of attitude motion as the spacecraft approaches perigee. These residuals were not, however, evident in data tables with low Sun angles ($\leq$ 22 degrees).

These data examples support a hypothesis that the fluctuations in the nadir angle residuals starting at the end of the shadow period for high Sun angle conditions originated with reflected IR radiation from the Sun. Figure 4.5-16 is an illustration of the DE-2 spacecraft showing the configuration of the low-gain antenna and support mast on the side of the spacecraft that is normally in shadow. It can be seen that, because of the mast (at Sun angles greater than 22 degrees), sunlight did have an indirect path into the bolometer telescope past the WHS mirror. Although special IR electronic signal blanking was provided to eliminate the thermal IR radiation from the structures viewed directly

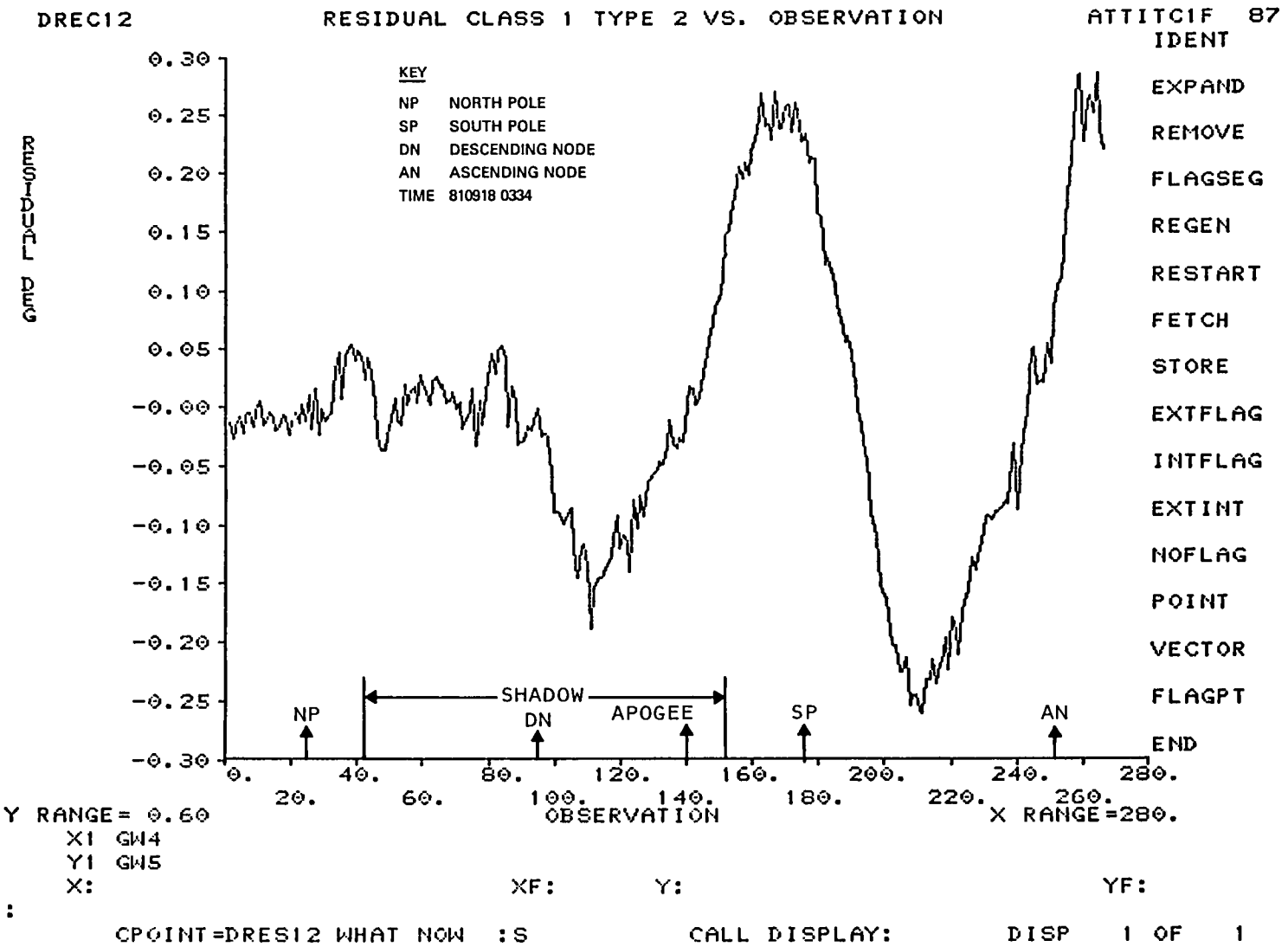

Figure 4.5-14. DE-2 Nadır Angle Residual Showing the Removal of Transponder Interference Effects

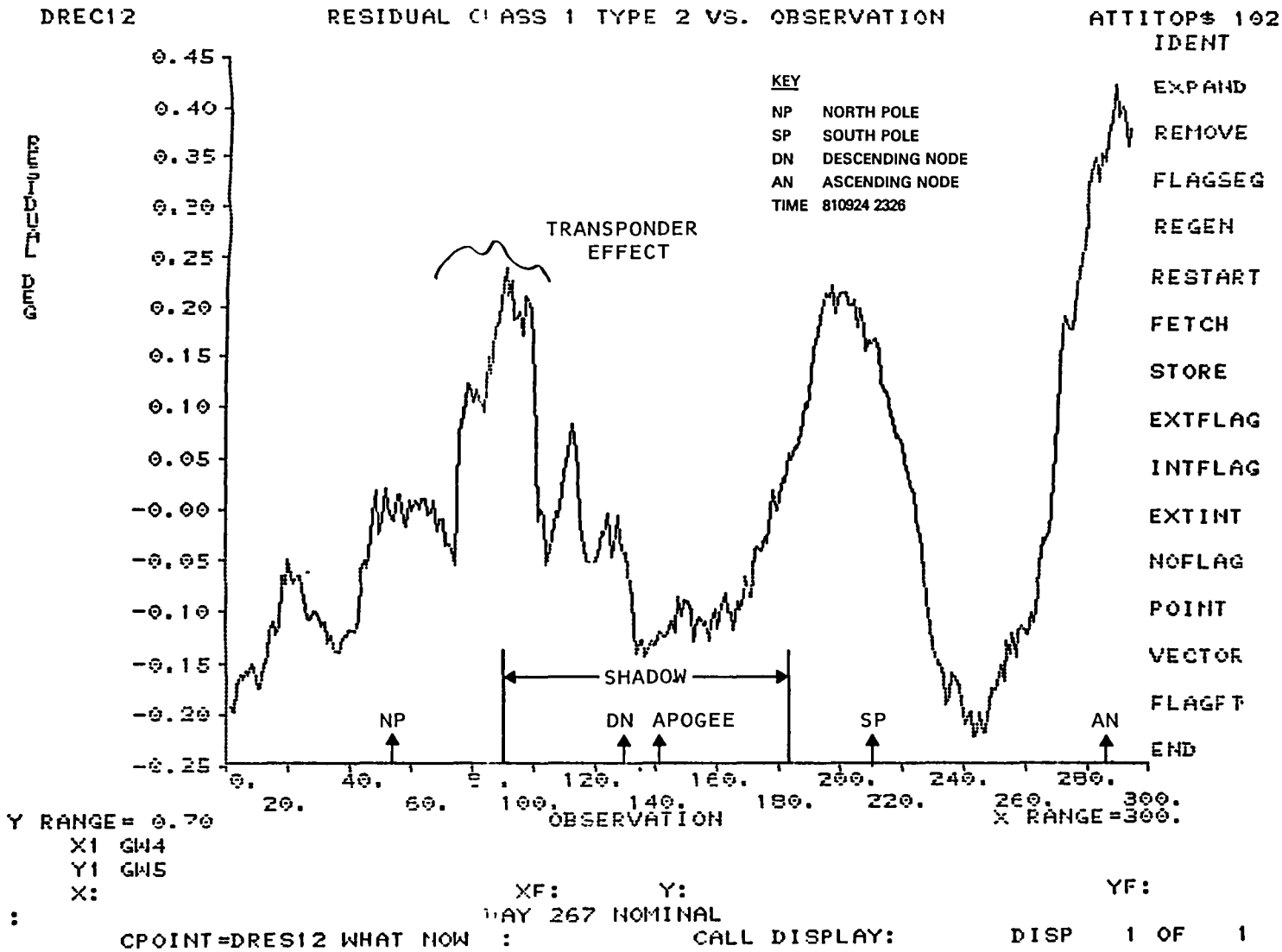

Figure 4.5-15. DE-2 Nadir Angle Residual at a 70-Degree Sun Angle for a Negative Orbit Normal Attitude

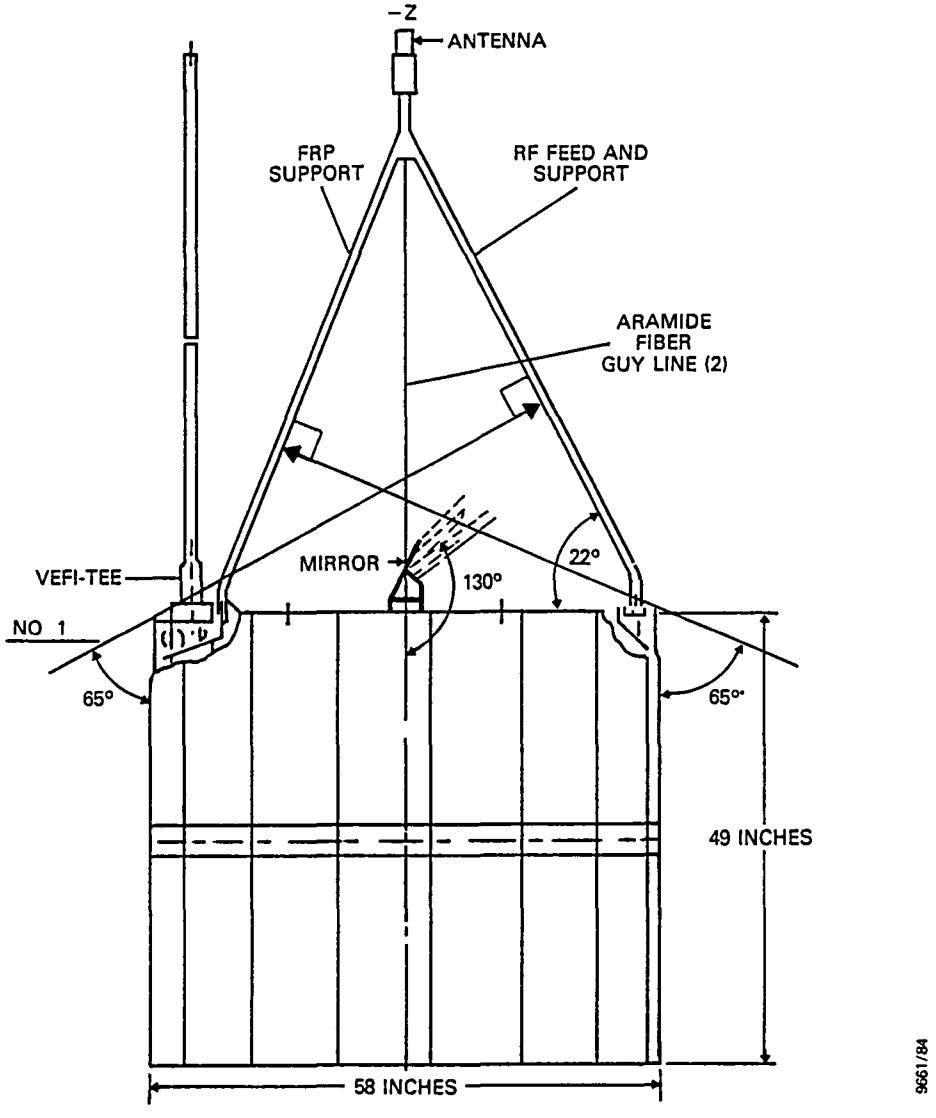

Figure 4.5-16. DE-2 Low-Gain Antenna and Support Mast

through the mirror, it is still possible for reflected sunlight to illuminate the bolometer telescope acceptance aperture at times when blanking is not active. Such an effect could modulate the bolometer output when it is viewing the cold reference of outer space. The rotating mirror thus acted as a chopper for the reflected and thermally radiated IR radiation from the radio frequency (RF) antenna support into the fringes of the bolometer FOV past the mirror.

An earlier analysis by RCA estimated the level of direct (through the mirror) interference from specularly reflected solar IR radiation off the cylindrical electrostatic probe (CEP) (Reference 44a). The RCA equation for the estimated ratio of IR energy from solar specular radiation from the AE CEP probe to Earth IR energy is

$$\frac{E_{ss}}{E_e} = \frac{\pi \gamma_s^2 W_s}{8 \theta_f^2 W_{213}} \left(\frac{R}{X}\right)$$

where E_{ss} = solar specular energy
E_e = Earth IR energy for an emittance W_{213} at 213K
γ_s = half angular width of the Sun
W_s = emittance of the Sun (W_s/W_{213} was 600)
θ_f = half angular width of the sensor FOV
R = probe radius
X = distance from the CEP to the IR scanners

For a probe radius of 0.084 centimeter and a distance of 33 centimeters, the equation yielded a ratio of 0.02. However, if this same equation is used for the DE-2 low-gain antenna support ($R \cong 1.27$ centimeters) with a distance X consistent with a path directly into the bolometer telescope past the WHS mirror (X = 60 centimeters or 23 inches), the result is a ratio of 0.15. Finally, although some flight

data analysis was performed on 3 days of data (August 7, 8, and 9, 1981) before the failure of the fine Sun sensor, no definitive conclusion could be established as to whether the IR radiance correction would have improved the accuracy of the DE-2 attitude solutions. The correction was not applied to the DE-2 definitive attitude data.

4.5.4 RESULTS AND DISCUSSION

Although the DE-2 WHS assembly was similar to the AE system, the system performance was probably poorer than the AE system. Three significant handicaps to the DE-2 system were the addition of significantly more IR background sources to the WHS end of DE-2; the location of the low-gain antenna, which caused the occurrence of RF interference (the transponder effect); and the change from a dual-sensor design to what was essentially a redundant single-sensor design.

The residuals displayed in Figure 4.5-14 were typical of the mission data and represent values twice those used in the prelaunch worst-case estimates for variations due to horizon radiance effects. A review of the procedures used to analyze the effects of horizon radiance variation on the DE-2 WHS system revealed, however, that both RCA and CSC had used a scanner rotation angle step size of 0.5 degree at the horizon for the Earth IR input pulse simulation. This step size was too coarse to reliably predict the response of the DE-2 derivative locator electronics to the intensity and shape characteristics of the Earth IR profiles. This, combined with the loss of the fine Sun sensor data for an accurate attitude reference, resulted in no significant results from the analysis of the WHS and Earth radiance model.

The review of the DE-2 mission support experience does offer a lesson, however. It showed that mistakes are often repeated. The transponder interference problem was experienced in the 1960s, and design guidelines for dealing with it were first developed at that time.

4.6 EARTH RADIATION BUDGET SATELLITE

The IR scanners on ERBS are similar to those used on Seasat; only the width of the IR passband and the electronics signal processor are different. An analysis was performed primarily to compute pitch and roll corrections to compensate for the effects of Earth IR horizon variations for application in the ground support ADS. The work described here is documented in References 12, 28, and 45. During ERBS mission support, the ADS is used to evaluate the accuracy of the ERBS onboard gyrocompass attitude solutions and to perform daily definitive attitude data processing if the accuracy of the gyrocompass solutions proves to be insufficient. Horizon radiance analysis for ERBS coincided with the analysis to evaluate the accuracy of the HRDB. During this process, it was discovered that the systematic pitch and roll corrections based on the HRDB could be improved.

The source of errors in the HRDB and the method of improvement were reported in the Nimbus/LIMS-HRDB radiance profile comparison analysis (Reference 12). A direct comparison of RAOBS July temperature profiles with those derived from Nimbus LRIR data supported this conclusion, as discussed in Section 2. The overall effect of the improvements to bring the HRDB into agreement with the Nimbus/LIMS and LRIR data was to increase the amplitude of the systematic pitch and roll correction predicted for ERBS.

4.6.1 MISSION REQUIREMENTS AND HARDWARE

ERBS was launched on October 5, 1984, by the Space Transportation System (STS). The spacecraft is illustrated in Figure 4.6-1. The mission can be summarized as follows:

- Orbit--Circular frozen at 610-kilometer altitude and 57-degree inclination; argument of perigee controlled to stay near 90 degrees; Sun passing from

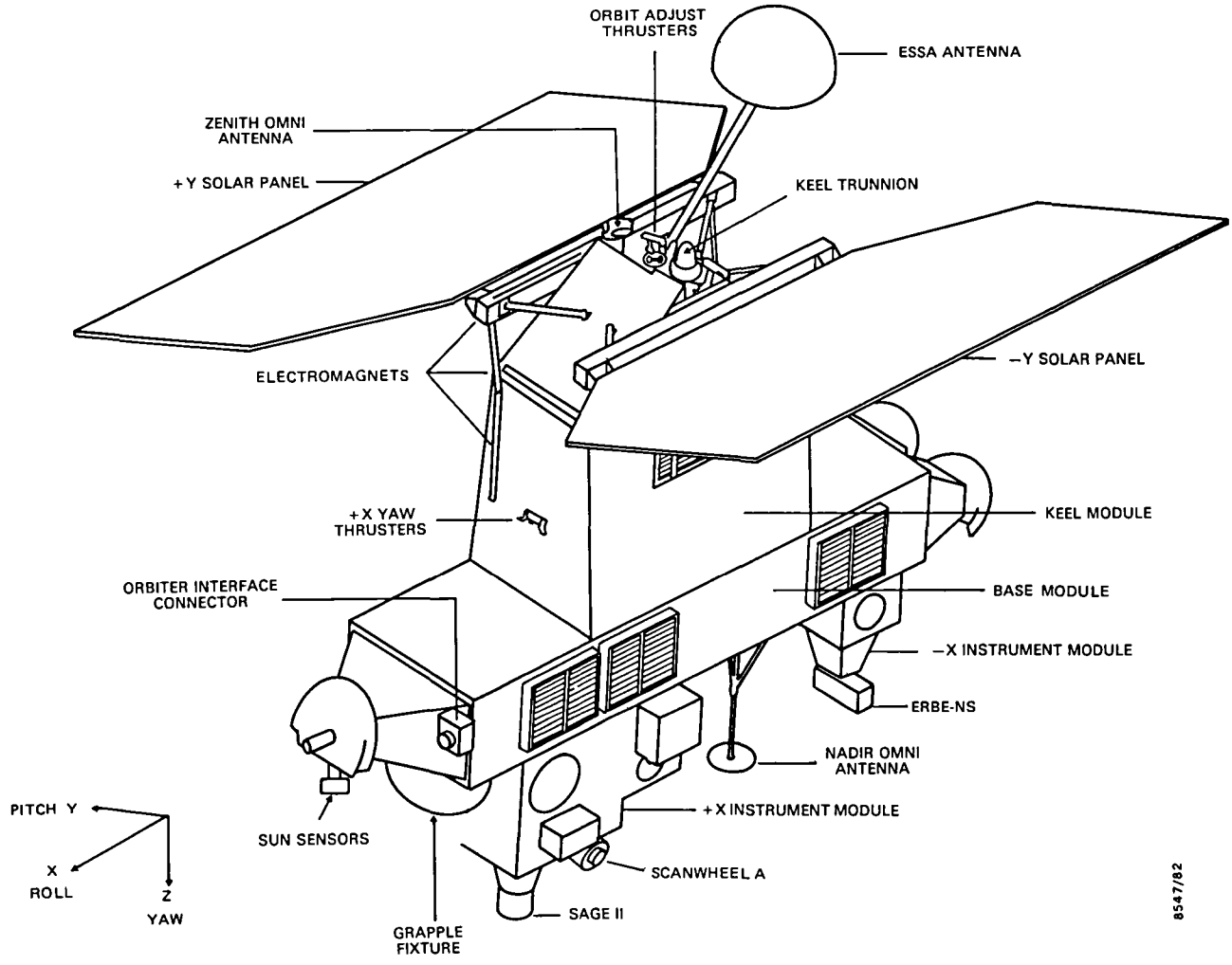

Figure 4.6-1. Earth Radiation Budget Satellite (ERBS)

the negative to the positive side of the orbit plane on approximately October 15, 1984

- Attitude configuration--Three-axis stabilized to null pitch, roll, and yaw in a geodetic reference frame; yaw equal to 0 degrees when the Sun is in the negative orbit normal hemisphere and 180 degrees when the Sun is in the positive orbit normal hemisphere; 180-degree yaw maneuvers required every 40 days
- Attitude determination hardware
  - Onboard input to the analog gyrocompass processors
    - -- IR scanner pitch and roll
    - -- Pitch, roll, and yaw rates from either of two 3-axis IRUs
  - Input to ground support software
    - -- Dual or single ITHACO Scanwheel IR horizon scanners for pitch and roll
    - -- Two Adcole two-axis fine Sun sensors for yaw and bias determination
    - -- Two three-axis IRUs for pitch, roll, and yaw rates
    - -- Three-axis magnetometer for coarse attitude determination
- Attitude control hardware
  - Pitch axis momentum wheel for pitch control, driven by IR-scanner-processed pitch error and rate signal
  - Roll/yaw control by pitch axis angular momentum inertial rigidity; roll error drives

magnetic dipole torque rods for pitch axis precession to orbit normal

- Differentially driven Scanwheel speed and magnetic dipole torque rods for nutation control
- Dipole torque rods for angular momentum control
- Four 0.45-lb hydrazine thrusters for 180-degree yaw turns
- Off-modulation of four 0.45-lb ΔV thrusters during orbit maneuver; thruster modulation by gyrocompass attitude error output
- Magnetic dipoles for acquisition mode and to lock on Earth magnetic field during attitude control emergencies

- Accuracy requirement
  - Nominal mission attitude--$\pm$0.25 degree (3σ) for pitch and roll and 1.0 degree (3σ) for yaw without Sun sensor data
  - Nominal attitude rates--$\pm$0.005 degree per second for pitch and roll and $\pm$0.01 degree per second for yaw without Sun sensor data
- Ground support system--Interactive system to provide
  - Near-real-time spacecraft attitudes for health and safety monitoring
  - Quality assurance of onboard analog attitude and attitude rate data
  - Backup 180-degree yaw maneuver planning; primary 180-degree yaw maneuver monitoring
  - Evaluation and maintenance of onboard electronic biases

- Data processing requirements
  - Near-real-time attitudes, one pass per day
  - Definitive processing--24 hours of data per day if requested, based on accuracy of onboard solutions
  - Weekly sensor and gyro bias determination
  - Weekly sensor performance monitoring
- Problems encountered
  - Transponder activity during contacts with the Tracking and Data Relay Satellite (TDRS) induced pitch sensing errors and stimulated control system activity.
  - Error in the Sun sensor assembly wiring led to an initial problem in interpreting fine reticle bits; this required a change in ground software to correct the error.

Section 3 discusses the prediction of ERBS pitch and roll errors induced by the nonuniformity of the Earth IR image and methods of assessing the accuracy of such predictions. CSC performed an analysis (Reference 45) to compute the pitch and roll correction required to reduce the effects of the nonuniformity of the Earth IR image on the mission attitude data. One objective of the analysis was to establish the specifications for the software to simulate the Earth-radiance-induced ERBS IR scanner pitch and roll output. Another was to evaluate the effects of Sun interference in the IR scanners. ITHACO, Inc., also performed an analysis to test the IR scanner system with simulated bolometer input radiance data.

The ERBS IR scanner locator logic and scan geometry are similar to those of the Seasat IR scanners. However, to

improve the performance of the system, the IR passband was narrowed. Because of the reduction in the IR signal that resulted from this, the time constants for the Earth pulse processing electronics were changed to increase the signal-to-noise ratio. The threshold adjustment zones were also changed. Figure 4.6-2 illustrates the passband for the IR scanners, and Table 4.6-1 lists the ERBS IR scanner modeling constants (Reference 45). The threshold adjustment zones for ERBS are 20 to 25 scan degrees from the AOS horizon and 15 to 20 scan degrees from the LOS horizon. The threshold voltage is continuously adjusted to be one-half the average voltage detected between these limits. The modeling of the optics was improved for ERBS to estimate the effects of FOV distortion by the rotating prism lens. (The FOV geometry used in the ERBS HRMU was discussed in Section 3 and is shown in Figure 3-2.) Figure 4.6-3 shows the circuit model for the ERBS IR scanner electronics simulation.

4.6.2 PREDICTED ATTITUDE ERRORS

The HRMU was used to predict the errors induced in the IR scanner pitch and roll output by variations in the Earth's IR intensity with latitude and season. Earth radiance profiles generated by integrating the simulated Earth IR spectra (from the LOWTRAN 5 program) over the ERBS IR passband were used as the Earth model input to the HRMU. Profiles were supplied for each month of the year at nine 20-degree-latitude intervals centered on the Equator. The profiles represented a longitudinally averaged Earth radiance model. Other input to the HRMU consisted of the nominal ERBS orbital parameters and the IR scanner geometry scan cone size, spin rate, and alignment in the spacecraft coordinate reference frame. The simulation was performed assuming a null attitude in the ERBS attitude reference frame and a spherical hard Earth. Thus, in the simulation, only the horizon profiles and optical and electronics response to

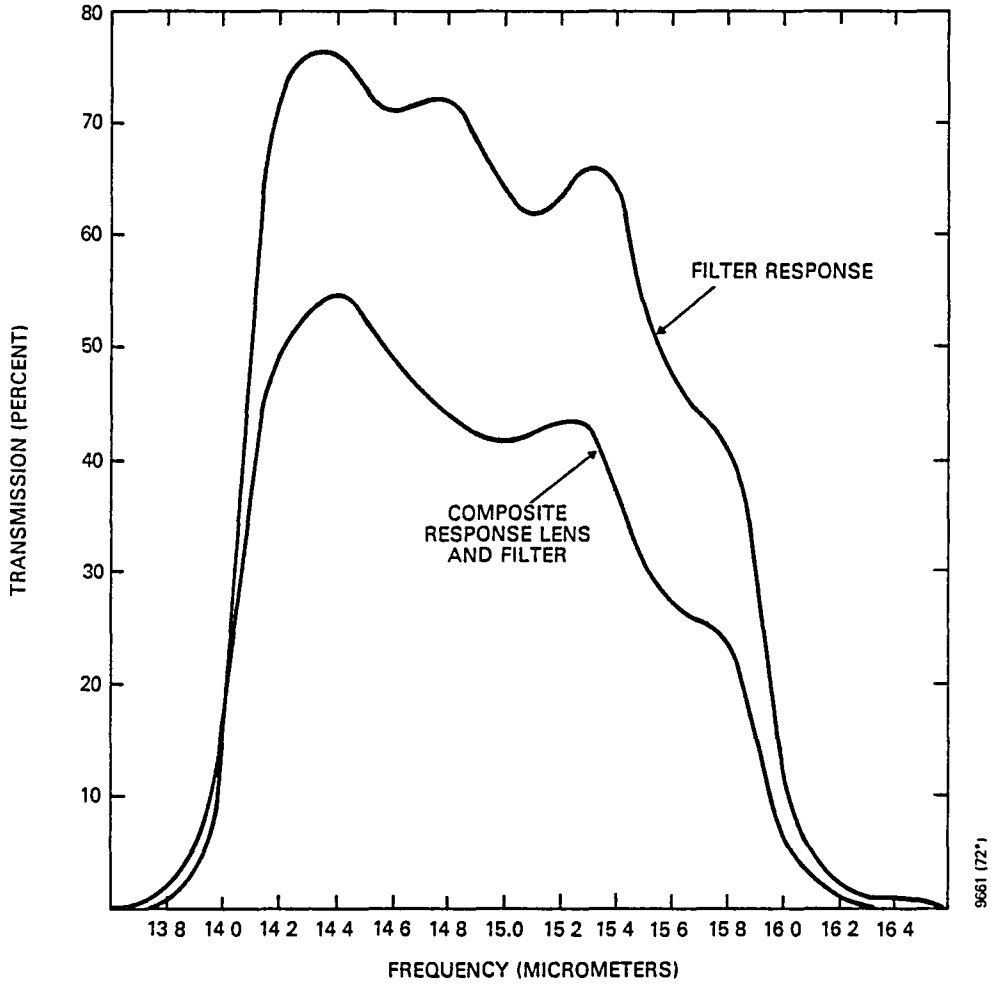

Figure 4.6-2. ERBS IR Optical Assembly Spectral Response

Table 4.6-1. HRMU Input Parameters

PARAMETER	DESCRIPTION	ERBS NOMINAL VALUE
α	SCANNER TILT ANGLE	+10 DEGREES (A) −10 DEGREES (B)
λ	SCANNER CONE ANGLE	+45 DEGREES (A) 135 DEGREES (B)
E	EARTH RADIUS	6367 47 KILOMETERS
E + S	ORBITAL RADIUS	6967.47 KILOMETERS
h_o	NOMINAL HORIZON HEIGHT	41 8 KILOMETERS
a	LOCATOR CONSTANT	22.5 DEGREES
b	LOCATOR CONSTANT	2.5 DEGREES
c	LOCATOR CONSTANT	17 5 DEGREES
d	LOCATOR CONSTANT	2 5 DEGREES
η	ROTATION ANGLE AT NOMINAL HORIZON	66 9 DEGREES
β	THRESHOLD CONSTANT	50 PERCENT
Q	FOV DISTORTION	1 80
δ	FOV SIZE CONSTANT	0 5 DEGREE
ω_0	WHEEL SPIN RATE	209.4 RADIANS/ SECOND (2000 RPM)
T_1	PEAKING AMPLIFIER TIME CONSTANT	18 MICROSECONDS
T_2	PEAKING AMPLIFIER TIME CONSTANT	98 MICROSECONDS
T_3	DC RESTORER AMPLIFIER TIME CONSTANT	103 4 MICROSECONDS
T_4	PREAMPLIFIER TIME CONSTANT	18 MICROSECONDS
T_5	PREAMPLIFIER TIME CONSTANT	15 8 MICROSECONDS
T_6	THRESHOLD NORMALIZER TIME CONSTANT	180 MICROSECONDS
T_C	THRESHOLD NORMALIZER CHARGING TIME CONSTANT	3200 MICROSECONDS
ω_a	NOISE FILTER AMPLIFIER FREQUENCY	1437 RADIANS/SECOND
ω_b	NOISE FILTER AMPLIFIER FREQUENCY	1468 RADIANS/SECOND

9617 (82)/84

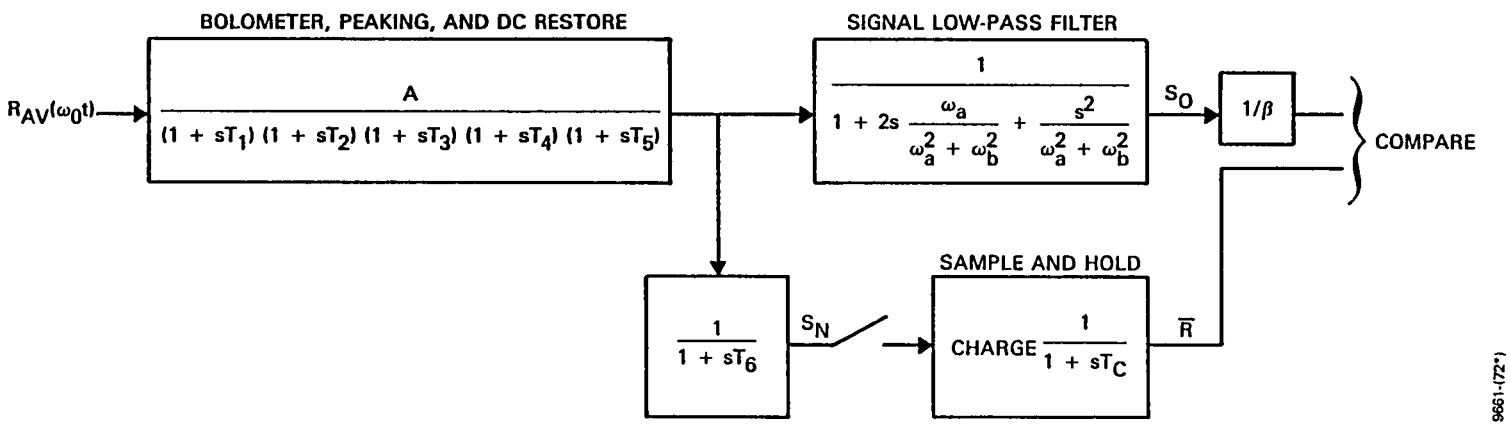

Figure 4.6-3. ERBS Earth Horizon Detection and Automatic Threshold Adjustment Circuit Model Used by the HRMU

these profiles caused the nonzero dual IR scanner error output.

4.6.2.1 ERBS IR Model Errors

Figures 4.6-4 through 4.6-7 illustrate the dual IR scanner errors predicted for the Earth IR model with the RAOBS temperature profiles for January and April. The ERBS ADS uses the errors predicted for January and April, along with similar results for the other 10 months, to correct the ERBS IR scanner pitch and roll data for the definitive data support processing mode. Extensive analysis has been performed to evaluate the accuracy of the predicted response shown in Figures 4.6-4 and 4.6-5. The errors in the modeled response of the IR scanners to Earth IR radiation originate from the Earth profile model, the IR scanner optics model, and the horizon detection electronics model.

Errors in the Earth profile model are described as differences between the IR image of the Earth represented by the model and the actual image of the Earth experienced by the flight system at the time of interest. The Earth model is an average model and, therefore, can only represent an average for any given month and latitude. Variations in the actual Earth IR radiation relative to the model will occur due to errors in the model and due to longitudinal variations in the actual Earth IR radiance from stratospheric (>20-kilometer altitude) and tropospheric (<20-kilometer altitude) temperature and cloud cover variability.

The analysis described in Section 2 comparing the Nimbus/LIMS data with its simulated counterpart showed that the RAOBS/LOWTRAN 5 average Earth model underestimates the IR brightness changes between the Equator and the poles for the winter and summer seasons. In particular, the winter pole is modeled too bright, and the summer pole is modeled too dim. The analysis also showed that longitudinal variability

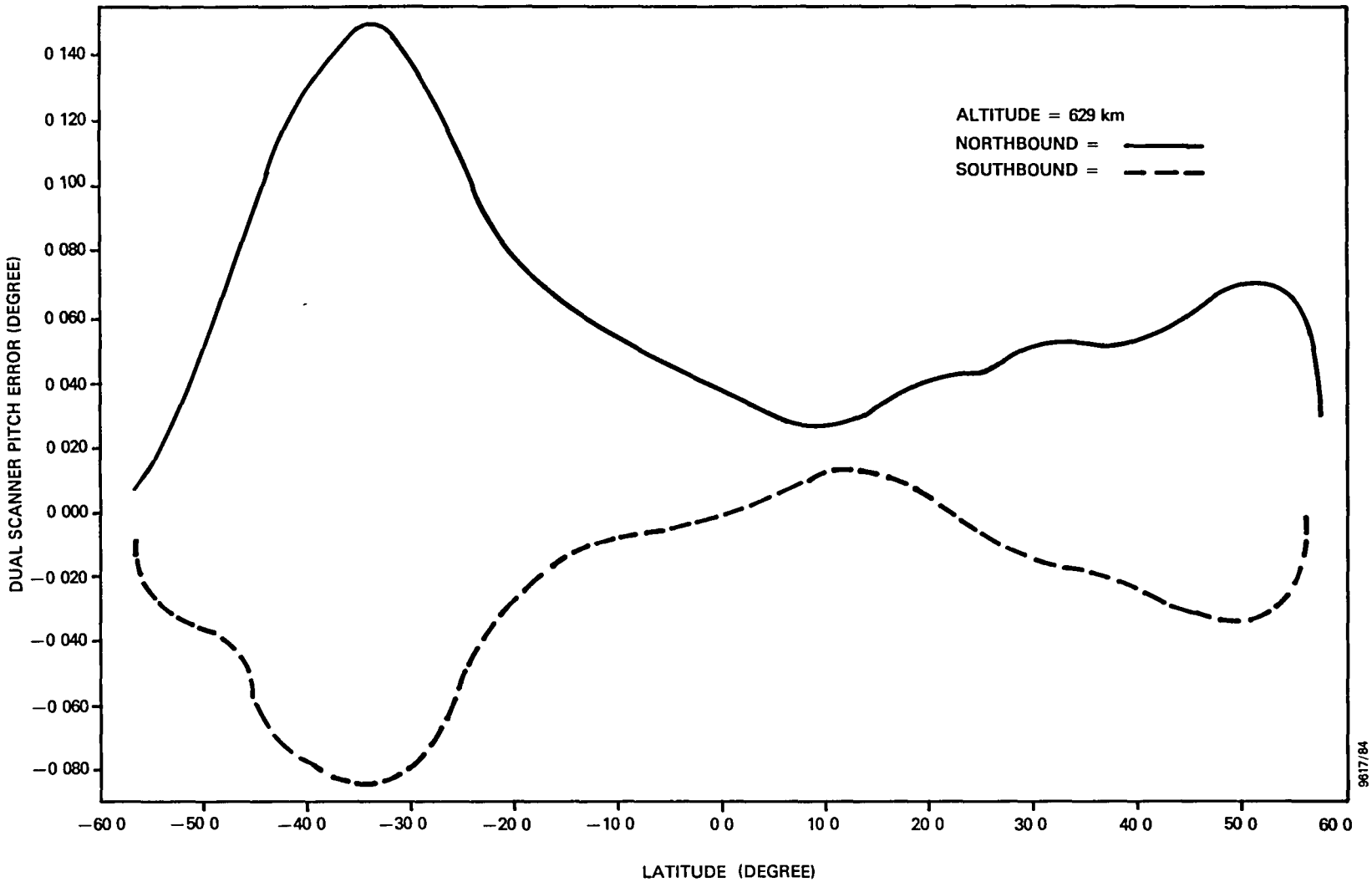

Figure 4.6-4. ERBS Dual IR Scanner Pitch Errors for January Radiance Data

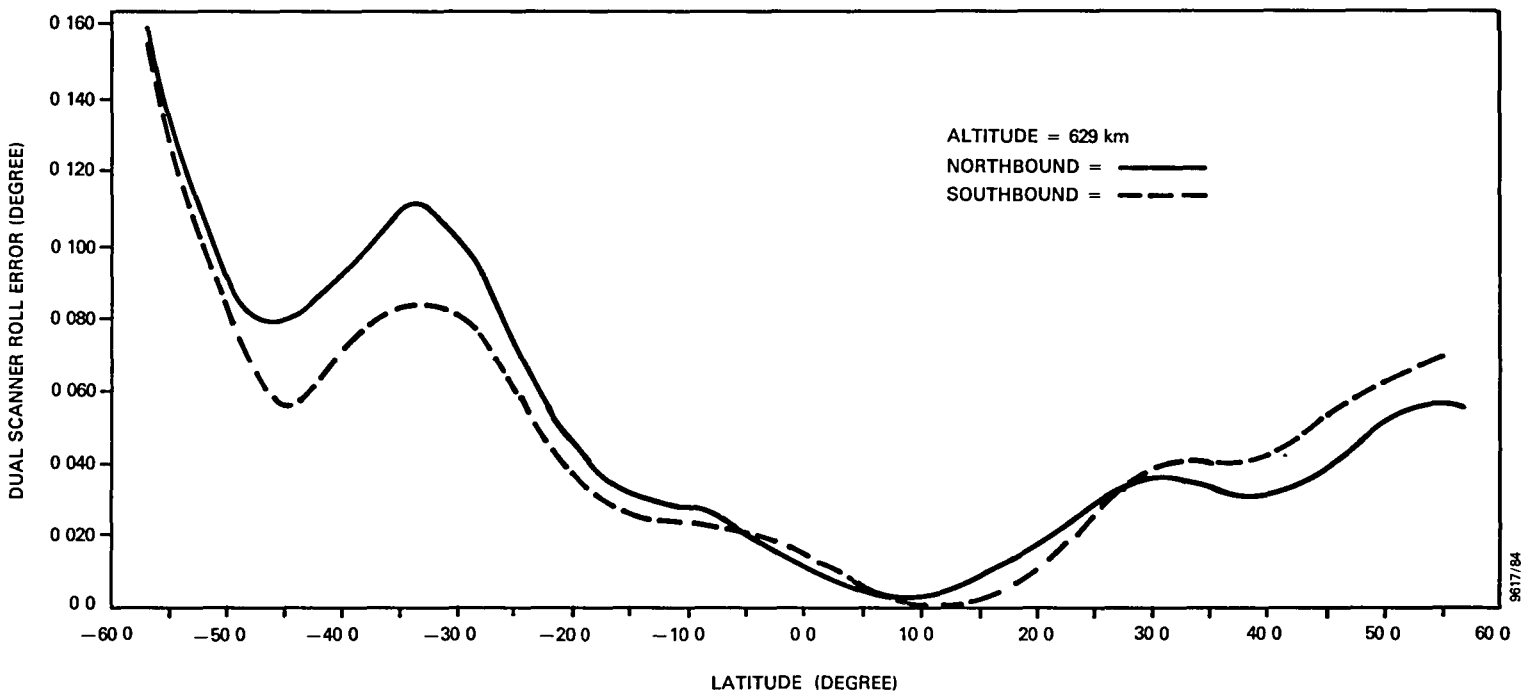

Figure 4.6-5. ERBS Dual IR Scanner Roll Errors for January Radiance Data

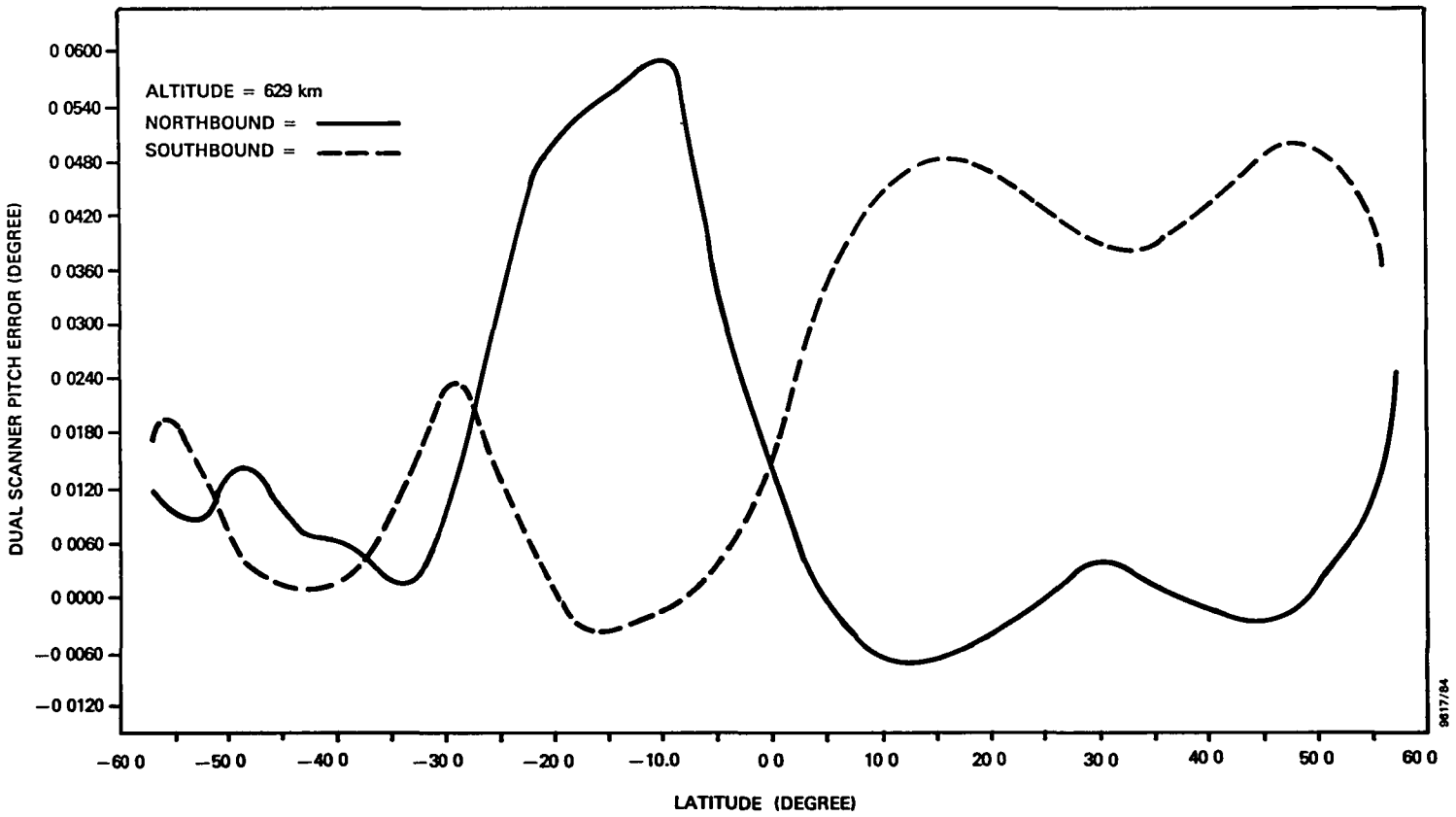

Figure 4.6-6. ERBS Dual IR Scanner Pitch Errors for April Radiance Data

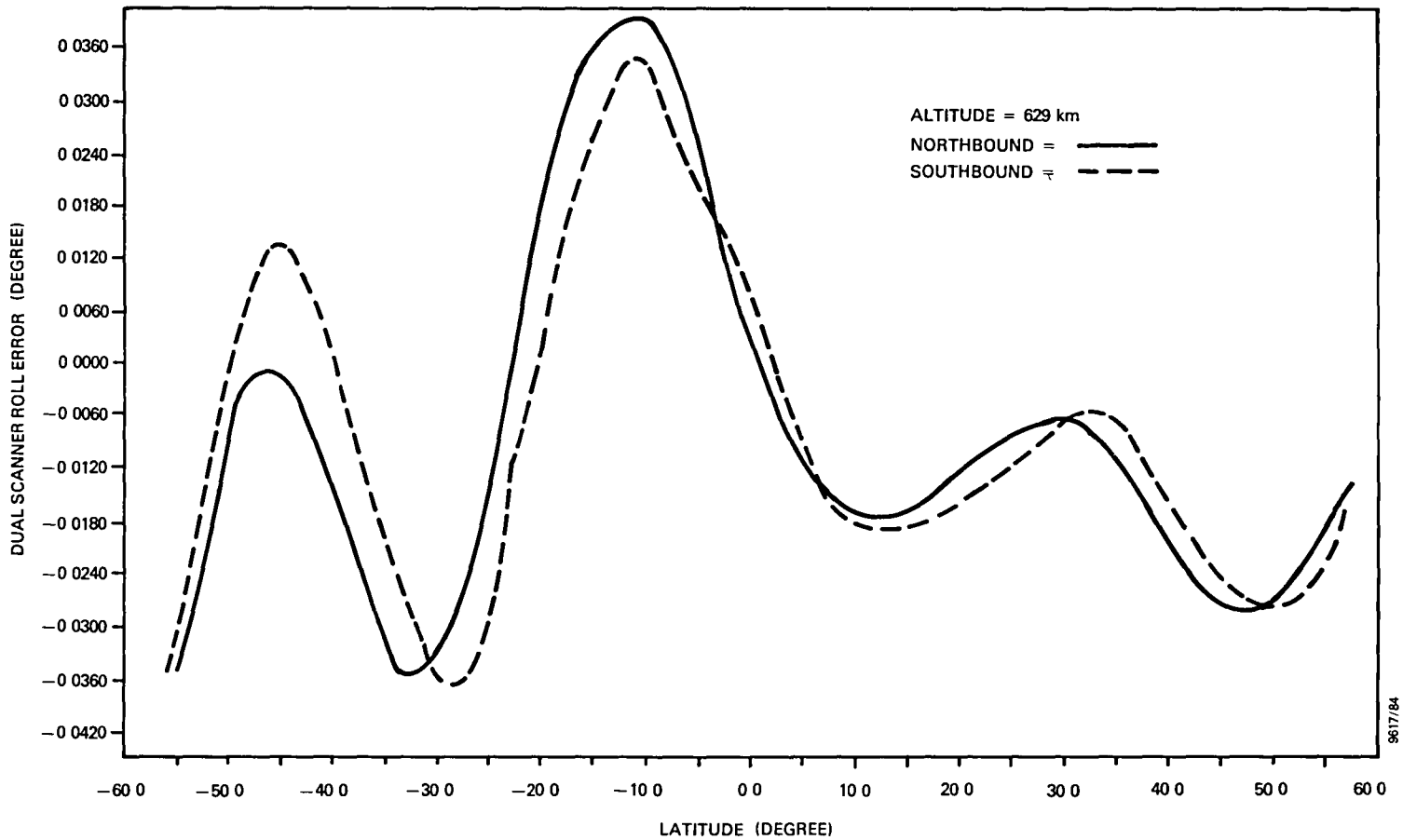

Figure 4.6-7. ERBS Dual IR Scanner Roll Errors for April Radiance Data

is extreme for polar winter conditions. Thus, the variability of the actual Earth IR image during these seasons at these latitudes will cause deviations in the flight data relative to the model. For ERBS, this variability was primarily due to stratospheric phenomena with time periods of a few days to a few weeks and with a geographic extent of one-fourth of a hemisphere.

The result is that variations in the flight data are expected to be a significant fraction of the total error in the predicted response of the IR scanners to the average model of the Earth IR image in the winter hemisphere. The predicted response of ERBS to Earth IR radiation in January consistently underestimates the response for the winter hemisphere with a peak difference of -0.1 degree for pitch and -0.14 degree for roll. The Nimbus/LIMS analysis indicated that the response for the northbound track in Figure 4.6-4 at 50 degrees latitude should be increased by 0.1 degree, and that the response for the southbound track at the same latitude should be decreased by 0.07 degree. The ERBS predictions underestimate the brightness for the summer hemisphere less severely, resulting in a peak systematic error of -0.05 degree. The Nimbus/LIMS analysis indicated that the response for the northbound and southbound tracks in Figure 4.6-4 at -35 degrees latitude should be increased by 0.05 degree.

The Nimbus/LIMS analysis also indicated, however, that the more extreme errors in the prediction of pitch and roll responses occur in the hemispheres where the flight data are expected to be most variable due to longitudinal radiance variability. The variation in the flight pitch and roll data relative to the model for these effects at 60^{o}N latitude in January is expected to reach extremes as high as

0.5 degree, with expected typical excursions of 0.25 degree. The duration of these excursions can be up to one-quarter orbit (25 minutes).

The other sources of error in the modeled response of the IR scanners to Earth IR radiation were also analyzed. No significant errors were encountered as a result of failure to incorporate the detailed IR scanner optics model (Section 3.2). CSC analysis did indicate some sensitivity of the predictions to approximations in the horizon detection electronics model. A more detailed discussion of this analysis (Reference 29) is presented in Section 3.5. The analysis was performed to determine the effect of approximating the ERBS IR scanner horizon detection electronics with a Seasat-like three-component transfer function and to determine the accuracy and stability of the computational procedure for a range of values of model parameters. The results of the analysis indicated variation in the computational model of about $\pm$0.05 degree. The more detailed optics and electronics models specified for ERBS produced results that were within 0.03 degree of the results produced with the single three-component transfer function model based on the Seasat HRMU (Reference 12). Furthermore, the results using a single-transfer-function approach agreed with those using both branches of the Earth pulse processing circuit (one for Earth detection, the other for threshold determination) as implemented in the ERBS HRMU. It was thus concluded that the electronics simulations are consistent as long as the timing characteristics (rise time and lag time of the pulse processing circuit) are preserved.

One limitation of the CSC approach to the electronic circuit simulation is the failure to model nonlinear effects such as pulse amplitude limiting and baseline restoration. This problem was addressed by ITHACO (Reference 46). Their analysis used simulated bolometer pulses that were generated

by CSC from the Earth IR model for each of the 12 months of the year using a detailed optics model. These Earth pulses were input to ITHACO's detailed digital model of the electronics incorporating the nonlinear components. The results of the ITHACO simulation for bolometer pulses generated from the January Earth data are illustrated in Figures 4.6-8 and 4.6-9. Overlaid on the ITHACO results (-) are the CSC results (X) corresponding to the same January radiance model and latitudes computed in the ITHACO analysis. As the figures show, the agreement is well within the 0.05-degree estimate of computational error attributed to the CSC results in this report. The roll error, however, presented a problem. To place the CSC results on the figure with the ITHACO results, the CSC results had to be multiplied by -1. The source of the discrepancy had not been resolved at the time of this report.

4.6.2.2 ERBS IR Scanner Sun Interference Effects

Both CSC and ITHACO estimated the effects of direct and near-direct impingement of the Sun on the space portion of the ERBS IR scan path. The CSC analysis (Reference 28) was based on estimates of the impulse response characteristics of the IR scanner signal processing electronics and a phenomenological analysis of the pulse width discrimination (Sun discrimination) circuit. The ITHACO analysis (Reference 46) used simulated Sun IR pulses, generated by CSC with the detailed optics model, to drive the bolometer input of ITHACO's digital simulation of the IR signal processor.

Figure 4.6-10 illustrates the CSC analysis for estimating the dual-scanner pitch and roll error from Sun interference at spacecraft sunrise. Sunrise is illustrated in row 1 by the processed Earth pulse arranged chronologically. The response of the ERBS Sun discriminator circuit elements to the AOS-to-index logic pulse (H_1 pulse, row 2) is illustrated

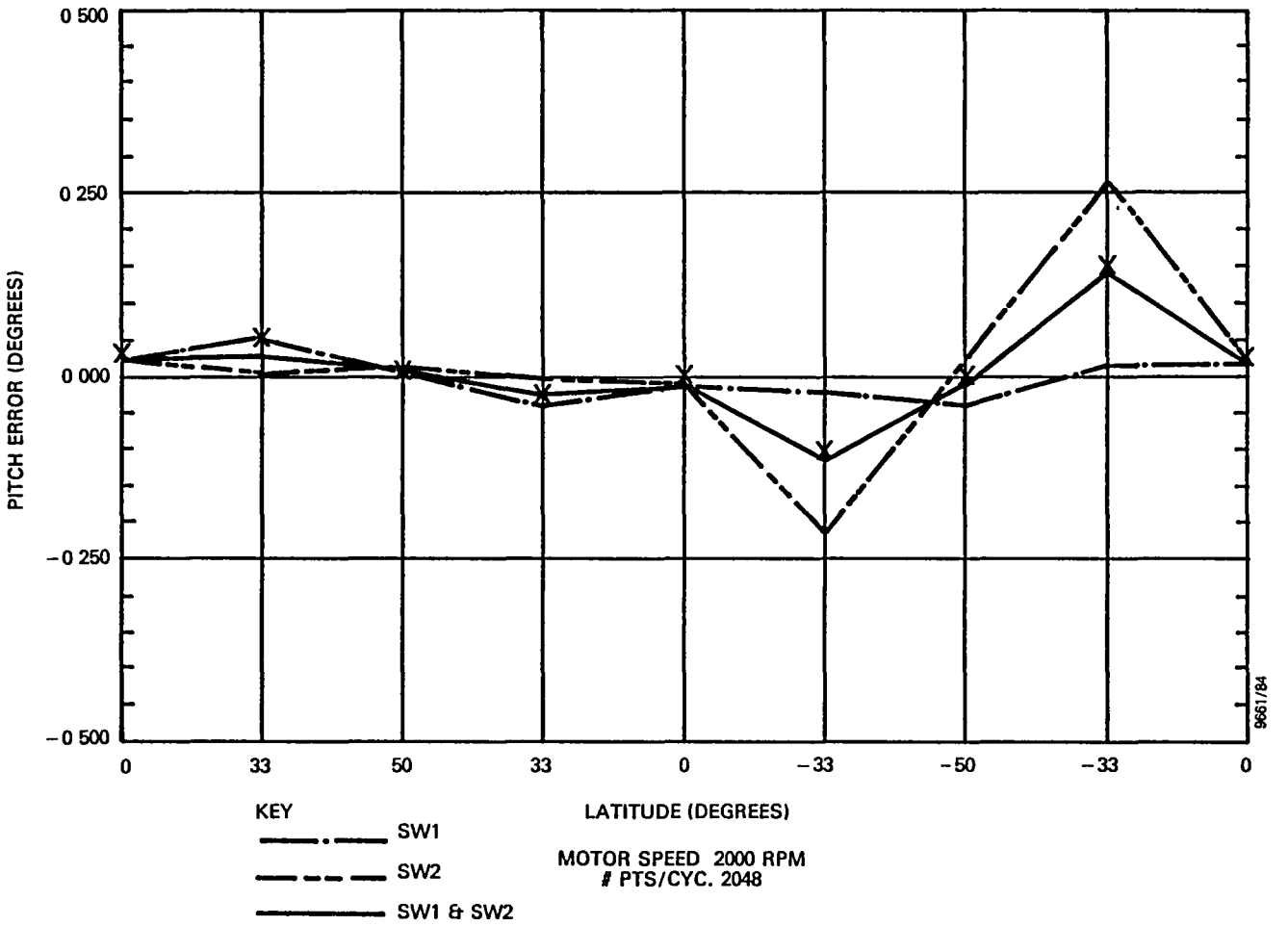

Figure 4.6-8. Pitch Error Computed by ITHACO (-) and CSC (X) for the January Radiance Model

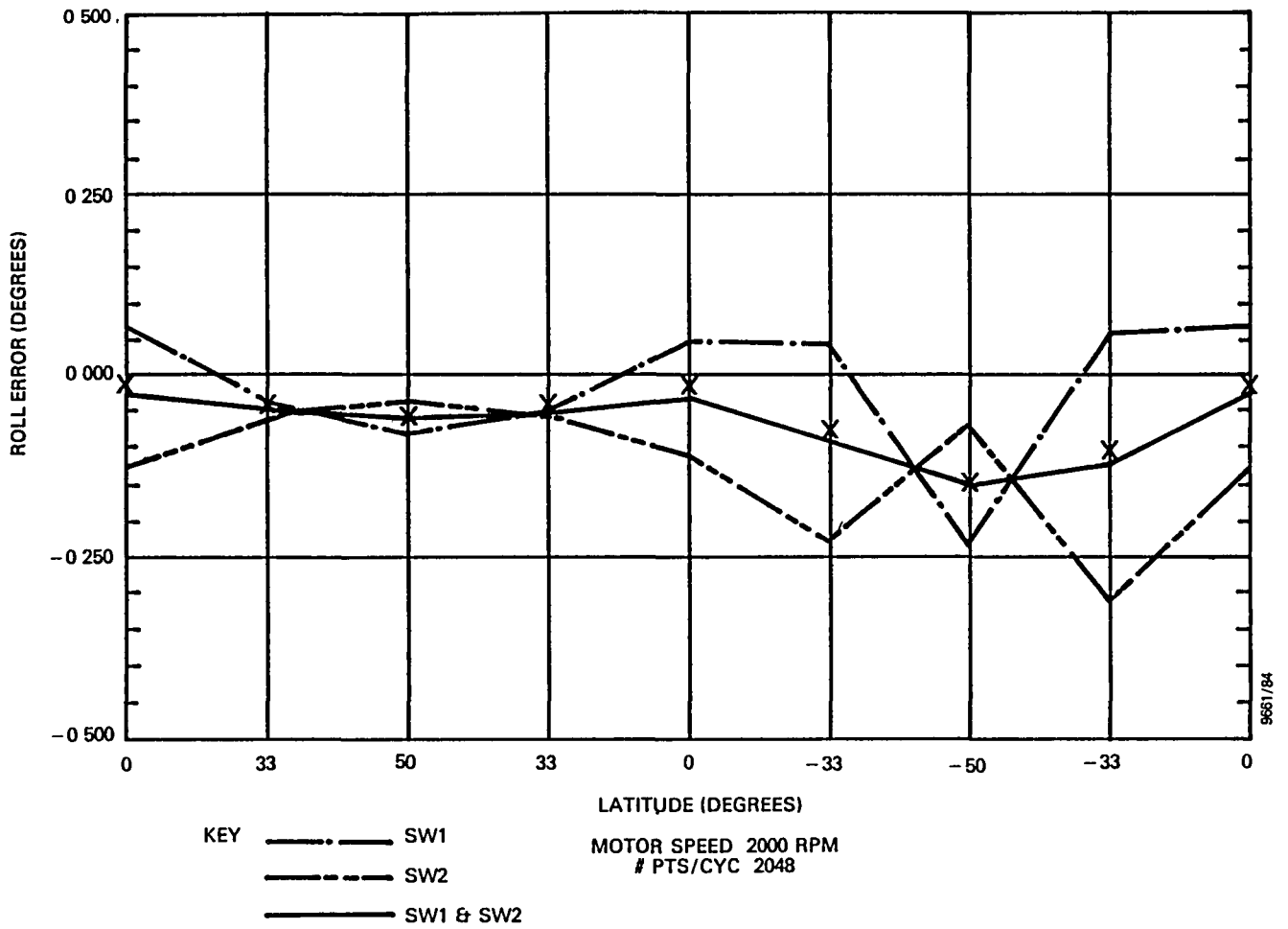

Figure 4.6-9. Roll Error Computed by ITHACO (-) and CSC (X) for the January 'Radiance Model (Note: CSC results were multiplied by -1.)

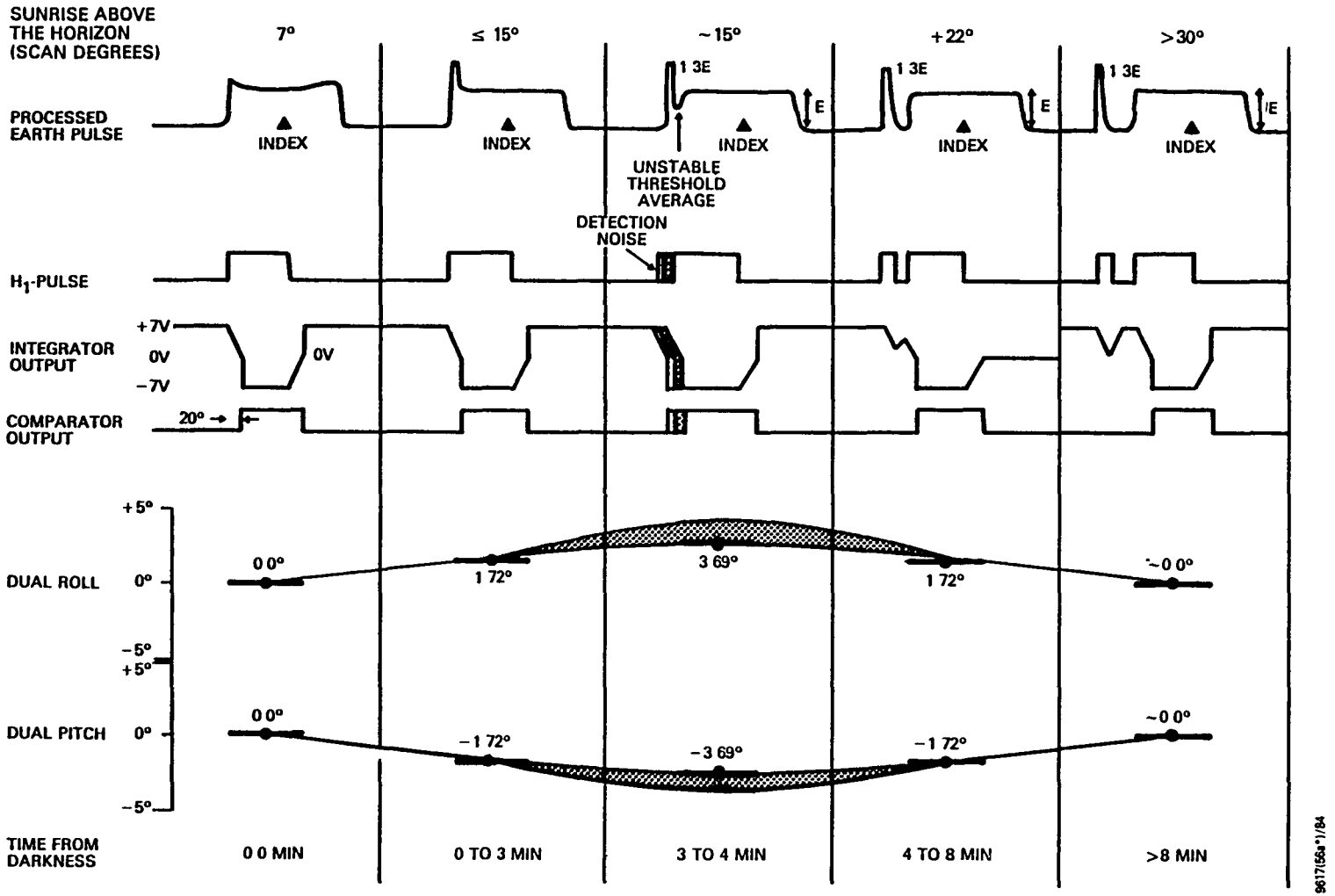

NOTE FOR THE SINGLE SCANNER RESPONSE, PITCH AND ROLL ERRORS SHOULD BE DOUBLED

Figure 4.6-10. Evaluation of Sun Interference Effects in the IR Scanner Signal Processor at Sunrise

in rows 3 and 4. The resultant roll and pitch errors are shown in rows 5 and 6. The shaded areas represent regions of unstable performance anticipated by the occurrence of a highly time-dependent trough at the threshold-level adjustment zone of the processed Earth pulse. Figure 4.6-11 illustrates a similar analysis of the characteristics of Sun interference at sunset. The peak amplitude of the errors predicted by CSC for sunrise and sunset interference depends on assumptions made about the Sun impulse response width, which varies with the geometry of the sensor FOV. A degree of uncertainty exists in the FOV analysis because the effects of scattered sunlight were not analyzed.

The ITHACO analysis, performed only for the sunrise geometry, studied nine locations and intensities for the Sun. Figure 4.6-12 illustrates the Sun, Earth, and FOV geometry for these tests. The results are summarized in Table 4.6-2. Comparison of these results with the CSC results is difficult because only a few cases are similar (simulations #1, #2, and #3). The results must be halved to convert them to equivalent dual IR scanner errors. The evolution of the errors from sunrise to a few minutes beyond sunrise is not analyzed, and larger errors appear at sunrise. The absence of a larger error in simulation #4 indicates that the CSC assumption for the width of the Sun impulse response was larger than the simulated response used by ITHACO. Thus, the peak error conditions were not simulated by ITHACO. These would occur at a scan angle slightly closer to the horizon than depicted for simulation #4.

Both analyses provide information about the Sun interference response. Larger errors are estimated for the interference at sunrise by the ITHACO simulation than by the CSC phenomenological analysis. It could be concluded that, if this indicates the starting point error for the sunrise interference, peak errors could equal or exceed those predicted by

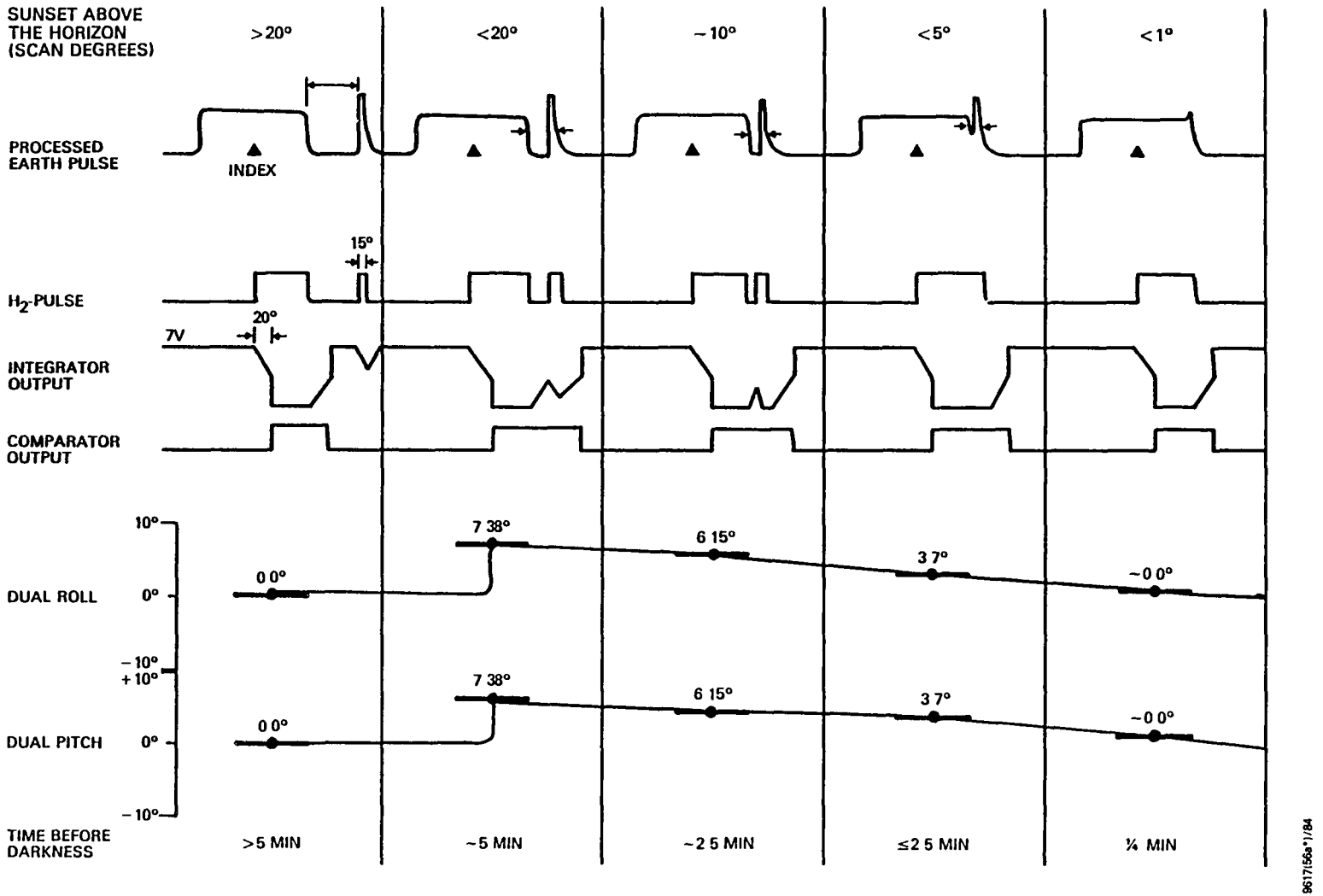

NOTE FOR THE SINGLE SCANNER RESPONSE, PITCH AND ROLL ERRORS SHOULD BE DOUBLED

Figure 4.6-11. Evaluation of Sun Interference Effects in the IR Scanner Signal Processor at Sunset

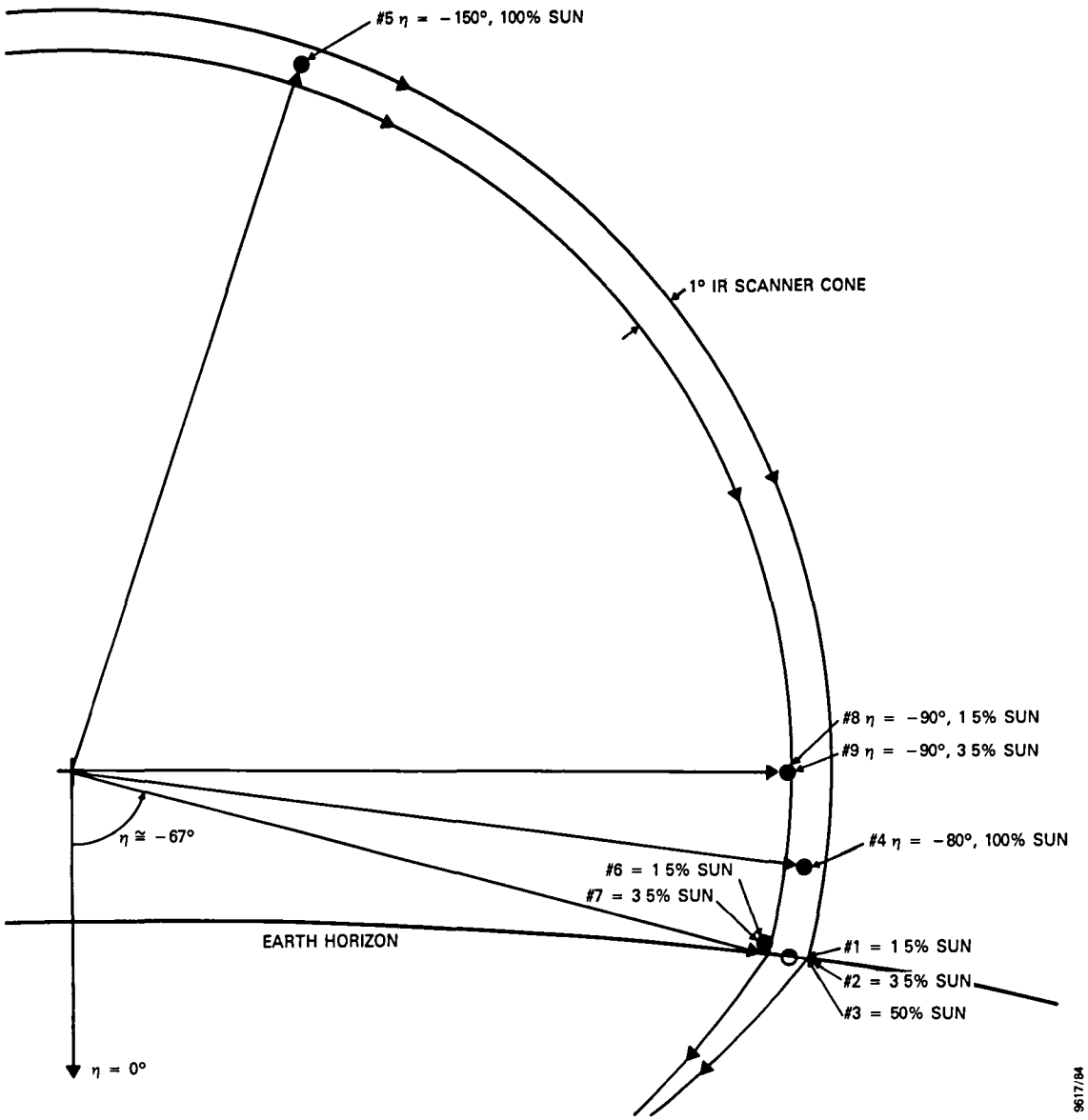

Figure 4.6-12. Geometry of the ITHACO Sun Interference Simulation Experiments

the CSC analysis when the Sun is between η equal to -70 degrees and η equal to -80 degrees. A dominant role will be played by the spacecraft control loop if Sun interference is allowed to occur; neither of the analyses studied this situation. If modest spacecraft attitude motion eliminates the Sun-induced errors to the control loop input, oscillatory attitude motions may occur, such as those experienced on AEM/SAGE. If this happens, the analyses discussed here would better describe the outer envelope of the IR scanner errors in the presence of the oscillating control loop response at sunrise.

Table 4.6-2. Summary of ITHACO Simulation Results for Sun Interference in the Single-Scanner Data Mode

SIMULATION NUMBER	SCAN ANGLE (degrees)	PERCENT OF MAXIMUM SUN PULSE	PITCH ERROR (degrees)	ROLL ERROR (degrees)
1	-67	. 1 5	-0 369	1.72
2	-67	3 5	-0 531	2 08
3	-67	50 0	-0 93	2 337
4	-80	100 0	-1 286	1 547
5	-150	100 0	-0 02	0 55
6	-68	1 5	-0 696	2 06
7	-68	3 5	-1 422	2 76
8	-90	1 5	-0 01	1 246
9	-90	3 5	-0 02	1 16

9617(56*)/84

4.6.3 MISSION DATA ANALYSIS

At the time of this writing, only a limited sample of ERBS telemetry was available for analysis. However, certain characteristics, not all expected, are discernible.

4.6.3.1 Flight Data Anomalies

One item of interest in the early postlaunch ERBS IR scanner analysis was the effect of cold clouds on scanner pitch and roll. As was discussed earlier in this document, ITHACO attempted to minimize these effects for ERBS by reducing the IR scanner bandwidth and modifying the scanner processing electronics. The evaluation of cold cloud effects for ERBS is, at this time, inconclusive. However, with only a limited amount of data from the first month of the ERBS mission, it can be stated that no obvious cold cloud signatures characteristic of those found for Seasat (Section 4.2) have been observed in the ERBS data. Dual-scanner pitch and roll data for three successive orbits on October 19, 1984, are shown in Figures 4.6-13 and 4.6-14, respectively. Apparent disturbances in these data at southern latitudes and near the North Pole are consistent in magnitude with cold cloud effects observed for Seasat. A closer examination of these periods, however, using ground attitude determination from an integration of gyro telemetry, reveals that the IR scanner pitch and roll data reflect true attitude motion by the spacecraft. This motion can be attributed to nutation induced by momentum dumping activity.

The third orbit in Figure 4.6-13 shows a transponder-induced pitch anomaly similar to that encountered with the DE-2 spacecraft (Section 4.5). This error is still under investigation, but has only been observed when the spacecraft is configured for high-power ground transmissions via the TDRS. Unlike DE-2, the ERBS pitch telemetry shows a change in pitch over a period of approximately 2 minutes. For DE-2, telemetry indicated an instantaneous change in the sensed pitch, followed by control system reaction to correct this error. Processing the ERBS gyro telemetry during these periods reveals that the IR scanner pitch may be correct in sensing actual spacecraft pitch errors. Thus, preliminary

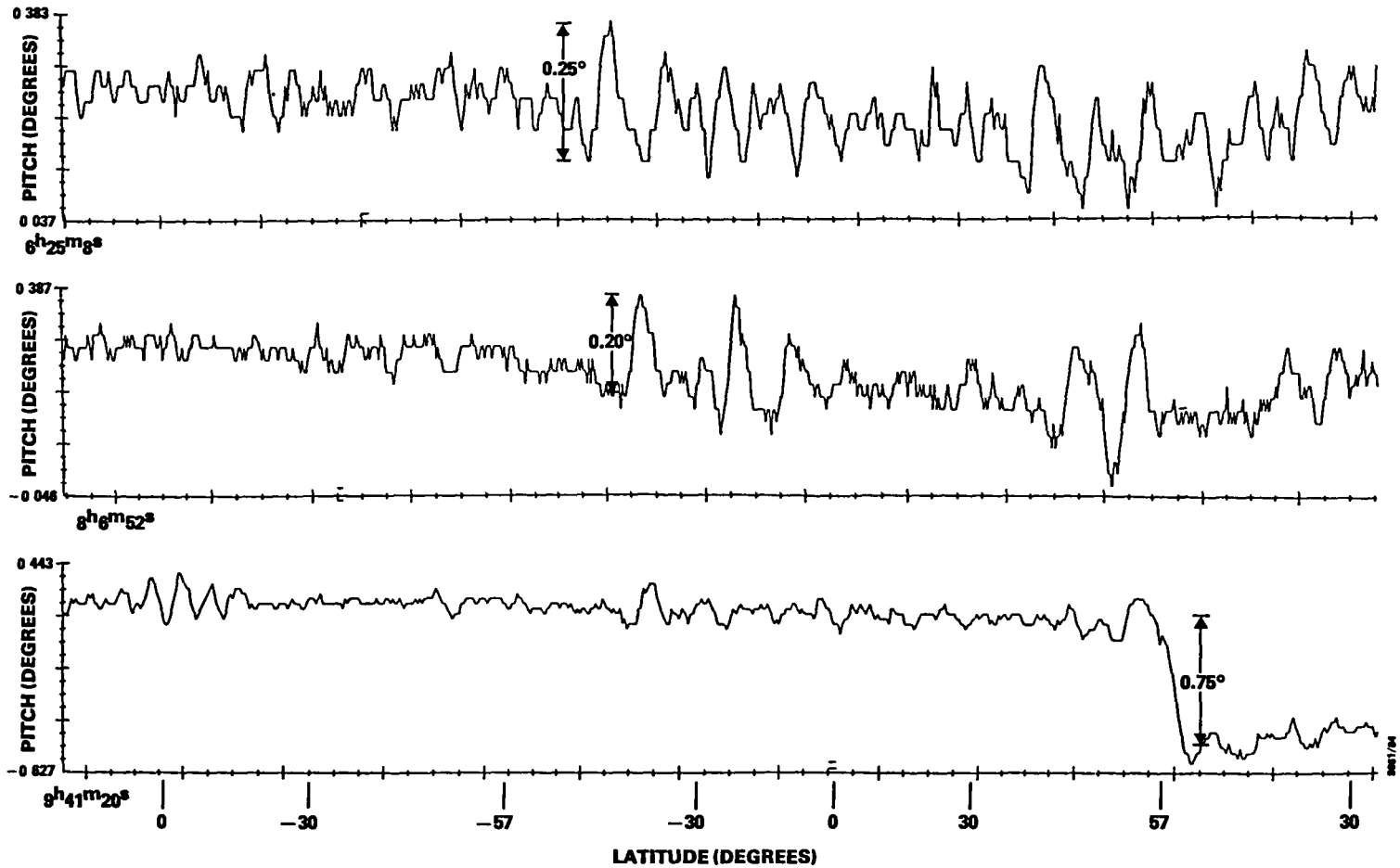

Figure 4.6-13. ERBS Dual IR Scanner Pitch Telemetry for Three Orbits on October 19, 1984

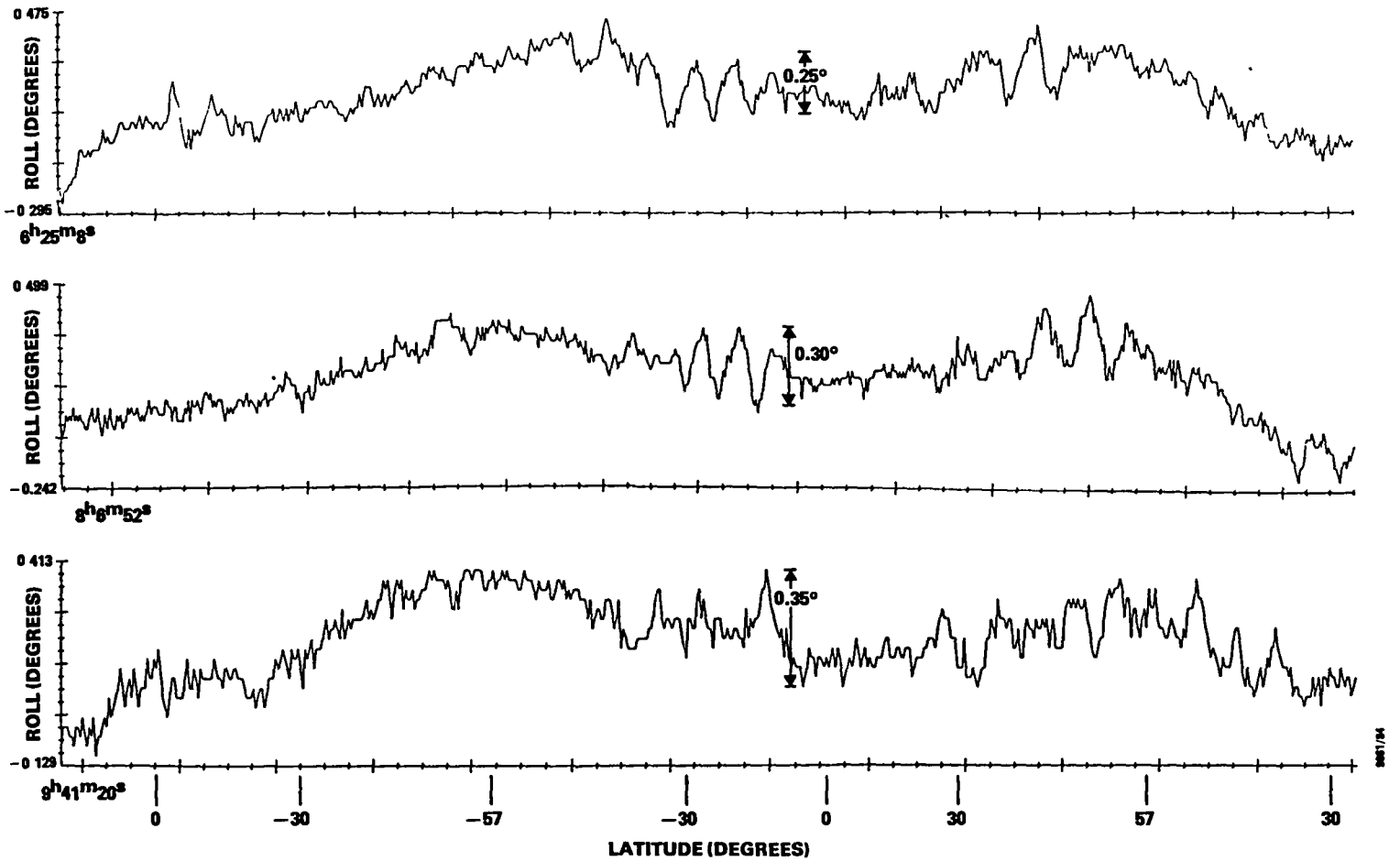

Figure 4.6-14. ERBS Dual IR Scanner Roll Telemetry for Three Orbits on October 19, 1984

analysis points toward some anomaly in the pitch control loop rather than an anomaly in the IR scanner sensing.

The ERBS fine attitude determination system (FADS) uses IR scanner pitch and roll errors, fine Sun sensor telemetry, and gyro telemetry. A batch least squares algorithm is employed, which solves for an attitude state (and gyro drift) at an epoch. Typically, an orbit of data is used. The gyros bring all measurements to a single point in time, thus reducing the effects of sensor noise and anomalies. A complete attitude history can be generated for the batch using the epoch attitude and gyros corrected for gyro drift. This method is effective in showing true spacecraft attitude motion in response to IR scanner anomalies caused by clouds, Sun interference, or other phenomena. Known corrupted scanner data may also be flagged and not used in the estimation of the epoch attitude.

Figure 4.6-15 provides an orbital plot of raw scanner roll, scanner roll corrected for horizon radiance using the HRDB, and ground roll computed using the FADS. The attitude solutions presented in this figure have not been compensated for any systematic bias in IR scanner output or in-flight determined misalignments. Figure 4.6-16 is a similar plot of the pitch data for the same orbit. An in-flight analysis of the effects of systematic variations in the Earth IR radiance of ERBS IR scanner data has not yet been performed. There are some preliminary indications, however, that the techniques employed by the FADS can be very effective in reducing short-term disturbances in IR scanner telemetry for attitude determination. There is also some evidence that these techniques might reduce the effect of errors in the HRDB. In one test case, the fine attitude determination algorithm was used to process a one-orbit batch of telemetry, first with a constant CO_2 altitude and then with the HRDB-derived CO_2 altitude. The difference in epoch attitudes (and in the

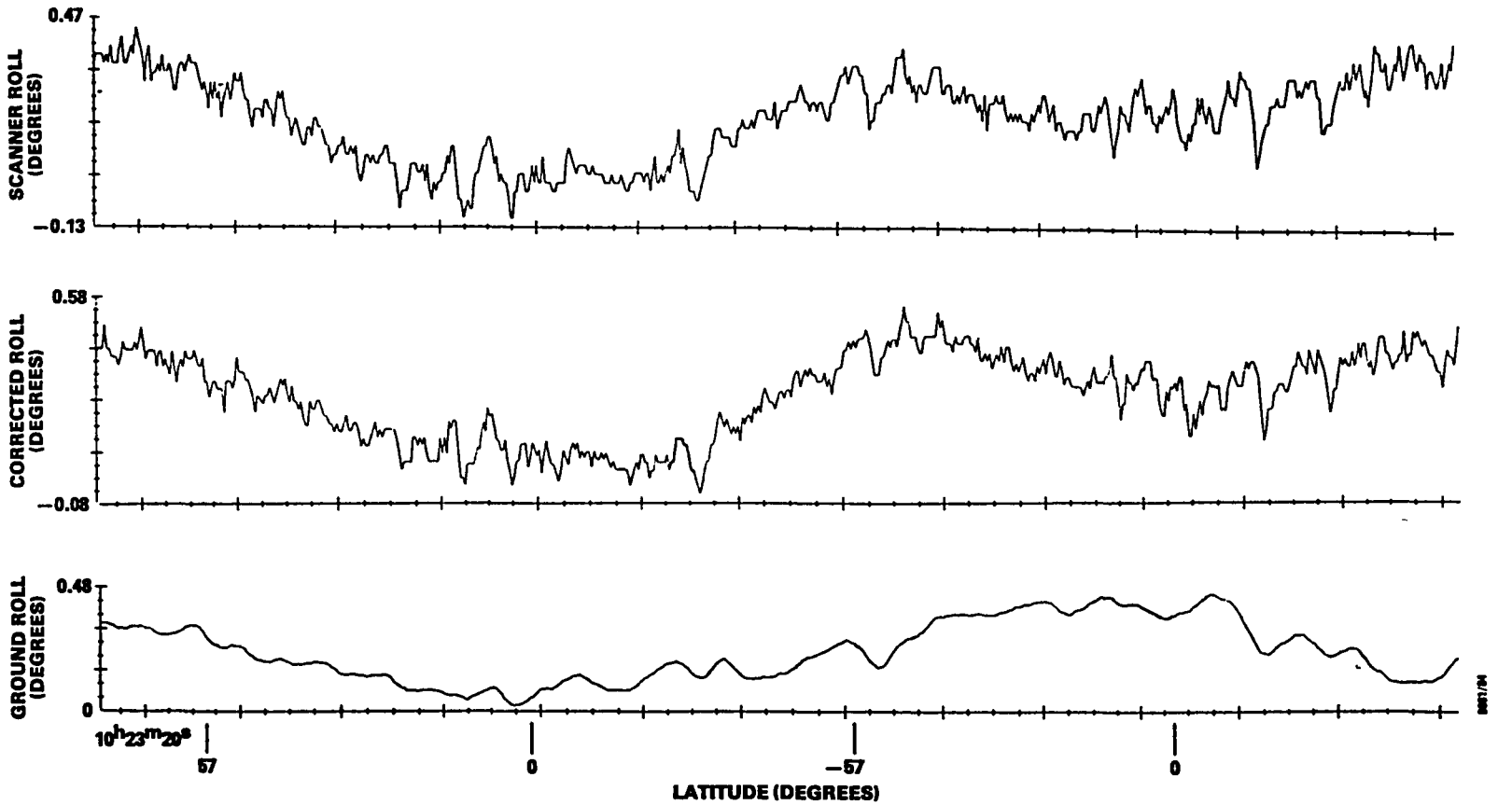

Figure 4.6-15. Scanner Roll, Corrected Roll, and Ground Roll From the ERBS FADS for One Orbit on October 16, 1984

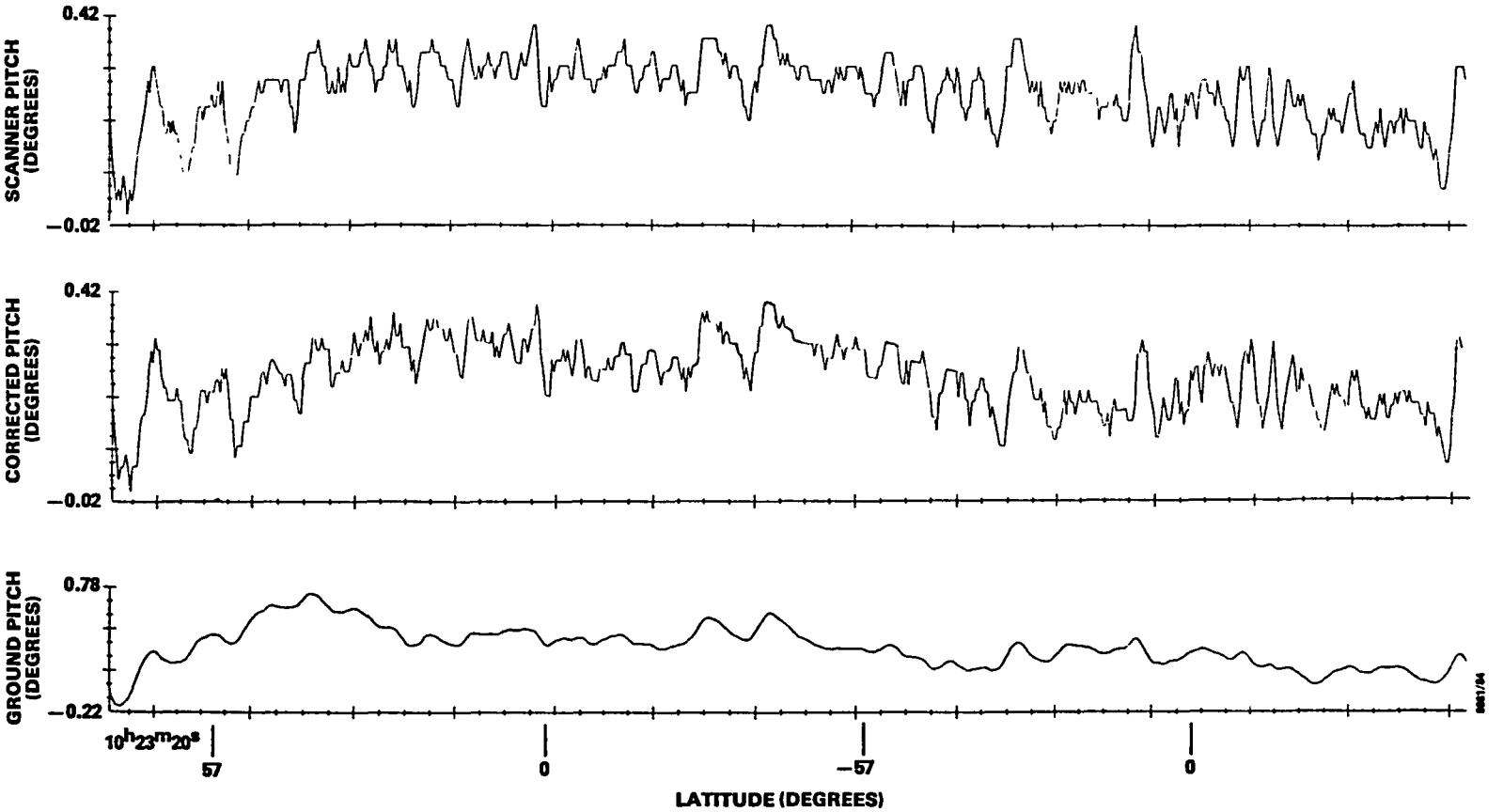

Figure 4.6-16. Scanner Pitch, Corrected Pitch, and Ground Pitch From the ERBS FADS for One Orbit on October 16, 1984

batch attitude history generated by propagating the epoch attitude using the gyros) was less than 0.02 degree for pitch, roll, and yaw. Further analysis is required, but these early results might be interpreted as an indication that the batch processing scheme used for ERBS may be an effective way to "average out" local disturbances and local errors in horizon radiance models.

4.6.3.2 Sun Interference Effects

The first and only period of Sun interference available for current analysis was encountered within 4 days after the ERBS launch. During this period, the spacecraft was flown using dual-scanner control. For future Sun interference events, the ERBS will fly in a single-scanner control mode, with the affected scanner turned off. The role played by the spacecraft control system and resulting spacecraft attitude motion is included in the following discussion of this first Sun interference period.

Nine sunrise events and six sunset events were observed over a 3-day period. There was some difficulty in observing Sun interference during these days because of extended periods at 90-degree pitch, which was required for orbit maneuver operations. With the cant in the IR scanner, a 90-degree pitch took the scan path away from the Sun. Observed attitude perturbations approached 3 degrees for pitch during both sunrise and sunset. Roll errors were as high as 1.4 degrees for roll at sunset and 0.8 degree at sunrise. Corresponding fine pitch and roll telemetry from the IR scanners had peak-to-peak transients of 3 degrees. The maximum observed pitch rate (orbital rate removed) was 0.04 degree per second, and maximum roll and yaw rates approached 0.02 degree per second.

Sun interference was observed over a 6-degree range in Sun angle. Sun interference periods were predicted using

software that determines the time when the Sun enters a zone of interference. A zone is nominally defined as a region 10 degrees wide centered on the null attitude scan path intersection with the Earth and extending 20 degrees above the horizon. By comparing predicted start and stop times of Sun interference with actual times, it was possible to estimate how far above the horizon the Sun affected the IR scanner. This range for both sunrise and sunset approaches 15 degrees, which is consistent with ITHACO predictions, although the present data base of Sun interference events is still too small to make a definitive determination. There is no evidence yet of Sun effects far (>20 degrees) above the horizon.

Figures 4.6-17 and 4.6-18 show the effects of Sun interference on the ERBS telemetry and spacecraft attitude as determined on the ground using the IR scanner, Sun sensor, and gyro data. These plots show sunrise and sunset interference periods on October 9, 1984, with a Sun angle (measured relative to the positive orbit normal) of 132.4 degrees. These were relatively large Sun "hits." Vertical lines on these plots show predicted interference start and stop times.

At the onset of Sun interference as the Sun rises above the horizon, sensed pitch and roll errors increase. Because the scanner B leading edge is affected, a negative pitch error and positive roll error are sensed and telemetered. The steady rise in these errors can be seen in Figure 4.6-17. The momentum wheel begins transferring momentum to pitch the spacecraft to correct the sensed pitch error. However, the pitch error grows faster than the pitch torque available from the momentum wheel to correct for the corrupted pitch error. Both gyro telemetry and processed ground attitude show a positive pitch motion by the spacecraft during this time. The spacecraft also begins to respond to the erroneous roll signal, but the response is slower due to the

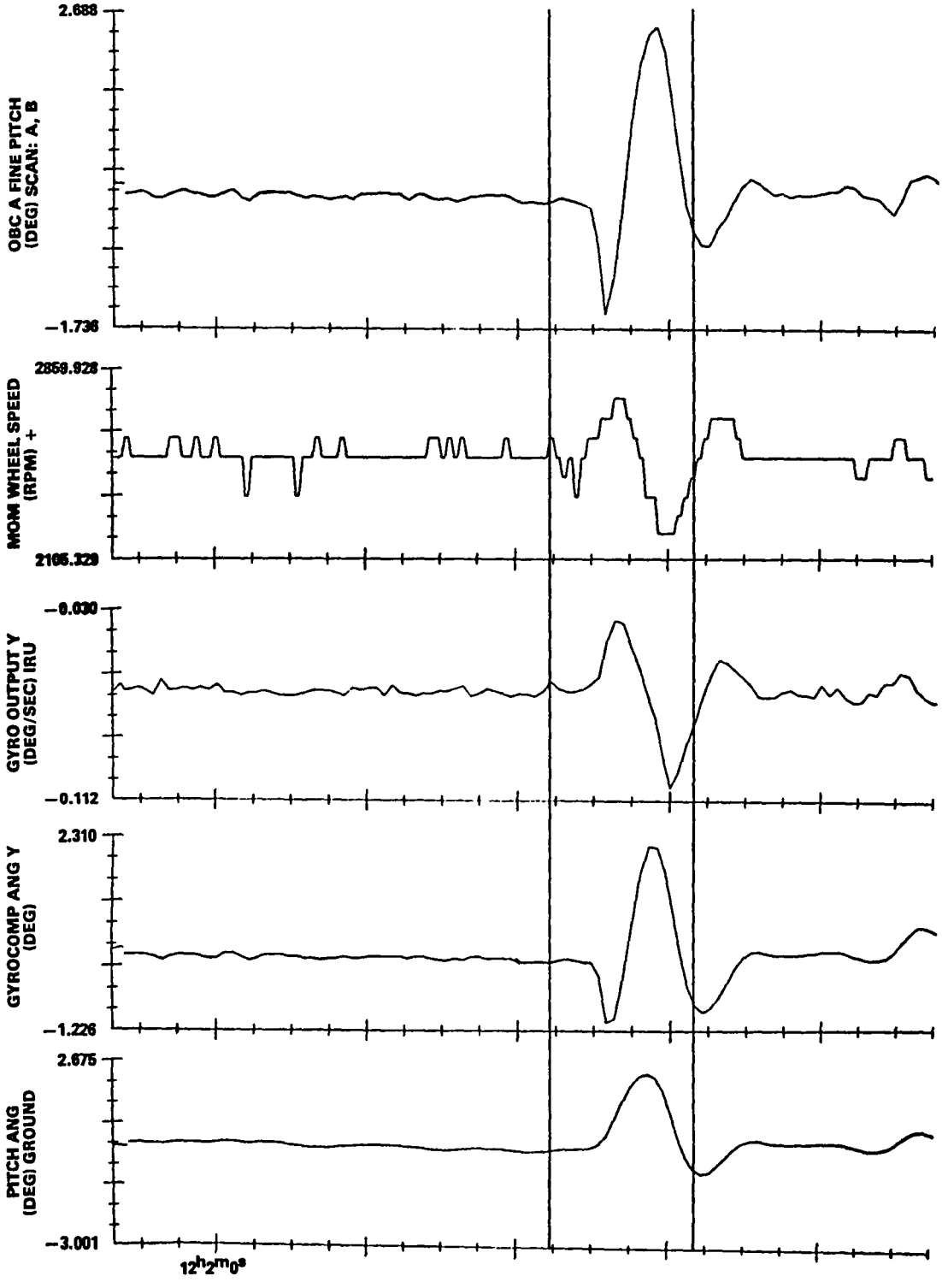

Figure 4.6-17. Sun Interference at Sunrise on October 9, 1984 (1 of 2)

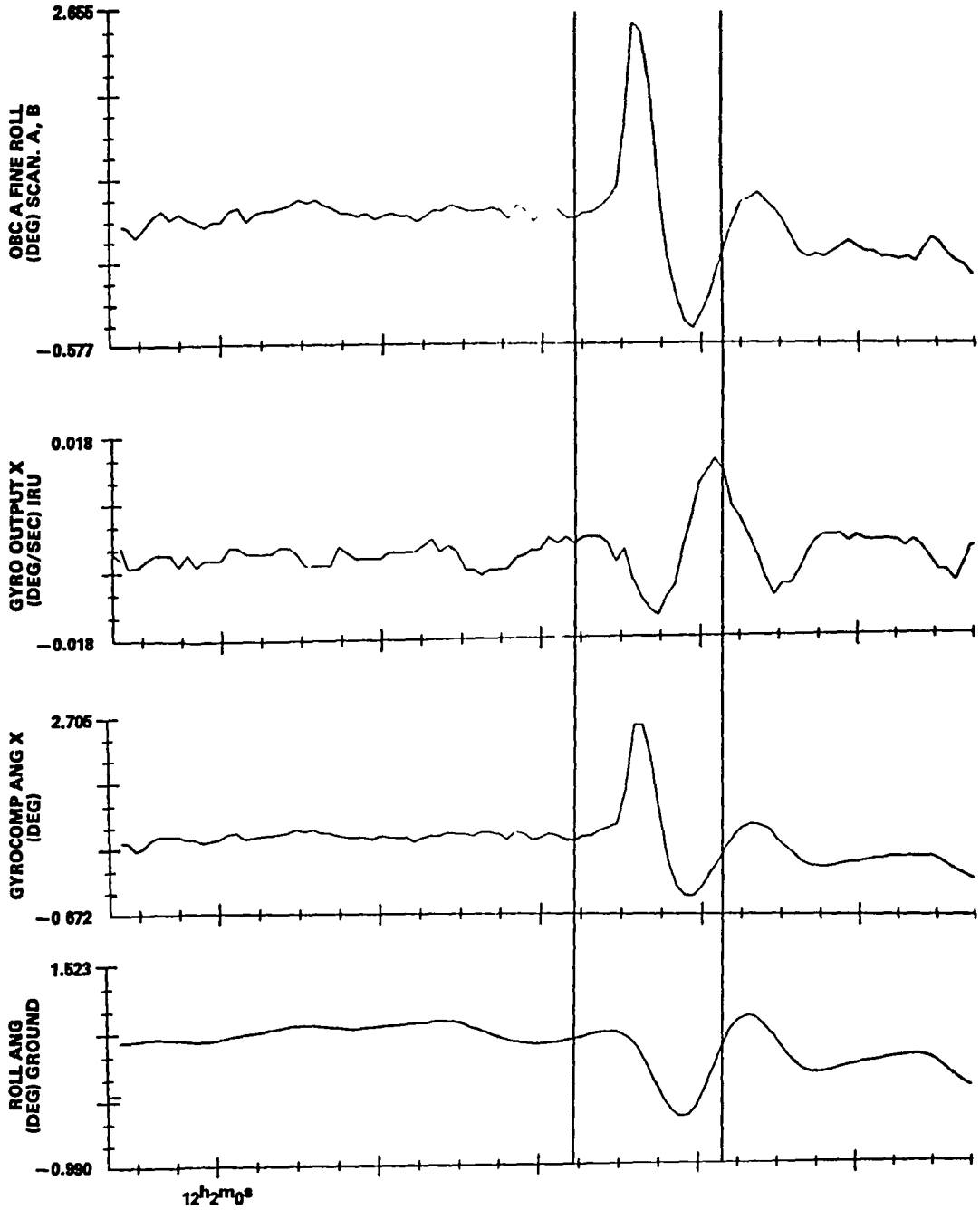

Figure 4.6-17. Sun Interference at Sunrise on October 9, 1984 (2 of 2)

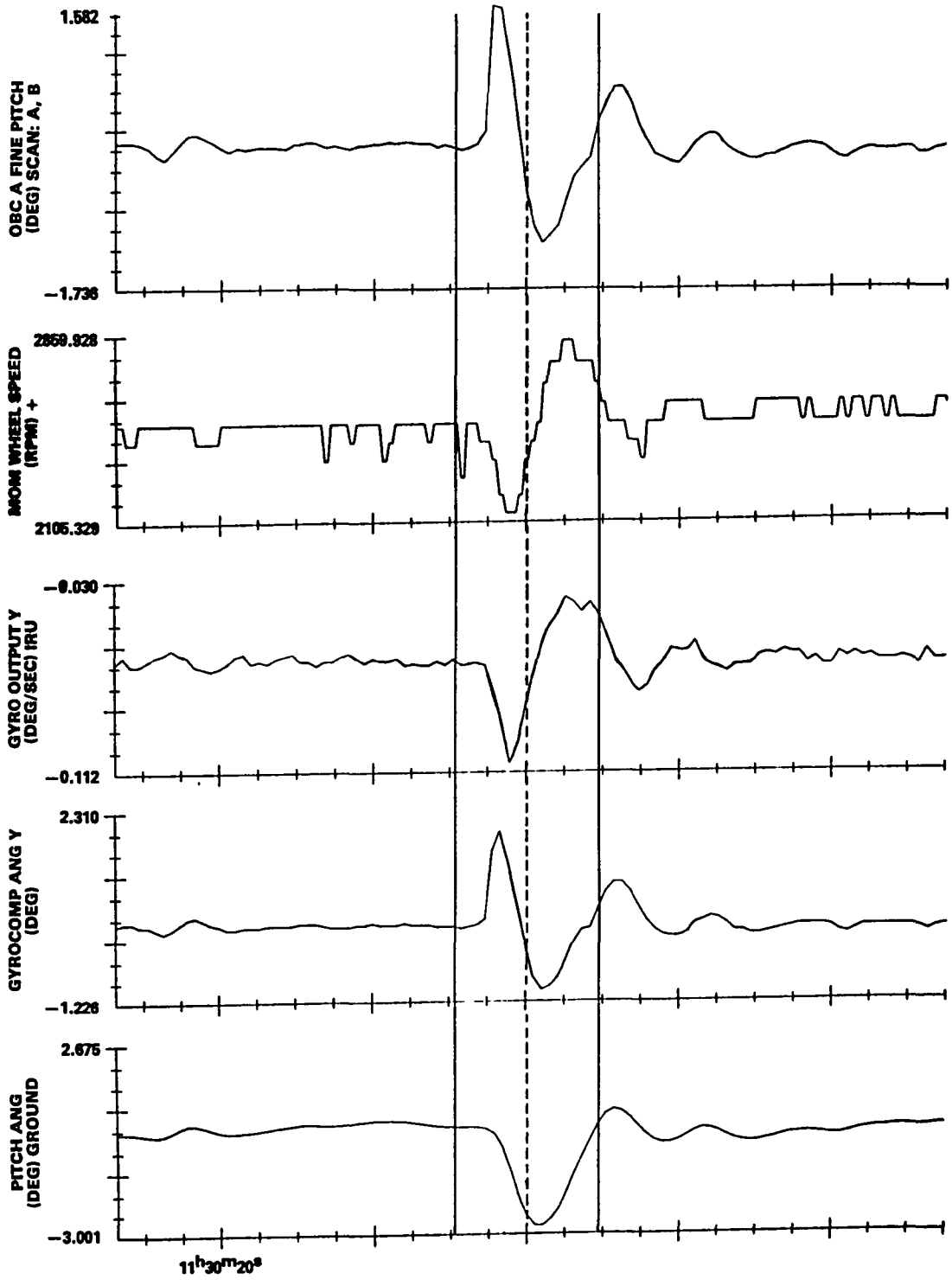

Figure 4.6-18. Sun Interference at Sunset on October 9, 1984 (1 of 2)

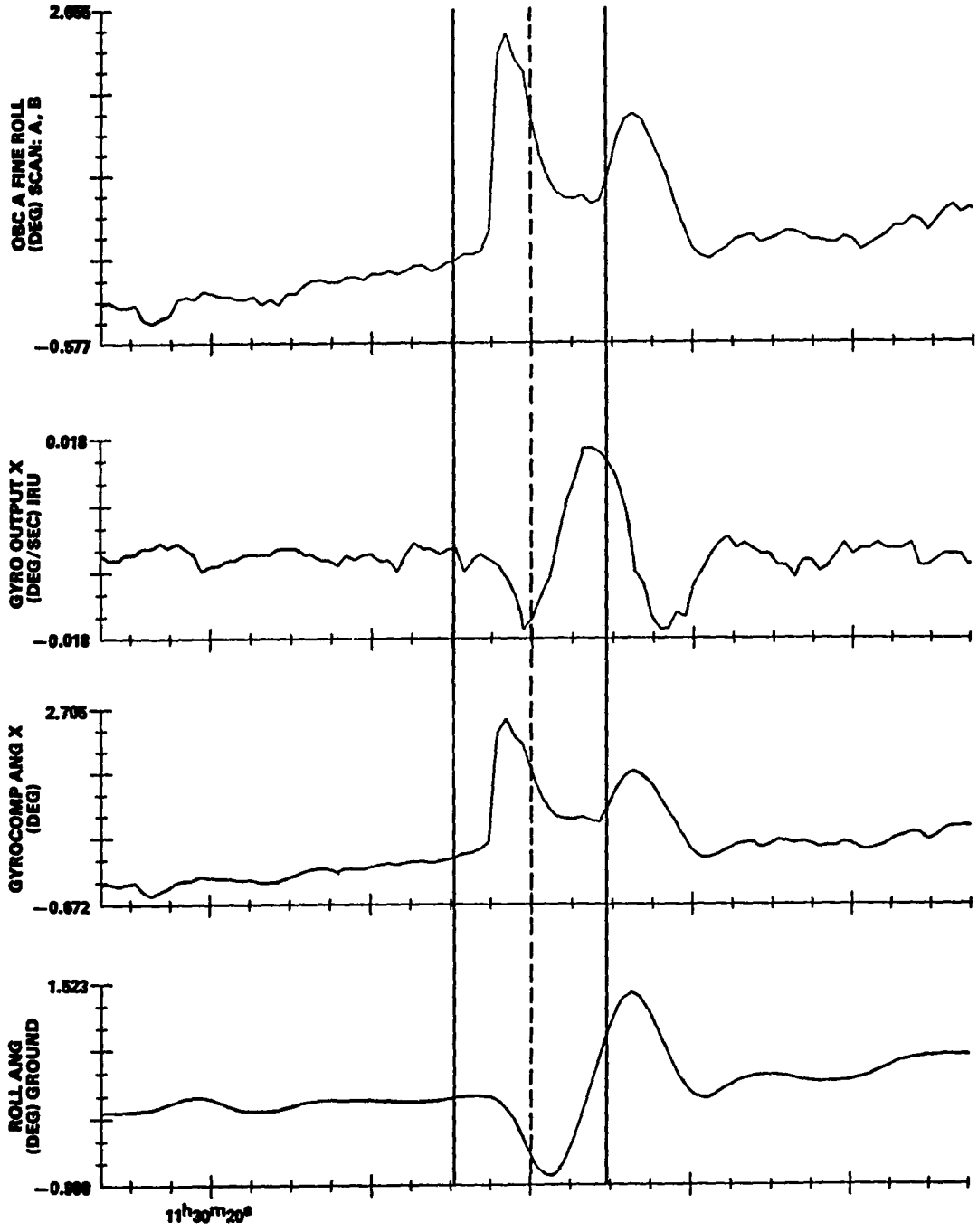

Figure 4.6-18. Sun Interference at Sunset on October 9, 1984 (2 of 2)

relative weakness of the magnetics used for roll control. At a point approximately 6 to 8 degrees above the horizon, the Sun discriminator circuit removes the Sun signal from the sensed Earth width. The IR scanner sees a true picture of the Earth and now responds to the positive pitch error that built up in response to control activity during the Sun interference period.

At some point approximately 10 degrees above the horizon with the Sun setting, the comparator output from the IR signal processor represents a combined Earth and Sun pulse (see Figure 4.6-11). Because the trailing edge of scanner B is affected during this interference period, a large near-instantaneous positive pitch error and roll error are immediately sensed (Figure 4.6-18). The magnetic control system responds with magnetic and momentum wheel activity. This activity, combined with the decrease in the comparator output, acts to reduce the sensed pitch and roll errors as the Sun begins to drop below the horizon. When the Sun signal is lost, residual attitude errors caused by the control system response to the Sun interference are properly sensed and corrected by the control system. Although the Sun interference effects shown in Figures 4.6-17 and 4.6-18 indicate a range of interference up to 10 degrees, other data showed Sun interference effects up to 15 degrees, as stated earlier.

4.6.4 RESULTS AND DISCUSSION

The ERBS IR scanner analysis has shown that, although the IR passband was narrowed to reduce the response of the scanner to cold clouds, a corresponding increase in the Earth pulse rise time and delay have increased the sensitivity to variations in the threshold adjustment voltage. Coupled with the effects of stratospheric warming events in the winter polar latitudes, this has reduced the possibility that the ERBS IR scanner has been improved relative to the Seasat system.

The results presented in Section 4.6.3, based on the limited amount of mission data available to date, do not provide any definitive determination of the ERBS IR scanner sensitivity to cold clouds. Further analysis of the ERBS mission data is required to answer this question.

The LIMS analysis (reported in Section 2) resulted in a significantly improved understanding of the Earth IR image and the limitations of a longitudinally averaged model of Earth IR radiation. This contributed greatly to the understanding of the ERBS IR scanner performance capabilities. Further understanding of the accuracy and reliability of the electronics circuit modeling method was established through parametric analysis with the modeling software and algorithm and through a direct comparison with the more complete approach by ITHACO including nonlinear effects. Some insight was also gained into the possibility of performing analyses to predict the IR scanner response to Sun interference. The limited amount of mission data has indicated that the Sun interference analysis was successful in predicting the magnitude and location of this effect. The usefulness of all of these efforts cannot, however, be determined until after the ERBS postlaunch data are analyzed in more detail.

4.7 ATMOSPHERE EXPLORER-3

Support for the AE-3 mission was provided by the GSFC ADCS and CSC for real-time attitude determination and control and for definitive attitude determination. The AE-3 spacecraft attitude mission support was unique because of the high attitude drift rates that were encountered during the low-altitude (135-kilometer) perigee passages. Spin axis precession rates as high as 1/3 degree per perigee passage were experienced, requiring activation of the Z-axis magnetic dipole as frequently as once every 6 hours to maintain the spacecraft attitude within 2 degrees of orbit normal. A major amount of attitude operation support resources was devoted to near-real-time attitude determination, attitude drift prediction, and attitude control command simulation and generation. Analyses were also performed to evaluate the performance of the IR sensors and to develop algorithms to correct the IR data and improve attitude determination accuracy. The improvements derived from experience with the AE-3 flight system were used to improve the AE-4 and AE-5 spacecraft and were subsequently applied to the support analysis for these spacecraft. References 47 through 49 present more details on the AE mission support analysis.

4.7.1 MISSION REQUIREMENTS AND HARDWARE

The AE-3 spacecraft, launched on December 16, 1973, was designed to study the physics of the lower thermosphere. The spacecraft was equipped with a hydrazine propulsion system for orbit control, which permitted systematic investigation of the atmosphere down to altitudes near 130 kilometers without committing to spacecraft reentry. The mission was thus characterized by (1) frequent orbit adjust maneuvers to raise or lower perigee and to maintain a predictable schedule of apogee decay, and (2) high attitude precession rates

because of the large aerodynamic torques experienced at perigee.

A cross-sectional view of the spacecraft in the AE series is shown in Figure 4.7-1. The AE-3 mission can be summarized as follows:

- Orbit--Three distinct phases:
  - An initial elliptical phase with perigee and apogee approximately at 150 and 4300 kilometers, respectively
  - A transition phase
  - A final circular phase at an altitude varying between 200 and 400 kilometers and inclination of 68.1 degrees
- Attitude configuration
  - Dual-spin spacecraft, with a momentum wheel providing a reference for stabilization
  - +Z-axis aligned along positive or negative orbit normal, in the direction of the Sun
  - Spacecraft body spin rate controlled at 4 rpm or despun relative to the nadir vector at selectable pitch angles
- Attitude determination hardware
  - Two body-mounted IR horizon sensors (BHSs) (Figure 4.7-2)
  - Two wheel-mounted IR horizon sensors (WHSs)
  - Sun sensor (digital solar aspect indicator (DSAI)) with 1-degree resolution for a 0- to 180-degree range from the spin axis

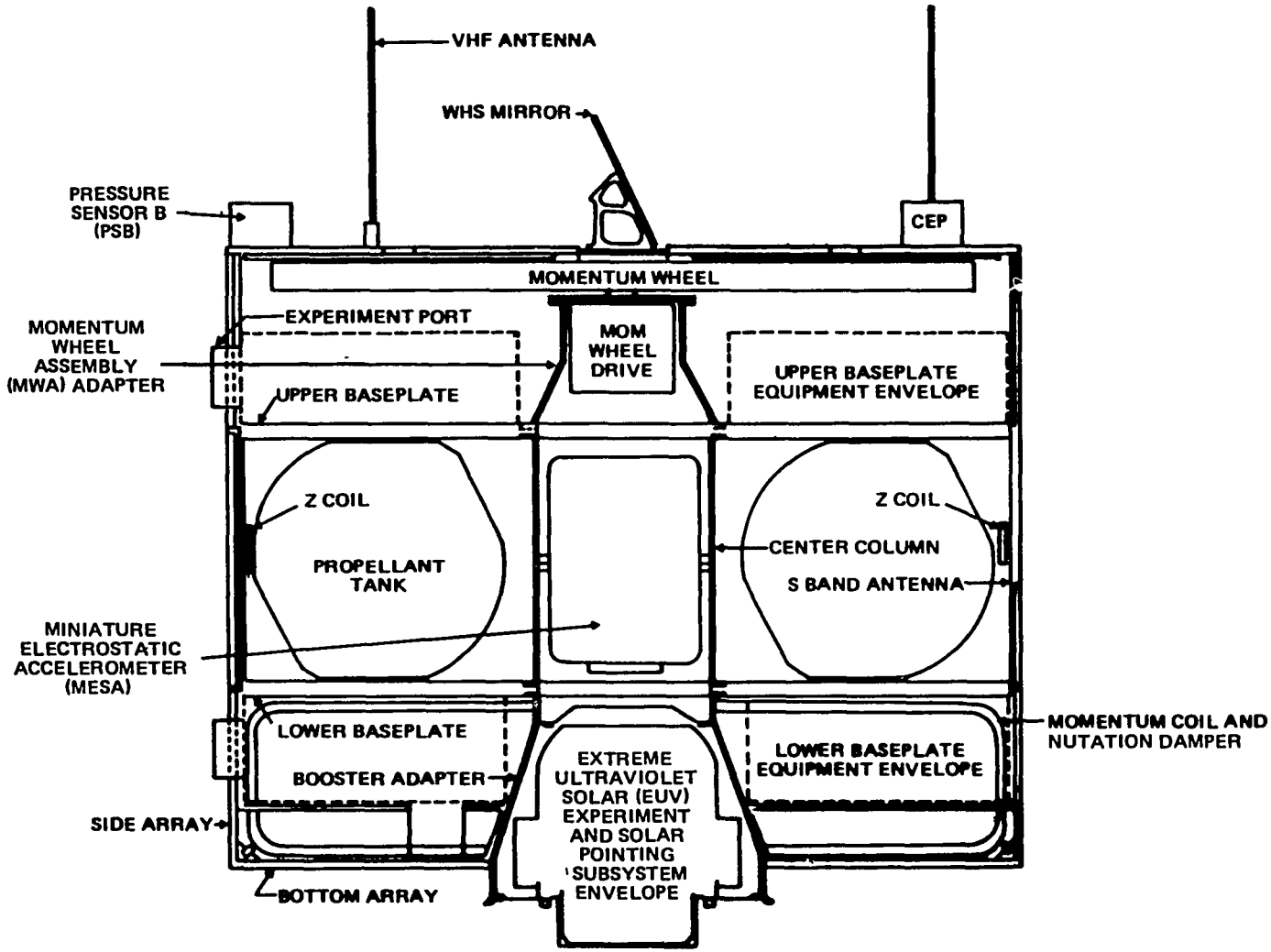

Figure 4.7-1. AE Cross-Sectional View

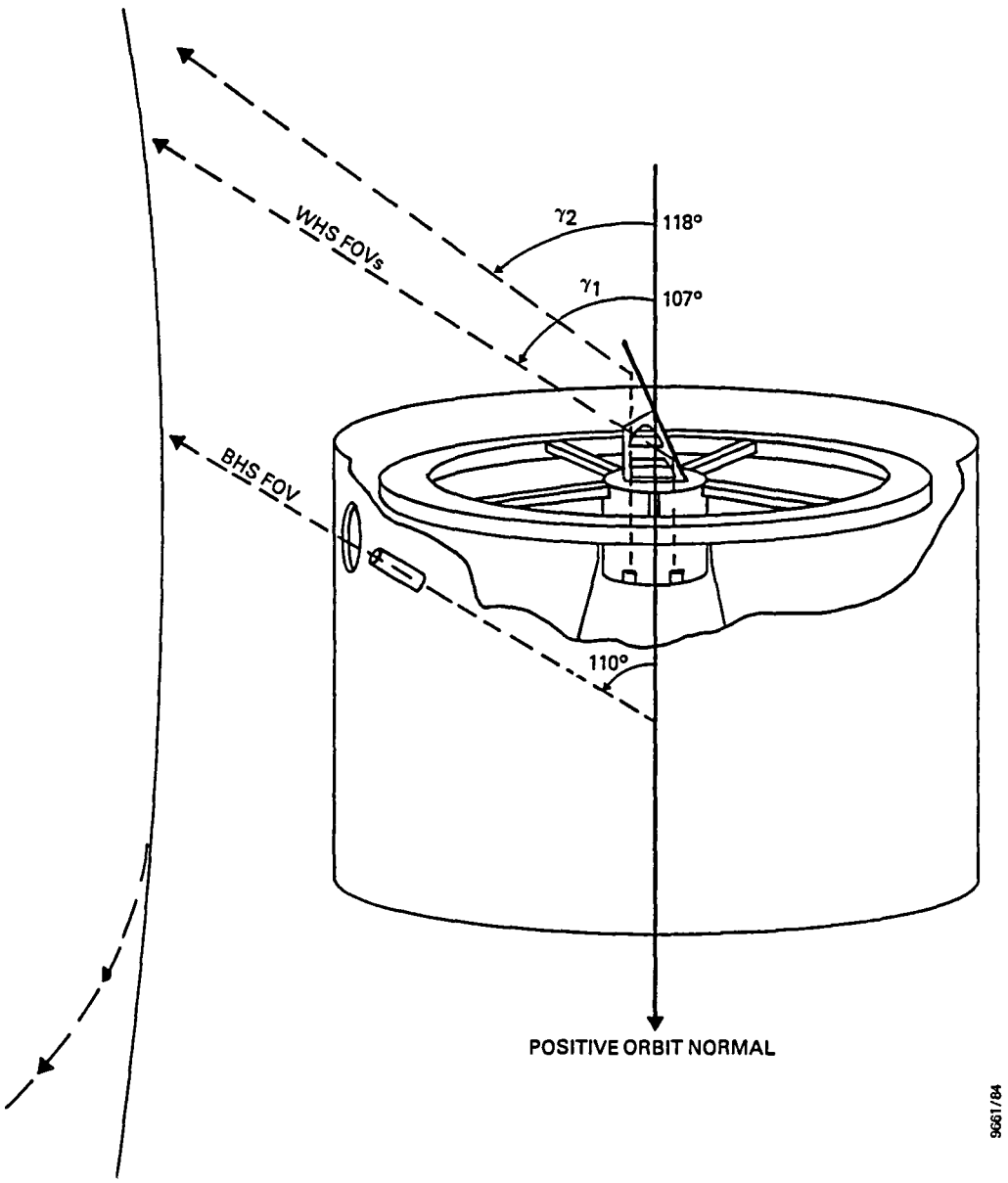

Figure 4.7-2. AE-3, -4, and -5 IR Sensor Earth Geometry for Operation at Positive Orbit Normal

- Magnetometer triad
- Sun-pointed system elevation gimbal

- Attitude control hardware
  - Momentum wheel assembly
  - Magnetic torque coils
  - Passive nutation dampers (liquid filled)
  - Automatic roll and pitch control via torque coils
  - Thrusters for yaw control

- Accuracy requirement
  - Maintain spin axis to within 2 degrees of orbit normal
  - Maintain total angular momentum to within 10 percent of 1200 inch pound seconds

- Ground support system--Interactive operating system

- Data processing requirements
  - Near-real-time attitude determination and drift prediction
  - Real-time attitude control command generation, as required
  - Definitive attitude processing of all data received

- Problems encountered
  - Noisy IR sensor data, with $\pm$0.8-degree (1σ) errors
  - Nutation hang-off

- Misalignment of the bolometer optical axis relative to the WHS spin axis, causing sinusoidal modulation of IR sensor data during 4-rpm operation
- High-attitude drift rates during low-altitude perigee passages, requiring frequent commanding of Z-axis coils to correct spin-axis precession

A closeup view with more detail of the angular momentum wheel, IR sensor bolometers, and WHS mirrors is shown in Figure 4.7-3. Figure 4.7-4 provides a detailed illustration of the Barnes Engineering Company bolometer assembly used for the WHS and BHS on the AE spacecraft (adapted from RCA horizon sensor detector specifications (Code 49671, RCA Part No. 1972769)).

The analysis performed on the AE-3 IR sensor flight data was primarily to enhance the accuracy of the definitive attitude solutions, although improvements in the near-real-time attitude solutions were also highly desired. Accuracy in near-real-time attitude determination tended to result in improvements in attitude drift prediction, with subsequent reductions in the operational support load.

4.7.2 MISSION DATA ANALYSIS

The usual postlaunch data processing support was provided to assess attitude sensor data for alignment and electronic biases. The AE-3 postlaunch data analysis provided a plausible explanation and modeling of the effects of a misalignment between the optical axis of the bolometers and the spin axis of the wheel-mounted scanning mirrors. The cause was postulated to be a bent shaft used to attach the T-plate to the body. This problem manifested itself as (1) an oscillation of the WHS data proportional to the spacecraft body spin rate and (2) a bias in the nadir angle (computed with

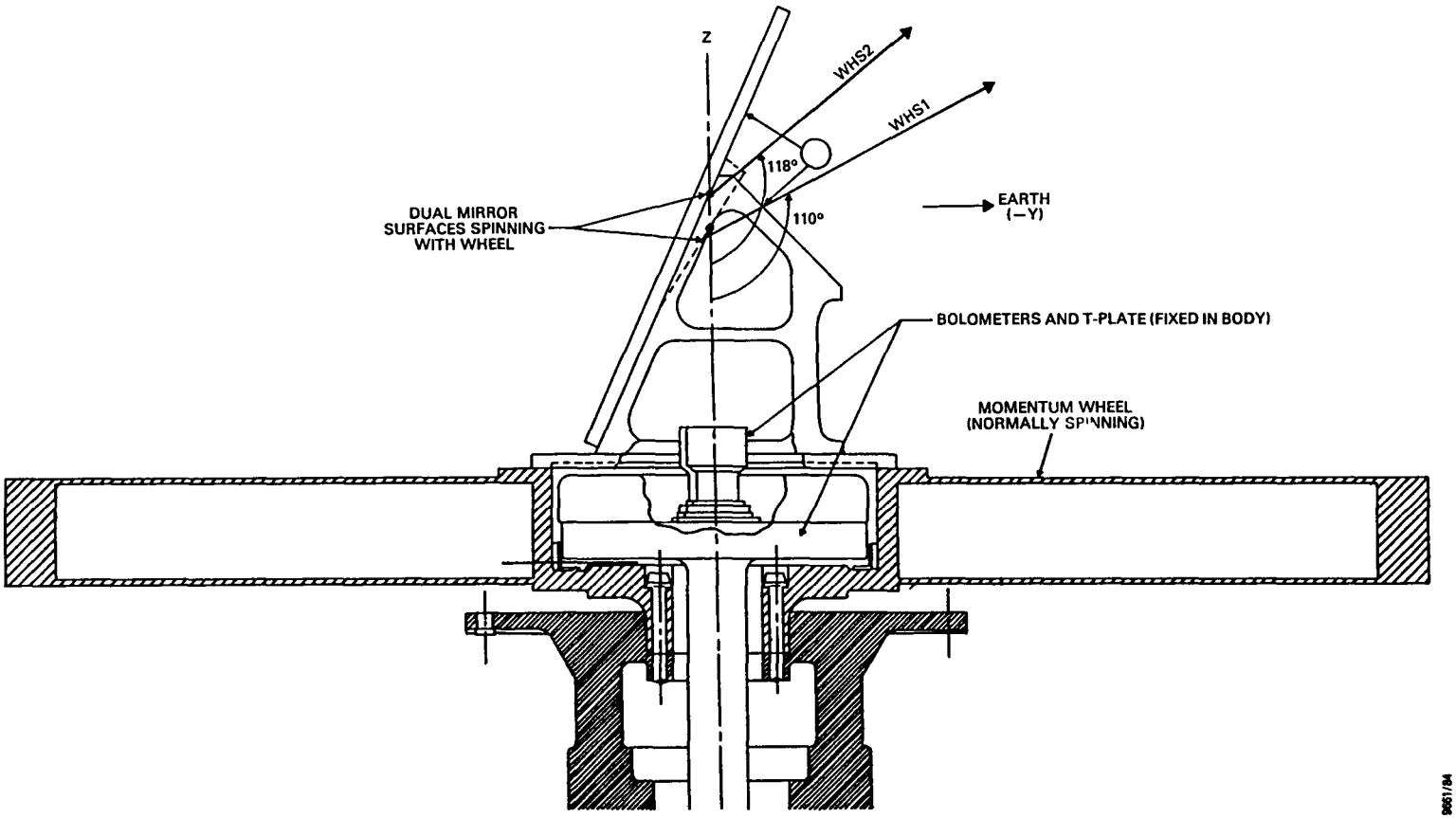

Figure 4.7-3. AE Wheel-Mounted Horizon Sensor Assembly With Momentum Wheel, T-Plate, Bolometers, and Dual Mirrors

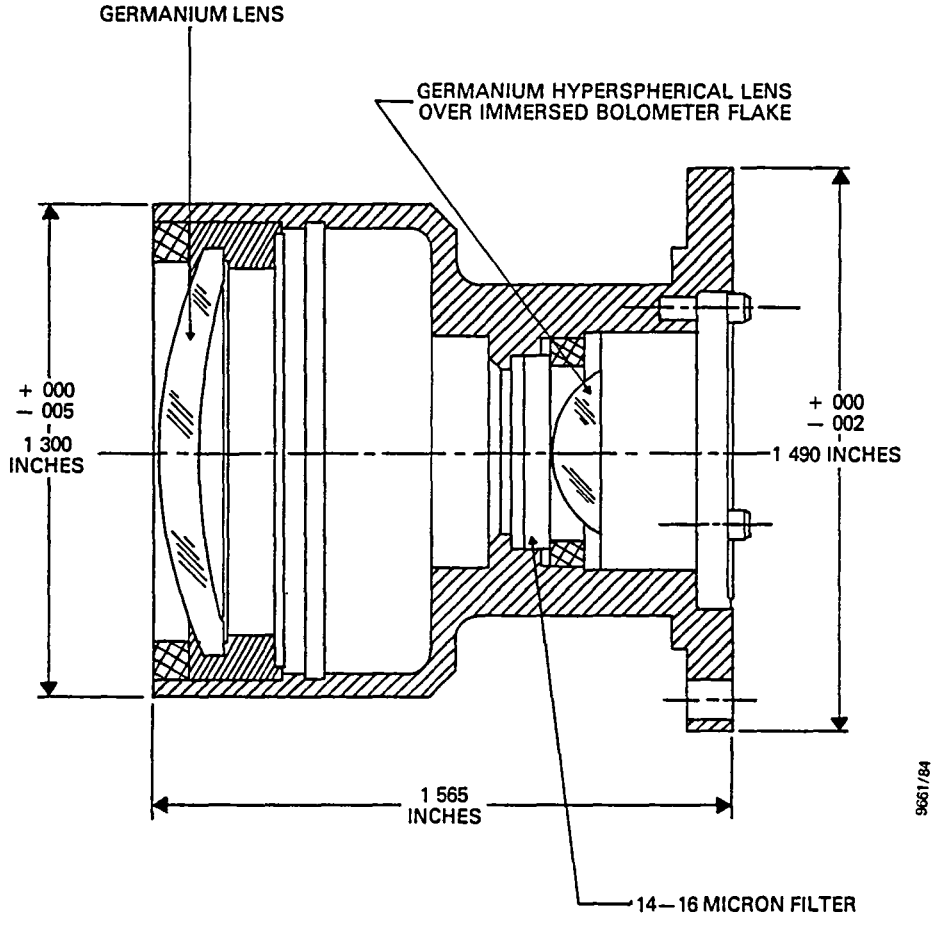

Figure 4.7-4. Barnes Engineering Company Bolometer Assembly for the AE and DE Series Spacecraft

the WHS Earth width data) as a function of pitch offset angle in the 1-rpo despun spacecraft mode.

The processed AE-3 WHS flight data for WHS1 and WHS2 midscan-to-Earth LOS angle is illustrated in Figure 4.7-5 and clearly shows the oscillating behavior at the spacecraft spin rate of 4 rpm. An example of the AE WHS data converted to spin axis-to-nadir vector angle (nadir angle) is illustrated in Figure 4.7-6. Here the spacecraft changed from 4 rpm to 1 rpo at 13:34:10 UT.

After establishing that the source of the oscillation in the WHS data was due to misalignment and not spacecraft nutation, a model to correct the nadir angle computed from this oscillating (4-rpm mode) WHS data was incorporated into the AE-3 ADS. The effects of applying this correction algorithm to the WHS data are illustrated in Figure 4.7-7, where the AE spacecraft goes from despun to spinning mode. As shown in the figure, the effect of the correction is to eliminate the step function bias that occurs between the despun and spinning modes and to reduce the oscillations in the computed nadir angles after the spacecraft reached 4 rpm.

4.7.3 RESULTS AND DISCUSSION

A major portion of the analysis effort on the AE-3 IR sensors was devoted to bias and alignment analysis. No detailed investigation was performed to analyze the data to determine the influence of horizon radiance variations for either the systematic effect or cold cloud and stratospheric anomalies effect. For this reason, a description of the AE IR sensor pulse processing electronics system and corresponding Earth IR radiance model was not included. An additional accomplishment of the AE-3 mission analysis effort related to IR sensor attitude data was the discovery of a wheel-speed-dependent bias in the Earth width angular measurements.

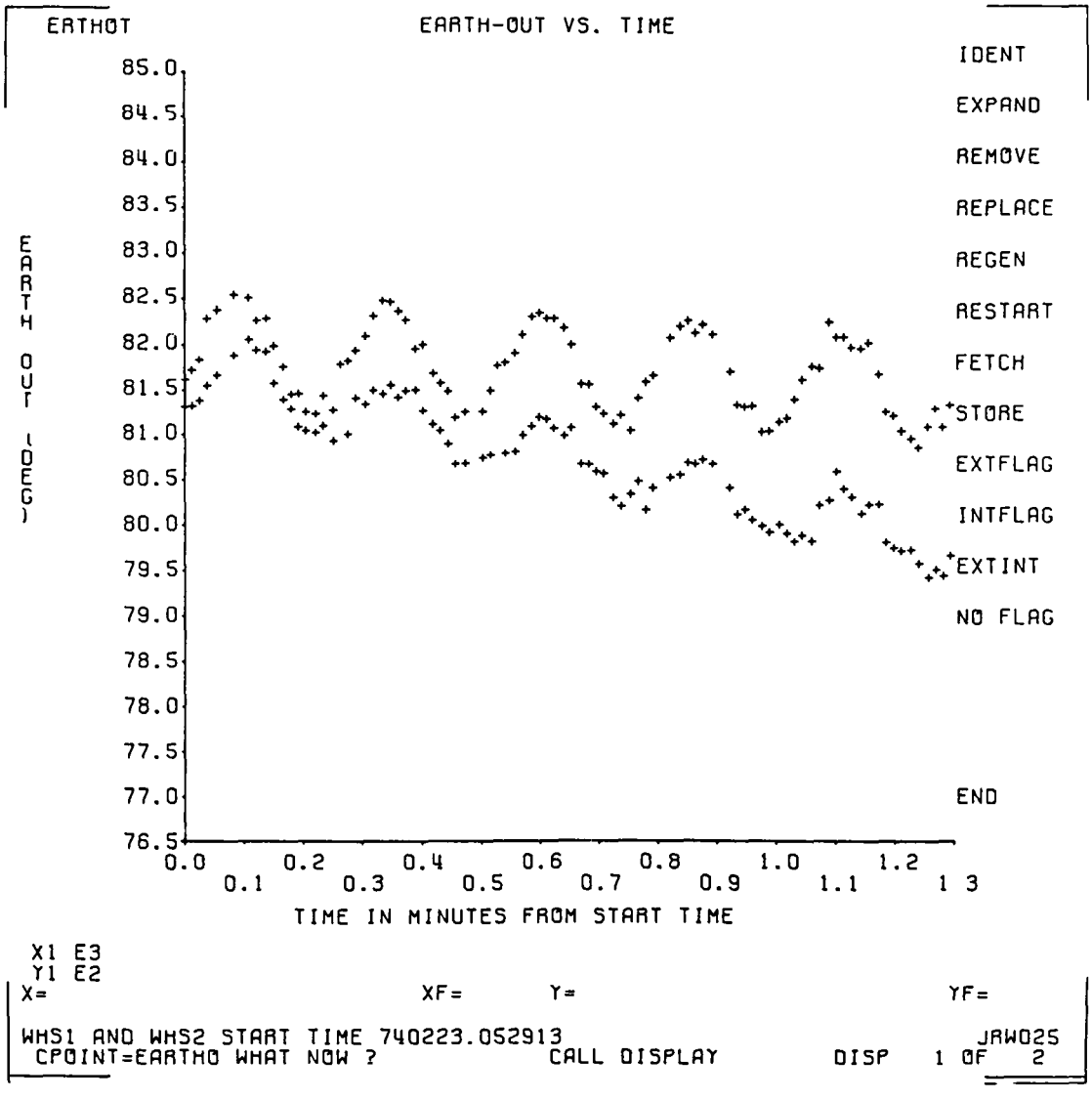

Figure 4.7-5. Sample AE-3 WHS Data Showing Oscillatory Behavior

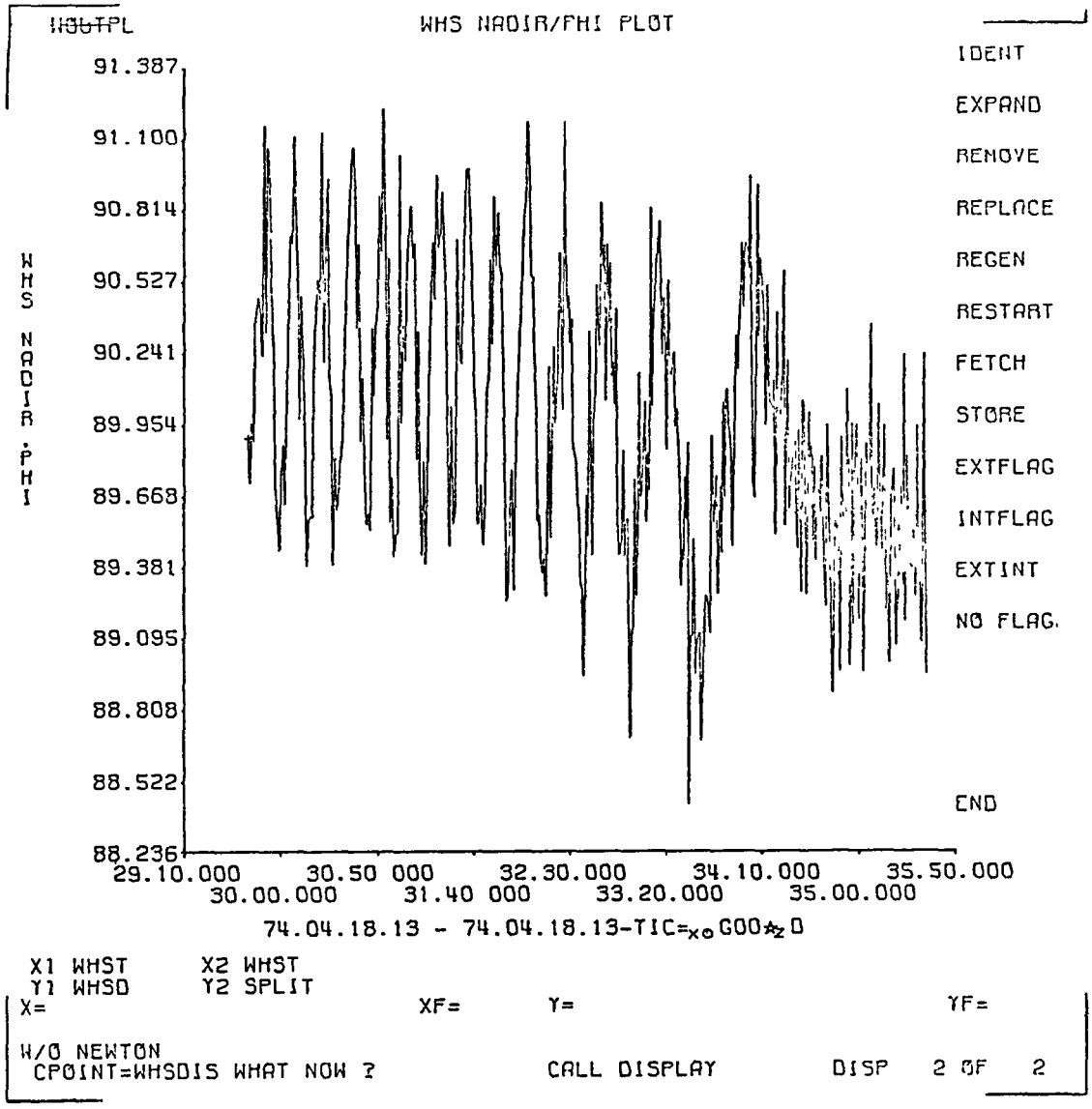

Figure 4.7-6. WHS Nadir Angles for Pass 1368 During the Transitional Period Without the Bolometer Offset Model

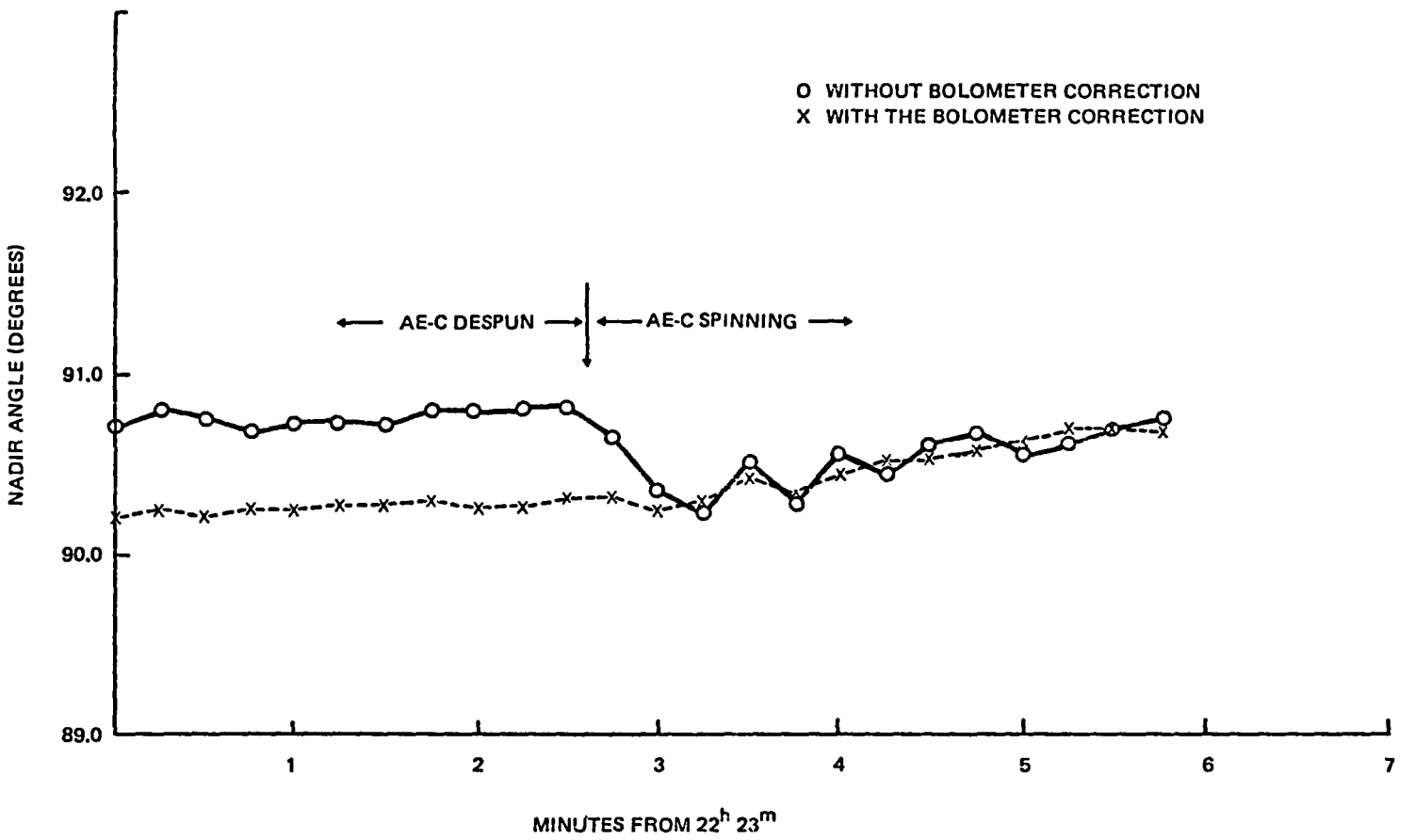

Figure 4.7-7. Effect of Bolometer Offset Correction on the AE-3 Nadir Angles, Despun Mode to Spinning Mode Transition

The IR sensor data were telemetered as a time interval for the wheel spin period, bolometer number 1 and number 2 Earth scan durations, and Earth electronics split pulse-to-body reference index duration (pitch offset). A fixed time bias in the Earth chord duration for Earth width 1 (EW1) and EW2 data became apparent, when Earth width times were converted to angles, as a wheel-speed-dependent Earth width angle error. Once this error was discovered, understood, and corrected, significant improvements were made in the real-time and definitive attitude solution accuracy.

The AE-3 mission attitude support analysis resulted in an understanding of the capabilities and limitations of ground support analysis applied in an effort to increase the accuracy of the attitude sensor data. The bolometer offset analysis showed that, given a good model of an effect, a self-consistent correction function for anomalous sensor performance could be applied, without the aid of a highly accurate sensor such as a star tracker or fine Sun sensor, although no absolute calibration could be achieved. An analysis of the effects of IR horizon radiance variations on the AE attitude solutions was not possible, however, with the low resolution (1 degree) of the DSAI flown on AE-3. The opportunity for performing such an analysis with the higher resolution solar pointing subsystem using definitive attitude data was missed during the period of active attitude support for this mission at GSFC. This happened because the emphasis of the attitude determination effort was on timeliness and attitude solution consistency. In addition, the attitude determination accuracy requirements on AE-3, -4, and -5 did not dictate an extensive effort in IR radiance modeling analysis.

4.8 GEOSTATIONARY OPERATIONAL ENVIRONMENTAL SATELLITE-5

The analysis of the effects of horizon radiance variations on the GOES-5 IR sensors made use of the OABIAS program, an analysis tool available in the ADCS program library. This bias determination program was applied to the GOES-5 IR sensor data to resolve the asymmetry in the model of the detected Earth angular radius that resulted from systematic horizon radiance effects during June atmospheric conditions. The analysis presented here is derived primarily from Reference 50.

4.8.1 MISSION REQUIREMENTS AND HARDWARE

The GOES series of spacecraft is a joint effort of NASA and NOAA to provide systematic, worldwide weather coverage. GOES-5 was launched from the Eastern Test Range on a Delta 3914 launch vehicle on May 22, 1981, at 22:29:00 UT. After third-stage spinup, the spacecraft was inserted into its transfer orbit at 22:52:57 UT. The apogee kick motor was fired on May 24, 1981, at 12:58:05 UT, to insert the spacecraft into the drift orbit. A series of attitude and orbit maneuvers were executed to place GOES-5 into a geosynchronous orbit, ending on June 6, 1981. After the attitude sensor biases were determined and spacecraft testing was completed, the responsibility for spacecraft support was transferred to NOAA on July 2, 1981. References 51 and 52 provide more information on GOES-5. The GOES-5 spacecraft is illustrated in Figure 4.8-1. The mission can be summarized as follows:

- Orbit--Three distinct orbits: transfer, drift, and final geosynchronous mission orbit
- Attitude scenario--Spin stabilized at 100 rpm, spin axis aligned approximately parallel to negative orbit normal

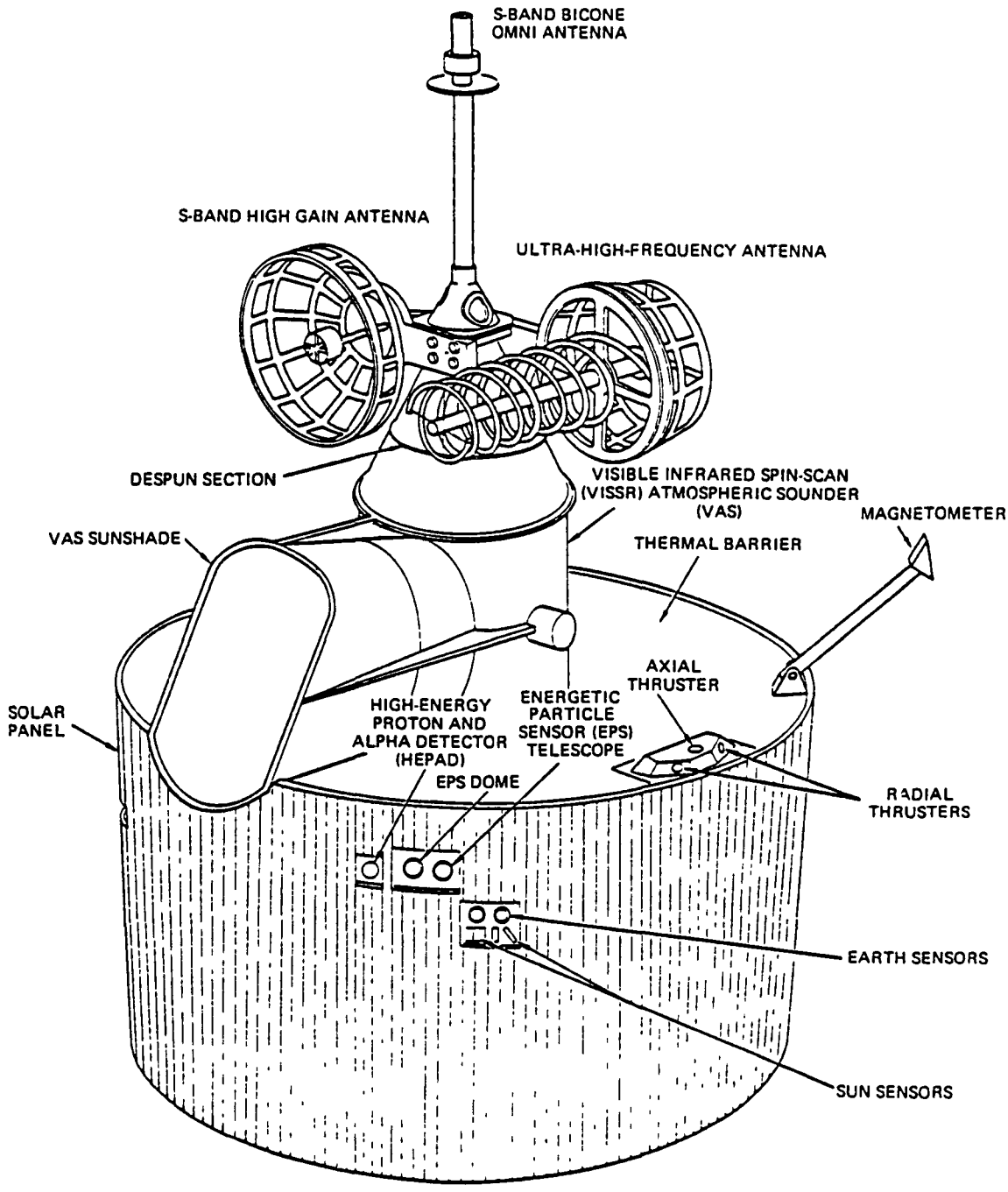

Figure 4.8-1. GOES-5 Spacecraft Configuration

- Attitude determination hardware
  - Two body-mounted IR horizon sensors (BHSs) with 1.5-degree square FOV, mounted with spin axes at 85 and 95 degrees from the spacecraft spin axis
  - Two Sun sensors (DSAIs)
- Attitude control hardware
  - Two hydrazine thrusters
  - Rotating fluid nutation damper
- Accuracy requirement
  - 2.0 degrees (3σ) during launch and checkout phase
  - One visible pixel (21 microradians) for imaging
  - 0.01 degree for pointing control in final mission mode
- Ground support system
  - Interactive system for attitude and bias determination as well as maneuver monitoring; used at GSFC
  - Visible and IR spin scan radiometer (VISSR) Image Registration and Gridding System (VIRGS) for attitude and orbit determination during mission mode; used at NOAA
- Data processing requirements--None

The two Earth sensors (ES) on GOES-5 (listed above as the BHSs) are IR radiometers operating in the 14- to 16-micrometer CO_2 absorption band. Each sensor has a square, 1.5-degree FOV. The optical axes of ES1 and ES2 are canted down from the spacecraft spin axis at angles of 85 degrees and 95 degrees, respectively.

The spinning motion of the spacecraft scans the sensor's FOV across the Earth, and the sensor processing electronics amplify and filter the detected Earth IR pulse. The processed Earth signal is threshold detected to produce AOS and LOS times, and these times are telemetered to the ground. The Earth sensor signal processor also provides a nadir-reference pulse to the antenna despin control electronics. A block diagram of the Earth sensing system is illustrated in Figure 4.8-2. The threshold detection logic is a fixed percentage of the peak Earth pulse level. The output pulse width at the half-peak level is approximately equal to the chord length of the Earth scan. The Earth scan geometry and a typical sensor output pulse are shown in Figure 4.8-3. The time required for the FOV to cross the Earth horizon, combined with the electronics time constant, delays the pulse and causes finite rise and fall times. AC coupling in the sensor electronics causes some of the decay in the signal amplitude as the sensor scans across the Earth, as well as an overshoot at the end of the pulse. Figure 4.8-4 is a Laplace transform diagram of the Earth sensor electronics.

GOES-5 telemetered data from only one Earth sensor at a time. To maximize Earth coverage during the transfer and drift orbits, the data batch was selected based on predictions of the Earth sensor coverage.

4.8.2 MISSION DATA ANALYSIS

During support of the GOES-5 mission, difficulty was encountered while trying to determine a set of biases that would remove systematic patterns in the measurement residuals. A second analysis of these data showed that the largest residuals were observed over the southernmost latitudes, where the detected horizon was lower than expected. The cause of this was attributed to seasonal variation in the IR horizon

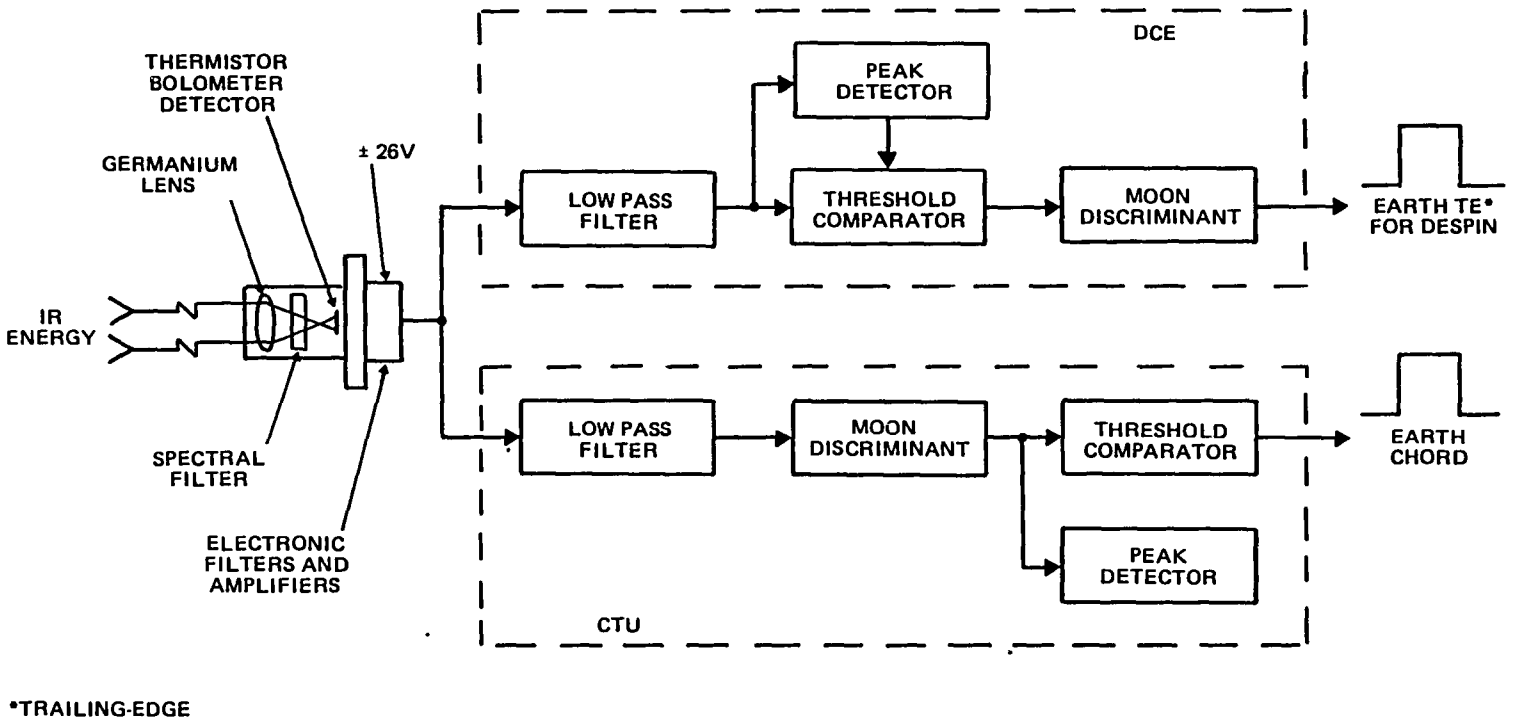

Figure 4.8-2. Block Diagram of the GOES-5 Earth Sensing System (Hughes Aircraft Company, 1978)

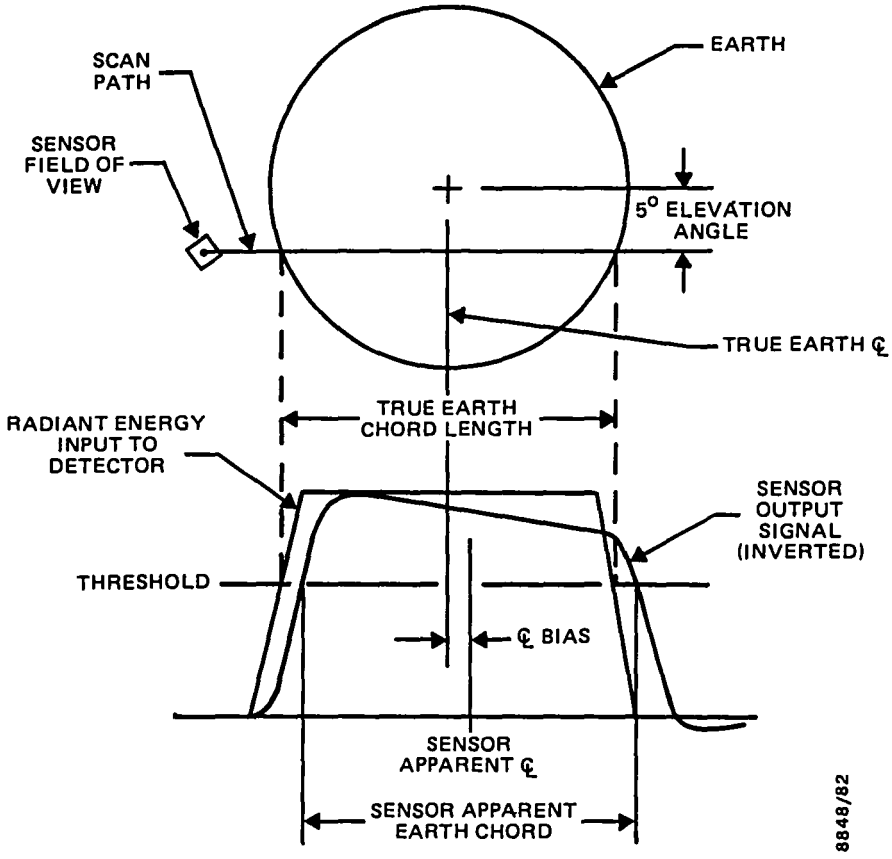

Figure 4.8-3. Typical Earth Sensor Output Pulse (Hughes Aircraft Company, 1978)

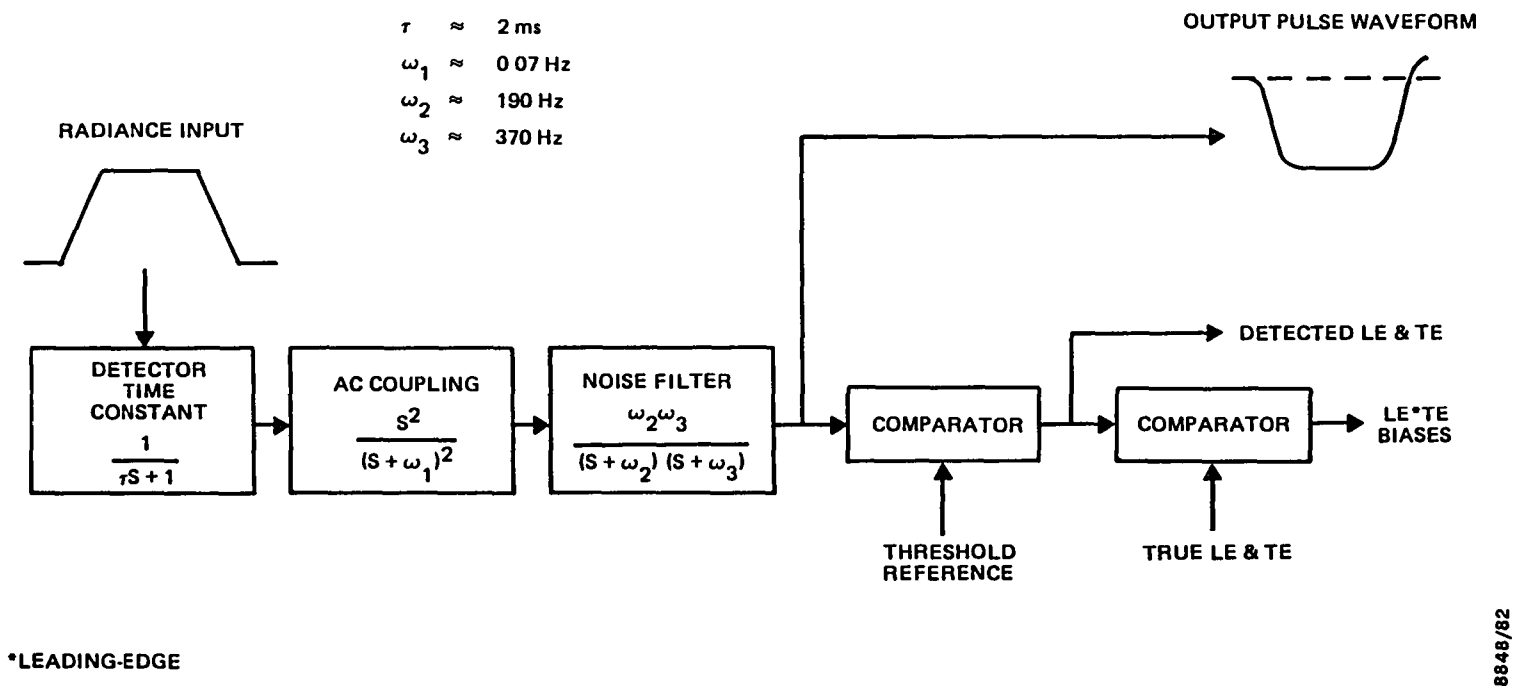

Figure 4.8-4. GOES-5 Earth Sensor Processing Electronics (Hughes Aircraft Company, 1978)

radiance (Reference 52). The analysis performed to check this conclusion (Reference 50) is reviewed below.

Figure 4.8-5 illustrates the spacecraft orbital geometry during the drift orbit. On June 2, 1981, the drift orbit was near circular (eccentricity of 0.0528), the orbit plane nearly coincided with the equatorial plane (inclination of 0.5273 degree), and the semimajor axis was 44,166.8 kilometers. The spin axis was in the orbit plane (right ascension (α) equal to 318.3 degrees, declination (δ) equal to 0.30 degree) such that it was parallel and antiparallel to the spacecraft velocity vector around perigee and apogee, respectively. As indicated in the figure, both sensors scanned the Earth for short periods (approximately 65 minutes each) near perigee and apogee.

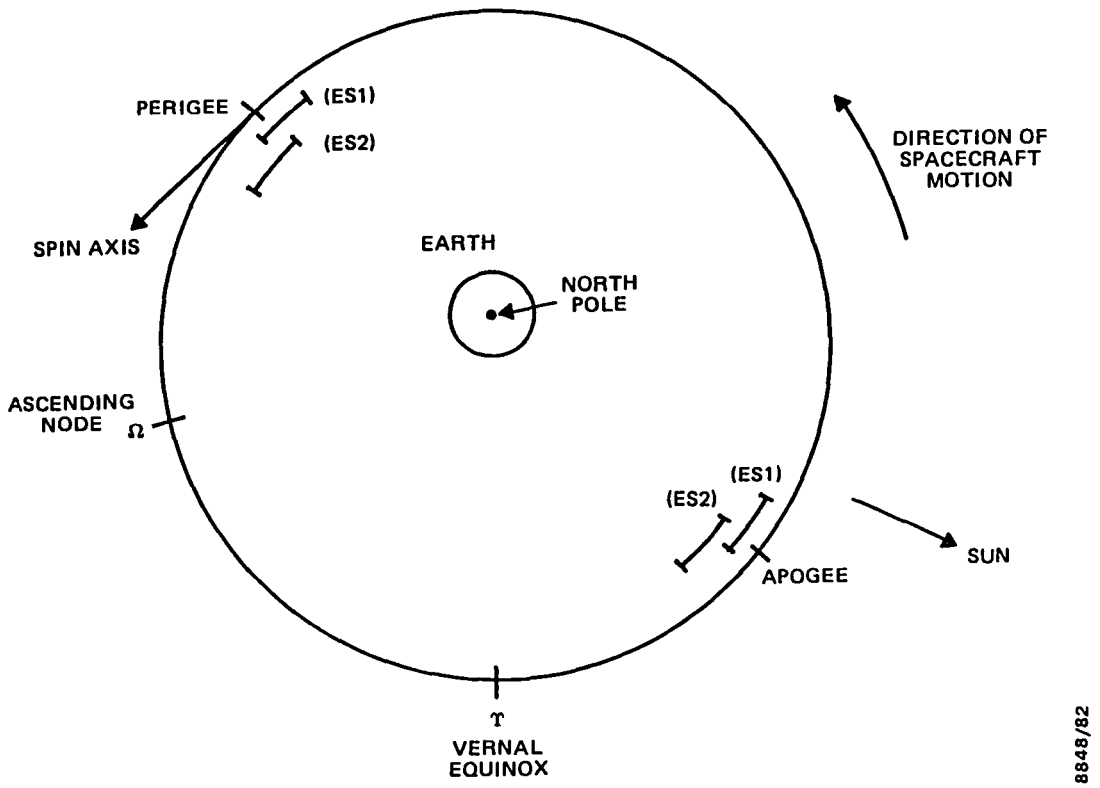

Figure 4.8-5. GOES-5 Configuration in Drift Orbit

The observed and predicted Earth-in and Earth-out crossing angle data from both sensors near perigee and apogee are plotted in Figures 4.8-6 and 4.8-7 for the time period 810602.0128 through 810602.0259 (YYMMDD.HHMM) and are typical of several passes that were taken. The predicted data were calculated using a single value of the Earth angular radius bias and sensor azimuth bias for both Earth edge crossings. As illustrated in Figure 4.8-6, the observed Earth-out data for both sensors agreed well with the predicted data, but the agreement between the observed and predicted Earth-in data was relatively poor. In Figure 4.8-7, the observed Earth-in data agree well with the predicted values, but the agreement between the observed and predicted Earth-out data is poor.

The analysis was repeated without restricting the Earth angular radius and sensor azimuth biases to identical values at the AOS and LOS edges. Except at the smaller Earth widths, reasonably good fits were obtained for the data, as illustrated in Figures 4.8-8 and 4.8-9. For this repeated analysis, the angular radius biases for the edge crossings in the Southern Hemisphere were always negative and larger than those for the edge crossings in the Northern Hemisphere. The results for the constrained and unconstrained cases are presented in Table 4.8-1, which is a corrected version of the table from Reference 50. (The table in Reference 50 contained data such that the Earth angular radius biases at apogee were inconsistent with the signs on the corresponding values in the original computer output.) The horizon crossing latitudes (for the transfer orbit attitude) near perigee and apogee are plotted in Figures 4.8-10 and 4.8-11. Near perigee, the Earth sensors acquired the Earth in the Southern Hemisphere and lost the Earth in the Northern Hemisphere. Horizon crossing latitudes ranged from the Equator to $\pm$56 degrees. When the sensors acquired or

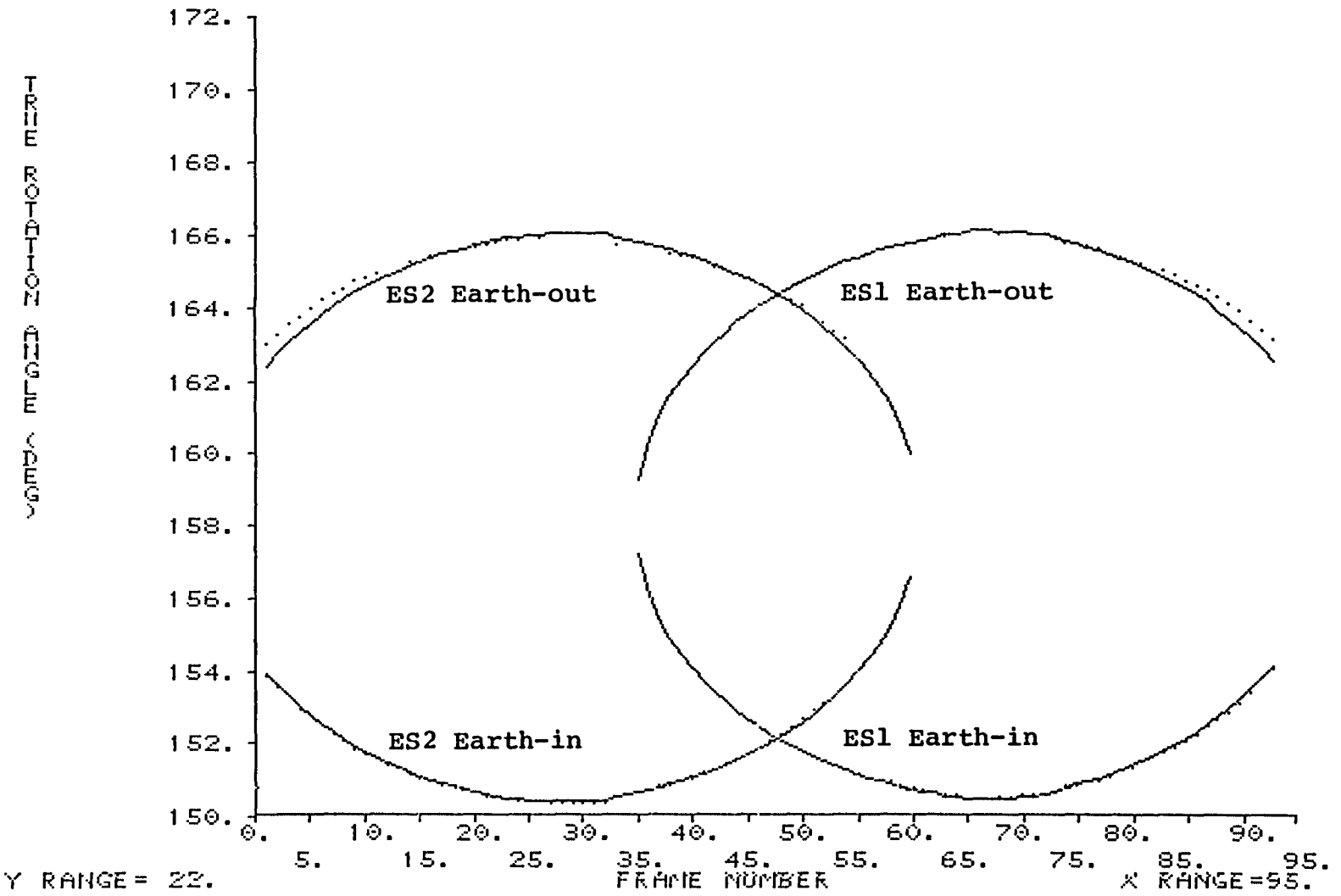

Figure 4.8-6. Observed (Dotted Curve) and Predicted (Solid Curve) Earth-In and Earth-Out Data Near Perigee; Biases Restricted to Equal Values

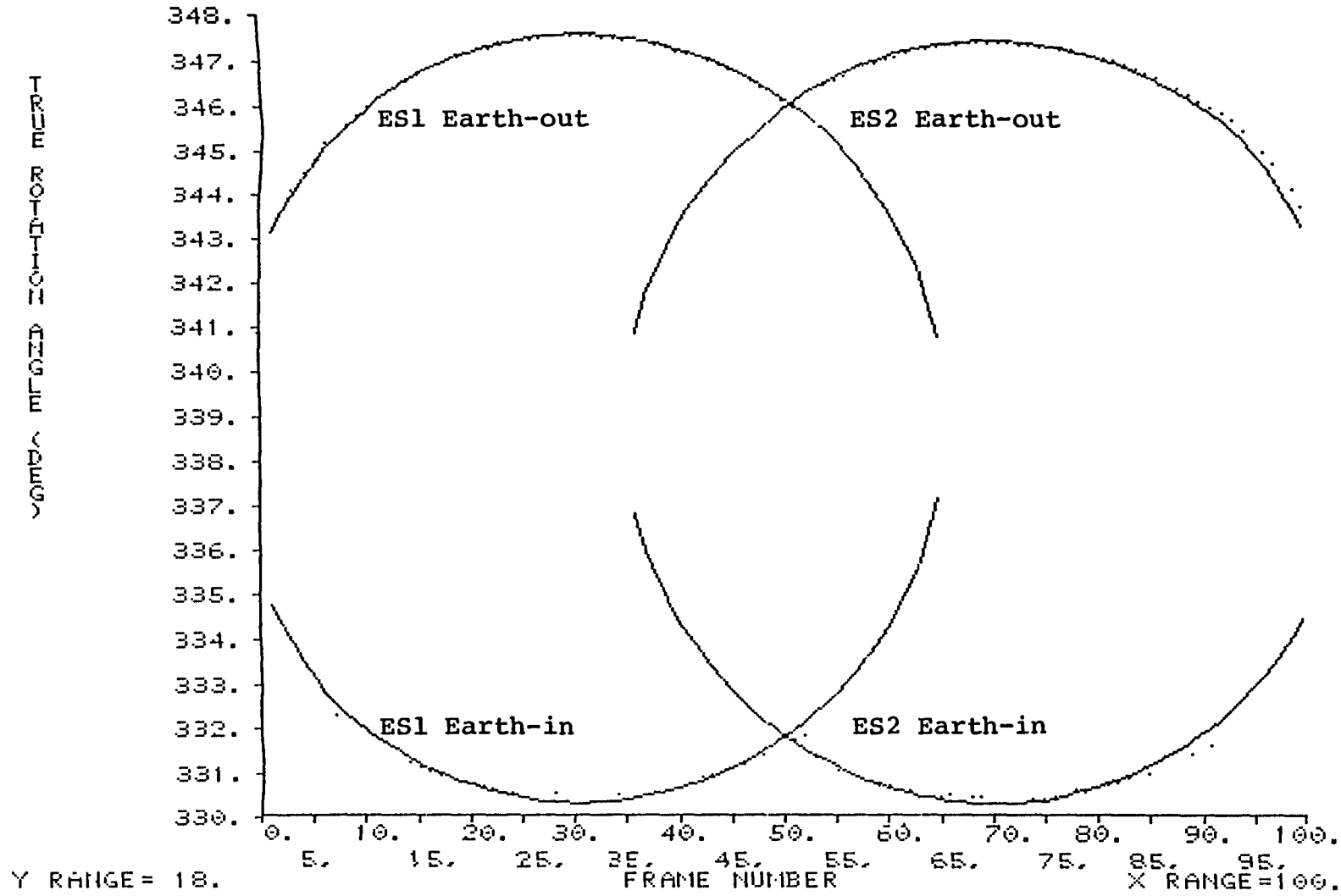

Figure 4.8-7. Observed (Dotted Curve) and Predicted (Solid Curve) Earth-In and Earth-Out Data Near Apogee; Biases Restricted to Equal Values

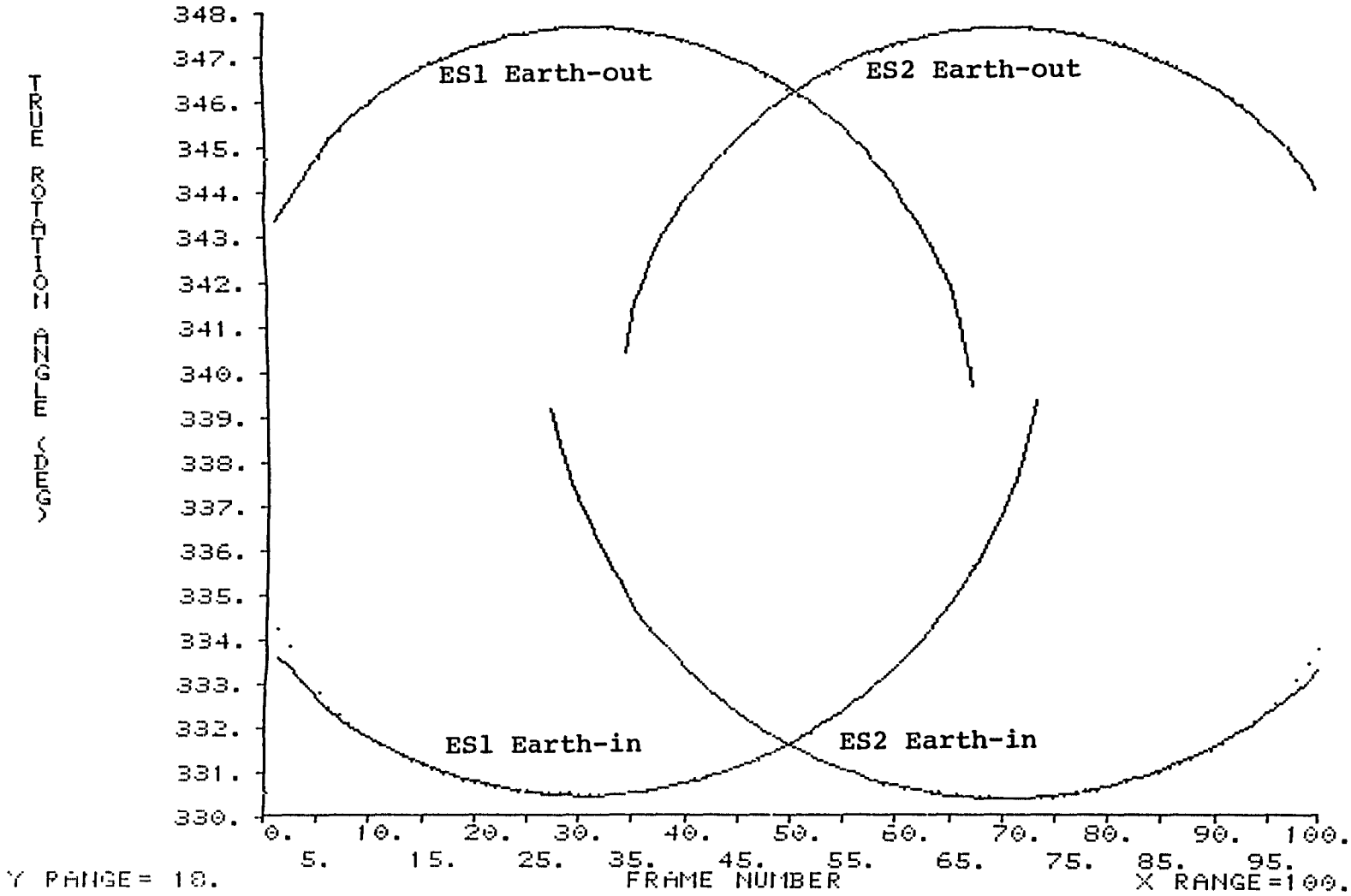

Figure 4.8-8. Observed (Dotted Curve) and Predicted (Solid Curve) Earth-In and Earth-Out Data Near Perigee; Unequal Bias Values Allowed

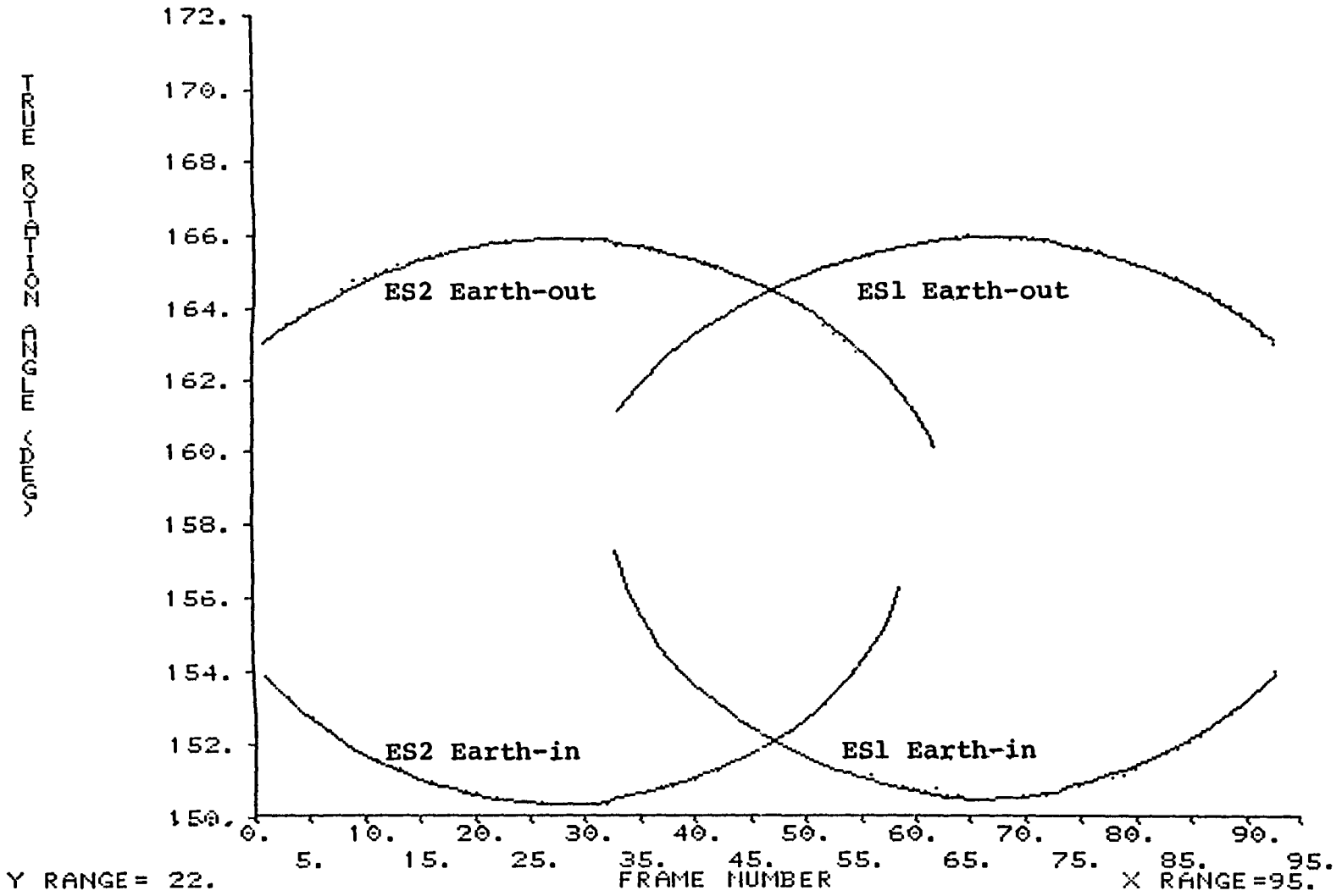

Figure 4.8-9. Observed (Dotted Curve) and Predicted (Solid Curve) Earth-In and Earth-Out Data Near Apogee; Unequal Bias Values Allowed

Table 4.8-1. Parameter Values Used To Generate the Observed-Versus-Predicted Data Plots

DATA	CASE	EARTH SENSOR	AZIMUTH BIASES (DEGREES)		ANGULAR RADIUS BIASES (DEGREES)	
			EARTH-IN	EARTH-OUT	EARTH-IN	EARTH-OUT
PERIGEE	CASE1	ES1	−2 41	−2 41	−0 13	−0 13
		ES2	−2 30	−2 30	−0 16	−0 16
	CASE 2	ES1	−4 45	−2 00	−1 81	−0 17
		ES2	−4 75	−1 61	−2 21	−0 46
APOGEE	CASE 1	ES1	−1 98	−1 98	−0 06	−0 06
		ES2	−1 99	−1 99	−0 07	−0 07
	CASE 2	ES1	−2 43	−0 56	−0 36*	−1 30*
		ES2	−1 83	−0 98	+0 21*	−0 86*

8848/82

NOTES EQUAL BIAS VALUES WERE ASSUMED FOR EARTH-IN AND EARTH-OUT HORIZON CROSSINGS IN CASE 1, UNEQUAL VALUES WERE ALLOWED IN CASE 2

POSTLAUNCH VALUES WERE USED FOR THE FOLLOWING BIASES (REFERENCE 52)

MOUNTING ANGLE BIAS FOR ES1 = −0 06 DEGREE
MOUNTING ANGLE BIAS FOR ES2 = −0 20 DEGREE
SUN SENSOR 1 BIAS = 0 13 DEGREE

AZIMUTH BIASES INCLUDE THE ELECTRONIC TIME DELAY

*THESE DATA ARE REPORTED WITH SIGNS REVERSED FROM THE ORIGINAL TABLE TO BE CONSISTENT WITH VALUES ON THE ORIGINAL COMPUTER OUTPUT

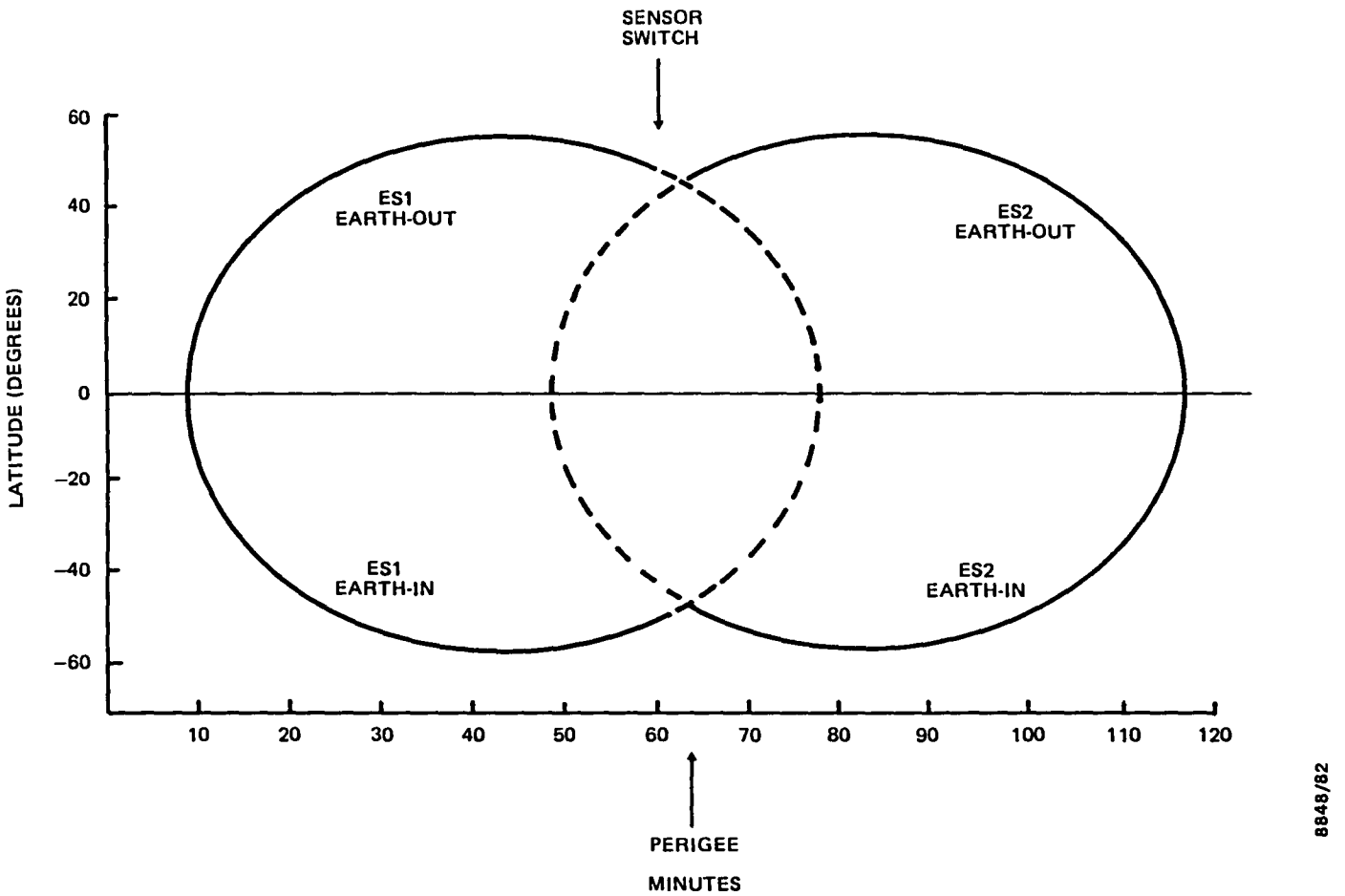

Figure 4.8-10. Horizon Crossing Latitudes Near Perigee

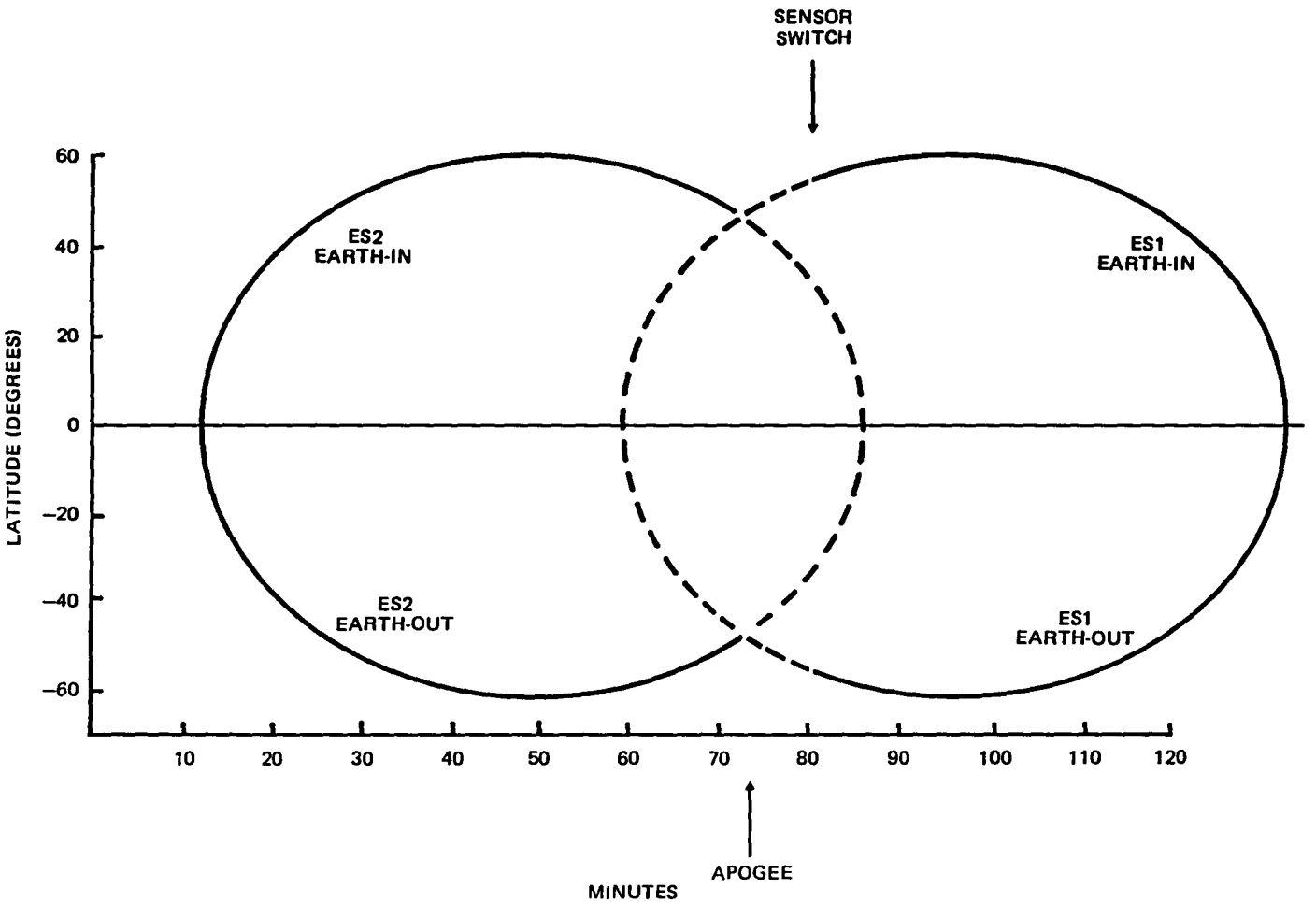

Figure 4.8-11. Horizon Crossing Latitudes Near Apogee

lost the Earth, the horizon crossing latitudes changed very rapidly. The situation near apogee was reversed so that the sensors acquired the Earth in the Northern Hemisphere and lost it in the Southern Hemisphere.

These results clearly indicated that the Earth sensors detected a lower Earth horizon in the Southern Hemisphere, which at the time of the data was the winter hemisphere. It was also discovered that it was not possible to model data taken as the sensor crossing latitudes changed rapidly. These results are summarized in the Earth model illustrated in Figure 4.8-12. The lower horizon altitude of the Southern Hemisphere is compensated for by an increased angular radius bias, but it leaves the low-latitude region in the Southern Hemisphere incorrectly modeled. This model of the Earth was satisfactory for the GOES-5 transition orbit attitude geometry. Further improvements would result, however, if a latitude-dependent parameter were incorporated into the Earth horizon altitude model.

4.8.3 RESULTS AND DISCUSSION

Reference 52 reported large errors in Earth-edge data taken in the drift orbit when the Earth sensors triggered in the southern latitudes. The cause of the errors was determined to be the season-dependent latitude variation in the horizon radiance. A second analysis of the problem confirmed the existence of differences between the observed and the predicted Earth sensor data from the drift orbit. The Earth sensors triggered at a lower altitude in the Southern (winter) Hemisphere than predicted by a uniform, horizon altitude model.

The differences between the observed and the predicted data were reduced when separate values of the Earth angular radius bias parameter were applied to the Earth-in and Earth-out crossings in the two hemispheres. A much larger

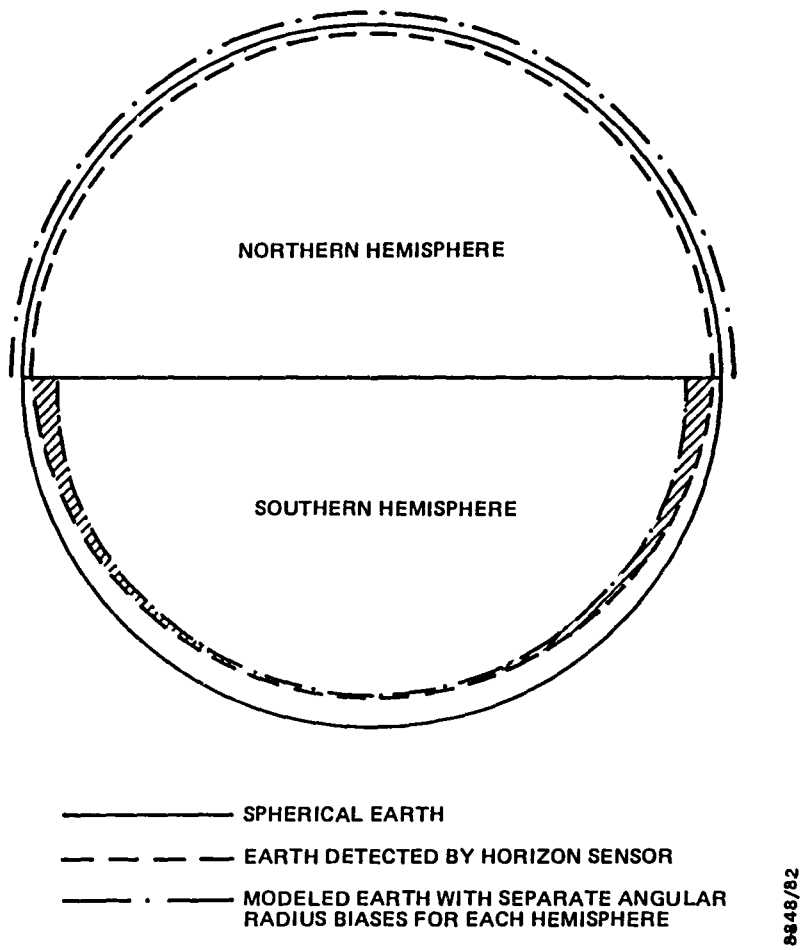

Figure 4.8-12. Modeled Earth in June for GOES-5

negative value for the Earth angular radius bias was required to predict the Earth edge crossings in the Southern Hemisphere accurately. It is interesting to note that the GOES-5 Earth sensors (employing a fixed percentage of the peak signal as their thresholding technique) showed significantly larger errors than the DE-1 sensors, which used a slope-sensitive thresholding technique.

When Earth sensors scan nearly constant latitudes, as in the GOES-5 nominal mission mode, latitudinal variations of the horizon radiance are not expected to affect Earth horizon measurements. When the spacecraft is in the transfer and drifts orbits, the Earth sensor incurs larger measurement errors than in the nominal mission configuration because of the large radiance variations experienced along the south-to-north scan line.

4.9 DYNAMICS EXPLORER-1

The DE-1 spacecraft was launched with the DE-2 spacecraft on a Delta 3913 launch vehicle. DE-2 was released first into a lower altitude orbit. Although the DE-1 and DE-2 spacecraft were a coordinated pair of satellites for science, the spacecraft differ significantly in their requirements for attitude determination and control support.

The DE-1 IR sensor data were analyzed using the mission support ADS software. No special support was required to correct the DE-1 attitude data for the effects of systematic horizon radiance variations. The data adjust subsystem of the DE-1 ADS did, however, have the capability of extending the Earth oblateness correction algorithm to include a correction to the Earth radius model that was proportional to the sine of the subsatellite latitude. This correction is functionally similar to that required for the model of systematic horizon radiance variations. Its use can be justified as an empirical method of improving the accuracy and reliability of the IR sensor data when the specified attitude solution accuracy requirements are not too high. This type of data correction is based primarily on deriving the correction from an analysis of flight data, minimizing the residuals between the IR sensor flight data and a model of that data including systematic radiance-variation-like correction functions.

The DE-1 mission data analysis illustrated the improvements in data accuracy that can be obtained as viewed through the data residuals. Even though improvements were realized, however, the suggested data correction procedure was not applied to the DE-1 definitive attitude data. The material presented in this section is derived from References 33 and 50.

4.9.1 MISSION REQUIREMENTS AND HARDWARE

DE-1 was launched from the Western Test Range at 09:55:00 UT on August 3, 1981. The DE-1 spacecraft is illustrated in Figure 4.9-1. The mission can be summarized as follows:

- Orbit--Polar with a 90-degree inclination, 683-kilometer perigee altitude, and 24,875-kilometer apogee altitude
- Attitude configuration
  - Spin stabilized at -10 rpm $\pm$0.1 rpm
  - Spin axis within 1 degree of orbit normal
- Attitude determination hardware
  - Two body-mounted IR horizon sensors (BHSs), similar to AE, with 2.5- by 2.5-degree FOV
  - Two single-axis Sun sensors (DSAIs) with $\pm$64-degree FOV; quoted accuracy of 0.1 degree for Sun angles less than 40 degrees
- Attitude control hardware
  - Four magnetic torque coils for spin axis precession and momentum control
  - Passive nutation dampers
- Accuracy requirement--0.3 degree (3σ) for Z-axis (spin axis) half-cone angle and for X-axis azimuth in spin plane
- Ground support system--Interactive processing
- Data processing requirements
  - Definitive solutions packaged as passes with approximately three nonoverlapping passes per day; results in generation of solutions for an average 50-percent duty cycle

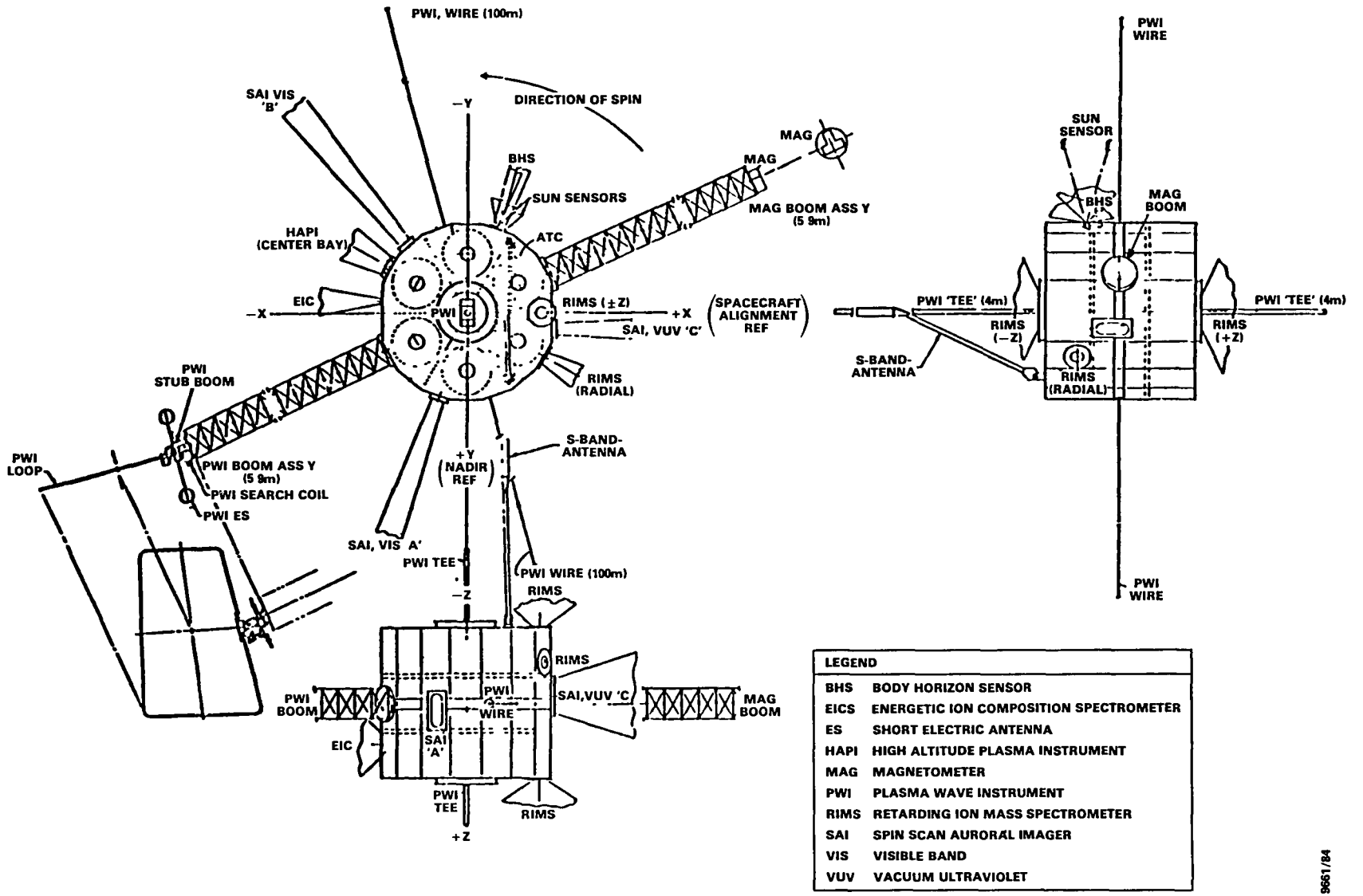

Figure 4.9-1. DE-1 Spacecraft Mission Configuration (Figure courtesy of RCA Astro Electronics)

  - Output data interval of 6 seconds
  - Turnaround in 2 to 5 days from receipt of telemetry data and definitive orbit data

- Problems encountered--Difficulty in azimuth determination related to
  - Cyclic accumulation of error due to 1-millisecond telemetry data resolution
  - Discontinuities from the merging of data segments with different time calibrations
  - Unmodeled variation in spin rate due to heating and cooling of 100-meter Plasma Wave Instrument (PWI) antenna wires
  - Early postlaunch discovery of inverted bits in the Sun sensor Gray code
  - Early postlaunch errors in the alignment calibration of the Sun sensors
  - Disabling of BHS1 by the command to turn off the spacecraft transponder, causing unexpected loss of data for BHS1 throughout the mission

At Delta separation, DE-1 had a spin rate of 64.5 rpm with the spin axis in the orbit plane. Upon acquisition of the Earth by the BHSs, a 22-day attitude maneuver was initiated to precess the spin axis from the orbit plane to 5 degrees from orbit normal. The maneuver was stopped for bias data collection, a spinup maneuver, and appendage deployment. Following deployment of experiment booms and the 63-meter portion of the PWI antennas, the spacecraft attitude was maneuvered to orbit normal and the second phase of the spinup maneuver was executed. The remaining 27 meters of the PWI antennas were then deployed, and the final spinup maneuver to establish the mission spin rate at 9.9 rpm was performed.

After all the acquisition maneuvers were completed, the sensor biases were determined, and DE-1 began mission operations on September 20, 1981.

The two DSAIs (DSAI1 and DSAI2) employed on DE-1 provide Sun angle information and a Sun reference pulse for timing purposes. The two BHSs (BHS1 and BHS2) locate the horizon of the Earth by detecting IR radiation. Mounted on the spacecraft in a "V" configuration (Figure 4.9-2), the BHSs are functionally independent altnough mounted in the same package. The BHS reference axis, R, lies in the spacecraft X-Y plane, 290 degrees from the +X-axis rotating in a positive sense about the +Z-axis. The optical axes of the sensors are in the R-Z plane, at angles 81 degrees and 99 degrees from the spacecraft Z-axis. The lens system in each sensor focuses IR radiation in the 14- to 16-micrometer range onto a bolometer. When the spinning motion of the spacecraft scans the sensor's FOV across the Earth, the sensor signal processing electronics amplify and differentiate the detected signal. Earth-in and Earth-out pulses are generated when the differentiated signals reach 50 percent of the peak values of the derivative of the previous Earth pulse. Figure 4.9-3 is a block diagram of the DE-1 BHS electronics. More details on the spacecraft and its sensors are presented in References 53 and 54.

4.9.2 MISSION DATA ANALYSIS

4.9.2.1 BHS Data

Four types of BHS data are used in the DE-1 ADS: Earth-in pulse time, Earth-out pulse time, Earth width time, and Earth midscan time. Earth-in and Earth-out pulse times are measured from the Sun event to the times when the BHS FOV encounters and loses the Earth, respectively. They are converted directly from the telemetered data. Earth width and Earth midscan times are data derived from the Earth-in and

Earth-out pulse times. Figures 4.9-4 and 4.9-5 are examples of telemetered BHS event time data converted to rotation angles and Earth width angles for February 8, 1982. The plots are of data taken near apogee. The DE-1 BHS data display remarkably low noise; except for a few abnormal points, the noise level is less than 0.05 degree.

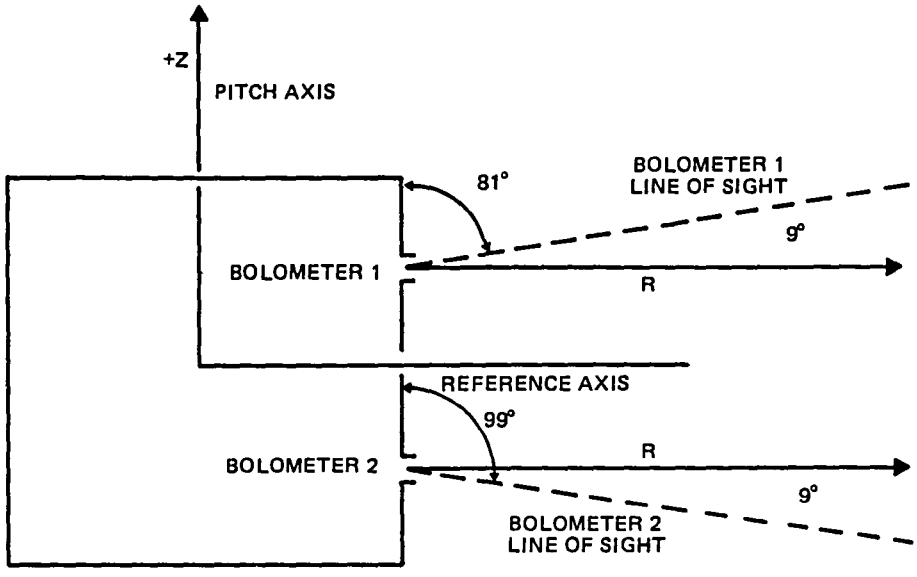

Figure 4.9-2. DE-1 Body-Mounted Horizon Sensor Geometry

It should be noted that BHS2 data appear either in the same minor frame as the DSAI2 Sun time or an even number of minor frames later. Both DSAI2 Sun times and BHS2 data times are thus subject to equal amounts of truncation. On the other hand, BHS1 data appear an odd number of minor frames later than the DSAI2 Sun times, and the amount of truncation differs by up to 0.5 millisecond. When DSAI2 is selected as the reference sensor for timing, BHS1 data therefore appear to have extra data noise of up to 0.5 millisecond (or 0.03 degree at 10 rpm). When DSAI1 is selected as the reference sensor, BHS2 data display that extra data noise. The

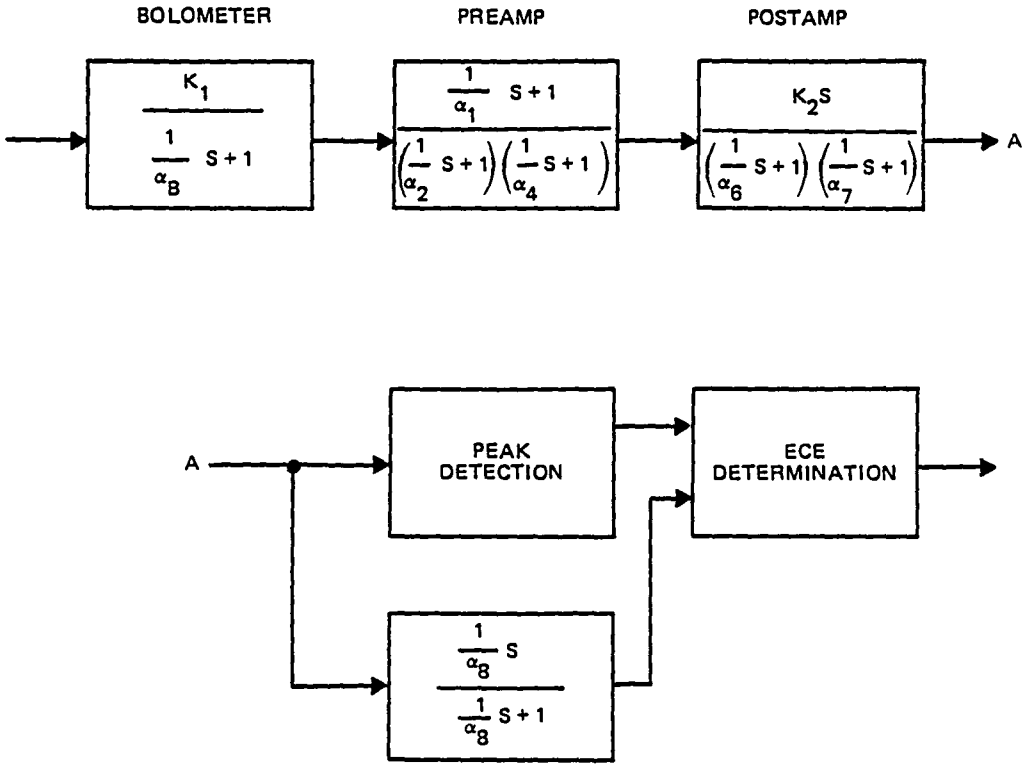

K_1	= 3 525E-5 V/W	α_4	= 404
K_2	= 122 5	α_6	= 1 13
α_B	= 286	α_7	= 201
α_1	= 1 03	α_8	= 0 01
α_2	= 102.5		

8848/82

Figure 4.9-3. DE-1 Body-Mounted Horizon Sensor Electronics

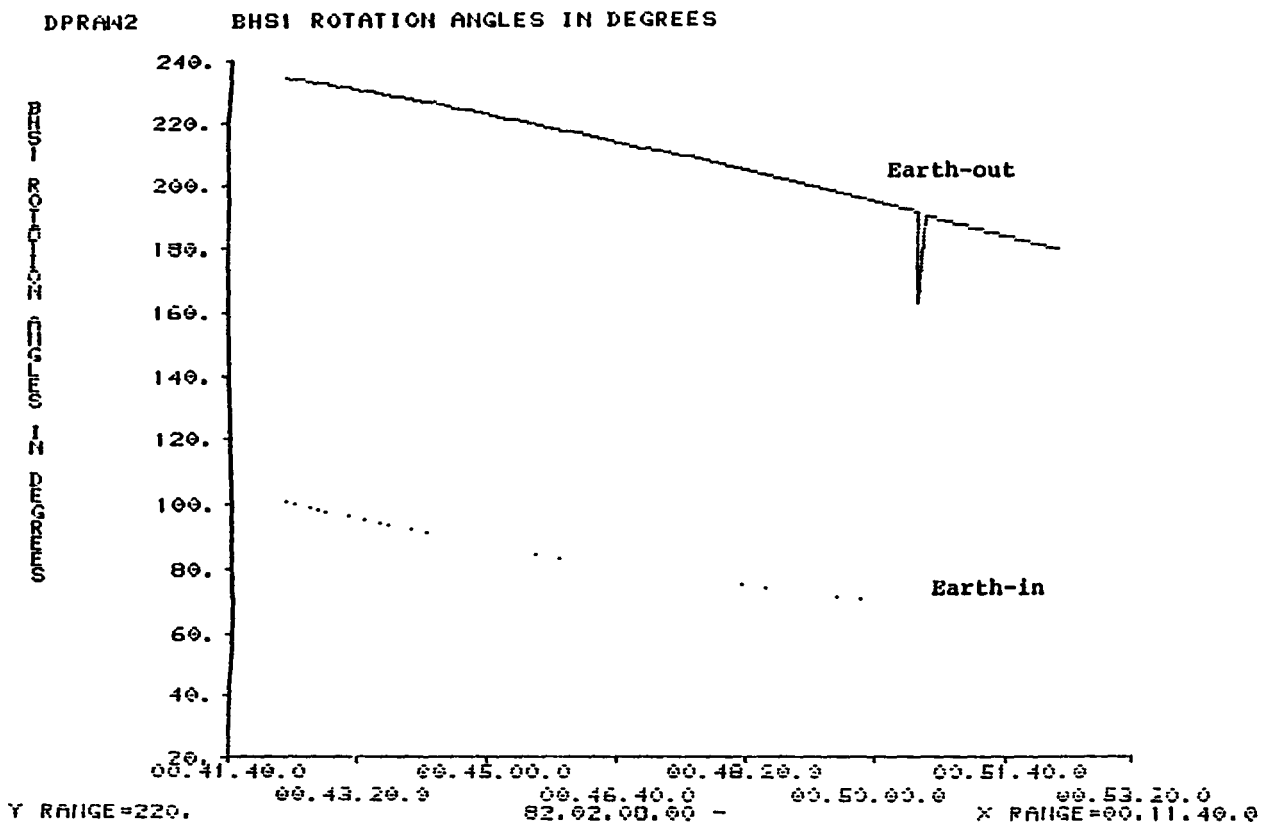

Figure 4.9-4. BHS1 Earth-In and Earth-Out Data for February 8, 1982

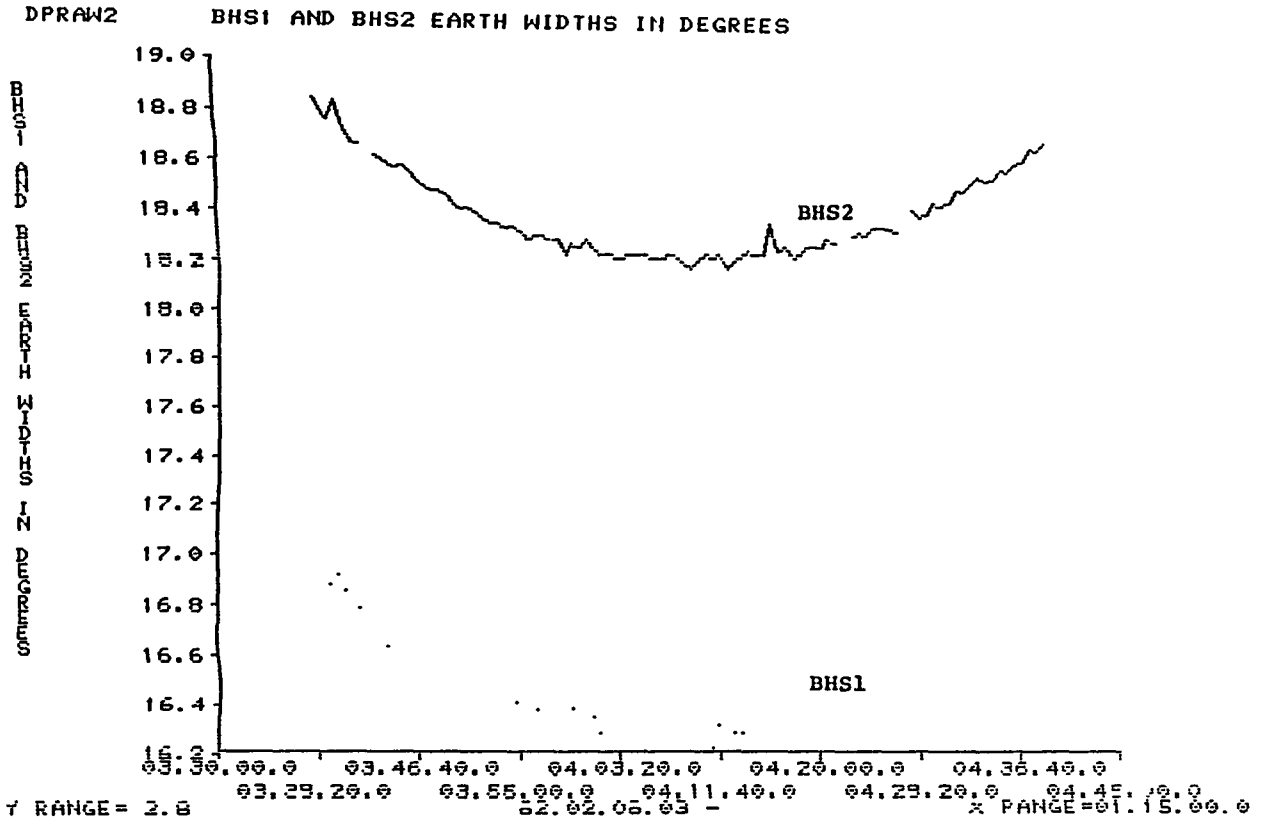

Figure 4.9-5. BHS1 and BHS2 Earth Widths Near Apogee for February 8, 1982

errors induced in the DE-1 attitude sensors by data tim- ing procedures are discussed further in Reference 55.

In the nominal DE-1 mission, the Sun interferes with each BHS for approximately 5 days, twice a year. The interference occurs whenever the Sun angle is within 2 degrees of the BHS scan cone and was first observed from BHS2 on September 10, 1981 (see Figure 4.9-6). The data showed that while the Sun was in the BHS2 FOV, BHS1 data looked normal but BHS2 was triggered by the Sun, producing fictitious Earth width data equivalent to the size of its FOV, defined by the solar IR intensity and Earth signal processing electronics.

Moon interference with the BHSs is observed when the nadir angle of the Moon is near 81 degrees (BHS1 mounting angle) or 99 degrees (BHS2 mounting angle); the illumination level of the Moon is high, i.e., a near-full Moon; and the Moon and the Earth are well separated. An example of the observed Moon interference with BHS1 is shown in Figure 4.9-7; only Moon-in signals were detected by the sensor. No detailed explanation of the Moon interference effect was established by the analysis of Reference 50. Because it is possible to predict the times of Sun/Moon interference with the BHSs accurately, these occurrences present no significant operational problems.

A systematic discrepancy between the observed BHS data and the predicted behavior, referred to as the Pagoda effect, occurs when the Earth width is small. The effect was seen in the DE-1 data during the attitude acquisition mode and is visible in the data of Figure 4.9-8. Although the phenomenon has not been explained in detail, the most likely origin is that the finite FOV size greatly distorts the sensed Earth chord when the BHS scan cone is nearly tangent to the

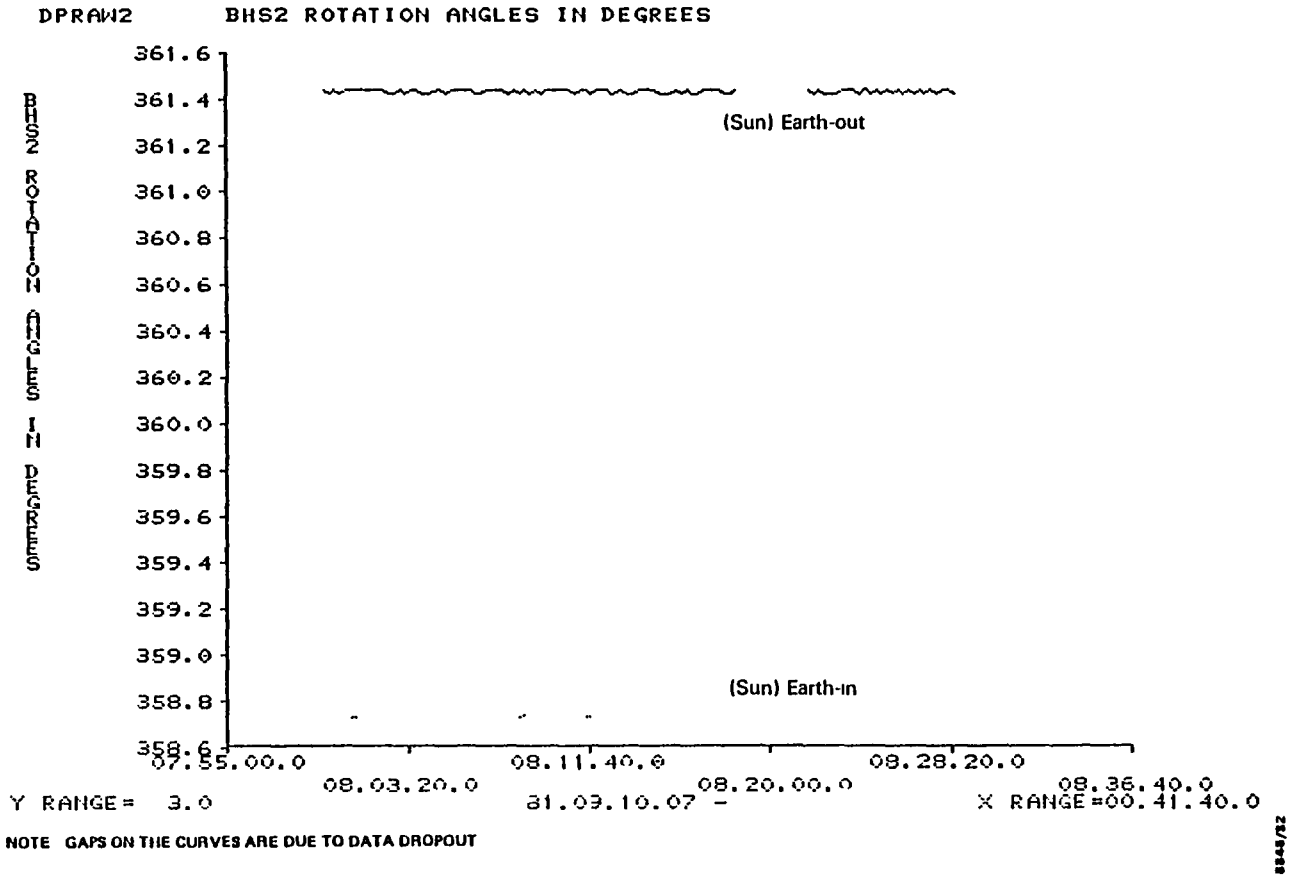

Figure 4.9-6. BHS2 Earth-In and Earth-Out Data During Sun Interference on September 10, 1981

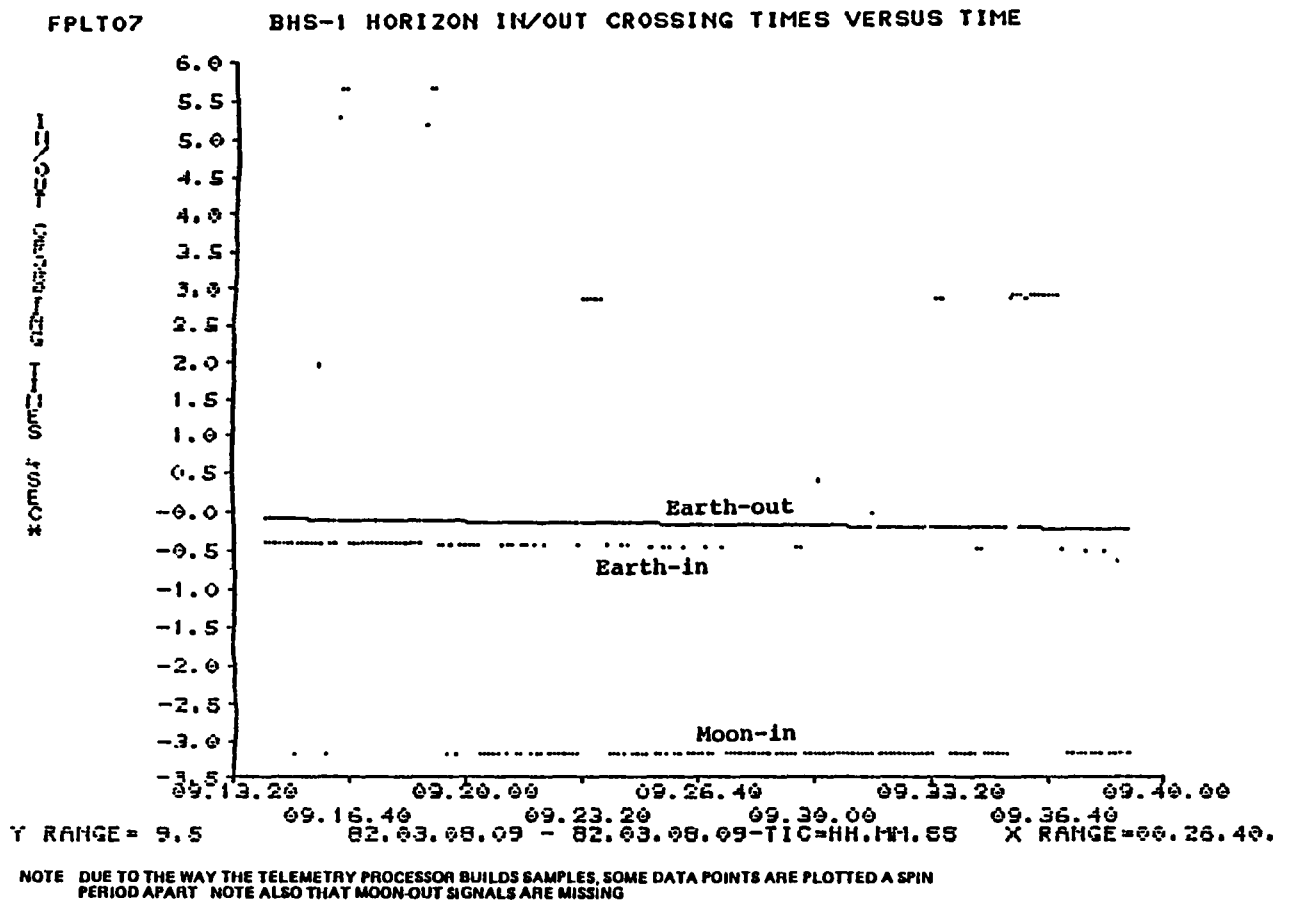

Figure 4.9-7. BHS1 Data Showing the Effect of Moon Interference

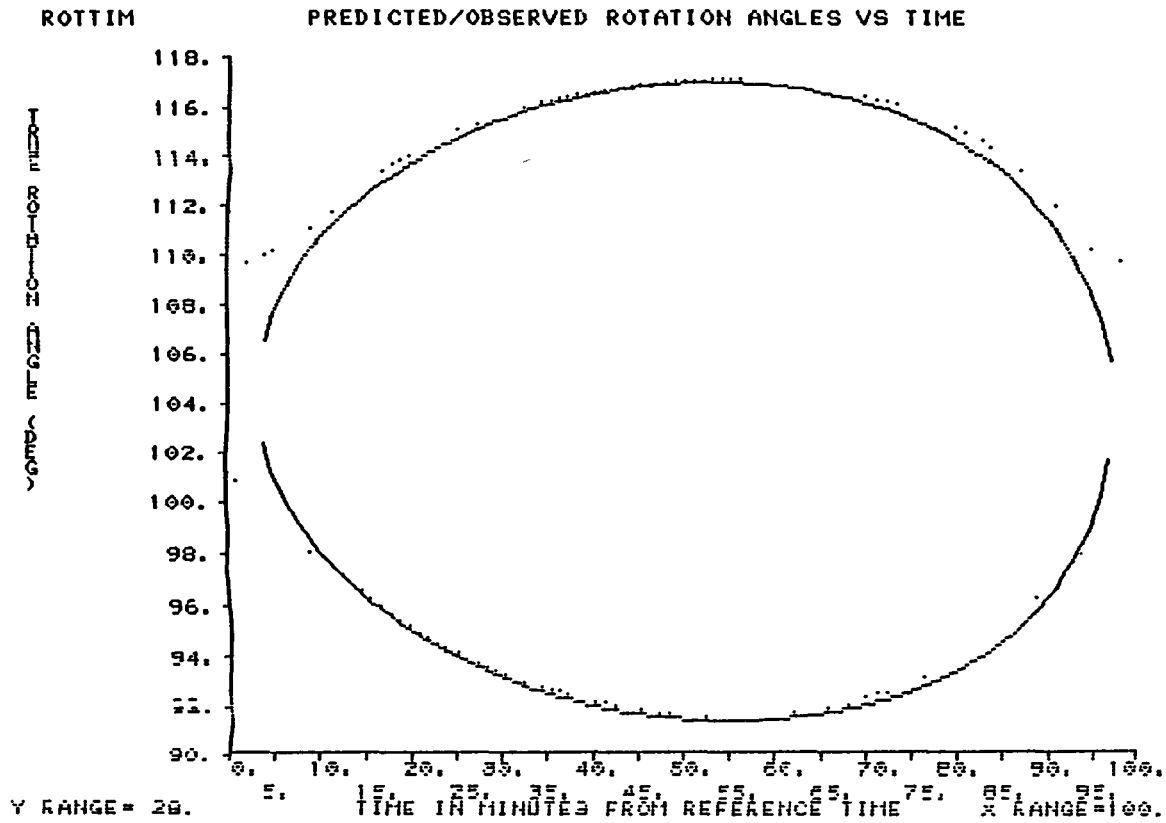

Figure 4.9-8. Observed BHS1 Data Showing the Pagoda Effect (Dotted Curve) and the Predicted Data (Solid Curve)

Earth disk. The effect is further amplified by the electronics in the Earth pulse processing circuit.

The RCA prelaunch simulation (Reference 56) of the DE-1 BHSs indicated a nominal delay in the hard Earth center relative to the split pulse; the split pulse leads the hard Earth center by 0.575 degree at apogee and 0.188 degree at perigee. To compensate for this altitude-dependent delay, the DE-1 ADS included a correction of the form

$$\Delta\phi = ar^2 + br + c$$

where $\Delta\phi$ is the correction for the electronic delay in degrees; r is the spacecraft range in kilometers; and a, b, and c are coefficients adjusted to fit the RCA simulation results. Studies with spacecraft flight data showed, however, that the BHS Earth midscan data still had large residuals after this correction was applied.

To investigate the reasons for the increased residuals in the off-orbit-normal case, the midscan residuals were computed without applying the correction and are shown in Figure 4.9-9, with the Earth width for each frame superimposed (the solid curve). The figure clearly indicates that the correction for the electronic delay is a function of Earth widths rather than spacecraft altitude.

4.9.2.2 Horizon Radiance Variations

Another conspicuous feature of the DE-1 BHS data emerged from examination of the residual plots. The BHS1 Earth-in residuals for October 31, 1981, show a maximum at Frame 44 and a minimum at Frame 55 (Figure 4.9-10); the BHS1 Earth-out residuals showed a similar pattern with a maximum at Frame 52 and a minimum at Frame 60. The Earth width data for these times show the resulting extrema that correspond to detected horizon latitudes of $\pm$90 degrees. Similar

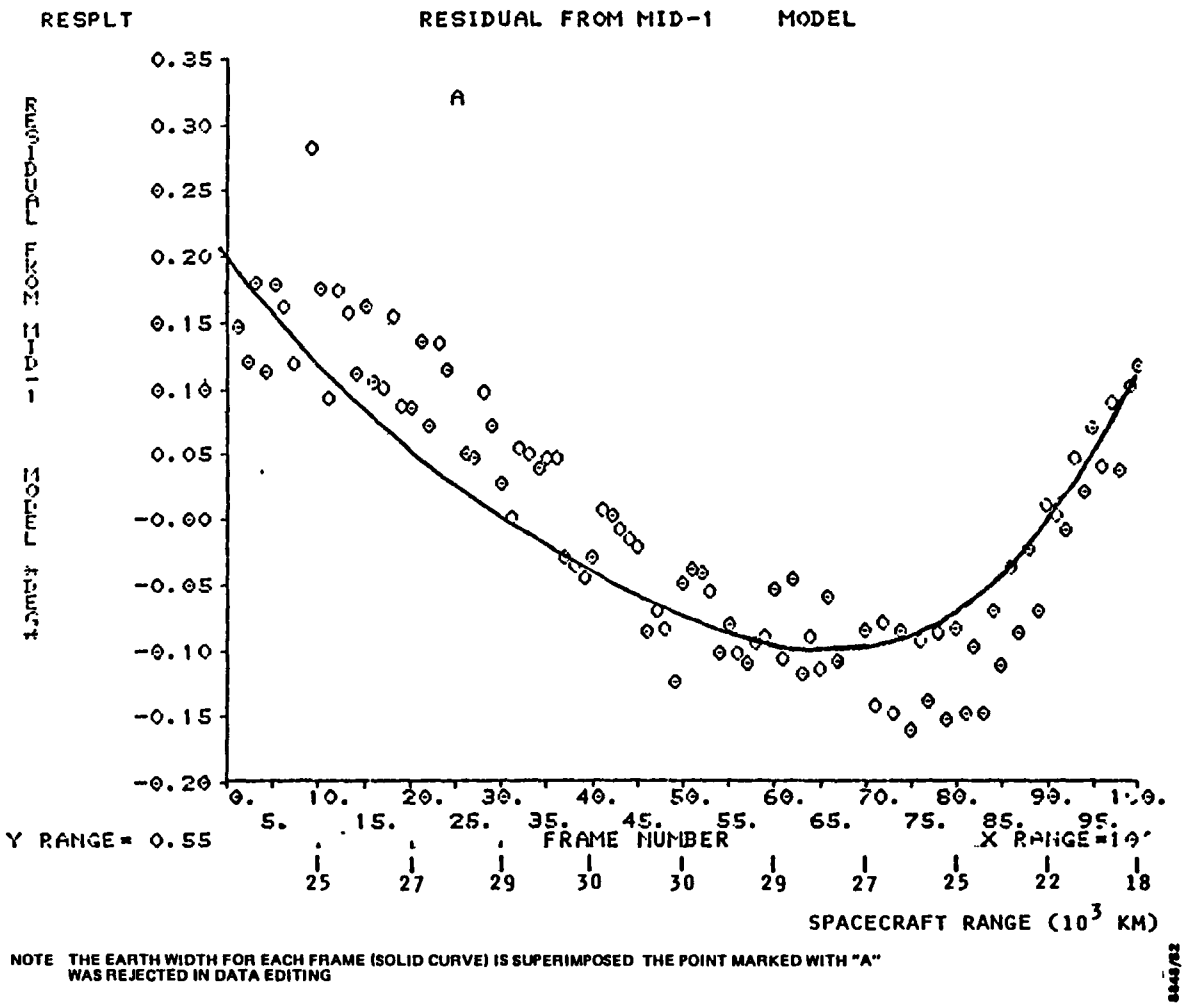

Figure 4.9-9. Earth Midscan Residuals for August 28, 1981 (Computed without the correction for the electronic delay)

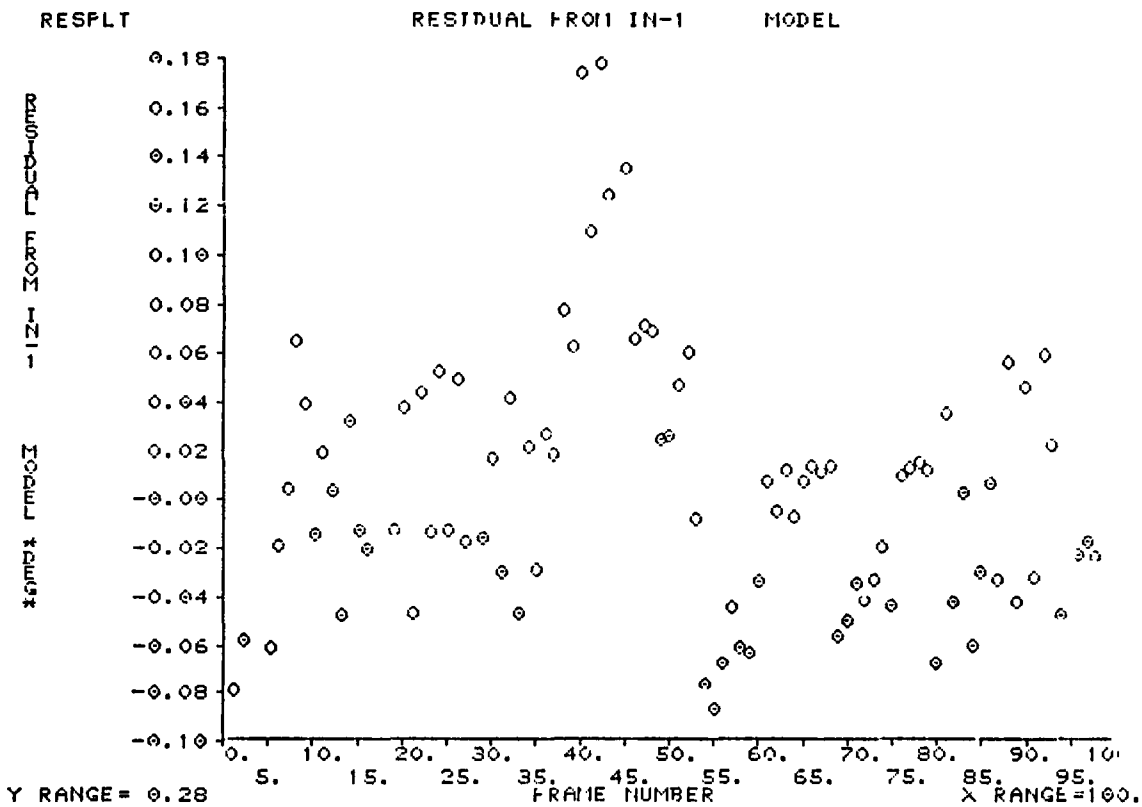

Figure 4.9-10. BHS1 Earth-In Residuals for October 31, 1981, Showing Maximum at Frame 44 and Minimum at Frame 55

observations were made in several different orbits, showing a definite correlation between extrema in Earth data residuals and detected horizon latitudes of ± 90 degrees.

To compensate for this anomaly, a latitude-dependent term, $f_2 \sin \lambda$, was used to adjust the Earth radius model,

$$R = R_{eq}(1 - f_1 \sin^2 \lambda + f_2 \sin \lambda)$$

where R_{eq} is the equatorial radius of the Earth, f_1 is the Earth flattening coefficient, λ is the latitude, and f_2 introduces a modification that is asymmetric with respect to the Equator. The f_2 coefficient changes with time of year to account for the seasonal variation of this correction. The BHS data residuals changed significantly when the asymmetric correction was introduced. Figure 4.9-11 shows the residuals in BHS1 data for selected values of the f_2 coefficient. The smallest residuals were obtained with f_2 equal to -0.001.

The results indicated that the model with a constant 38-kilometer IR horizon altitude caused 7-kilometer errors, which correspond to 0.2 degree in edge-triggering data, 0.15 degree in Earth width data, and 0.1 degree in midscan data. The spacecraft altitude is the dominant factor in the sensitivity of the residuals to error in the IR horizon altitude model. The largest residuals occur when the points with scan latitudes near ± 90 degrees occurred at perigee. An Earth width error of 0.1 degree at perigee can cause an error of up to 0.4 degree in the nadir angle computation and, subsequently, that much error in the computed attitude.

To observe the seasonal variation of the horizon radiance through BHS data, full-orbit data were taken in each season: October 31, 1981, for autumn; February 8, 1982, for winter; March 14, 1982, for spring; and July 14, 1982, for summer.

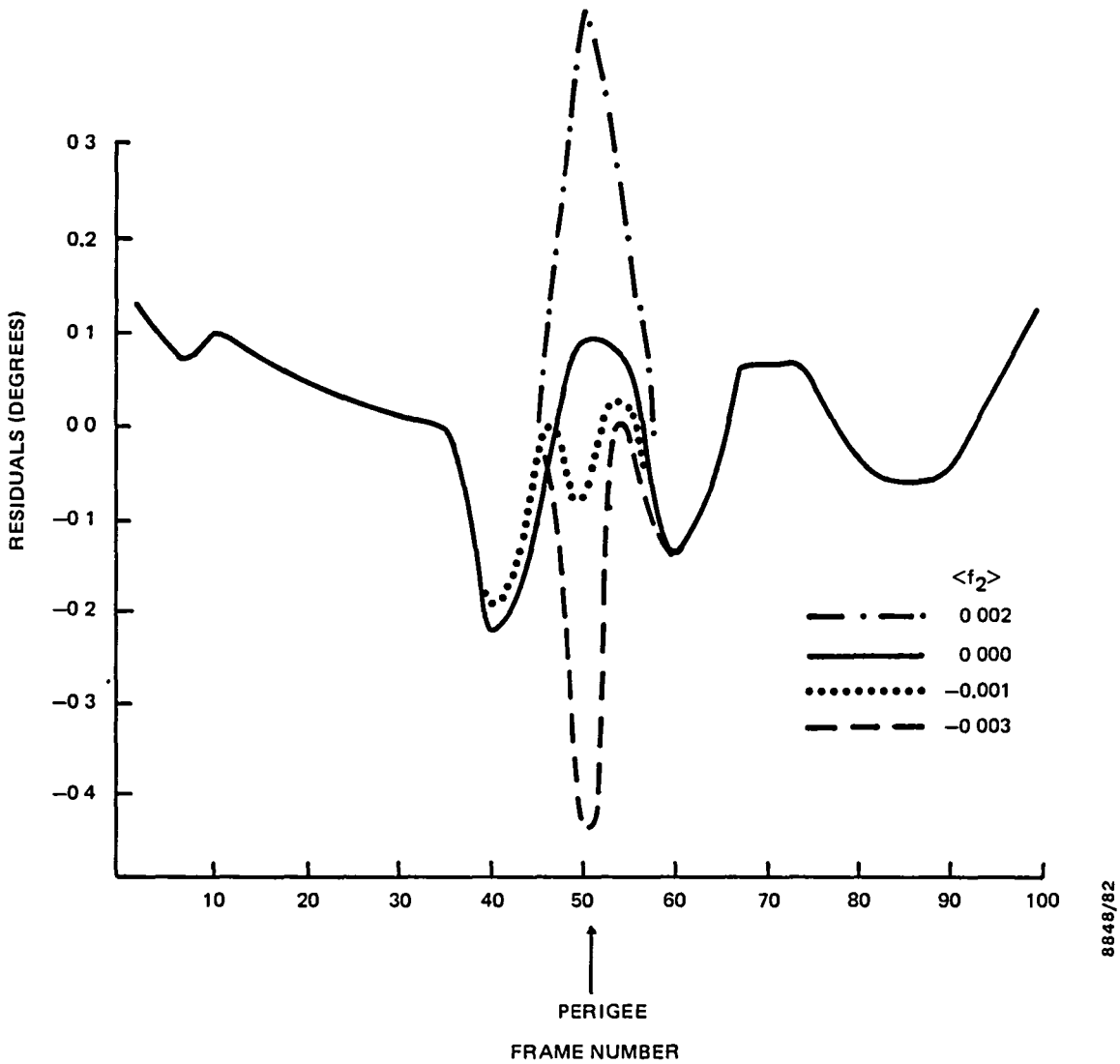

Figure 4.9-11. Variation of BHS1 Earth Width Residuals With the Value of the f_2 Coefficient, Autumn (October 31, 1981)

The f_2 coefficient that minimized the BHS Earth-in and Earth-out residuals was computed for each season.

For the winter data (Figure 4.9-12), -0.001 was still the optimum value for f_2. For the spring data (Figure 4.9-13), an f_2 coefficient value of 0.0 showed the minimum residuals, indicating that the nominal CO_2 height of 38 kilometers was good enough for the Earth model. Sizable residuals were, however, detected in some of the spring data when the BHS scanned the northern midlatitudes. For the summer data (Figure 4.9-14), the optimum f_2 coefficient value was 0.0005, which means that the nominal CO_2 height (38 kilometers) was overestimated by 3 kilometers near the South Pole. Closer examination of the Earth-out data was not possible, however, because the 16-minute shadow after perigee passage eliminated the Sun sensor reference data. Table 4.9-1 summarizes these observations of the seasonal variation of the horizon radiance.

Table 4.9-1. Season Variation of the Horizon Radiance

DATE	ARGUMENT OF PERIGEE (DEGREES)	SHADOW	BEST f_2 VALUE	ESTIMATED CO_2 HEIGHT AT THE SOUTH POLE (KILOMETERS)
OCTOBER 31, 1981 (AUTUMN)	254	NONE	–0 001	45
FEBRUARY 8, 1982 (WINTER)	220	NONE	–0 001	45
MARCH 14, 1982 (SPRING)	209	32 MINUTES NEAR APOGEE	0 0	38
JULY 14, 1982 (SUMMER)	168	16 MINUTES NEAR PERIGEE	0 0005	35

4.9.3 RESULTS AND DISCUSSION

The analysis of the DE-1 IR data showed that it was necessary to model the Earth radius with a north-south latitude asymmetry to minimize the residuals between the data and the

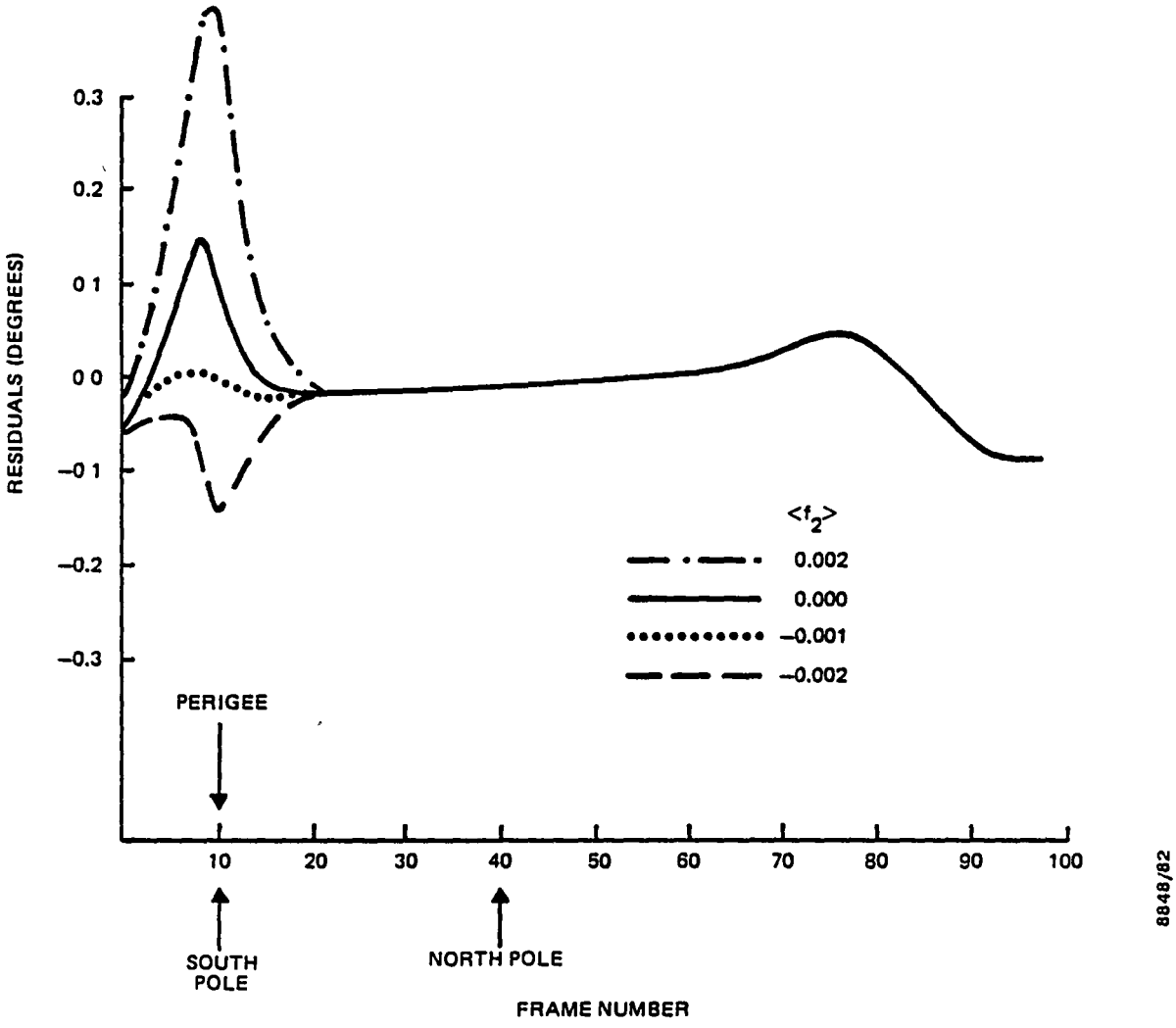

Figure 4.9-12. Variation of BHS1 Earth-Out Residuals With the Value of the f_2 Coefficient, Winter (February 8, 1982)

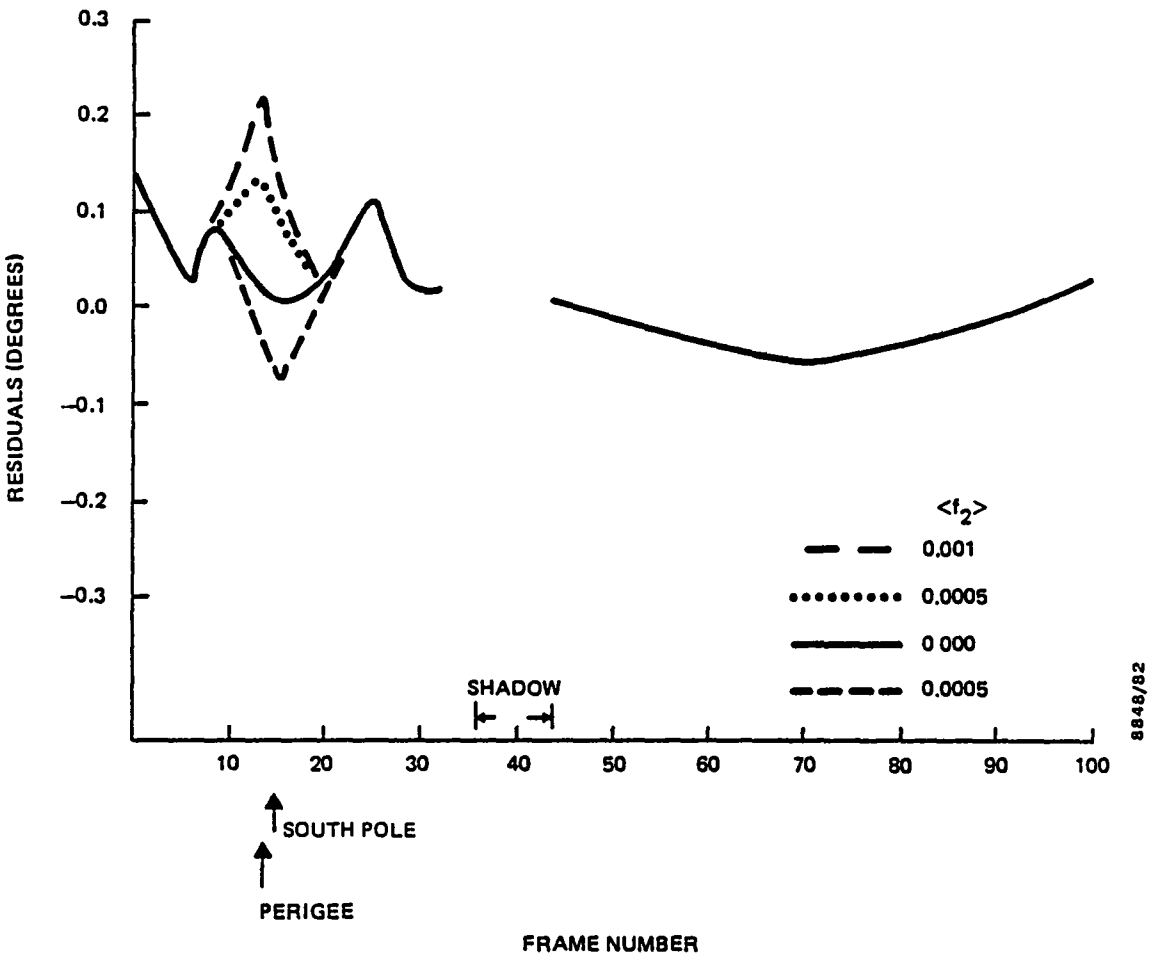

Figure 4.9-13. Variation of BHS2 Earth-Out Residuals With the Value of the f_2 Coefficient, Spring (March 14, 1982)

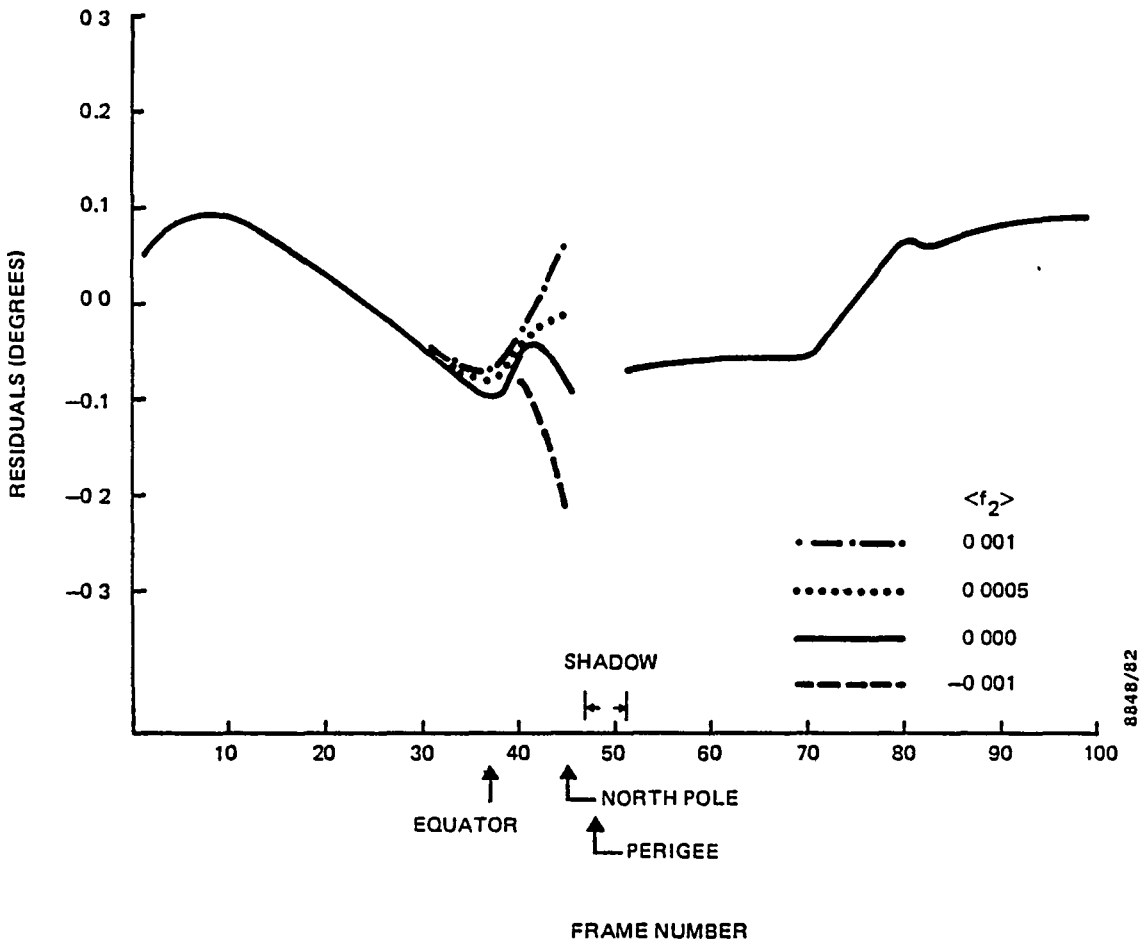

Figure 4.9-14. Variation of BHS1 Earth-In Residuals With the Value of the f_2 Coefficient, Summer (July 14, 1982)

data model, and that this component of Earth radius model had a seasonal dependence. The analysis therefore showed clear evidence for the effects of systematic variations of the Earth IR radiance on the DE-1 BHS data. It was also shown that a modest improvement in the accuracy of the data can be achieved by applying a simple correction function proportional to the sine of spacecraft latitude.

This method of correction lends itself to preflight determination of the coefficient f_2 (of the sine of latitude), with followup postlaunch flight data analysis to refine the estimates on a seasonal or monthly schedule. This sine-of-latitude correction function is a less exact procedure than that applied for other missions using a seasonal Earth radiance model and detailed IR sensor geometry and electronics model. It can, however, lead to significant improvements in the accuracy of the data for mission such as DE-1 and GOES-5 with high-altitude Earth sensing geometry and less stringent attitude accuracy requirements.

4.10 SOLAR MESOSPHERE EXPLORER

SME is a spin-stabilized scientific satellite operated by students and scientists at the University of Colorado. Five science instruments on board were designed to measure atmospheric concentrations of oxygen, ozone, nitrogen dioxide, and water vapor. The method was to scan the Earth disk at the 5-rpm spacecraft spin rate in various optical and IR bands. A four-channel IR radiometer was to be cooled to 130K without cryogenics, using a specially designed radiative antenna assembly opening into the antisolar direction. The four-channel IR radiometer scanned the Earth at the 6.3-, 9.6-, and 15-micrometer (wide and narrow) bands, and thus offered an opportunity to compare the measured 15-micrometer profiles with the LOWTRAN 5/RAOBS model of those profiles. However, because of a failure in the heat sink attachment of the 15-micrometer bolometer, these data were not available. An extensive analysis was performed on the SME BHS sensor data (Reference 57) to determine a global horizon triggering altitude model for attitude data correction. More details on the material presented in this section are available in References 13, 57, 58, 59, and 60. Several of the figures are taken from Reference 13.

4.10.1 MISSION REQUIREMENTS AND HARDWARE

SME was launched on October 6, 1981. The spacecraft structure and dimensions are illustrated in Figure 4.10-1. The mission can be summarized as follows:

- Orbit--Circular, near-polar, Sun-synchronous, with 97.6-degree inclination and 534-kilometer altitude
- Attitude configuration--Spin stabilized; spin axis along orbit normal (Figure 4.10-2), but switched to a constant Sun angle mode early in the mission

(PAGE TITLE)		1 REPLACES PAGE(S)	2 PAGE NO. 1400.2
SME ON-ORBIT		DATED	3. DATE FEBRUARY 1980
4 PROGRAM TITLE	5 MISSION(S) SME	6 PROGRAM NO.	7 REVISION NO.

8 DESCRIPTION

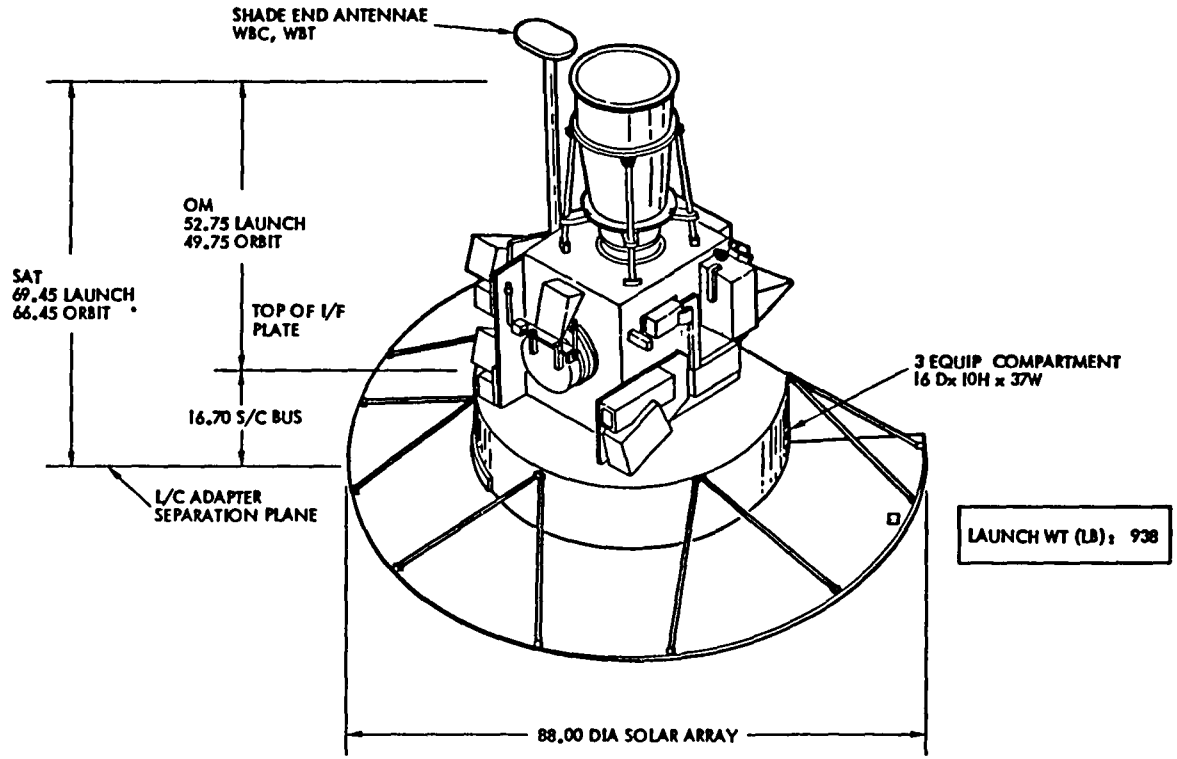

JPL 3420 11/78

Figure 4.10-1. SME Spacecraft Configuration

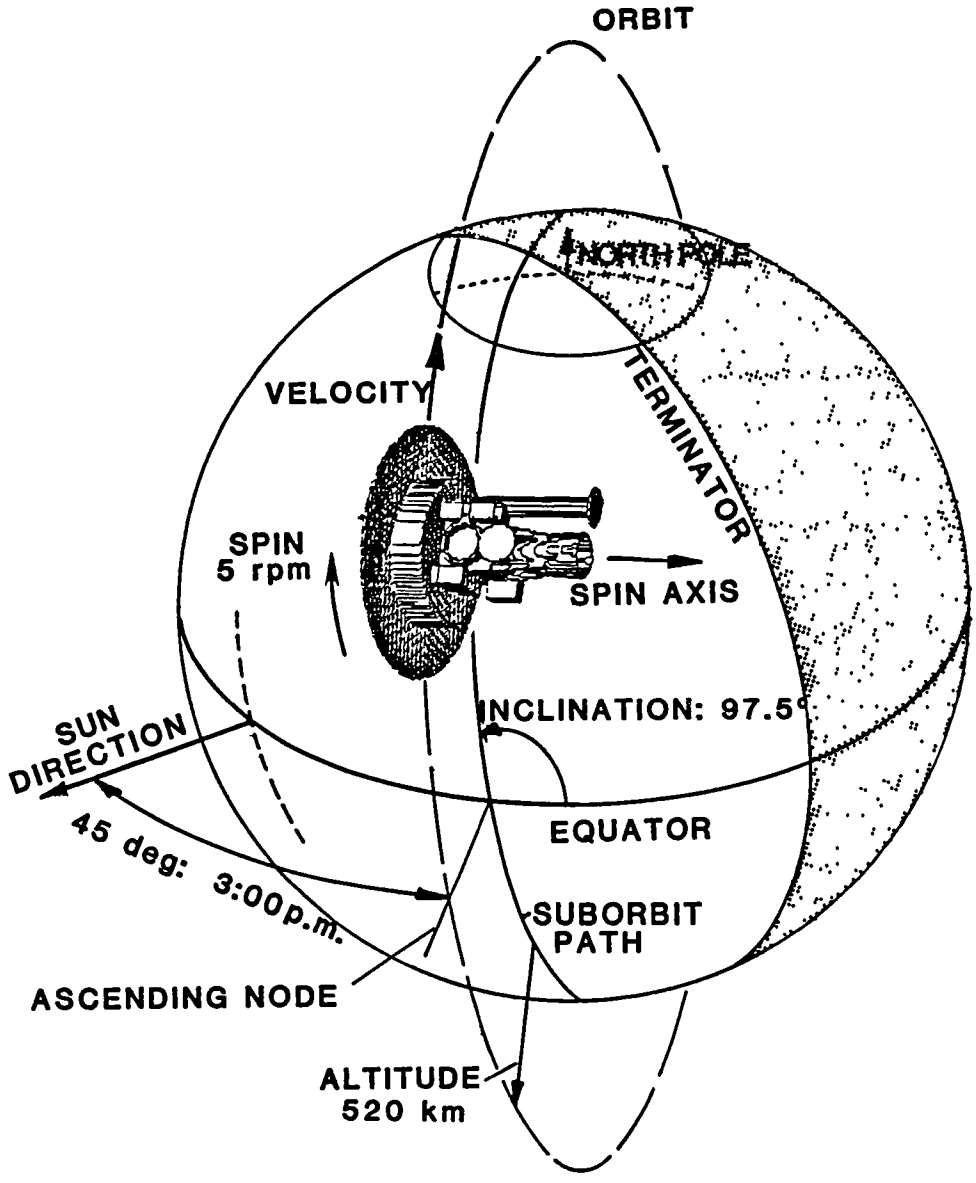

Figure 4.10-2. SME Orbit Geometry

- Attitude determination and control hardware
  - Two body-mounted IR horizon sensors (BHSs) (Figure 4.10-3) with derivative locator logic
  - Automatic onboard control loop, later switched to open-loop mode
  - Magnetometers
  - Magnetic torquing coils
- Problems encountered--Failure of the heat sink attachment caused loss of radiometer data in the CO_2 band.

The horizon edge times for the BHSs were established at the center of the derivative pulse for the rising and falling edges of the IR Earth pulse. Figure 4.10-4 shows the IR passband for the BHSs. The data available for analysis of the detected horizon tangent height were not the times of the individual horizon crossings, because of some onboard data processing. The three data types available in the telemetry were the average of the A and B sensors' Earth-in times, the average of the A and B sensors' Earth-out times, and the B sensor's Earth-out time.

4.10.2 MISSION DATA ANALYSIS

The analysis performed on the SME BHS data by the University of Colorado was supported by a grant from the ADCS at GSFC. Early analysis of the SME BHS data (Reference 57 and 58) compared horizon triggering altitudes derived for SME. The analysis used a version of the GSFC/CSC HRMU, the altitude of the 5-millibar pressure level from the National Meteorological Center (NMC) data base, and the science data adjusted for differences between the pressure-altitude scale and the geometric altitude. In the last case, the science measurement profiles were compared with profiles derived by using an Air Force atmospheric model to obtain a tangent

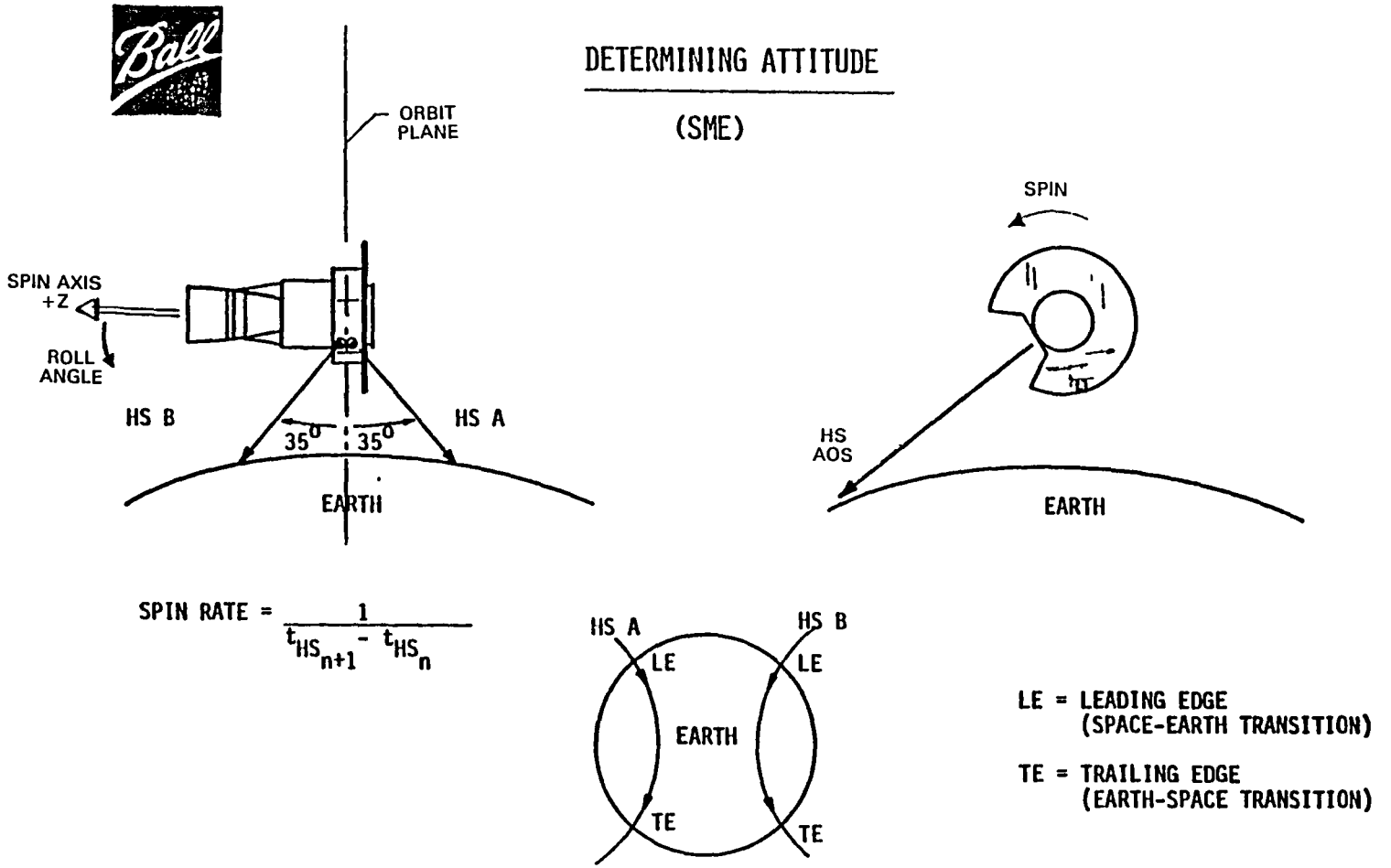

Figure 4.10-3. SME BHS Geometry

height scale adjustment for the sensed spacecraft pitch angle. These earlier comparisons showed similarities between the various methods only in the amplitude of the corrections, which were shown to be generally less than 3 kilometers for April data. The general appearances of the HRMU triggering altitudes and NMC 5-millibar altitudes were correlated with the lower altitudes occurring in the Southern Hemisphere but anticorrelated in the Northern Hemisphere.

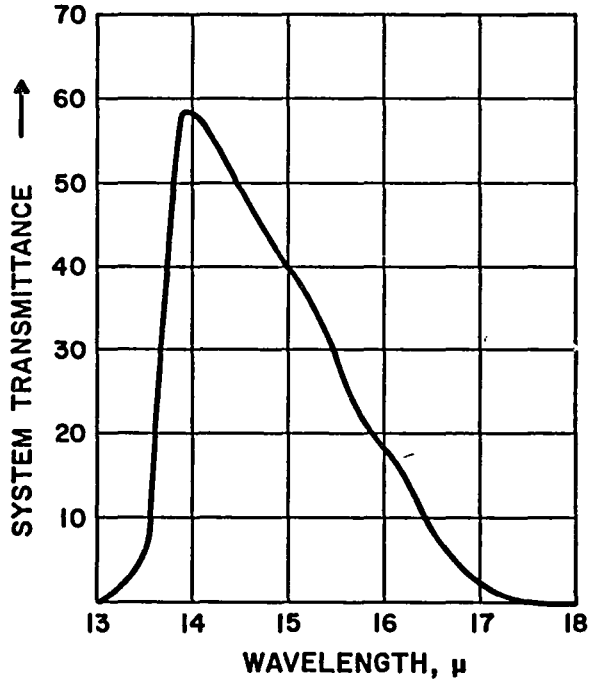

Figure 4.10-4. SME BHS IR Passband

After this early attempt, analysis was extended to a new approach that involved modeling the SME horizon triggering time history over data spans of 9000 seconds duration. This spin dynamics model was formulated as follows:

$$\theta(t_i) = \sum_{j=1}^{10} C_j \, F_j \, (t_i)$$

where θ represents a spin angle measurement at a limb pulse time t_i, C_j represents constants that determine the relative contribution of each effect, and F_j represents time-dependent model functions that can influence the predicted schedule of horizon crossing angles. This model of the horizon triggering angles was then applied in a least squares algorithm to the BHS data to determine the C_j's. In the order in which they are labeled, the F_j's represented (1) the initial pitch, (2) the average inertial spin rate, (3) the spin rate change due to eddy current drag in the Earth's magnetic field, (4) the change in the spin rate due to thermally induced, moment-of-inertia variations, (5) the time lag in the sensed solar panel temperature used to model the inertial variations, (6) the altitude of the 5-millibar pressure level, (7) the temperature of the 5-millibar pressure level, (8) an offset horizon altitude bias relative to 35 kilometers, (9) the BHS azimuth alignment error, and (10) the BHS elevation alignment error.

Using this approach, the model for the BHS triggering altitude is derived from the coefficients C_6, C_7, and C_8, which produce a minimum in the data residuals. Again, the 5-millibar altitude and temperature data were obtained from the NMC data base. The results for January, April, July, and December data are presented in Figures 4.10-5 through 4.10-8 (Reference 13). The composite effect from the three terms is displayed as the NMC model. The raw data points, which are the NMC altitudes plus the residuals from the 10-parameter fit, are compared with the HRMU results using the LMSC Seasat radiance profiles in the upper portion of the figures.

4.10.3 RESULTS AND DISCUSSION

The accuracy of the analysis to determine the true BHS triggering horizon altitudes is quoted as better than 2.0 kilometers (1σ) (Reference 60). Comparisons of the NMC-derived

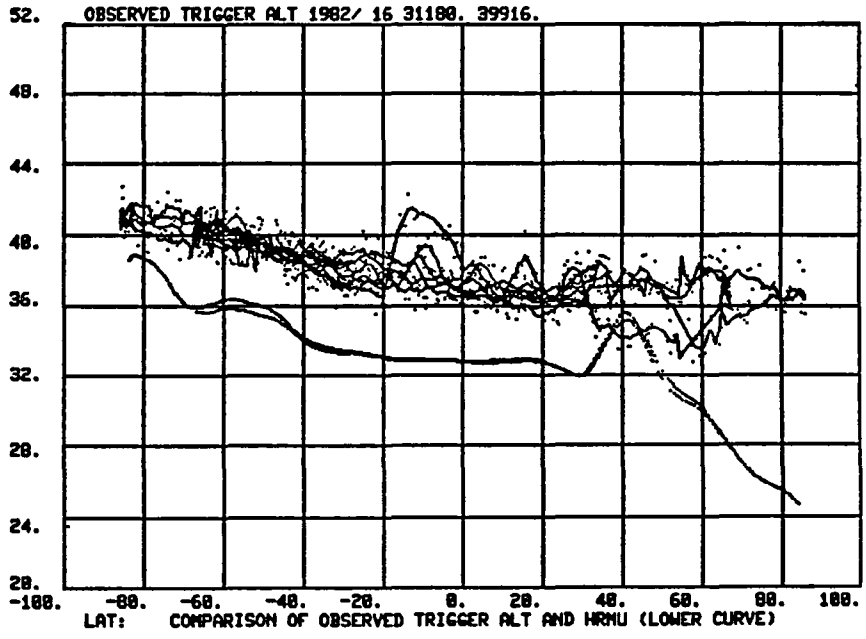

SPIN RUN FOR 1982 16 31180. 39916.

START,STOP,NPTS,NPNTS 1 2016 2016 2016 BB=-C.1e1C2E+02

DM=	1.306	CONST	TIME	MAG	TEMPINT	TEMP	NMC ALT	NMCTEMP	ZOFFSET	AZIMCOR	ASPCORR	DET= 0.9037E-04
NMILC=	0	5.9992	-0.5114	0.2212E-06	0.8512E-05	-0.2185E-03	1.33321	-0.25501	-4.46454	2.43000	-1.73129	PPM= 23.7059
TAU=	-25.7	0.44C9E-04	0.260CE-07	0.3490E-10	0.1767E-08	0.1255E-05	C.10922	0.01014	0.11896	0.00000	C.04729	BB= -16.1024

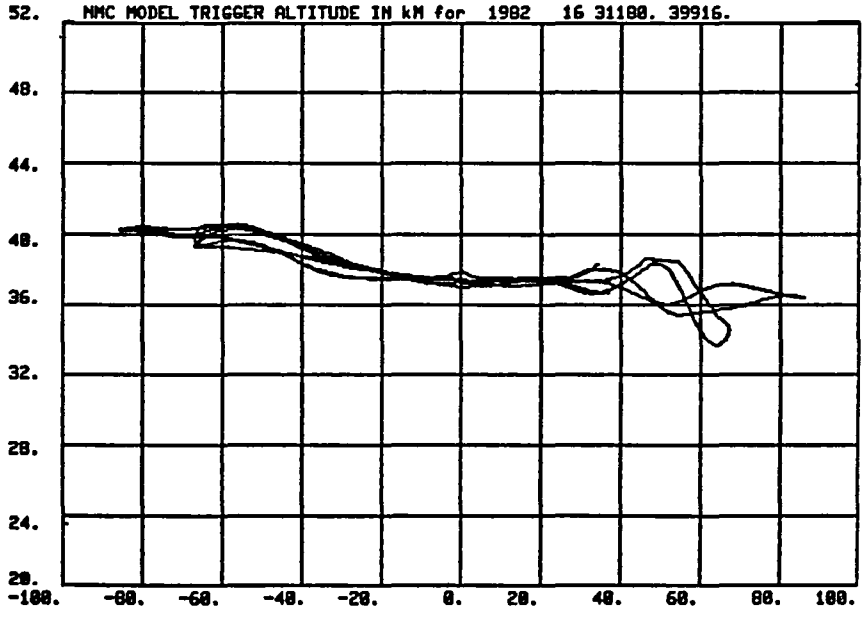

Figure 4.10-5. Comparison of SME Horizon Triggering Height Models for January Atmospheric Conditions

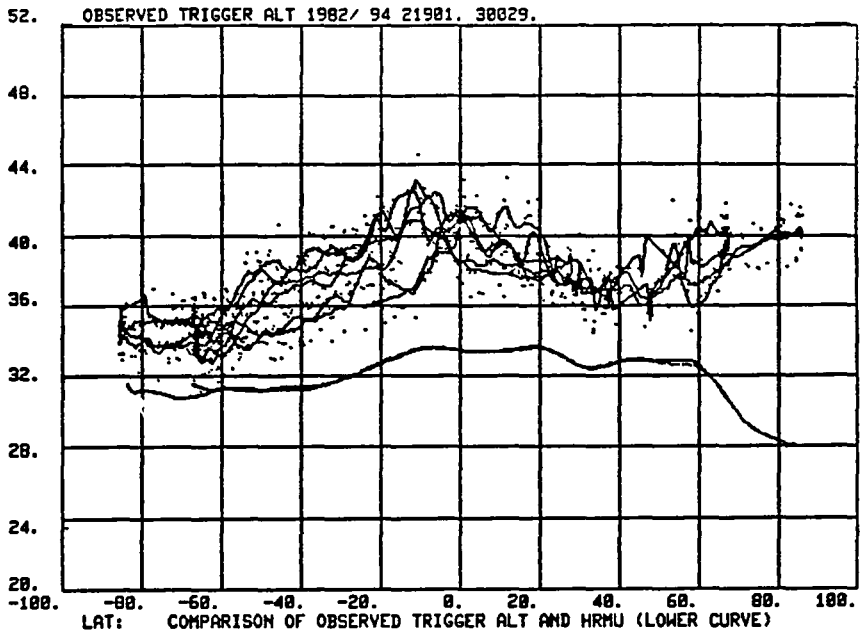


```
SPIN RUN FOR  1982   94  21901.  30029.
************************************      ************************************
START,STOP,NPTS,NPNTS      1 1890 1890 1890  BB=-0.19543E+02
 DH=    1.463     CONST       TIME       MAG        TEMPINT     TEMP      NMC ALT  NMCTEMP  ZOFFSET  AZIMCOR  ASPCORR  DET=  0.1582E-0
NWILD=     0     5.4590    -0.5084 0.2248E-06 0.8343E-05-0.288CE-03  1.02326 -0.27224 -3.38768  2.43000 -1.53297  PPM=    23.3765
TAU=  -34.5 0.5831E-04 0.4007E-07 0.5725E-10 0.2252E-08 0.1543E-05  0.10942  0.00565  0.10179  0.00000  0.05648  BB=   -19.5434
```

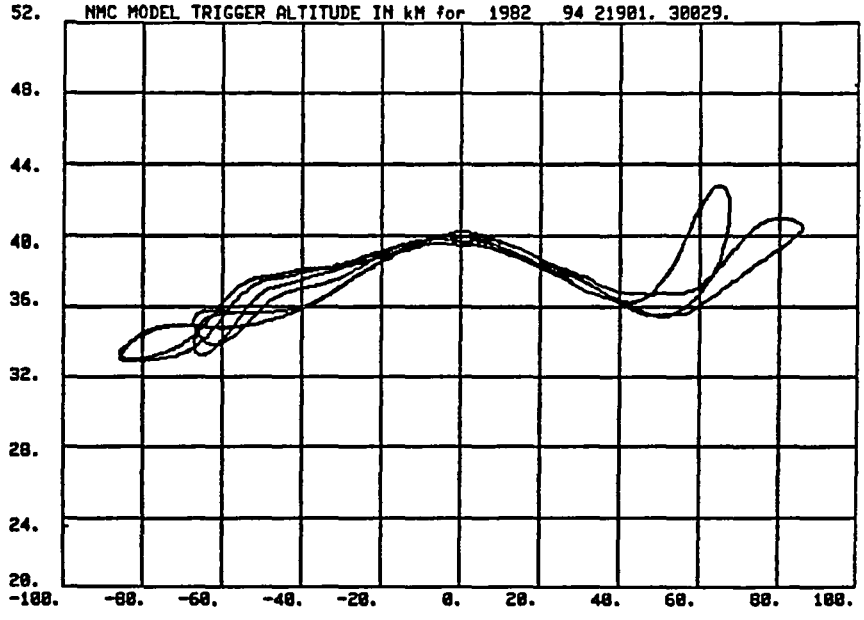

Figure 4.10-6. Comparison of SME Horizon Triggering Height Models for April Atmospheric Conditions

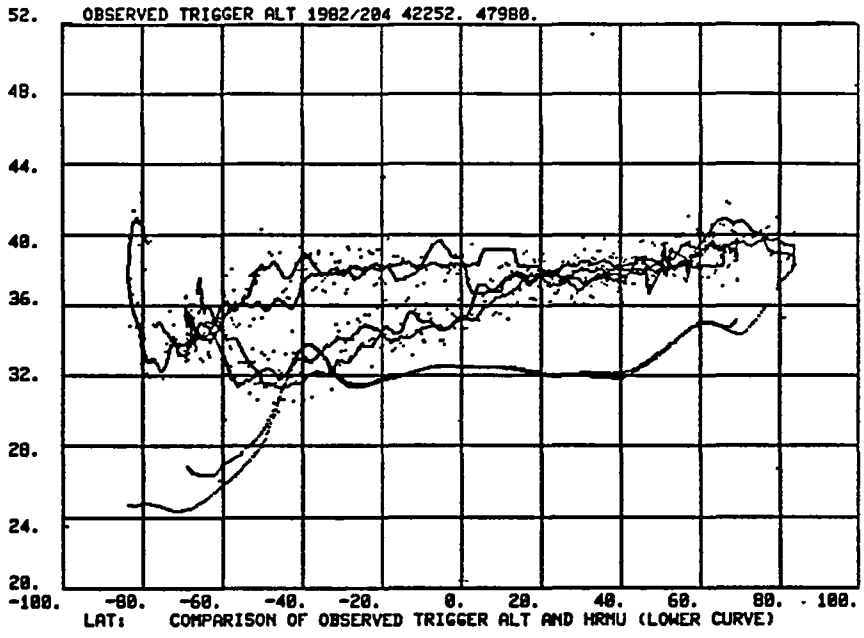

SPIN RUN FOR 1982 204 42252. 47980.

START,STOP,NPTS,NPNTS	1 1323 1323 1323	BB=-0.21835E+02										
DH= 1.628	CONST	TIME	MAG	TEMPINT	TEMP	NMC ALT	NMCTEMP	ZOFFSET	AZIMCOR	ASPCORR	DET=	0.7961E-0
NWILC= 0	5.0816	-0.5128	0.2409E-06	0.8174E-05	-0.2199E-03	1.77292	-0.33657	-2.98206	2.43000	-2.40585	PPM=	22.7034
TAU= -26.9	0.1881E-03	0.2019E-06	0.5740E-09	0.3565E-08	0.9240E-05	0.06779	0.00840	0.06019	0.00000	0.07611	BB=	-21.8354

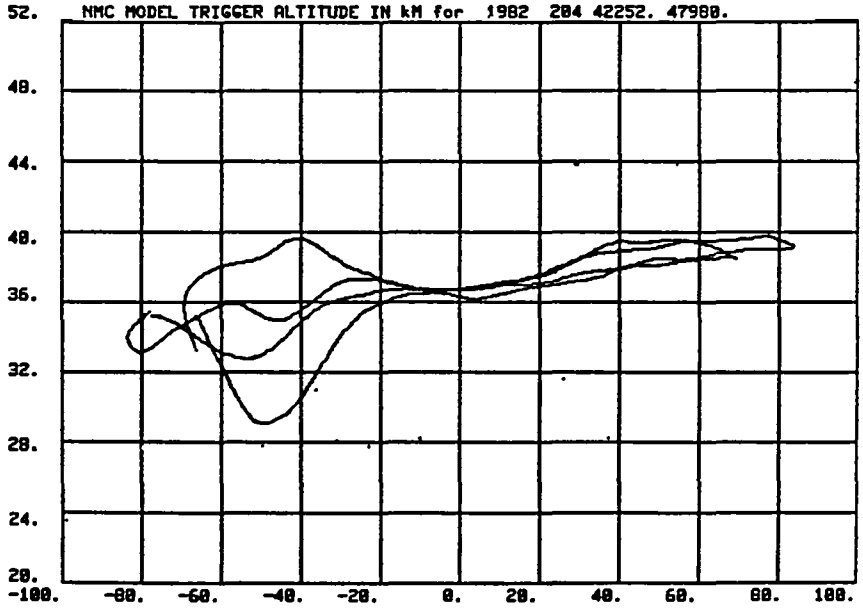

Figure 4.10-7. Comparison of SME Horizon Triggering Height Models for July Atmospheric Conditions

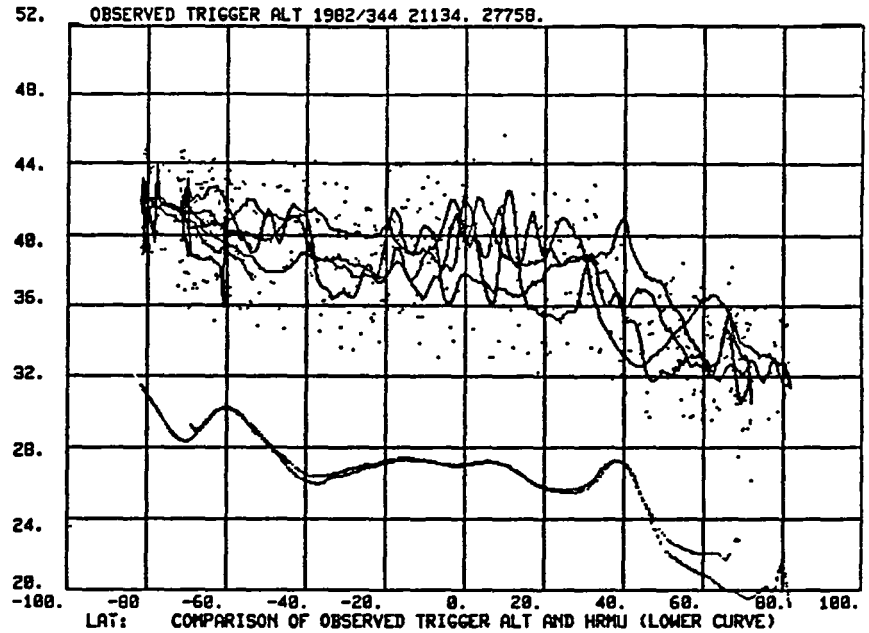

SPIN RUN FOR 1982 344 21134. 27758.

START,STOP,NPTS,NPNTS 1 1581 1581 1581 BB=-0.15776E+02

DM=	2.082	CONST	TIME	MAG	TEMPINT	TEMP	NMC ALT	NMCTEMP	ZOFFSET	AZIMCOR	ASPCORR	DET=	0.3185E-0
NWILC=	0	9.0390	-0.5135	0.2324E-06	0.8237E-05	-0.2301E-03	0.06051	-0.18879	-3.09578	2.43006	-1.81766	PPM=	22.8450
TAU=	-27.9	0.1321E-03	0.1086E-06	0.2066E-09	0.3660E-08	0.4244E-05	0.14238	0.01089	0.15406	0.00000	0.08404	BB=	-15.7755

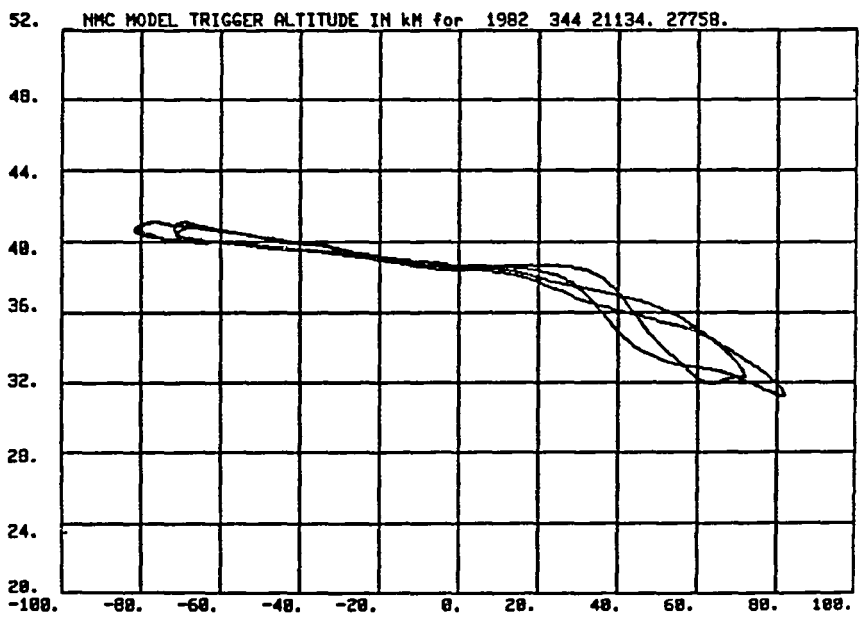

Figure 4.10-8. Comparison of SME Horizon Triggering Height Models for December Atmospheric Conditions

horizon triggering altitudes with those derived by the HRMU are consistent with this estimate of accuracy. The LMSC/Seasat radiance profiles differ from those that would be derived for SME in four fundamental ways: They are computed for a wide 15-micrometer passband, are derived totally from Northern Hemisphere data inverted in season to represent the Southern Hemisphere, are extrapolated over the poles, and are longitudinally averaged. Even so, the general latitude trend for January, April, and July altitudes tends to be similar. There is, however, a tendency for the NMC model data to predict higher triggering altitudes over the winter poles. This tendency in the NMC data could be attributed to the occurrence of somewhat localized stratospheric warming events at longitudes of the data spans tested. It could also be an effect caused by some unmodeled factor in the response of the IR sensor to the polar radiances experienced during the flight. It is shown in an analytical experiment with the Landsat-4 conical IR scanner model (see Section 4.11) that the response of the derivative locator logic shows a nearly direct correspondence with the altitude variation of the horizon profile, and that the response to profile brightness variations was smaller but not strictly linear in brightness.

Following the example of the Landsat-4 experiment, a test of the response of the SME sensors to profile altitude and brightness variations could provide support for the results of the SME analysis. That is, it could show that the value of -0.26 kilometer per degree Kelvin reported for the effect of profile brightness variations (which are nearly proportional to the temperature of the atmosphere at 30 kilometers, or 5 millibars) is close to that derived from an analysis of the circuit model using a fixed-altitude variable-brightness profile model.

The SME analysis shows an approach that can be developed into an operational method for sensor data correction. If a method of obtaining and quickly translating the NMC altitude, pressure, and temperature data into a daily Earth-detected IR horizon adjustment model can be achieved, significant improvements in the accuracy of attitudes derived from IR sensors are possible. The accuracy improvements depend, however, on the choice of pressure level or levels (3, 5, or 10 millibars) and which form of response to altitude and temperature is appropriate. The model depends on the details of each IR sensor design, which should be established with a proper analysis of each design using techniques similar to those employing the HRMU and LOWTRAN 5 programs.

4.11 LANDSAT-4

Landsat-4 was equipped with the Multimission Modular Spacecraft (MMS) ACS augmented for an emergency safehold attitude control mode with two ITHACO conical IR horizon scanners. The MMS ACS module provided an accurate onboard attitude reference derived primarily from data from two fixed-head star trackers and a set of three-axis IRUs processed by an attitude algorithm operating in the spacecraft onboard computer (OBC). Because the IR scanner data are input to the spacecraft control loop only during the override emergency safehold attitude mode, most of the attitude telemetry data from Landsat-4 could be used to evaluate the performance characteristics of the conical scanners. The error signal in these scanners, unlike those of previous scanners that drove the spacecraft control loop, is a simple sum of errors caused by spacecraft attitude and sensing errors. The sensing errors are due to Earth oblateness, spacecraft altitude changes due to a nonzero orbital eccentricity, sensor electronic and alignment biases, Earth horizon sensing noise, and variations in the IR image of the Earth. A sensing error is thus referred to here as that part of the sensor signal that is not strictly a result of attitude motion.

The Landsat-4 attitude system data are useful for comparing a model of the Earth IR image with the actual Earth IR image as viewed through the IR passband and electronics processor of the conical scanners. There are three major features of the Earth IR model represented by radiance profiles of the type derived by Honeywell, Lockheed, and CSC and measured in Project Scanner and Nimbus-6 LIMS. The first is the profile brightness, which is typically the radiance intensity at a tangent height near 0 kilometers and which varies with latitude and season. The second is the tangent height of the profile 50-percent intensity point, which typically occurs above a tangent height of 30 kilometers. This latter feature

has not been analyzed in this report for latitudinal and seasonal variations. This is because a major portion of the variation in the altitude of the detected horizon for scanners with normalized threshold locator logic (such as those on Seasat and ERBS) can be accounted for by the variations in the model of profile brightness. Even the fixed-threshold detection systems (such as that on Magsat) were strongly influenced by the model of profile brightness. The Landsat-4 conical scanners with derivative locator logic provide a good opportunity to evaluate the dependence of the tangent height of the 50-percent point on latitude and season. The third feature is the width of the edge of the profile, which is a function of the temperature lapse rate in the stratosphere. The sensitivity of the conical scanner to the slope at the edge of the profile is reduced by the integration effects related to the scanner FOV angular width, the scan rate, and the signal processor timing characteristics.

The discussion presented here is derived from the GSC analysis documented in Reference 13a. Most of the illustrations are from that report.

4.11.1 MISSION REQUIREMENTS AND HARDWARE

Landsat-4 was launched on July 16, 1982, by a Delta launch vehicle. The spacecraft is illustrated in Figure 4.11-1 (Reference 61). The mission can be summarized as follows:

- Orbit--Sun synchronous with 98.2-degree inclination, 710-kilometer nominal altitude, perigee frozen at the northernmost latitude, and descending node at 9:30 a.m. local time
- Attitude configuration--Pitch (Y) axis along negative orbit normal, roll (X) axis along nominal flight velocity vector, and yaw (Z) axis along the nadir vector

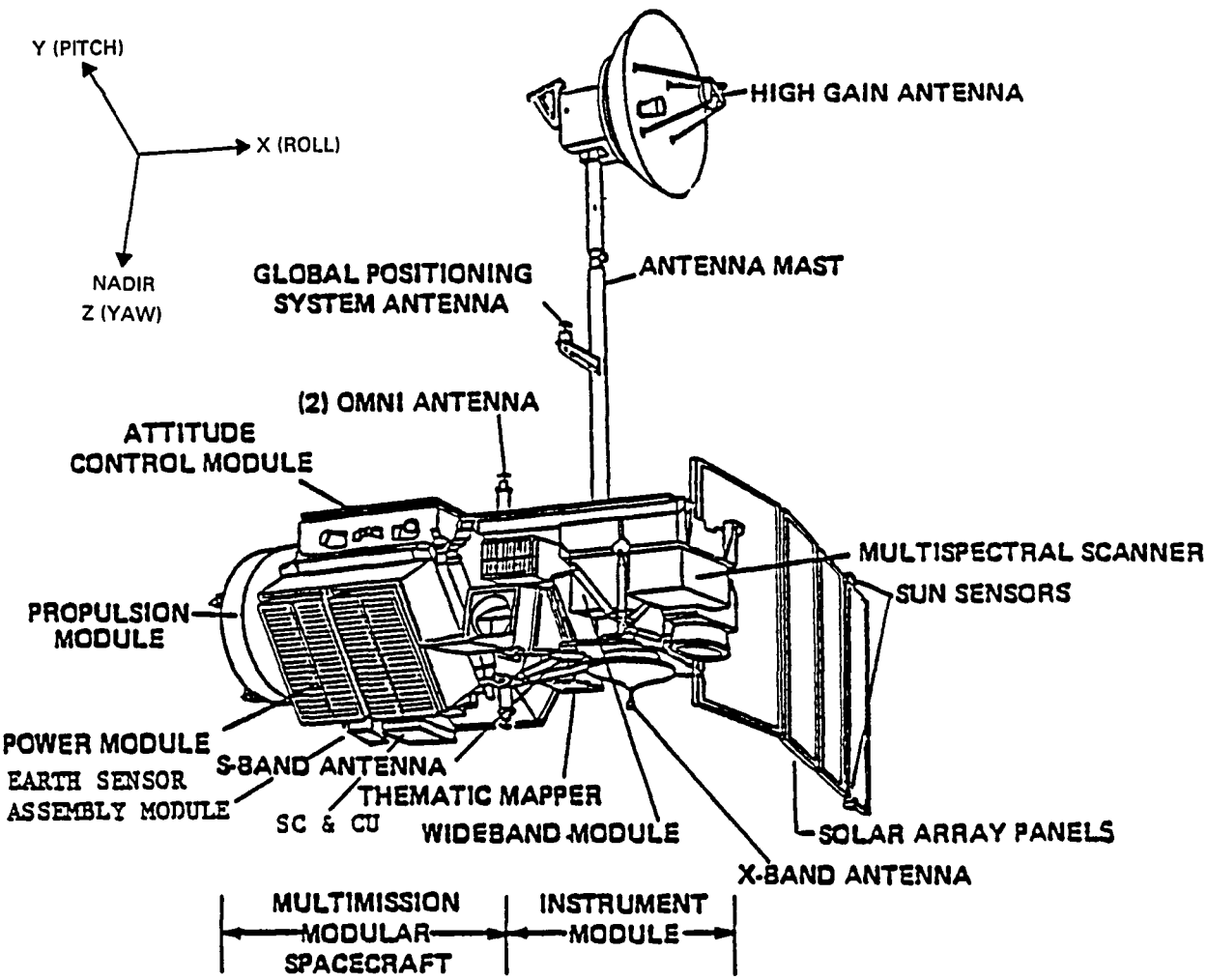

Figure 4.11-1. Landsat-4 Spacecraft

- Attitude determination hardware
  - Two fixed-head star trackers
  - Set of three-axis IRUs
  - Two fine Sun sensors
  - Two conical IR horizon scanners (Figure 4.11-2, Reference 62)
- Attitude control hardware
  - Four reaction wheels
  - Three-axis magnetometer
  - Magnetic torque rods
  - Hydrazine thrusters
- Accuracy requirement--$\lesssim$ 0.01 degree
- Ground support system--None by GSFC ADCS
- Problems encountered
  - Frequent loss of OBC attitude during early mission phase due to the inability of the FHSTs to locate selected guide stars
  - Partial loss of power associated with thermal effects on the solar panels

The conical scanners scan the Earth at 120 rpm on a 45-degree scan cone with the scan cone axis tilted 24 degrees toward the Earth from the local horizontal. In this report, the scanners are referred to as Earth sensors 1 and 2. The Earth sensor 1 (ES1) scan cone views the Earth along the aft portion of the spacecraft horizon with its cone axis lying in the plane defined by the negative roll axis and the Z-axis. The Earth sensor 2 (ES2) cone is on the right side of the spacecraft in the Y/Z plane. Figure 4.11-3 illustrates the geometry, with the sensors scanning counterclockwise around the axis of the 45-degree cone.

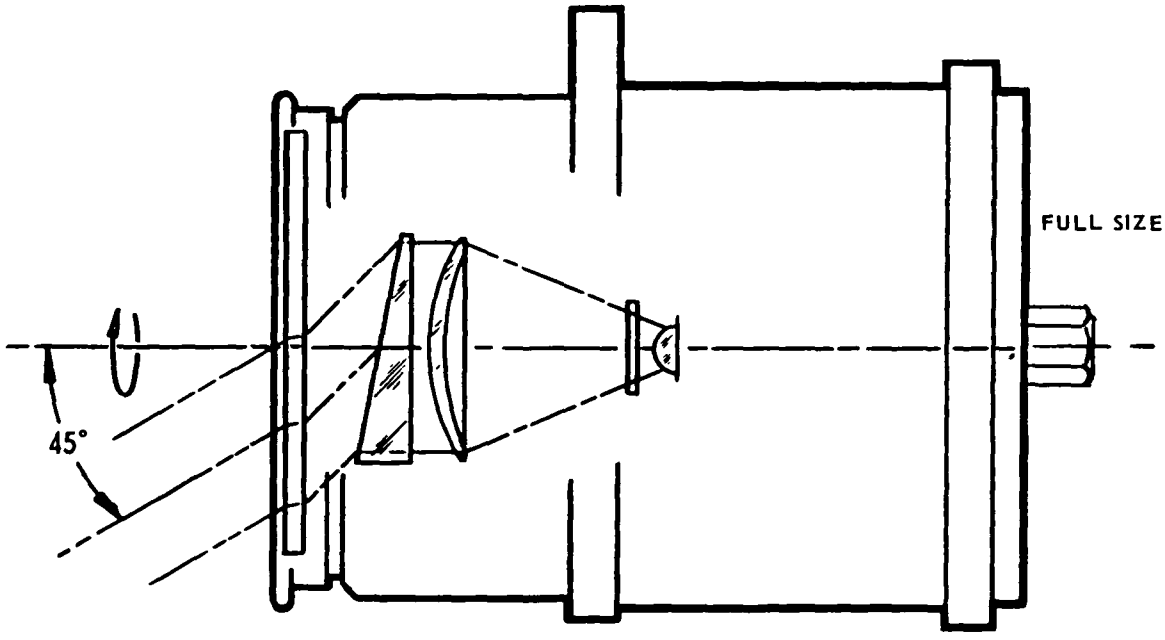

Figure 4.11-2. Landsat-4 Conical Scanner

The conical scanners detect the Earth horizon using normalized derivative locator logic. The Earth IR pulse from the bolometer is differentiated to provide a positive pulse at AOS and a negative pulse at LOS. The peak positive and negative values of these derivative pulses are used to adjust a threshold level that is one-half of the peak derivative. The Earth AOS horizon crossing time is the average time between the rising and falling transitions of the output pulse through the threshold voltage. Figure 4.11-4 illustrates this technique. Figure 4.11-5 is a graphical representation of the Landsat-4 conical scanner footprint as the spacecraft travels northward in its orbit.

4.11.2 MISSION DATA ANALYSIS

GSC, under contract to the ADCS at GSFC, performed an in-depth analysis of the Landsat-4 conical scanner data (Reference 13a) using full-day intervals of flight data for a total of 28 days between August 1982 and September 1983.

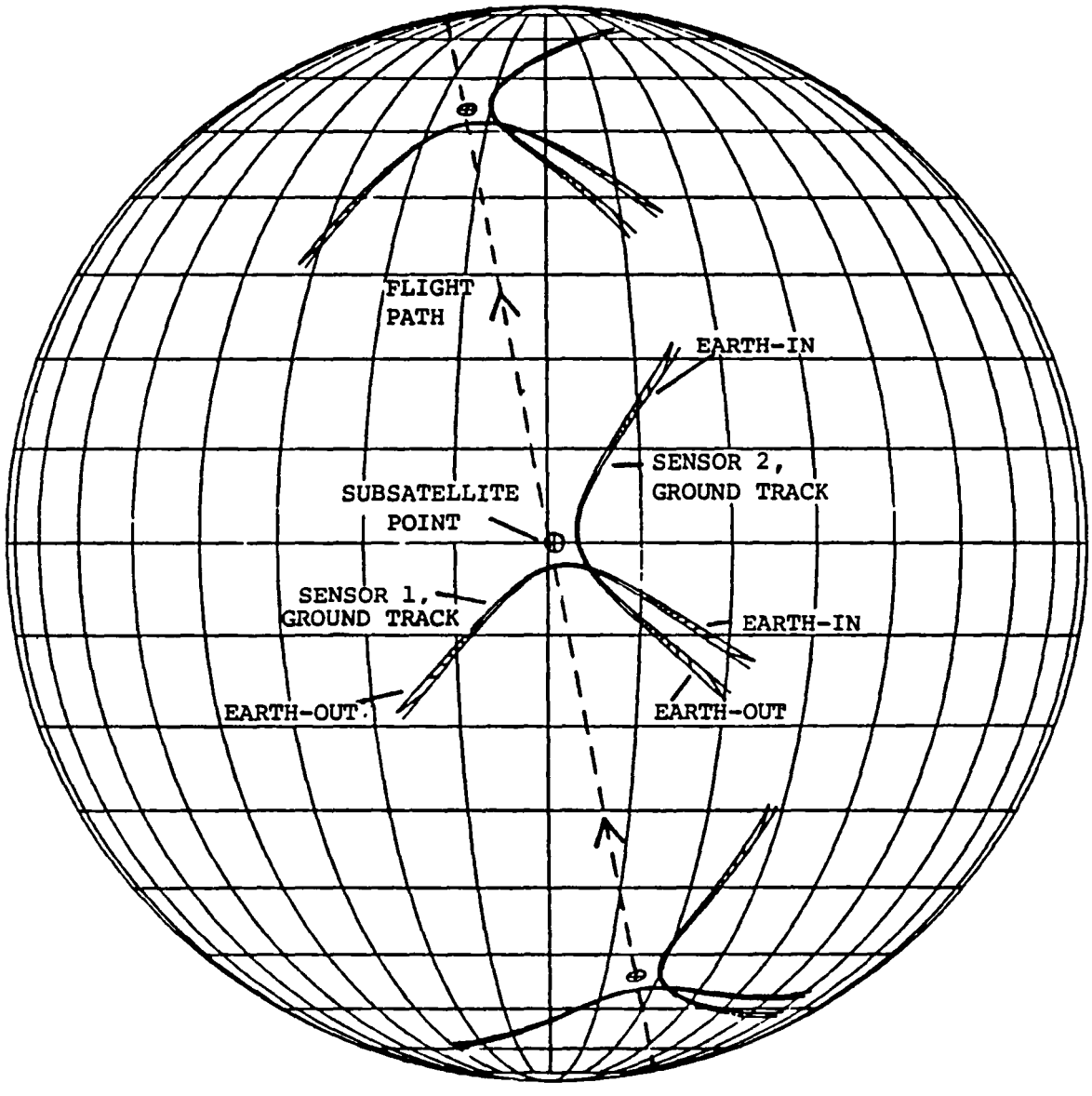

Figure 4.11-3. Earth Scan Geometry of the Landsat-4 Conical Scanners

Their approach used the OBC reference attitudes, which varied less than 0.02 degree peak to peak and were generally within ±0.02 degree of zero pitch, roll, and yaw. The quoted accuracy of the reference attitudes was 36 arc-seconds (0.01 degree). These reference attitudes were used in an analytical model of the conical scanner data. This model added the effects of Earth oblateness and orbital altitude variations to the reference attitude. The model data were then subtracted from the conical scanner Earth-width and Earth-phase pitch and roll flight data to obtain residuals for comparison with predictions of the effects of horizon radiance variation. The effects of horizon radiance variation were predicted using the HRDB to obtain a set of Landsat-4 Earth radiance profiles. These profiles were used as input to sensor simulation software similar to the HRMU (described in Section 3). Figure 4.11-6 illustrates the impulse response function for the electronics model used in the GSC simulation software.

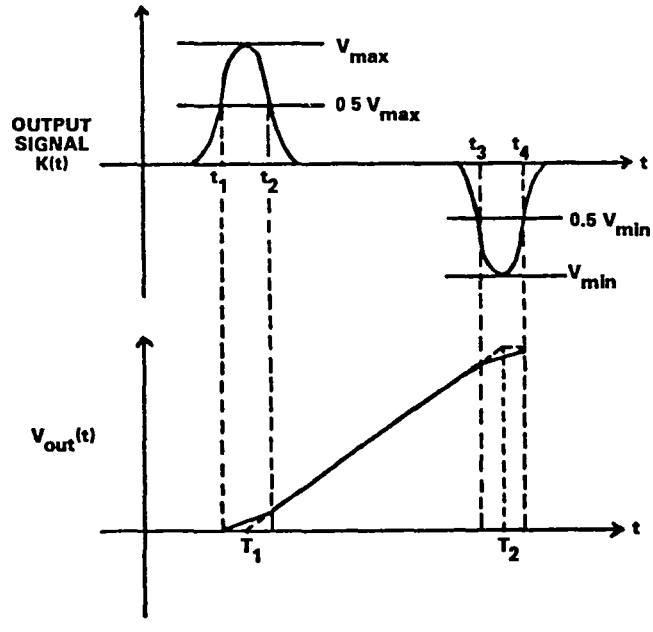

Figure 4.11-4. Landsat-4 Conical Scanner Derivative Locator Method

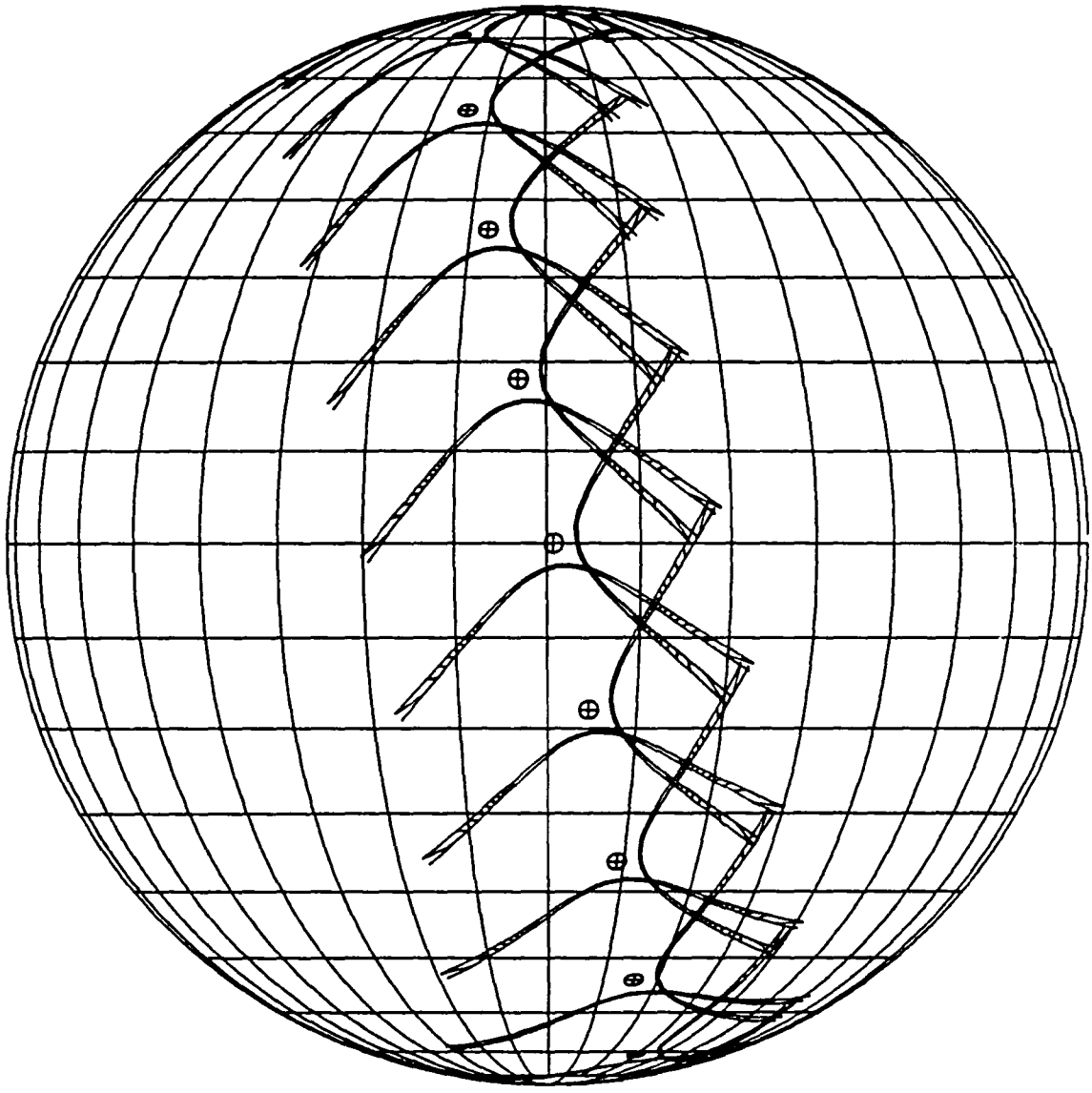

Figure 4.11-5. Landsat-4 Conical Scanner Ground Track on the Earth at 5-Minute Intervals; Ascending Node View

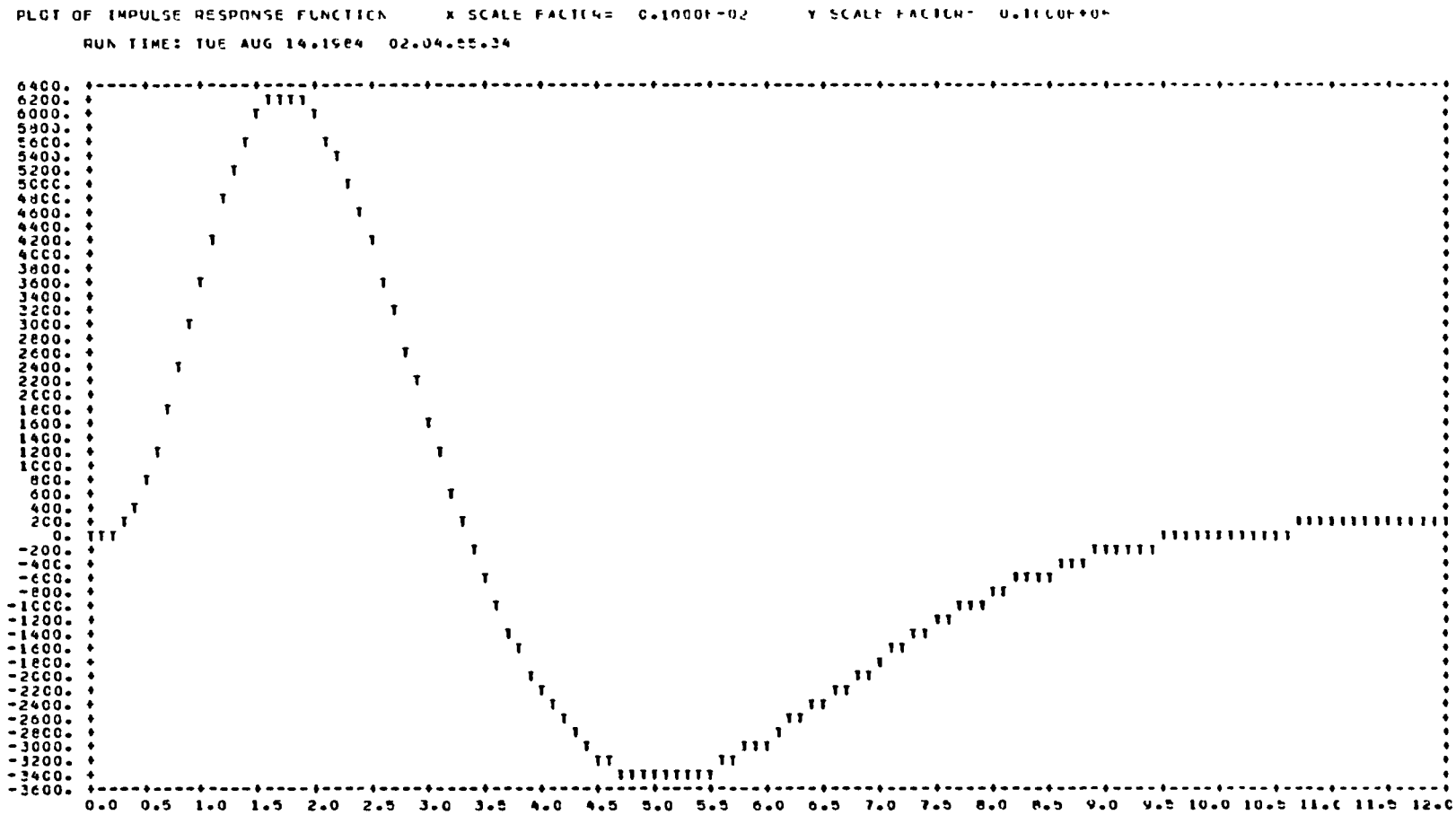

Figure 4.11-6. Landsat-4 Conical Scanner Electronics Model Impulse Response Function

The GSC analysis also included flight data showing the effects of solar and lunar IR radiation and cold clouds on the conical scanner output. Their report (Reference 13a) discusses the noise characteristics of the data and a test of an analytical method of IR data correction using a truncated Fourier series at the orbital period to represent the horizon-radiance-induced errors. The emphasis of this report will be to review the GSC analysis of the effects of systematic radiance variation.

4.11.2.1 Errors Induced by Systematic Radiance Variations

The predicted ES1 and ES2 pitch errors (single solid curves) are compared with the flight data (multiple curves) in Figure 4.11-7. The predicted curves were artificially shifted to provide a better comparison of features in the data. The figure shows pitch errors as a function of orbit phase angle from ascending node for 15 data spans. The GSC analysis concluded that the Landsat-4 Earth profile model generated with the HRDB successfully predicts many of the key features in the residual errors; however, many details in the amplitude and timing features of the predicted errors provide mixed results. In general, the HRDB was only moderately suitable for a model of the Earth IR horizon used to predict the corrections to the Landsat-4 conical scanner data.

An analytical experiment was performed for this report to understand more about which characteristics of the Earth's IR horizon stimulate the Landsat-4 conical scanner error response and to help interpret the GSC analysis. Two fictitious Earth IR horizon models were generated using an HRDB-derived Landsat-4 July equatorial radiance profile. Figure 4.11-8 is an example of this profile showing the three major features of the profile model.

The first fictitious data set (the scaled radiance model) was generated by substituting a scaled version of the equatorial

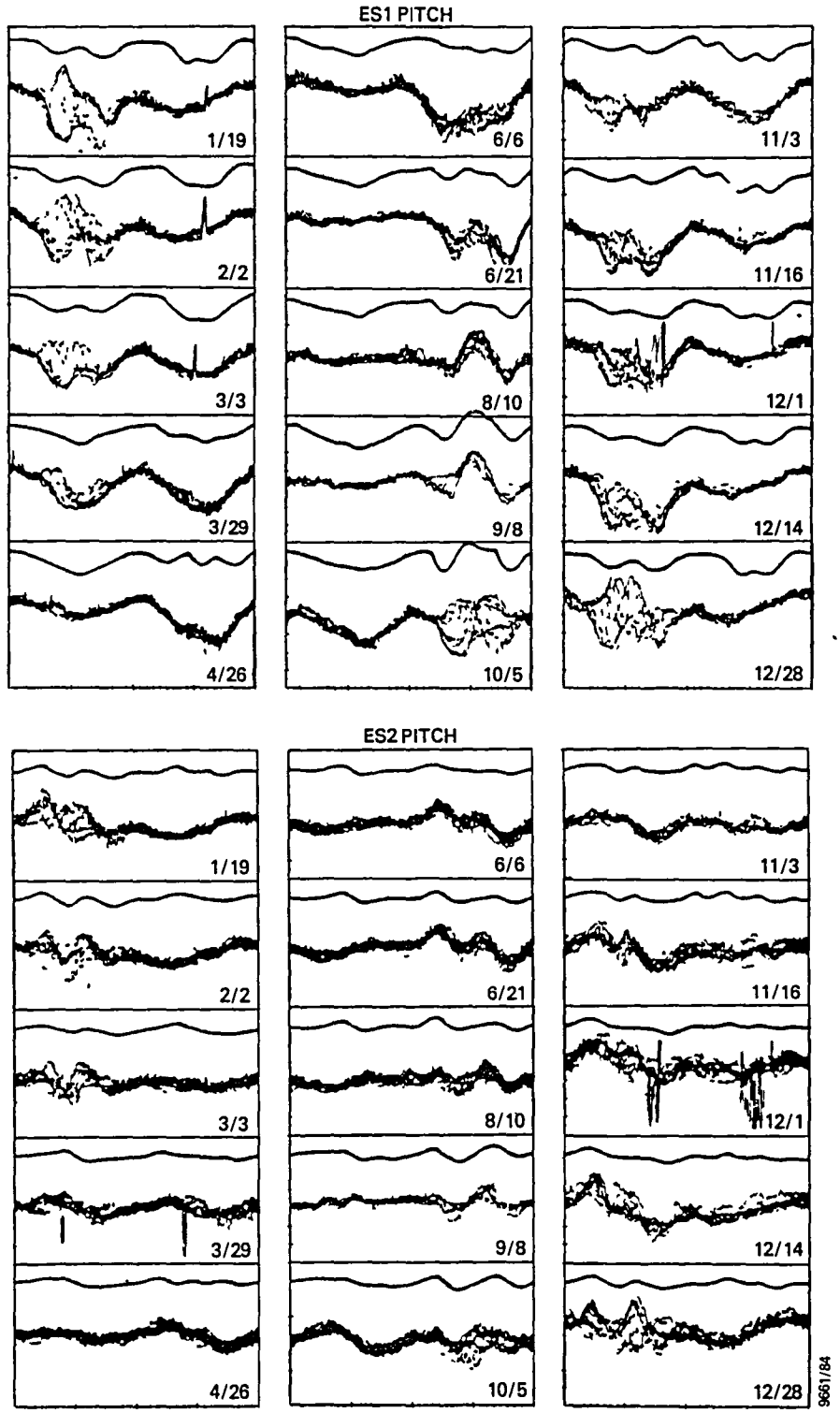

Figure 4.11-7. Residual Errors Compared To Predicted Radiance Effects (The predicted functions are offset for comparison.)

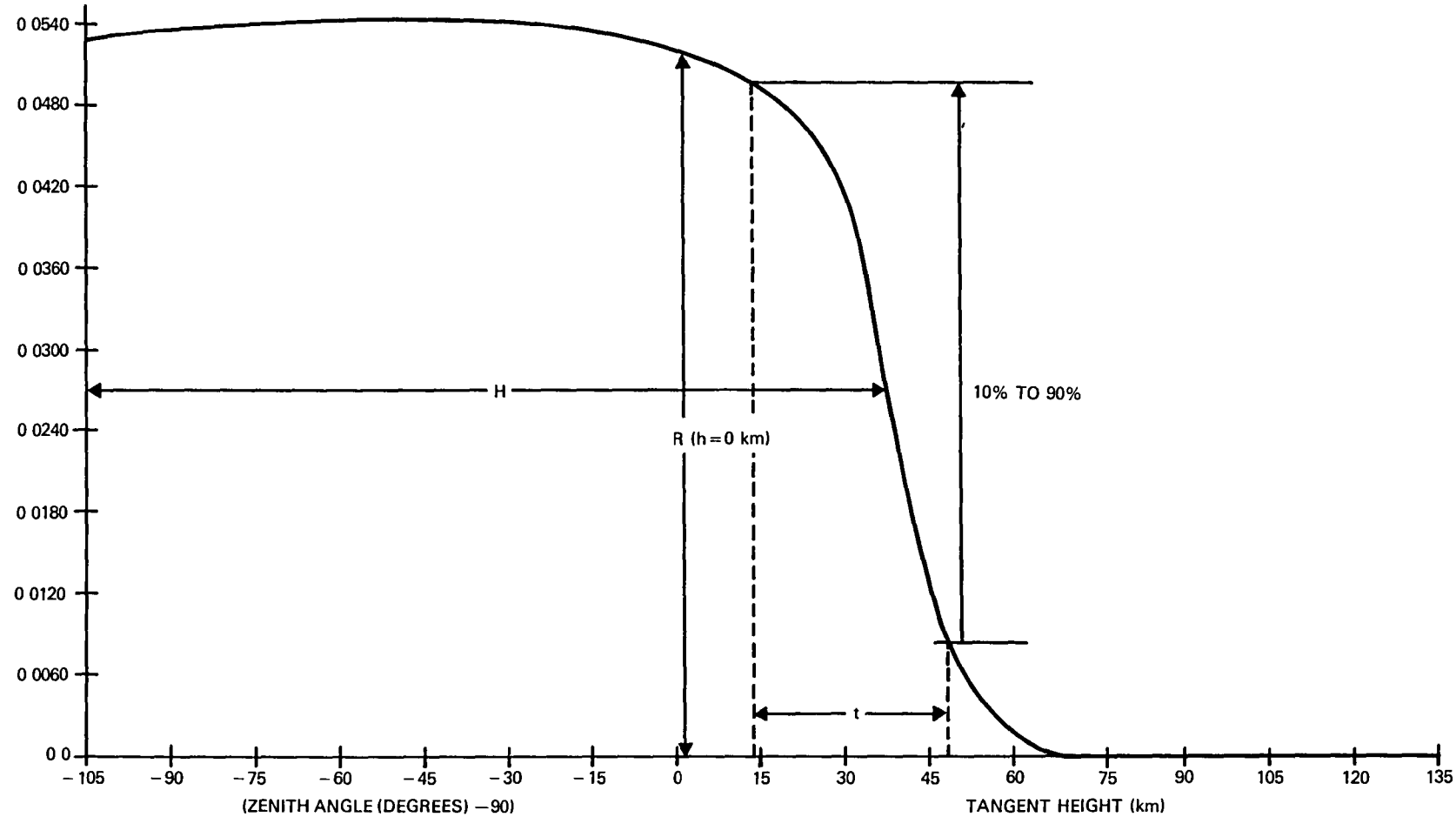

Figure 4.11-8. Horizon Profile Sample Showing Three Characteristic Features (Brightness of 0-kilometer tangent height, R; altitude of the 50-percent point, H; and width of rise, t)

profile for each latitude bin from the South Pole to the North Pole. The scaling factors were 0.76, 0.88, 1.0, 1.0, 1.0, 1.0, 1.12, 1.20, and 1.24 for the profiles from 80°S to 80°N at 20-degree latitude intervals. The Earth IR model thus possessed no latitude-dependent effect in the tangent height variation of the radiance profiles (except for a scale factor), ensuring that the derivative generated by a scan from space to Earth into any single profile would have the same shape. The goal was to test the amplitude insensitivity of the Landsat-4 derivative locator logic. Figure 4.11-9 shows the 0-kilometer profile brightness versus latitude for this Earth IR model. A second radiance data set (shifted tangent height model) was created by raising and lowering the tangent height of the 50-percent radiance point on the July equatorial profile to represent the whole Earth profile model from 80°N to 80°S. The tangent height adjustments were 3.0, 1.5, 0.0, 0.0, 0.0, 0.0, 0.0, -3.0, and -6.0 kilometers from 80°N to 80°S.

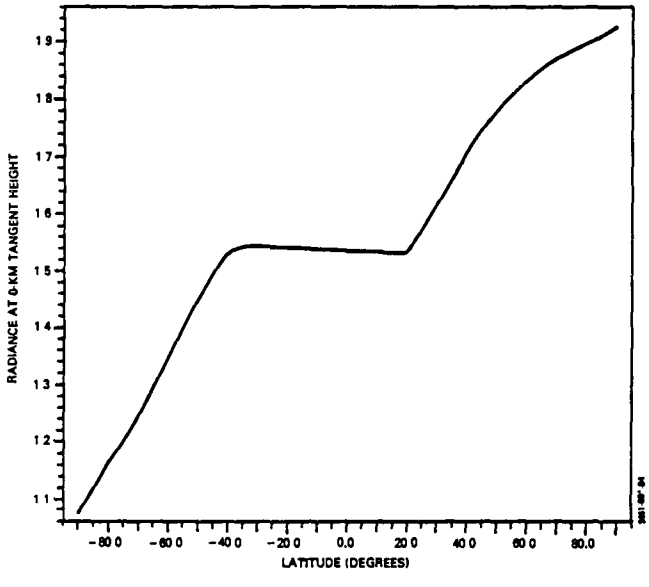

Figure 4.11-9. Latitude Dependence of the Scaled Radiance Model

The scaled radiance model was based on observations from the Nimbus-7 LIMS data and other arguments supporting such a brightness scaling of the HRDB (Section 2.5). The tangent height adjustments were made from evidence in the Honeywell data analysis, supported by Project Scanner measurements. No information about the tangent height dependence could be obtained from the Nimbus LIMS data because of the arbitrary calibration of the tangent height scale for that data. Because of the limitations that have been noted for the RAOBS-generated HRDB (which depends heavily on an extrapolation to a standard midlatitude atmospheric temperature profile above 30 kilometers), no analysis of the tangent height variations in a normalized version of this data set has been performed.

Figure 4.11-10 illustrates the results of a simulation with the scaled radiance model; Figure 4.11-11 shows the results of the simulation with the shifted tangent height model. The figures show Earth-in and Earth-out triggering heights versus orbit phase angle from the ascending node in the upper two segments and pitch and roll errors versus the phase angle in the lower two segments. The error output for this more extreme scaled radiance (brightness variation) model is relatively low, but not zero, as would be expected if the derivative locator logic were responding totally as a normalizing function. Another point to be noted is that the sensor model responds almost linearly to the changes in the tangent heights of the profiles. In addition, when both effects are combined, they have a tendency to cancel. Figure 4.11-12 compares Earth width pitch errors from the two effects, both separately and combined.

The residuals output for the June 22, 1983, data from Reference 13a are presented in Figure 4.11-13. The figure indicates that the Earth radiance profile as viewed by Landsat-4 appears to vary in a manner that could be explained by the

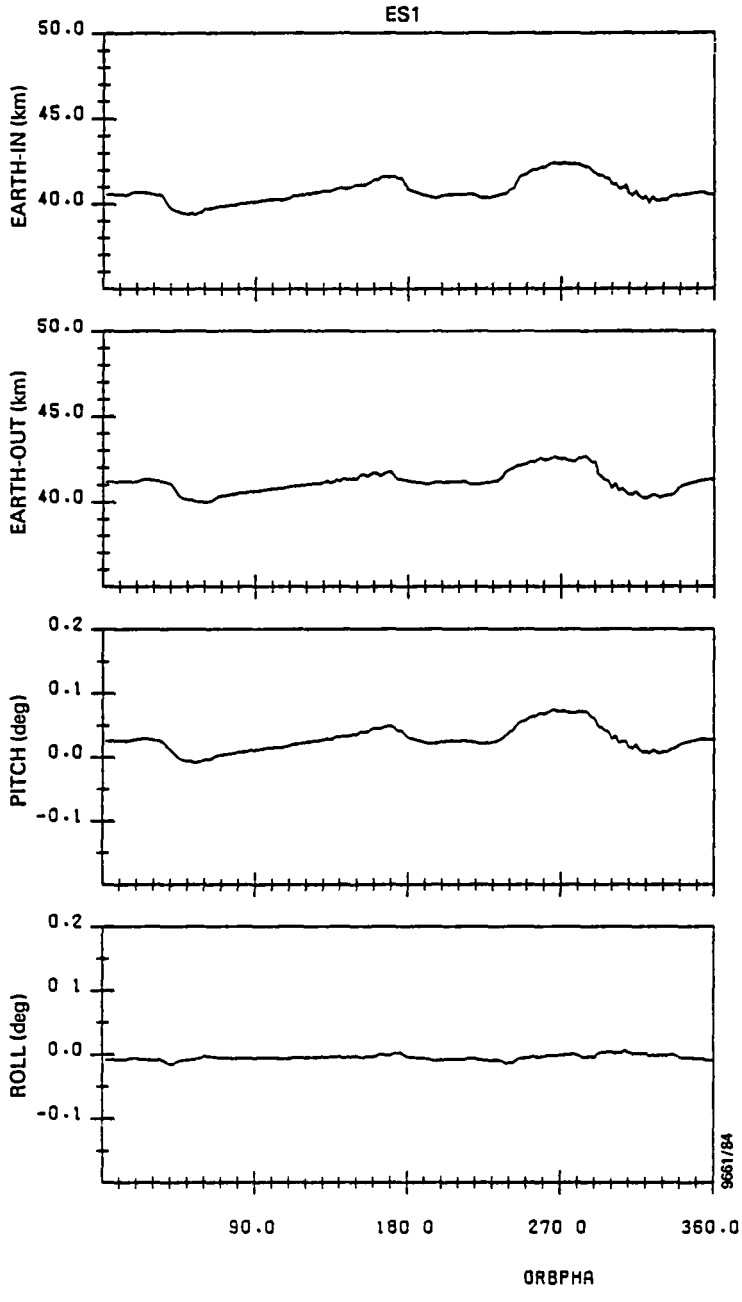

Figure 4.11-10. Response of Landsat-4 to Scaled Radiance Model (1 of 2)

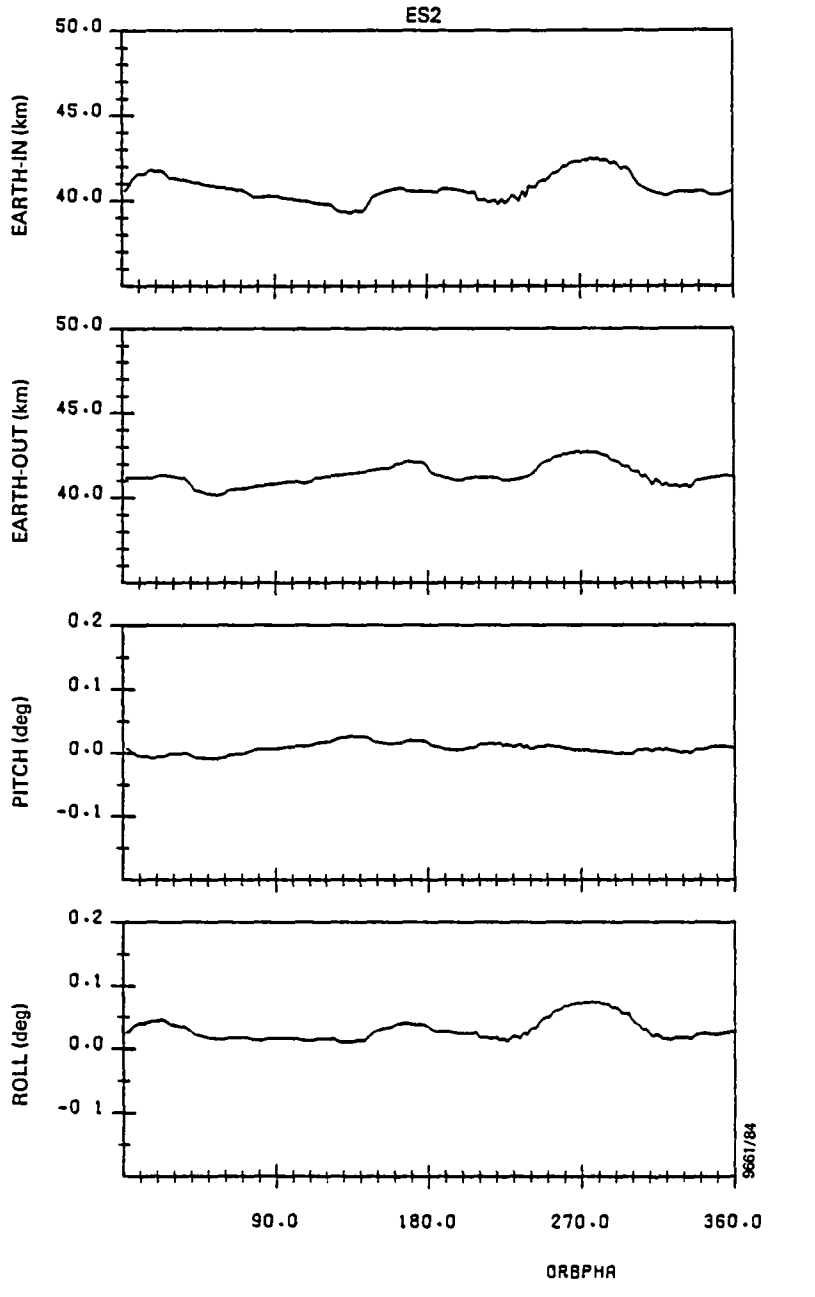

Figure 4.11-10. Response of Landsat-4 to Scaled Radiance Model (2 of 2)

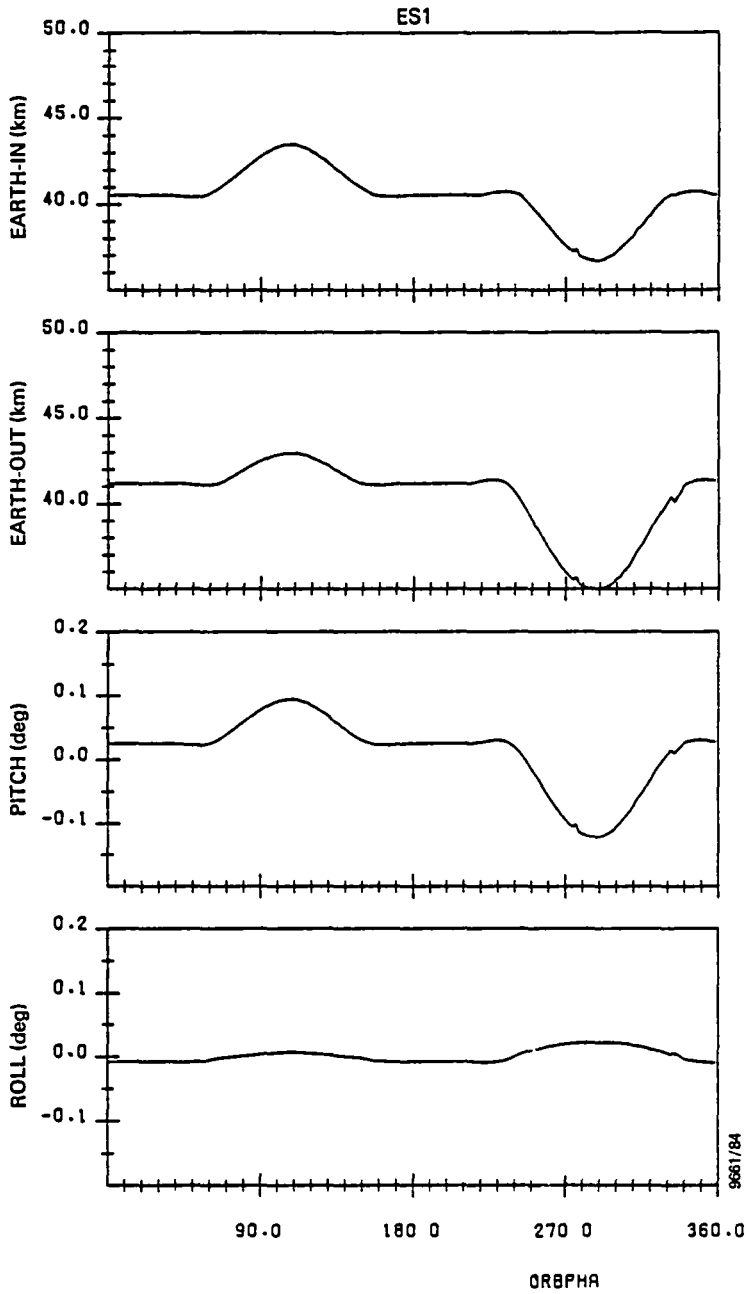

Figure 4.11-11. Response of Landsat-4 to Shifted Tangent Height Model (1 of 2)

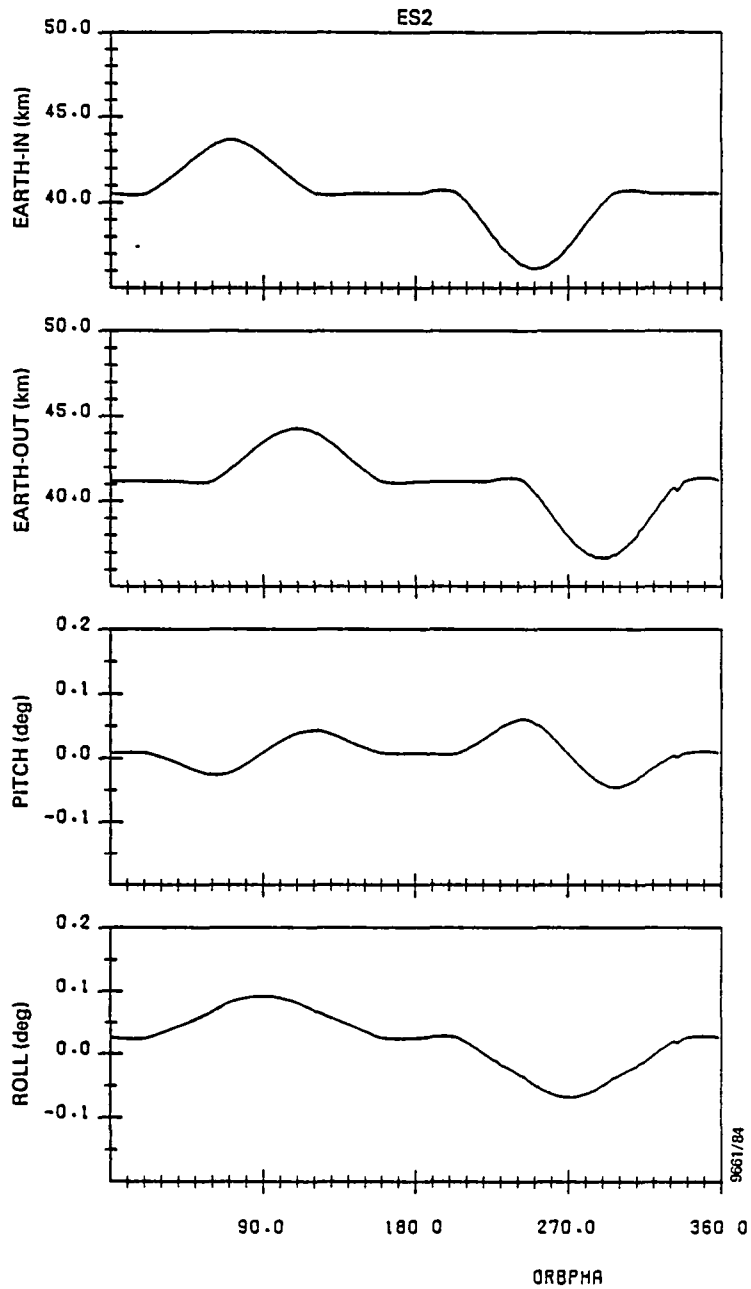

Figure 4.11-11. Response of Landsat-4 to Shifted Tangent Height Model (2 of 2)

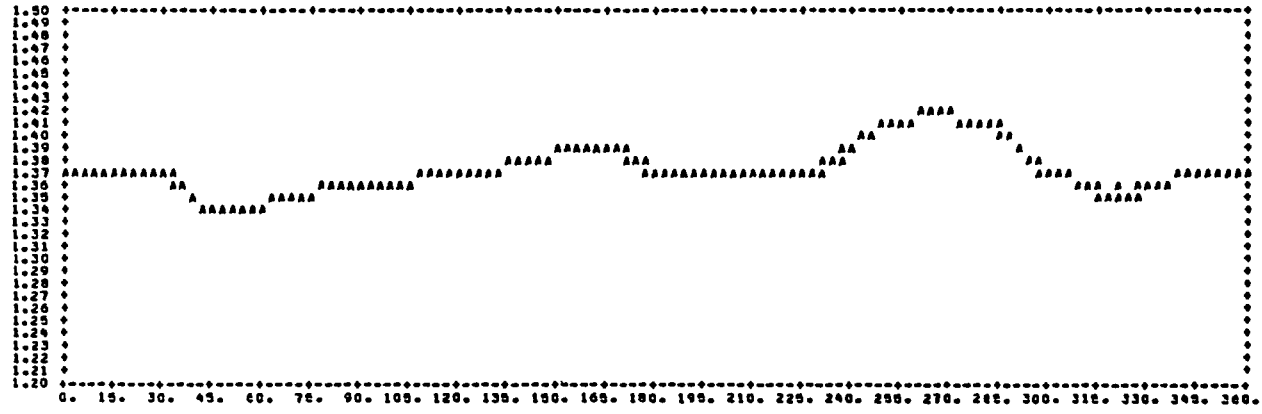

(a)

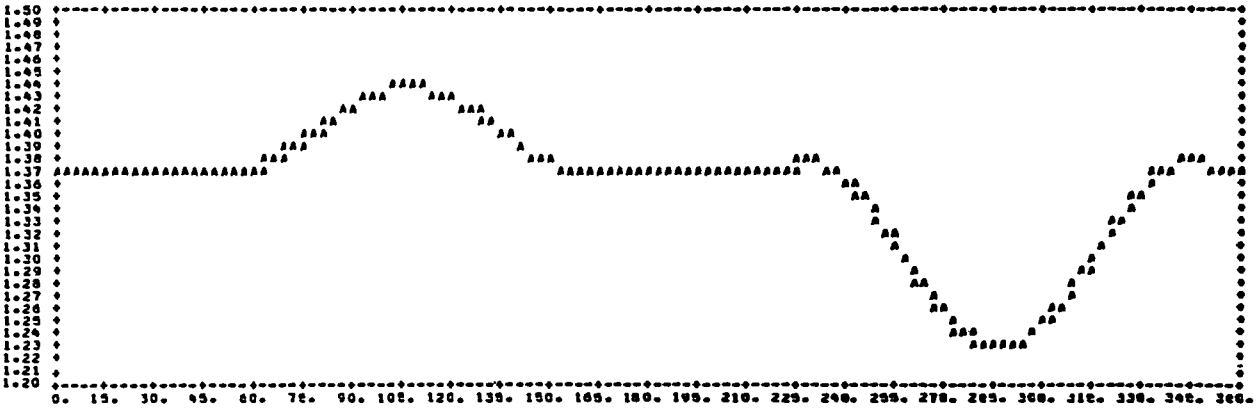

(b)

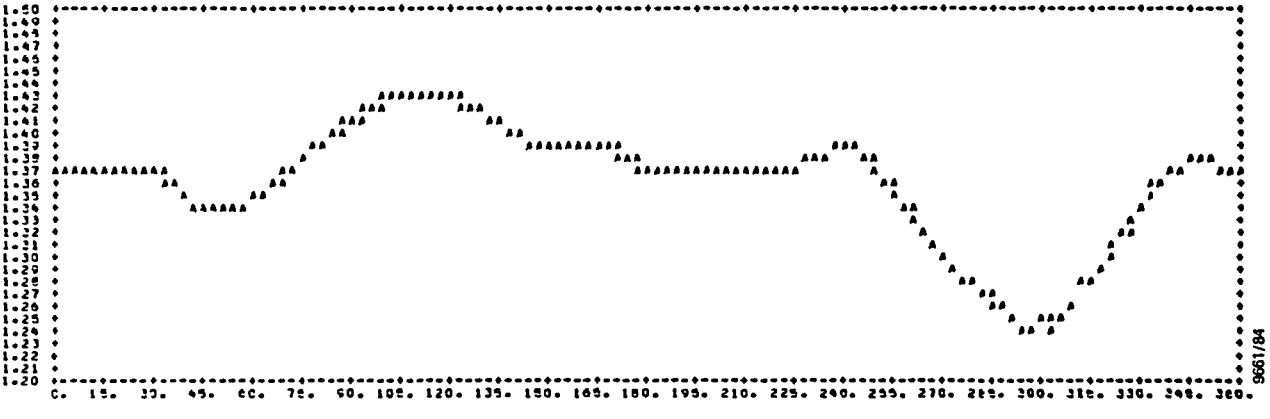

(c)

Figure 4.11-12. Comparison of Earth Width Pitch Errors
(a) Scaled Radiance Model
(b) Shifted Tangent Height Model
(c) Combined

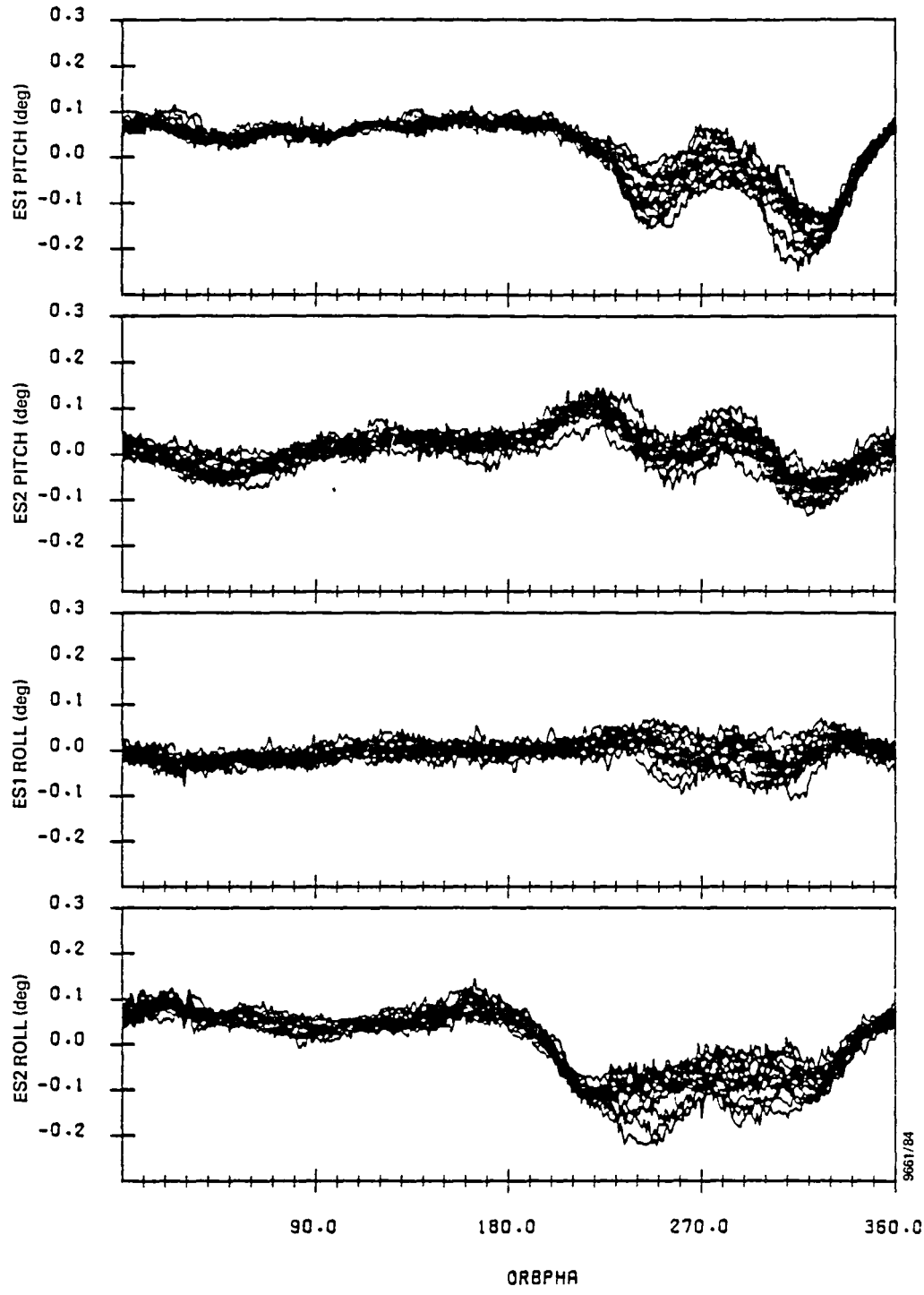

SCANNER RESIDUAL ERRORS IN DEGREES FOR NOMINAL CALIBRATION
WITH EARTH OBLATENESS. OBC ORBIT AND OBC REFERENCE ATTITUDE
EFFECTS MODELLED AND CONSTANT BIASES REMOVED
DATA START TIME:830621.225929155
END TIME:830623.012243587

Figure 4.11-13. Residual Errors From Oblate Earth Model for Data Span on June 21-23, 1983

interaction of the brightness and tangent height effects. The actual summer hemisphere appears more uniform than modeled. The fictitious profiles with a greater negative (0.05 degree) depression occur in about the same location as the brightness-induced errors in Figure 4.11-10. However, a 0.05-degree positive error tends to fill this trough, possibly indicating a more local and less than 3-kilometer increase in the polar tangent heights. In the southern portion of the orbit, a deep negative error (0.3 degree) characteristic of twice the tangent height adjustment of the fictitious model (-6 kilometers) appears to be partially filled or canceled by the positive error due to the decrease in brightness of the southern polar horizon profiles. The brightness adjustment that would cause such a large positive error is two or three times lower than the fictitious model value of 0.76.

The evidence suggests that a likely representation of the atmospheric radiance profiles (derived from the data of Figure 4.11-13) is a complex tangent height model rather than the simple monotonically increasing or decreasing model coupled to the brightness dependence. The example in Figure 4.11-13 was chosen because of its clear trend in all orbits for a full day of data. Two weeks later in July, atmospheric conditions in the winter hemisphere are similar, but not as symmetric (Figure 4.11-14). A January example illustrated in Figure 4.11-15 had similar results for the latitude-inverted atmospheric conditions. The figure illustrates the greater degree of irregularity in the Northern (winter) Hemisphere.

4.11.2.2 Sun and Moon Interference Effects

Interference in the Landsat-4 conical scanners from the Sun and Moon occurred when the Sun or Moon entered a portion of

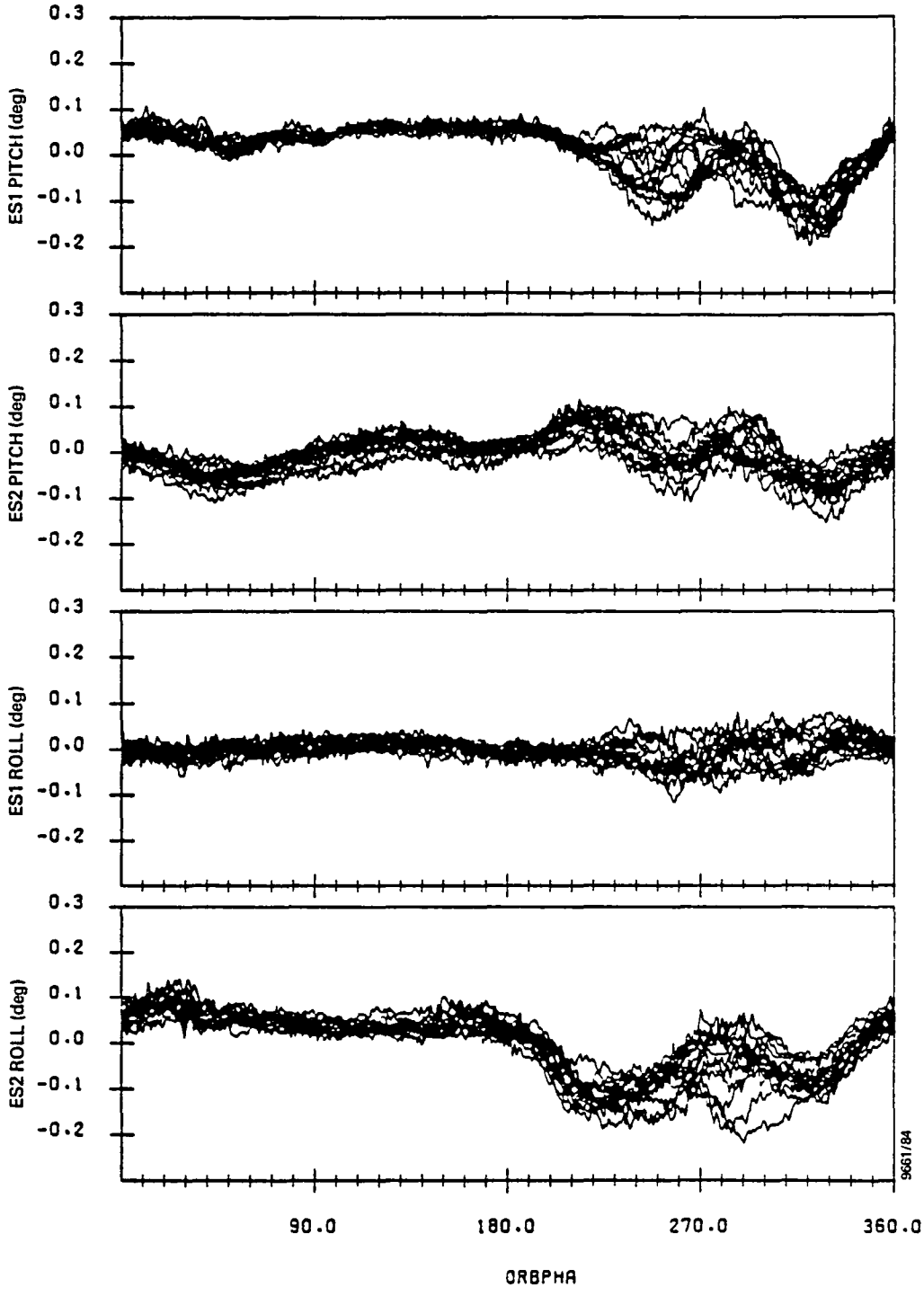

Figure 4.11-14. Residual Errors From Oblate Earth Model for Data Span on July 6-7, 1983

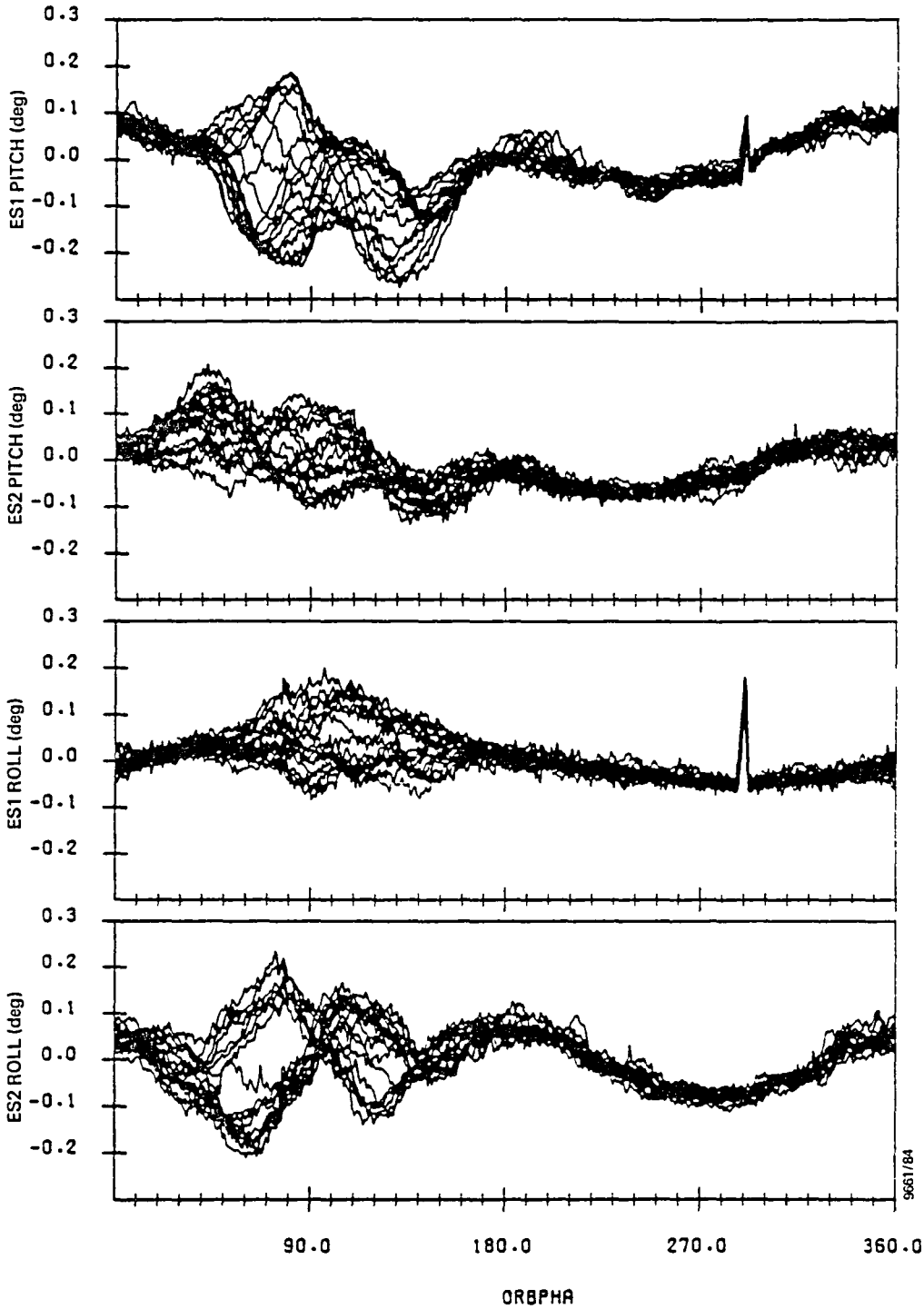

SCANNER RESIDUAL ERRORS IN DEGREES FOR NOMINAL CALIBRATION
WITH EARTH OBLATENESS, OBC ORBIT AND OBC REFERENCE ATTITUDE
EFFECTS MODELLED AND CONSTANT BIASES REMOVED
DATA START TIME:830119.063608627
END TIME·830120.120626114

Figure 4.11-15. Residual Errors From Oblate Earth Model for Data Span on January 19-20, 1983

the scan cone that was not electronically blanked. Electronic blanking was in effect for 122 scan degrees centered on the space portion of the scan. For the nominal Earth scan width angles near 96 degrees, a 71-degree portion of the scan (from 61 degrees past zenith to 48 degrees before nadir) was vulnerable to interference. Only ES1 was vulnerable to Sun interference; Figure 4.11-16 illustrates the Sun/Earth geometry for this sensor as viewed from orbit normal. Moon interference is possible in both sensors; Figure 4.11-17 illustrates the Sun, Moon, and Earth geometry for ES2 as viewed from behind the spacecraft.

Data plots illustrating the effects of the Sun on the conical scanner residual plots for the pitch and roll channels are presented in Figure 4.11-18. The influence of the Moon at full brightness on roll data from ES1 and pitch data from ES2 is illustrated in Figures 4.11-19 and 4.11-20, respectively. During these orbits, the angle between the Moon and orbit normal changed from 123 to 136 degrees. Moon interference with ES2 occurs twice per orbit in the AOS and LOS portions of the scan cone as the Moon rises and sets.

The Landsat-4 flight data thus demonstrate the degree to which the conical scanner output is modified by Sun and Moon IR radiation for the Landsat-4 flight geometry. The data also show that the electronic blanking system performed well for these sensors. Because of constraints imposed by the Landsat-4 attitude control requirements, it was not possible to analyze interference conditions showing the extremes occurring when the Sun crosses the scanner cone near the Earth horizon. A more detailed analysis of the evolution of Sun and Moon interference on a timescale of seconds would have contributed significantly to the understanding of the optical properties of these sensors. No significant interference effects were established from cold clouds in the scanner FOV.

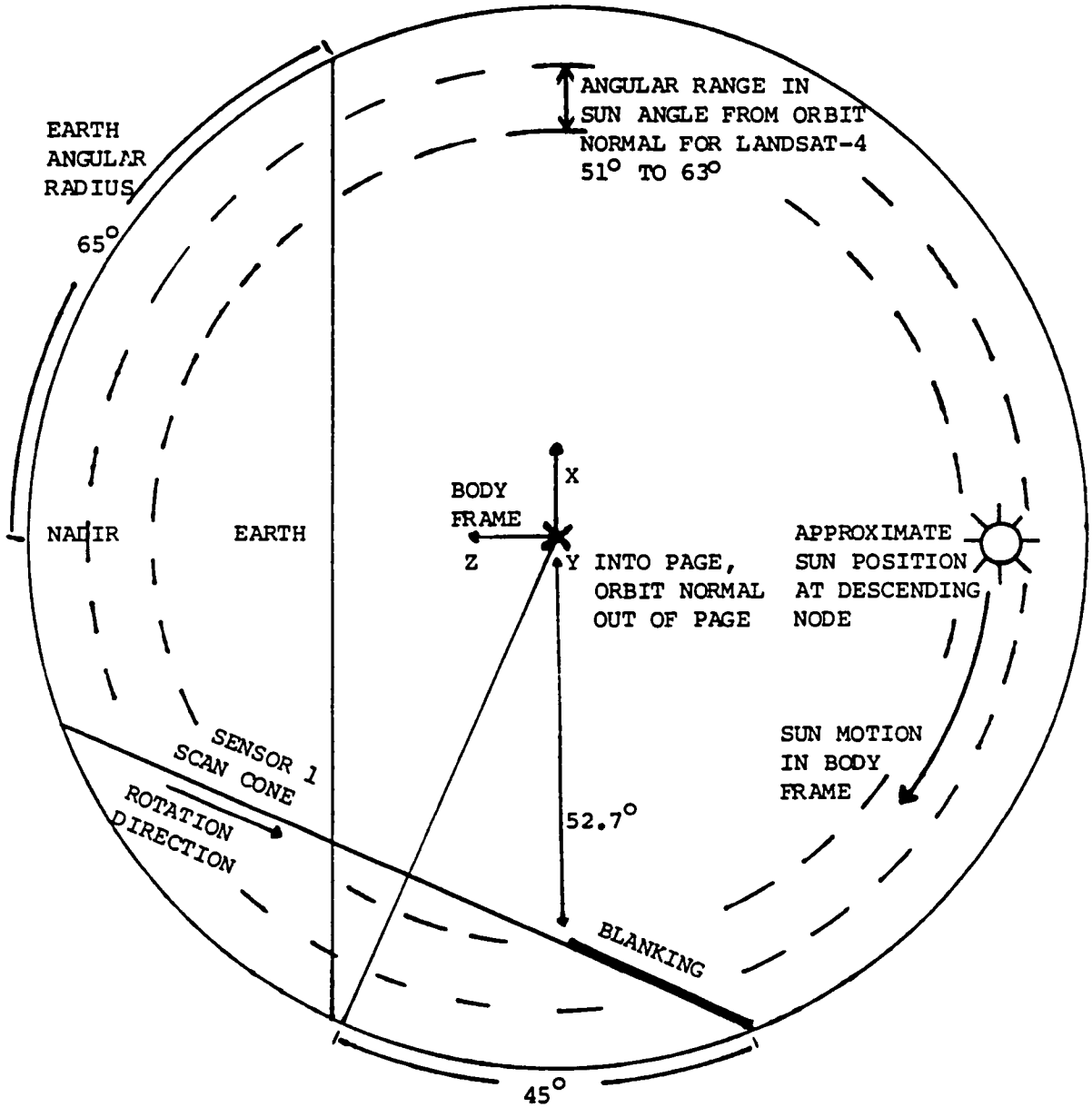

Figure 4.11-16. Sun Position and ES1 Scan Cone Geometry for Landsat-4

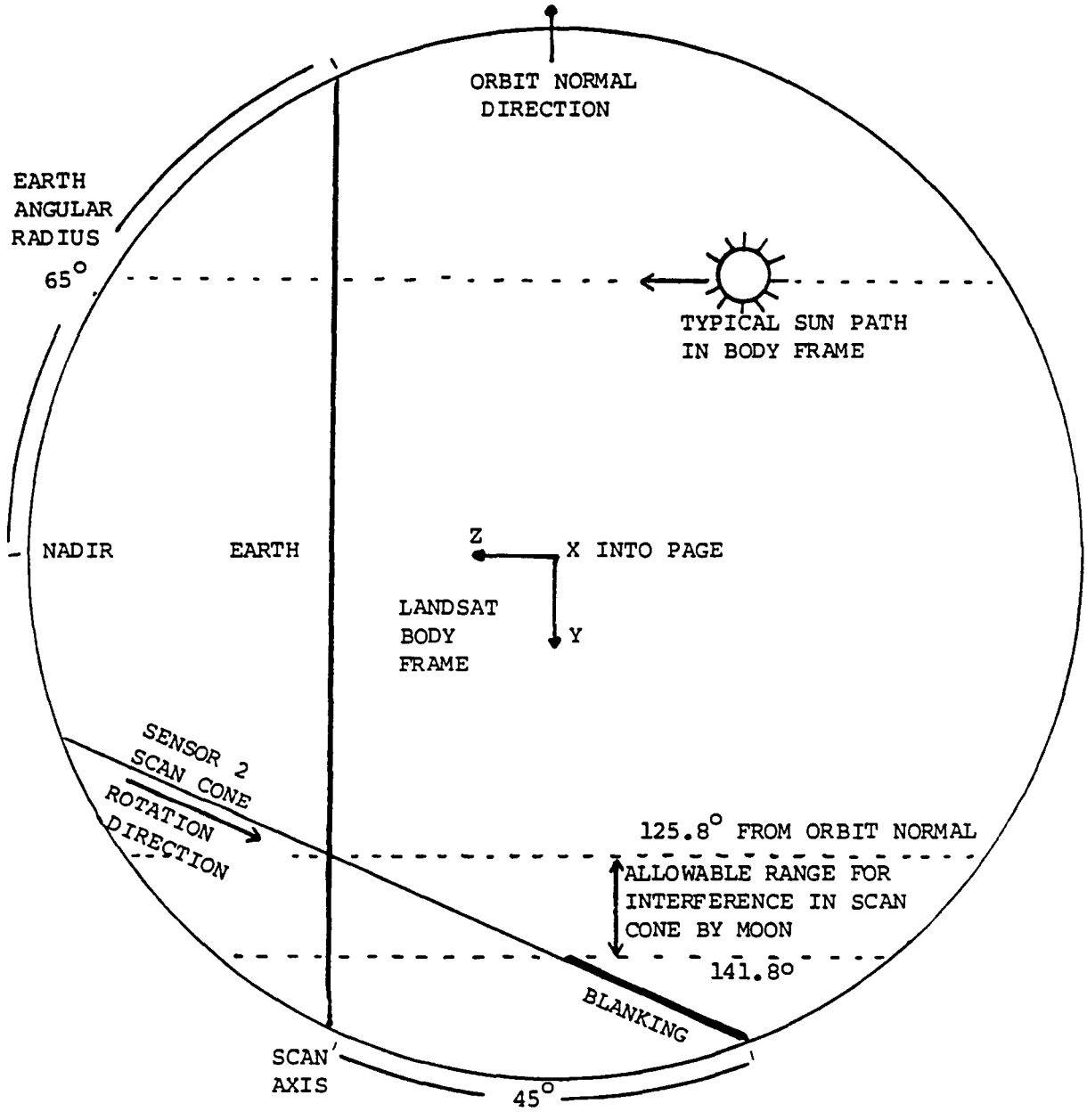

Figure 4.11-17. ES2 Scan Cone Geometry Indicating Allowable Range for Interference in Scan Cone by Moon

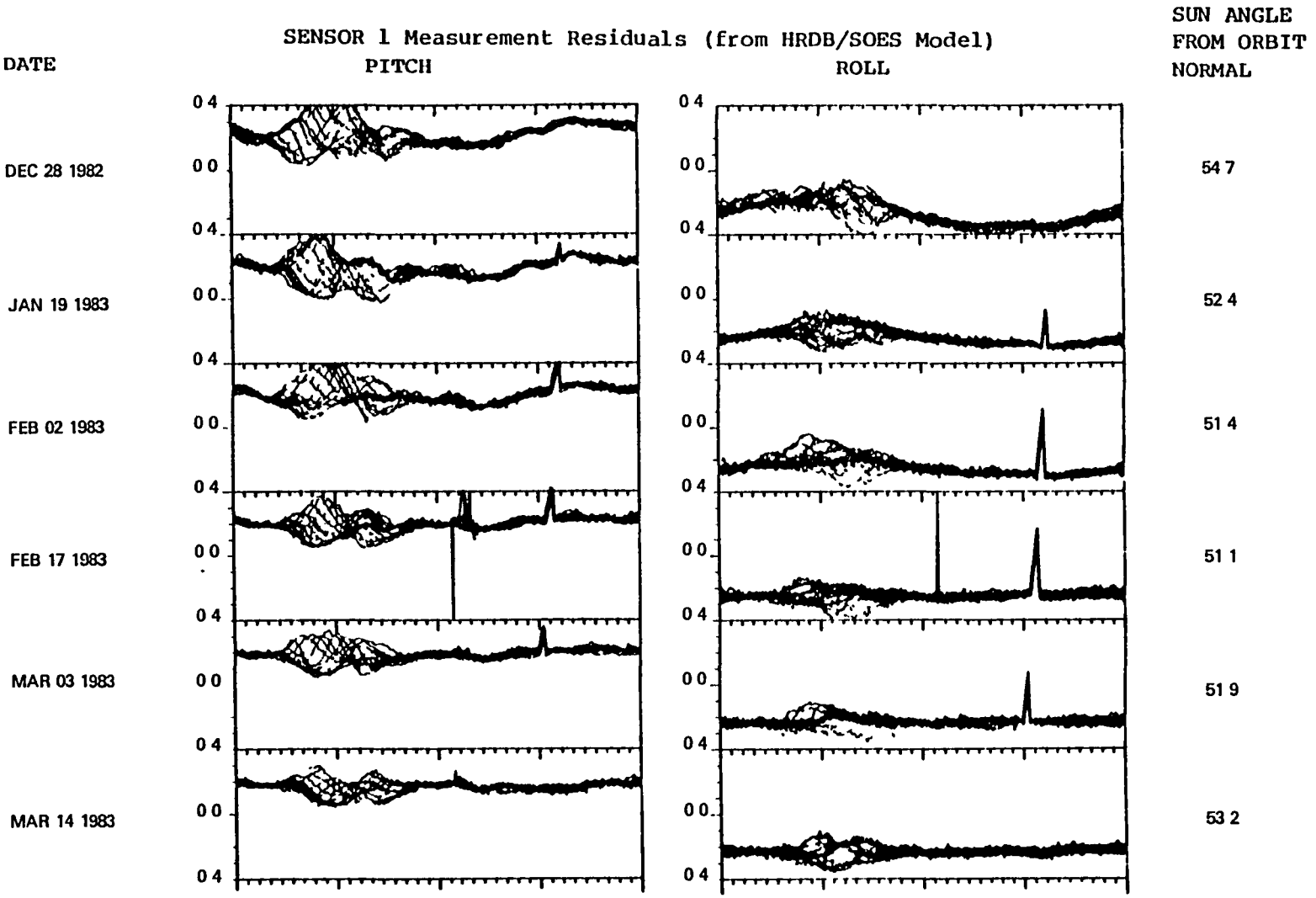

Figure 4.11-18. ESl Residual Errors for Six Dates Illustrating Sun Interference Appearance for Various Sun Angles From Orbit Normal

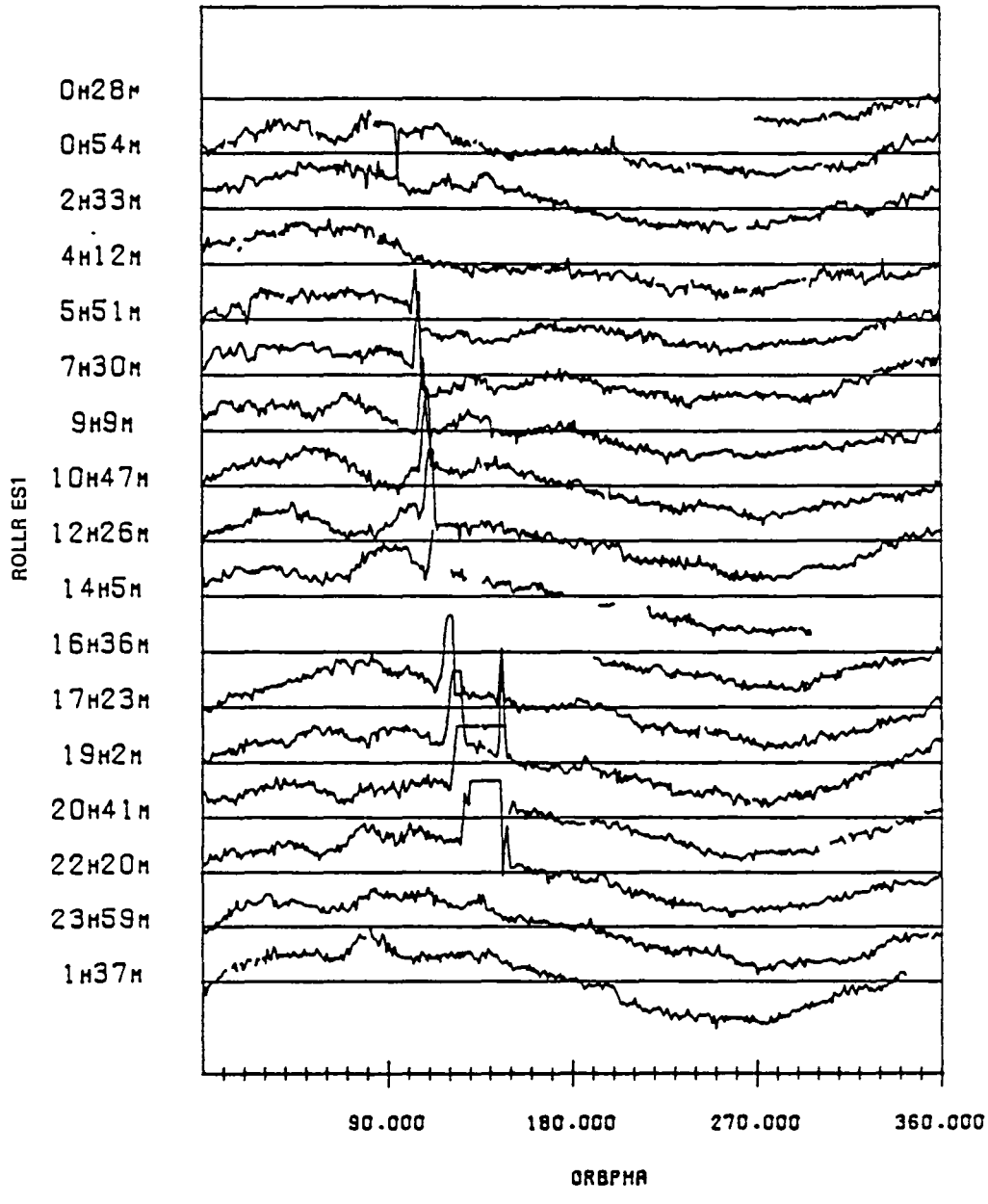

Figure 4.11-19. ES1 Roll Data With Full Moon Interference on December 1, 1982 (The angle between orbit normal and the Moon evolved from 123 to 136 degrees.)

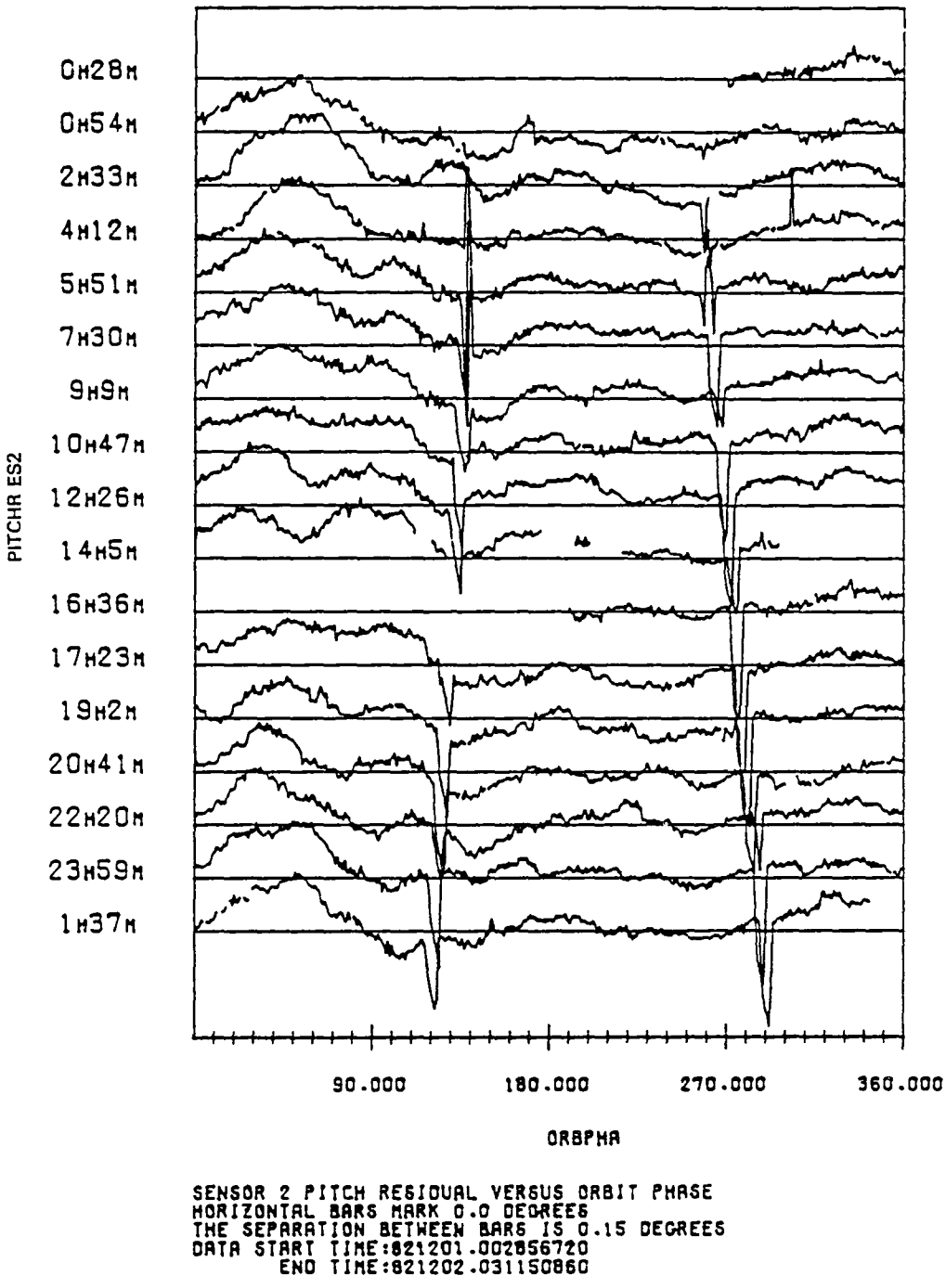

Figure 4.11-20. ES2 Pitch Data With Full Moon Interference on the AOS and LOS Portion of the Scan on December 1, 1982

4.11.3 RESULTS AND DISCUSSION

The Landsat-4 mission offers an excellent opportunity to evaluate the performance of the ITHACO conical IR horizon scanner. The flight data analysis offers insights into methods for processing and correcting attitude determination data on future missions that apply these scanners either as active components of the control loop or as backup and primarily passive components, as in the Landsat-4 mission. The goal of the Landsat-4 analysis was to determine the attitude accuracy that can be achieved with the conical scanner system; with all corrections applied and neglecting the winter hemisphere, this is 0.08 degree (3σ). This is slightly better than the estimates made by Dodgen and Curfman (Reference 6), who estimated a 3-kilometer (1σ) horizon altitude detection accuracy for a single-beam scanner. Three kilometers is roughly equivalent to a 3σ Earth width measurement error of 0.18 degree which, when applied to one limb, will cause a 0.09-degree pitch error. The estimates of Dodgen and Curfman stated that this accuracy level is achievable after the application of an accurate model of the Earth IR radiance.

Figure 4.11-21 is a summary of the pitch and roll standard deviations from sensor Earth width and phase measurements resulting after various stages of GSC model subtraction. The quoted 0.08-degree accuracy is a result derived from the data illustrated in the bottom row of this figure. The degree to which the individual scanner data can be improved to the accuracy of the Dodgen and Curfman estimate is a function of the accuracy of the horizon radiance model.

It can be seen from the figure that the HRDB model appears to reduce the 3σ errors in the phase channels to about 0.12 degree, with some evidence of a seasonal dependence in the standard deviations remaining. It is apparent from the

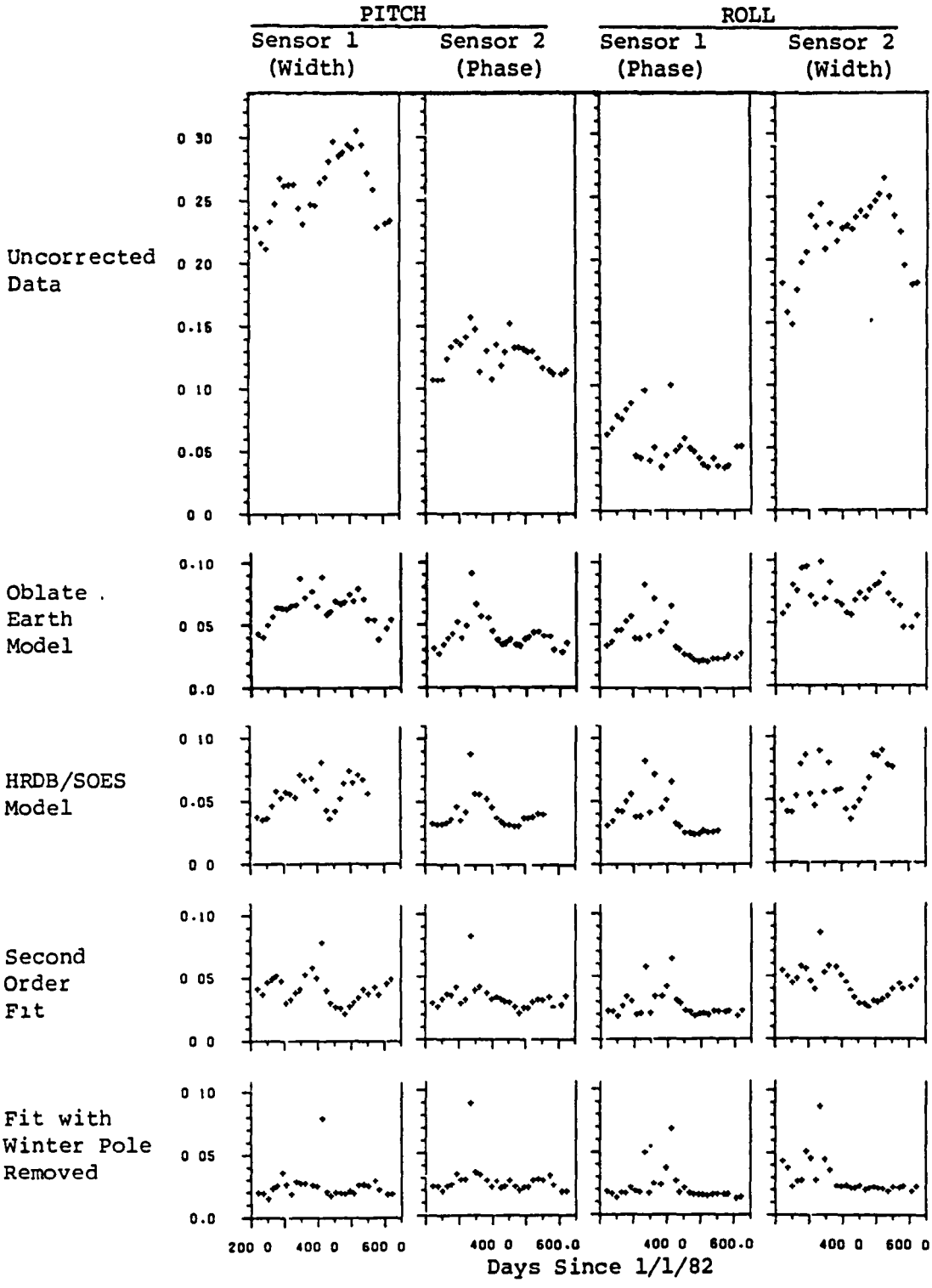

Figure 4.11-21. Pitch and Roll Standard Deviation Statistics for All Data Spans Processed Five Different Ways

experiments with the fictitious profile model (Section 4.11.2.1) and the analysis reported in Section 2 that the HRDB model has obvious shortcomings. For scanners with derivative locator logic, such as those on Landsat-4, a major component of the profile model is the variation in the tangent height with latitude and season. Thus, until a better model of the Earth radiance profiles is established, the 3σ accuracy of the conical scanner data (phase measurements in the third row of Figure 4.11-21) is between 0.12 degree and 0.18 or 0.22 degree, depending on the season and month of year. This assumes unrealistically that every other source of error in a mission with conical scanners can be resolved to the same accuracy as the reference attitude in Landsat-4 (i.e., generally 36 arc-seconds). For most missions using IR scanners as the primary attitude reference and as drivers of the spacecraft control loop, the problem is not as straightforward.

The Earth radiance profile model can be improved, using the residuals from Landsat-4 to determine the model of the profile tangent height. GSC applied alignment and bias errors of up to 0.25 degree to the IR scanner data to produce these results. In-flight determination of these quantities is typically complicated by the absence, or the presence of only limited amounts, of data from an accurate attitude reference.

4.12 TIROS-N/NOAA-7

NOAA-7 was the third satellite in the TIROS-N series. Although no mission support attitude analysis was performed by the ADCS, the mission is of interest here because it employed a static Earth IR sensor, the Earth Sensor Assembly (ESA), built by Barnes Engineering Company. CSC (under contract to GSFC) performed an analysis to evaluate the response of the ESA to the HRDB, the Earth radiance profile model discussed in Section 2.4 (Reference 50). The following discussion reviews that analysis and compares the CSC results with those obtained from the analyses by Ward et al. of Barnes Engineering Company (References 63 and 64).

4.12.1 MISSION REQUIREMENTS AND HARDWARE

The TIROS-N series of spacecraft, operated by NOAA's National Environmental Satellite Service, provide data for the global weather experiment and the world weather watch. This series, consisting of eight satellites in Sun-synchronous, near-polar orbits, is the third generation of the operational environment satellite series and complements NOAA's network of GOES weather satellites.

NOAA-7 was launched from the Western Test Range on an ATLAS-F booster on June 23, 1981. The prime contractor for the satellite bus, as well as for spacecraft integration and testing, was RCA Astro Electronics. A postlaunch report on the mission's attitude determination and control system performance is presented in Reference 65.

The TIROS-N/NOAA-7 spacecraft is illustrated in Figure 4.12-1 (Reference 65). The mission can be summarized as follows:

- Orbit--Sun-synchronous, near-polar, circular, with 98.8-degree inclination and 850-kilometer altitude

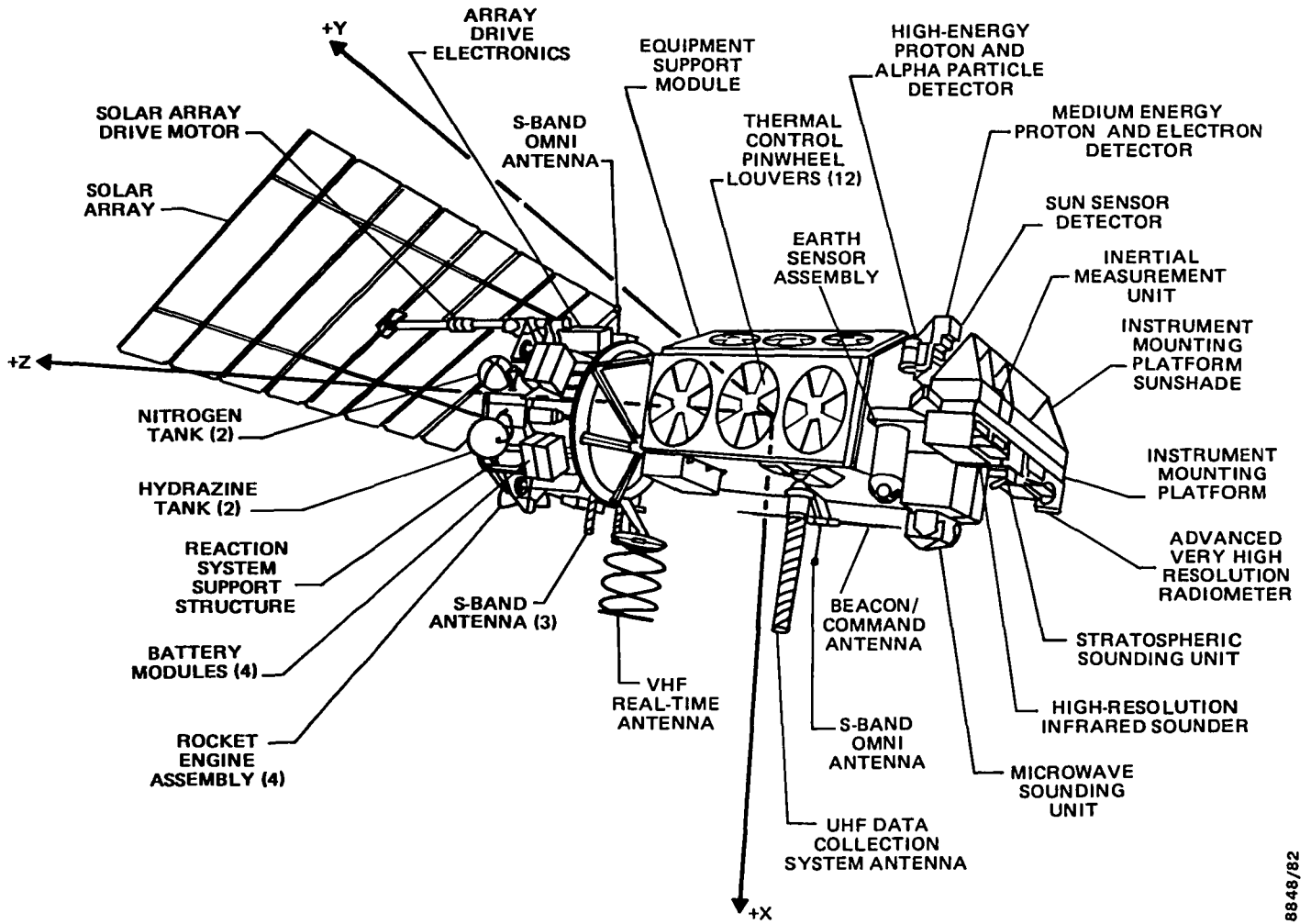

Figure 4.12-1. TIROS-N/NOAA-7 Spacecraft

- Attitude configuration--Pitch (Z) axis nominally along positive orbit normal, yaw (X) axis along the nadir vector, and roll (Y) axis nominally opposite the instantaneous spacecraft velocity vector (Figure 4.12-2, from Reference 66)
- Attitude determination and control hardware--Attitude determination and control subsystem (ADACS), consisting of the following:
  - Earth Sensor Assembly (Figures 4.12-2 and 4.12-3)
  - Single-axis digital Sun sensor assembly
  - Four gyros
  - Four reaction wheel assemblies
  - Two roll/yaw coils
  - Two pitch torquing coils
- Accuracy requirement
  - Control--0.2 degree (3σ) relative to the local geodetic frame, for each axis
  - Determination--0.1 degree (3σ) relative to the local geodetic frame, for each axis
- Ground support system--None

The ADACS is an automatic, zero-momentum, Earth-pointing control system. Rate information is derived from the IRU, which contains three orthogonal and one skewed, strap-down, rate-integrating gyros. The reaction wheels are unloaded periodically by two air-core magnetic coils. Emergency wheel unloading and despin capability is available using nitrogen thrusters. All attitude control calculations are performed by an onboard computer that reads the attitude sensors and calculates control torques to the wheels every

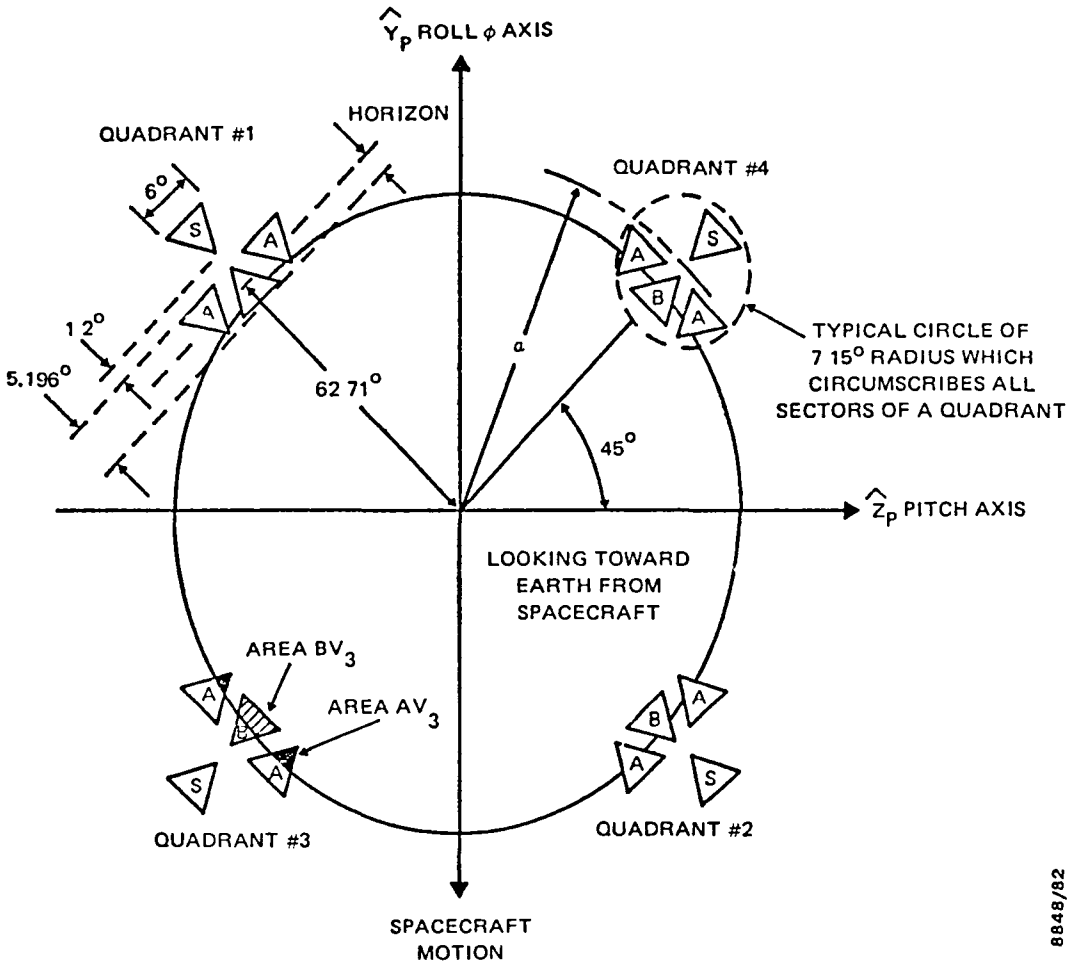

Figure 4.12-2. Earth Sensor Assembly Sensing Geometry

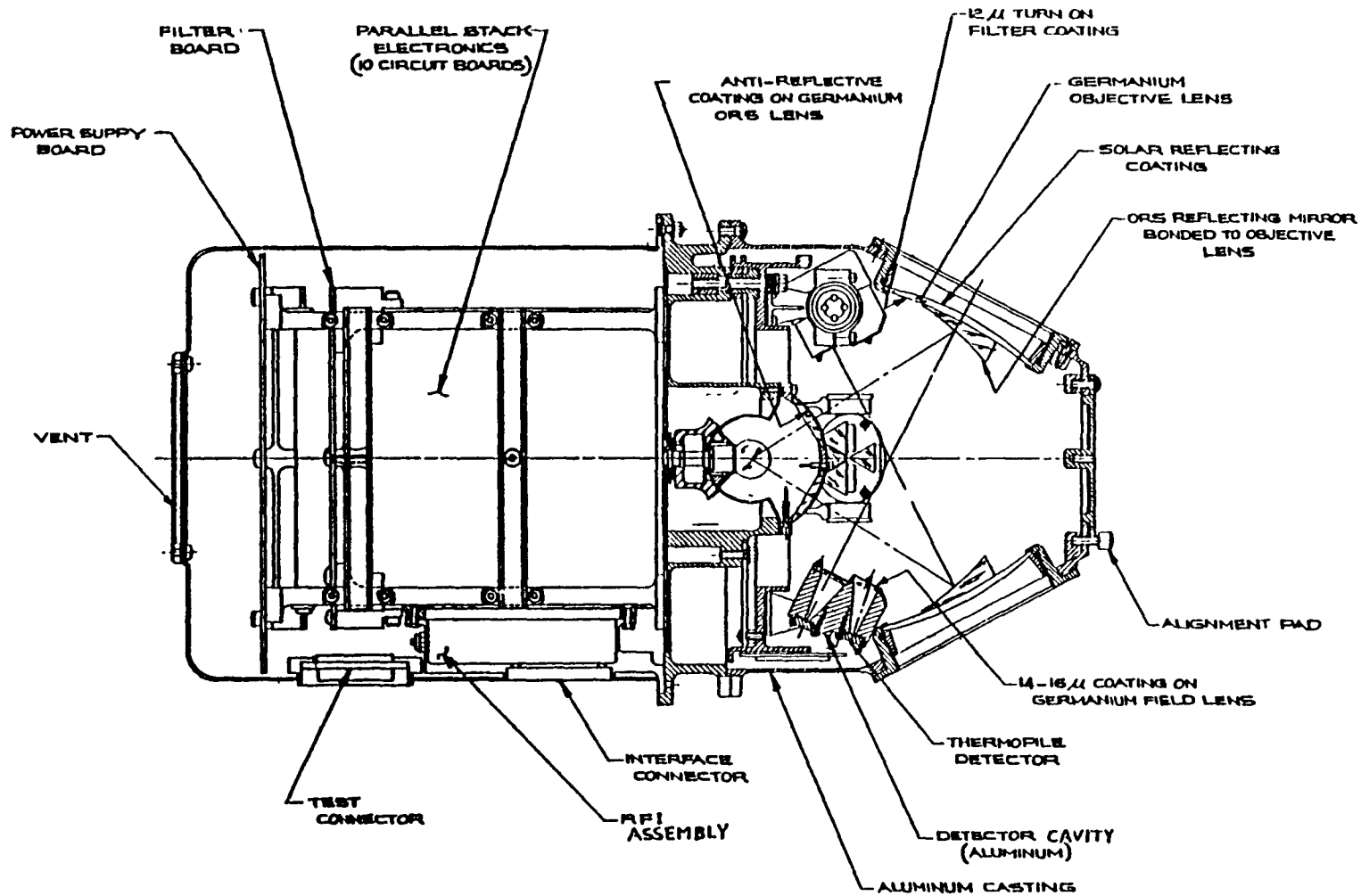

Figure 4.12-3. Cross-Sectional View of Earth Sensor Assembly

half second. The spacecraft ephemeris is computed by the geometric data (GEODAT) software module, which is periodically used to update an onboard table of parameters via ground command. The yaw error calculated with the Sun sensor assembly output is used to update the IRU yaw attitude calibration once per orbit. Attitude changes between updates are derived from the combined output of the pitch, yaw, and roll gyros.

The ESA is a static IR sensor designed to operate over an altitude range of 740 to 926 kilometers. The ESA independently views a segment of the horizon in each of four quadrants and provides four sets of measurements for pitch and roll attitude determination (Figure 4.12-2). The two A-detectors in each quadrant are connected in parallel and produce a single averaged output to minimize errors due to radiance gradients along the horizon. The output from the A- and B-detectors is used to calculate the horizon penetration in the quadrant. This penetration is a pure number ranging from 0 to 1, where 1 represents total penetration. The S detectors view cold space and measure the amount of energy that the detectors in each quadrant are losing to space. A major design feature of the ESA is an offset radiation source that reduces the net radiation loss to space by supplying heat equally to all detectors. The 12 independent detector (A, B) outputs are sequentially sampled by a commutator and multiplexed into a single electronic processing channel to eliminate channel asymmetry. A low-noise preamplifier provides the proper drive levels for the 16-bit analog-to-digital converter. The digitized radiance signals are formatted and provided, on request, to the control interface unit. The digital signal is supplied to the spacecraft data processor every 0.5 second for attitude computation. The digitized radiance signals from the four space-viewing detectors are also fed to the offset radiation

source controllers, where they are used to regulate the amount of heat generated. The spectral band of the ESA is determined by the filter on the lens and by the absorption characteristics of the germanium optical elements. The composite spectral response is shown in Figure 4.12-4 (Reference 50).

4.12.2 PREDICTED ATTITUDE ERRORS

The study by CSC (Reference 50) used the HRDB generated by the LOWTRAN 5 program from 1972 radiosonde observations to model atmospheric radiance (Reference 18). The HRDB data were integrated over the ESA spectral response function to create a data base containing integrated horizon radiance profiles for NOAA-7.

A simple orbit generator was used to compute the spacecraft ephemeris from the following orbital elements:

- Semimajor axis, 7224.35 kilometers
- Eccentricity, 0.0
- Inclination, 98.8 degrees
- Ascending node, 90.0 degrees
- Argument of perigee, 0.0 degrees
- Mean anomaly, 0.0 degrees

This combination of semimajor axis, eccentricity, and inclination resulted in a circular, Sun-synchronous orbit.

The total radiation on each detector (R_A or R_B) was computed, and the horizon penetration in each quadrant, X_i, was obtained as follows:

$$X_i = \left(\frac{2R_A}{R_A + R_B} \right)_i \qquad i = 1, 2, 3, 4$$

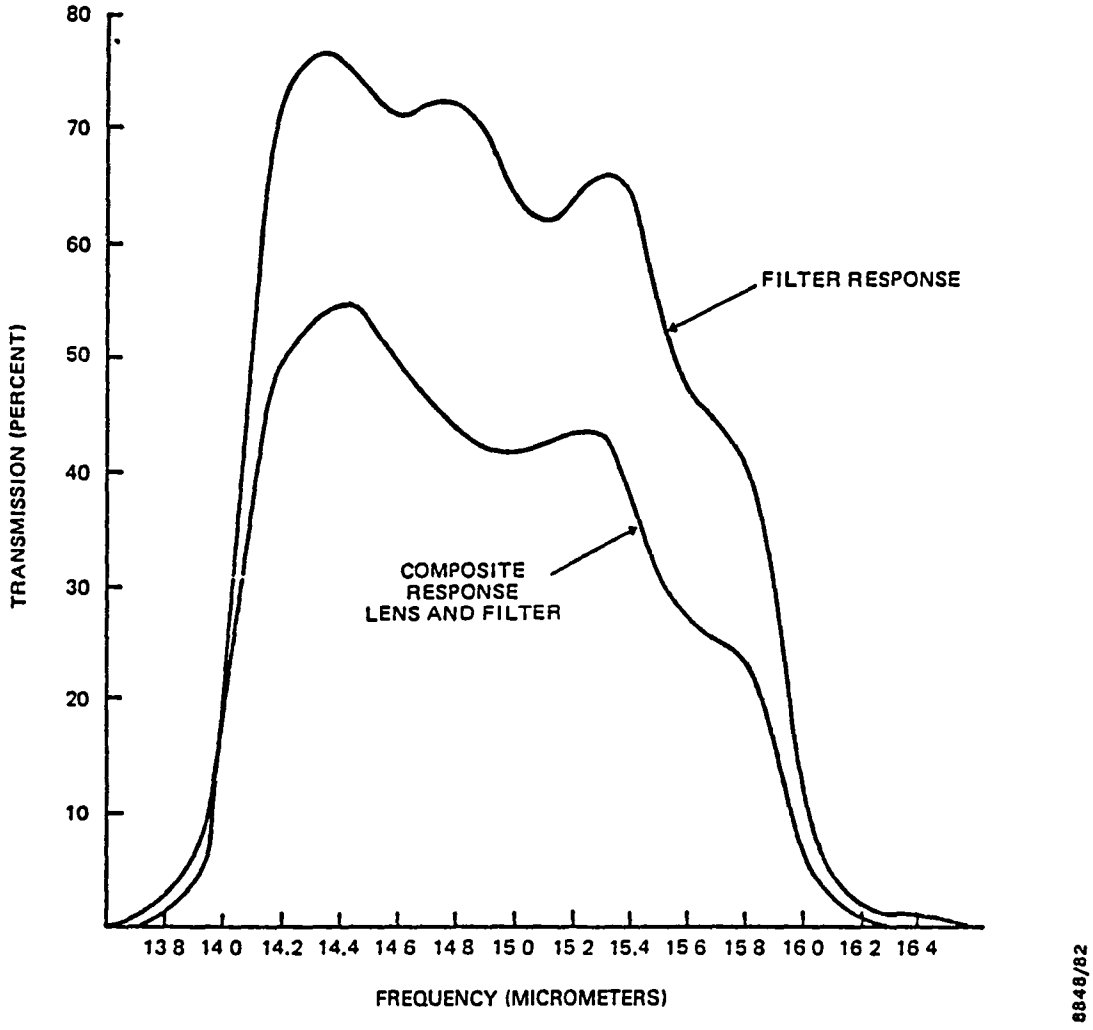

Figure 4.12-4. Optical Assembly Spectral Response

The spacecraft pitch (p) and roll (r) errors were then computed (allowing for a 45-degree rotation from the sensor frame to the spacecraft pitch and roll axes) as follows:

$$\begin{pmatrix} -p \\ r \end{pmatrix} = \frac{1}{\sqrt{2}} \begin{pmatrix} 1 & 1 \\ -1 & 1 \end{pmatrix} \begin{pmatrix} \frac{X_1 - X_2}{2} \\ \frac{X_3 - X_4}{2} \end{pmatrix}$$

The computed pitch and roll errors for July using the HRDB are shown in Figures 4.12-5 and 4.12-6. The ordinate shows the pitch or roll error in degrees, and the abscissa represents the orbit phase angle from the ascending node in degrees.

A similar computation by Barnes Engineering Company (Reference 63) used an updated version of the CORPS program developed by Honeywell. The input temperature profiles to the CORPS program were obtained from an LMSC data base compiled and reported in 1967 (Reference 67). Like the temperature profile data used by LMSC for the Seasat IR scanner analysis (Reference 8), these were Northern Hemisphere data, latitude inverted to provide a full-Earth IR horizon model over the year. One limitation of this model is that it results in temperatures that are too high over the South Pole in July.

The Barnes Engineering results (Reference 63) for pitch and roll errors from January data are illustrated in Figure 4.12-7. The data in this figure were replotted to allow comparison with the corresponding CSC results. The sign of the data has been adjusted to agree with the later report of the results (Reference 64). When compared with the original CSC HRDB results (Figures 4.12-5 and 4.12-6), the Barnes Engineering results show twice the peak-to-peak pitch and three times the zero-to-peak roll variation of the original CSC results.

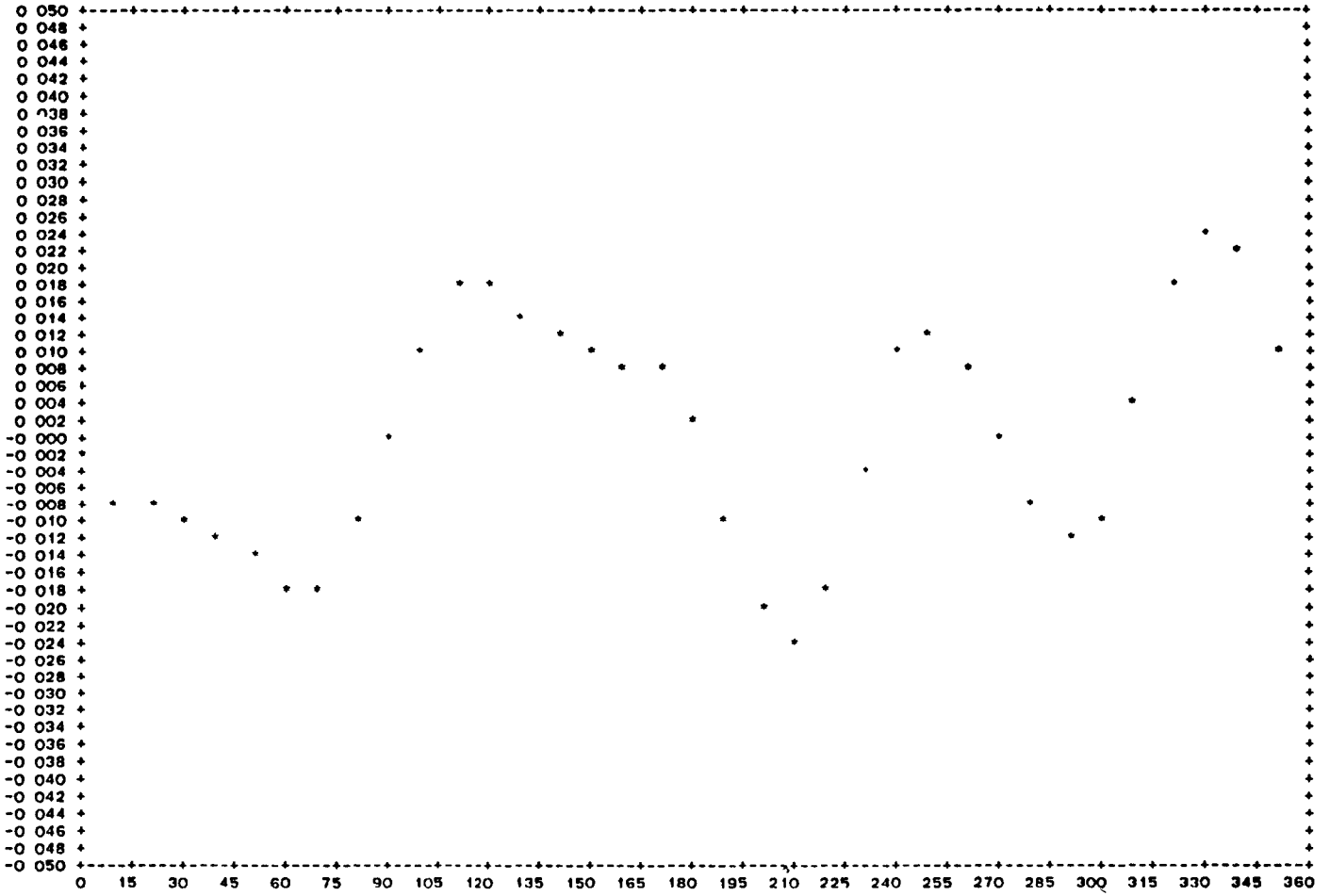

Figure 4.12-5. Pitch Response of the TIROS-N/NOAA-7 ESA to the Nominal CSC HRDB July Radiance Model

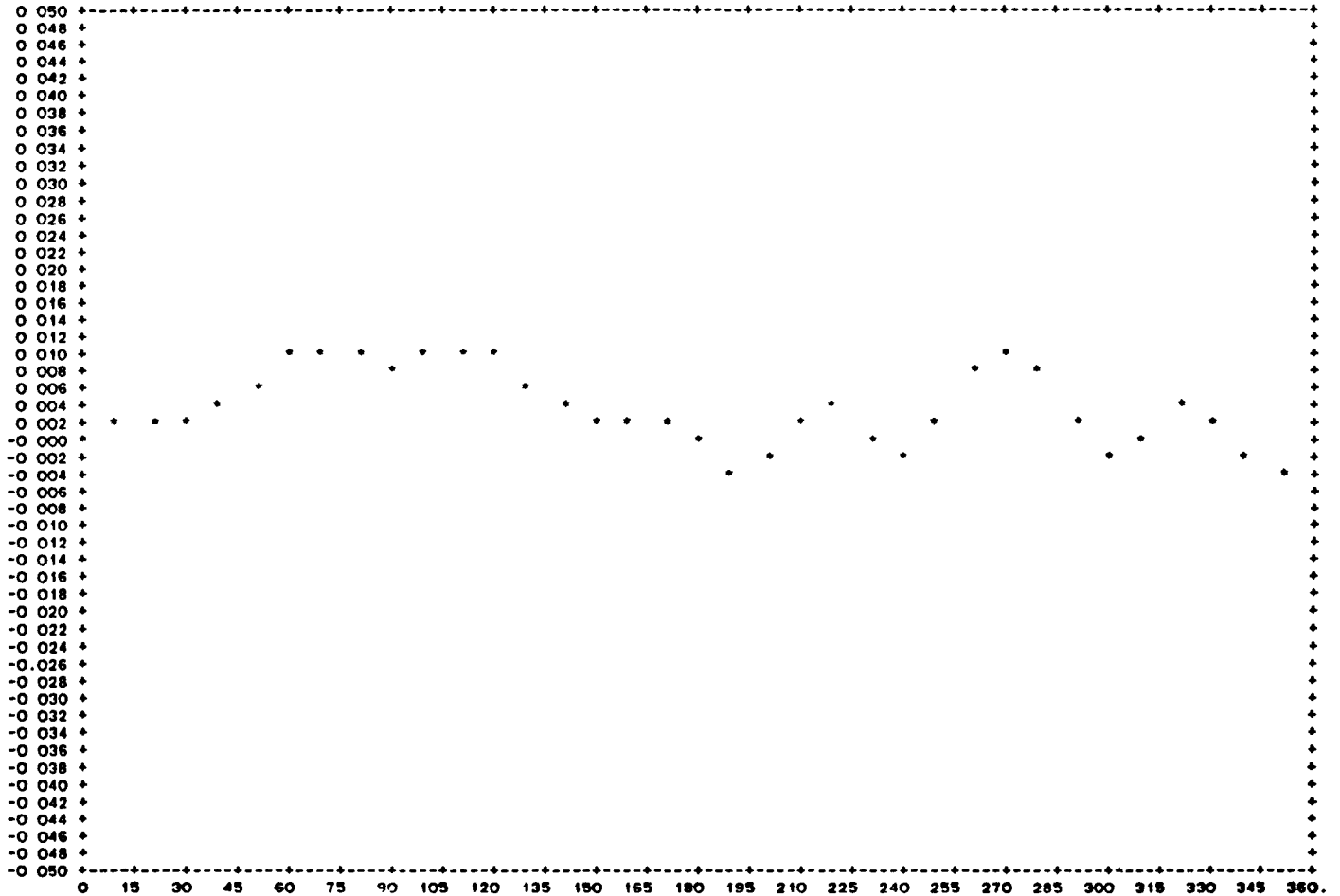

Figure 4.12-6. Roll Response of the TIROS-N/NOAA-7 ESA to the Nominal CSC HRDB July Radiance Model

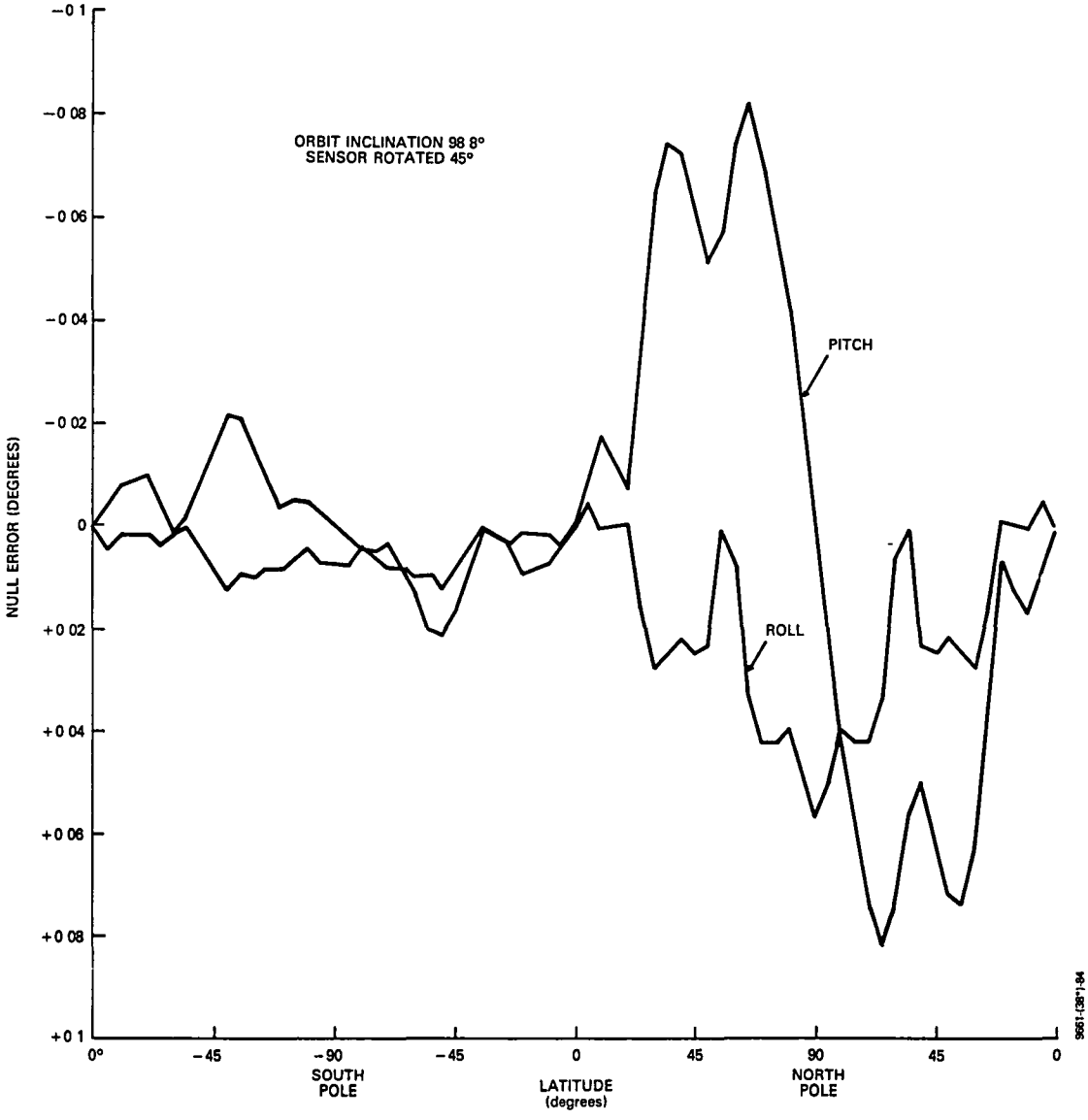

Figure 4.12-7. Pitch and Roll Error at Null Attitude Versus Latitude of the TIROS-N/NOAA-7 ESA for the Barnes January Radiance Model

When the HRDB profiles are adjusted to agree with the Nimbus-6 LRIR data (see Section 2.5), the peak-to-peak amplitude of the pitch errors predicted by the CSC analysis increases to 0.1 degree and the roll errors increase to 0.02 degree. The CSC results with the adjusted July profile model are illustrated in Figures 4.12-8 and 4.12-9. The January results from Barnes Engineering Company and the July results from CSC are analytically compared by adjusting the orbit angle of the January data 180 degrees relative to the July data. The CSC radiance model result still appears to predict one-half the roll error and slightly less pitch error than the Barnes analysis. The sign of these results is consistent with the definition of the pitch and roll axes illustrated in Figure 4.12-2.

4.12.3 MISSION DATA ANALYSIS

In their analysis of the attitude data from NOAA-7, Ward et al. (Reference 64) attempted to extract the horizon radiance component of the pitch variation by two methods. The first method used spacecraft gyro data and a model of the pitch motion that included the effects of Earth oblateness and orbit eccentricity. The difference between the model and the gyro data was attributed to control system response to ESA errors. The second method used ESA data to derive the radiance intensity in each quadrant of the ESA. The results from the first method were inconclusive, but with refinement the method could prove useful. The results from the second method show radiance intensities with the same general shape as those computed from the atmospheric radiance model (Reference 63). The model did not, however, match the amplitude extremes indicated by the ESA measurements.

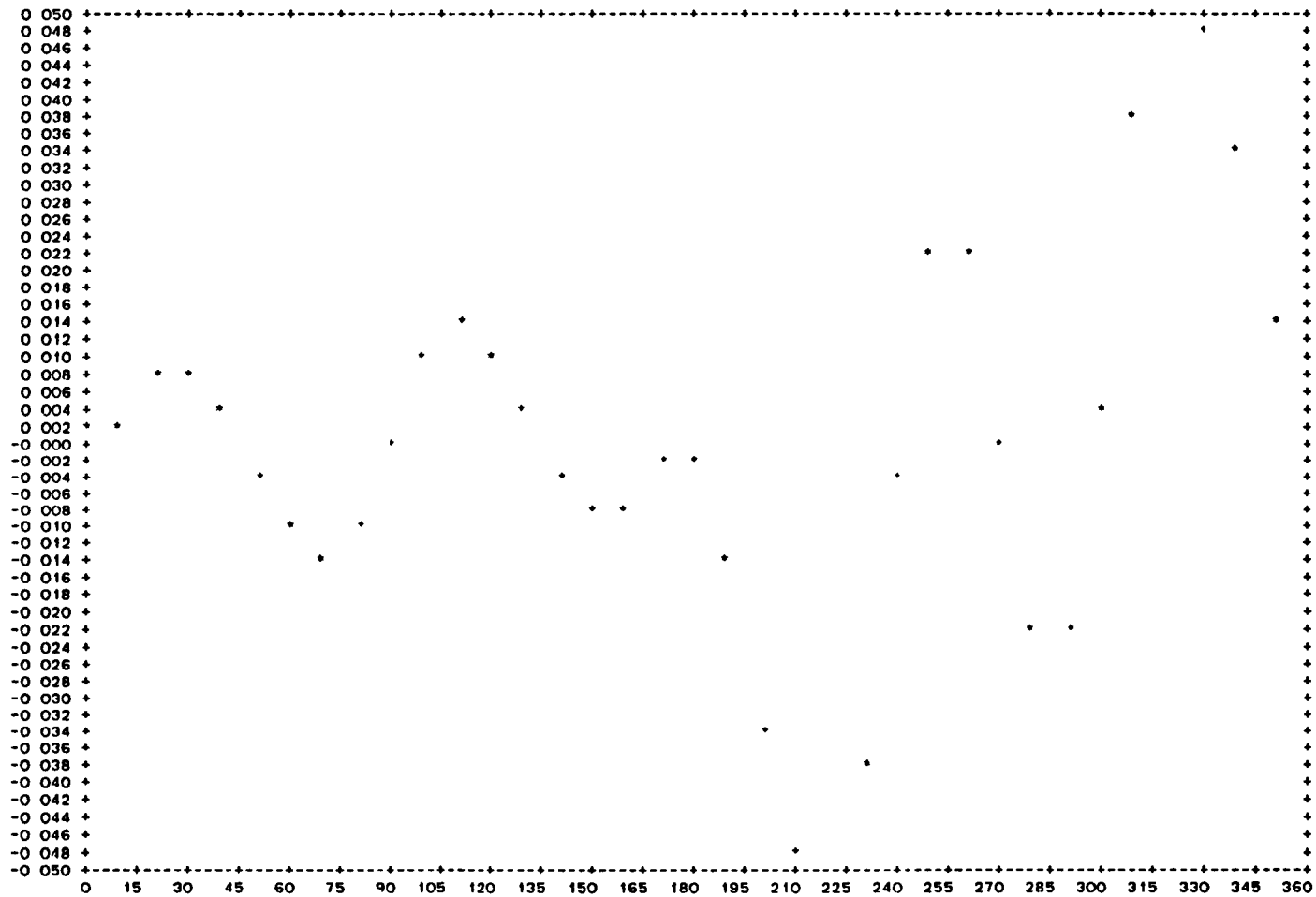

Figure 4.12-8. Pitch Response of the TIROS-N/NOAA-7 ESA to the Modified CSC July Radiance Model

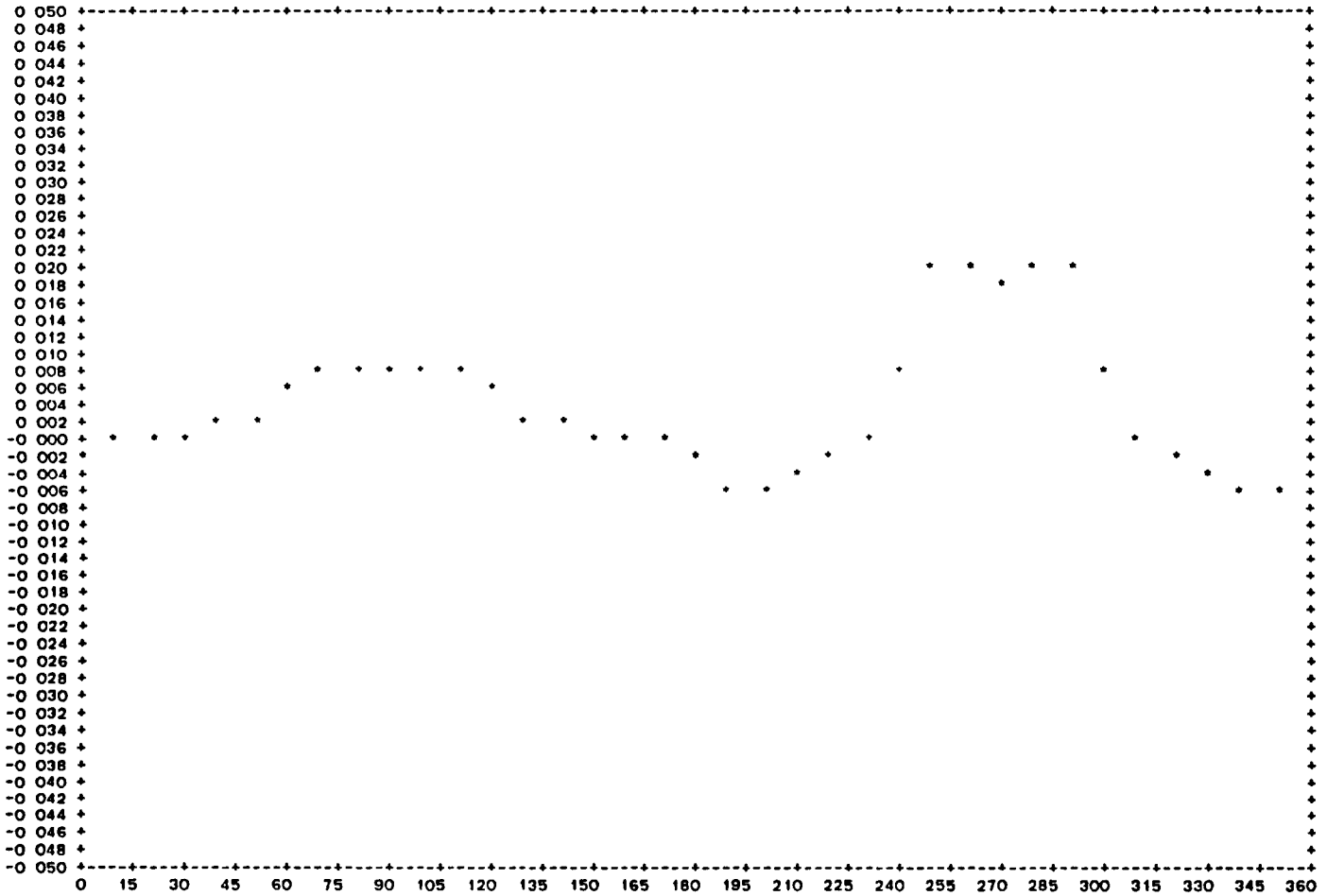

Figure 4.12-9. Roll Response of the TIROS-N/NOAA-7 ESA to the Modified CSC July Radiance Model

4.12.4 RESULTS AND DISCUSSION

The analysis of the NOAA-7 ESA response to the original HRDB resulted in the lowest error response that had been computed to that time for an Earth IR sensor system. Subsequent analysis by CSC (reported in Section 2) demonstrated that part of this low error response was due to IR radiance profile modeling errors in the HRDB. A comparison of the CSC results with results from a similar analysis by Barnes Engineering Company further supported this explanation. When the CSC model of the ESA was rerun using a July Earth radiance model adjusted to agree with Nimbus-6 LRIR temperature profiles, the predicted pitch and roll errors increased to values nearer those obtained by Ward.

The significance of the results of modeling the ESA can be summarized as follows. The error signal from a single quadrant of the ESA is independent of the horizon radiance intensity in that quadrant. Therefore, raising and lowering the radiance intensity uniformly in the A and B FOV sectors, either in the flight system or in the simple "integration of the FOV" analytical model, should not change the X_i output from that quadrant. A change in the ESA error output will be caused by (1) changes in the radiance gradient in the lateral (horizontal) and sky-to-Earth directions within a sector FOV array and (2) increases and decreases in the tangent height of the edge of the Earth IR profile in a given sector.

The change in response observed between the nominal and adjusted HRDB profile models was induced by an increase in the north/south radiance gradient. This is a lateral gradient influencing the pitch errors in the midlatitudes and a sky-to-Earth gradient for roll errors at the maximum latitudes of the orbit. Changes in the radiance across the 6-degree triangular FOVs shift the output away from the values that

would be obtained if the radiance were uniform. Increases in brightness toward the apex of the A-detector FOV will have more effect on the B-detector FOV output. Similarly, increases in brightness toward the apex of the B-detector FOV will have a greater effect on the A-detector FOV output relative to a uniform horizon bisecting the centers of the A- and B-detector FOVs. Changes in the horizon profile edge tangent height have a direct influence on the output of the ESA. Thus, the degree to which either the CSC or Barnes estimate of errors reflects the actual flight response may depend on the accuracy with which either horizon profile model represents the latitude dependence of the profile edge tangent heights.

A modest effort was made to analyze NOAA-7 flight data by Ward et al. (Reference 64) in which the general features of the sensed Earth radiance were correlated with the Earth radiance model. The measured radiance data showed larger extremes than predicted by the model used in their work. A detailed analysis of flight data from the NOAA-7 ESA could add significantly to the development of a good representative Earth IR horizon profile model and should be pursued in the future.

SECTION 5 - CONCLUSIONS AND RECOMMENDATIONS

This document surveyed 10 years of experience in applying IR Earth horizon sensors to attitude determination and performing analyses to model the performance of these sensors. The massive Project Scanner study was reviewed for the purpose of establishing the state of the art (circa 1969) and making this information available to current users. The IR sensor modeling analysis and IR sensor flight data analysis were based primarily on those missions that were the direct responsibility of the ADCS at GSFC. Flight data and analysis from missions such as SME, TIROS-N, and Landsat-4 were included to illustrate alternative analysis approaches and to extract specific information about the Earth radiance. The material presented supports the following observations:

- Early spaceflight experience (1960s) with IR sensors established guidelines for IR attitude sensor design, operation, and space system integration that are still valid and necessary considerations for current versions of the IR sensing systems.

- The analysis of the behavior of the Earth's IR profile in the 15-micrometer band by LRC and Honeywell established an understanding of the physical factors influencing the Earth's IR image in that band and resulted in a method of deriving the IR profile intensities from atmospheric temperature profiles. The Project Scanner radiance profile measurements confirmed the validity of these procedures for the homogeneous summer atmosphere conditions. They also illustrated the degree to which the horizontal nonuniformity characteristic of the high-latitude winter atmosphere caused disagreement between the measured and computed radiance profiles using data over a given geographic location.

- Flight data analysis from the Seasat-1, AEM/SAGE, DE-2, and Magsat missions showed that most of the effects cautioned against by the flight experience in the 1960s occurred again to a lesser degree in the 1970s.

- Using the results of the Earth IR profile analysis and the Project Scanner measurements of Earth profiles, limits on attitude performance accuracy were established for a hypothetical IR scanner system with the output data corrected by an oblateness-like IR Earth radiance model. The errors established were assumed to originate primarily from the unmodeled variations in the Earth's IR image.

- The prelaunch analysis of the Seasat-1 IR scanner demonstrated that valuable information about the in-flight performance of an Earth sensing system can be obtained with a longitudinally averaged, latitude-dependent Earth IR profile model tailored to the specific sensor and reasonably accurate models of the Earth scanning geometry and sensor signal processing electronics. In addition, the analysis provided a means of estimating the oblateness-like radiance errors for postlaunch attitude data enhancement.

- The Seasat-1 flight data analysis verified the existence of cold cloud effects in the flight data and confirmed the preflight analysis that predicted the magnitude of these effects.

- The development of a capability by GSFC and CSC to generate IR Earth profile models tailored to a given IR sensor passband showed that the LOWTRAN 5 program was analytically sufficient, but that the input Earth temperature profiles were inadequate to represent the high-latitude seasonal effects. This latter result was established by a direct comparison of the analytical representation of the Nimbus/LIMS data with the Nimbus/LIMS Profile-R flight data.

- The review of Nimbus/LIMS Profile-R data performed to evaluate the accuracy of the GSFC/CSC Earth IR model also demonstrated the degree of variability of the Earth IR image in the narrow and wide CO_2 passbands centered at 15 micrometers. This provided representative models of the degree and geographical extent of atmospheric IR radiance variability that enhanced the reliability of analysis to estimate the magnitude of these effects on the IR sensor attitude sensing accuracy.

- Detailed ray trace analysis of the IR scanner field of view showed that, for the ERBS flight system modeling, the detail was inconsequential. However, the analysis showed that the effect is significant for the ground calibration where the assumption of an object at infinity does not hold.

- An evaluation of the IR sensor modeling software showed that, for the most part, only general features (rise times, gain, and delays) in the signal processing are necessary for reliable results. The evaluation also indicated that great care should be taken to ensure the accuracy of the integration procedures in computing the IR input pulse and in convolving this pulse with the electronics response function to obtain the output pulse.

- Analysis of the Landsat-4 IR sensor data using an accurate (<36 arc-sec) attitude reference from the OBC showed that improved performance has been achieved with the derivative locator logic used in the conical scanner, when compared to the normalized threshold and fixed-threshold sensors. Conclusive data on the latitude dependence of the Earth IR horizon tangent height was not, however, obtained from the Landsat-4 data, because the derivative locator logic showed significant sensitivity to the brightness variations in the IR profiles.

- The Landsat-4 IR sensor analysis also showed that the limit of an ideal IR sensor attitude accuracy is in the range of 0.1 degree (3σ) with the winter hemisphere removed, which agrees approximately with the estimates by Dogden and Curfman in 1969. However, when an accurate reference attitude is not available and the winter hemisphere is included, the 3σ accuracy is still between 0.15 and 0.20 degree.

- Analysis of SME data demonstrated an alternative method of horizon altitude estimation and data correction using the temperature and altitude of the 5-millibar level from the NMC data base.

Overall, the analyses presented in this document confirm the existence of a systematic season- and latitude-dependent horizon radiance effect in the IR scanner data. The accuracy of modeling this effect is currently limited by shortcomings in the temperature profile data used to synthesize the radiance profiles. Improvements in the temperature profile data base supported by Nimbus/LIMS data and Nimbus/LRIR data can be made to enhance the overall accuracy of the Earth IR radiance model. With these improvements and the application of an associated oblateness-like correction to IR scanner data, accuracies would still remain between 0.15 and 0.2 degree for flight systems. Further enhancement in the accuracy of the Earth IR model can be obtained for systems with derivative locator logic by analysis to improve the understanding of the latitude dependence of the tangent height of the radiance profiles. Some evidence for this exists in the Project Scanner data and in the Landsat-4 data, when the influence of brightness variations is adequately accounted for in the flight data.

Improvements in the accuracy of the methods using longitudinally averaged radiance profiles can be achieved by compiling a comprehensive data base of world temperature profiles from the NMC. Furthermore, with methods similar to those used for analysis of the SME data, it may be possible to correct IR scanner data on a daily basis. This procedure would involve using the most strongly correlated parameters, such as the temperature and altitude of the 5-millibar level, to derive a local (longitude and latitude dependent) horizon altitude correction. Whether significant improvements in the quality of the flight data can be made, using a local daily model of the Earth IR profiles, again depends on the degree of horizontal uniformity in the atmosphere viewed by the flight system.

Finally, although improved attitude sensing accuracy is one of the goals influencing the IR sensor designs and supporting analyses presented in this document, it is equally important to understand the IR sensing technology and the factors that influence the performance accuracy of the various sensors. It is hoped that this document will assist the reader in the rapid assimilation of information that was acquired over a decade of mission support analyses. It is also hoped that the information presented in this document increases the probability of success in the application of IR sensors in future spaceflight missions.

GLOSSARY

ACS	attitude control system
ADACS	attitude determination and control subsystem
ADCS	Attitude Determination and Control Section
ADS	attitude determination system
AE	Atmosphere Explorer
AEM	Applications Explorer Mission
AOS	acquisition of signal
APL	Applied Physics Laboratory
ATS	attitude transfer system
BHS	body-mounted IR horizon sensor
CEP	cylindrical electrostatic probe
CORPS	Comprehensive Radiance Profile Synthesizer
CSC	Computer Sciences Corporation
DC	direct current
DE	Dynamics Explorer
DSAI	digital solar aspect indicator
EMI	electromagnetic interference
ERBS	Earth Radiation Budget Satellite
ESA	Earth Sensor Assembly
FADS	fine attitude determination system
FHST	fixed-head star tracker
FOV	field of view
FSS	fine Sun sensor
GOALS	Geometric Optical Analysis of Lens Systems
GOES	Geostationary Operational Environmental Satellite
GSC	General Software Corporation
GSFC	Goddard Space Flight Center
HCMM	Heat Capacity Mapping Mission
HRDB	Horizon Radiance Data Base
HRMU	Horizon Radiance Modeling Utility
IPAT	Inverted Profile Archival Tape
IPD	Information Processing Division

IR	infrared
IRU	inertial reference unit
JCL	job control language
LASP	University of Colorado Laboratory for Atmospheric and Space Physics
LIMS	Limb Infrared Monitor of the Stratosphere
LMSC	Lockheed Missiles and Spacecraft Company
LOS	loss of signal
LRC	Langley Research Center
LRIR	Limb Radiance Inversion Radiometer
LTE	local thermodynamic equilibrium
MIT	Massachusetts Institute of Technology
MMS	Multimission Modular Spacecraft
NASA	National Aeronautics and Space Administration
NCAR	National Center for Atmospheric Research, Boulder, Colorado
NCC	National Climatic Center, Asheville, North Carolina
NMC	National Meteorological Center
NOAA	National Oceanic and Atmospheric Administration
NSSDC	National Space Science Data Center
OBC	onboard computer
OGO	Orbiting Geophysical Observatory
OID	optical intensity distribution
PWI	Plasma Wave Instrument
RAOBS	radiosonde observations
RCS	reaction control system
rpm	revolution per minute
rpo	revolution per orbit
SAGE	Stratospheric Aerosol Gas Experiment
SAS	Small Astronomy Satellite
SME	Solar Mesosphere Explorer
SMS	Synchronous Meteorological Satellite
STP	standard temperature and pressure
SWA	Scanwheel assembly
TDRS	Tracking and Data Relay Satellite

TIROS	Television Infrared Observation Satellite
USGS	U.S. Geological Survey
UT	universal time
VIRGS	VISSR Image Registration and Gridding System
VISSR	visible and IR spin scan radiometer
WHS	wheel-mounted IR horizon sensor

REFERENCES

1. National Aeronautics and Space Administration, NASA SP-8033, Spacecraft Earth Horizon Sensors, December 1969

2. --, NASA CR-724, The Synthesis of 15-μm Infrared Horizon Radiance Profiles From Meteorological Data Input, J. C. Bates et al., 1967

3. --, NASA CR-725, The Analysis of 15-μm Infrared Horizon Radiance Profile Variations Over a Range of Meteorological, Geographical, and Seasonal Conditions, J. R. Thomas et al., April 1967

4. --, NASA TN-D-4741, Infrared Horizon Profiles for Summer Conditions From Project Scanner, T. B. McKee, R. I. Whitman, and R. E. Davis, August 1968

5. --, NASA TN-D-4905, Infrared Horizon Profiles for Winter Conditions From Project Scanner, R. I. Whitman, T. B. McKee, and R. E. Davis, December 1968

6. J. A. Dodgen and H. J. Curfman, Jr., "Accuracy of IR Horizon Sensors as Affected by Atmospheric Considerations," Proceedings of the Symposium on Spacecraft Attitude Determination, September-October 1968, SAMSO-TR-69-417, vol. 1, pp. 161-168, December 1969

7. Computer Sciences Corporation, CSC/TM-76/6229, Modeling of the Earth's 15-Micrometer CO_2 Horizon Radiance Profile, J. E. Richey, November 1976

8. Lockheed Missiles and Space Company, GCS/3979/6211, Atmospheric Radiance Profiles for the ITHACO Horizon Sensor, P. L. Keithley and W. G. Uplinger, April 1977

9. Computer Sciences Corporation, CSC/TM-77/6064, Infrared Horizon Scanner Attitude Data Error Analysis for Seasat-A, M. C. Phenneger, C. Manders, and C. B. Spence Jr., July 1977

10. Air Force Geophysics Laboratory, Report AFGL-TR-80-0067, Atmospheric Transmittance/Radiance: Computer Code LOWTRAN 5, F. X. Kneizys, E. P. Shuttle, et al., February 1980

11. Computer Sciences Corporation, CSC/TM-77/6133, A Comparison of Radiosonde Temperature and Humidity Profile Data Bases, R. A. Nieman, August 1977

12. --, CSC/TM-83/6177, Evaluation of the Horizon Radiance Data Base (HRDB), M. C. Phenneger and S. P. Singhal, November 1983

13. University of Colorado, Laboratory for Atmospheric and Space Physics, Final Report for Contract NAS 5-27359. Studies of the Solar Mesosphere Explorer: Dynamics and Horizon Sensor Performance, G. M. Lawrence and J. R. Cowley, Jr., December 1983

13a. General Software Corporation, GSC-TR8401, Landsat-4 Horizon Scanner Performance Evaluation, S. Bilanow et al., January 1984

14. Computer Sciences Corporation, CSC/TR-78/6007, Seasat-A Attitude Analysis and Support Plan, W. T. Nutt, M. C. Phenneger, et al., April 1978; also NASA X-581-78-9

15. Lockheed Missiles and Space Company, GCS/4001/6211, Effect of Clouds on Seasat-A Horizon Sensor, P. L. Keithley and W. G. Uplinger, July 1977

16. National Aeronautics and Space Administration, NASA CR-1858, Atmospheric Effects on Infrared Multispectral Sensing of Sea-Surface Temperature From Space, P. Anding, R. Kauth, and R. Turner, 1971

17. Computer Sciences Corporation, CSC/TM-81/6038, Infrared Horizon Radiance Data Base Feasibility Study, N. Gupta, March 1981

18. --, CSC/TM-82/6118, Horizon Radiance Data Base: Generation and Data Description, S. P. Singhal, July 1982

19. --, CSC/TM-77/6138, User's Guide to RAOBS Climatology Programs, R. A. Nieman, 1977

20. National Aeronautics and Space Administration, Goddard Space Flight Center, "The Limb Radiance Inversion Radiometer (LRIR) Experiment" (Section 7), The Nimbus-6 User's Guide, J. Gille et al., February 1975

21. --, "The Limb Infrared Monitor of the Stratosphere (LIMS) Experiment" (Section 4), The Nimbus-7 User's Guide, J. Russell and J. Gille, August 1978

22. National Center for Atmospheric Research (Boulder, Colorado), User's Guide for the Limb Radiance Inversion Radiometer (LRIR) Data Set, J. Gille et al., February 1984

23. --, NG-67, Nimbus Observation Processing System (NOPS) Requirements Document, Tape Specification T564111, LIMS Profile-R Tape, R. Stephenson, May 1978

24. Computer Sciences Corporation, CSC/SD-78/6032, Horizon Radiance Modeling Utility System Description and User's Guide (Preliminary), W. Nutt and M. C. Phenneger, March 1978

25. --, CSC/SD-84/6007, Earth Radiation Budget Satellite (ERBS) Horizon Radiance Modeling Utility (HRMU) User's Guide and System Description, E. J. Burgess, June 1984

26. Scientific Calculations, Inc., GOALS (Geometric Optical Analysis of Lens Systems), 1967

27. Computer Sciences Corporation, CSC/SD-81/6017, User's Guide for the GOALS (Geometric Optical Analysis of Lens Systems) Program as Enhanced and Modified for the VAX-11/780 Computer, J. Bowser, March 1981

28. Computer Sciences Corporation, CSC/SD-82/6013, Earth Radiation Budget Satellite (ERBS) Attitude Ground Support System (AGSS) Functional Specifications and Requirements, G. Nair et al., September 1982

29. --, Informational Memorandum, "Horizon Radiance Modeling Utility (HRMU) Analysis Study," M. C. Phenneger and T. H. Lee, January 1984

30. --, CSC 3000-37600-01TM, Star Camera Support System Requirements Updates to Small Astronomy Satellite-C (SAS-C) Attitude Support System Specifications and Requirements, L. Fallon, B. Gambhir, and M. Rubinson, March 1976

31. --, CSC/TR-76/6012, Evaluation of the Small Astronomy Satellite (SAS-3) Scanwheel Attitude Determination Performance, S. G. Hotovy, M. G. Grell, and G. M. Lerner, July 1976

32. --, CSC/TR-79/6008, Seasat-1 Postlaunch Attitude Analysis, G. F. Manders, M. C. Phenneger, S. Bilanow, and K. W. Chan, June 1979

33. --, CSC/TM-82/6120, Feasibility of Autonomous Attitude Determination for the Cosmic Background Explorer (COBE), K. R. Hall et al., September 1982

34. --, CSC/TM-79/6223, Applications Explorer Missions-2/ Stratospheric Aerosol and Gas Experiment (AEM-2/SAGE) Postlaunch Report, D. P. Niebur, September 1979

35. --, CSC/TM-79/6187, AEM-2/SAGE Instantaneous Body Rate Analysis, D. P. Niebur and D. G. Trahan, August 1979

36. --, CSC/TM-79/6073, AEM-B/SAGE Attitude Analysis, C. B. Spence, March 1979

37. --, CSC/SD-78/6065, AEM-B/SAGE Attitude System Functional Specifications and Requirements, D. P. Niebur, July 1978

38. --, CSC/TM-81/6043, Magsat Infrared Horizon Scanner Data Evaluation Report, S. Bilanow, March 1981

39. --, CSC/TM-81/6036, High-Precision Attitude Determination for Magsat, F. Vanlandingham et al., March 1981

40. Johns Hopkins Applied Physics Laboratory, S4A-3-059, Component Transfer Functions of the Various Pitch Control Loops of Magsat, Memorandum from K. J. Hefferman to G. H. Fountain

41. Computer Sciences Corporation, CSC/TR-81/6003, Dynamics Explorer Attitude Analysis and Support Plan, C. Sturch et al., May 1981

42. --, CSC/SD-80/6096, DE-B Horizon Radiance Modeling Utility (HRMU) System Description and User's Guide (Preliminary), R. Shendock, 1980

43. --, CSC/TM-81/6264, Azimuth Angle Computation for the Dynamics Explorer-2 Spacecraft, M. Phenneger, December 1981

44. RCA Corporation, RCA Note No. 2.2.4-10, ESASIM and ESBSIM, The Computer Simulation for the DE-A and DE-B Earth Sensors, J. B. Antley and W. V. Fuldner, February 1980

44a. --, RCA Note No. DN-521-5.7.2 (AE), The Effects of a Heated Probe in the Horizon Sensor Field of View, G. Schmidt, Jr., December 1971

45. Computer Sciences Corporation, CSC/TM-84/6071, Earth Radiation Budget Satellite (ERBS) Attitude Analysis and Support Plan, M. Phenneger, J. Rowe, et al., August 1984

46. ITHACO, Inc., Engineering Report 92319, Revision B, ERBS Horizon Sensor Error Analysis Final Report, April 26, 1984

47. Computer Sciences Corporation, CSC/3000-25800-03TN, Bolometer Model Tests for AE-C, M. G. Grell, December 1974

48. --, CSC/TR-75/6018, Atmosphere Explorer-D and -E Attitude Determination and Control Prelaunch Report Analysis and Operational Plan, M. C. Phenneger et al., October 1975

49. --, CSC/TM-75/6004, Horizon Sensor Behavior of the Atmosphere Explorer-C Spacecraft, J. R. Wertz et al., May 1975

50. --, CSC/TM-82/6155, Study of DE-1, GOES-5, and TIROS-N Fixed-Body Horizon Sensors, Y. R. Kwon, September 1982

51. --, CSC/TM-81/6130, Flight Dynamics Postlaunch Report for the Geostationary Operational Environmental Satellite-5 (GOES-5), J. A. Erickson, D. R. Brown, and D. B. Woodside, June 1981

52. --, CSC/TM-81/6149, Geostationary Operational Environmental Satellite-5 (GOES-5) Attitude Postlaunch Report, H. L. Hallock et al., July 1981

53. OAO Corporation, Dynamics Explorer-A and -B Attitude System Functional Specifications and Requirements, December 1979

54. RCA Astro-Electronics, Document No. AE R-4355, Dynamics Explorer Spacecraft System Baseline Definition, October 1980

55. Computer Sciences Corporation, Memorandum, "The Dynamics Explorer-1 (DE-1) Azimuth Determination Procedure With Descriptions of Flight Data and Azimuth Rate Anomalies, M. C. Phenneger, January 1982

56. RCA Corporation, Design Note No. 3.3.2-034-DN, DE Earth Sensor Analysis - Supplement 1, T. J. Furia and J. Antley, October 1980

57. K. D. Stewart et al., "Attitude Control of the SME Satellite--A Flight Experience," AAS Annual Rocky Mountain Guidance and Control Conference, Paper 82-046, Keystone, Colorado, February 3, 1982

58. J. R. Cowley, Jr., and G. M. Lawrence, "Earth Limb Altitude Determination for Solar Mesosphere Explorer," AIAA 21st Aerospace Sciences Meeting, paper AIAA-83-0429, Reno, Nevada, January 10-13, 1983

59. G. M. Lawrence and J. R. Cowley, Jr., "A Presentation of SME Horizon Sensor Analysis at GSFC," September 29, 1983

60. G. M. Lawrence and J. R. Cowley, Jr., "Spin Dynamics and Horizon Sensor Performance for the Solar Mesosphere Explorer," AIAA/AAS Astrodynamics Conference, paper AIAA-84-2022, Seattle, Washington, August 20-22, 1984

61. General Electric Space Division, Landsat-D Jitter Review, May 1980

62. ITHACO, Inc., IPS 0006, Conical Earth Sensor, July 1979

63. K. A. Ward, "Modeling of the Atmosphere for Analysis of Horizon Sensor Performance," Proceedings of the International Society for Optical Engineers, vol. 327, pp. 79-88, January 1982

64. K. A. Ward, R. Hogan, and J. Andary, "Horizon Sensor Errors Calculated by Computer Models Compared With Errors Measured in Orbit," Proceedings of the International Society for Optical Engineers, vol. 327, pp. 67-78, January 1982

65. National Aeronautics and Space Administration, Goddard Space Flight Center, NASA X-480-79-14, TIROS-N Attitude Determination and Control System (ADACS), J. Andary and C. Dunker, April 1979

66. RCA Astro-Electronics, TIROS-N System Design Report Volume 2, May 1976

67. Lockheed Missiles and Space Company, LMSC-677318, Earth Limb Radiance Profiles for the 15-Micron Carbon Dioxide Absorption Band, J. W. Burn, W. G. Uplinger, and P. P. Morris, March 1967

BIBLIOGRAPHIC DATA SHEET

1. Report No.	2. Government Accession No.	3. Recipient's Catalog No.
NASA TM-86181		

4. Title and Subtitle	5. Report Date
INFRARED HORIZON SENSOR MODELING FOR ATTITUDE DETERMINATION AND CONTROL: ANALYSIS AND MISSION EXPERIENCE	March 1985
	6. Performing Organization Code 554
7. Author(s)	8. Performing Organization Report No.
M. C. Phenneger, S. P. Singhal, T. H. Lee, and T. H. Stengle	85B0147
9. Performing Organization Name and Address	10. Work Unit No.
Flight Dynamics Division/Code 554 NASA/Goddard Space Flight Center Greenbelt, Maryland 20771	11. Contract or Grant No.
	13. Type of Report and Period Covered
12. Sponsoring Agency Name and Address	
National Aeronautics and Space Administration Washington, D.C. 20036	14. Sponsoring Agency Code

15. Supplementary Notes

M. C. Phenneger, S. P. Singhal, and T. H. Lee: Computer Sciences Corporation, Silver Spring, Maryland.
T. H. Stengle: Goddard Space Flight Center, Greenbelt, Maryland.

16. Abstract

The work performed by the Attitude Determination and Control Section at the National Aeronautics and Space Administration/Goddard Space Flight Center in analyzing and evaluating the performance of infrared horizon sensors is presented. The results of studies performed during the 1960s are reviewed, several models for generating the Earth's infrared radiance profiles are presented; and the Horizon Radiance Modeling Utility, the software used to model the horizon sensor optics and electronics processing to compute radiance-dependent attitude errors, is briefly discussed. Also provided is mission experience from 12 spaceflight missions spanning the period from 1973 to 1984 and using a variety of horizon sensing hardware Recommendations are presented for future directions for the infrared horizon sensing technology.

17. Key Words (Selected by Author(s))	18. Distribution Statement
Horizon sensors, Infrared sensors (spacecraft), Attitude control, Attitude determination	Unclassified - Unlimited Subject Category 19

19. Security Classif. (of this report)	20. Security Classif. (of this page)	21. No. of Pages	22. Price
Unclassified	Unclassified	482	A21

For sale by the National Technical Information Service, Springfield, Virginia 22161.

GSFC 25-44 (10/77)

☆U S GOVERNMENT PRINTING OFFICE 1985 -537 -086/ 48 REGION NO 4

End of Document